The Dissertation Committee for Wing Shun Kwan Certifies that this is the approved version of the following dissertation:

Laboratory Investigation into Evaluation of Sand Liquefaction under Transient Loadings

Committee:

Chadi S. El Mohtar, Supervisor

Steven L. Kramer

Ellen M. Rathje

Brady R. Cox

Loukas F. Kallivokas

Laboratory Investigation into Evaluation of Sand Liquefaction under Transient Loadings

by

Wing Shun Kwan, B.S.; M.S.C.E.

Dissertation

Presented to the Faculty of the Graduate School of

The University of Texas at Austin

in Partial Fulfillment

of the Requirements

for the Degree of

Doctor of Philosophy

The University of Texas at Austin

December 2015

Dedication

To my family for their limitless

support and encouragement

Acknowledgements

My college education has been a very challenging and life-changing process. I found that it is a true blessing to have the opportunity of working with people who define the state of the art in the field. I owe a great debt of gratitude to all my teachers and mentors, for their instructions and advices.

I would like to offer my special thanks to my doctoral advisor, Dr. Chadi El Mohtar, for continuous supports in the past four years. I would also like to express my sincere gratitude to Dr. Steven Kramer at the University of Washington for his financial support, advice, and reviews for this research. This project could not have been completed without his valuable insight and support. My heartfelt appreciation also goes out to Dr. Ellen Rathje, Dr. Brady Cox, and Dr. Loukas Kallivocas, for their time and effort to serve on my dissertation committee. Their guidance has greatly contributed to this research project.

My journey was wonderfully enriched by other colleagues. I am indebted to Mr. Federico Castro, the geotechnical laboratory manager at UT Austin, who provided much assistance with testing. Special gratitude is also extended to Dr. Jisuk Yoon, who shared the office and many insightful research ideas during my first year in Austin. I also want to thank my other colleagues, especially the undergraduate researchers (Mr. Christian Hogan, Ms. Patricia Bennett, Ms. Molly Coffman, and Mr. Aqshems Nichols), who had made my time in the laboratory much more enjoyable.

The author gratefully acknowledges the direct and indirect financial support of this study by the National Science Foundation, George E. Brown, Jr. Network for Earthquake Engineering Simulation Research program, under Grant No. 0936408, and the Civil, Architectural and Environmental Engineering Department of the University of Texas at Austin.

Lastly, I want to acknowledge my spiritual home, the Hyde Park Chinese Baptist Church at Austin, for the friendships and prayers. I am truly thankful to my parents (Miu Lan Leung, and Yuk Kuen Kwan), my wife (Yu Yuk Ng), and son (Paul Kwan), for their

endless support. My wife has made a lot of sacrifices so that I could do my best on the academic path I have chosen. Her encouragement has always reminded me what's truly important in life, and turned my fears of failure into aspiration for accomplishments. Last but not least, endless praise and thanksgiving go to my God.

Laboratory Investigation into Evaluation of Sand Liquefaction under Transient Loadings

Wing Shun Kwan, Ph.D.

The University of Texas at Austin, 2015

Supervisor: Chadi S. El Mohtar

The current laboratory procedures for evaluating liquefaction potential are still the same as 40 years ago, with minor updates. The complex seismic loading motions are simplified to a series of uniform harmonic sinusoidal loading cycles with amplitudes related to the maximum amplitude of a given ground motion; liquefaction resistance is then evaluated as the load generating liquefaction in a predefined number of harmonic loading cycles. The simplified methods of loading and resistance characterizations are a crude proxy and provide limited information in predicting the time of liquefaction triggering and therefore, the expected effects/damage of seismic events. Specific details of the time of soil liquefaction within a ground motion can be better understood from laboratory testing. Among the available element-level types of cyclic testing, cyclic simple shear (CSS) tests are the most popular and commonly used. The CSS tests provide a satisfactory simulation of seismic induced in-situ stresses.

A testing program consisting of a series of multi-stage undrained direct simple shear tests was performed using the hydraulically-actuated GCTS cyclic simple shear apparatus. The apparatus had been modified and upgraded so that it is capable of applying user-specified, transient loading histories to Nevada Sand soil samples. Reconstituted specimens were prepared by the wet pluviation method at two different densities, 40% and

70%, followed with back-pressure saturation and K_0 consolidation. The shearing phase was conducted in three distinctive stages: (1) Scaled transient stress histories, (2) modulated sinusoid with a taper-up shape stress histories, (3) static monotonic loads. All shearing stages were performed under continuous undrained conditions.

This research program had two major motivations. The first motivation is to provide element-level tests subjected to transient loadings, so that the soil responses of excess pore pressure generation and shear strain along the time domain can be measured. The transient loading was selected from a suite of ground motions with different spectral and temporal characteristics to cover a wide range of possible ground motions. The second motivation is to investigate the performances of four Intensity Measures (IMs): CAV_5, Arias Intensity, Normalized Energy Demand and PGA magnitude. These IMs were proven to be more efficient predictors of soil responses than peak acceleration. The experiments provide a database that can systematically illustrate the response of liquefiable materials subjected to transient ground motions before and after liquefaction; such a database was virtually non-existent prior to this study. Therefore, the data generated in this study supports the development of improved and more informative procedures for the evaluation of liquefaction potential, the effects of liquefaction, post-liquefaction responses, and more accurate constitutive models for liquefiable soils.

Table of Contents

List of Tables

List of Figures

CHAPTER 1: INTRODUCTION

1.1 BACKGROUND

Soil liquefaction is a major urban seismic risk and its effects on the built environment have been proven to be extremely devastating. Earth embankments may lose stability; bridges may lose support from their pile foundations; underground utility lines may break because of the differential settlement; sloping ground may slide on liquefied layers, and buildings may suffer a 'punching shear' type of foundation failure. Those catastrophic losses by soil liquefaction were well observed and documented in almost all of the major earthquakes in the past half-century: 1964 Alaska, USA; 2015 Gorkha, Nepal; 2014 Iquique, Chile; 2011 Christchurch, New Zealand (Figure 1.1).

Modern study of soil liquefaction began after the Niigata and Alaska earthquakes in 1964, and the basic procedure used today are the same as the one developed by Seed and Idriss (1971), by comparing some measures of seismic loading and soil resistance. While major refinements have been made in the characterization of soil resistance, the loading side, a transient earthquake motion, is still commonly represented by a single point, the peak ground acceleration (PGA) plus a rough approximation for magnitude and duration of the ground motion. Physical modeling, both in research and practice, utilizes equivalent harmonic sinusoidal loading with constant amplitudes and different number of loading cycles to mimic the seismic loading. In general, this method works well in deterministic analysis when only a single worst case scenario is considered. Due to the emerging demands of performance-based earthquake engineering (PBEE), more accurate and informative approaches of earthquake loading characterization are desired in order to reduce the epistemic uncertainty under the probabilistic frameworks. Recent numerical

studies have proven that evolutionary intensive measures (IMs) perform better than PGA (Kramer and Mitchell 2006; Abegg 2010). Coupled with the advancement in geotechnical testing equipment that is no longer constrained to applying simple harmonic loading, there is a need and opportunity for establishing the first experimental program that focuses on the characterization of earthquake loading instead of liquefaction resistance. As such, the loading conditions should extend to realistic, transient loading histories.

Earthquake motions can have very different time-domain characteristics. Some display one dominant pulse at a given point of the loading, whereas others contain many pulses with similar amplitudes. Using a single point to represent a ground motion is too coarse (Figure 1.2). A few evolutionary intensity measures, such as Arias intensity (Kayen and Mitchell 1997), CAV_5 (Kramer and Mitchell 2006), and normalized energy demand (Green 2001), have been proposed for possible better characterization of earthquake loading for liquefaction evaluation. These IMs are typically calculated by integrating a function of acceleration or energy over time and only require one parameter to represent ground motion, as opposed to two parameters (PGA and MSF) in the current stress-abased procedures. Therefore, those IMs provide a possible correlation with the cumulative damages, pore pressure generation (r_u) and shear strain (γ), and more importantly, potentially lead to the identification of liquefaction initiation timing.

Soil properties change drastically upon the triggering of liquefaction, transforming a soil deposit from solid state to a liquid one. The stiffness of the overall soil deposit decreases rapidly upon liquefaction triggering, and therefore, the ground response changes from one that can withstand high forces to one that impose large deformations to structures. The damages induced by liquefaction to structures predominately occur after liquefaction initiation. Obviously, if the remaining motion is short and frail, the expected damage would be minimal. On the other hand, when the remaining motion is long and with excessive

significant ground shaking, the expected damage will be catastrophic. For that reason, significant improvement can be made in evaluating the hazard if the timing of liquefaction initiation can be reasonably predicted and brought into the procedure. Knowing the timing of liquefaction can allow dividing design ground motions into pre- and post- triggering components, which would lead to better prediction of the hazard effects.

In order to accurately predict the initiation timing and effects of liquefaction, an optimum ground motion intensity measures need to be identified through experimental methods. Element testing in the laboratory showing the soil responses under transient loading is ideal for this investigation, because the testing allows the researchers to identify the timing of liquefaction triggering under many different transient loading histories. The resulting data can then be used to investigate the optimum intensity measures for predicting pre- and post-liquefaction response. This approach explores the use of timing information to improve the accuracy of predictions of the effects of liquefaction (e.g. lateral spreading).

Figure 1.1. Liquefaction damages in built environments. (a) 2014 Chile earthquake (M_w = 8.8). Collapsed and shifted spans at Raqui 2 Bridge due to liquefaction. (b) 1999 Kocaeli earthquake (M_w = 7.4). Liquefaction-induced bearing capacity failure. (c) 1964 Alaska earthquake (M_w = 9.2). Liquefaction induced landslide at Prince William. (d) 2007 Peru earthquake (M_w = 8.0). Liquefaction and lateral spreading of the marine terrace induced failure of the Pan American highway embankment fill

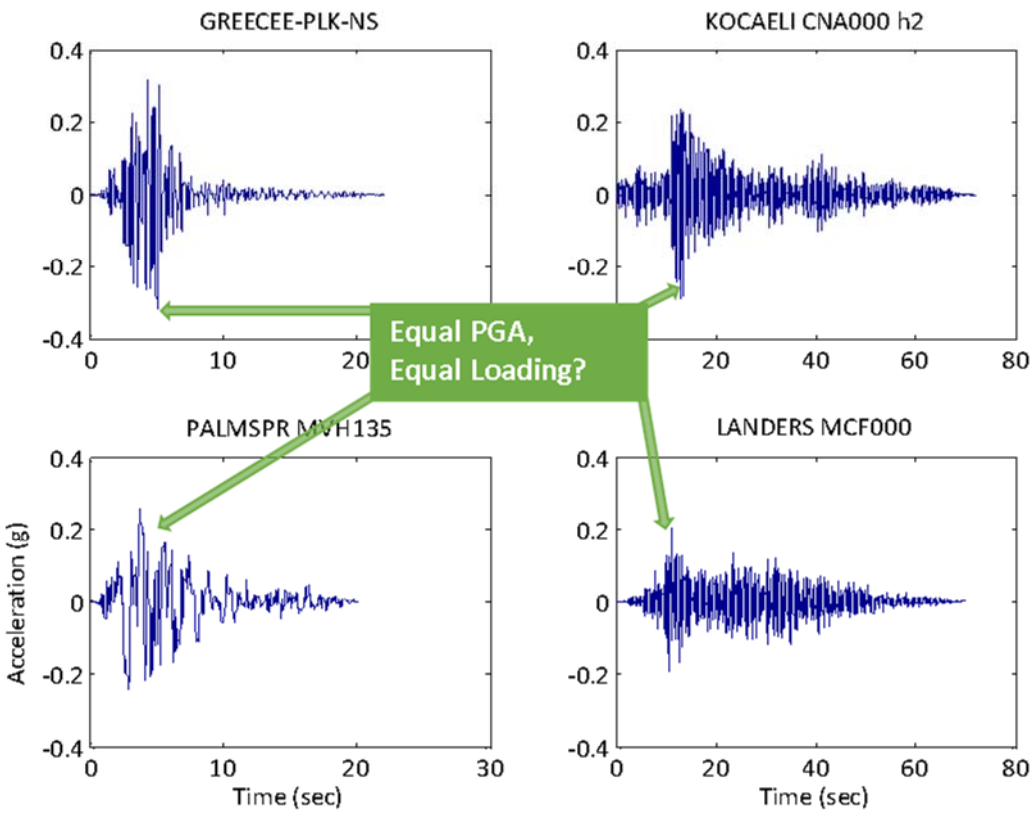

Figure 1.2. Four different ground motions scaled to the same PGA.

1.2 RESEARCH OBJECTIVES

With the increasing demand of practicing performance-based earthquake engineering, PEBB (Figure 1.3), the state of liquefaction hazard evaluation can and should be advanced. The PBEE framework requires probabilistic characterization of both earthquake loading and soil resistance to liquefaction, which can be significantly improved by reducing uncertainty in those characterizations (or predictions). A framework or model with low uncertainty (or high accuracy) yields a higher factor of safety against the soil liquefaction for a given hazard level. Therefore, this dissertation documents a research

project that reduces uncertainty in characterizing earthquake loading, which gives rise to more efficient and economic seismic designs, thereby increasing public safety.

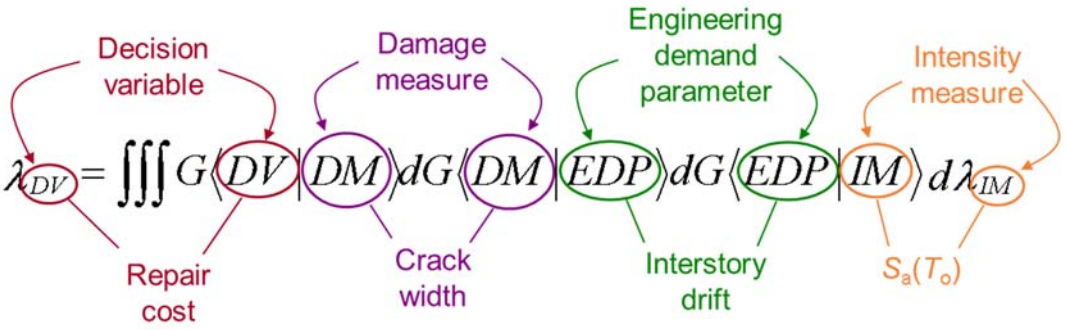

Figure 1.3. Framework for the Performance-based Earthquake Engineering (Kramer and Mitchell 2006).

While the past research efforts have been focused on the characterization of soil resistance to liquefaction, little attention has been given to the characterization of earthquake loadings in the past half-century. The most popular method is still the one suggested by Seed and Idriss (1971), which represents a complex and transient ground motion by a single point- its maximum value, and a coarse approximation of earthquake duration. The method suppressed the spectral and temporal characteristics of ground motions; therefore, the current practice contains significant uncertainty that can be reduced by using proper intensity measures.

The time dimension has been overlooked in the existing liquefaction hazard evaluation procedures. Not only is an earthquake-intensity accumulated with time, the response of a structure sitting on liquefied soils will be highly influenced by the remaining intensity of seismic loading after the liquefaction initiation. Consequently, effective

prediction on the timing of liquefaction triggering can be very helpful for the next generation framework of liquefaction evaluation in the future.

Experimental studies on the topic of soil liquefaction have never ceased in the past half-century. From testing program of cyclic triaxial (Seed and Lee 1966; Castro 1969) in the early days to bi-directional cyclic simple shear in the recent studies (Kammerer 2002; Rutherford 2012), numerous research projects have been conducted to investigate the soil resistance to liquefaction under different soil types or loading conditions. Nevertheless, a very limited number of previous experimental studies looked into the issue of earthquake loading characterization. For this reason, most experimental investigations of liquefaction resistance were performed on soil specimens subjected to uniform harmonic loading. This research project aims to experimentally look into the potential improvements of earthquake loading characterization. Therefore, a database and analyzes of cyclic simple shear tests that systematically illustrates the responses of liquefiable soils to very distinctive spectral and temporal characteristics of transient ground motions is generated and performed. The input motions were scaled in a way that the test specimens were loaded to trigger liquefaction at the later part of ground motions. This kind of systematical data is virtually non-existent before this project, including laboratory, field and large-scale centrifuge testing. The data supports the development of the next generation liquefaction evaluation procedure in three ways: (1) to gain insight into soil responses (development of excess pore pressure and shear strain) under transient loading, (2) to investigate the effects of post-liquefaction loadings, and (3) to improve the development of constitutive models for liquefiable soils.

To summarize, this study is motivated by the following objectives:

1. To optimize the performance of a Cyclic Simple Shear apparatus.

2. To establish reconstitution procedures for sand specimen, at both loose and dense states.
3. To identify the optimum IMs that can provide the best estimates of liquefaction potential, so as to improve the accuracy of earthquake loading characterization.
4. To identify the optimum IMs that can provide the best prediction of liquefaction effects, in order to reduce the uncertainty in earthquake damage predictions.
5. To provide valuable data for constitutive model calibrations.

1.3 ORGANIZATION OF DISSERTATION

This dissertation consists of eight chapters. Succeeding from the first chapter's introduction, chapter two launches a review of research in soil liquefaction, which contains enormous research efforts in the past half-century. Chapter two mainly focuses on reviewing the literature of sand behavior under monotonic and cyclic loading, which complements the understanding of the simple shear test results, and liquefaction hazard evaluation procedures. Chapter three starts with the review of different types of cyclic element testing: simple shear, triaxial, and torsional shear; followed by presentations of the project-specified testing apparatus and procedures.

Chapter four summarizes different kinds of preliminary testing and results, including direct simple shear tests, triaxial tests, and preliminary cyclic simple shear tests, which are very important for calibrating and optimizing the performance of the project-specified testing apparatus, and finalizing the specimen reconstitution procedures. Chapter four also introduces a new design of the UT cyclic simple shear apparatus. Chapter five summarizes the simple shear testing results that are categorized by different types of loading: 1) harmonic, 2) modulated sinusoid, 3) transient, and 4) stage two taper up,

Chapter six focuses on the pre-liquefaction motion (up to liquefaction initiation), establishing and analyzing the experimental data from the cyclic simple shear tests subjected to transient loadings, to identify the optimum evolutionary intensity measure for predicting liquefaction initiation. The intensity measures are evaluated based on two criteria, the matching and/or correlating with the excess pore pressure generation and shear strain development.

Chapter seven discusses and analyzes the post liquefaction response based on the portion of CSS data recorded after the liquefaction initiation. Preliminary data of post-liquefaction monotonic response is also included. The goal is to identify an intensity measure that best matches and/or correlates with the recorded cumulative post-liquefaction shear strain.

To conclude the dissertation, chapter eight gives a summary of the major findings in this study, and suggests future research areas. The dissertation ends with appendices that encompass all of the test results, and detailed procedures of loose and dense specimen reconstitution. The plots are color coded, each containing subplots of stress-time, r_u-time, strain-time, stress-strain, and stress path. The organization of the test results in the appendices is fully explained in chapter five.

Chapter 2: Literature Review and Background

2.1 INTRODUCTION

The term "liquefied" was perhaps first introduced and documented by Hazen (1920) and usually used interchangeably with another term, "quicksand" (Hazen 1920 and Terzaghi 1947). In the early days, liquefaction was used to introduce the catastrophic failure of saturated earthworks, particularly in earth dams constructed using the hydraulic method of dam construction. The phenomenon of liquefaction induced by static loading has drawn wide attention after the classic work by Casagrande (1936) and the case history of Fort Peck Dam slide in 1938, which involved about 7.5 million m^3 of soil and cost eight lives. Even though there was a debate among the review board that the Fort Peck Dam slide was mainly due to shear failure of the shale foundation, the effect of static liquefaction was well recognized. The 1938 case history has been a humbling experience of the possible consequences of soil liquefaction; therefore, compacting sand fills in dam has become a practice after this tragedy.

A physical sand model subjected to dynamic loading to simulate earthquake loading resulting in "liquefaction" was first documented by Mogami and Kubo (1953). Liquefaction induced by seismic loading was then greatly recognized after the devastating earthquakes in Anchorage, Alaska and Niigata, Japan in 1964. Numerous research was conducted on the topic over the half century since the 1964 earthquakes. Notably, Professor Harry Bolton Seed and his colleagues at UC Berkeley provided tremendous literature in the field during the period of 1960s to 1980s. Today, "soil liquefaction engineering" is a semi-mature field, and practitioners can design in these extremely complicated conditions with a level of confidence.

2.2 LIQUEFACTION TERMINOLOGY

Although the term liquefaction has already been introduced for almost a century, there is still no consensus on a clear definition in the geotechnical engineering community. In fact, the mechanism of liquefaction is a very complicated subject, rendering it more or less a piece of art instead of science, which echoes the vision of Professor Terzaghi:

*"Soil Mechanics arrived at the borderline between science and art. I use the term "art" to indicate mental processes leading to satisfactory results without the assistance of step-for-step logical reasoning…To acquire competence in the field of earthwork engineering one must live with the soil. One must love it and observe its performance not only in the laboratory but also in the field, to become familiar with those of its manifold properties that are not disclosed by boring records…"*at the 4th International Congress on Soil Mechanics, England , 1957 (Goodman 1999).

The "art" part has generated various definitions of liquefaction, which confuses the geotechnical engineering community. In the early days, the effect of liquefaction was usually observed in the failure of earthwork site and relate to the knowledge of the seepage pressure. The earlier definitions were very broad and without any quantitative criteria, as in the following examples:

- "*The sudden decrease of the shearing resistance of a quicksand from its normal value to almost zero without the aid of a seepage pressure*" (Terzaghi 1947)
- *Soil deformation caused by monotonic, transient, or repeated disturbance of saturated cohesionless soil under undrained conditions* (Mogami and Kubo 1953)
- *Liquefaction of saturated sand is caused by a substantial reduction in its shear strength which, in turn, is caused by the development of high pore pressure induced by monotonically or cyclically applied strains* (Castro 1969).

- *"The act or process of transforming any substance into a liquid"* (Committee on Soil Dynamics of the Geotechnical Engineering Division 1978).
- *Liquefaction is defined as the transformation of a granular material from a solid to a liquefied state as a consequence of increased pore-water pressure and reduced effective stress* (Marcuson 1978).

Up to the present time, the geotechnical engineering community generally defines liquefaction as a phenomenon in which the strength and stiffness of a soil are reduced by earthquake or other rapid loading, and it is accompanied by the generation of excess pore pressures and large induced deformations (laterally and vertically). Liquefaction is not only limited to cohesionless sand, but can also occur in soils with fines and/or gravels. The scope of this dissertation is limited to the behavior of clean sand.

There are two major failure phenomena or mechanisms in liquefaction: (1) flow-type failure and (2) cyclic mobility. The flow-type liquefaction occurs when the strength of the soil is reduced below the stress required to maintain equilibrium (i.e. shear stress is greater than residual strength at the liquefied state), and can be triggered by monotonic or cyclic loading. When this phenomenon arises, the static shear load will continue to cause the soil mass to deform to a very large range. Flow liquefaction can occur before the effective confining stress is reduced to zero, and the consequence can be catastrophic. This mechanism is usually found in saturated loose sand.

Cyclic mobility is a phenomenon in which the shear strength of soil is progressively reduced by the excess pore pressures generated during cyclic loading. Unlike flow liquefaction, the shear stress causing cyclic mobility is less than the residual strength of the liquefied sand. This mechanism can occur in loose and dense sands. The deformations

resulting from cyclic mobility are lower than those experienced during flow failures. The two liquefaction mechanisms are further discussed in Section 2.3.

2.2.1 Liquefaction Triggering Criteria

Numerous effort has been invested in improving the problem of inconsistent definitions, but the problem could not be resolved unless the phenomenon can be quantified. In order to define the onset of liquefaction, the excess pore water pressure ration (r_u, ratio of excess pore pressure to initial effective stress prior to loading) equal to 1.0 criteria is very promising and theoretically sound. When the generated pore pressure is equal to the effective confining stress, the shear strength of the sand becomes zero and liquefaction occurs. However, this criterion is not universal adapted as researchers reported that r_u of 1 is not always achievable and liquefaction could occur at lower values of r_u. Ishihara (1993) suggested that the r_u value in silty sands or sandy silts may level out at around 90 to 95 percent. Wu et al. (2004) reported that a pore pressure ratio $r_u = 1.0$ might not be achievable in many situations, such as in dense clean sand and/or in sloping ground. Moreover, the pore pressure-based criterion does not capture the failure mechanism of the liquefiable soil; with the same situation of $r_u = 1.0$, excessive (flow-type) deformation could occur in a loose sand sample, while limited (cyclic mobility) deformation is more likely for a dense sand sample.

An alternative to the pore pressure-based criterion is the strain-based criterion, which provides better information on the seismic performance. The cyclic strain approach has more fundamental connotations than the cyclic stress approach (Dobry and Ladd 1980). Ladd et al. (1989) presented a testing program with a cyclic-strain approach, and concluded that there is a threshold cyclic shear strain (of 10^{-2} % approximately) below which pore

pressure would not buildup. Ladd et al. (1989) reported that this threshold is independent of relative density and confining pressure but is dependent on the overconsolidation ratio (OCR).

The strain-based criterion for the initiation of liquefaction has gained popularity in the recent studies. Laboratory based research used either cyclic triaxial or cyclic simple shear testing to quantify the strain level to approximate the occurrence of zero effective stress. However, the different shearing mechanisms (triaxial, torsional and simple shear) provide different measurements of shear strain at liquefaction. Hence, the liquefaction criterion measured using simple shear is different from that measured using triaxial testing. It should be noted though that deformations/strains are much harder to measure in the field than in laboratory. The following table (Table 2.1) summarizes a few projects that investigated liquefaction triggering strain-based criteria:

Table 2.1 – Summary table for research projects on liquefaction triggering criterion (DA = Double Amplitude)

	Test type	Criteria*
Seed and Lee (1966)	CTX	20% DA
Ishihara (1993)	CTX	5% DA
Wu et al. (2004)	CSS	6% DA

2.3 UNDRAINED BEHAVIOR OF SAND

Sand behavior highly depends on its initial state (density and confining stress) before being loaded. The frameworks of "soil state" can effectively predict the tendency (contraction or dilation) of soil particles, or, for undrained conditions, the generation of

positive versus negative water pressure. Such prediction would allow for a preliminary assessment of liquefaction susceptibility. There are two popular frameworks available for the evaluation of a soil state, the critical void ratio (CVR) and the steady state line (SSL). The relative position between the initial state of soil and the location of CVR or SSL controls the sand behavior.

The framework of critical void ratio (Casagrande, 1936) was developed based on the results from drained triaxial tests sheared under displacement control. Professor Casagrande concluded that every cohesionless soil has a certain critical density, in which state it can undergo any amount of deformation or actual flow without volume change. The critical state was later defined by Roscoe et al. (1958): *"the state at which a soil element continues to deform at constant stress and constant void ratio"*. Figure 2.1 graphically shows the stress path and concept of CVR. The CVR line distinguishes the contractive and dilative behaviors. If the soil state plots above the CVR line, a contractive response (during drained shearing) or positive excess pore pressure generation (during undrained shearing) is expected, and the sand is susceptible to the flow liquefaction. If the soil state plots below the CVR line, a dilative response (during drained shearing) or negative pore pressure generation (during undrained shearing) is expected. For such sands, cyclic mobility is more probably than flow liquefaction.

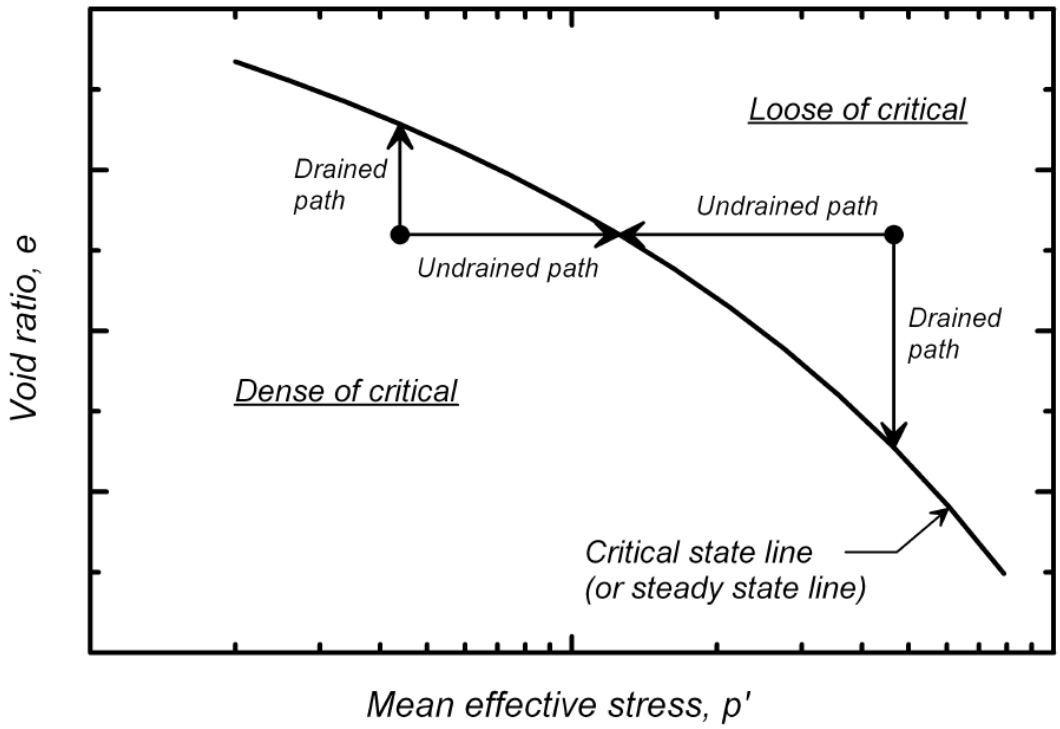

Figure 2.1: The stress paths for monotonic undrained loading of saturated sand at different densities (Idriss and Boulanger 2008).

The steady state (Castro, 1969) has been regarded as a better framework than the CVR for the evaluation of liquefaction susceptibility. Castro (1969) performed a series of stress-controlled undrained triaxial tests. Castro reported that a steady state line (SSL) exists below and parallel to the CVR line on the e-log p' plot, and is usually demonstrated in a three-dimensional space (e, σ' and τ) as shown in Figure 2.2. The SSL addresses the existence of "flow structure", which the grains orient themselves so that the least amount of energy is lost by frictional resistance when flowing. CVR doesn't address this issue. The concept of steady state is later described by Poulos (1981): *"the state of deformation for a mass of particles in which the mass is continuously deforming at constant volume, constant normal effective stress, constant shear stress and constant velocity."* At steady state, the

shearing resistance of the liquefied soil is proportional to the effective confining stress, and useful for estimating the shear resistance at very large deformations.

The SSL line is useful for evaluating the susceptibility of liquefaction of soil, given its initial state. On the e-σ' plot, if the initial state of a sand sample is located above the SSL, the sample is susceptible to flow liquefaction, provided that the static shear stress greater than the shear strength of liquefied sand. On the other hand, if the initial state of a sand sample is located below the SSL, the sample is not susceptible to flow liquefaction but cyclic mobility. Cyclic mobility can take place above or below the SSL for loose or dense sands, respectively.

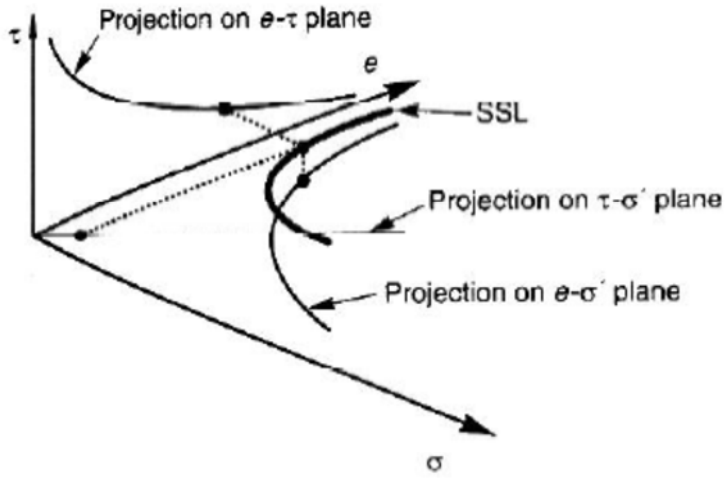

Figure 2.2: 3-D steady-state line shows projection on e-τ plane, τ-σ' plane and e- σ' plane (Kramer 1996).

2.3.1 Monotonic loading

While the soil state could evaluate the susceptibility of liquefaction, well-planned element-level testing programs are needed to investigate the detail of soil behavior and

mechanism, such as stress-strain relationship and stress path. Castro (1969) provided the pioneer work on systematically showing the undrained static behavior, and initiation of liquefaction of sand at different densities. Depending on initial density and confining stress, three different types of stress-strain responses (A, B and C) from anisotropically consolidated specimens were reported and shown in Figure 2.3.

- Specimen A illustrates a response of strain softening after reaching the peak strength at small strain, which has been widely regarded as the 'true' or 'flow-type' liquefaction phenomenon (Castro, 1969; Casagrande, 1975; Seed, 1979; Chern, 1985). Clearly, the steady state is reached at an early stage of loading.
- Specimen B shows a phase transformation from a relatively limited strain softening response to a strain hardening behavior. Castro (1969) termed this response as limited liquefaction, while Ishihara (1993) termed it as quasi steady state.
- Specimen C, the densest specimen, demonstrates a contractive response shortly followed with a dilative response. Clearly, the specimen is not susceptible to flow liquefaction at the given density and stress level.

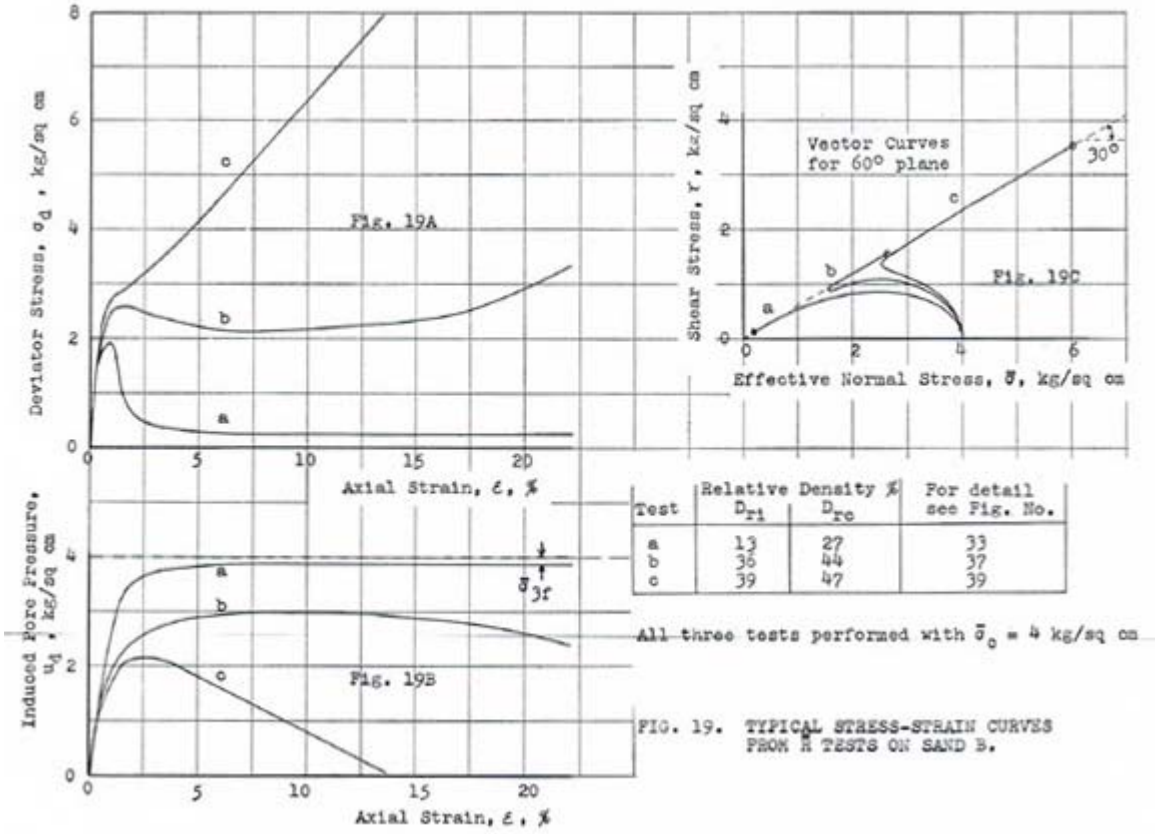

Figure 2.3: Typical monotonic stress-strain curves of sand at different initial states (Castro 1969).

Experimental studies of saturated sand under undrained static loading was further enhanced by many other investigators. For example, Ishihara (1993) conducted a triaxial testing program on saturated Toyoura sand under a wide range of confining stresses (0.1 to 30 atm). Figure 2.4 shows the dependence of sand undrained response on the initial density and confining stress. The findings agree with Castro (1969), and provide an insight on the quasi-steady-state, a transitional phase between the peak and steady state. The quasi-steady-state strength can be substantially smaller than the residual strength and usually takes place at strains of a few percent.

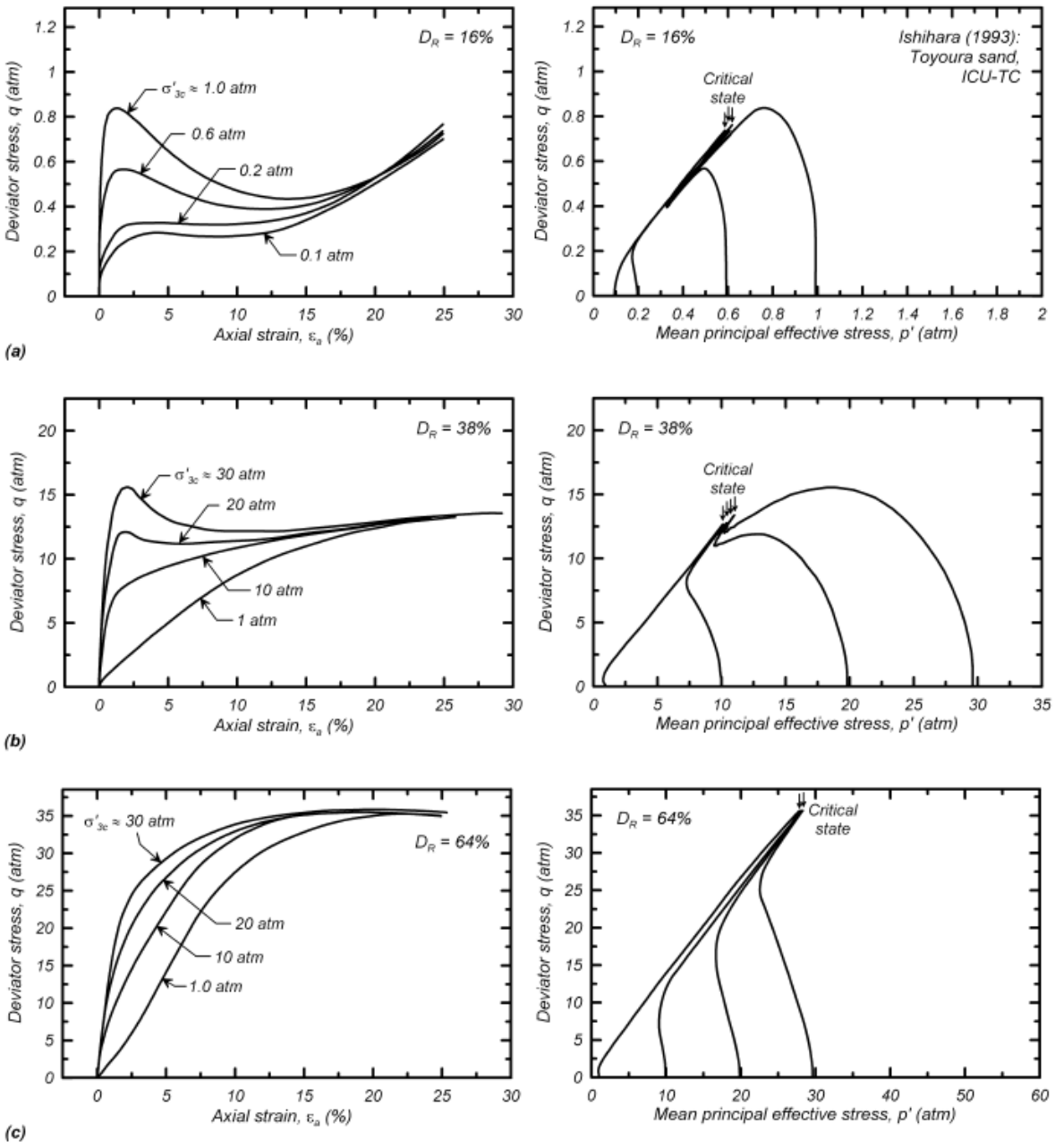

Figure 2.4: Monotonic loading response of saturated Toyoura sand in triaxial compression tests (Ishihara 1993); (a) D_r = 16%, (b) D_r = 38%, (c) D_r = 64%.

2.3.2 Cyclic loading

Vibration, or high-frequency cyclic loading, is proven to be an effective way to densify sand samples under drained condition, because the particles are reorganized into a denser configuration while dissipating excess pore pressure. However, when the drainage is prevented, the restriction to volumetric strains result in excess pore water pressures instead. Figure 2.5 shows a typical undrained cyclic simple shear test on a medium dense sand specimen (D_r = 62%) sheared under harmonic sinusoidal loading at a frequency of 0.2Hz. The stress path and stress-strain relationship are shown on Figure 2.6, and the fifteenth cycle is highlighted in red (r_u reaching unity). The test result shows that the generated excess pore pressure is accumulated under the undrained cyclic loading, which eventually results in a large amount of deformation. The induced shear strain is small until the fifteenth cycle, which shows that limited deformations will occur unless liquefaction is triggered or very close to it. The basics mechanism of excess pore pressure development at the grain size level is discussed in section 2.4. Deformation, or shear strain, is highly dependent on the r_u value in addition to the relative density and soil type. For a loose specimen, a significant amount of shear strain can be developed when r_u exceeds 0.6. For a dense specimen, limited amount of shear strain is expected to develop, even when r_u reaches 1.0. The smaller amount of deformation is regarded as the phenomenon of cyclic mobility.

For a test specimen of loose to medium density under typical vertical confining stress, the specimen is initially located at the “loose of critical” side of the critical state line plot (Figure 2.2). After generating a certain amount of excess pore pressure, the vertical effective stress would become low enough to reposition the state passing the critical state line to the “dense of critical”. For example, in the CSS test results shown in Figure 2.5, the soil response during the 15^{th} loading cycle exhibits this phase transformation phenomena.

Since stress reversals are involved in cyclic loading, the state of soil bounces back and forth across the critical state line and gives alternating contractive and dilative behaviors under the low effective confining stress due to the high generated excess pore pressure. The alternation between the contractive and dilative behavior is defined as phase transformation by Ishihara (1993). Figure 2.6 shows the stress-strain and stress path of a CSS test, and the fifteen cycle (highlighted in red) demonstrates the phase transformation. Figure 2.7 tracks the condition of loading at the fifteen cycle of the CSS test.

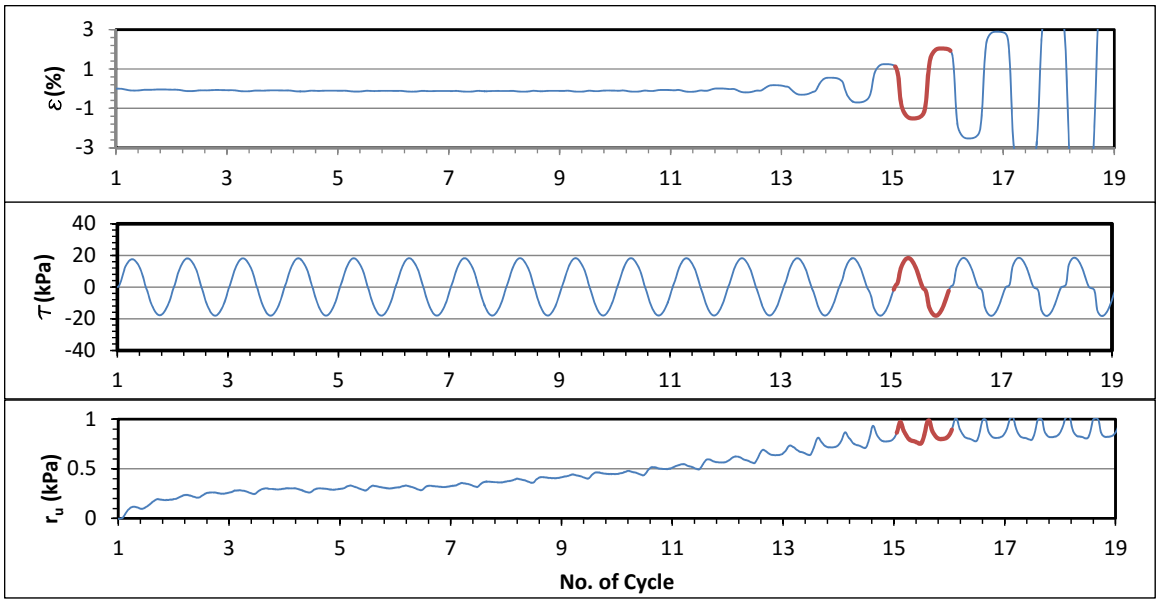

Figure 2.5: Test result from a CSS test under harmonic loading. Shear strain response (Top); Shear stress history (middle); Pore Pressure Ratio (Bottom).

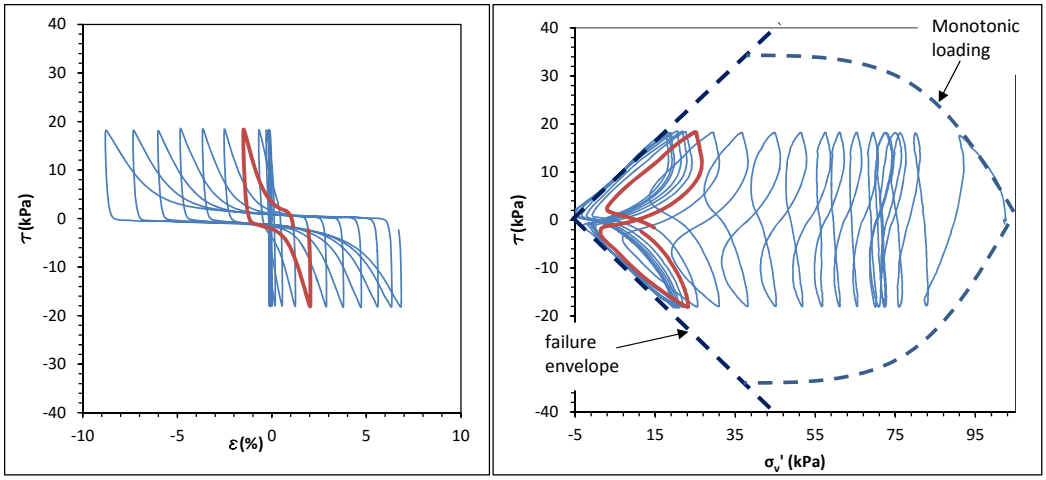

Figure 2.6: Test result from a CSS test under harmonic loading. Stress-Strain relationship (Left); Stress path (Right).

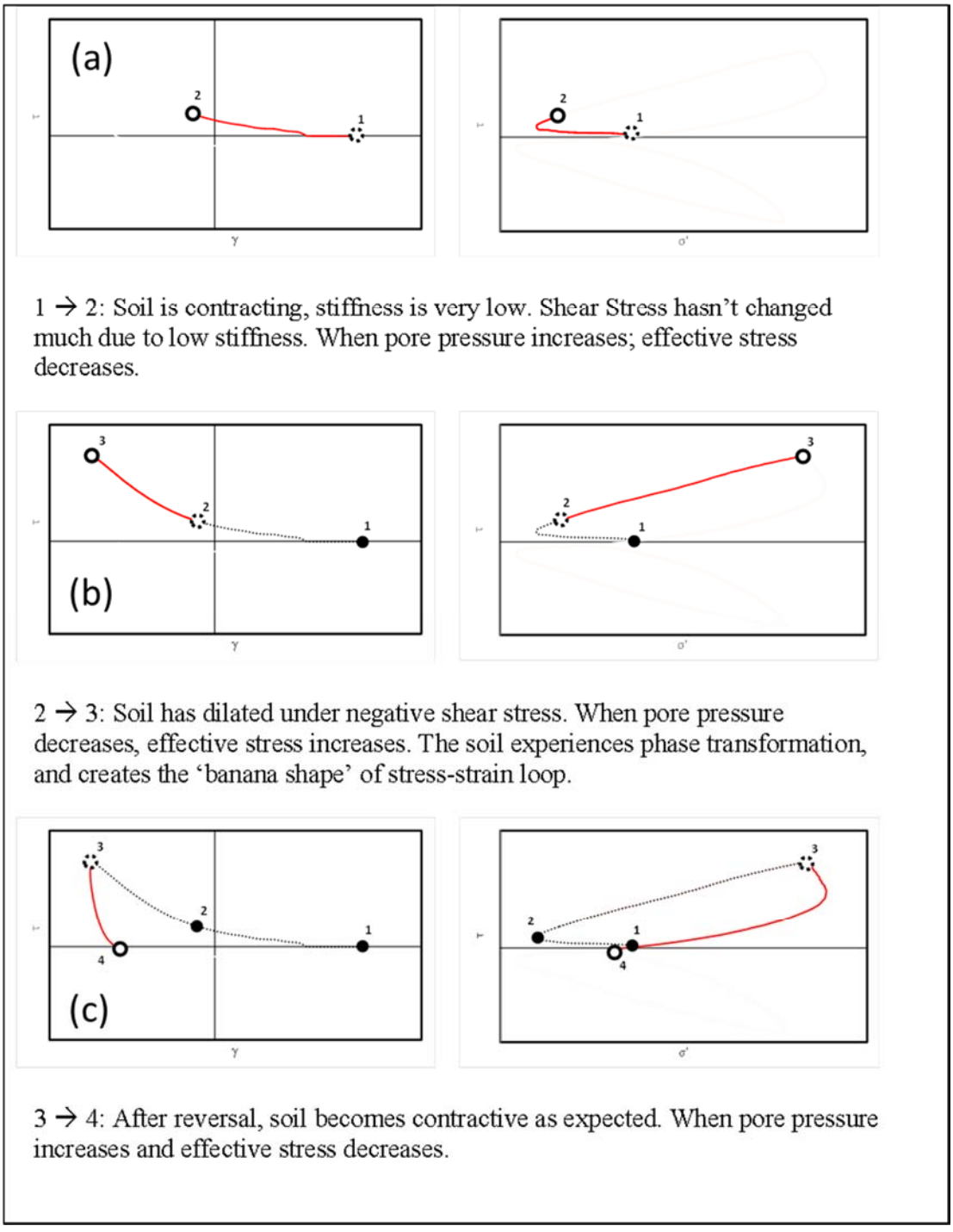

Figure 2.7a-f: Tracking of the loading condition of a phase transformation cycle. Stress-strain relationship on the left; stress path on the right (open dotted circle = starting point; open solid circle = end point).

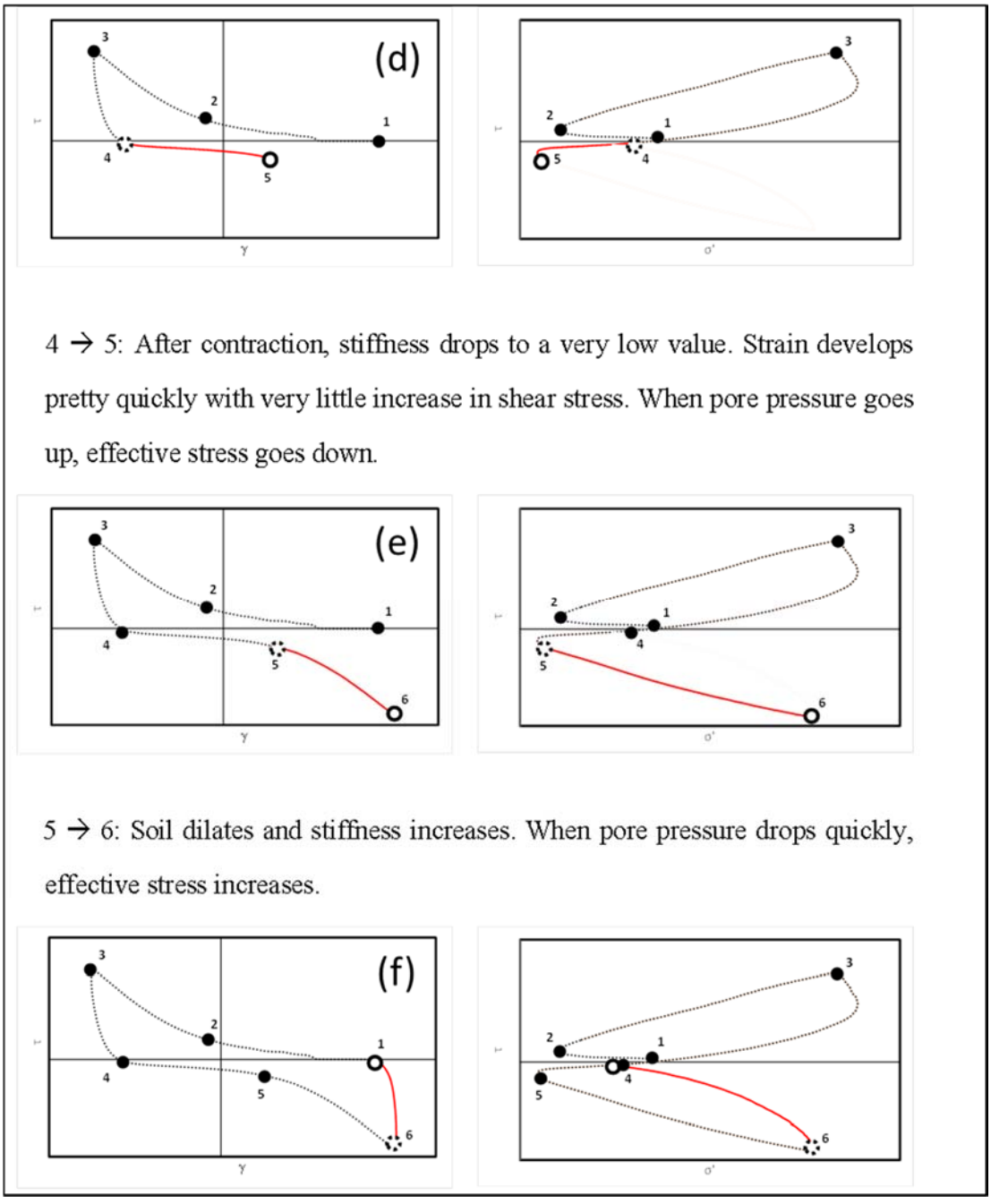

4 → 5: After contraction, stiffness drops to a very low value. Strain develops pretty quickly with very little increase in shear stress. When pore pressure goes up, effective stress goes down.

5 → 6: Soil dilates and stiffness increases. When pore pressure drops quickly, effective stress increases.

Figure 2.7a-f (cont.): Tracking of the loading condition of a phase transformation cycle. Stress-strain relationship on the left; stress path on the right (open dotted circle = starting point; open solid circle = end point).

2.4 EXCESS PORE PRESSURE GENERATION

Prior to a seismic event, the saturated soil deposit is assumed to be under a ‘at rest’ condition, in which the soil particles are in contact with a number of adjacent particles. The overburden weight and surcharge above ground that are placed on top of the soil grains provide contact forces between the particles, which hold the soil mass structurally sound and attributes to the shear strength of the deposit. Dynamic shear stresses and shear strains generated by the earthquake or blasting cause slip at particle to particle contacts. Individual particles have the tendency to get closer to each other, into a denser configuration. Since the applied loads are rapid, there is no time for the water in the pore space to escape, and hence it prevents the reconfiguration of soil particles. As a result, there is a generation of excess pore pressure, under the undrained condition, because of the tendency for densification. The generated water pressure reduces the contact forces between the soil particles, and therefore can lead to an instable deposit. If the level of ‘shaking’ is high, the generated excess pore pressure could become high enough to force the soil particles to be out of contact leading to liquefaction. Even with a r_u value of 0.6 (generated pore pressure equal to 60 percent of initial confining stress), the soil mass could lose significant amount of shear strength. Therefore, predicting excess pore pressure generation at a given site is one of the keys of seismic design.

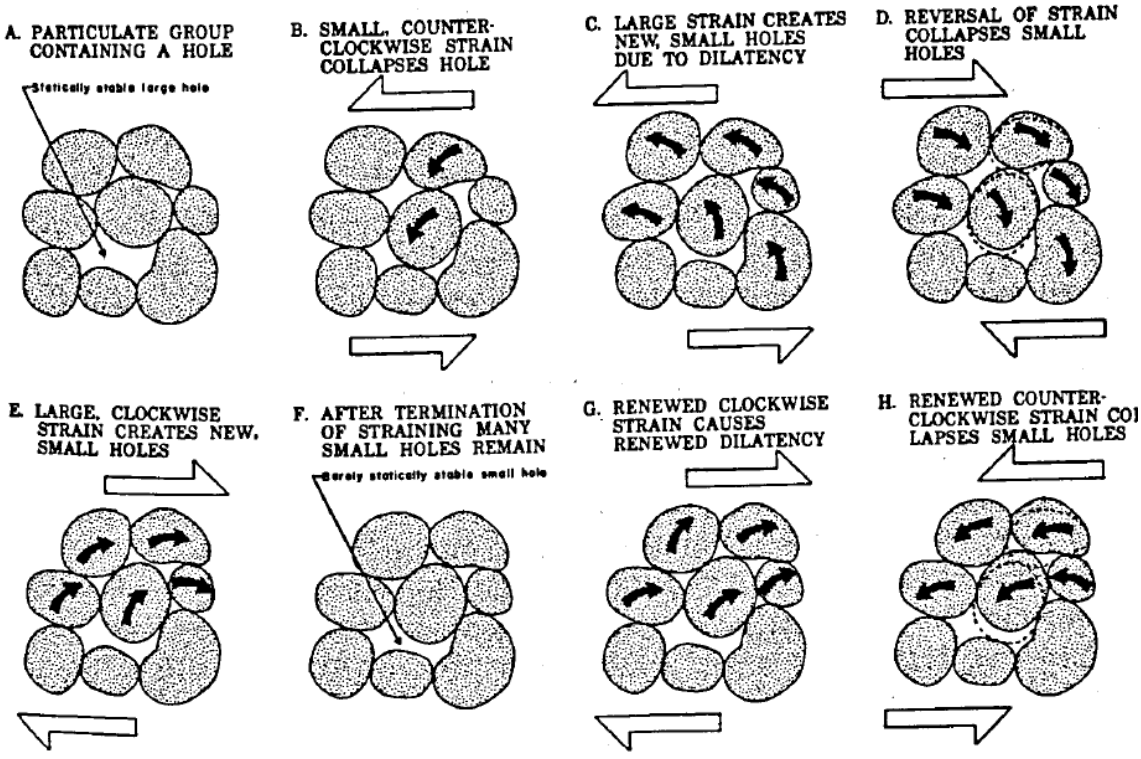

Figure 2.8: Idealized cross sections of a particulate group showing packing changes that occur during cyclic loading (Youd 1977)

The generation of excess pore pressure is a very complicated phenomenon, involving dissipation and redistribution of water pressure within the soil mass. Density, fine content, and stress level are the main parameters that affect the rate of excess pore pressure development. Numerous studies have been aimed to predict or model excess pore pressure development under cyclic loadings.

2.4.1 Pore Pressure Generation Prediction Based on Laboratory Test

The rate of pore pressure development in cyclic loading tests was observed by different investigators in the laboratory. One of the most direct way is to measure the pore

pressure development under undrained element level test. It is noteworthy that the pioneers are Lee and Albeisa (1974) who used cyclic triaxial test on different types of sand and DeAlba et al. (1976) who used cyclic simple shear test on sand with different densities. The undrained tests were conducted under harmonic stress cycles, and the generated pore pressure was monitored under each cycle. The results show that the rate of normalized excess pore pressure (r_u) buildup fell into a range, as indicated in Figure 2.9 and 2.10. The empirical relationship between r_u and the cyclic ratio, r_N (number cycle normalized by the number of cycles to reach liquefaction), is:

$$r_N = [\frac{1}{2}(1 - cos\pi \cdot r_u)]^{\alpha} \qquad [2.1]$$

in which α is a function of the soil properties and test conditions.

In order to apply the laboratory element test results to evaluate liquefaction in the field, the method of equivalent number of cycle (N_{eq}), which converts a time-history of shear stress into a number of uniform stress cycles (Seed et al. 1975), is used. Even though the prediction is totally empirical, the test results from Lee and Albeisa (1974) and De Alba et al. (1975) provided reasonable and practical estimations of excess pore pressure generation under cyclic loading at the present time. The test result has been adopted in many later models of dynamic soil behavior.

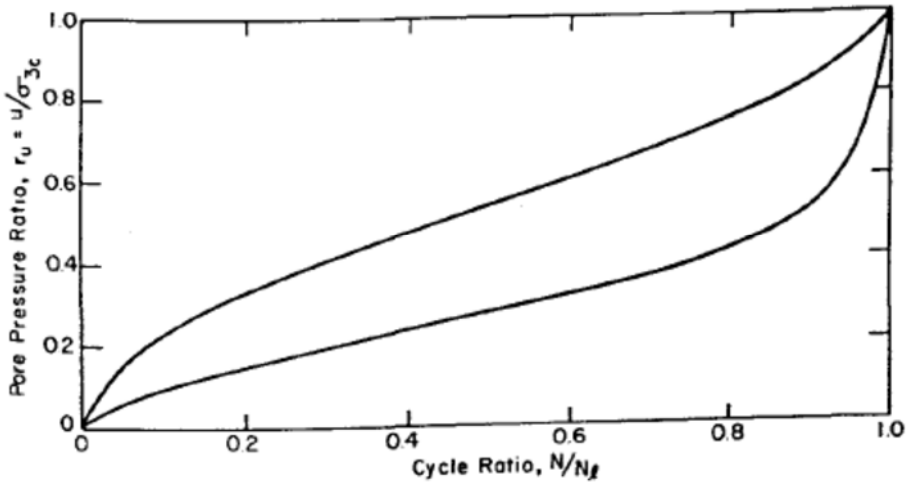

Figure 2.9 Rate of Pore Pressure Buildup in Cyclic Triaxial Tests (Lee and Albeisa 1974)

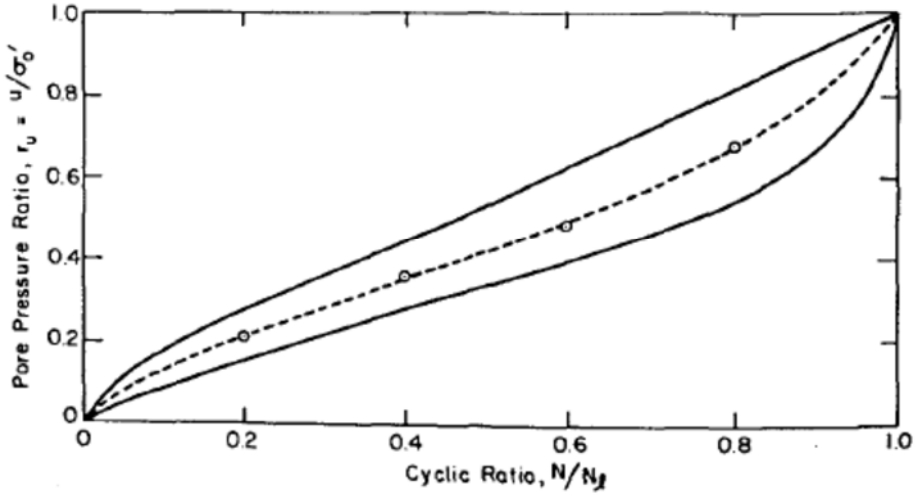

Figure 2.10 Rate of Pore Pressure building up in Cyclic Simple Shear Tests (De Alba et al. 1975).

Drained cyclic tests were also performed to simulate liquefaction and the test results were used for predicting pore pressure generation, by correlating volume reduction to pore pressure generation (Martin et al. 1975; Finn et al. 1977; Byrne 1991). Drained testing is often preferred to undrained testing because of the ease of specimen preparation. Drained

tests under constant volume using the cyclic simple shear were used by (e.g., Shaw and Brown 1986; Wijewickrem 2010) to determine the liquefaction resistance of soils. In these tests, the pore pressure is assumed to be equal to the decrease in the vertical effective stress due to the densification of the soil under cyclic loading. Dyvik et al. (1987) reported the test results on Drammen clay obtained by the undrained tests and constant volume tests are equivalent for practical purposes. Martin et al. (1975) firstly proposed a concept of volumetric compatibility that the change in volume of soil voids is equal to the net change in volume of sand structure:

$$\frac{\Delta u n_e}{K_w} = \Delta\epsilon_{vd} - \frac{\Delta u}{\bar{E}_r} \qquad [2.2]$$

where Δu is the increase in residual pore pressure for a loading cycle; K_w is the bulk modulus of water; n_e is the porosity; $\Delta\epsilon_{vd}$ is the reduction in volume of sand structure due to slip deformation; and $\bar{E}_r$ is the tangent modulus. The concept allowed the implementation of effective stress analysis, since the excess pore pressure can be estimated by linking the increment of volumetric strain per cycle of load with the shear strain. Equation (2.2) can be expressed as:

$$\Delta u = \frac{\Delta\epsilon_{vd}}{\frac{1}{\bar{E}_r}+\frac{n_e}{K_w}} \qquad [2.3]$$

The Martin et al. (1975) method wasthen modified and improved by many researchers (Finn and Byrne, 1976; Finn et al., 1977; and Byrne, 1991). The computation of induced excess pore pressure is embedded in a few plasticity models for predicting cyclic behavior, such as the UBCSAND (Beaty and Byrne 2011).

2.5 DEFORMATION AFTER LIQUEFACTION INITIATION

One of the most severe damages from liquefaction hazard results from excessive shear displacements (lateral spreading) when the strength of liquefied soil is significantly reduced, as shown in the San Fernando earthquake of 1971 (Figure 2.11), and bridge foundation movements of the Snow River Bridge in the Alaska earthquake of 1964. Geotechnical earthquake engineering research has historically focused on evaluating the pre-liquefaction soil resistance, but the response of the liquefied soil has received limited attention. In the past, it was believed that the most effective way of minimizing loss associated with liquefaction-induced sliding was to prevent the triggering of liquefaction. Therefore, high cost was spent on soil improvement or remedial measures. However, when the consequences of large deformations are possibly acceptable for a given structure or site, it may be economically advantageous to ensure the stability against sliding after the triggering of liquefaction (Seed 1987). Also, Performance Based Earthquake Engineering (PBEE) provides a probabilistic framework to evaluate the risk associated with liquefaction hazard at a given site (Mayfield et al. 2010). Therefore, a better estimation of the resulting deformations is in needed in order to advance the liquefaction evaluation procedure.

Figure 2.11: San Fernando, California, Earthquake February 1971. Building at San Fernando Valley Juvenile Hall located astride the margin of a lateral spread that produced 3 feet of horizontal ground displacement (USGS 2013).

2.6 EVALUATION OF SHEAR STRENGTH AND DISPLACEMENT OF LIQUEFIED SOIL

Steady-state strength at which the soil deform continuously may not be valid for post-liquefaction analysis because the cyclic loading rearranges the soil profile into zones with different densities, with higher density at the bottom and lower one at the top. Given this possibility, there may be multiple steady-state strengths, depending on the void ratios (Seed 1987). Because of the complexity, the characterization of undrained strength of liquefied soil in practice is heavily depended on empirical approaches. The Seed and Harder (1990) (Figure 2.12) method has been widely used to estimate the liquefied soil's residual strength, which is correlated with the soil density ($N_{1,60}$) only. As indicated in Figure 2.12, the data consist large scatter, because those data is obtained from back

calculation using limit equilibrium analyses, which assumed different failure surface to determine the minimal shear strength. The method contains several uncertainties and the 33rd percentile bound is conservative.

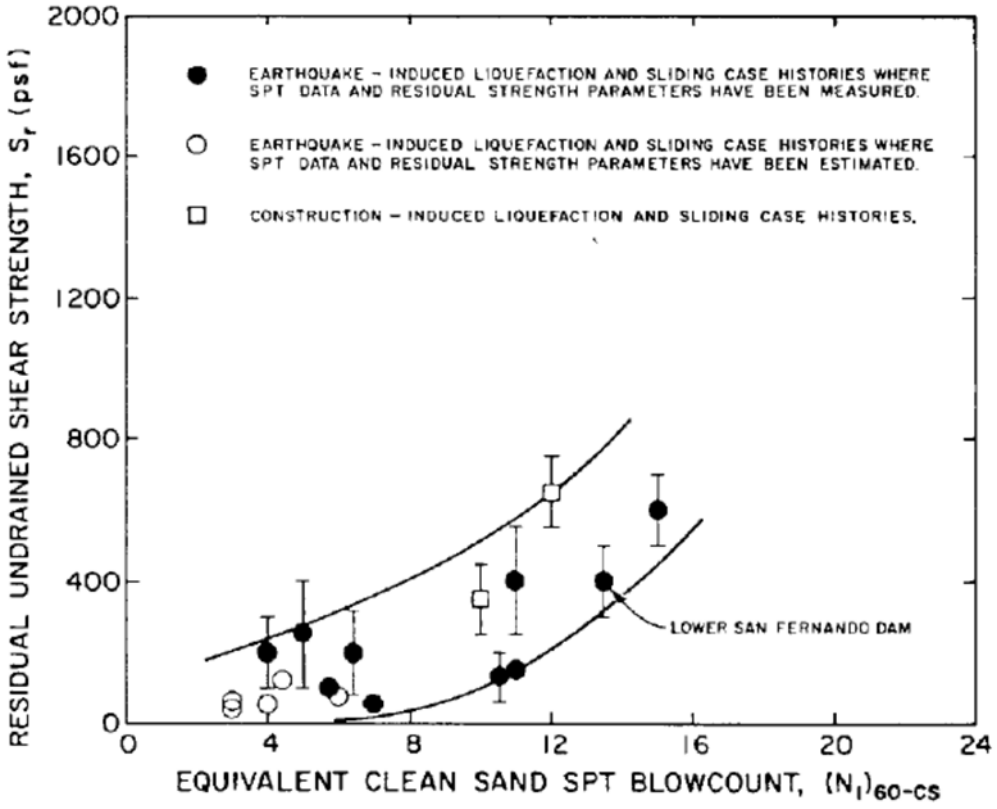

Figure 2.12: Relationship between corrected clean sand blow count and undrained residual strength from case studies (Seed and Harder 1990).

Liquefaction induced lateral deformation is another important assessment. Using multiple linear regression, Barlett and Youd (1992) developed an empirical model correlating lateral ground displacement to a few physical parameters, such as earthquake magnitude and thickness of saturated sand layer. The model was based on a huge database of earthquake induced lateral deformation in the U.S. and Japan, and attempted to capture

the effect of topography and soil conditions. However, the method is restricted to earthquake magnitudes between six to eight, and soil conditions of sandy to silty within 10 meters depth from the ground surface. There are two models, free-face and ground-slope.

Free-face model: $logD_H = -16.3658 + 1.1782M_w - 0.9275logR - 0.0133R + 0.6572logW + 0.3483logT_{15} + 4.5720\log(100 - F_{15}) - 0.9224(D_{50})_{15}$ [2.4]

Ground-slope model: $logD_H = -16.3658 + 1.1782M_w - 0.9275logR - 0.0133R + 0.4293logS + 0.3483logT_{15} + 4.5720\log(100 - F_{15}) - 0.9224(D_{50})_{15}$ [2.5]

where D_H is the estimated lateral ground displacement in meter; M_W is the moment magnitude; R is the horizontal distance from seismic energy source in kilometer; T_{15} is the cumulative thickness (in meters) of a saturated granular layers with $(N_1)_{60}$ less than 15; F_{15} is the average fine content (in percent) for the granular layers comprising T_{15}; $(D_{50})_{15}$ is the average mean grain size (in millimeter) for the granular layer layers comprising T_{15}; W is the ratio of height of the free face to the horizontal distance between the base of the free face and the point of interest; S is the ground slope in percent. Figure 2.13 indicates the performance of the free face model, which shows a certain level of uncertainty exist.

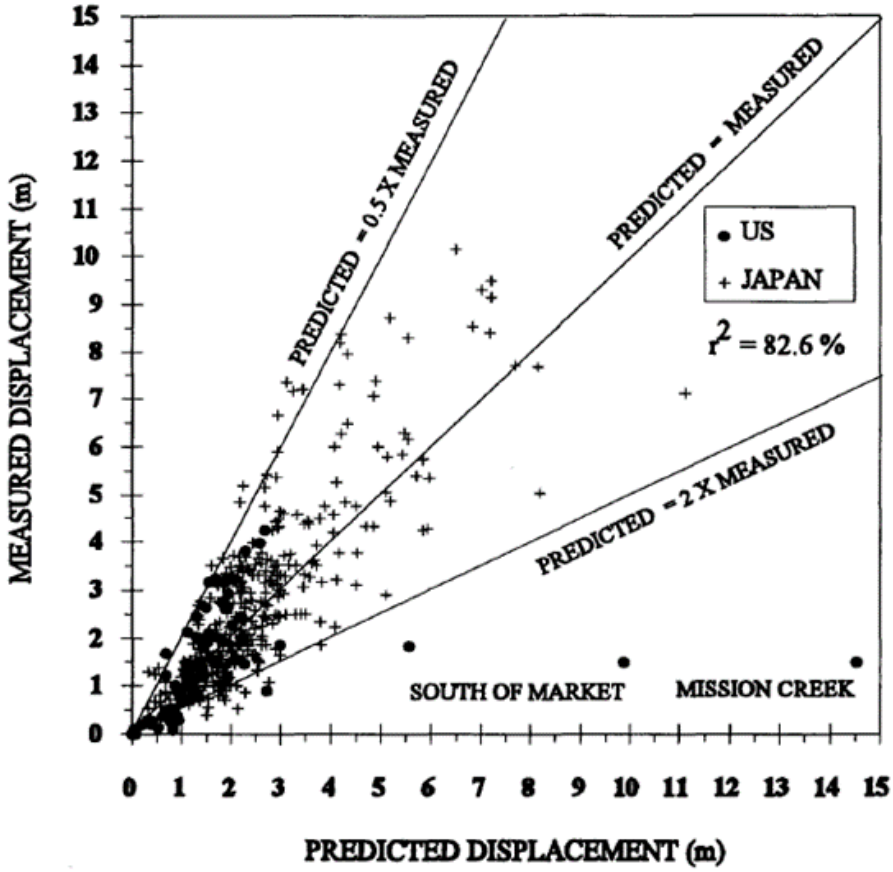

Figure 2.13: Comparison of predicted and measured displacement from the Barlett and Youd model (Barlett and Youd 1995).

2.7 Post-liquefaction Stress-Strain Behavior

Shear strength of liquefied sand highly depends on the level of shear strain, which can vary from of a few to hundred percent. In order to reasonably predict the earthquake-induced deformation, there is a need for studying the stress strain relationship of liquefied soil, which is still a geotechnical novelties that have not yet been comprehensively and systematically explored. A better understanding on liquefied soil responses at the element level can improve the development of geotechnical structure constitutive modeling.

Several studies have employed laboratory modeling to simulate liquefaction triggering and monitor the monotonic undrained response of sand immediately after the liquefaction initiation. Vaid and Thomas (1995) are the pioneers who experimented on this topic, by conducting monotonic loading following cyclic loading in a triaxial setup, and found that generally there is a low stiffness region followed by a dilative response region (Figure 2.14). Vaid and Thomas (1995) also reported that post-liquefaction dilation is dependent on the density of the soil and the confining stress level applied. However, the loading mechanism of triaxial setting has proven to be an improper way of simulating earthquake waves, because of the 90 degrees rotation of the principal axes during the stress reversal as well as the inaccurate approximations of area of specimen at high axial strains. Also, laboratory compression tests overestimate the residual strength. Instead, simple shear and torsional shear testing, which provide better simulation of seismic loading, are adopted in recent research projects to investigate the stress-strain relationship of liquefied soil.

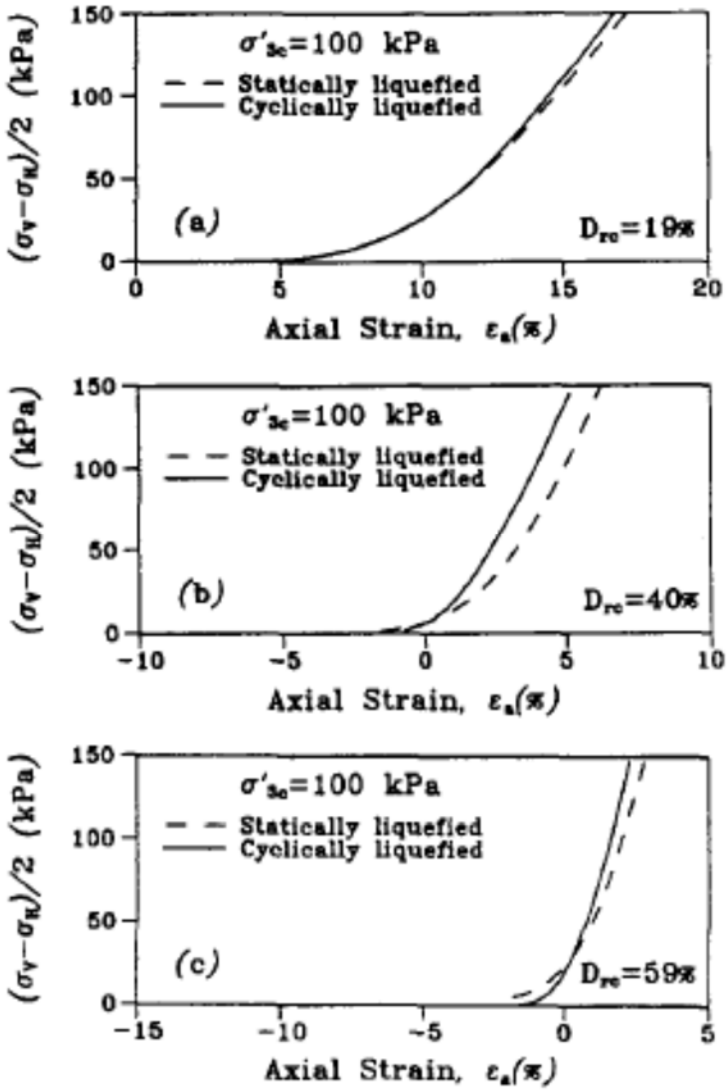

Figure 2.14: Comparison of Monotonic Response Following Liquefaction by Cyclic and Static Load/Unload Cycle (Vaid and Thomas 1995).

A few researchers (Kano et al. 2008; Sivathayalan and Yazdi 2013 and Dahl et al. 2014) studied this topic with either cyclic simple shear or cyclic torsional devices, and generally agree that a there is a minimal stiffness region under loading immediately after the liquefaction initiation. The low stiffness region ranges from a few to several tens of a percent (Kiyota et al. 2008). Post-liquefaction stress-strain behavior can also be accessed

with cyclic loading (Wu et al. 2004), which the findings generally concur with those observed from monotonic loading. The change from almost zero stiffness to a dilative response is due to particle rearrangement or change of fabric during liquefaction, which was experimentally proven to be a function of shear strain level, density, stress level, sand type (angularity and gradation) and fine content (Kokusho et al. 2004; Kano et al. 2008; Sitharam et al. 2009; Sivathayalan and Yazdi 2013; Dahl et al. 2014). For example, Sivathayalan and Yazdi (2013) observed a correlation between the dilation response and particle angularity. Dahl et al. (2014) examined the effect of two soils with different fines content, and the amount of fines impacts the post-liquefaction responses. The pre-liquefaction loading history should affect the post-liquefaction stress-strain relationship. Sitharam et. al (2009) asserted that the post-liquefaction response is greatly depend on the axial strain induced prior to initial liquefaction. Sivathayalan and Yazdi (2013) and Dahl et al (2014) use maximum shear strain to represent the effect of pre-liquefaction loading and correlate with the post-liquefaction effect (Figure 2.15).

Although previous studies have proven the dependence of the dilation response on a few factors, they are deficient because they only employed harmonic loadings to represent actual earthquake motions and trigger initial liquefaction. An earthquake motion can vary significantly in amplitude and frequency over its duration; therefore, the irregular pattern of pulses can alter the particle arrangement. It is important that the post-liquefaction behavior of sand in response to transient loadings be observed to provide more accurate models of the response of a liquefied sand when monotonically loaded. Moreover, to build upon the results found by Sivathayalan and Yazdi (2013), the effects of different transient loadings, instead of harmonic loading, on post-liquefaction dilation response to sands with contrasting particle angularity are required for further examination.

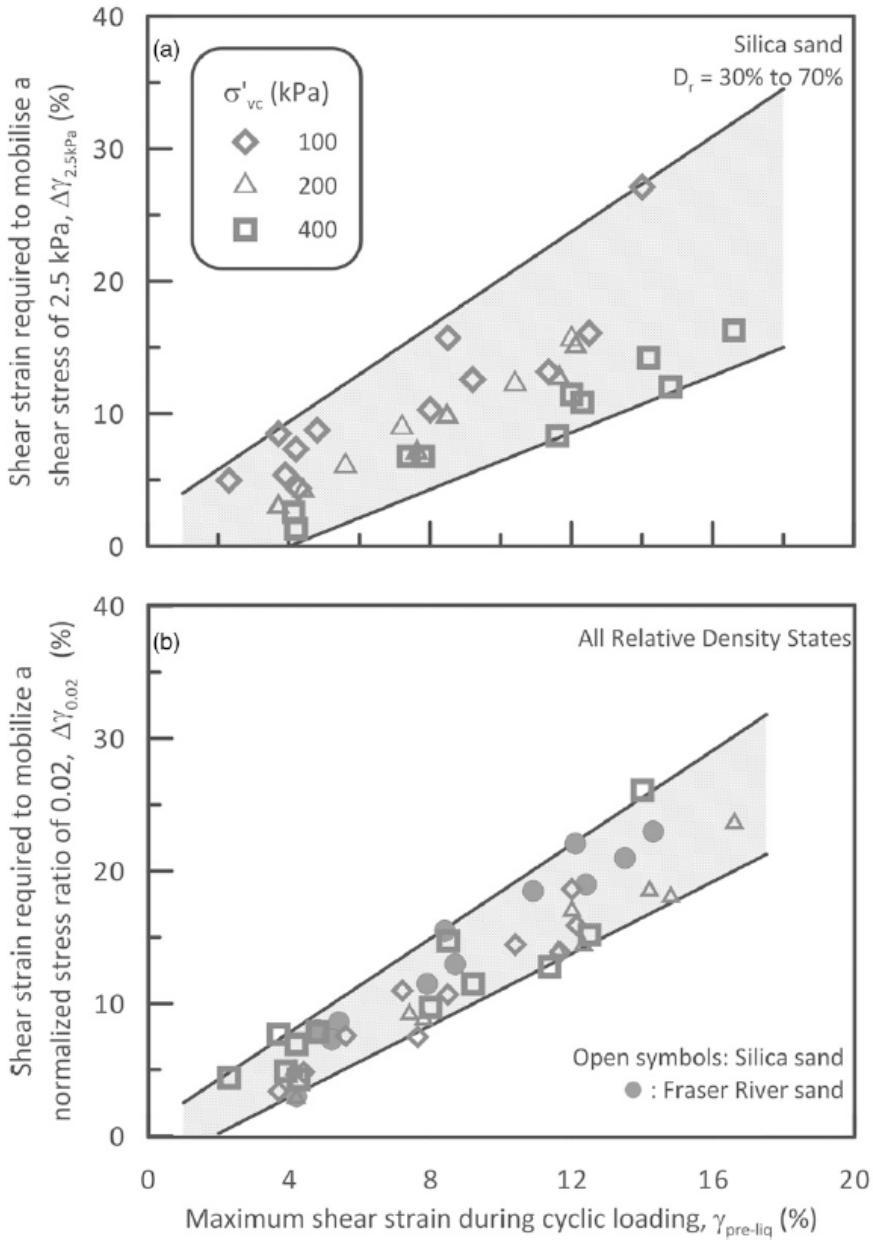

Figure 2.15: Influence of maximum pre-strain on the range of postliquefaction deformation at essentially zero stiffness (Sivathayalan and Yazdi 2013).

2.8 NUMERICAL SIMULATION OF SEISMIC DESIGN FOR GEOTECHNICAL STRUCTURES

Numerical simulation of liquefiable soil under cyclic undrained loading is very important for predicting earthquake-induced deformation of geotechnical structures in liquefaction hazard evaluation. The seismic response of geotechnical structures, such as earth dam and slope, can be numerically simulated by the integration of many elements comprising the structure. During an event of soil liquefaction, successful numerical simulations of soil responses for geotechnical structures require constitutive models that can reasonably predict the soil behavior of a soil element under dynamic loadings. Many advanced constitutive models, such as PM4sand (Boulanger and Ziotopoulou 2015), UBCSAND (Beaty and Byrne 2011), Pressure-Dependent-Multi-Yield Surface (Yang et al. 2003) and Boundary surface hypoplasticity (Wang et al. 1990), were developed in the past three decades for the purpose of soil liquefaction hazard evaluation. Those advanced models are built on plasticity theories with many different assumptions and modificaitons. For example, PM4sand model was initially built upon a two-surface plasticity model combined with critical state soil mechanic framework (Manzari and Dafalias 1997). The laterest version of PM4Sand (3rd version) follows the basic framework of Dafalias and Manzari (2004) with modifications on the fabric formation and history, plastic modulus relationship, dilatancy relationship, elastic modulus relationship, sloping ground effect and the logic for tracking previous initial back-stress ratios. The UBCSAND and PM4sand models are particularly popular, because they can be implemented in a commercial program, FLAC (Itasca 2011), which is commonly used in the practice of geotechnical earthquake engineering.

In addition to plasticity models, there are many other researchers trying to simulate or predict the consequence of soil liquefaction. Kiku and Tsujino (1996) used a simplified

method by Yoshida et al. (1993) to simulate the basic stress-strain of liquefied soil behavior. The authors concluded that the sand properties may change during the cyclic loading before and after liquefaction; therefore, it is necessary to modify the internal friction angle and other parameter values to improve the sand behavior in the high stiffness region. The results were compared with torsional shear tests with Toyoura Sand. Shamoto et al. (1997) proposed constitutive relations for liquefied sand based on the analyses of mechanism, relative compression, and plasticity theory. The authors divided the volumetric strains into two components, reversible dilatancy and irreversible dilatancy. Also, the authors reported two shear strain components, one that depends on change in effective stress and the other that does not. Sitharam et al. (2009) reported a model with discrete element method (DEM) to simulate the drained and undrained post-liquefaction stress-strain behaviors. The authors proposed a few new micromechanical parameters such as the average coordination number and induced anisotropic coefficients to model the change of fabric and particle rearrangements during liquefaction. Two series of cyclic triaxial test, drained and undrained, were provided to validate the model.

Nevertheless, the core part of all models were developed based on observations from experimental test results of harmonic loading (cyclic simple shear or cyclic triaxial tests). For both physical and numerical simulation, representing a transient ground motion by an equivalent number uniform cycle is too coarse, because the temporal and spectral characteristic of earthquake motions are overlooked. High-quality cyclic simple shear data that systematically illustrate the response of soils subjected to transient ground motion is needed. Those experimental data can be used to compare with the numerical simulations from those numerical models at the element level. The recognition of such limitations through single-element modeling are essential for improving the practice of numerical simulation of geotechnical structures.

2.9 EVALUATION OF LIQUEFACTION HAZARDS

Common deterministic procedures for soil liquefaction evaluation consist two characterizations: soil resistance to liquefaction and earthquake loading. The resistance of a soil to liquefaction is termed as a cyclic resistance ratio (CRR), which has been widely correlated to a few in-situ indexs: 1) standard penetration resistance, SPT, 2) cone penetration resistance, CPT and 3) shear wave velocity, V_s. These correlations are based on case histories that classifying seismic sites either having liquefied or not having liquefied under the level of shaking induced by the earthquake.

Different evaluation procedures adopt different approaches to characterize the earthquake loading, such as peak ground acceleration (Seed and Idriss 1971), arias intensity (Kayen et al. 1997), cumulative average velocity (Kramer and Mitchell 2006) and normalized energy demand (Green 2001). For the most commonly used procedure in practice, loading is characterized by the peak absolute value of the shear stress acting at the interested vertical stress level, cyclic stress ratio (CSR). The peak stress can be computed by a site response analysis, but is much more commonly obtained by using a simplified procedure (Seed and Idriss 1971) that relates to PGA. Knowing CRR and CSR, the potential for liquefaction is then deterministically evaluated in terms of a factor safety, which is a ratio of CRR to CSR.

Probabilistic models for liquefaction hazard evaluation have been developed (e.g., Cetin et al., 2004, Juang et al., 2012; Kayen et al. 2013) and become more and more popular in the past decade. These models estimate a probability of liquefaction triggering based on indices, such as SPT, CPT or PGA. However, neither the current deterministic nor probabilistic approach provides prediction on when liquefaction occurs and the consequences of induced shear deformation.

2.9.1 Characterization of Soil Resistance to Liquefaction

In-situ index testing (e.g., SPT, CPT and V_s) is the dominant approach in practice to characterize soil liquefaction resistance because of the extensive available databases and past experience. In addition, there are soil characteristics that are hard to characterize, such as aging, cementation and previous seismic history which make in-situ based approaches advantageous. Cyclic Resistance Ratio (CRR), can be correlated to in-situ test parameters such as SPT (Seed and Idriss 1971; Youd et al. 2001; Boulanger and Idriss 2014), CPT (Robertson and Wride 1998; Moss et al. 2006; Boulanger and Idriss 2014), and the shear wave velocity V_s (Andrus and Stokoe 1997; Andrus et al. 2009; Kayen et al. 2013):

$$CRR_{M=7.5,\sigma'_{vc}=1} = \exp\left(\frac{(N_1)_{60cs}}{14.1} + \left(\frac{(N_1)_{60cs}}{126}\right)^2 - \left(\frac{(N_1)_{60cs}}{23.6}\right)^3 + \left(\frac{(N_1)_{60cs}}{25.4}\right)^4 - 2.8\right) \quad [2.6]$$

$$CRR_{M=7.5,\sigma'_{vc}=1} = \exp\left(\frac{q_{c1Ncs}}{540} + \left(\frac{q_{c1Ncs}}{67}\right)^2 - \left(\frac{q_{c1Ncs}}{80}\right)^3 + \left(\frac{q_{c1Ncs}}{114}\right)^4 - 3\right) \quad [2.7]$$

where equations [2.6] and [2.7] are the derived correlation between CRR and penetration resistances that are expressed via SPT and CPT respectively (Idriss and Boulanger 2004). In the terms $(N_1)_{60CS}$ and q_{c1Ncs}, the subscript 'cs' indicates clean sand. The equations are corrected to earthquake magnitude of 7.5 by using the magnitude scaling factor (MSF) and effective overburden stress of σ'_{vc}= 1 atm by using the overburden correction factor, K_σ:

$$CRR_{M=7.5,\sigma'_{vc}=1} = \frac{CRR_{M,\sigma'_{vc}}}{MSF * K_\sigma} \quad [2.8]$$

These correlations are generally based on logistic regression of case history data involving sites with liquefiable soils that are subjected to strong ground motion. For each site, the level of ground motion loading (PGA or CSR) is estimated and plotted as a

function of some measure of the soil's density (e.g., $(N_1)_{60cs}$, q_{c1Ncs}, and V_{s1}) (Figure 2.16 and 2.17). The above relationships are then developed by creating curves that separate the conditions in which liquefaction has been observed from the cases where liquefaction was not observed. It is important to note that this approach is mainly correlation based, and is only able to predict whether the site could potentially experience liquefaction or not. In-situ index testing can only provide a very rough estimation on surface deformation (Figure 2.18).

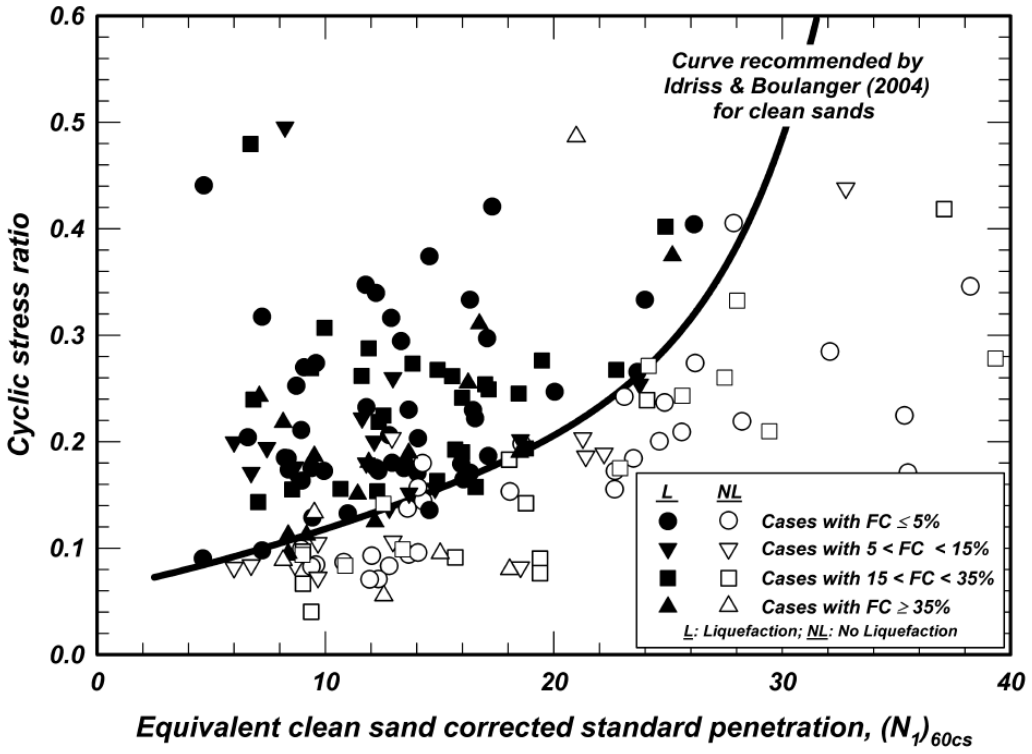

Figure 2.16: SPT case history of liquefaction in cohesionless soils with various fines contents plotted versus their equivalent clean sand (N1)60cs values for M =7.5 and σ'vc = 1 atm (Idriss and Boulanger 2008)

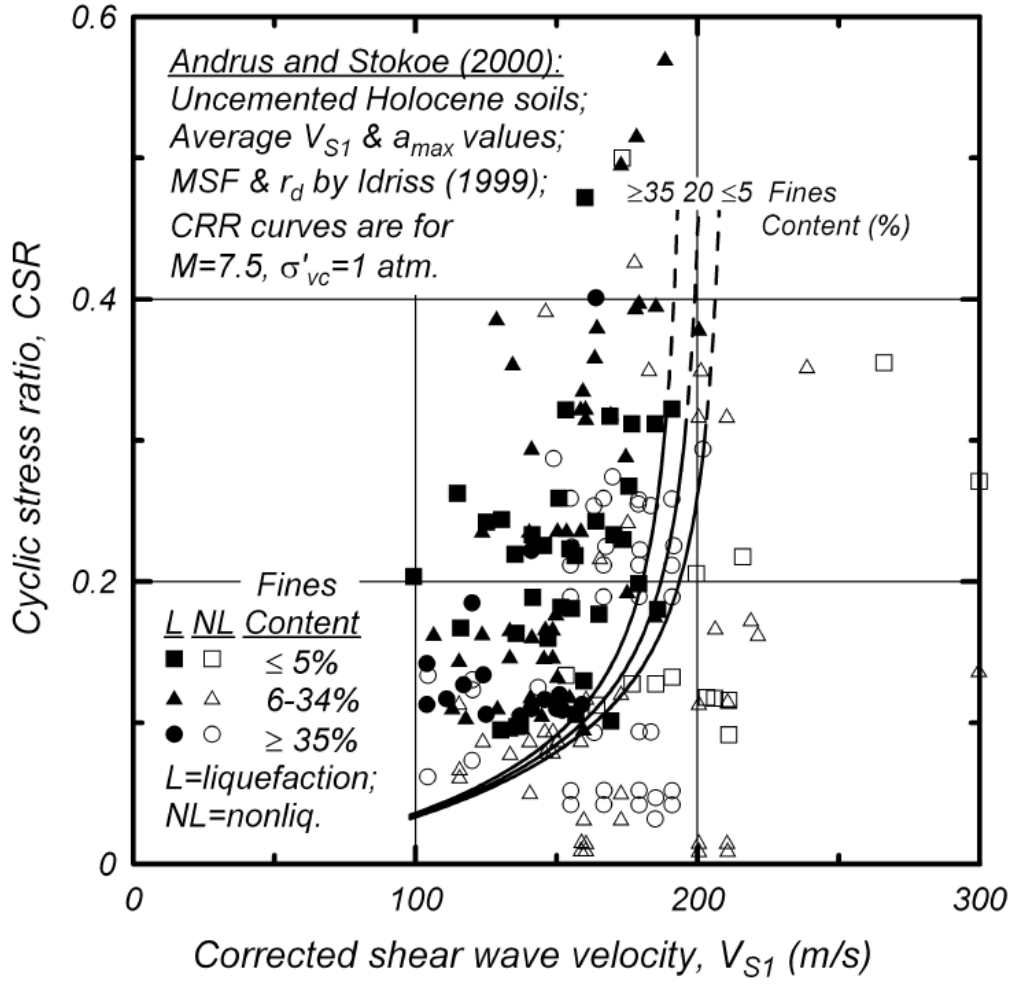

Figure 2.17: V_{s1}-based liquefaction correlation for clean uncemented sands (Andrus and Stokoe 2000).

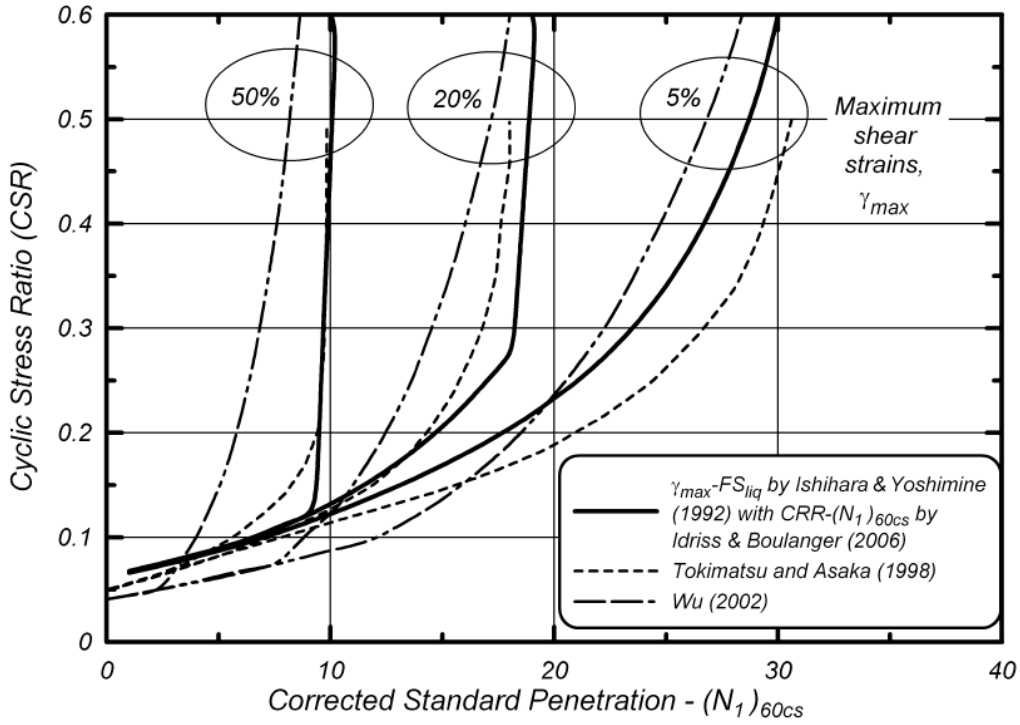

Figure 2.18 Comparison of the relationship among CSR, SPT, $(N_1)_{60cs}$, and maximum shear strain for three levels of maximum shear strain (Idriss and Boulanger 2008).

2.9.2 Characterization of Earthquake Loading

Even though major refinements have been made on evaluating soil liquefaction resistance, the most common way to characterize an earthquake loading, Cyclic Stress Ratio (CSR), is still mainly based on the framework reported by Seed and Idriss (1971):

$$CSR = 0.65 \frac{PGA}{g} \cdot \frac{\sigma_{vo}}{\sigma'_{vo}} \cdot r_d \qquad [2.9]$$

where PGA is the Peak Ground Acceleration, g is gravitational acceleration, σ_{vo} is the total vertical overburden stress, σ'_{vo} is the effective vertical overburden stress, and r_d is the depth

reduction factor (Figure 2.19). Eq. (2.9) can be modified to account for the effects of the duration of the event by the use of a magnitude scaling factor (MSF) that works to increase CSR for events less than Magnitude of 7.5, and decrease CSR for events greater than M7.5. With the MSF serving as a crude proxy for duration, the earthquake loading is chiefly represented by a parameter, PGA.

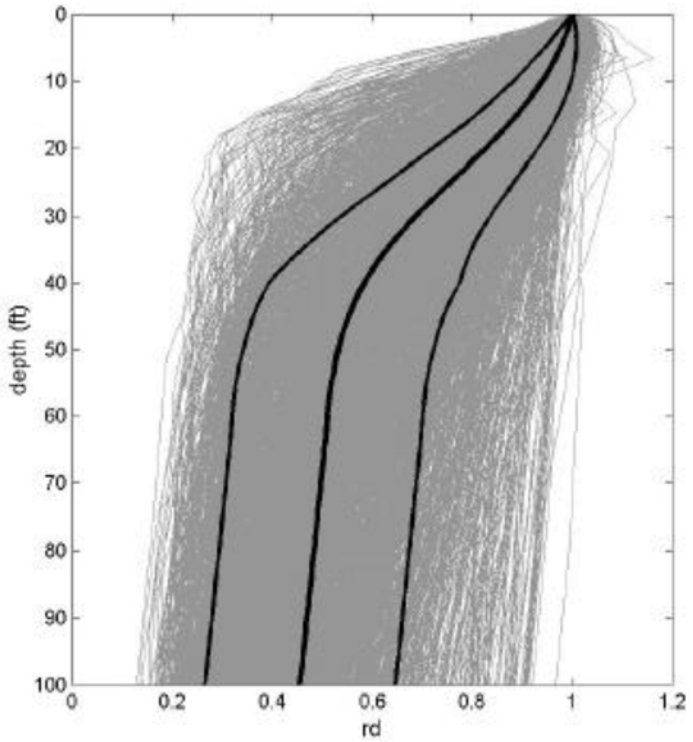

Figure 2.19: r_d Results from Response Analyses for 2,153 Combinations of Site Conditions and Ground Motions, Superimposed with Heavier Lines Showing the Mean and + 1 Standard Deviation Values for the 2,153 Cases Analyzed (Cetin and Seed, 2004).

There are a few correlations for the MSF (Seed and Idriss 1982; Ambraseys 1988; Arango 1996; Andrus and Stokoe 1997; Youd and Noble 1997), and are compared in

Figure 2.20). MSF can also be derived by combining correlations of the number of equivalent uniform cycles versus earthquake magnitudes, and laboratory-based relations between CRR and number of uniform stress cycles (Boulanger and Idriss 2004).

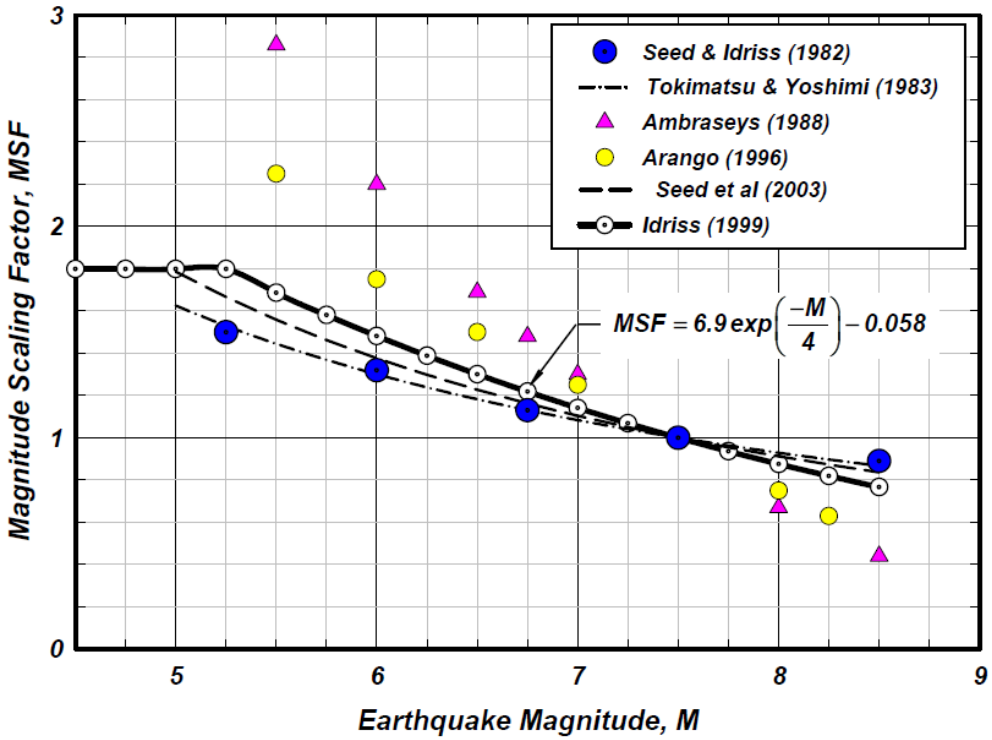

Figure 2.20: Comparison of the MSF relation for sands (Idriss and Boulanger 2004).

The MSF can also be evaluated from a given ground motion by transforming it into an equivalent number of cycle. Liu et al. (2001) developed a procedure for calculating the equivalent number of cycle at time t, $N_{eq}(t)$. By identifying the stress reversal (zero crossing) point, a random and transient ground motion is divided into a number of pulses, and the amplitude of each pulses can be determined and normalized. $N_{eq}(t)$ is estimated by

scaling in accordance to the scheme of Seed (1975) and summing the amplitudes of pulses. Knowing the development of $N_{eq}(t)$, Liu et al. (2001) came out with an evolutionary MSF(t) correlation by considering both laboratory data and field evidence:

$$MSF(t) = \exp[1.3 - 0.41*\log(N_{eq}(t))] \qquad [2.10]$$

Alternatively, Idriss and Boulanger (2004) recommends a MSF(t) correlation related to $N_{eq}(t)$ that is only based on laboratory data:

$$MSF(t) = \left(\frac{N_{M=7.5}}{N_{eq}(t)}\right)^b \qquad [2.11]$$

where b is a curve fitting parameter of the CSR versus number of cycles to liquefaction curve under harmonic loading. Idriss (1999) suggested b = 0.337 for clean sand. N_M=7.5 is number of uniform cycles for M = 7.5, and is equal to 15. With the MSF, the duration-corrected cyclic stress ratio can be calculated as:

$$CSR_{M=7.5} = \frac{CSR}{MSF} \qquad [2.12]$$

Since N_{eq} (t) can be calculated in a form of summation over time, so does the MSF factor. The MSF factor decreases with increasing the number of loading pulse in a given ground motion. The two parameters, MSF(t) and maximum peak ground acceleration (a_{max}) can be combined in to an evolutionary intensity measure, PGA_m:

$$PGA_m(t) = \frac{\max(a(t))}{MSF(t)} \qquad [2.13]$$

Since the recent improved procedures for determination of equivalent cycles for individual ground motions (Liu et al., 2001; Green and Terri 2005), the new methods offer a potential for more accurate, motion-specific characterization of earthquake loading. In fact, other than PGA, there are many alternative analytical approaches to characterize liquefaction loading from a given ground motion, which termed as Intensity Measures.

2.10 INTENSITY MEASURES (IMS)

Many researchers have proposed different analytical approaches to characterize earthquake loading. Up to the present time, the most widely adopted practice in geotechnical earthquake engineering, CSR-approach is presented in section 2.6. In fact, there are other paths to tackle the problem, and offer potential ways for improving the evaluation of liquefaction hazard. In the following section, three other intensity measures are presented: 1) Arias Intensity, 2) cumulative absolute velocity, and 3) normalized energy demand. Those methods generally require integrations of a particular form (acceleration, velocity, or energy) over the time domain of given ground motions, analogizing the build-up of excess pore pressure or cumulative damage of earthquake loading. Although the other methods may require more computation work, they are more informative and can potentially evaluate the liquefaction effect as compared to the CSR-approach. The use of performance-based earthquake engineering (PEBB) would accelerate the trend of IM application. Instead of evaluating a single "worst-case" scenario, a few to hundreds of ground motions are considered in the framework of PEBB. IM such as CAV_5 has been proven to be an efficient predictor (Kramer and Mitchell 2006), and therefore greatly reduced the uncertainty in performance-based evaluation of liquefaction hazard.

The effects of liquefaction hazard (e.g., induced lateral spreading and settlement) are mainly triggered by the loading that occur after liquefaction initiation. A recent numerical study, Abegg (2010), emphasizes the importance of identifying the timing of liquefaction. Therefore, IMs to characterize earthquake ground motions are divided into pre- and post-liquefaction components, and provid better prediction in the pre- and post-liquefaction effects. Due to the dramatic change of soil properties, the best IM for predicting pre-liquefaction soil response is not necessary the same as the best IM for predicting post-liquefaction effect. Abegg (2010) has numerically proven that I_a and CAV_5 are the efficient and sufficient IMs for correlating the pre-liquefaction effect, pore pressure ratio, and CAV_5 is the most efficient and sufficient predictor of liquefaction-induced ground surface lateral displacement.

2.10.1 Arias Intensity

Kayen and Mitchell (1997) proposed a ground motion parameter, Arias Intensity (I_a) for evaluation of liquefaction potential by quantifying the earthquake shaking intensity. I_a encompasses both amplitude and duration of earthquake motion; therefore, it leads to a single parameter for the liquefaction evaluation. On the contrast, the CSR-approach requires two separated parameters, PGA and MSF. The authors claim that the approach does not require arbitrary magnitude correction factor(s). The cumulative arias intensity adds up both orthogonal-horizontal (x-y) components of motion (I_h):

$$I_h = I_{xx} + I_{yy} = \frac{\pi}{2g}\int_0^{\infty} a_x^2(t)dt + \frac{\pi}{2g}\int_0^{\infty} a_y^2(t)dt \qquad [2.13]$$

where, I_h represents the sum of the two-component energy per unit weight and is given in units of length per time. a(t) is the horizontal acceleration time history in the correspondent direction. Finally, g is the gravity.

A liquefaction curve which resembles the CRR curve in the CSR-approach (IM vs. density) was also developed by Kayen and Mitchell (1997). The curve serves as a borderline separating a series of case histories of liquefied soils versus soils that didn't liquefy during earthquakes. Therefore, the susceptibility of liquefaction can be computed in a form of factor of safety: F.S. = I_{hb} / I_h. This procedure characterize a given motion entirely as a static value, without separating the pre- and post-liquefaction components, disregarding the timing of liquefaction.

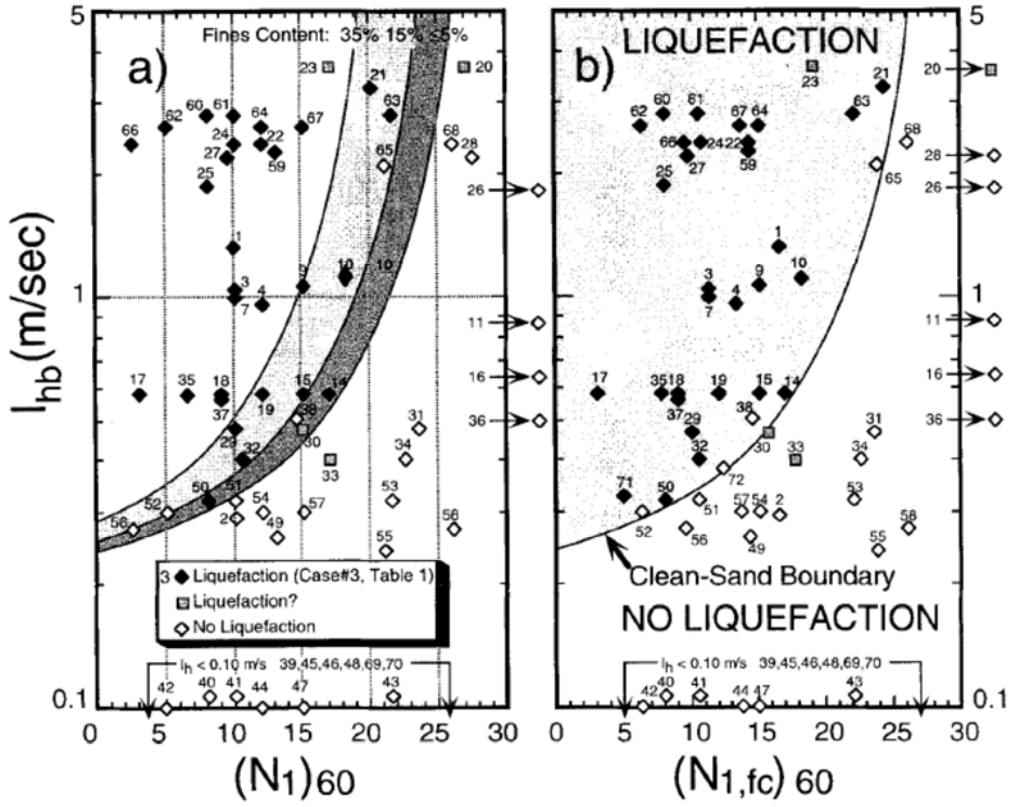

Figure 2.21: Liquefaction curve developed by Kayen and Mitchell (1997). (a) Plot without Fines Content Correction; (b) Plot with Fines Correction to Equivalent "Clean Sand". I_{hb} is the Arias Intensity required to trigger liquefaction.

$$\log(I_{hb}) = 1.234 \cdot 10^{-6}\left(N_{1,60cs}\right)^5 - 6.956 \cdot 10^{-5}\left(N_{1,60cs}\right)^4 + 0.001421\left(N_{1,60cs}\right)^3 - 0.01132\left(N_{1,60cs}\right)^2 + 0.04162\left(N_{1,60cs}\right) - 0.6227 \quad [2.14]$$

2.10.2 Cumulative Absolute Velocity

Kramer and Mitchell (2006) reported a new ground motion intensity measure, CAV_5, and suggested it is more closely related to excess pore pressure generation in potentially liquefiable soils than other intensity measures, including peak acceleration and Arias intensity. CAV_5 is a ground motion parameter integrating the absolute value of

acceleration over the time domain of the history, and the subscript $_5$ means a 5 cm/sec^2 threshold acceleration. An amplitude of less than 5 cm/sec^2 is not considered because the small acceleration in the ground motion records have little effect on pore pressure generation. The common unit for CAV_5 is in cm/sec, and is defined as:

$$CAV_5 = \int_0^\infty \langle \chi \rangle \, |a(t)| dt \;\; where \; \langle \chi \rangle = \begin{cases} 0 \; for \; |a(t)| \leq 5 cm/sec^2 \\ 1 \; for \; |a(t)| \geq 5 cm/sec^2 \end{cases} \qquad [2.15]$$

Like Arias intensity, CAV_5 also only requires one parameter. Besides, the theory of wave propagation (i.e. $\nu = \varepsilon_x v_p$, where ν is particle velocity, ε_x is strain and v_p is the wave propagation velocity) shows that the particle velocity is related to shear strain, which has been proven to have significant impact on pore pressure generation (Dobry et al. 1982). By evaluating nearly 300 intensity measure candidates through the response of nine different soil profile and more than 450 ground motions, Kramer and Mitchell concluded CAV_5 is an efficient and sufficient parameter, which produces little dispersion in predicting excess pore pressure, and is conditionally independent of magnitude and distance. Similarly, a liquefaction curve was also developed by the CAV_5 approach (Figure 2.22). The borderline, Equation 2.17, separates a series of case histories of either having liquefaction or no liquefaction by the earthquake. Therefore, the susceptibility of liquefaction can be computed in a form of factor of safety:

$$\text{F.S.} = CAV_{5,\text{ required for liq}} \; / \; CAV_{5,\text{ actual motion}}. \qquad [2.16]$$

The procedure disregarded the timing of liquefaction as if the I_a evaluation procedure. Entire ground motion is considered without breaking down into two components, pre-liquefaction and post-liquefaction.

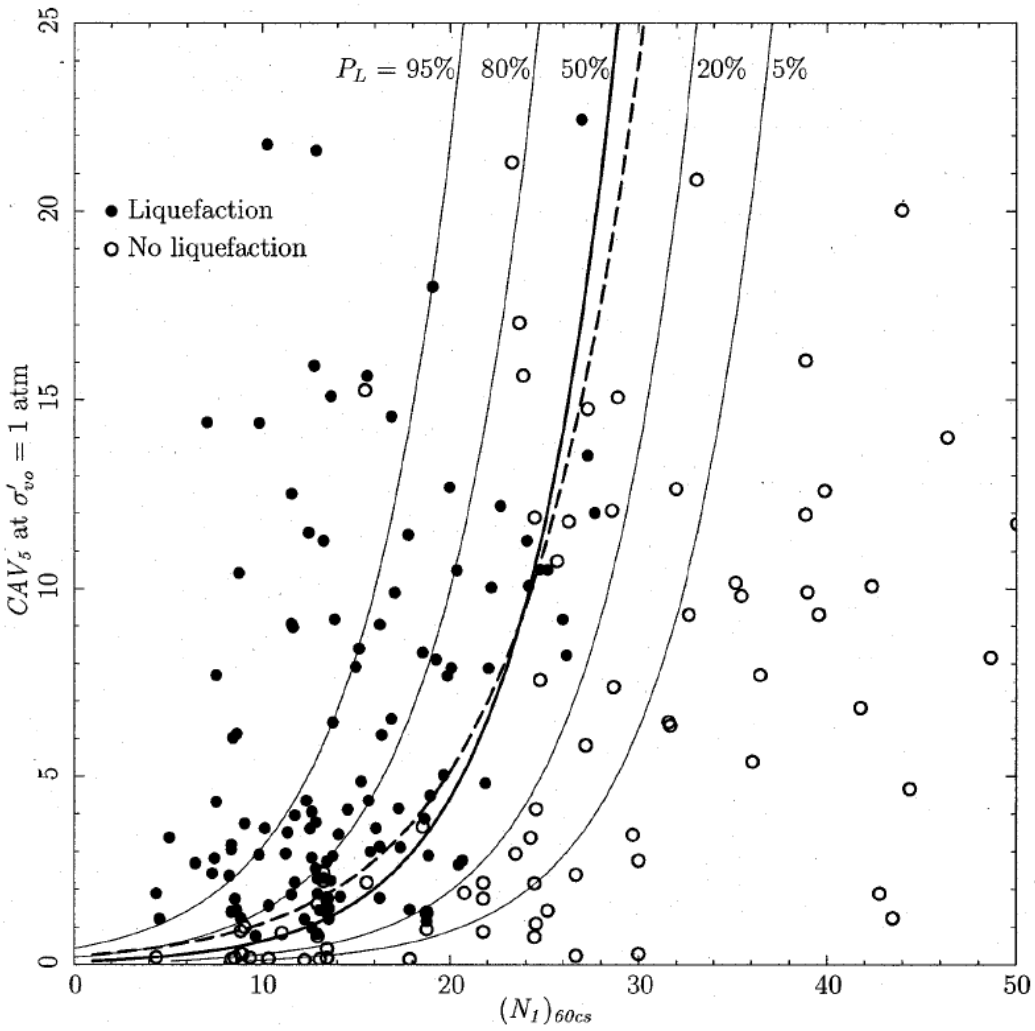

Figure 2.22: Liquefaction curve for CAV_5 (Mayfield 2007).

$$\ln(CAV_5) = \frac{N_{1,60cs} - 4.20\ln\left(\frac{\sigma'_{vo}}{p_a}\right) - 9.45}{6.47} \qquad [2.17]$$

2.10.3 Normalized Energy Demand (NED)

Green (2001) developed energy-based pore pressure generation models to evaluate liquefaction potential, which compares the energy dissipation by frictional mechanisms during relative movement of sand grains (Capacity) and the energy dissipated in soil during an earthquake (Demand). A linearized hysteretic model is adopted to calculate the energy dissipated in a soil element under cyclic loading. By this concept, NED, is calculated as the cumulative energy dissipated per unit volume (ΔW) of soil and normalized by the initial mean effective confining stress (σ'_{mo}). Figure 2.23 illustrates the dissipated energy per unit volume for an equivalent cycle of loading, which is the area of the hysteresis loop. Therefore, unlike CAV_5 and I_a, NED is not a ground motion parameter, but an interpretation from the soil stress-strain response. Green (2001) suggests using equivalent linear site response analyses to obtain the require soil response. The cumulative energy dissipated per unit volume of a soil element (ΔW_T) can be calculated by the trapezoidal rule:

$$\Delta W_T = \frac{1}{2}\sum_{i=1}^{n-1}(\tau_{i+1} + \tau_i)(\gamma_{i+1} - \gamma_i) \qquad [2.18]$$

where, τ_i is shear stress at the i^{th} cycle, γ_i is shear strain at the i^{th} cycle, and n is the number of cycle in a given cyclic motion.

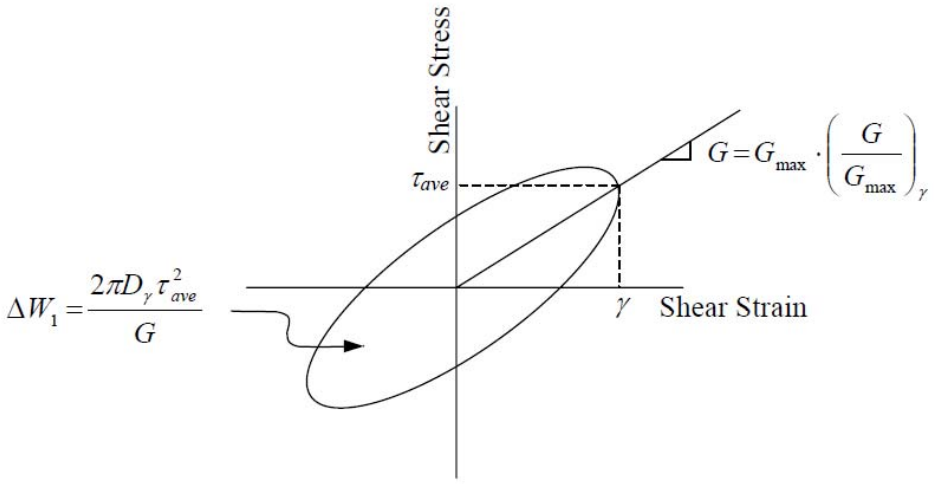

Figure 2.23: Calculation of dissipated energy for a loading cycle (Green 2001).

Green (2001) also reported a liquefaction curve and developed an empirical approximation (Equation 2.19) that is based on 126 earthquake case histories, separating those with occurrence of liquefaction from those without it. The intensity measure, NED, is plotted against SPT N values (Figure 2.24), and the liquefaction curve is interpreted as the normalized energy capacity (NEC). As a result, the susceptibility of liquefaction can be computed in a form of factor of safety: F.S. = NEC / NED.

$$NEC = 1.195 \cdot 10^{-4} \exp\left(0.185 \cdot N_{1,60CS}\right) \qquad [2.19]$$

Like the other two procedures above, the NED liquefaction evaluation does not take the timing of liquefaction into account. Entire ground motion is considered.

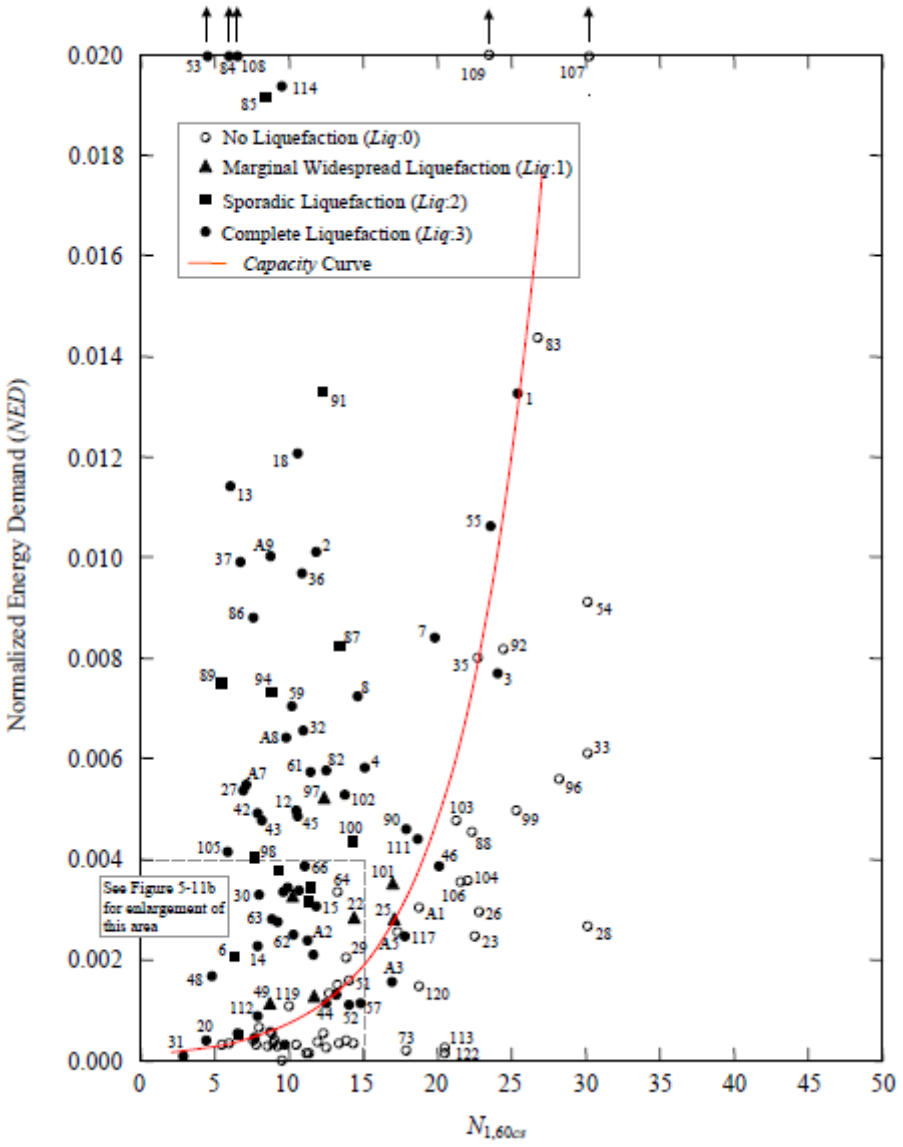

Figure 2.24: Energy-based Capacity curve based on 126 earthquake case histories (Green 2001).

2.11 CONCLUSION

In current practice, the potential for liquefaction is commonly evaluated as the ratio of soil resistance to earthquake loading, in a form of factor of safety, F.S. = CRR/CSR.

Clearly, the CSR-based procedure can only give a binary outcome, liquefied or not liquefied, and cannot provide in-depth evaluation, such as the likelihood of hazard and liquefaction effects. This approach worked well in the early days when evaluation of liquefaction was based on a deterministic approach using singular "worst-case" scenario. However, such an approach is no longer desirable within the new Probabilistic Seismic Hazard Analysis framework where many different earthquake scenarios can contribute to the seismic hazard for a given site. Additionally, it cannot capture all aspects of the complicated time-domain characteristics of ground motions. This dissertation presents a set of high-quality experimental data that systematically illustrate the response of soils subjected to transient ground motion (instead of an equivalent number of harmonic loading cycles). Such tests can help improve current liquefaction evaluation procedure by incorporating time characteristics of ground motions, and can also aid in the calibration of constitutive models for liquefiable soils.

Chapter 3: Simple Shear Testing Program

3.1 INTRODUCTION

The testing program that focus on earthquake loading characterization consisted of a series of multi-stage undrained direct simple shear tests performed on loose to dense, saturated, and reconstituted cohesionless specimens. This testing program was designed to evaluate the soil responses under undrained transient loadings, and the consequent stress-strain behavior after liquefaction has occurred. Distinct ground motions were selected to represent earthquake motions with different time domain characteristics. Element-level data that systematically illustrates the response of soils subjected to transient ground motion is virtually non-existent in the literature and the current research provides the earthquake geotechnical engineering community with a much needed data set.

The simple shear tests were conducted in three stages, consisting of different types of loadings: (1) Scaled transient stress histories, (2) modulated sinusoid with a taper-up shape stress histories, (3) static monotonic loading (Figure 3.1). All stages were performed under undrained condition without allowing any drainage in between stages. Stage 2 was skipped if liquefaction occurred during stage 1's loading.

The objectives of this testing series are twofold. Firstly, the test results provided insights into soil behavior before and after liquefaction. Secondly, the high-quality experimental data is critical for the development of an improved, more informative procedure for evaluation of liquefaction potential and post-liquefaction damage. In order to meet these objectives in the laboratory, both the specimen and the imposed loading must replicate the in-situ condition as closely as possible. Obtaining "undisturbed" samples is not economically feasible for this study; therefore, specimens were reconstituted using the

method of water sedimentation, which closely simulates the natural depositional processes. This chapter presents an overview of cyclic simple shear testing apparatus, testing program for this study and specimen preparation procedures.

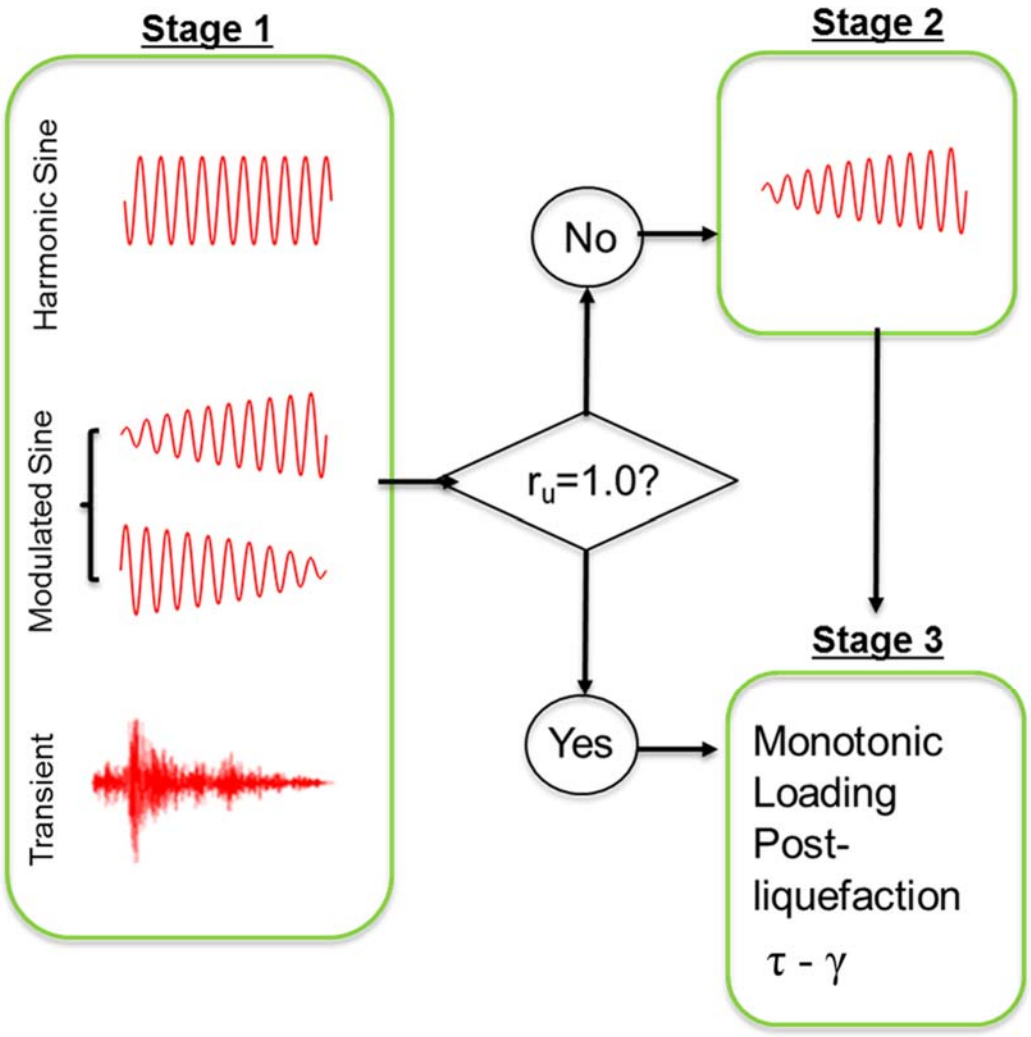

Figure 3.1: Stages of the CSS testing program.

3.2 LABORATORY CYCLIC ELEMENT TESTING

Liquefaction of loose, saturated sand has been the topic for extensive laboratory research over the past 50 years. Cyclic loading due to upward propagating shear waves generate excess pore pressure within saturated soils during seismic events. The upward propagating dynamic shear waves produce an irregular shear stress history of various frequencies and amplitudes in the soils. The duration of the seismic loading is usually assumed to be short enough to prevent drainage, even for clean granular deposits. Specific details of the mechanisms by which soil liquefaction develops were studied using laboratory testing. Cyclic triaxial (CTX), torsional, and cyclic simple shear (CSS) tests are the most commonly used methods for soil element-level cyclic testing.

3.2.1 Simple Shear

CSS testing is used for this project, so the mechanism of simple shear is discussed here, and the comparisons of simple shear versus triaxial and torsional test are covered in the latter sections. The applied loading on a soil element in multiple practical situations can be simulated using the simple shear test (Figure 3.2), such as the bottom part of a slope slip surface and upward propagating seismic shear wave.

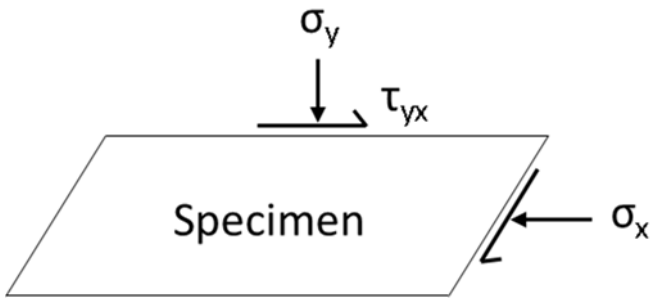

Figure 3.2: Components of simple shear stress

The essential requirements for simple shear are uniform strains along the height of the specimen and plane strain (no strains in the plane perpendicular to the direction of shear loading), both of which are typically achieved by rigid lateral confinement. Rubber membrane reinforced with a spiral winding of wire or Stacked Rings are commonly used for lateral confinement. Despite that the plane strain condition is well maintained at the consolidation stage, Roscoe (1953) has proven the shear stresses at the specimen's top and bottom could be non-uniform during the shearing stage. The normal stress could also be non-uniformly distributed (Figure 3.4). The non-uniformities are severe at the edges. This shortcoming can be explained by the lack of complimentary shear stresses on the sides (Figure 3.3). While the shear stress is applied from the top or bottom platen, there is no method to impose a balance shear stress at the sides. Past research projects have proven that the imbalance in forces create a tendency for the soil specimen to rock during the cyclic loading or tilt in monotonic loading (Franke et al. 1979; Vucetic and Lacasse 1982).

The rocking problem can be minimized by using a larger diameter to height ratio (D/H) of specimen. Amer et al. (1987) compared saturated sand specimens with D/H ratio range 3 to 12 and found similar results. Similarly, the effect of the absence of complimentary shear stresses can be significantly reduced with a D/H greater than four. A D/H of greater than four is used in this project. Besides, a larger D/H ratio can reduce the potential problem of pore pressure redistribution within the sand specimen, particularly with a slow loading rate.

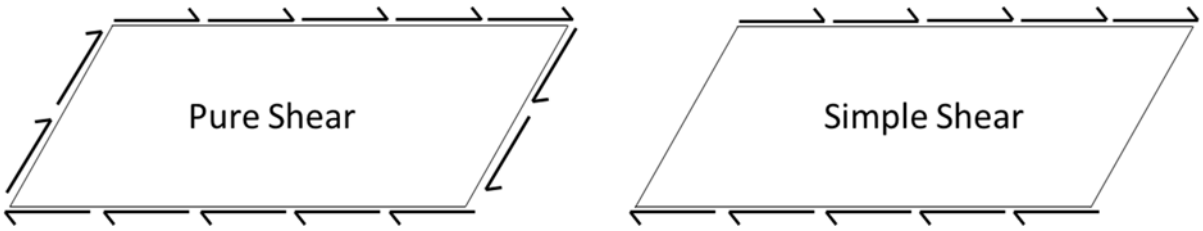

Figure 3.3: Pure Shear vs. Simple Shear

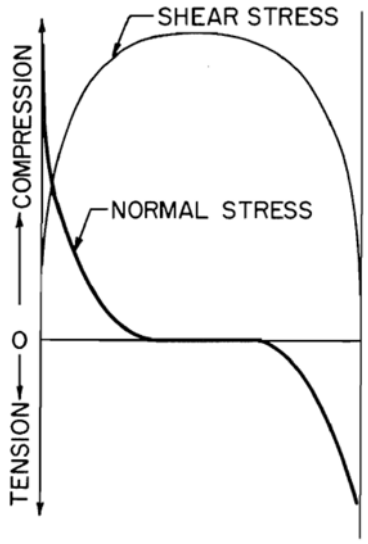

Figure 3.4: Distribution of stresses in simple shear from elastic analysis (Roscoe 1953)

Figure 3.5 illustrates the physical modeling of seismic loadings in a cyclic simple shear setup. Prior to a seismic event, a soil element is in a "at rest" condition, which is experiencing a vertical overburden stress without lateral strain, since the horizontal direction is infinitely long, compared with the vertical depth. This is also called "K_0 consolidation". To achieve the K_0 condition in a CSS setup, a soil specimen is consolidated

under a normal load, and constrained with a horizontal confinement, such as stacked rings (Figure 3.5a). The soil specimen is bounded by the top and bottom platens. The top platen is constrained in the horizontal direction but free to move along the vertical direction. The bottom platen is mounted on a shaking table that connected to an actuator.

During a seismic event, a series of upward shear waves propagate through a soil element (Figure 3.5b), which is modeled by applying cyclic loadings at the bottom platen through the roller base shaking table. The relative movement between the bottom platen and top platen is measured, and therefore the corresponding shear strain can be calculated. Because of the rapid dynamic loading, there is no time for the excess pore pressure to escape between the soil pore spaces. This phenomenon is simulated by undrained loading in the CSS setup, of which the drainage is prevented during cyclic loading and the excess pore pressure inside the soil specimen is measured. Liquefaction initiation is commonly defined as the generated excess pore pressure is equal or very close to the effective vertical confining pressure (i.e. $r_u = 1.0$).

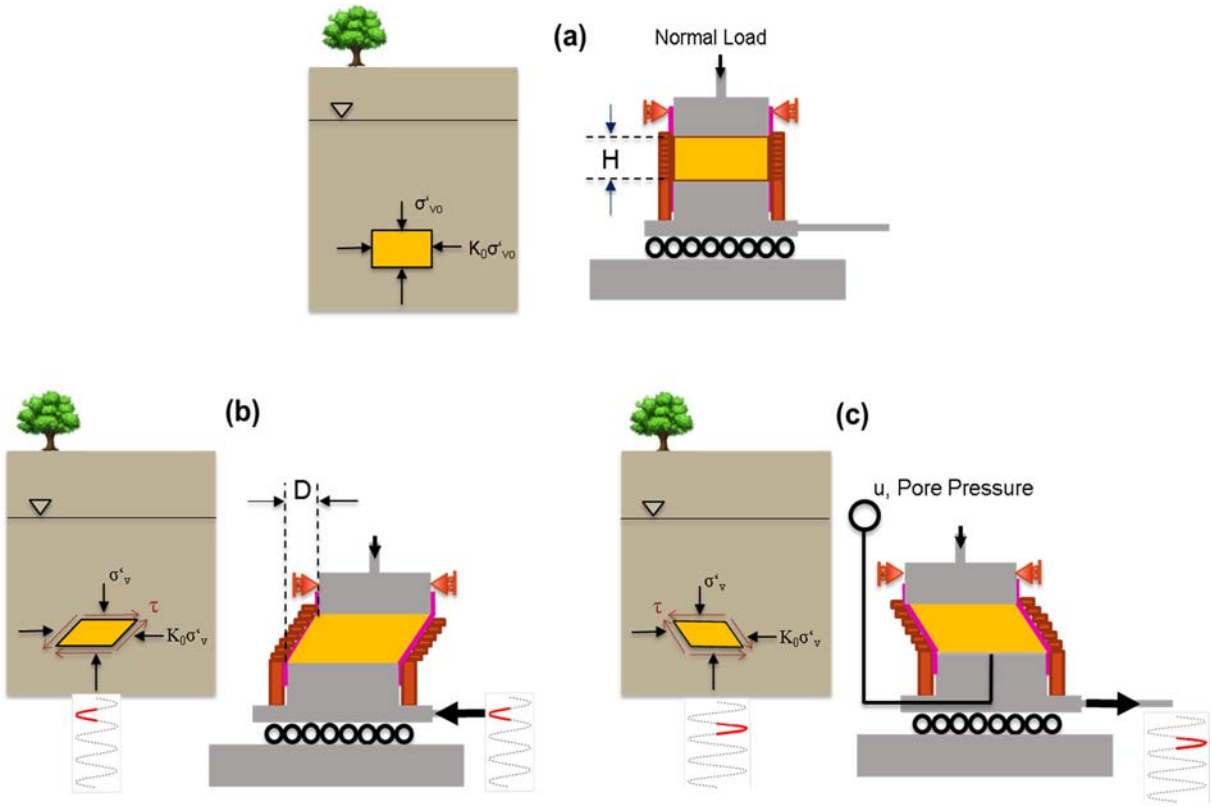

Figure 3.5: Illustration of cyclic simple shear modeling. (a) at rest condition (b) during seismic loading (c) stress reversal.

3.2.2 Cyclic Simple Shear Test vs. Cyclic Triaxial Test

Cyclic triaxial equipment was first used to evaluate liquefaction (Seed and Lee 1966; Castro 1969). CTX still remains popular nowadays, because it is widely available and is the simplest to operate among the available test types. Nevertheless, it is a well-accepted fact that CSS test provides better simulations of in-situ stresses for seismic hazard evaluation than CTX because it is capable of producing a more accurate representation of the seismic loading conditions that occur in the field (Boulanger et al. 1993). The 'simple shear' mechanism allows the principal stress axes to rotate smoothly during cyclic loading,

as compared to the CTX where the principal axes instantaneously rotate 90 degrees upon loading reversal (Figure 3.6). Another advantage of CSS over CTX is the relatively high diameter to height ratio (D/H ≥ 4), which allows for a relatively uniform stress field within the active portion of the sample and minimizes the pore pressure redistribution due to cyclic loading. CSS testing also allows for K_0 consolidation to prevent any lateral strain during consolidation. Instead of applying cell pressure through a non-reinforced latex membrane, lateral confinement in simple shear is attained through the use of NGI-type wire-reinforced latex membranes or stacked rings. Because of the different mechanisms, the CSS and CTX impose different loading stresses, and the cyclic stress ratios used in the tests are different. Idriss and Boulanger (2008) reported a correlation of cyclic resistance ratio (CRR) between the simple shear (SS) and isotropically consolidated undrained (ICU) triaxial (TX) test:

$$CRR_{ss} = \left(\frac{1+2(K_0)_{ss}}{3}\right) CRR_{TX} \qquad [3.1]$$

where K_0 is the coefficient of lateral earth pressure at rest. For normally consolidated sand, K_0 would be about 0.45 to 0.5.

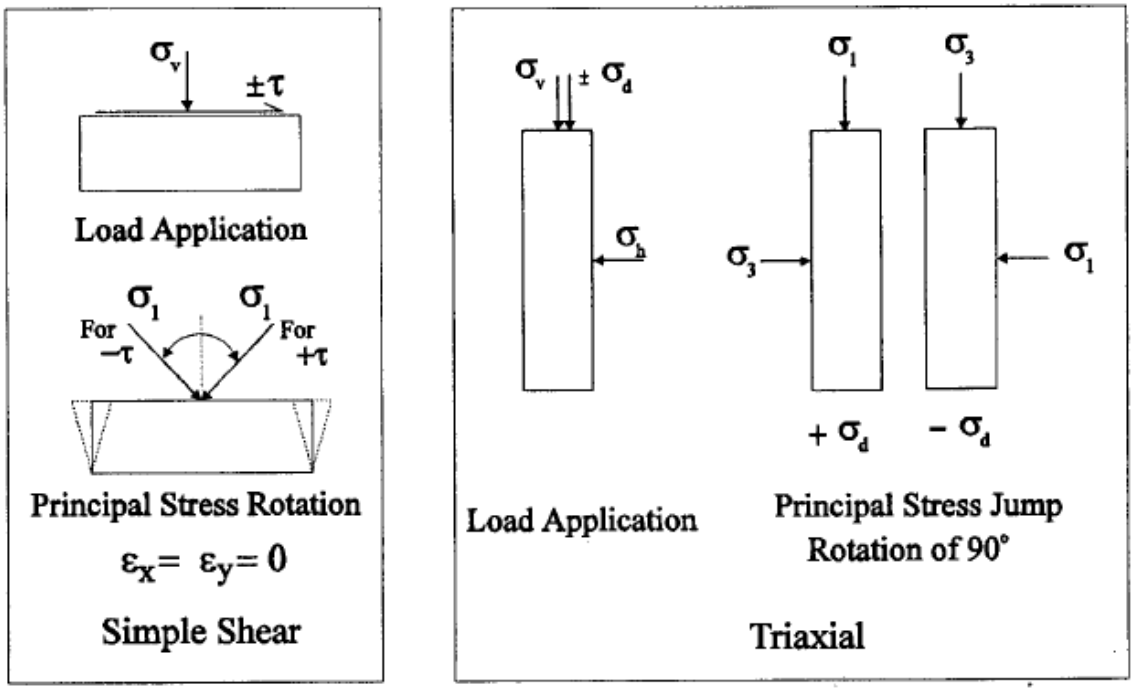

Figure 3.6: Simple shear and triaxial loading conditions (Sivathayalan 1994).

3.2.3 Cyclic Simple Shear Test vs. Cyclic Torsional Test

The CSS test provides a better stress-uniformity over the width of specimen than cyclic torsional test. Figure 3.7 illustrates the stress and strain condition in torsional simple shear; Figure 3.8 shows a torsional shear apparatus. Non-uniform stress distributions in simple shear apparatus were reported (Saada 1983) because of the lack of complementary shear stresses at the vertical boundaries. However, this shortcoming can be improved by increasing the specimen's diameter to height ratio (D/H). A D/H ratio greater than four was used for this study. The selected D/H ratio is consistent with many recent cyclic simple shear testing research (Boulanger et al. 1991, Kamerer 2002, Wu 2002, and Hazirbaba 2005). On the other hand, the torsional force may provide a highly non-uniform stress distribution to the specimen. When shearing a cylindrical specimen, the developed strains

are zero at the center and reaches maximum at the edge. The hollow cylinder configuration of the cyclic torsional test was designated to address this problem. However, the hollow configuration increases the specimen's boundary area significantly, which may generate greater stress non-uniformity at large strain levels. Moreover, the D/H ratio for cyclic torsional test is typically low. Therefore, pore pressure redistribution is a potential problem when the tall specimen is being sheared from the top. Pore pressure redistribution may cause "local" densification, and make the overall specimen density to be non-uniform.

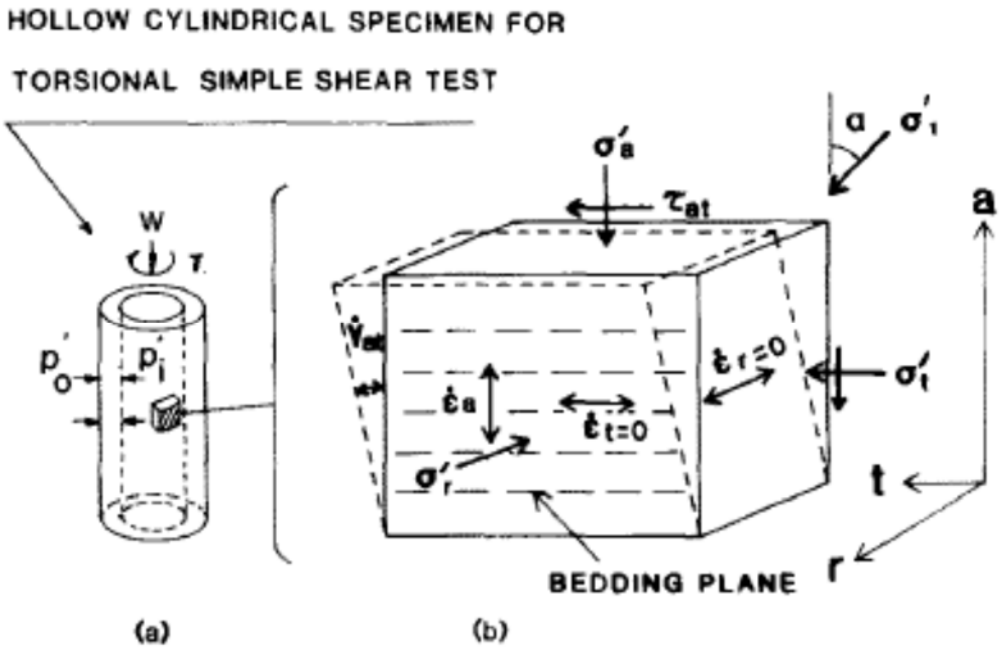

Figure 3.7: Stress and strain condition in torsional simple shear specimen (Tatsuoka et al. 1989).

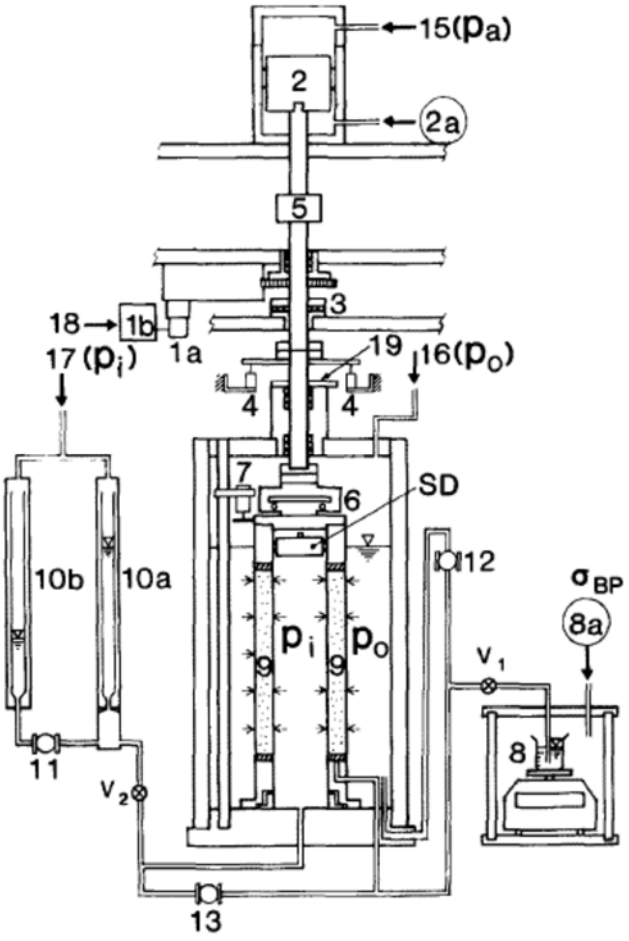

Figure 3.8: Torsional shear apparatus (Tatsuoka et al. 1989).

3.3 CYCLIC ELEMENT TEST WITH IRREGULAR LOADINGS

In the past two decades, a number of element level liquefaction research projects were performed in cyclic simple shear setting, mainly because of its advantages over the other two equipment discussed above. Out of these testing, a significant improvement was made on upgrading the loading capacity from uni-directional to bi-directional, which provided a better simulation of sloping ground (K_α condition) and seismic loading (Ishiara

and Yamazaki 1980; Boulanger et al. 1993; and Rutherford 2012). Nevertheless, a large majority of testing in the past were limited to harmonic sinusoid wave loading. Liquefaction resistance is represented by the number of cycles that the soil sample can withstand. This approach works well when comparing the liquefaction resistance of different soil specimens. However, the characteristic of excess pore pressure generation is limited to linear increase rate (except the first cycle), and deformation (shear strain) is restricted to a symmetrical harmonic sinusoid response. On the other hand, the response of saturated sands under transient loadings is closely related to the time domain characteristic of the input motion. A harmonic sinusoid series would overlook the complicated spectral and temporal characteristic of a ground motion. Therefore, translating a transient ground motion time history into a series of uniform shear stress cycles is oversimplifying the complexity of earthquake loading.

Japanese researchers, Dr. Fumio Tastsuoka and his colleagues, conducted some research programs investigating undrained stress-strain behavior of sand subjected to irregular or earthquake loadings (Tastsuoka and Silver 1981; Tastsuoka et al. 1982a; Tastsuoka et al. 1982b; Tastsuoka et al. 1986 and Pradhan et al. 1988). Numerical models were developed to predict the maximum and time history of shear strain amplitude under a given earthquake or modulated sinusoidal loading. In order to validate the numerical models, limited number of cyclic torsional simple shear tests were conducted with two recorded ground motions. Tastsuoka and Silver (1981) tested the specimen prepared by the method of wet tamping by running cyclic simple shear tests. However, the testing method was limited to constant volume test and the specimens were consolidated without lateral confinement. Also, the number of test is limited because the testing program from previous research work was used to prove or validate a particular formulation or proposed model(s). Therefore, each of the previous cyclic element testing programs under non-uniform load

consisted of only a few tests. Figure 3.9 displays one of such test. A testing program providing high-quality experimental data that systematically illustrate the response of liquefiable soils to transient ground motions is in need.

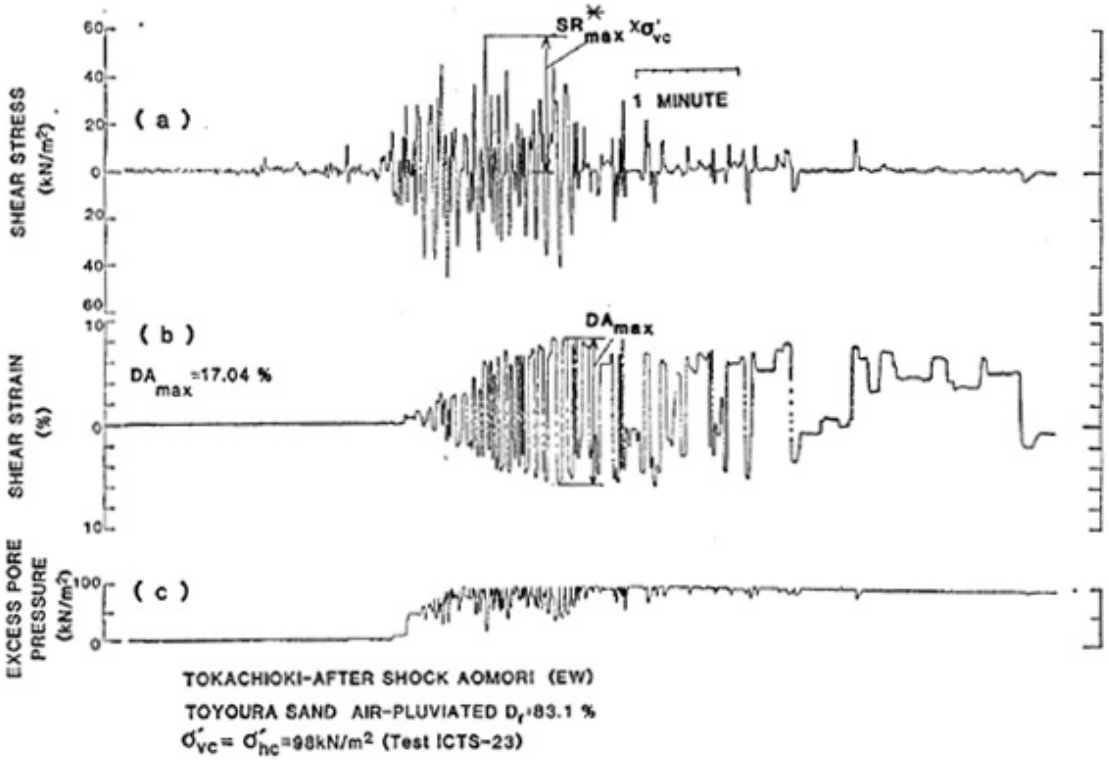

Figure 3.9: A test result from a cyclic torsional shear apparatus under irregular loading. (a) shear stress, (b) shear strain, and (c) excess pore pressure. Toyoura Sand of Dr = 83.1% (Tatsuoka et al. 1986).

3.4 THE UT MODIFIED GCTS CYCLIC SIMPLE SHEAR SYSTEM

The University of Texas (UT) Cyclic Simple Shear Apparatus (Figure 3.10) was used for this research project. This device was originally manufactured by the Geotechnical Consulting and Testing System (GCTS). The system is operated by a computer using a window-based program, and uses a closed loop, electro-hydraulically actuated, servo valve that controls shearing in the horizontal direction at the bottom of the specimen under load or displacement controls. The apparatus accepts four-inch diameter specimens, and was designed to impose a chamber pressure, which allows for conventional back-pressure saturation procedure (a unique feature that is not available in most CSS setups and therefore, allows for running true undrained tests rather than constant volume tests). The apparatus was originally set up at UT for a cyclic strain-controlled testing program, and is documented in Hazirbaba (2005).

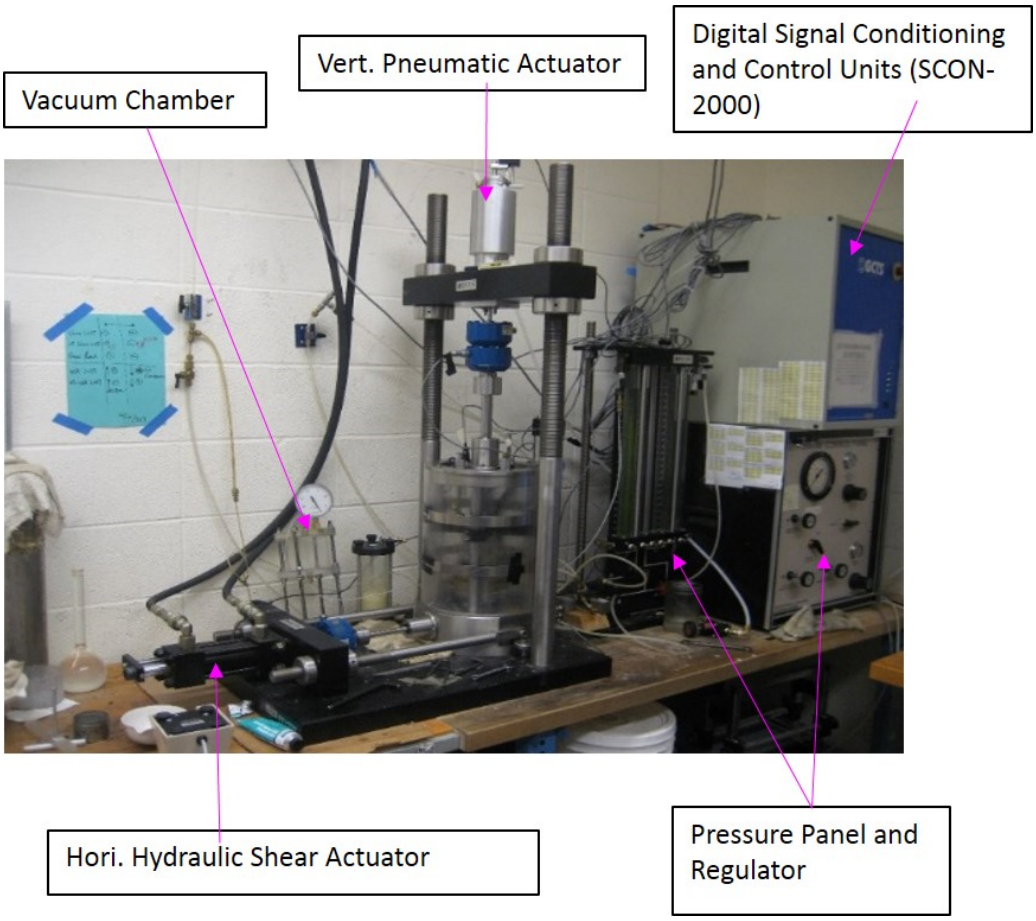

Figure 3.10: The UT modified GCTs Cyclic Simple Shear (UTCSS) Apparatus

3.4.1 Upgrades on the UT Cyclic Simple Shear (UTCSS)

The original GCTS Model SSH-100 Cyclic Simple Shear apparatus was operated by a DOS-based program, and contained a servo valve that digitally controlled three closed loops (axial load, shear load and cell pressure). Also, the apparatus was designed for an alternation of converting to a cyclic triaxial set-up, so that axial and shear loads were both hydraulically actuated. In order to improve the performance of the horizontal shear actuator

and add the capacity of applying user-specified, transient loading histories to the soil samples, the following changes and upgrades were made:

1. The new digital electronics (SCON-2000) replaced the old analogue signal conditioners. The main feature of this upgrade was to allow the system applying desired loading histories at frequencies of up to 20 Hz under stress- or strain-controlled conditions. The new system allows for "on the run" adjustment of the gain factors to account for the reduced specimen stiffness after liquefaction.
2. The axial hydraulic actuator was replaced by an axial pneumatic piston, and the cell pressure changed to manual control from servo valve control. This change maximized the performance of the horizontal shear actuator, as the horizontal shear actuator became the only closed loop of the system. The pneumatic piston vertically provided more stable static load than the hydraulic actuator as the pneumatic piston was able to maintain the vertical stress constant as the cyclic loading was applied and reduced the changes in vertical stress due to specimen rocking (the hydraulic actuator stiffness is too high compared to the pneumatic piston and resulted in higher changes in vertical stresses due to minimal vertical rocking).
3. The cell and pore pressure transducers configuration was redesigned. The old configuration had a section of pressure panel that had softer tubes, and the tubes were expanding under pressure in undrained condition (the original design had the tubes extending about 12 inches outside the cell to the pore pressure and cell pressure sensors). The compliance of the tubes led to lower B-values, since the excess pore pressure could not be maintained within the soil specimen. Therefore, the softer tubes were removed and the transducers were moved as closely to the chamber as possible (Figure 3.10).

4. The horizontal shear actuator assembly alignment was reconditioned and realigned. The shear roller assembly bearings were greased to reduce friction.
5. A new split mold for stacked was designed and manufactured for specimen preparation using stacked rings. More details are covered below in the specimen preparation method section.
6. A new aluminum bracket (Figure 3.13) was designed and manufactured to minimize bending of the top platen during shearing. Design drawing of the bracket is shown on Figure 3.9.

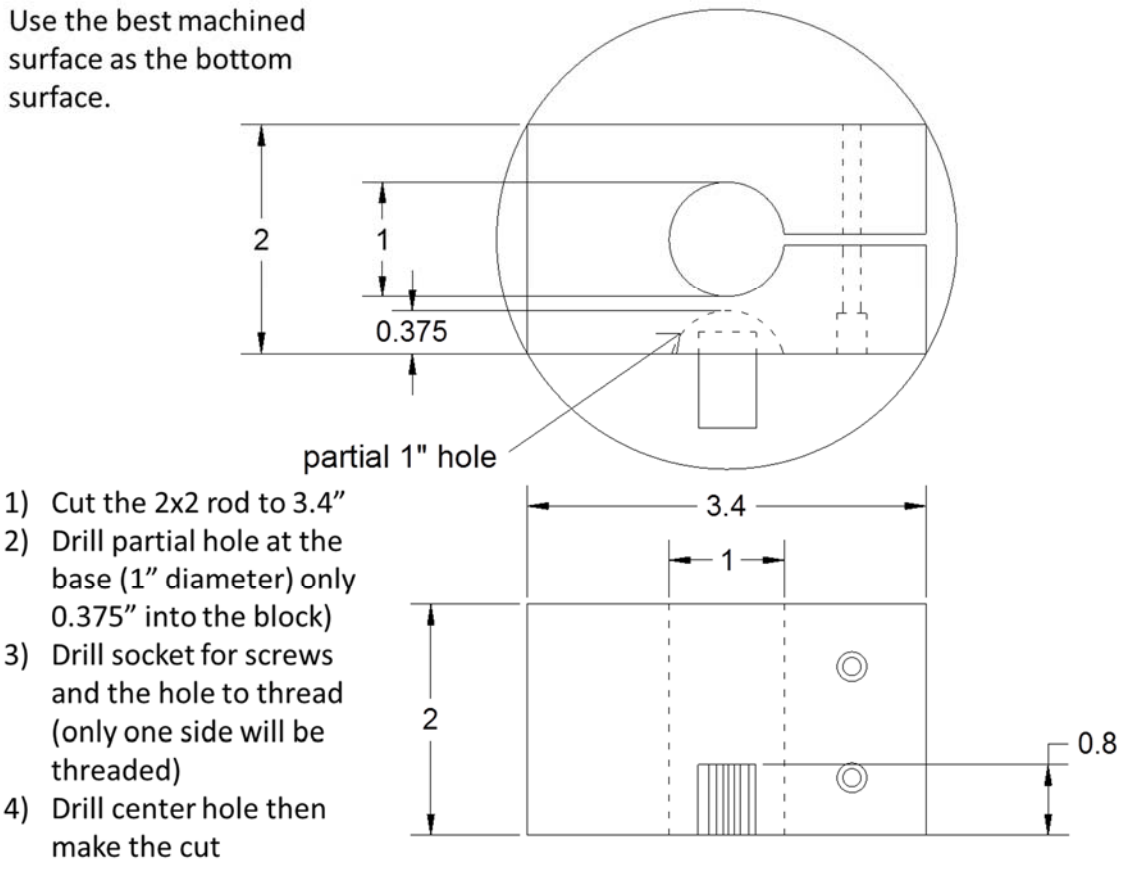

Figure 3.11: The design of the aluminum bracket for minimizing the rocking problem.

3.4.2 UTCSS Instrumentation

Table 3.1 summarized the instrumentation and Figure 3.14 illustrated the sensor configuration for this research project. There are two load cells: One is set up vertically outside the pressure chamber monitoring the applied vertical load; the other one is set up underneath the shear roller assembly to measure the horizontal shear load. Since the horizontal load cell is located inside the pressure chamber and under the soil specimen, the shear force measurement is not affected by the cell pressure (no need for out-push compensation). On the other hand, uplift compensation was included due to the cell pressure for the vertical load cell measurements. The detailed correction is discussed in section 3.9 below.

There are four linear variable differential transformers (LVDTs) for measuring displacements. Two of these LVDTs are placed externally parallel to the shear actuator assembly (horizontal) and the air piston assembly (vertical); the other two LVDTs (smaller range but better resolution) are positioned internally within the cell on the specimen itself for more accurate measurements. The internal vertical LVDT was used to monitor any volumetric change during consolidation and rocking of the top platen during shearing. Rocking is calculated by comparing the values between the external (positioned at the center of the specimen) and internal (positioned at the edge of the specimen, Figure 3.14) LVDTs. The internal horizontal shear LVDT was set up to measure the movement of the bottom platen relative to the top one. Chapter 5 reports detail calculation on rocking when the soil specimen is loaded under cyclic loading. Due to the potential of top platen rocking/tilting during shearing, relative movement between the two platens is a better representation of shear deformation than the displacement of the bottom platen. Therefore, a special design was used to measure the relative displacement between the two platens which consisted of an L-shape bracket attached to the top platen that extends to the

horizontal level of the bottom platen and serves as a reference for the internal shear LVDT (Figure 3.13).

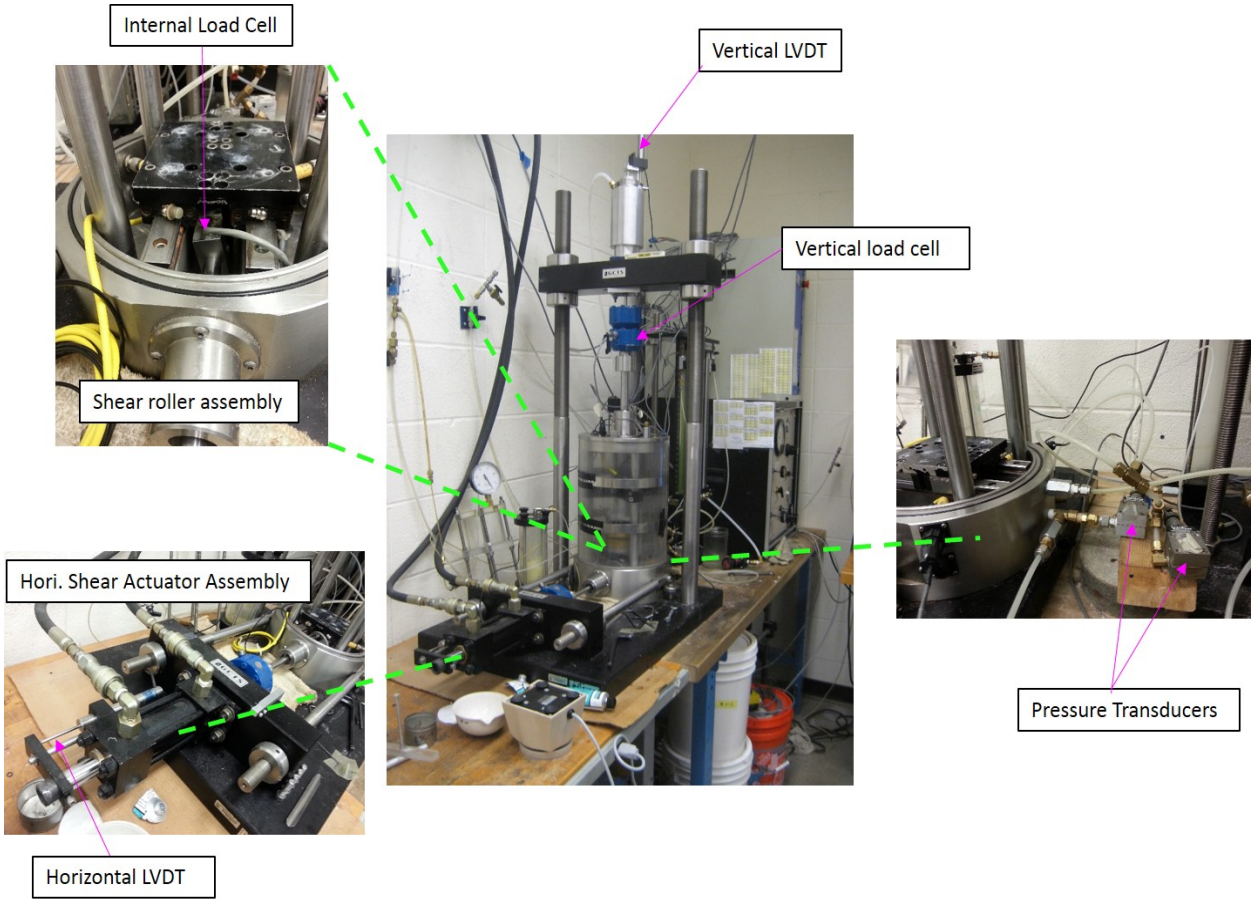

Figure 3.12: UTCSS instrumentation setup

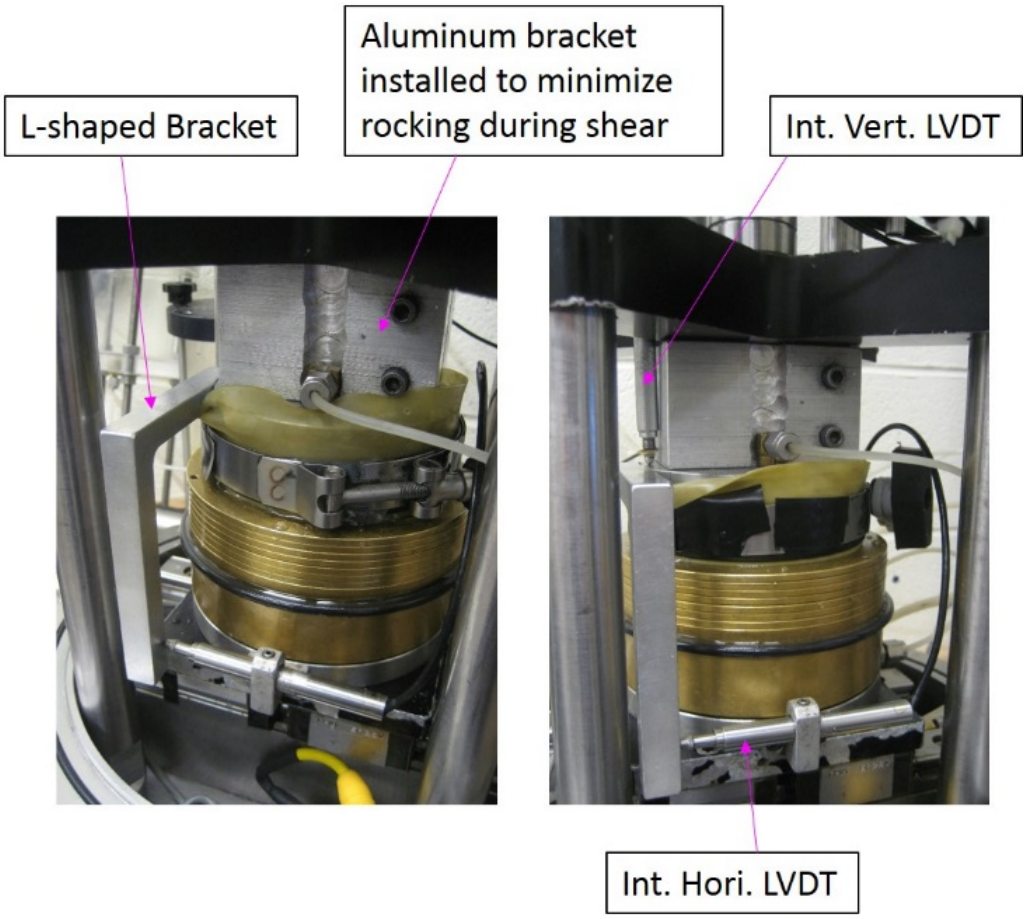

Figure 3.13: Internal Instrumental setup

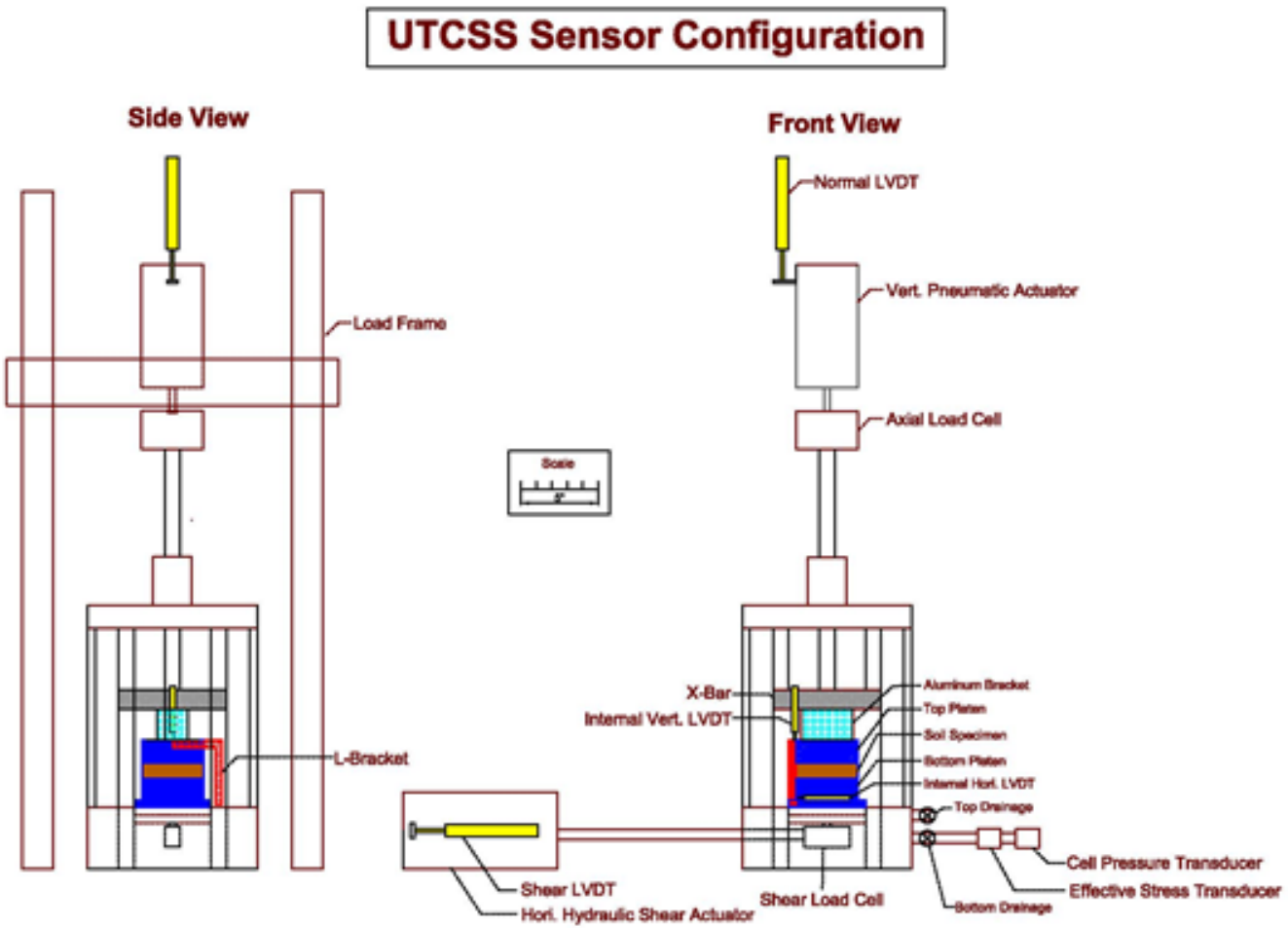

Figure 3.14: UTCSS sensor configuration.

There are also two differential pressure transducers for measuring the cell and "effective" pressures (Figure 3.14). The "effective" pressure differential transducer measures the difference between the applied cell pressure and the pore pressure at the base of the specimen.

Table 3.1: Instrumentation used for Simple Shear Testing

Measurement	**Instrument**	**Range±Sensitivity**
External Axial Deformation	Vertical LVDT	±25.4mm±0.02mm
External Shear Deformation	Horizontal LVDT	±25.4mm±0.02mm
Internal Axial Deformation	Miniature Axial LVDT	±5.0mm±0.0026mm
Internal Shear Deformation	Miniature Horizontal LVDT	±5.0mm±0.0026mm
Vertical Load	Load Cell	1000 lbs±0.50 lbs
Shear Load	Internal Load Cell	2000 lbs±1.00 lbs
Cell Pressure	Pressure Transducer	860 kPa ±2.15kPa
Effective Pressure	Pressure Transducer	140kPa±0.35kPa

3.5 TEST MATERIALS

All CSS tests were performed on Nevada Sand, a uniform, fine size, angular sand with a mean size of about 0.2 mm. The tested soil was obtained from Rensselaer Polytechnic Institute Center for Earthquake Engineering Simulation. This sand has been widely used for many centrifuge research projects at RPI including the tests performed in conjunction with this study; therefore, using Nevada Sand allowed us to compare the test results from this project with those obtained from the centrifuge testing. The sand properties are presented in Table 3.2 and the particle size gradations is shown in Figure 3.15. The minimum density of soil was determined by ASTM D4254; maximum density by ASTM D4253. Table 3.2 also compares the tested soil with that in other research projects using Nevada Sand (Kammerer et al., 2000 and Arulmoli et al., 199). Kammerer et al. (2000) used a different method, the modified Japanese method and the dry tipping method, to determine the minimum and maximum void ratio of Nevada Sand. According to the USCS, the tested soil (C_c = 1.13, C_u = 2) is classified as a uniform sand (SP).

Since water sedimentation was used for specimen reconstitution, a small amount of fines were separated before and after deposition (Figure 3.15); however, the effect of fines segregation is considered negligible.

Table 3.2: Properties of Nevada Sand

Source	G_s	$\gamma_{d,\,min}$ (KN/m^3)	$\gamma_{d,\,max}$ (KN/m^3)	e_{max}	e_{min}
Kammerer et al. (2000)	-	13.87	17.09	0.89	0.53
Arulmoli et al. (1992)	2.67	13.87	17.33	0.89	0.51
This Study	2.67	15.14	17.09	0.76	0.56

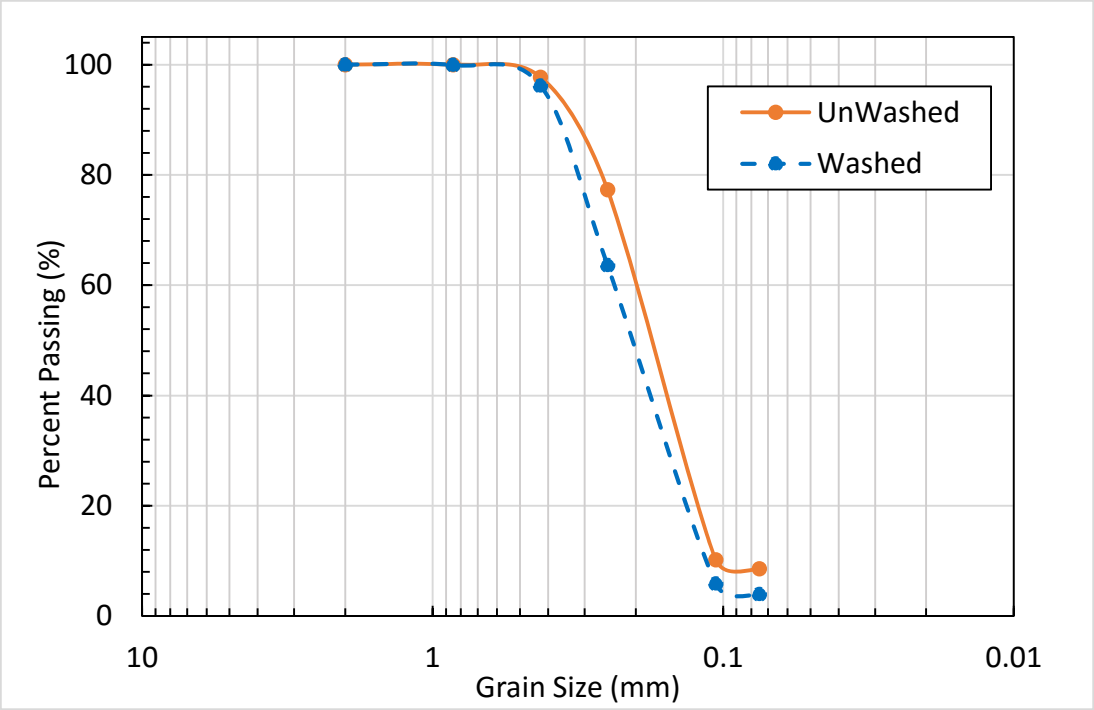

Figure 3.15: Grain size distribution for Nevada Sand before and after water sedimentation

3.6 USE OF STACKED RINGS AND THE NEW SPLIT MOLD

Instead of applying cell pressure through a latex membrane to achieve K_0 conditions, lateral confinement in direct simple shear testing is maintained through the use of NGI-type wire-reinforced latex membrane or stacked rings to provide lateral constrain while applying a vertical stress. WR is commonly used in academic liquefaction testing (Bjerrum and Landva, 1966; Boulanger et al., 1993; Kammerer et al., 2002), but is not the only option. Stacked rings (Ishihara and Yamazaki, 1980) are also available and attractively simple in sample preparation. In fact, the use of stacked rings has become more popular in engineering practice over the past ten to twenty years after automated simple shear apparatuses became commercially available. Stacked rings are usually sold along

with the commercial equipment for its cost effectiveness and durability. Baxter el al (2010) and Kwan and El Mohtar (2014) show that the two confinement systems provided comparable test results in direct simple shear testing on clays and sands, respectively. Considering the large amount of testing for this research project, the use of stacked rings was a more sustainable choice than the NGI type wire-reinforced membrane for the lateral confinement. In order to reduce frictional resistance between the rings during shearing, lubricant oil was applied between the stacked rings for each test. The performance of stacked rings versus that of wired reinforced membrane is discussed in chapter four.

Split molds are commonly used to aid preparing cohesionless element level soil specimens. A standard split mold is used to stretch the wire-reinforced or unreinforced latex membrane and ensure a circular cross-section before siphoning the sand in. The split mold is then removed after securing the top platen (and applying vacuum for the case of unreinforced membranes with or without stacked rings). The use of split molds and the NGI type wire-reinforced membrane made the sand reconstitution progress manageable. However, the use of traditional split mold in conjunction with stacked rings could be a disadvantage, because the stacked rings needed to be slid down after the removal of split mold (Figure 3.16) and while the specimen is under vacuum. The sand specimen could be disturbed when the stacked rings were being slid down or a gap might exist between the membrane and the rings which would lead to lateral deformations once the vacuum is removed and the normal stresses are increased.

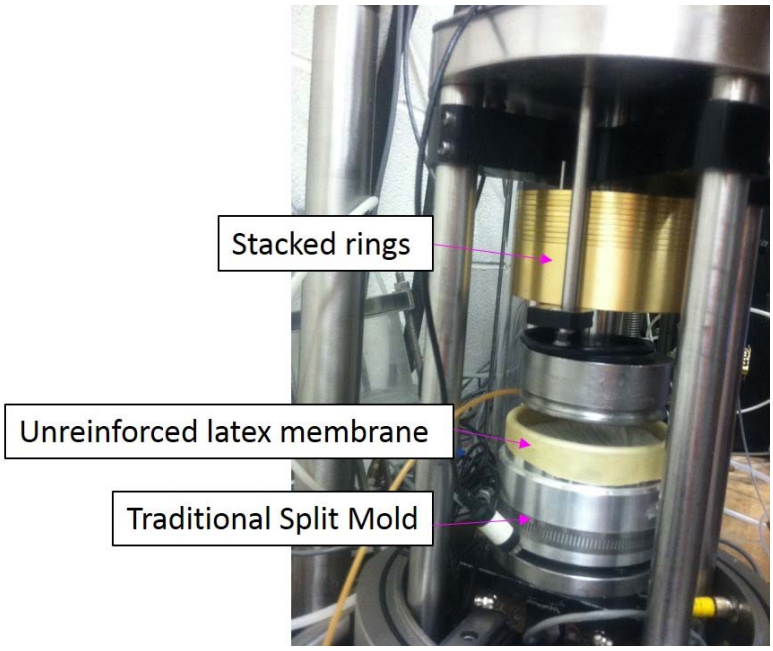

Figure 3.16: Set up of Stacked Rings with a traditional split mold

The specimen preparation procedure with stacked rings was improved by adopting a new aluminum split mold that was designed and manufactured for this study (Figure 3.17). Figure 3.18 shows engineering drawing of the newly designed split mold. The new split mold surrounds the stacked rings as well as the latex membrane, which is very similar to the one used in Ishiara and Yamazaki (1980). When a vacuum is applied, the latex membrane is pulled in contact with the stacked rings to avoid any gap between the two. The new design eliminated the potential of soil sample disturbance, and improved the efficiency of the preparation procedure of the stack rings specimen.

Figure 3.17: The new split mold for stacked rings

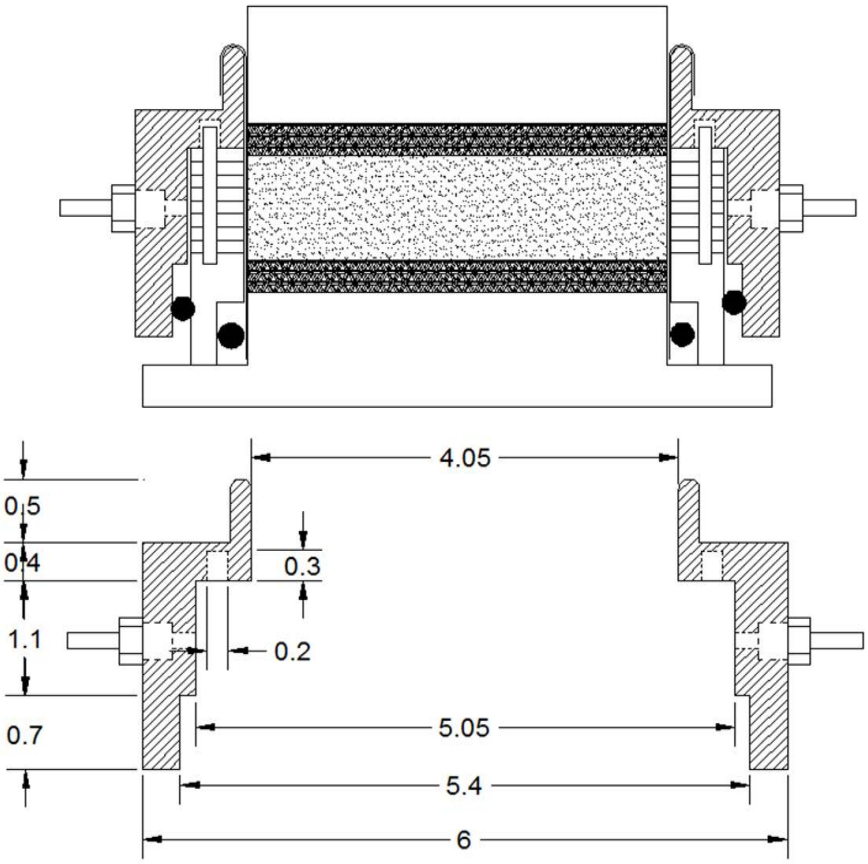

Figure 3.18: Design drawing of the new split mold

3.7 SPECIMEN RECONSTITUTION PROCEDURES

Laboratory approaches to the measurement of field liquefaction resistance are limited in engineering research and practice by the high cost of obtaining "undisturbed" samples. A high quality coarse-grained sample could be collected by the "frozen sampling" technique, which allows for some preservation of the in-situ properties (e.g., age, cementation, seismic history). However, this sampling technique is very expensive and requires laboratory sample handling at freezing temperatures. Therefore, most laboratory studies tend to recreate element-size soil specimens with a fabric that is close to the in-situ

conditions. Various sample preparation techniques were developed, such as dry funnel deposition, water sedimentation, slurry deposition, moist tamping, and air pluviation. Past research studies (Mulilis et al. 1977; Jang and Frost 1998; Vaid et al. 1999; Wood and Yamamuro 1999) have shown that the specimen reconstitution method greatly influences the measured monotonic and cyclic behavior of sand (Figure 3.19). In order to identify the most suitable reconstitution method to resemble the in-situ soil conditions, researchers compared the stress-strain behavior of reconstituted soil to that of 'undisturbed' frozen samples (Yoshimi et al., 1994; Vaid et al., 1999). The results showed that the water sedimentation method most closely simulated the fabric of the natural alluvial and hydraulic fill sands. On the other hand, specimens reconstituted by moist tamping are relatively non-uniform (Vaid et la., 1999). The results from Vaid et al. (1999) are shown in Figure 3.20. As a result, the water sedimentation reconstitution technique has been widely adopted in recent liquefaction laboratory research to understand the liquefaction phenomenon (Kammerer et al., 2002 and Wijewickreme, 2010).

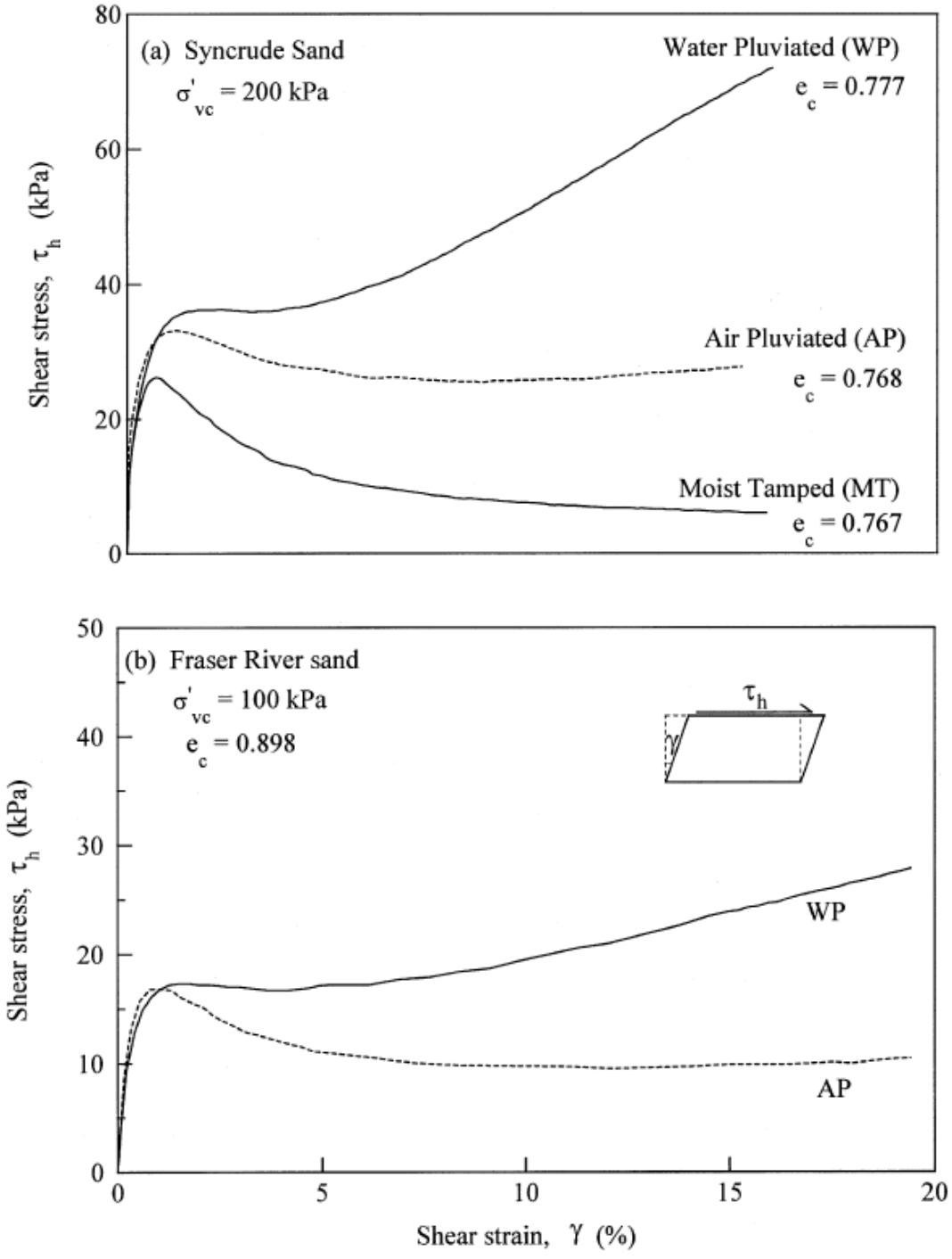

Figure 3.19: Simple Shear response of specimens reconstituted by different techniques: (above) Syncrude sand, (below) Fraser River sand (Vaid et al. 1999)

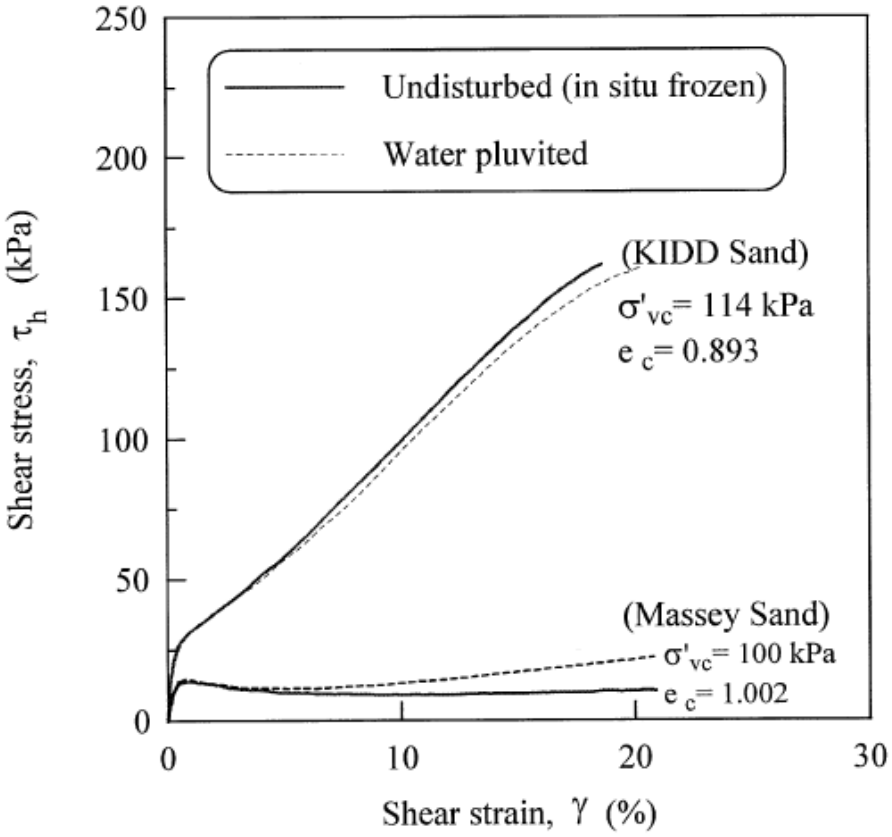

Figure 3.20: Comparison on undrained simple shear response of undisturbed (in-situ frozen) and specimen reconstituted by water sedimentation method (Vaid et al. 1999)

Water sedimentation was selected as the method for specimen reconstitution in this study. The repeatability of creating specimens with uniform densities and sand grains packing was important for comparison of response under transient loading and the preliminary specimen preparation exploration showed that the water sedimentation provided the most repeatable results. The details of specimen preparation methods at specific density range are discussed in the following sections.

3.7.1 Loose Specimen Preparation

This section describes the specific procedure for creating a saturated simple shear loose specimen for the UTCSS apparatus. The procedure was similar to the one employed by Kamermer et al. (2002), but with some modifications. First, a designated amount of sand was placed and mixed in a 500 mL volumetric flask filled halfway with water. In order to achieve a satisfactory level of saturation, the water-sand mixture, and both the top and bottom platens, were boiled for at least 30 minutes, and given a few hours to cool down. The drain lines and volumetric flask were fully filled with de-air water, and the flask was capped and sealed with a strip of latex membrane. The new split mold and membrane are then assembled on the bottom platen and vacuum is applied to have the membrane adhering to the rings. The inside of the membrane was then filled with de-aired water up to the final height of the specimen and a custom-made screen was placed on top of the bottom platen. Then, the flask was inverted and inserted into the water inside the membrane before removing the membrane strip. The saturated sand was siphoned with a circular pattern in the mold. As the sand slowly went down from the flask, an equal amount of volume of water from the mold was forced upward. After the majority of soil was deposited, the water inside the inverted flask became unclear, which was an indication of fine separation. A small amount of fine particles which were too small and light fell down by their own weight. The total weight of the segregated fines was around 0.2 g out of the total 314 g of sand used to prepare a loose specimen. Before the inverted flask was taken out, the removed membrane strip was used again to seal the tip of inverted flask. No air bubbles should be introduced if the procedures were conducted with great care.

The screen was then pulled up gently to allow the sand to rain through it. The raising rate of the screen would affect the specimen density. The slower the rate was; the looser the density is. Any remaining sand on top of the screen was dried and weighted after

the screen was pulled out. The sand specimen surface was leveled by a custom device that spins at a constant depth from the top of the mold. It was important to make the sand surface as level and smooth as possible before lowering the top platen. Any irregularities in the top of the sand can result in non-uniform normal stresses and can increase rocking significantly.

Custom pluviation screens were created to aid preparation of uniformly loose specimen (Figure 3.23). The devices were designed to provide a level and rigid screen allowing the soil to rain through it under water. The screen opening was 0.85 mm, slightly greater than the largest grain size of Nevada Sand, according to the sieve test (Figure 3.15). Figure 3.23a shows the first design, a screen attached to a plastic tube. However, this design failed to create specimens with relative density less than 45% and to improve the density uniformity. The wall thickness of the device allowed a gap between the sand and membrane; therefore, the sand particles tended to roll toward the membrane when the device was being raised. To address this problem, the second device used steel wire (Figure 3.23b), and it provided more uniform specimens.

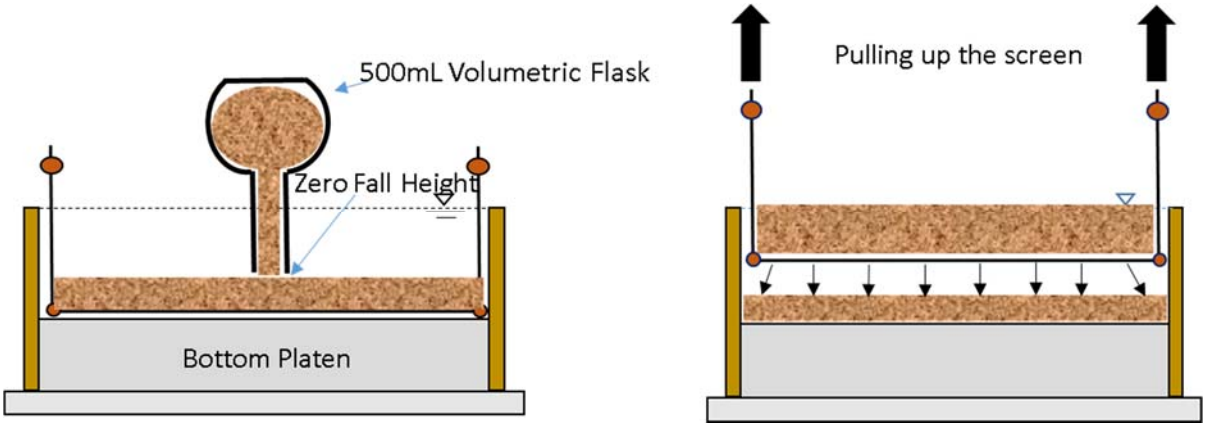

Figure 3.21: Loose specimen preparation procedure. Picture on the left shows the soil siphoning; picture on the right shows the construction of loose sand specimen. The soil particles rain through the screen.

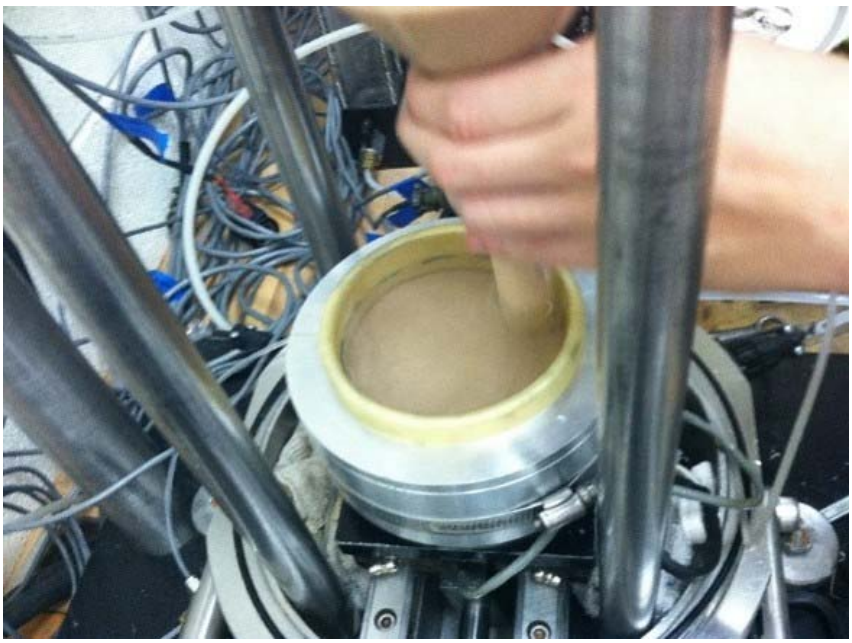

Figure 3.22: Siphoning Sand

Figure 3.23: First design pluviation screen (a. left), Second design pluviation screen (b. right).

3.7.2 Dense Specimen Preparation

Current literature shows limited information on the testing of direct simple shear dense sand specimens. Limited attention was given to liquefaction behavior of medium dense to dense sand in the past, so very little good quality element level cyclic testing is available. However, this set of data is important for learning the effects of site remediation, which can involve densifying the saturated loose soil as an option for ground improvement. Effects of sample preparation techniques were studied (Mulilis et al. 1977), but documentation of water-pluviated dense specimen ($D_r > 70\%$) reconstitution is virtually non-existent. Densification of samples was usually achieved by some forms of vibration, which were various on different types of CSS apparatus. To create a dense sample, Kamermer et al. (2002) tapped the sample through the base cap to provide required

vibration. For the setup of UTCSS, the bottom platen was required to fix at the shear roller assembly before sand deposition; therefore, there was no room to provide vibration (tapping) through the base.

Four densification methods, as summarized in Table 3.3, were attempted in this study, and evaluated by comparison to the loose sand (under the same vertical stress) on a CSR vs. N_f plot (Figure 3.24). At least three dense specimens (D_r = 70 to 90%) were prepared using each of the methods, and loaded under different CSR values. The test results showed that the method of "surface vibration with two layers" provided a significant higher resistance than the loose sand curve, and was concluded as the most appropriated method for this study, because it effectively densified the sand. On the other hand, the other three methods produced specimens with only a slightly higher resistance than the loose samples, which indicated that the applied vibration could not uniformly penetrate the whole sample. The more energy was uniformly applied to the saturated sample, the greater the liquefaction resistance was. Detailed step by step specimen reconstitution procedures (loose and dense) are documented in Appendix B.

Table 3.3 Different methods of preparing dense specimen

Methods	Procedures	Comments / Remarks
[1] Vibration with the shear actuator under a normal load	First, the sand was siphoned into the mold/membrane. After the top platen was applied (before the split mold was dissembled), a dead weight (5.5kg) was added on top of it. The specimen was then vibrated by applying a 2Hz, strain-controlled vibration of 2 mm peak-to-peak amplitude from the shear actuator.	With the applied top platen, the sand specimen was vibrating almost at an "undrained" condition. Since the pore pressure cannot be dissipated, this method cannot densify the sand efficiently.
[2] Tapping on the side of split mold	After depositing sand under water, vibration was applied by tapping the side of the slit mold with a rubber hammer.	The vibration cannot penetrate through the longer dimension (4" Dia). So, the specimen was heavily disturbed at the circular edge, but remained undensified at the center.
[3] Surface vibration with one layer	A custom device (Figure 3.23) was created for applying uniform vibration to the sand surface. The device included a metal thread attached to a 3.96" Dia plastic plate. Holes were drilled on the plastic plate to allow drainage. The device was placed on the top sand surface, and an inverted vibratory table was turned on and attached to the tip of metal thread, to provide vibration to the soil specimen. After the water-sand mixture escaped from the plastic plate drainage holes, the vibratory table was removed. The escaped sand was dried and weighed.	The drilled holes on the plastic plate were designed for pore pressures dissipation during vibration. However, this set up were found to be ineffective, because the vibration could not penetrate the one-inch thickness.
[4] Surface vibration with two layers	The method is similar to the one above, except reconstituting the soil specimen with two layers. Figure 3.23 illustrates this preparation method.	The ½" layers allowed vibration to penetrate through the entire thickness, when Δu dissipated through the holes. This method was found to be effective.

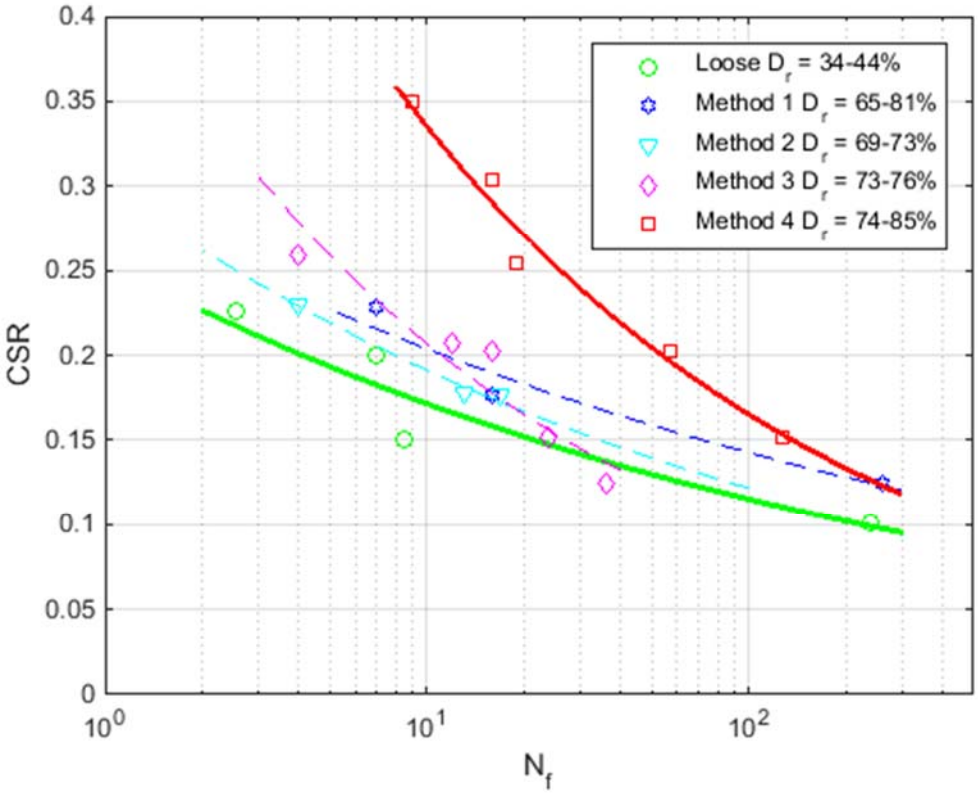

Figure 3.24: Comparison of different dense specimen preparation methods

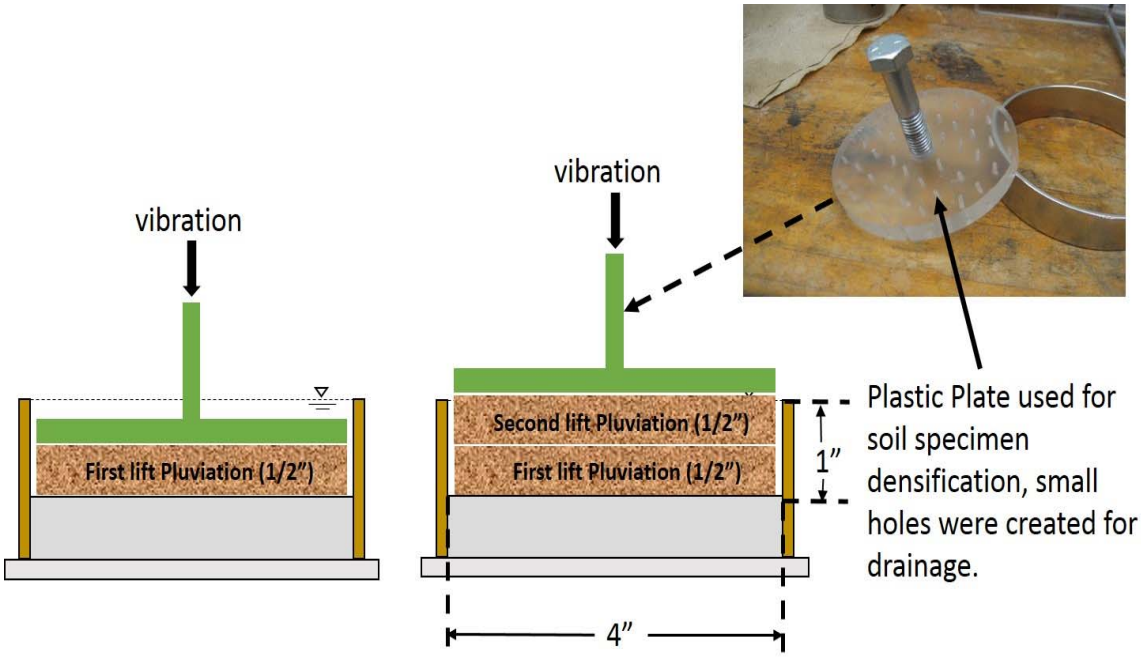

Figure 3.25: "Surface vibration with two layers" preparation procedure illustration

3.8 SPECIMEN SATURATION AND CONSOLIDATION

The entire test procedure (prior to shearing) for this study can be divided into two parts: (1) specimen reconstitution and (2) saturation and consolidation. The reconstitution methods are described in section 3.7 and a full list of UTCSS test procedures are covered in Appendix B.

After reconstituting a soil specimen, the top platen was placed on the top of the sand and sealed by a hose-clamp on top of at least five O-rings. The hose-clamp was modified by attaching sand paper on the inner wall so that the potential of O-rings and the hose-clamp slipping against each other when tightening is minimized. Earlier tests showed that when the pore pressures inside the specimen are 70 kPa higher than the cell pressure, the O-rings were no longer sufficient to isolate the specimen from the cell. Therefore, the

hose-clamps were used to provide additional seal and prevent the pore pressures from leaking out during undrained loading.

After placing the top platen, a seating vertical stress and small vacuum (about 10 kPa) were applied to the specimen before the split mold was removed. At this point, the height of the specimen was recorded and the density was calculated. The cell was then assembled and a cell pressure of 15 kPa and vertical stress of 50 kPa were applied. The cell pressure was selected based on a k_0 value of 0.3, which is smaller than the k_0 value (about 0.4) provided by the lateral confinement. Back pressure saturation was then applied to the specimen using traditional techniques. After a "B-value" of 0.92 or greater was achieved, the specimen was consolidated to the desired final stresses. The lower B value (as compared to 0.95 which is commonly used for sands) was considered sufficient due to the smaller particles size of Nevada Sand and a higher targeted density.

At the consolidation stage, the cell pressure was increased to 30 kPa and the vertical stress to 100 kPa. The change in specimen height was recorded, and the final specimen density was calculated at the end of consolidation. Prior to the application of the shearing, no horizontal shear stress was imposed on the specimen so that level ground conditions could be simulated during testing. Throughout the saturation and consolidation stages, the shear actuator assembly was under displacement control at the "zero" position. During the shearing stage, an approximately constant vertical load was maintained by the pneumatic actuator. The shearing stage was terminated after the entire ground motion history was applied (including any additional stages of tapper up loading or static loading) or a single amplitude shear strain of 15% was achieved.

3.9 REQUIRED CORRECTIONS

Frictional forces were induced in both the vertical and horizontal directions during consolidation and shearing, respectively. Therefore, two corrections were required so that the compliance of the UTCSS apparatus can be isolated from the soil response. The ball bearing connection at the top of the pressure chamber provided frictional force when the specimen was loaded vertically; the stacked rings and the shear roller assembly provided additional resistances when the specimen was sheared. In order to quantify these frictions, water specimen tests were performed for the horizontal resistances, and vertical friction test was conducted for the vertical resistance.

3.9.1 Water Test

Water specimens were created to investigate the shear resistance provided by the two confining systems, stacked rings (SR) and wire reinforced membrane (WR), and the ball bearings of the shear actuator assembly. Water is assumed to have no shear resistance, and therefore the measured resistance during shearing is contributed by the confining system and friction within the equipment. Figure 3.26 shows the water tests results. At a small strain (<1%), the resistances from SR and WR both increased quickly to 0.5 kPa, and the measured resistances are very close to each other. In both systems there is a sharp increase in shear stress right after shearing starts, followed by a linear increase at a flatter slope up to a shear strain of 25%. Since the magnitudes of the systems' resistance were relatively small, a simple linear model with a y-intercept was used to correct the measured shear stresses during later tests. Both systems had a very similar y-intercept (a measure of the friction in the loading mechanism rather than resistance of the confinement); however, the increase in resistance of the SR with increasing shear strain is slightly higher than that

of the WR after the initial spike. With the obtained shear resistance at a given strain level, the CSS test data can be corrected.

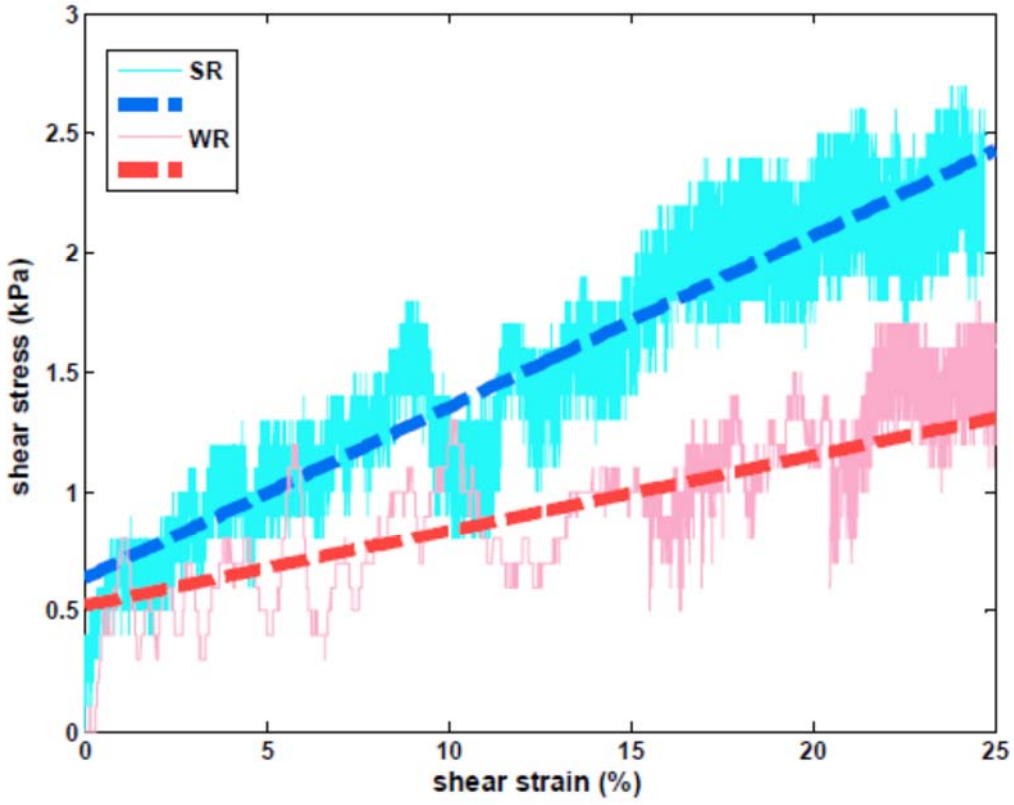

Figure 3.26: Stress-Strain plot for water specimens under different confining systems

3.9.2 Vertical Friction Test

The UTCSS vertical load cell is located outside of the pressure chamber, and therefore, the vertical load measurement included frictional forces in the ball bearing connection and the X-bar (Figure 3.27). Vertical friction test was performed to quantify the vertical frictional resistance of the UTCSS apparatus when applying consolidation stresses.

In additional to the original load cell (#1), an extra load cell (#2) was set up on top of the shear roller assembly (Figure 3.27), and a range of vertical loads (10 to 110 kPa) were applied. The two load cells would provide the same measurement if the UTCSS vertical alignment was frictionless. The measured differences between the top (#1) and bottom (#2) load cells were due to frictional resistance. Figure 3.28 illustrates the measured values, and the data was used for vertical load corrections. In addition, since the vertical load cell is located on top of the top platen and vertical piston, the vertical load measurement was corrected for the weight of the three components (Load cell (#1), vertical piston and top platen).

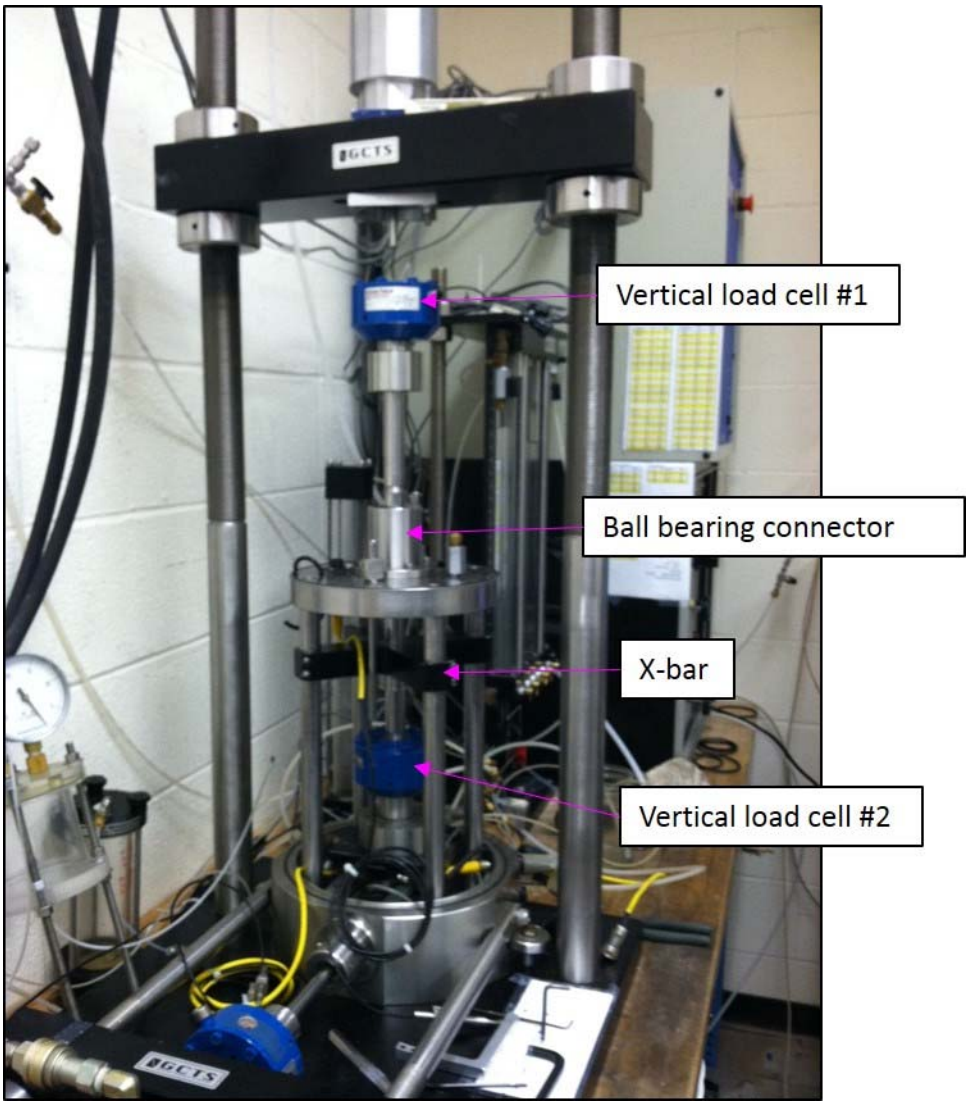

Figure 3.27: Setup of vertical friction test

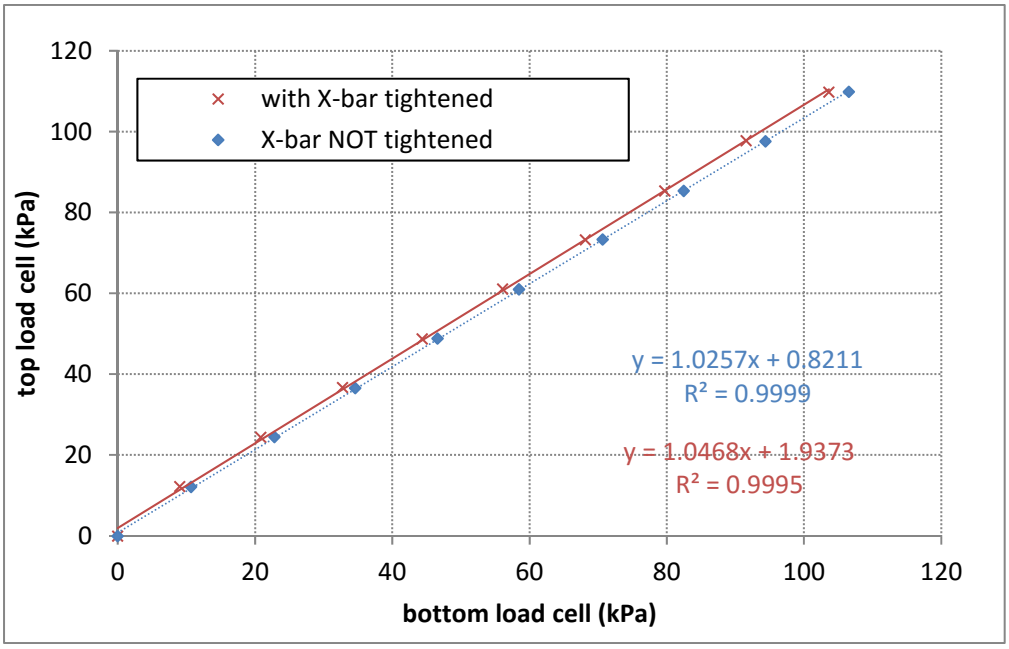

Figure 3.28: Vertical friction test data.

3.10 CONCLUSION

A testing program that consists of multiple stages to study the behavior of liquefiable soil before and after liquefaction initiation is introduced in this chapter. A review of simple shear testing principles are discussed and compared with other similar testing, such as triaxial and torsional shear. The advantages and limitations of CSS testing are discussed.

The configuration of the main testing apparatus for this research project, the University of Texas Cyclic Simple Shear (UTCSS) is covered in detail in this chapter. The original apparatus was manufactured by GCTS, but significant modifications were made in order to optimize the apparatus' performance. Moreover, additional instrumentations (internal LVDTs) are installed for more precise measurements. Unlike previous research projects that conducted simple shear testing, this project adopted stacked rings, and instead

of NGI type wired reinforced membrane, for specimen lateral confinement. A special split mold is manufactured for the use of stacked rings during specimen preparations.

Reconstituting high quality sand specimens is the key of success for this project. Wet pluviation, which is considered the best reconstitution method on mimicking sand deposition is used. Two density ranges (loose and dense) of specimens are targeted, and each of the loose and dense specimen has its own construction procedure. In order to create a uniform loose specimen, the sand particles rain through a custom made screen. For the dense specimens, vibration is applied in pursuance of densifying the sand. The dense specimen construction method is an unprecedented procedure that cannot be found in previous research. Last but not least, vertical and horizontal frictions that are embedded in the apparatus are quantified for data correction.

Chapter 4: Preliminary Testing and Results

4.1 INTRODUCTION

This chapter reports the procedures and results of Direct Simple Shear (DSS) and Isotropic Consolidated Undrained (ICU) tests that aid to create the CSS testing procedures. The DSS tests were set up to compare the performance of reinforced membrane versus stacked rings as a mean to achieve K_0 consolidation; the ICU tests were conducted to investigate the differences in soil properties under different specimen reconstitution methods. In addition, preliminary results of CSS tests under irregular loading are also documented.

4.2 DIRECT SIMPLE SHEAR TEST

One of the main features of CSS tests is allowing K_0 consolidation, which can be achieved by either using wire-reinforced membranes (WR) or stacked rings (SR). WR, adopting the NGI-type wire-reinforced latex membranes is commonly used in the academic research projects: Bjerrum and Landva 1966, Boulanger et al. 1993, Kammerer et al. 2002. On the other hand, SR is also available and more popular in engineering practices, because of its cost effectiveness and durability. Figure 4.1 illustrates the setups of the two devices.

Neither WR nor SR can provide complimentary shear stresses on the slides (Figure 3.3). Therefore, non-uniform shear stresses are expected from the top and bottom of the specimen. It is necessary to study the effects of using WR and SR, which may affect the simple shear test results. A detailed review of simple shear mechanism is documented in Section 3.2.1. Measuring the horizontal forces on the lateral confinement side walls is the most direct way to quantify the differences between the two confining systems. However,

the circular shape of the devices prevents an easy and economical way of acquiring the measurements. Alternatively, direct simple shear tests (DSS) can be used to compare the performances of wire-reinforced membranes (WR) and stacked rings (SR) in a simple shear setup. Any difference resulted from the two confining systems will be reflected on the DSS stress-strain curves. Therefore, if the SR and WR provide the same amount of lateral stresses, the stress-strain curves resulted from SR and WR should be very similar. Baxter et al. (2010); Kwan and El Mohtar (2014) compared DSS test results from WR and SR. Baxter et al. (2010) performed constant volume DSS tests on cohesive soils, and concluded that the two confining devices provide comparable results.

Kwan and El Mohtar (2014) intends to compare the performances of the two different confining systems in CSS testing on sand (liquefaction test). Hence, constant normal load tests, instead of constant volume tests, were conducted to simulate the undrained CSS tests with pore pressure measurements. Figures 4.2 and 4.3 demonstrate the DSS test results (stress-strain and volume-strain) on two kinds of sand, Monterey #0/30 and Washed Mortar. Overall, the two confining systems provide comparable test results, expect the two tests with Washed Mortar sand under higher vertical stresses (100 and 150 kPa). In fact, Washed Mortar sand is a relatively well grade and more angular soil (with more individual larger soil particles), and the vertical stress of 150 kPa is very close to the consolidation stress limit of the NGI-type WR (C=1.0). Therefore, greater discrepancy between WR and SR is found in denser and more angular sand under relatively high vertical stresses. For the sand type (Nevada sand, Figure 3.13) and stress level that are conducted in the CSS testing program, using stacked rings should give comparable results with using wire-reinforced membrane.

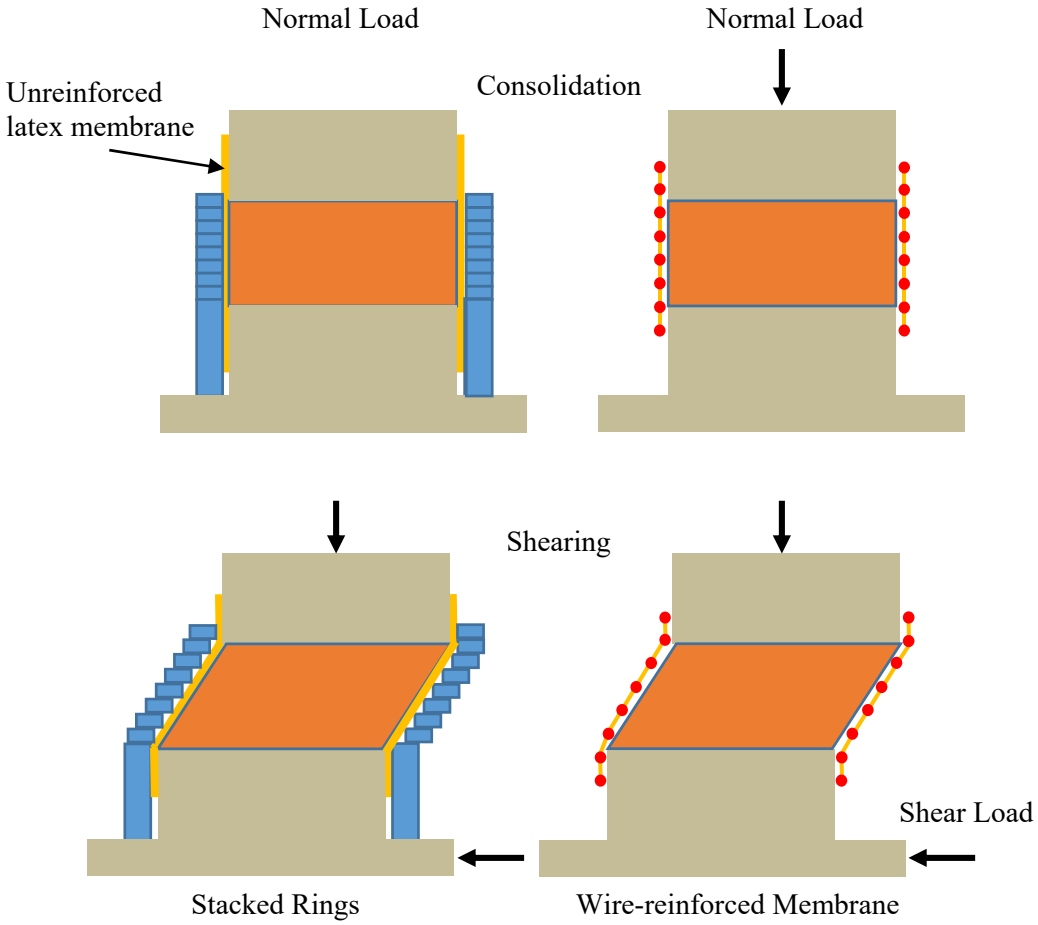

Figure 4.1: Setup of Stacked Rings and Wire-reinforced during consolidation and shearing (Kwan and El Mohtar 2014).

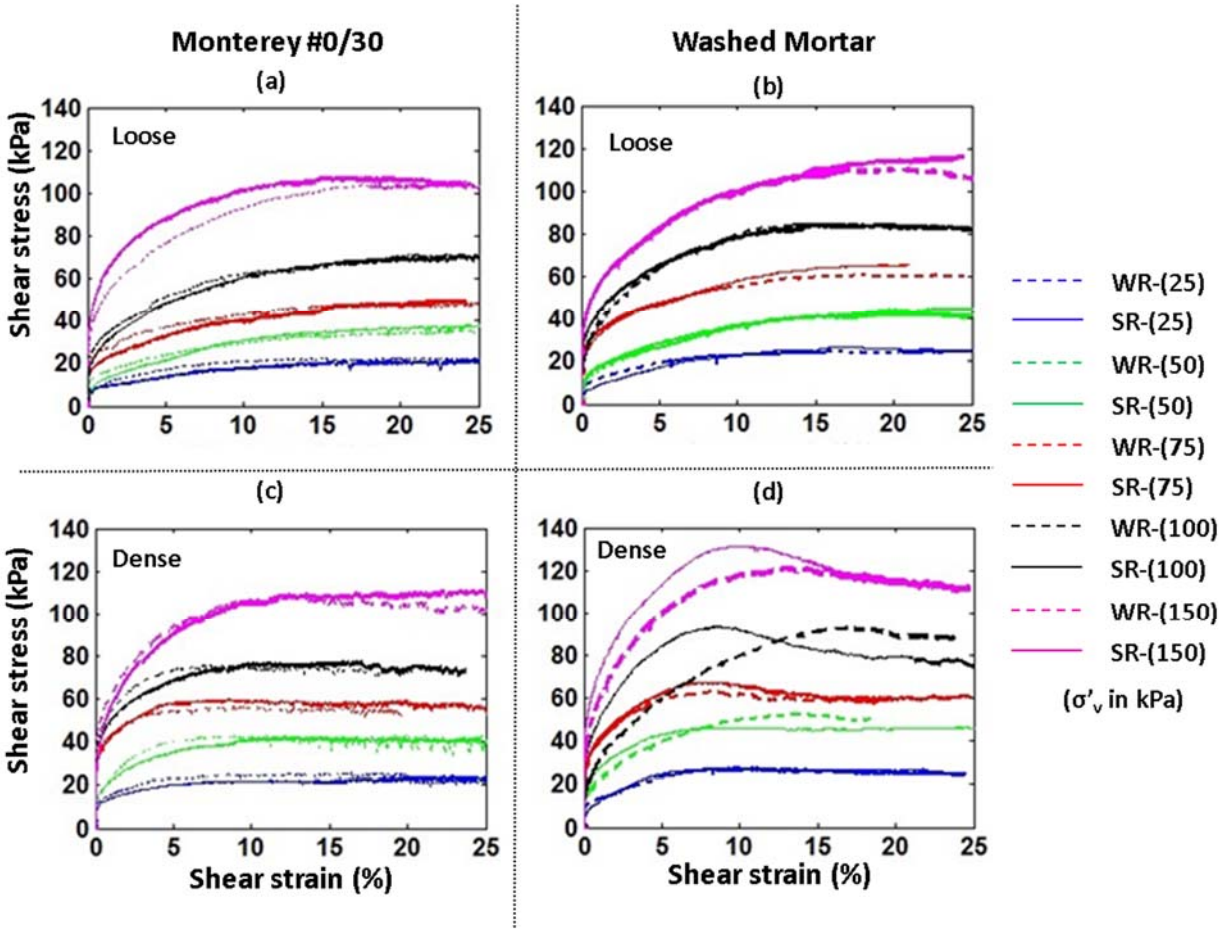

Figure 4.2 (a-d): DSS test shear stress verses shear strain results (Kwan and El Mohtar 2014).

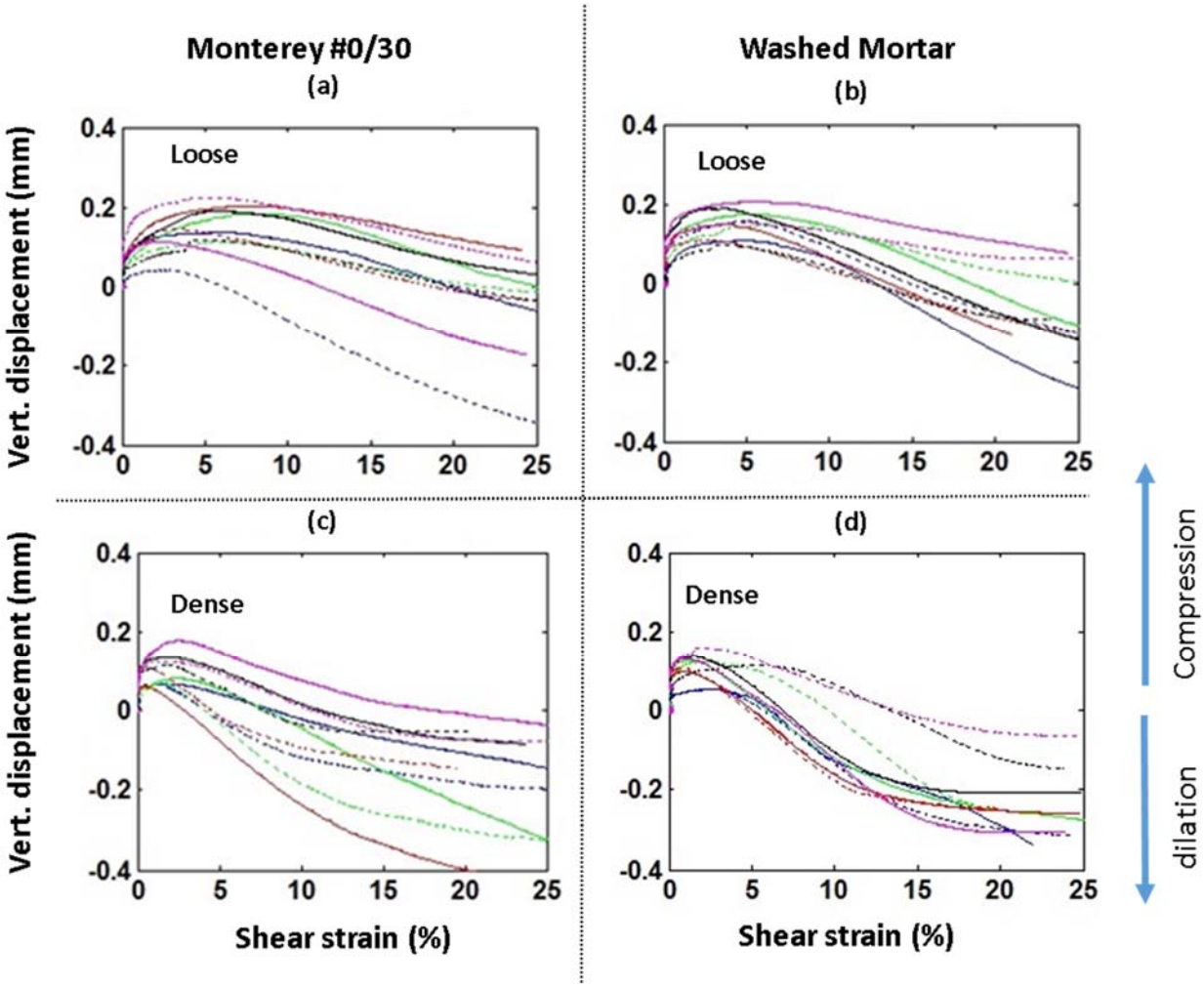

Figure 4.3 (a-d): DSS test vertical displacement verses shear strain results (Kwan and El Mohtar 2014).

4.3 TRIAXIAL ICU TESTS

Eight Isotopically Consolidated Undrained (ICU) triaxial tests were conducted for two goals: (1) to study the soil properties of Nevada Sand at different density ranges under static loading, and (2) to compare the monotonic sand behavior under the two different depositional techniques, wet and dry pluviation. The cylindrical specimens generally measured 50 mm in diameter by 100 mm diameter in height. The ICU tests were performed with a typical triaxial frame that was manufactured by GeoTac. Specimens with two relative density ranges were created (loose and dense), and consolidated to different effective confining stresses, ranging from 50 kPa to 350 kPa.

The dry pluviation method starts with placing the spout of a funnel on the bottom of a split mold. The pluviation was done in a circular manner to maintain a constant soil level throughout the height of the specimen. To create a loose specimen, the dry sand was deposited into the funnel, and the funnel was slowly raised up with almost zero drop height. Therefore, a low energy state is achieved. To create a dense specimen, the split mold was gently tapped in a symmetrical pattern after sand deposition. The top platen of the soil specimen was connected to the top drainage lines of the triaxial cell, and a vacuum of approximately 20 kPa was applied before removing the split mold. The cell was then filled with water and placed in the automated triaxial machine. Careful measurements of the membrane thickness, the heights of the platens, porous stones, and filter papers, along with the specimen height and diameter were taken to create accurate calculations of soil volume. Afterward, the specimen is flushed with CO_2 for about 30 minutes and de-aired water before back pressure saturation. After a "B-value" of 0.95 or greater was achieved, the specimen was consolidated to desired confining stress level. While the LVDTs monitored the height of specimen, the relative density was calculated.

The wet pluviation method used to create triaxial specimens was the same as the one used to create simple shear specimens. Prior to pluviation, the sand was placed in a volumetric flask half-filled with water, and boiled for at least 30 minutes. After the water-sand mixture had cooled down, the flask was capped and sealed with a soft plastic strip. The inside of the spilt mold was filled with de-aired water up to the rim, and a custom-made screen was placed on top of the bottom porous stone. Then, the flask was inverted and inserted into the water inside the split mold. After removing the sealing plastic strip, the saturated sand was siphoned with a circular pattern in the mold. The screen was then slowly pulled up to allow the sand to rain through it. The slower the rate of pulling up the screen is, the looser the relative density is. To create loose specimens, a very slow raising rate of screen was adopted. To create dense specimens, like the CSS procedure, the specimens were constructed in two lifts. Half of the amount of designated sand was siphoned into the split mold for each lift, and densification was achieved by symmetrical pattern of tapering at the split mold. Figure 4.4 illustrates a Nevada sand specimen after construction and shearing.

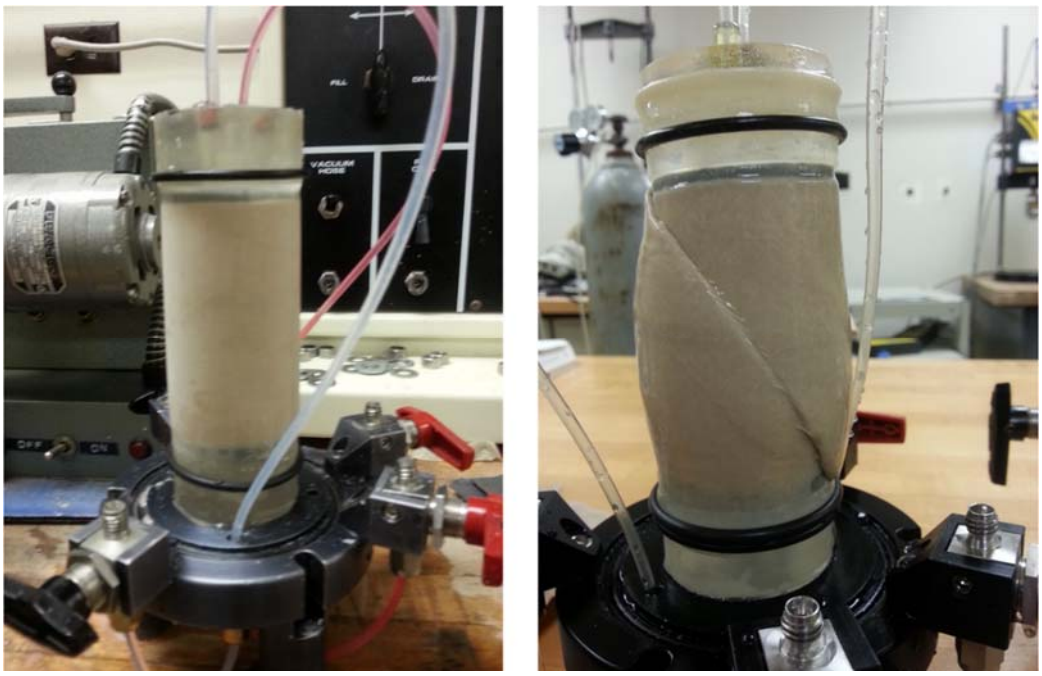

Figure 4.4: Pictures of reconstituted Nevada sand ICU test specimen. Before test (left). After test (right).

Figure 4.5 and 4.6 demonstrate the stress paths and soil strength envelops that were developed from six ICU tests. The six specimens were all prepared by the wet pluviation method. At each density range, three tests were performed at different effective confining stresses. The strength envelops defined by the critical state shear stress and corresponding friction angles (φ_{cs}) were obtained. Comparing the two envelops, ($\varphi_{cs} = 33.52^{o}$) and ($\varphi_{cs} = 30.75^{o}$), the critical state friction angle for the dense soil specimens is about 10 percent stronger than that established for the loose specimens.

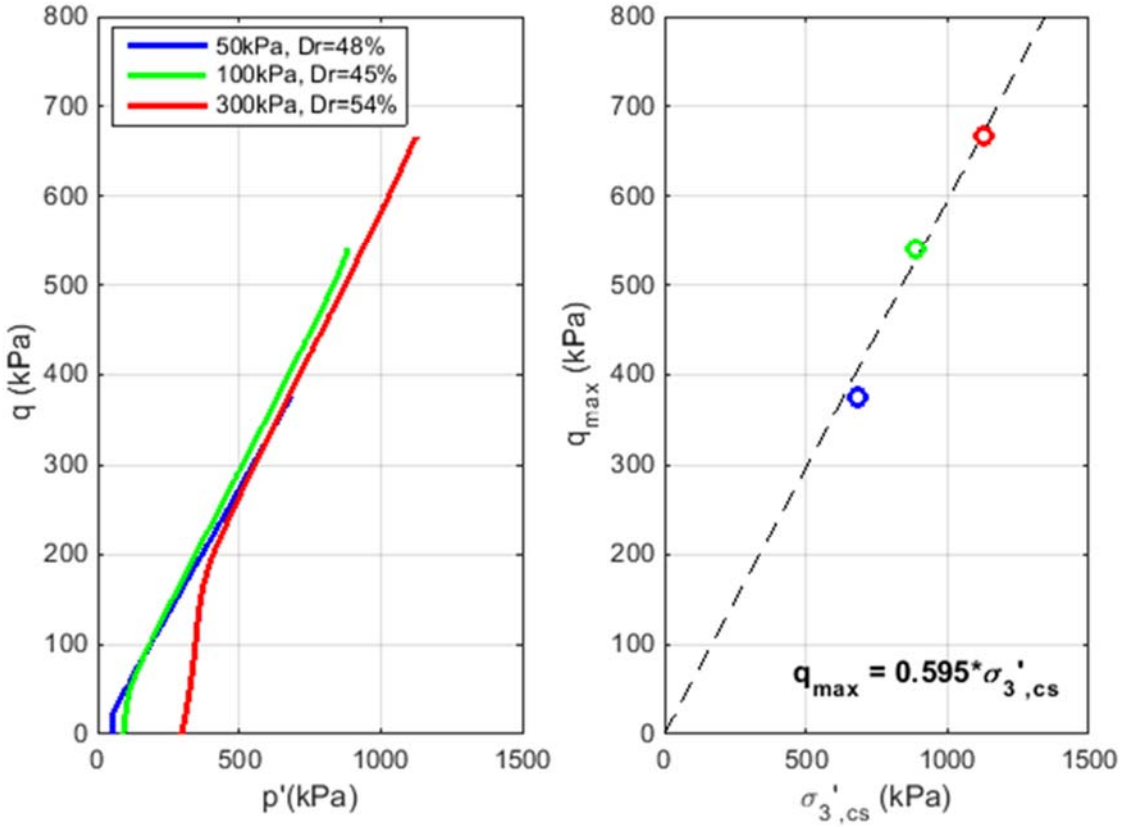

Figure 4.5: ICU test result for loose specimens reconstituted by the wet pluviation method. Stress path (left). Soil strength envelop (right).

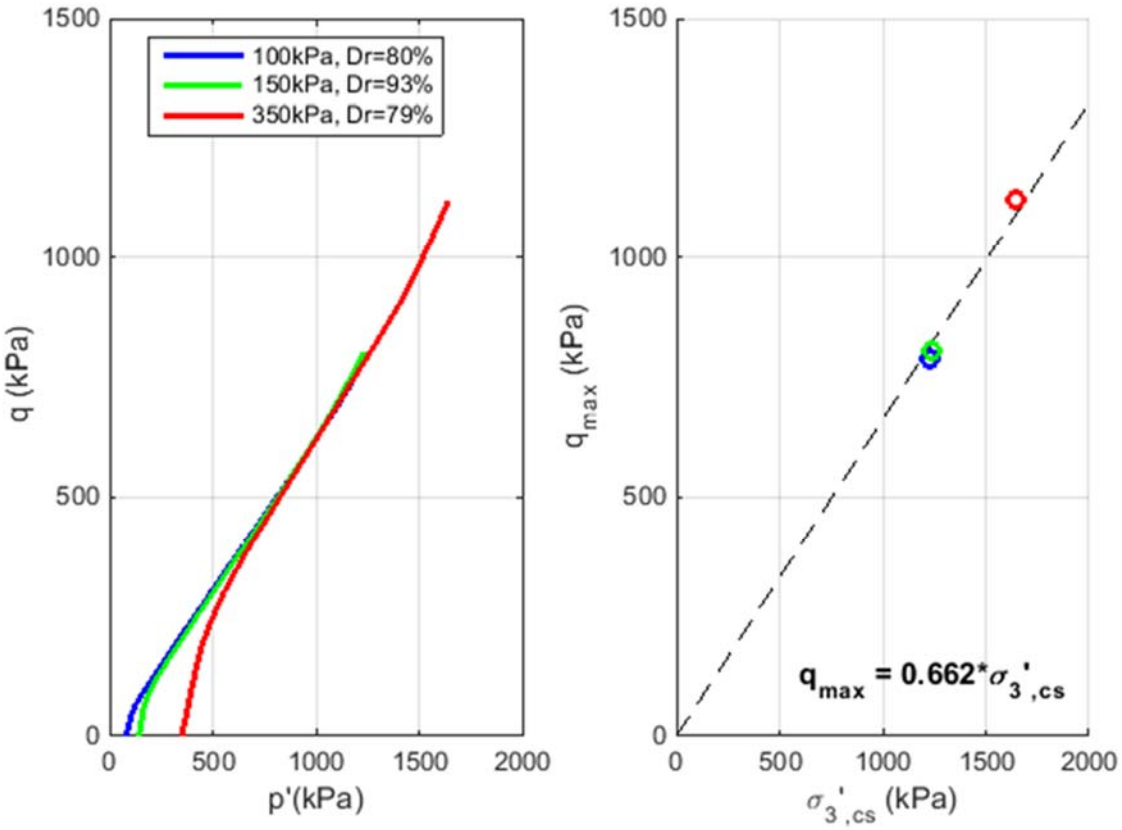

Figure 4.6: ICU test result for dense specimens reconstituted by the wet pluviation method. Stress path (left). Soil strength envelop (right).

Two additional ICU tests were performed on specimen prepared by the dry pluviation method, and hence, the test results can be used to compare with those generated from wet pluviation method. Figure 4.7 shows the stress path of four ICU tests (two prepared by dry pluviation and two by wet pluviation). While there are limited test results, the wet pluviation method appears to produce specimens with a slightly stiffer response. Overall, both the specimen preparation methods provide comparable stress paths.

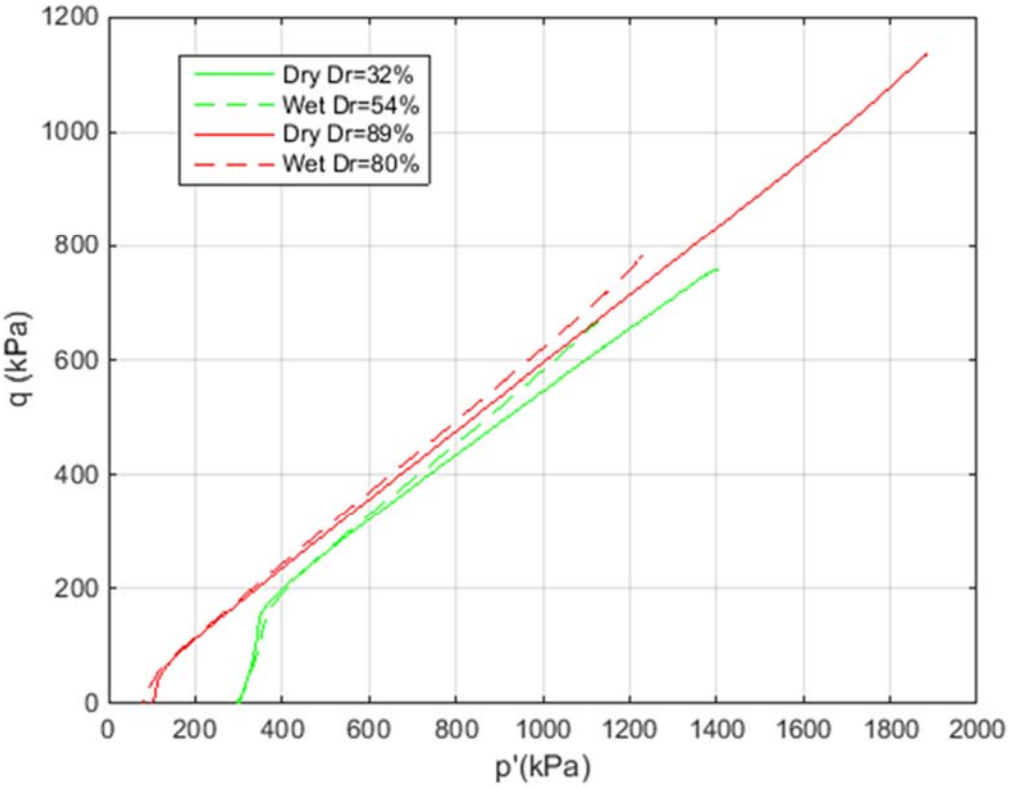

Figure 4.7: Stress Path showing the comparison of dry and wet pluviation methods.

4.4 PRELIMINARY CSS TEST

Prior to optimizing the UTCSS apparatus performance and establishing effective specimen reconstitution procedures, many CSS tests were conducted as part of the apparatus and testing procedure calibration process. The test result is affected by the shortcomings of excessive rocking and/or non-uniform soil density. Even though the quality of those tests are questionable, no value in studying the data of each test individually; however, there are a number of tests that are valuable when comparing the

test results as a group that the apparatus bias and specimen reconstitution procedure are consistent.

There are two testing programs of CSS test that were loaded with stress controlled, undrained, and irregular sinusoid loading. All tests were performed before completely addressing the issues of excessive rocking and specimen density uniformity. Nevertheless, the test result from one test relative to other tests under similar loading provide valuable insights, which are very useful for determining the final testing procedure for the overall research project. In addition, the irregular sine motions can serve as an intermediate step between the harmonic and transient loadings, for revealing soil responses (pore pressure generation and induced shear strain).

4.4.1 Irregular Sine Motions

The first testing program was setup to investigate the sand responses under a series of loading, which composed of nine uniform loading cycles plus a double-amplitude loading cycle at different locations (2^{nd}, 4^{th}, 6^{th}, 8^{th} and 10^{th} cycle), as depicted in Figure 4.8. For each CSS test, the specimen was loaded at least five times with different motions, designed to study the seismic history effect. After each loading, which built up a residual excess pore pressure in the sand, the pore pressure was allowed to dissipate and the specimen to reconsolidate under the initial effective vertical stress. As an example, after being saturated and consolidated to 100 kPa, a specimen was subjected to a sinusoid loading that was peaking at the 2^{nd} cycle under undrained condition. Before applying the second round of loading that is peaking at the 4^{th} cycle, the drainage valve connected to the base of the specimen was reopened to allow for pore pressure dissipation. This step was repeated, thereby motions peaking at 6^{th}, 8^{th} and 10^{th} cycles were loaded.

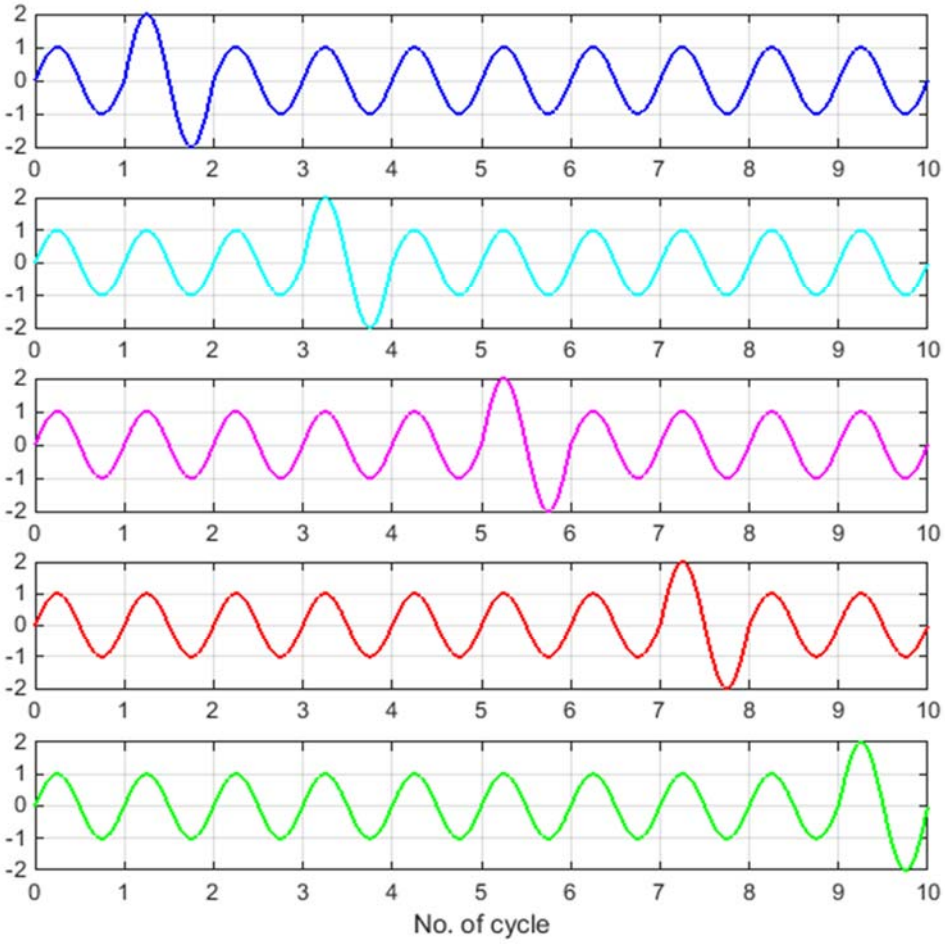

Figure 4.8: Irregular sinusoid motions. Nine uniform cycles plus a special cycle with double amplitude at different locations (2nd, 4th, 6th, 8th and 10th).

Figure 4.9 encompasses the test result of five CSS tests under first round of irregular sinusoid loading (i.e. no pre-loading effect), which depicts the soil responses under motions with difference peaking loading cycles. The most severe damage (excess pore pressure generation) is found in the test peaking at the 2nd loading cycle; the least damage is recorded in the test peaking at the 10th cycle. More importantly, the loading peaking at the second cycle provided a much earlier liquefaction initiation than that any of the other loadings.

The other loadings reached or got close to achieve liquefaction initiation towards the end of the loading.

Figure 4.10 shows the results of the second loading on six CSS tests sheared with the same second cycle high peak loading after different first round of loading (different history effect). The test results are consistent with previous experimental finding (Seed et al. 1975; Seed et al. 1988) that the seismic history would increase resistance to liquefaction in subsequent undrained loading even though the specimens underwent no significant change in density. The increased resistance may be due to change in the structure of the sand skeleton or an increase in the lateral earth pressure coefficient, K_0 (Seed et al. 1975). However, the experimental finding of seismic history improving liquefaction resistance appears to contradict with the recent field evidences from the series of earthquake that shook Christchurch, New Zealand in 2010 and 2011 (Cubrinovski et al. 2011). The re-occurrence of liquefaction reveals that seismic history may not increase the liquefaction resistance in the field. Pore pressure upward dissipation during and after liquefaction may alter the structure of sand deposit. Problems of model scaling may also limit the capability of experiments to simulate an actual seismic event in the field. Further research effort is needed in the topic of "seismic history effect".

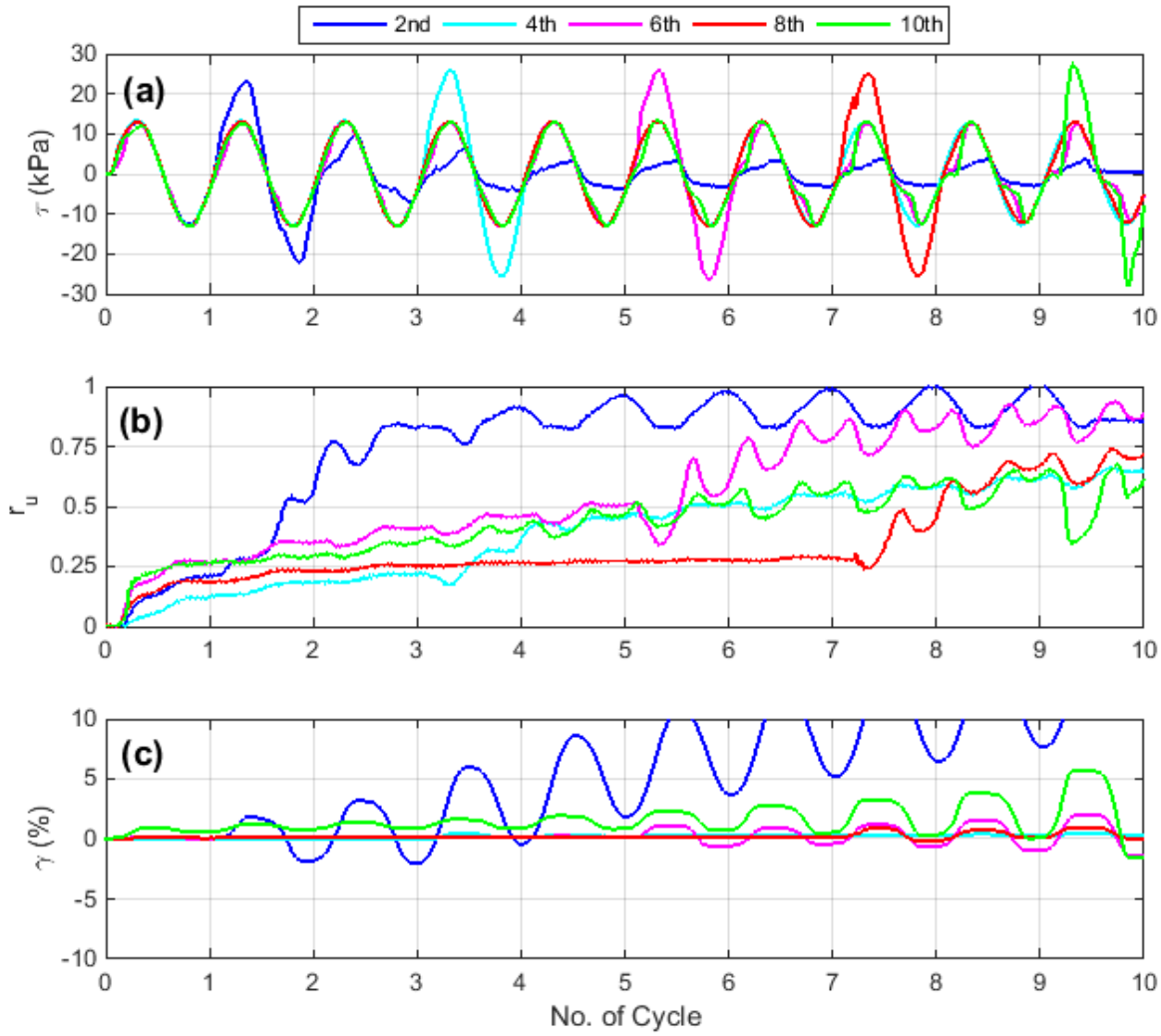

Figure 4.9: Test results of irregular Sine loading. First round loading with different motions (i.e. no seismic history)

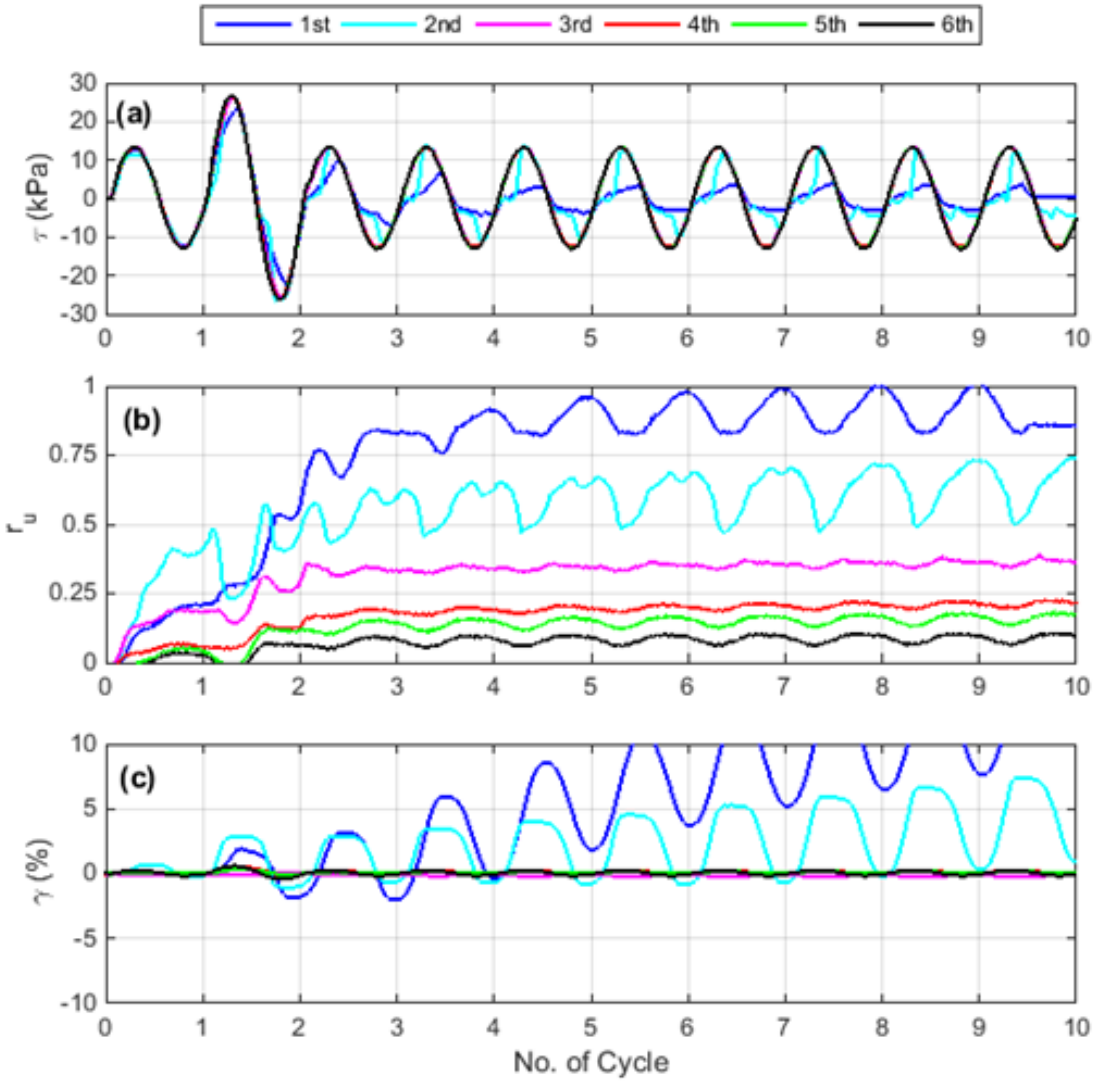

Figure 4.10: Test results of second round of irregular Sine loading on specimens with different pre-loading histories.

4.4.2 Taper Sine Motions

The second testing program consisted four taper sinusoid motions. Figure 4.11 illustrates the test result of the four CSS tests, which each included twenty loading cycles, taper-up or taper-down. According to the current liquefaction evaluation procedures

(covered in chapter 2), taper up and down motions are characterized to have the same amount of seismic loading, because the amplitudes of cycles are the same. Therefore, the induced excess pore pressure and shear strain are expected to be similar. However, the test result shows that the soil response is highly depend on the type of taper motion. The excess pore pressure generation is progressively increasing under taper up loading, but levelled after five cycles of loading during the tapper down loading leading to very different final r_u values. Moreover, the shear strain induced by the taper up motions were significantly higher than those by the taper down motions. Figure 4.12 shows a test result that consists both taper up and taper down in the same motion. The test result confirms that the taper down motion after taper up loading has limited or no effect on excess pore pressure generation.

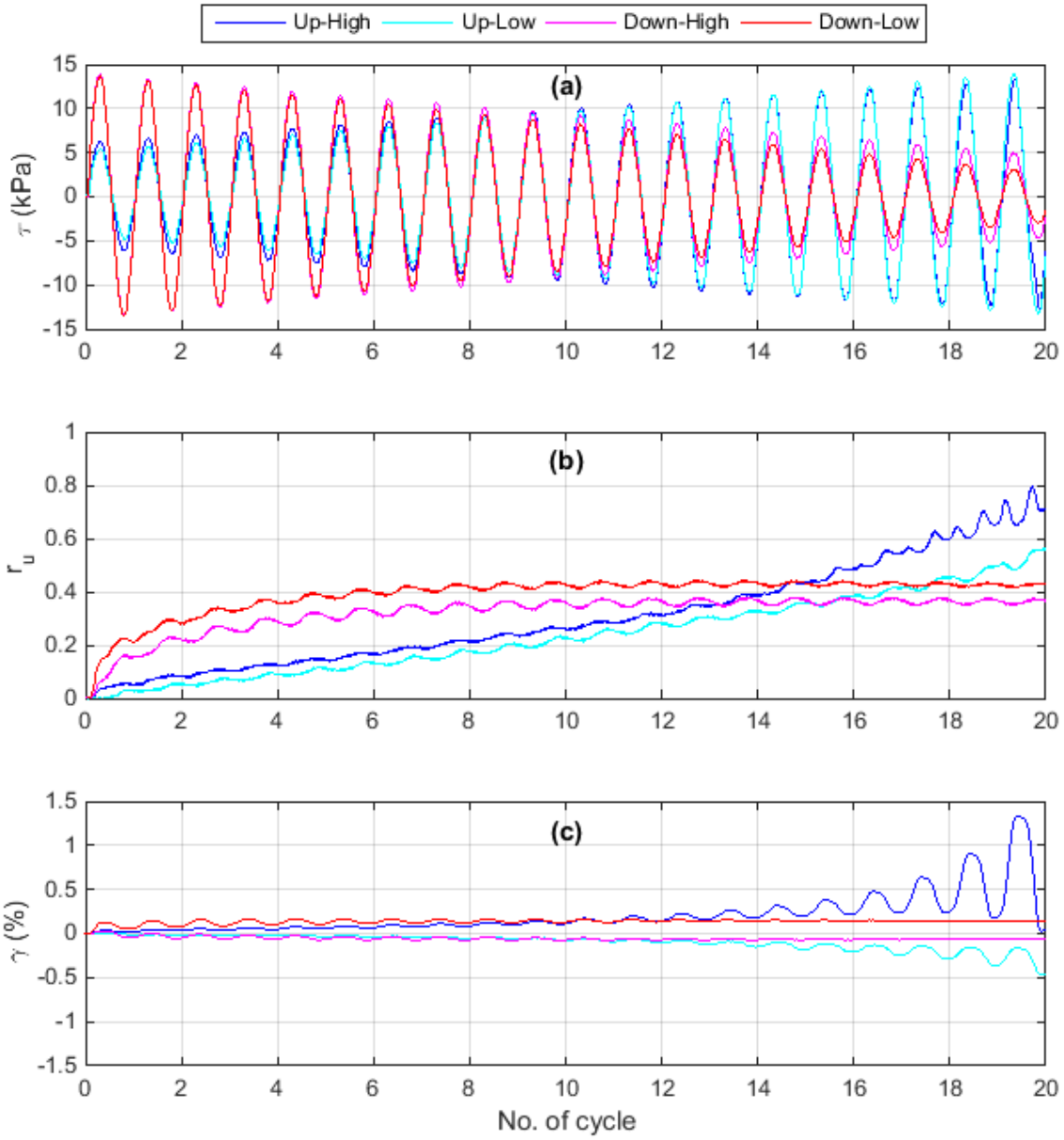

Figure 4.11: Taper Motion test results.

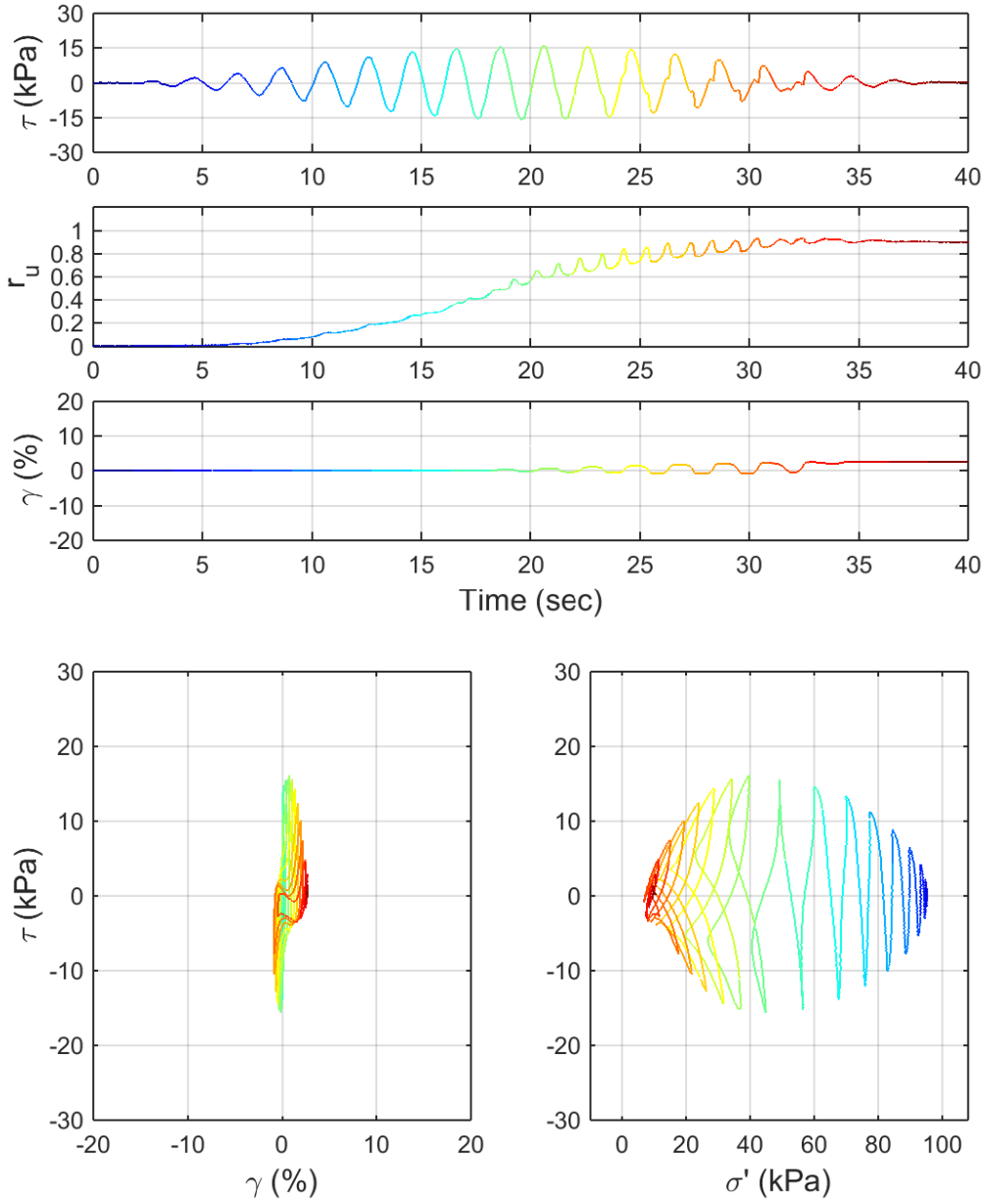

Figure 4.12: Test results of a new modulated sine loading.

4.4.3 Conclusion

The following conclusions are drawn for the future testing through the two preliminary testing programs:

1. Seismic history increases the liquefaction resistance of sand specimen in the laboratory setting; therefore, repeatedly loading the same soil specimen is overestimating the liquefaction resistance. Each prepared specimen can only be tested one time for pre-liquefaction responses.
2. The development of excess pore pressure and induced shear strain highly depends on the order of stress cycles in a given loading.
3. The simple but yet irregular sinusoid motions are helpful for establishing basic principles of undrained soil responses beyond those developed by harmonic motions.
4. The results overall give insights that representing a complicated transient loading by a simple harmonic loading ignores the impact of the time characteristics of the loading history on the liquefaction potential. A more advanced parameter or measure is needed to capture the temporal and spectral characteristics of ground motions.

4.5 UTCSS APPARATUS UPGRADE

In order to improve the quality of simple shear testing, a new UT CSS apparatus was designed (Figure 4.13 c) with a main feature of high overall rigidity. The key component of the new apparatus are a pair of steel walls that can hold a pneumatic actuator aligning and lock with the top platen (Figure 4.13 a). The steel walls were custom made in order to accommodate the soil specimen reconstitution procedures. The wall thickness varies to accommodate the split mold (0.45” wall thickness) and actuator (1.5”). The new

apparatus accepts both stacked rings and wire-reinforced membrane as the confining system. Figure 4.14 depicts the details of shear walls. Overall, the system provides a high level of restraint against lateral deflection or rotation and minimizes rocking or tilting under cyclic or monotonic loadings.

The second major modification is that the hydraulic shear actuator is bought as close to the shaking table as possible (Figure 4.13 b). Such that, it possibly eliminate all the miss alignment at the horizontal shaft, and enhances the performance of the hydraulic actuator. Moreover, the shaking table, connecting bear bearings, and rails are all replaced with new parts. The new design also allow two testing configurations: 1) constant volume and 2) undrained testing. A two feet long acrylic cell tube is manufactured such that it provides a chamber for cell pressure. The new UTCSS is designated to conducted post-liquefaction monotonic tests that the specimen is loaded to high strain level while experiencing dilation. The current UTCSS configuration provides excessive tilting while the specimen is stiff at a high strain level.

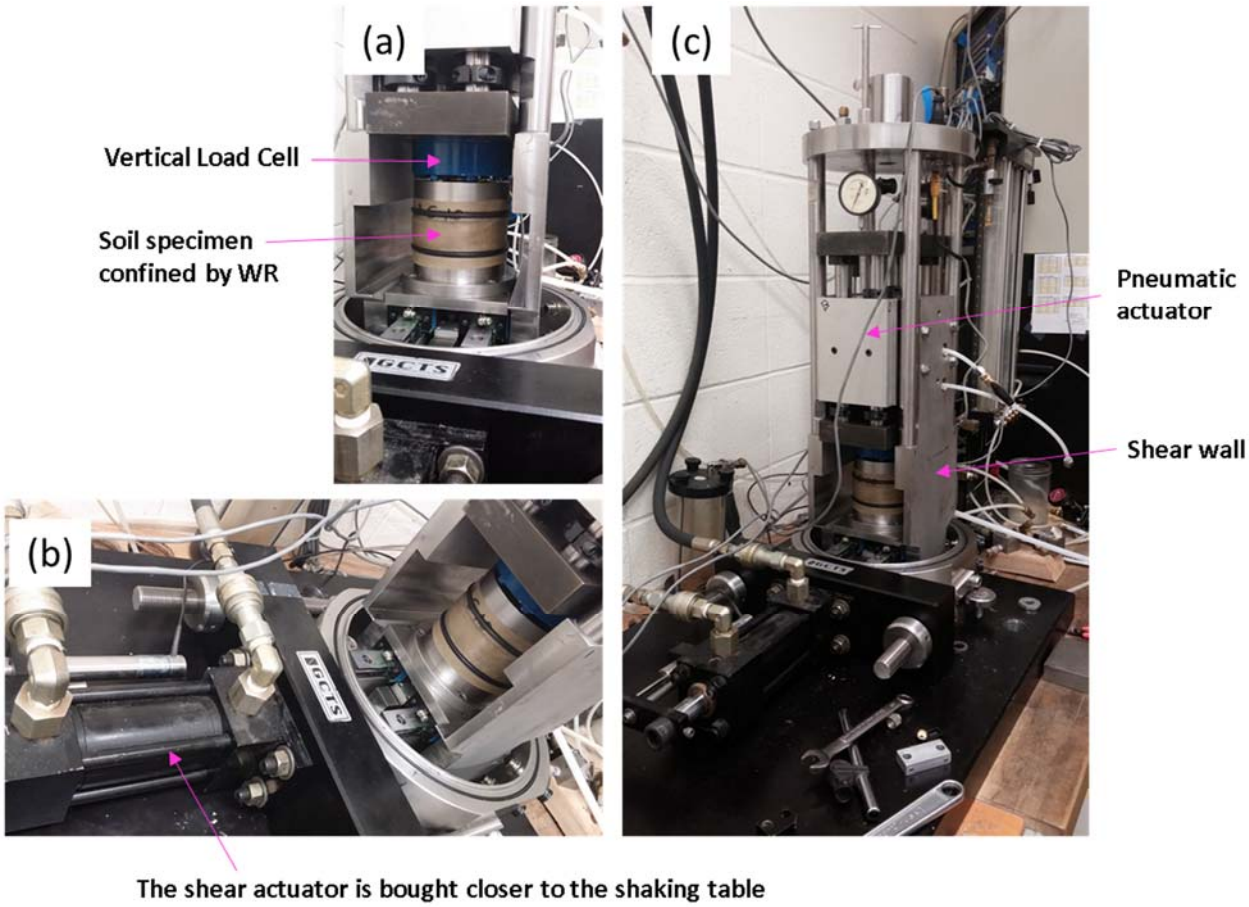

Figure 4.13 (a-c): New design of the UTCSS. (a) The location of the vertical load cell. (b) The new configuration of the actuator and shaking table. (c) Overall new setup.

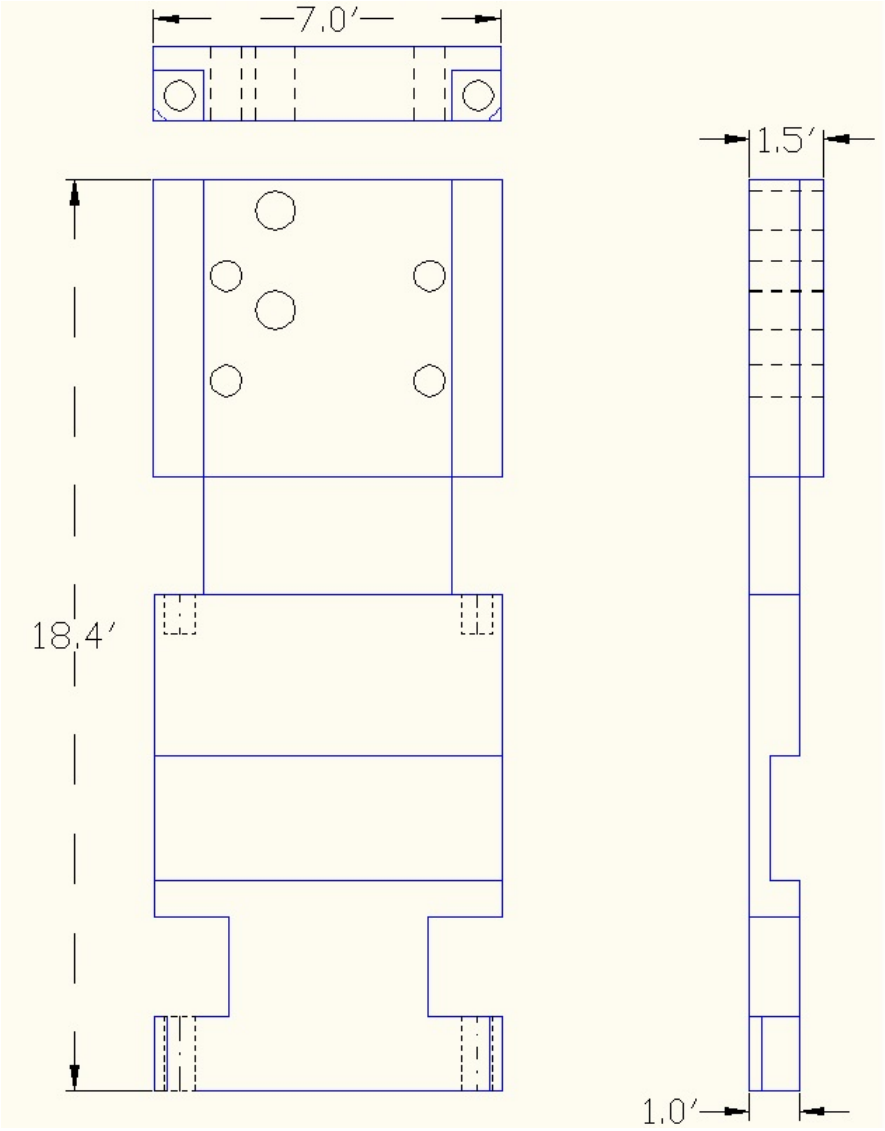

Figure 4.14: Design drawing for the shear walls of the new UTCSS apparatus.

Chapter 5: Simple Shear Testing Results

5.1 INTRODUCTION

A total of 175 tests from a testing program of simple shear on Nevada sand are presented in this chapter. The tests were conducted after the UTCSS apparatus was well calibrated with minimized degree of rocking at the top platen. Soil specimens were prepared following the methods described in chapter 3 (Sections 3.7.1 and 3.7.2) in order to achieve representable density ranges. Therefore, the tests presenting in this chapter are high quality and can be used for constitutive model calibration. There are five groups of testing based on different types of loadings: 1) Harmonic Sinusoid, 2) Modulated Sinusoid, 3) Transient, 4) Stage 2 Taper Up, and 5) Post-liquefaction Monotonic. All undrained tests were performed under load control, except the fifth group. Figure 5.1 displays the number of tests performed in each group. Discussion of the post-liquefaction monotonic data is covered in Chapter 7. Plots for the result for each test, including measured shear stress, shear strain response (γ), pore pressure ratio (r_u), stress-strain and stress path are presented in Appendixes A1 to A7. All plot traces were color-coded with respect to time to allow for direct comparison between the time history and stress-strain and stress path plots.

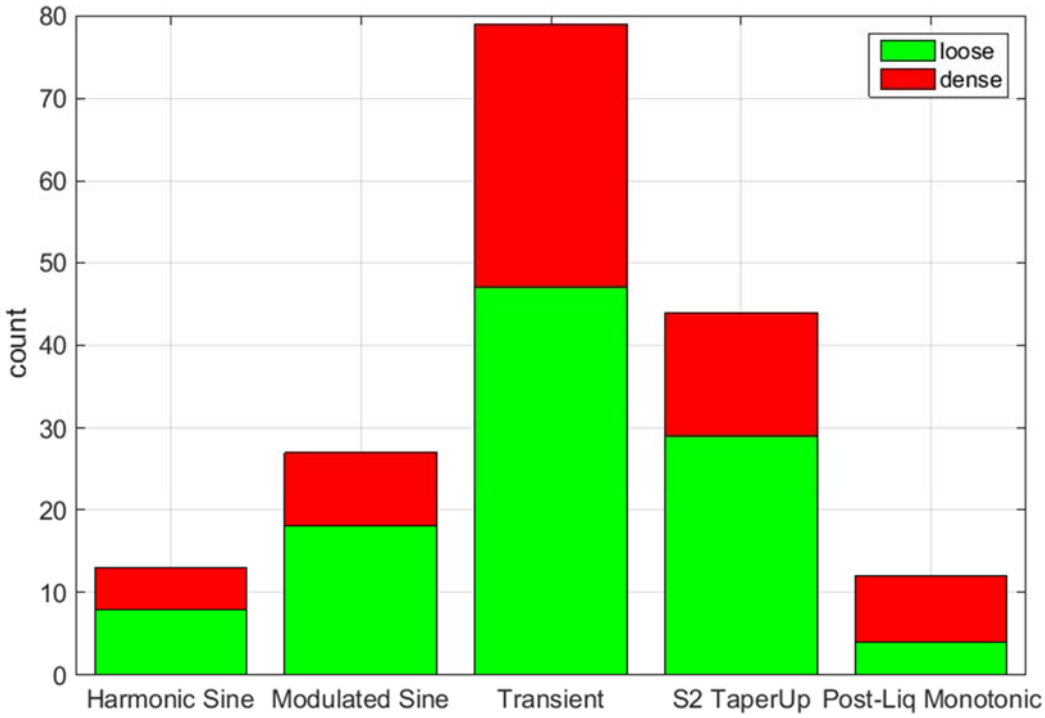

Figure 5.1: Histogram showing the number of testing in different testing groups. Green bars represent testing that was performed in loose specimens; red bars represent tests in dense specimens.

5.2 HARMONIC LOADING

The CSS tests with harmonic loading were performed under a vertical effective confining stress of 100kPa and at level ground condition ($K_\alpha = 0$). Liquefaction triggering is defined as r_u reaching unity. In order to optimize the performance of the shear actuator, all tests were conducted at a frequency of 0.2 Hz. A slower cyclic rate also allows better pore pressure measurement, since the pressure transducer is connected to the bottom of the specimen. Previous research have shown that the effect of frequency on the number of cycles to liquefaction for clean sand at a given cyclic stress ratio is not significant in stress

controlled loading (Riemer et al. 1994). Figure 5.2 depicts a CSS test result under harmonic loading. The loose specimen was liquefied in 13 cycles. As indicated in the second and third rows of subplots, the excess pore pressure increases linearly until achieving a r_u value of one, and the shear strain develops significantly more after liquefaction initiation. Stress-strain plot and stress path are also presented, and both of them are reasonably systemic along the zero shear stress axis, indicating level ground ($K_\alpha = 0$) condition.

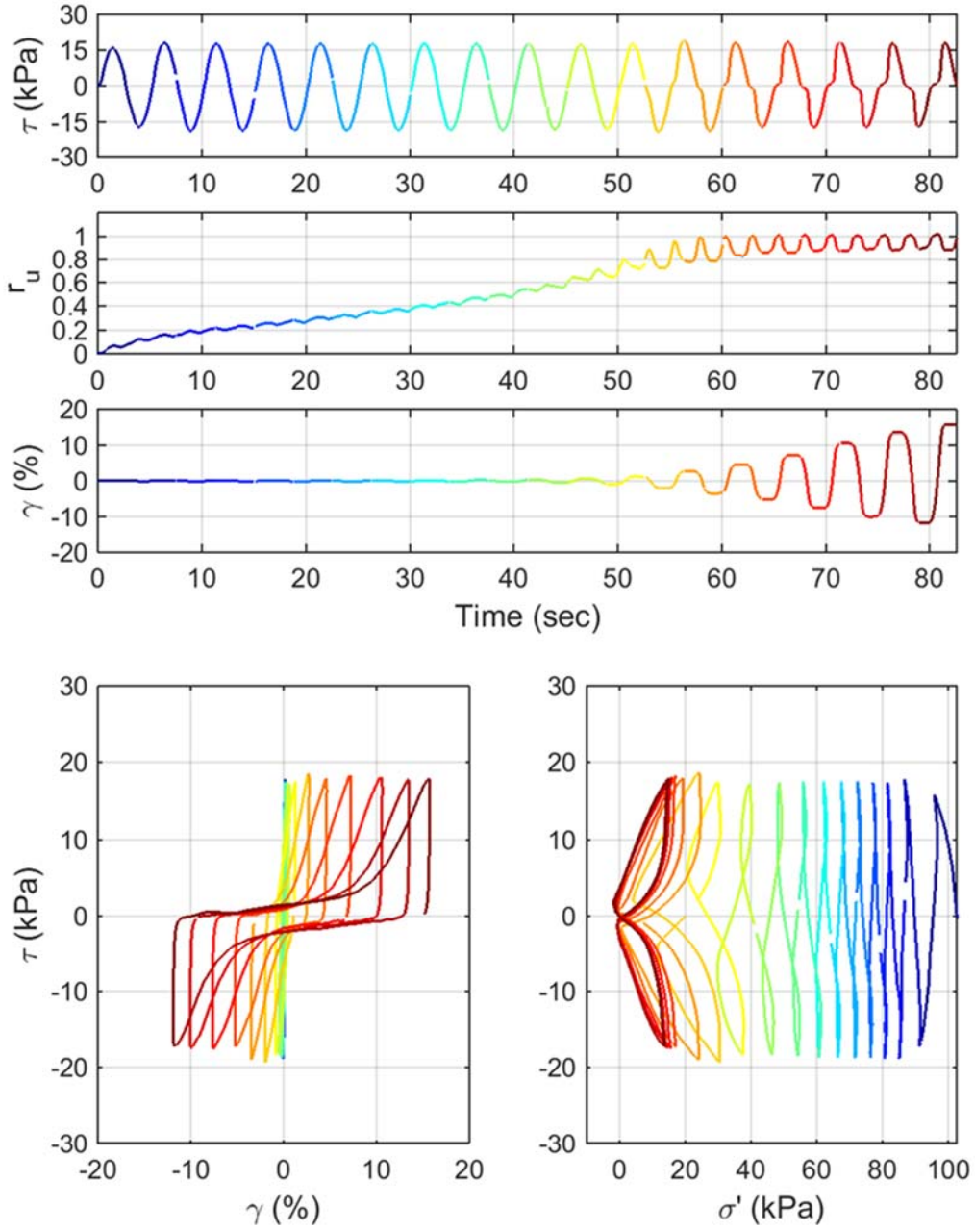

Figure 5.2: A CSS test result under harmonic loading (Test ID: 20130327, D_r = 49%)

The liquefaction resistance of soil can be characterized by a CSR vs. N_f curve, which provided the numbers of cycle (N_f) required to liquefy the specimens when shearing at a constant cyclic stress ratio (CSR). CSR values are defined based on the measured shear stresses normalized by initial effective vertical stresses:

$$CSR = \frac{\tau_{ave}}{\sigma'_{v,initial}}, where\ \tau_{ave} = \frac{\tau_{max} + \tau_{min}}{2} \qquad [5.1]$$

Figure 5.3 illustrates the CSR vs. N_f curves for the loose and dense Nevada sand specimens. The correlation between CSR and N_f is closely approximated using the formula:

$$CRR = a \cdot N^{-b} \qquad [5.2]$$

with –b as the slope of a straight line on a log(CSR) versus log(N_f) plot. In this study, b = 0.181 for the loose and 0.298 for the dense sand were obtained. Idriss (1999) used b = 0.337 for clean sand to derive a magnitude scaling factor relation for sand-like soils. CSS tests under harmonic testing are summarized in table 5.1, and a plot for each test can be found in Appendix A.2.

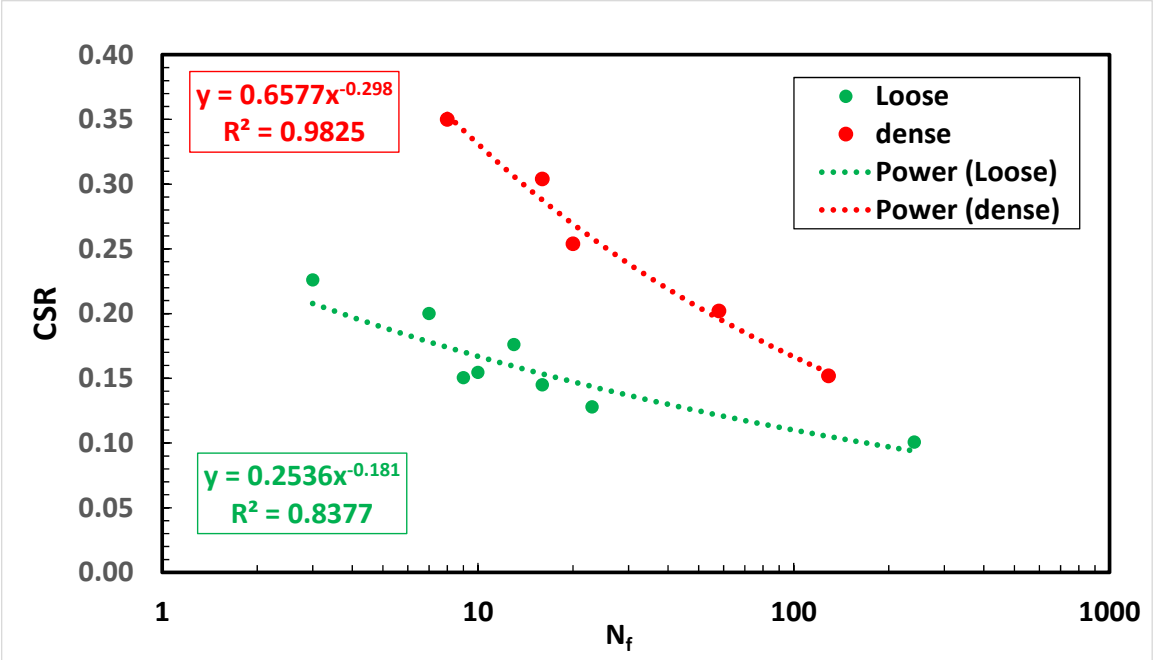

Figure 5.3. CSR vs. N_f plot for loose and dense Nevada sand specimens.

Table 5.1: Summary of CSS tests under harmonic loading.

test ID	Dr (%)	CSR	N_f
20130327	49	0.176	13
2013032902	39	0.200	7
2013040102	34	0.151	9
20130404	51	0.128	23
20130406	41	0.226	3
20130424	44	0.101	241
20130525	55	0.145	16
20130523	55	0.155	10
2013051502	85	0.152	129
20130516	85	0.202	58
2013051602	74	0.254	20
20130517	79	0.304	16
20130711	78	0.350	8

5.2.1 Recorded Rocking

Mechanical compliance that leads to relative rocking motion between the top and bottom platens should be minimized. However, the original design of the GCTS CSS apparatus has not addressed this issue well. The system was not sufficiently stiff and caused an excessive rocking at the top platen. To address this problem, an aluminum block was designed and installed on the top platen to increase the rigidity and restricting the rocking motion. In addition, two LVDTs were used to measure vertical displacements at two different locations; at the vertical actuator and at the edge of the top platen. The measurements can be used to observe volumetric changes during consolidation and rocking or tilting at the top platen during shear. Tilting or rocking occurs when monotonic or cyclic loads apply. If the top platen remains perfectly flat, the two vertical LVDTs should provide synchronous readings. If there is rocking, the amount of tilting can be quantified by the difference of the two vertical LVDTs. From the results of the CSS tests under harmonic loadings, the degree of rocking at the top platen depends on a few factors: 1) the stiffness of the soil specimen (i.e. relative density), 2) number of loading cycle, and 3) input shear stress amplitude. In this study, rocking is quantified as the following:

$$\text{Max. R}ocking = \frac{\max\left(LVDT_{center}(t) - LVDT_{edge}(t)\right)}{H} * 100\% \qquad [5.3]$$

where H is the height of the soil specimen, $LVDT_{center}$ is the normal LVDT (Figure 3.13), $LVDT_{edge}$ is the internal vertical LVDT (Figure 3.13).

Figure 5.4 illustrates the relationship between the cyclic loading amplitude (CSR) and recorded rocking. The degree of rocking is found to increase with the amplitude of shear stress. Extensive rocking was found in a test with CSR = 0.1, because it was loaded with a very high number of cycles (N_f = 241). N_f is found to have no significant effect on

the amount of rock unless over 200 cycles of loading. Also, excessive rocking is found in the test with the highest CSR input of 0.35. These two tests were omitted when calculating the overall rocking of the testing program because the CSR level and number of loading cycles are not relevant to other tests with different types of loading, particularly the transient loadings.

As seen in figure 5.5, a higher amount of rocking is found in the higher range of r_u. This consequence more likely is due to the fact that the higher shear displacements has been mobilized, particularly post-liquefaction. Figure 5.6 displays the amount of rocking increases with the shear stain level. At a relative small strain level ($<10^{-2}$ %), both loose and dense specimens provide similar amount of rocking. As a matter of fact, 10^{-2}% is the threshold shear strain that excess pore pressure starts to be generated, reported by Dobry et al. (1982). After the threshold, the dense tests give significantly higher amount of rocking than the loose tests, which leads to an observation that the amount of rocking is depended on specimen's stiffness. Under the current UTCSS configuration, the combination of high shear displacement and stiff specimen may lead to excessive rocking or tilting. For CSS testing, the two criteria are not fulfilled, because when the specimen is intact, the shear strain level is low ($<10^{-2}$ %); when the shear strain level is high, the specimen has been softened. However, the two criteria for excessive tilting may be found in the testing of post-liquefaction monotonic loading, due to the dilative response of liquefied sand at large strain. More details on the post-liquefaction are covered in section 7.2.

From the harmonic CSS test results, upon liquefaction initiation, the level of rocking is generally estimated as 1% for the loose specimens and 2.5% for the dense specimens.

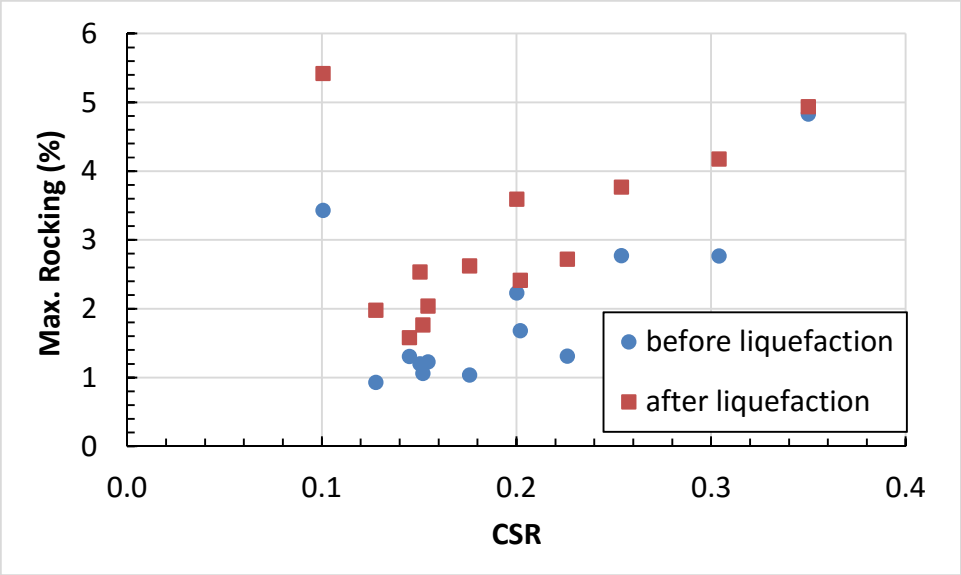

Figure 5.4: Max. Rocking vs. CSR from the CSS tests with harmonic loading.

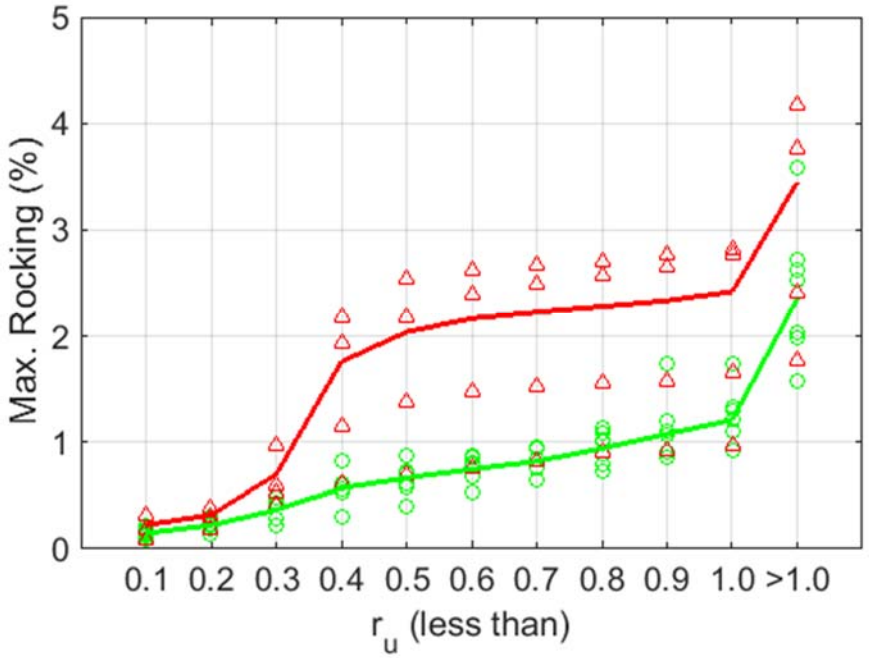

Figure 5.5: Amount of Rocking [%] at different levels of r_u values. Open green circle represents tests on loose specimen. Open red triangle represents tests on dense specimen. The green and red lines represent the average values of the amount of rocking at the corresponding r_u level.

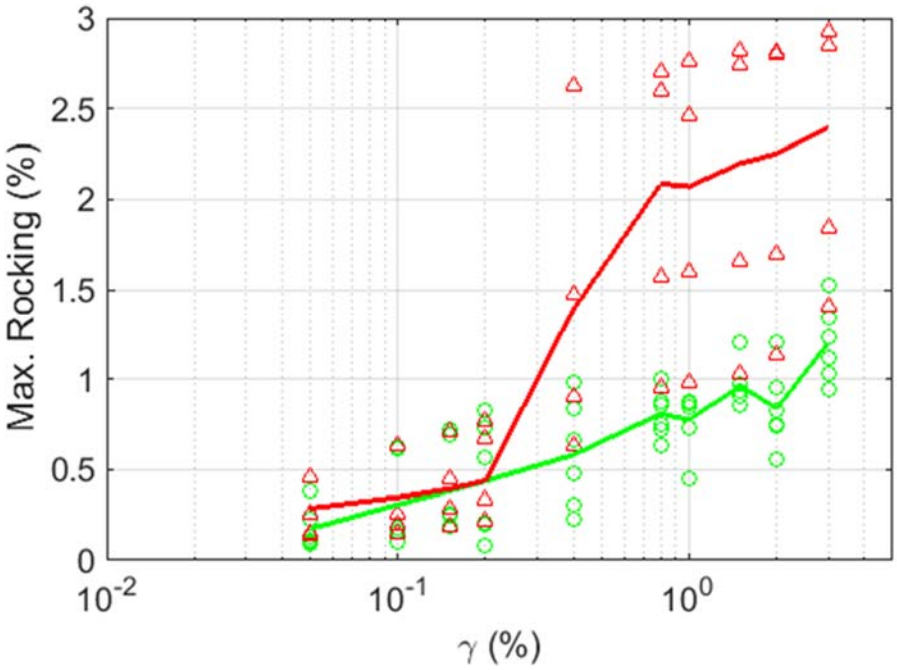

Figure 5.6: Amount of Rocking [%] at different levels of shear strain values. Open green circle represents tests on loose specimen. Open red triangle represents tests on dense specimen. The green and red lines represent the average values of the amount of rocking at the corresponding shear strain level.

5.3 MODULATED SINUSOID LOADING

While the modulated sinusoid and tamper motions present a more simplified loading sequence than the transient loading, these tests are useful for illustrating the soil response under loading beyond uniform cycles. It can potentially establish some basic principles of soil responses before advancing to transient loadings, for which the motions are random and complicated. Unlike the motions illustrated in chapter 4.4.2., the modulated sinusoid motions consist of harmonic and taper components. The taper-up motions consisted of ten taper-up cycles with various increasing rates, followed by ten uniform cycles (Figure 5.7). The taper down motions consisted often initial uniform cycles,

followed by ten taper-down cycles with different decreasing rates (Figure 5.8). The baseline motion for these tests was a harmonic loading with twenty uniform-amplitude cycles. The taper amplitudes were generated from a sinusoid uniform function by a multiplying factor, $(t/10)^n$, where t is the time in the corresponding motion, and n is a constant varying from 0.1 to 10 (0.1, 0.2, 0.4, 0.67, 1, 1.5, 2.5 and 10). The tests are grouped in three sets:

1) taper up motions on loose sand (Figure 5.9)
2) taper down motions on loose sand (Figure 5.10)
3) taper up motions on dense sand (Figure 5.11)

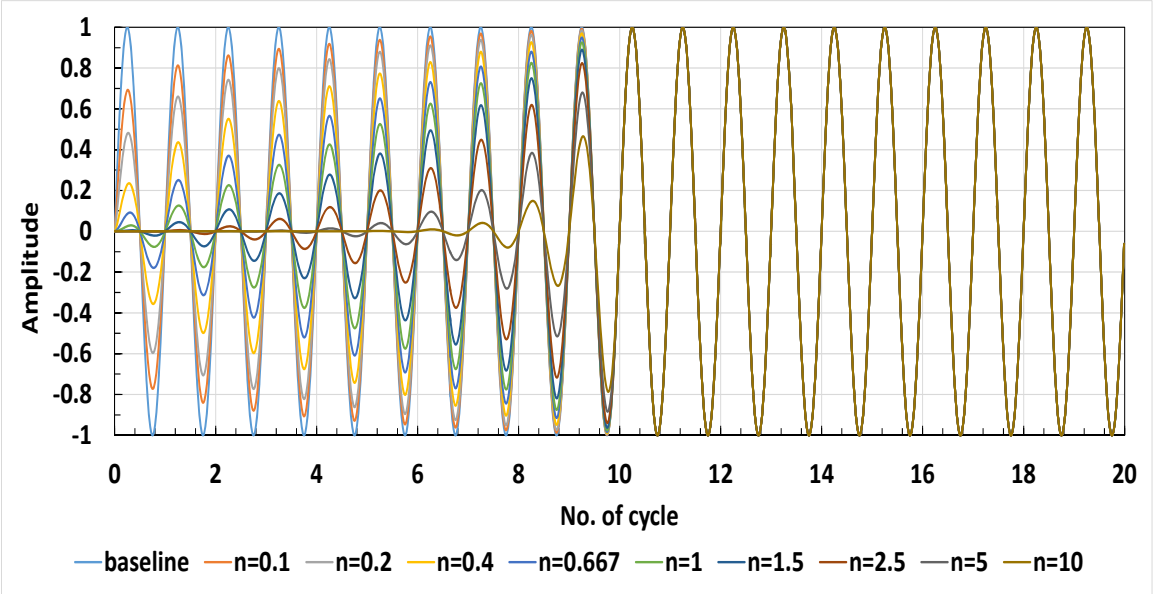

Figure 5.7: Input taper up motions

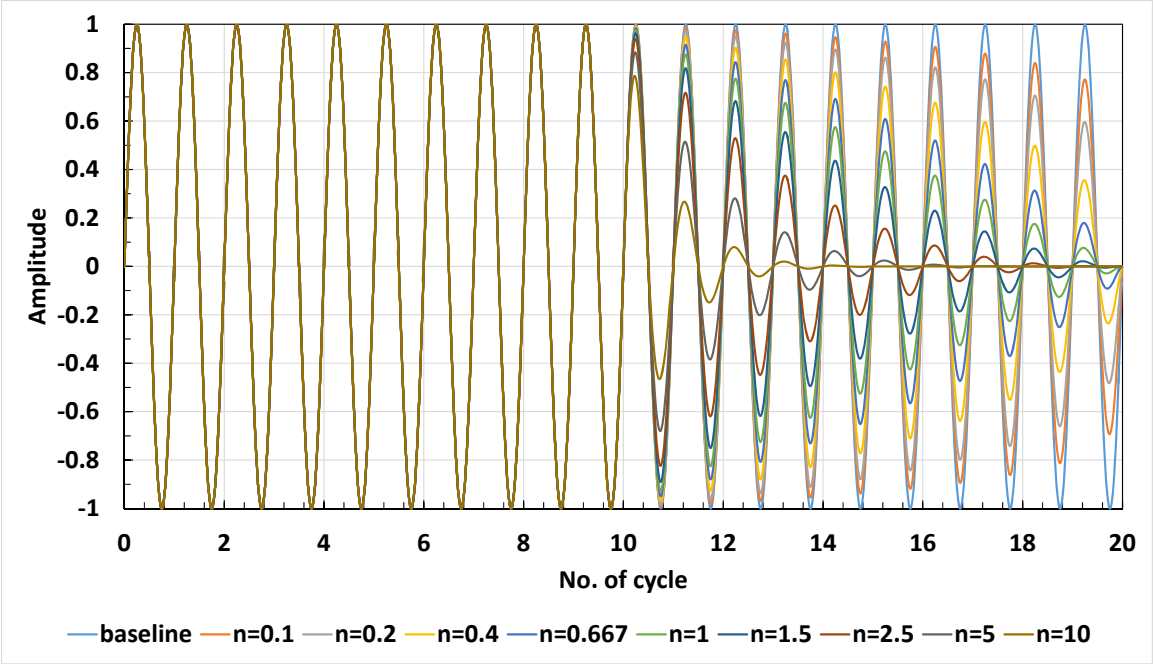

Figure 5.8: Input taper down motions

5.3.1 Taper Up Loading on Loose Sand

The first set of tests consist a series of taper up motions followed by ten uniform cycles. A constant CSR was selected for all tests (based on the peak-peak value of the uniform loading cycles); the CSR value was selected as best estimate to trigger liquefaction at the end of the input motions (Figure 5.9). For the five tests with a similar relative density of over 50% (n = 0.1, 0.2, 0.4, 0.67 and 1.5), the development of pore pressure generation is found to be related to the n value; the higher the increasing rate in tapering, the higher the pore pressure generation rate (Figure 5.10). Moreover, it is surprising that the test with a taper motion of n=0.1 is providing a more severe damage than the baseline motion, which is expected to be the worst case scenario because the 20 uniform cycles are at the highest loading amplitude. This finding implies that a series of ascending pulse at a specific rate

may generate more excess pore pressure than a series of uniform loading at maximum amplitude. In other words, a taper motion, even with a smaller amplitude per cycle, can cause more damage than the uniform cycle composed with higher amplitudes. This data set suggests the ascending rate of n = 0.1 is critical, because another test with n=0.2 shows a significantly smaller excess pore pressure generation, compared to the baseline motion. These results imply that the preceding cycle amplitude can impact the responses under the current cycle. The test results here provide a useful database for potentially refining the practice of number of equivalent cycle concept by adding a weighted factor that consider the amplitude of the preceding cycles.

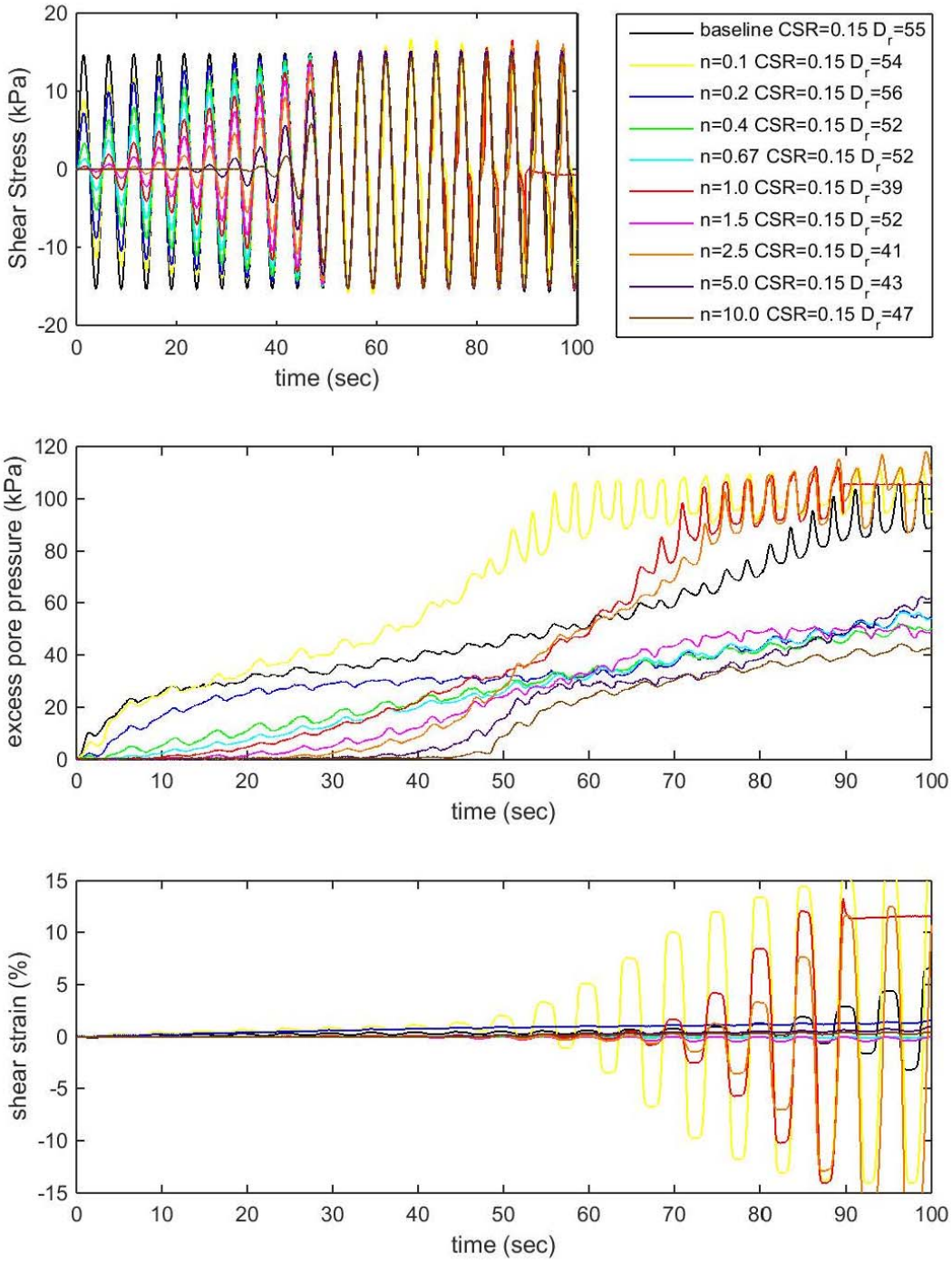

Figure 5.9: Test results of taper up motions on loose specimens. Measured shear stress at the top, pore pressure generation at the middle and shear strain at the bottom.

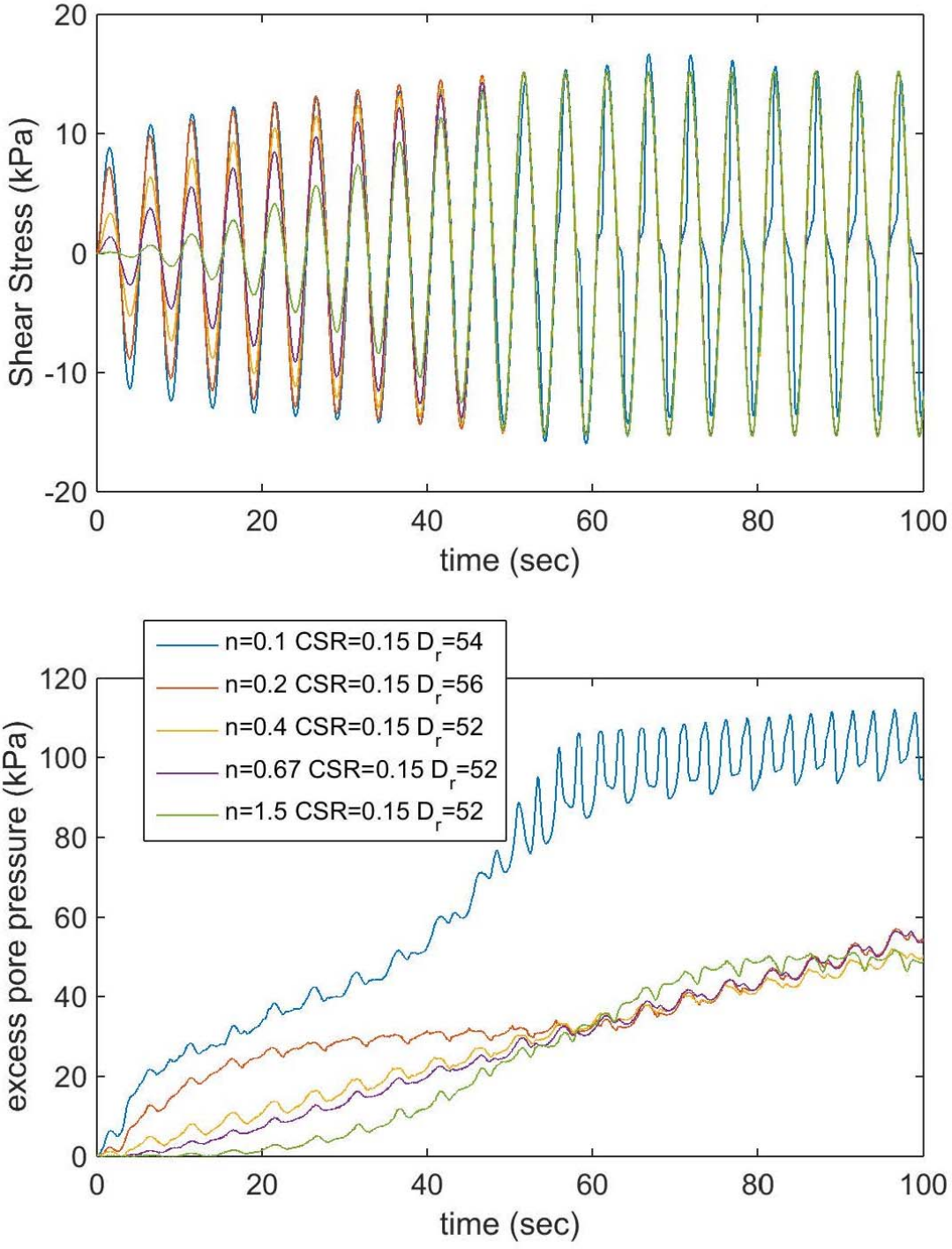

Figure 5.10: Five tests from the first set of taper up motion showing comparable pore pressure generation.

5.3.2 Taper Down Loading on Loose Sand

Various CSR were applied to the second set of data (Figure 5.11), i.e. the taper down motions on loose specimens. The applied CSR for each test was designated to trigger liquefaction at the end of the applied motion. Compared to the first set of tests (taper up), the pore pressure generation is limited when the taper down motions were loaded (11^{th} to 20^{th} cycle). The pore pressure generation is basically leveled out after the first ten cycles of uniform loading. Figure 5.12 compares the responses of pore pressure generation from eight different tests under the taper up and taper down motions. The responses are very different. The taper up motions, depending on the shear stress amplitude, continuously generated excess pore pressure throughout the twenty cycles. However, for the taper down motions, the taper down portion almost has no effect on the pore pressure generation after the ten preceding uniform cycles. This finding is attributed to the importance of order in the shear stress cycle. Given the same shear stress amplitudes and number of cycle, the undrained soil response can be very different if the order of stress cycle (taper up or taper down) is different. Regrettably, the current stress-based liquefaction evaluation procedure cannot address the spectral differences, since both taper up and taper down motions are characterized by the same maximum amplitude only.

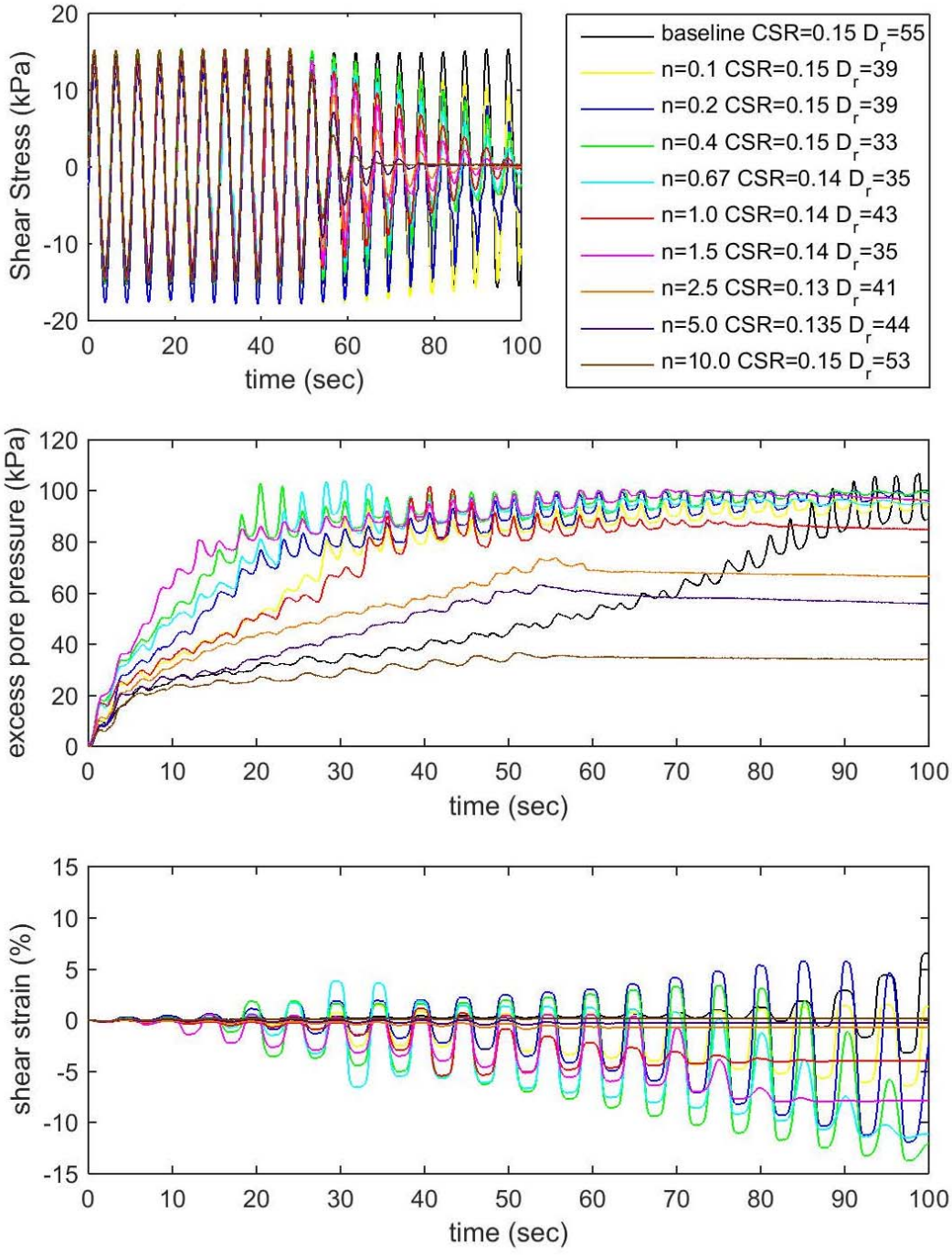

Figure 5.11: Test Results of Taper Down Motions on Loose Specimens. Measured shear stress at the top, pore pressure generation at the middle and shear strain at the bottom.

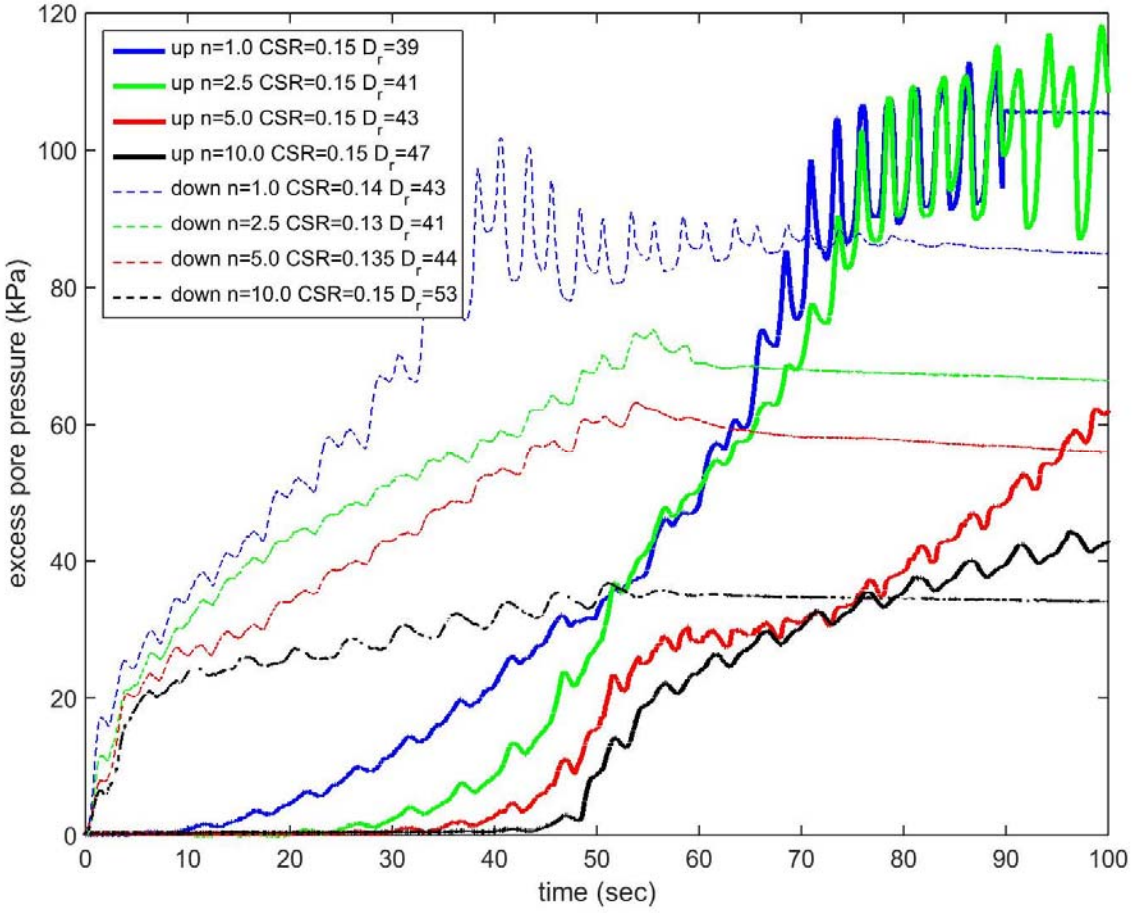

Figure 5.12: Comparing the response of pore pressure generation between the taper up and taper down motions.

5.3.3 Taper Up Loading on Dense Sand

The taper up motions were repeated with the dense soil specimens, and the test results (Figure 5.13) also show that a more severe damage is found in the n = 0.1 taper up motion (yellow) than the baseline motion (black). This set of data confirmed that, even in dense sand, a more severe damage could be found in a motion with smaller amplitudes and an increasing rate than the baseline motion of uniform cycles. Overall, the excess pore pressure generations agree with the results from the loose tests, progressively increasing.

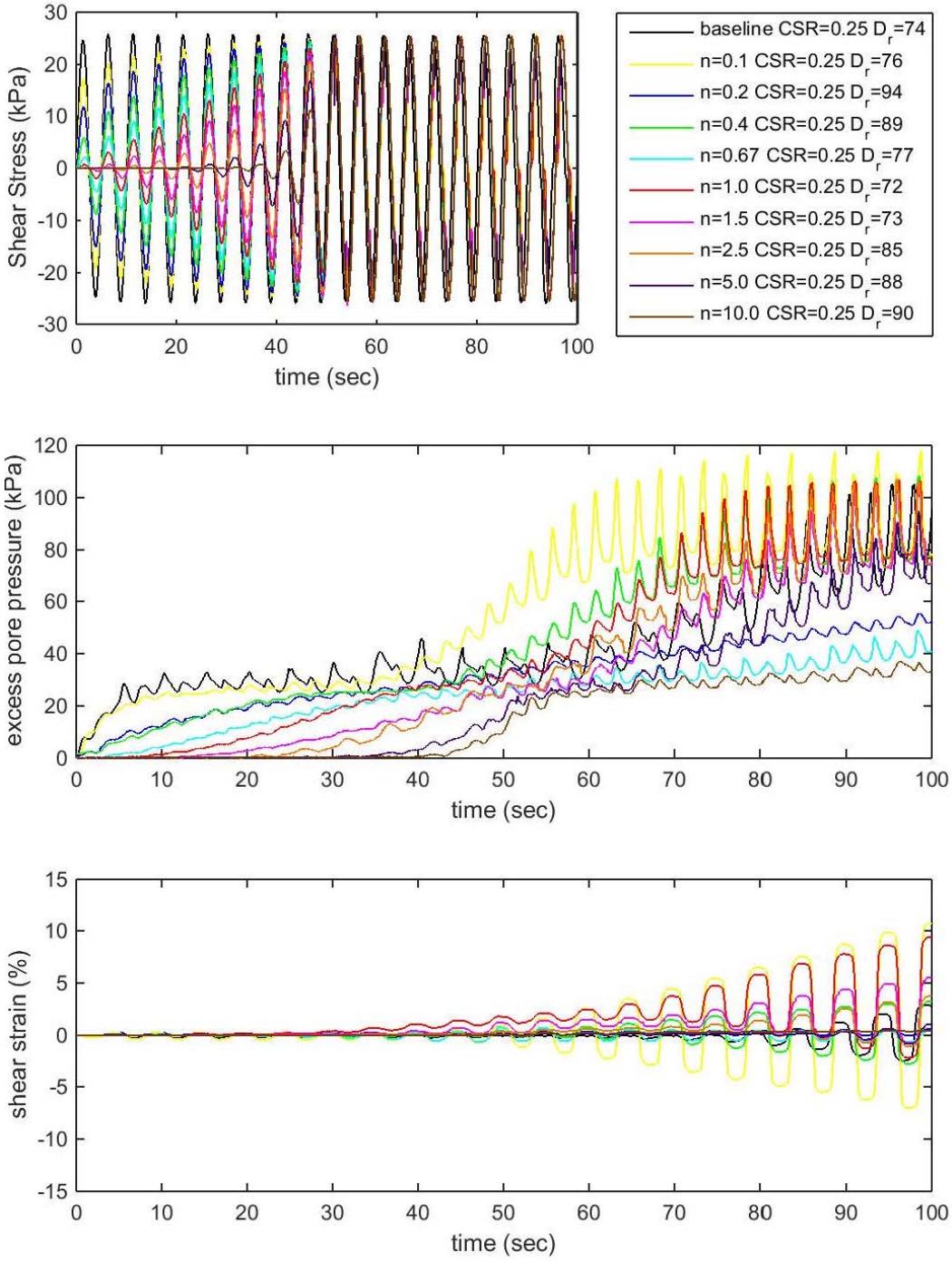

Figure 5.13: Test results of taper up motions on dense specimens. Measured shear stress at the top, pore pressure generation at the middle and shear strain at the bottom.

From the three sets of modulated sinusoid data, the following conclusions are made:

1. The order of stress cycle matters. Even though with the same shear stress amplitudes, ascending or descending pattern dictates the soil responses.
2. The relative amplitude of preceding cycle matters. Both the loose and dense test results indicate that greater excess pore pressures were generated in tests with n = 0.1 ascending rate than in tests with constant maximum amplitudes.

5.4 TRANSIENT LOADINGS

79 tests (47 loose and 32 dense) were performed under transient loading with 22 different ground motions. The tests were divided into three sets, and the grouping is in accordance to the investigation purpose. Each set will be discussed later. The ground motions were selected from the PEER NGA strong motion database, and converted into shear stress time histories. At the shearing stage of each test, a scaling factor was estimated and applied to adjust the shear stress amplitude, so that liquefaction was triggered towards the end of each transient loading. In fact, the scaling factor was mainly selected based on trial-and-error. Some scaling factors were 'overshoot', and therefore liquefaction were triggered in the early part of applied motions. Some scaling factors were 'underestimated'; hence, lower r_u values were achieved even after the application of the complete ground motion. Figure 5.14 displays the number of test at different r_u ranges.

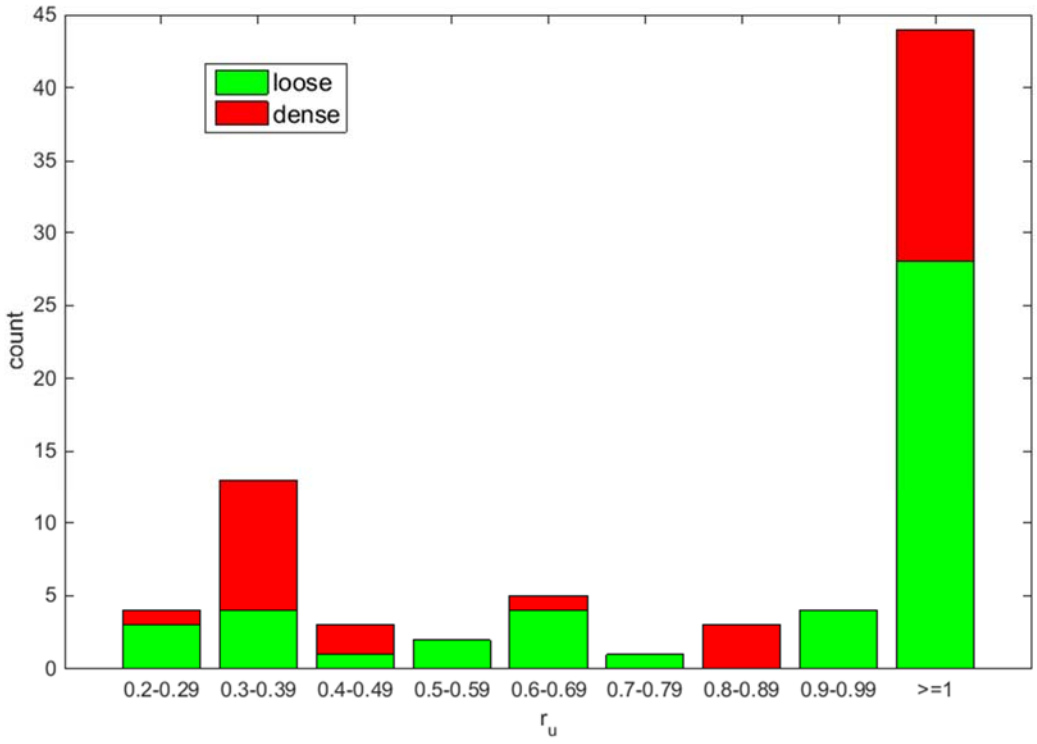

Figure 5.14: Histogram on CSS transient loading test achieving different r_u values

The details of each test such as stress path and stress-strain plots can be found in Appendixes A.4 and A.5. An example of these results is presented in Figure 5.15. Compared with the CSS test result under harmonic loading (Figure 5.2), the test under transient loading reflects much more complicated stress strain plot and stress path. The generation of excess pore pressure is no longer linear. Moreover, the stiffness of the liquefied soil decreases rapidly upon liquefaction initiation; consequently, the specimens reduce its ability to carry high frequency content while enhancing its ability to carry low frequency content. Moreover, the closed loop, electro-hydraulically actuated piston is not able to match the high deformations required to reach the target stresses with the dramatic decrease in soil stiffness (the system settings are optimized to match the loading pattern in

the pre-liquefaction phase. Therefore, the recorded shear stress histories do not match the input transient loadings beyond liquefaction as can be seen in Figure 5.16.

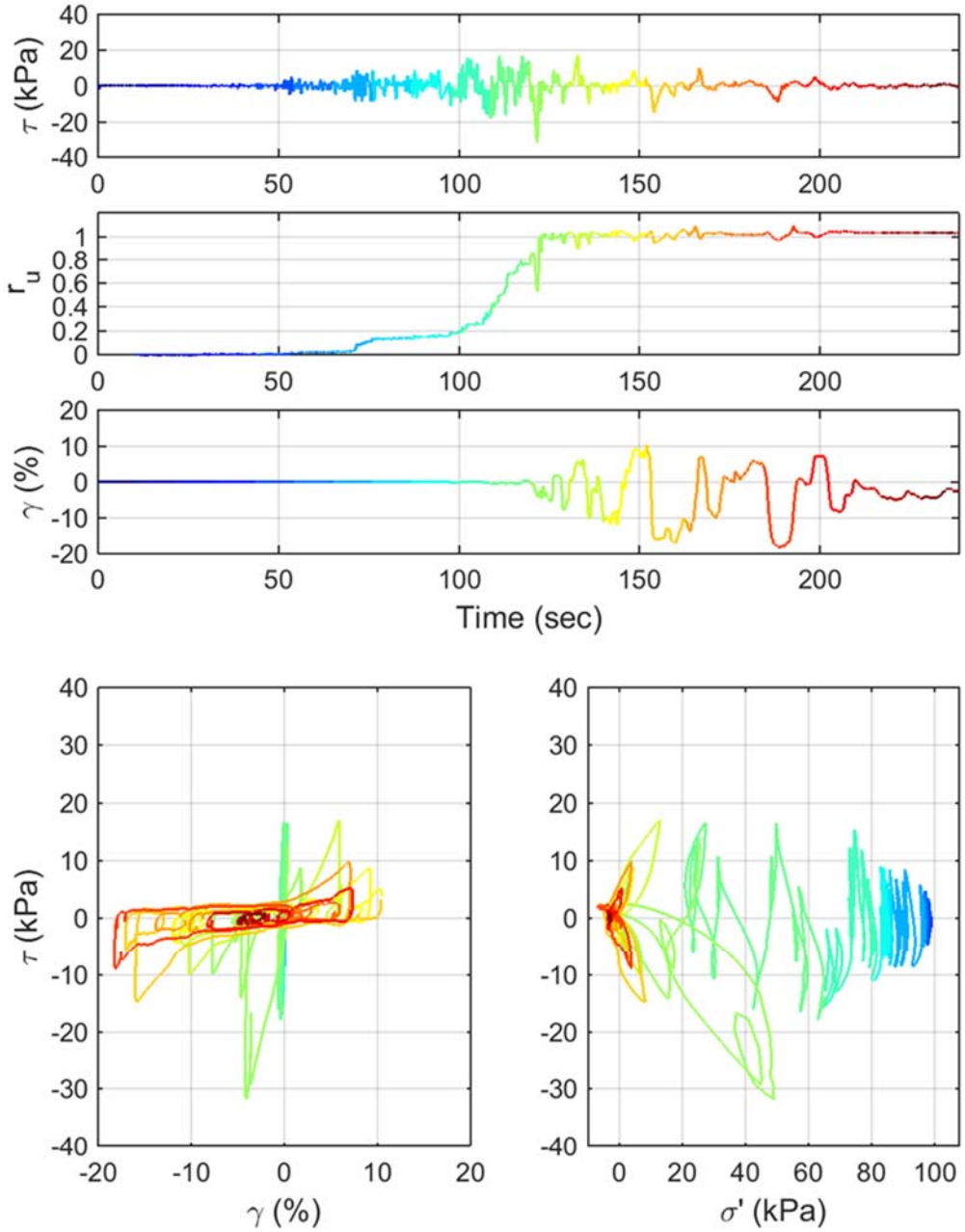

Figure 5.15: A CSS test result under transient loading (Test ID: 2013021502, D_r = 47%).

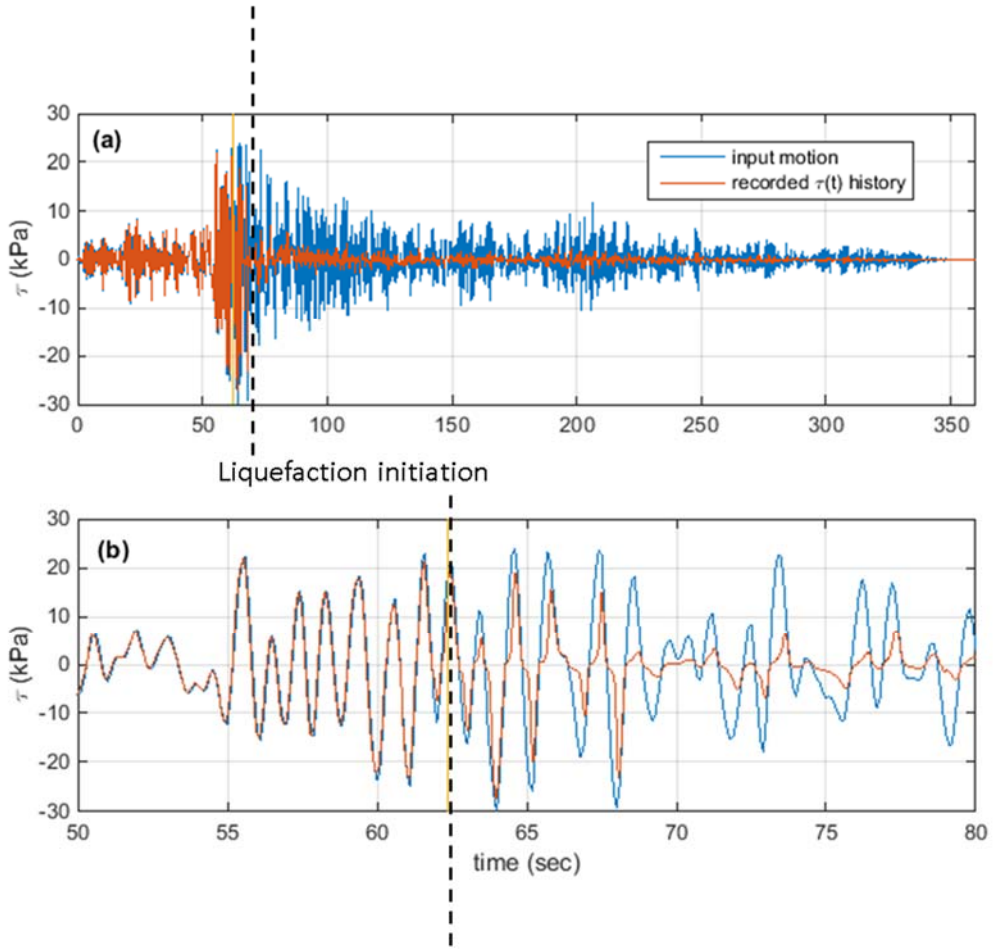

Figure 5.16: Comparison on input and recorded shear stress time history (Test ID: 130117, Ground Motion: NGA_no_1157_CNA000).

The results presented in this chapter are focused on the overall perspective of ground motion loading and excess pore pressure generation in the CSS database.. In order to compare all tests on the same plot, the x-axis is normalized by the liquefaction time of each test specifically and data is plotted up to time of liquefaction only. Figure 5.15 shows the normalized cumulative sum of the shear stress square (normalized by its values at liquefaction) on the y-axis, $N.\Sigma\,\tau^2\,(t)$ (Equation 5.4), to reflect how the loading is building building up for each of the transient loading histories.

$$N.\Sigma\,\tau^2\,(t) = \frac{\int_0^t \tau^2\,(t)\,dt}{\int_0^{t_{liq}} \tau^2\,(t)\,dt} \qquad [5.4]$$

Squaring the shear stress time history allows to account for the absolute magnitude of both, positive and negative, shear stresses and the integration over time provides the cumulative loading up to a specific time. $N.\Sigma\,\tau^2\,(t)$ is the cumulative shear stress square normalized by the cumulative value at the time of liquefaction (t_{liq}).

Figure 5.17 illustrates the variety in loading build-up for the different transient loadings adopted in this research project and Figure 5.18 displays the development of r_u under these loads. Figure 5.17 also shows the the differences of the $N.\Sigma\,\tau^2\,(t)$ development development between harmonic and transient loading. On the normalized plots, the harmonic loadings almost provide a linear-proportional relationship between the loading and time, and a narrow band of pore pressure generation buildup, indicating that harmonic loading may not be a good representation of ground motions, which have very different time-domain characteristics. For the transient ground motions, the loading can build up relatively quick (if the ground motion dominant peaks are at the earlier stages of the loading time similar to NGA #107 in red), or relatively slow if the dominating pulses are located at the tail end of ground motion (NGA #1792 in green). In order to improve the characterization of earthquake loading, a more sophisticated method is needed. Figure 5.19 compares the CSS data from this research project with data reported by DeAlba (1976), which conducted cyclic simple shear tests on Monterey #0/30 sand. The harmonic loading results from this study matches well with the results from DeAlba, 1976.

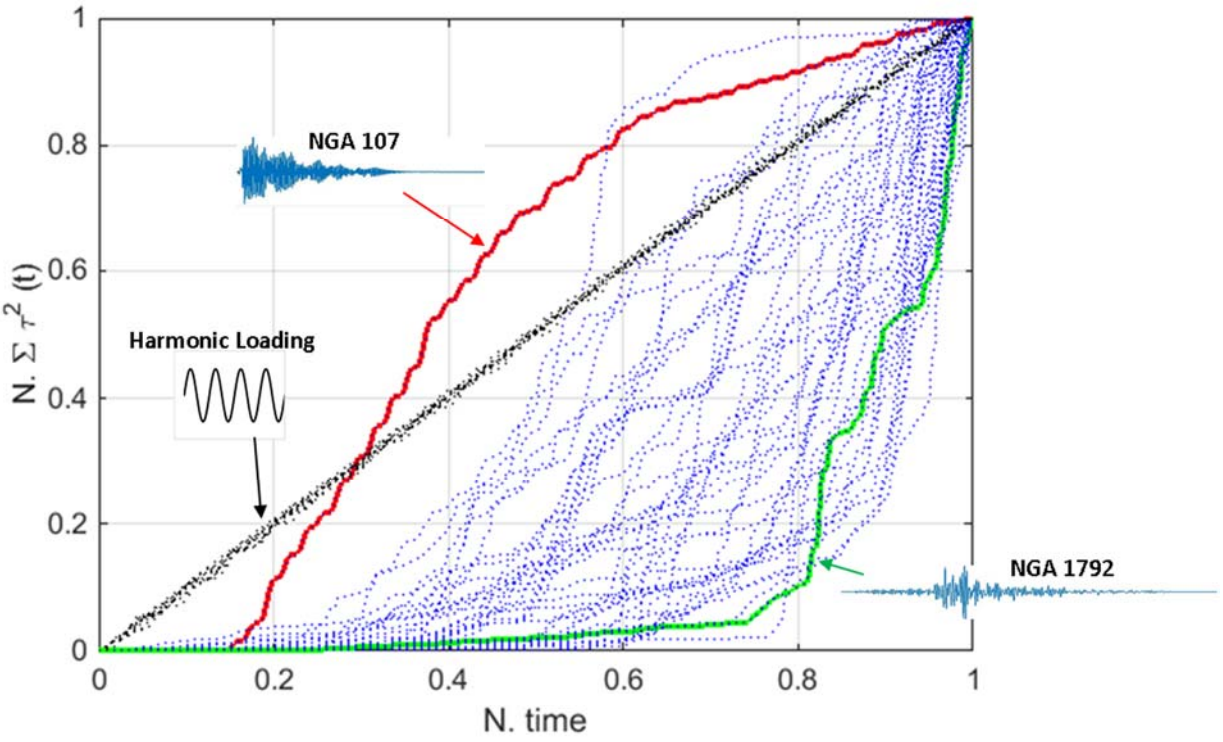

Figure 5.17: $N.\Sigma\,\tau^2$ (t) vs. normalized time for the 23 CSS tests under transient loading achieving r_u = 1.0 and uniform harmonic loading plots. Blue dot lines represent transient loading; black dot lines represent harmonic loading.

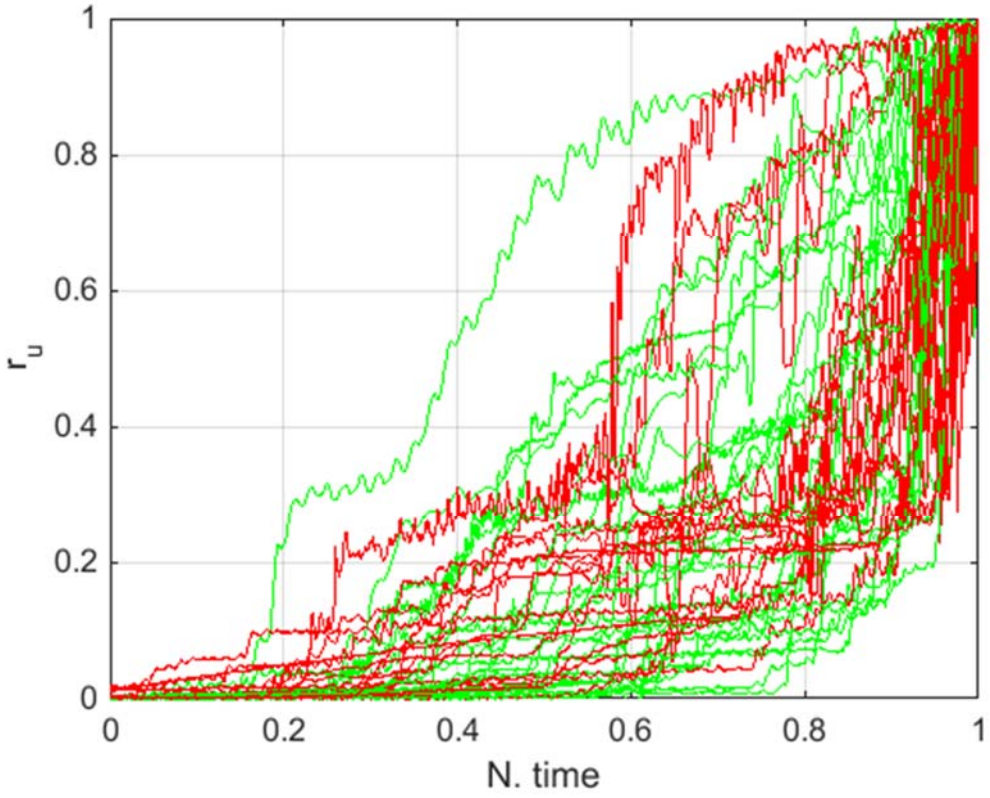

Figure 5.18: r_u vs. normalized time for the 23 CSS tests under transient loading achieving $r_u = 1.0$. Green lines represent the loose specimens; red lines represent the dense specimens.

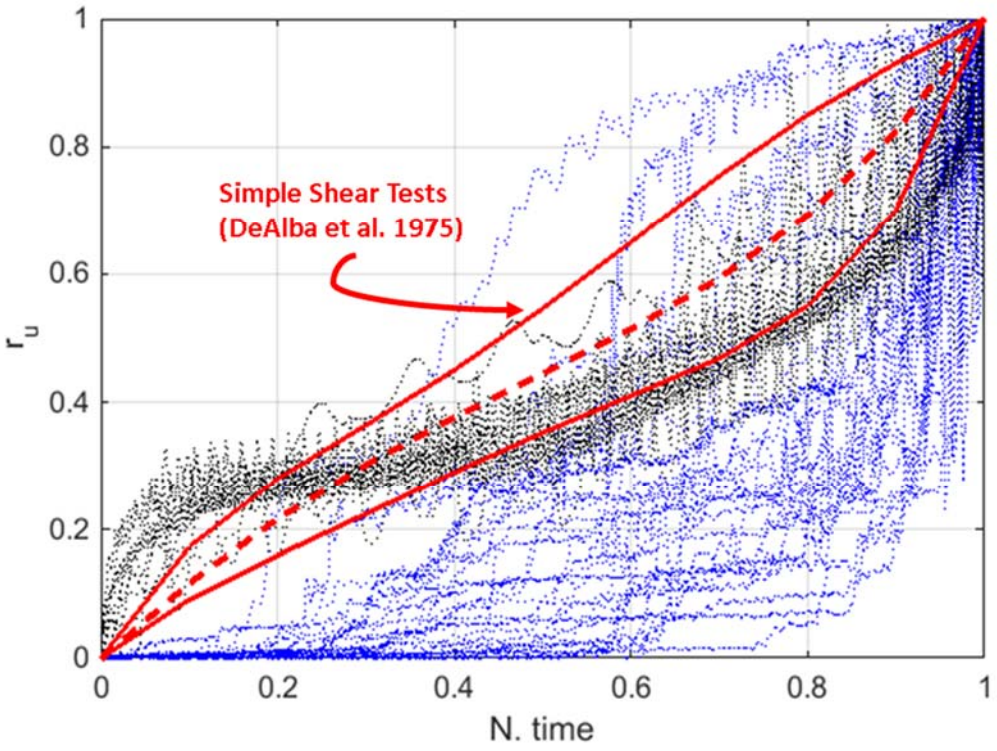

Figure 5.19: Comparing the differences of excess pore pressure generation between transient loadings and harmonic loadings. Blue dot lines represent transient loading; black dot lines represent harmonic loading, Red lines represent the results from DeAlba et al (1975).

5.4.1 Ground Motion Selection

The previous testing result from the modulated sinusoid loading suggests that pore pressure generation is highly dependent on the order of shear stress pulses. The transient loading test results consistently show that the major amount of excess pore pressure is generated from a few dominant pulses, which were located at the early or later part of a ground motion. However, the current stress-based procedures for characterizing earthquake loading have only a very crude estimation of the ground motion duration and are incapable of addressing the time domain characteristic of ground motions. Therefore,

a more detailed framework on characterizing the earthquake loadings is needed. The proposed model should be evolutionary and matched the rate of excess pore pressure generation with time. A few IMs such as CAV_5, I_a, NED and PGA_M have been proposed by different researchers as potential candidates. Twenty two ground motions were selected to study the undrained soil response before and after liquefaction initiation, and evaluate the efficiency of the current evolutionary intensity measures in characterizing the loading. The 22 ground motions are grouped into three sets:

1) Investigation of CAV_5 and PGA_M,

2) Rate of energy build up, and

3) Processed transient motions.

5.4.1.1 Ground Motion Selection for the Investigation of CAV_5 and PGA_M

The first set consists of nine ground motions that were selected to investigate the predictive capabilities of CAV_5 and PGA_M. The ground motions were primarily picked from the database of Abegg (2010), which documented many more ground motions that were selected from the PEER NGA database for numerical studies. Figure 5.20 illustrates the nine motions, with their peak amplitudes normalized to a unity. Each motion in this set contains very different time-domain characteristics, from short to long duration, low to high frequency content, and one dominant pulse to a few dominant ones. This set of ground motion includes loadings that can yield very high CAV_5 values (NGA No. 880, 1534 and 1157) and very low CAV_5 values (NGA No. 484, 695 and 249). Moreover, extreme values in PGA_m are also considered. High PGA_m, such as NGA No. 1792 and No. 149, mean the ground motion contain a dominant pulse. Whereas, a ground motion composing with

similar amplitude is characterized as low PGA_m (e.g. NGA No. 527). The following table summarizes the first set of ground motion:

Table 5.2: Summary of the first set of ground motion.

Set	Motion	feature
1	NGA_no_484_PLK-NS.AT2	low CAV_5
	NGA_no_880_MCF000.AT2	high CAV_5
	NGA_no_1534_TCU107N.AT2	high CAV_5
	NGA_no_1157_CNA000.AT2	high CAV_5
	NGA_no_695_A-RO3000.AT2	low CAV_5
	NGA_no_249_L-FIS090.AT2	low CAV_5
	NGA_no_1792_12543090.AT2	high PGA_M
	NGA_no_527_MVH135.AT2	low PGA_M
	NGA_no_149_G04360.AT2	high PGA_M

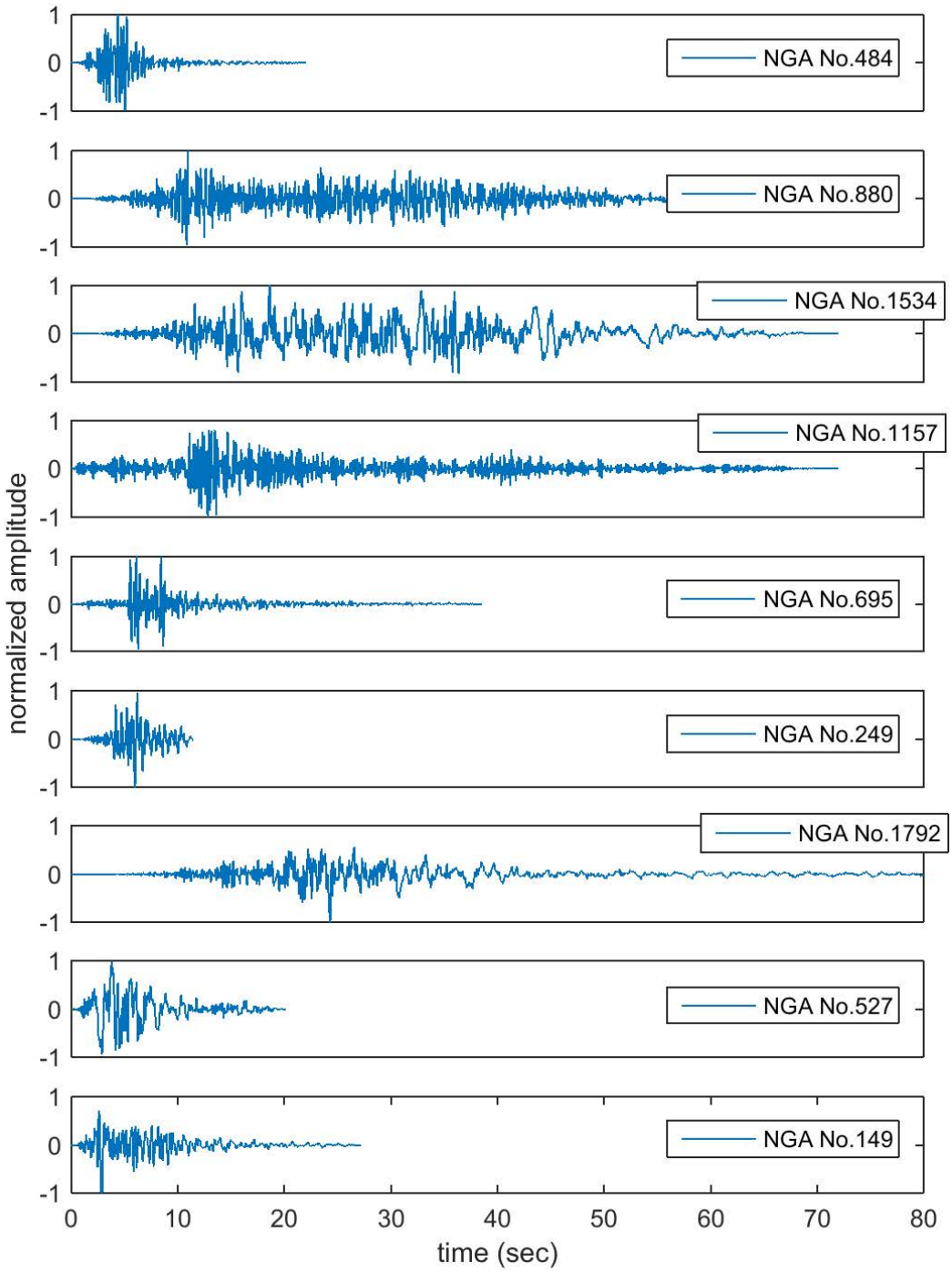

Figure 5.20: Ground motions selected for use based on IM behavior.

The test results can also be used to validate the current CSR based liquefaction procedure, since the input shear stress amplitudes are scalable. If the tests were conducted using transient loading histories with similar MSF adjusted CSR values, the results should have a similar binary outcome, liquefied or not liquefied. Section 5.4.2. covers the validation of the procedure.

5.4.1.2 Rate of Energy Build Up

The second set consists of seven ground motions (Figure 5.21 and Table 5.3) that were selected to investigate how the order of shear stress pulses governing the soil response. Each ground motions provides different rates of energy buildup, which are displayed in Figure 5.22, indicating by the $N.\Sigma\,\tau^2\,(t)$. Noticeably, NGA-107 has the fastest fastest rate of loading buildup. Figure 5.23 show that the excess pore pressure generation developments, which appear similarly to the ways that $N.\Sigma\,\tau^2\,(t)$ develop. Again, the test with NGA-107 shows fastest rate in pore pressure generation.

Table 5.3: Summary of the second set of ground motion.

Set	Ground Motion
2	NGA_no_107_B-OAP180.AT2
	NGA_no_288_A-BRZ000.AT2
	NGA_no_587_A-MAT083.AT2
	NGA_no_724_B-PLS135.AT2
	NGA_no_755_CYC195.AT2
	NGA_no_988_CCN360.AT2
	NGA_no_1020_H12090.AT2

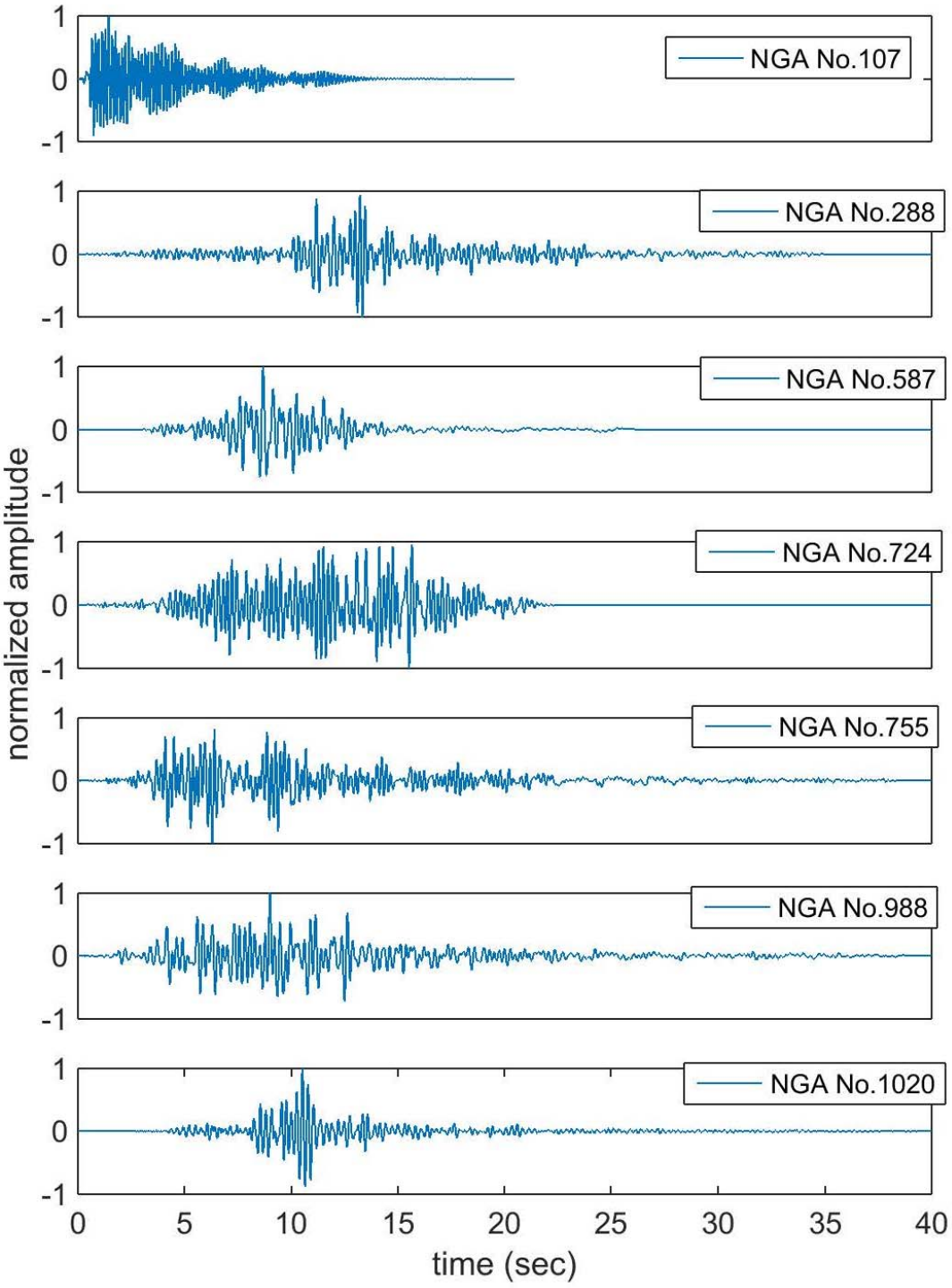

Figure 5.21: Ground motions selected based on the rate of energy buildup.

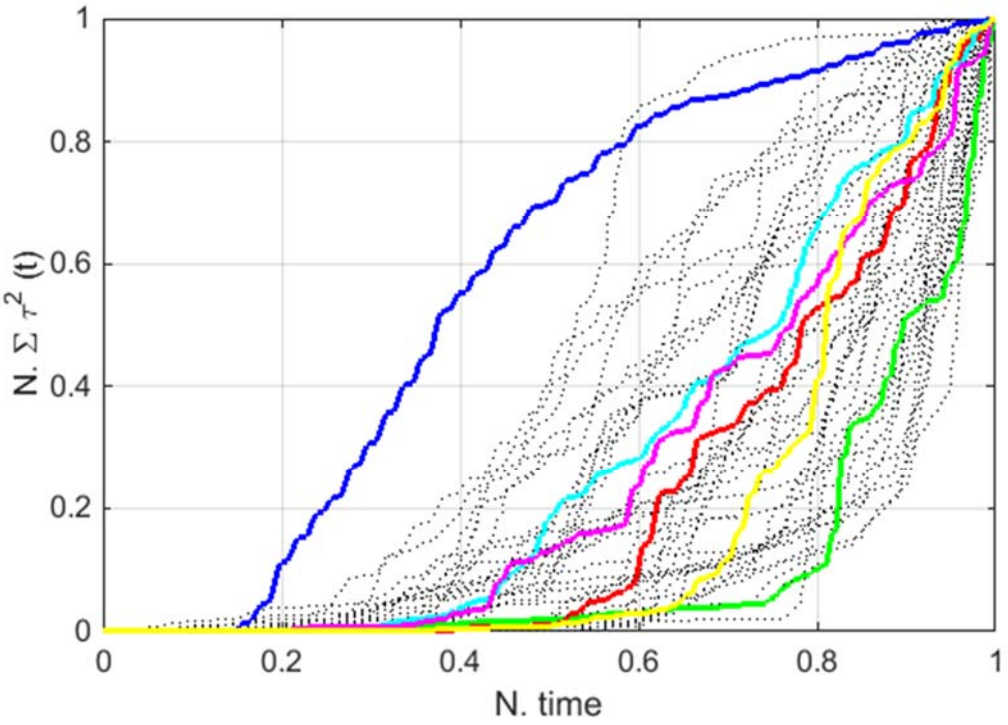

Figure 5.22: $N.\Sigma\,\tau^2$ (t) vs. N. time, highlighting tests from the Group 2 ground motions. blue = NGA-107, green = NGA-288, red = NGA-755, cyan = NGA-724, magenta = NGA988, and yellow = NGA-587

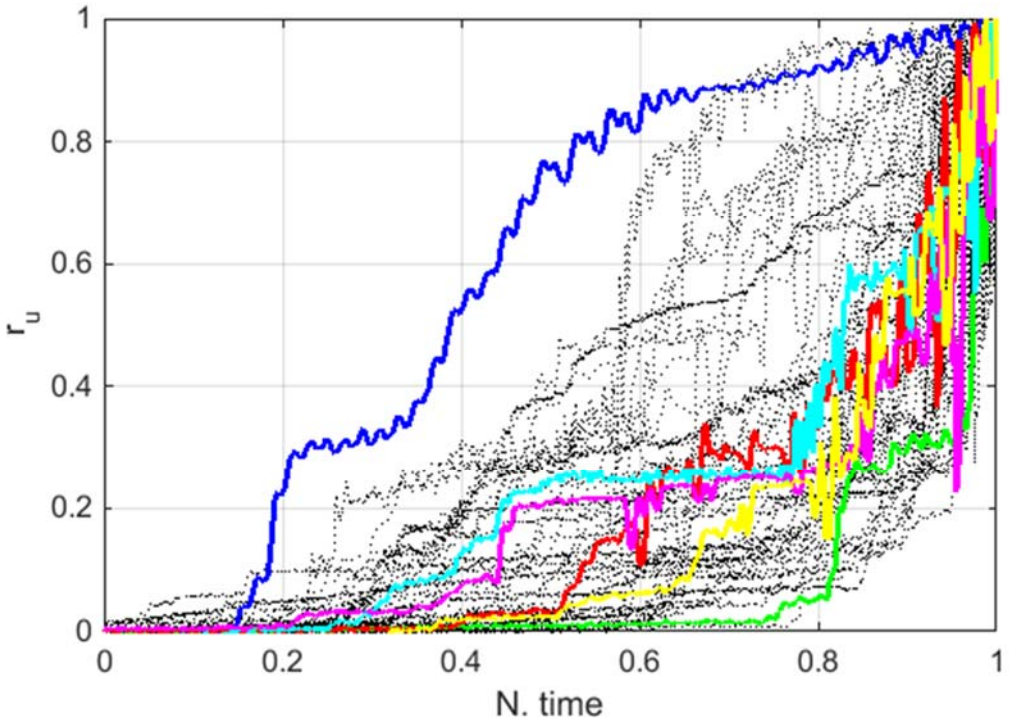

Figure 5.23: r_u vs. N. time, highlighting tests from the Group 2 ground motions. blue = NGA-107, green = NGA-288, red = NGA-755, cyan = NGA-724, magenta = NGA988, and yellow = NGA-587

5.4.1.3 Processed Transient Motions

The third set consists of six loading histories (Table 5.4 and Figure 5.24) that were generated in ProShake. Those ground motions produce the largest difference between the shear stress and acceleration time histories at a given depth. The list of the motions is:

Table 5.4: Summary of the third set of ground motion.

Set	Motion
3	6530_2A
	7030_2A
	7030_1A
	6530_2B
	7030_2B
	6530_1B

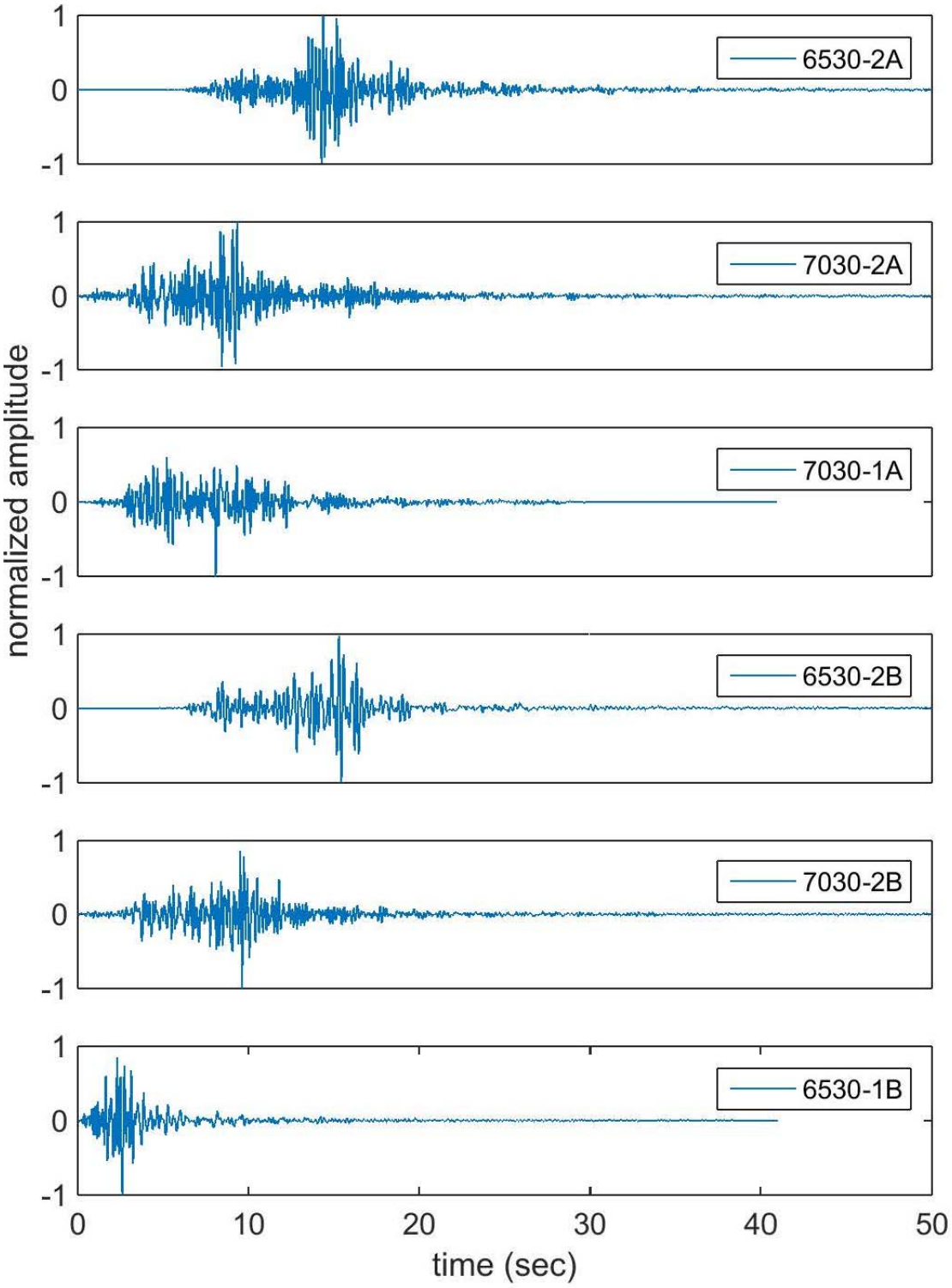

Figure 5.24: The third set of Ground Motions.

5.4.2 Evaluation of Stress Based Liquefaction Procedure

The CSS transient loading data provides an opportunity to evaluate the current stress based liquefaction procedure, which characterizes an earthquake loading solely by the peak amplitude and MSF factor. Therefore, given a few different ground motions at the same soil site, if their adjusted CSR values, $CSR_{M=7.5}$ (Equation 5.6), are very close, then the liquefaction evaluation should give the same binary outcomes: liquefaction or no liquefaction.

$$CSR_{M=7.5} = \frac{CSR}{MSF} \qquad [5.6]$$

Kwan et al. (2014a) evaluated four CSS transient loading tests that contain very distinctive loading histories in the time domain, but have very similar values of $CSR_{M=7.5}$ and relative density. The sand and vertical overburden stresses are identical. According to the stress based evaluation procedure, the outcome of the four cases should be very similar, either all four specimens to be liquefied or not liquefied. Nevertheless, the CSS test results showed that two tests liquefied while the other two tests achieved very low r_u values (Table 5.5). This preliminary study implies that the current simplified liquefaction evaluation procedure is not enough to reflect very different transient loadings. A better way to characterize earthquake loadings is much needed in order to advance the liquefaction evaluation procedure.

Table 5.5: Summary for the selected CSS tests on evaluation of stress based liquefaction procedure (Kwan et al. 2014a)

Test No.	D_r (%)	Ground Motion	$CSR_{M=7.5}$	r_u
1	73	GREECE-PLK-NS	0.264	<0.4
2	74	KOCAELI_CNA000_h2	0.276	1
3	72	PALMSPR_MVH135	0.270	1
4	73	LANDERS_MFC000	0.260	<0.4

5.5 STAGE TWO TAPER UP LOADING

A second stage, taper up loading, was applied on the specimens that did not liquefy after the first stage of undrained loading (Figure 3.1). Figure 5.25 shows the taper up motion, which is composed of a series of harmonic loading pulses with increasing amplitudes. The initial peak to peak amplitude was set at 70.8 N, with the amplitude of each of the following pulses increasing by 20N. This stage of loading is continued until the specimen liquefies. Figure 5.25 demonstrates a typical test result (Test ID: 121228), for which an r_u of 0.29 was achieved from stage one transient loading and 19 cycles of taper up motion was followed to liquefy the specimen. There are 45 CSS tests (30 loose and 15 dense) that included a second stage of loading. The results from all the taper up loading tests are documented in Appendix A.6.

It is obvious to expect that the number of cycle required to liquefy the sand specimen highly depends on the intensity attained in stage one. Therefore, the higher 'damage' achieved in stage one, the less number of cycle is required to trigger liquefaction in stage two. To quantify seismic damage or liquefaction triggering criteria, there are two parameters, excess pore pressure ratio (r_u) or shear strain (γ). Figure 5.26 illustrates the relationship between the maximum r_u value achieved in stage one and the number of taper up cycle required to initiate liquefaction (r_u = 1.0) in the second stage. At a low $r_{u,max}$ value

(<0.4) after the first stage, there is apparent discrepancy of number of cycle required in stage two, from 12 to 35. For a higher $r_{u,max}$ value (>0.4), a crude correlation between the x- and y- axes is observed (i.e., increase in stage two No. of cycle and decrease in stage one $r_{u.max}$).

Figure 5.27 demonstrates the relationship between the maximum absolute shear strain ($|\gamma_{max}|$) attained in stage one loading and the number of cycle required to cause either the single absolute amplitude of 3% or maximum absolute amplitude. The results show that the correlations in shear strain depend on soil density. There are two crude trends, one for the loose tests and one for the dense tests.

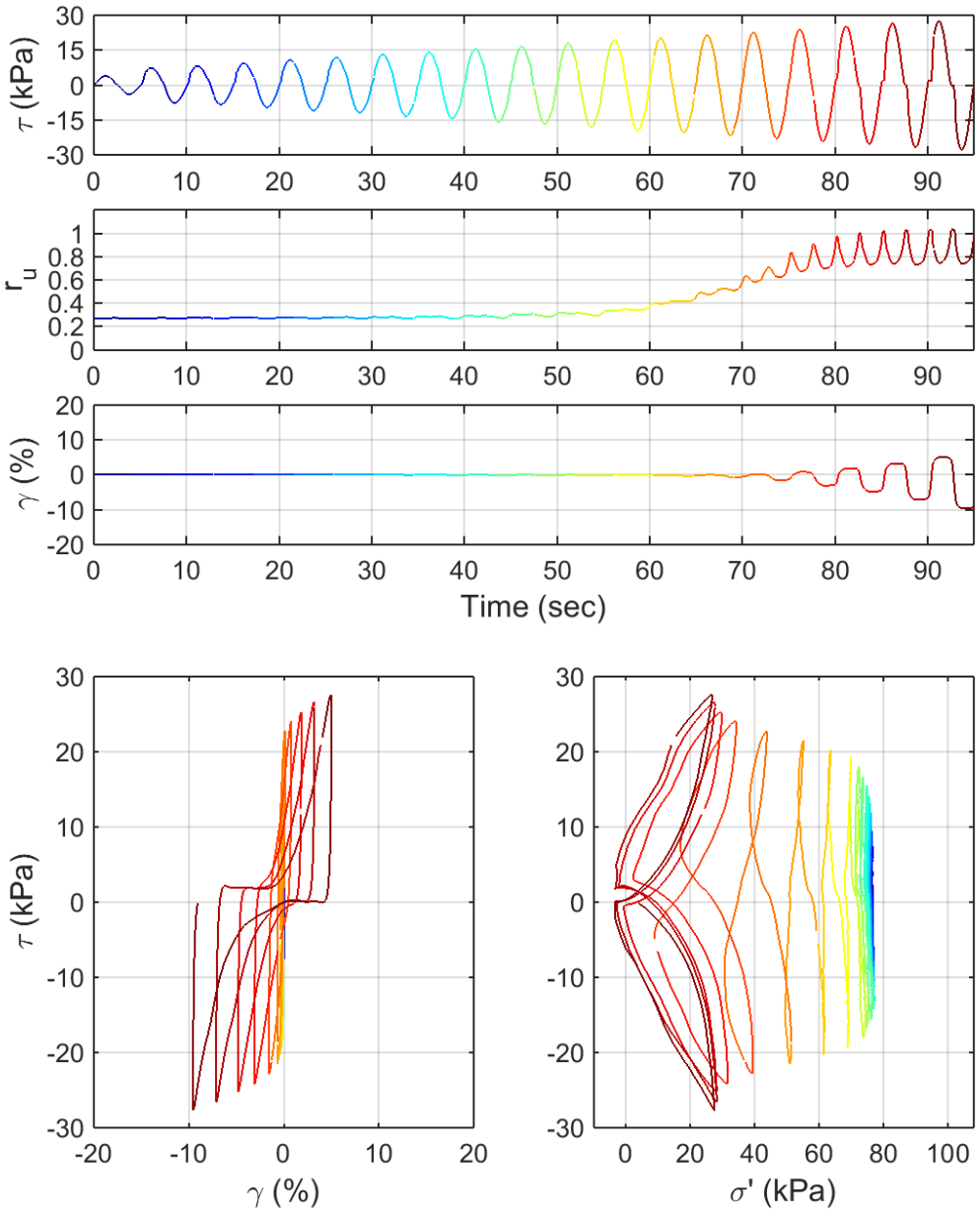

Figure 5.25: A typical second stage test result (Test ID: 121228).

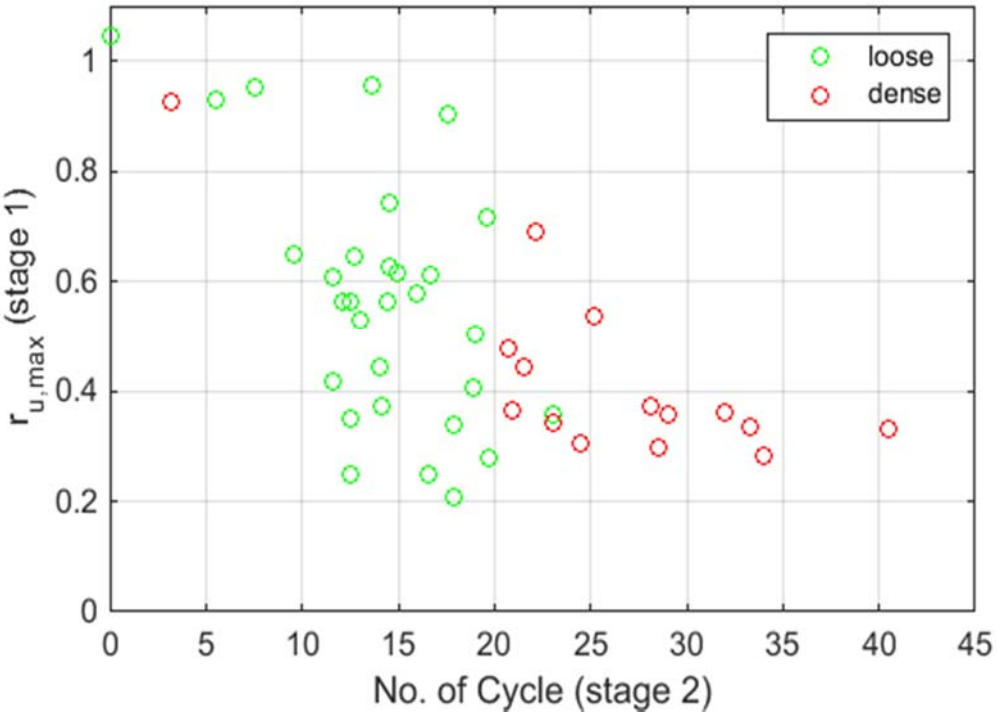

Figure 5.26: Summary plot of number of taper-up cycle required (stage two) to reach r_u = 1.0 (stage 2) given the prior maximum achieved r_u (stage one).

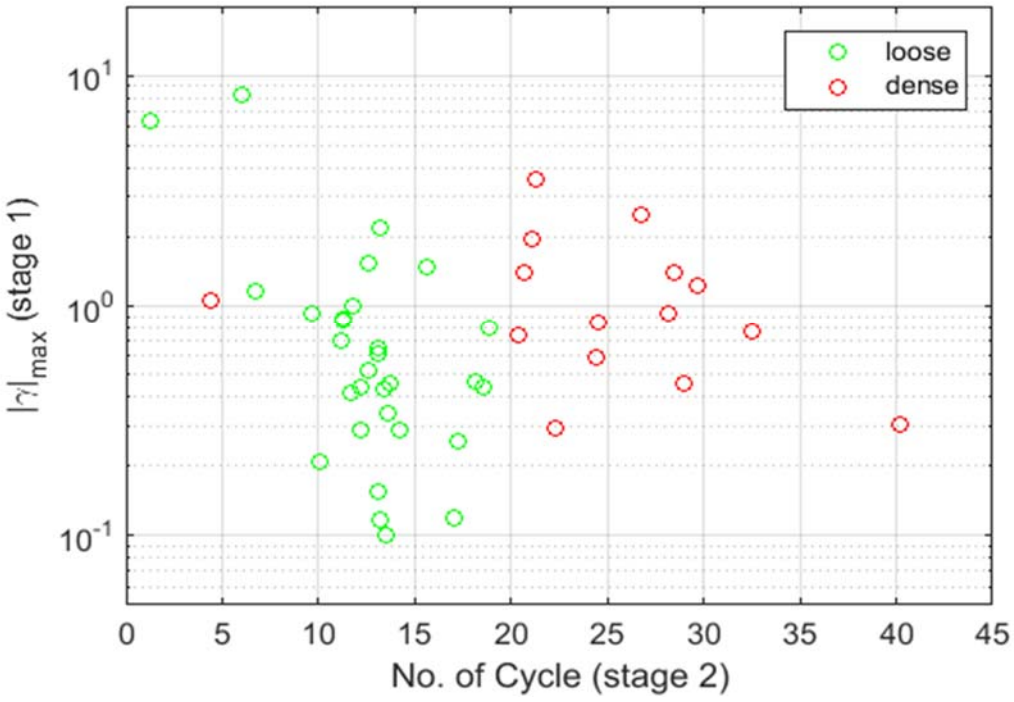

Figure 5.27: Summary plot of number of taper-up cycle required (stage two) to reach r_u = 1.0 (stage 2) given the prior maximum achieved shear strain (stage one).

While the damage can be accessed by r_u or shear strain, earthquake loading, or ground motion intensity, can be represented by intensity measures (IMs). The detail calculation of each IM is documented in Chapter 2.10 and more in-depth analyses are shown in Chapter 6. Here, IMs are used to characterize stage one loading and study its correlation with the number of cycle required to liquefy the specimens in stage two (Figure 5.28). The results show that CAV_5, I_a, NED values from the first stage scatter with the number of required cycle from the second stage, except PGA_m. It is interesting to observe that the higher PGA_m value attained in the first stage of loading, the higher number of cycle required in the second stage.

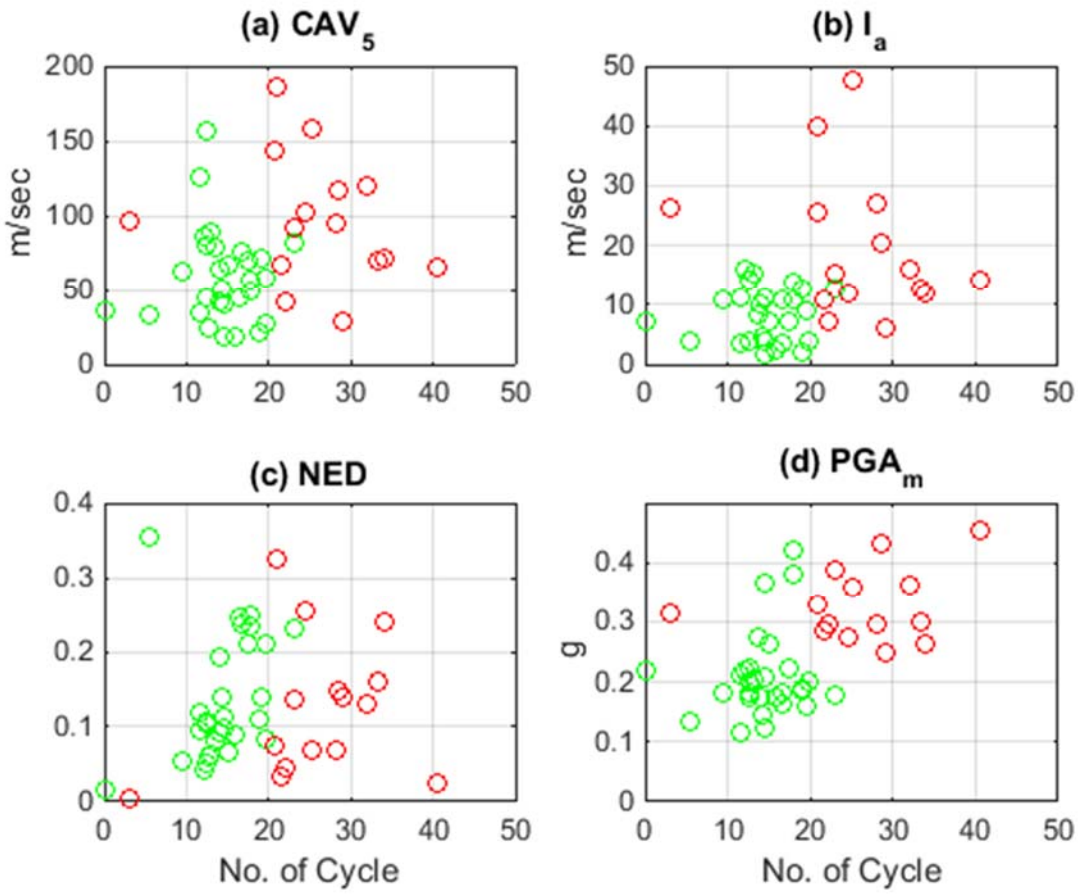

Figure 5.28: Results on the correlation between stage one IM values and stage two required number of cycle to liquefy specimens. (open green dots = loose specimens; red open dots = dense specimens).

5.6 CONCLUSION

Chapter 5 presents the available data resulting from this research program. Only the data from tests performed after making all improvements to the CSS setup are included in this chapter. The data is grouped in accordance to the different types of loading: 1) harmonic, 2) new modulated sinusoid, 3) Transient, and 4) Stage two taper up. The first group of data provides information that evaluates the full capabilities and limitations of the

UTCSS apparatus. From the data reported in the second to the forth group, comparisons are made among the same group, which elucidates the very strong influence stress path has on the responses of sand. A number of specific analyses are covered in Chapters 6 and 7.

The testing program represents an unprecedented step in reproducing the complexities of actual ground motions and provides crucial information for the validation of the current and development of future liquefaction evaluation procedures. Each test result is plotted and documented in Appendixes A1 to A7. The CSS tests under loadings of new modulated sine and transient motions are available at NEEShub (Kwan et al. 2014 b-e). These digital records include the time histories of the stress, strain, excess pore pressure, and vertical effective stress. The relative density, test ID, and information regard the UTCSS apparatus are also documents and readily available through NEEShub.

Chapter 6: Evolutionary Intensity Measures: Pre-Liquefaction

6.1 INTRODUCTION

This study provides valuable experimental data to evaluate whether using Intensity Measures (IMs), such as CAV_5, I_a, NED and PGA_m, to characterize earthquake loading can potentially improve the current liquefaction evaluation procedures. The next generation liquefaction evaluation procedure should be more accurate and informative by providing an estimation of liquefaction initiation time and expected damage (such as induced lateral displacement and settlement).

During a seismic event, both the loading and damage are accumulating with time, and liquefaction occurs when the accumulation of damage is higher than a threshold value (e.g. r_u = 1.0). To simulate an earthquake loading in the laboratory, a shear stress time history is input to the CSS setup, and the associated damage can be measured by the induced excess pore pressure (r_u) and shear strain (γ %). Meanwhile, the loading resisted by a specimen can be translated into an intensity measure that is evolutionary with time. Figure 6.1 demonstrates the accumulation of IM values (i.e. a measure of ground motion intensity) over time (a normalized time is used to compare loadings with different durations).

IMs have previously shown its potentials of tracking earthquake induced damages, such as pore pressure generation and lateral displacement, based on numerical modeling of ground response under different loadings. This chapter evaluates the performance of IMs when predicting the development of r_u and shear strain. Figure 6.2 illustrates the evolution of different IMs (calculated from CSS measured shear stress time histories) with the increase of excess pore pressure. The main goal of this chapter is to identify the optimum

IM that is the best in tracking excess pore pressure generation and shear strain development upon liquefaction initiation.

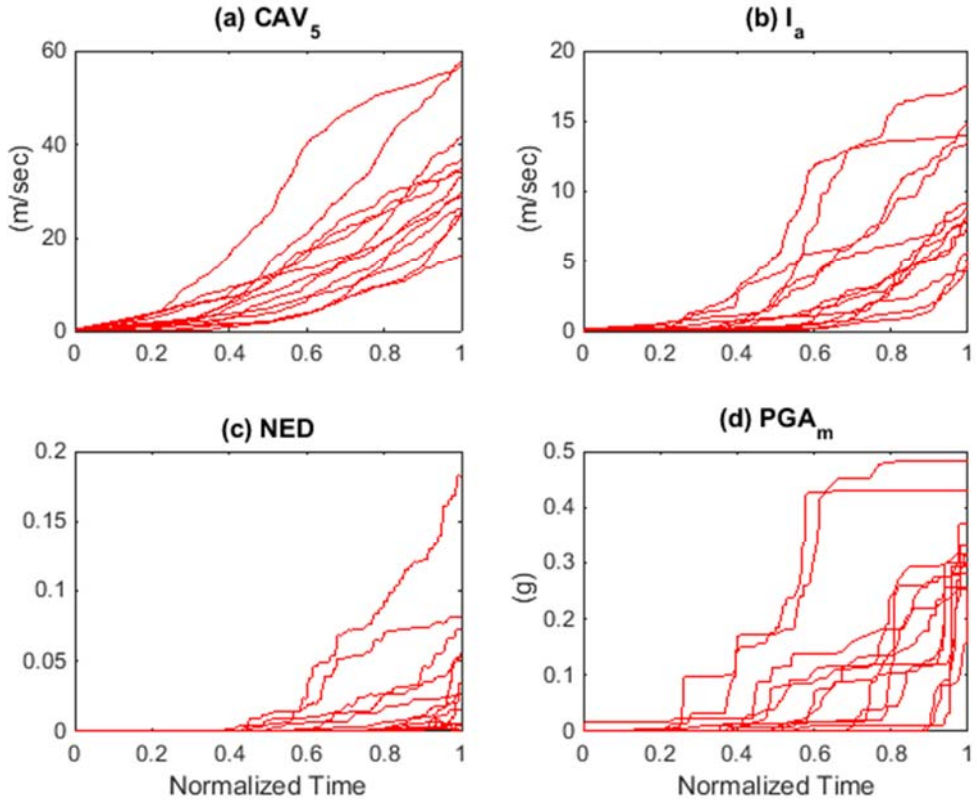

Figure 6.1. Evolutionary IM values vs. normalized time. 13 dense CSS test results are shown. For each test, the time is normalized by the timing of liquefaction initiation.

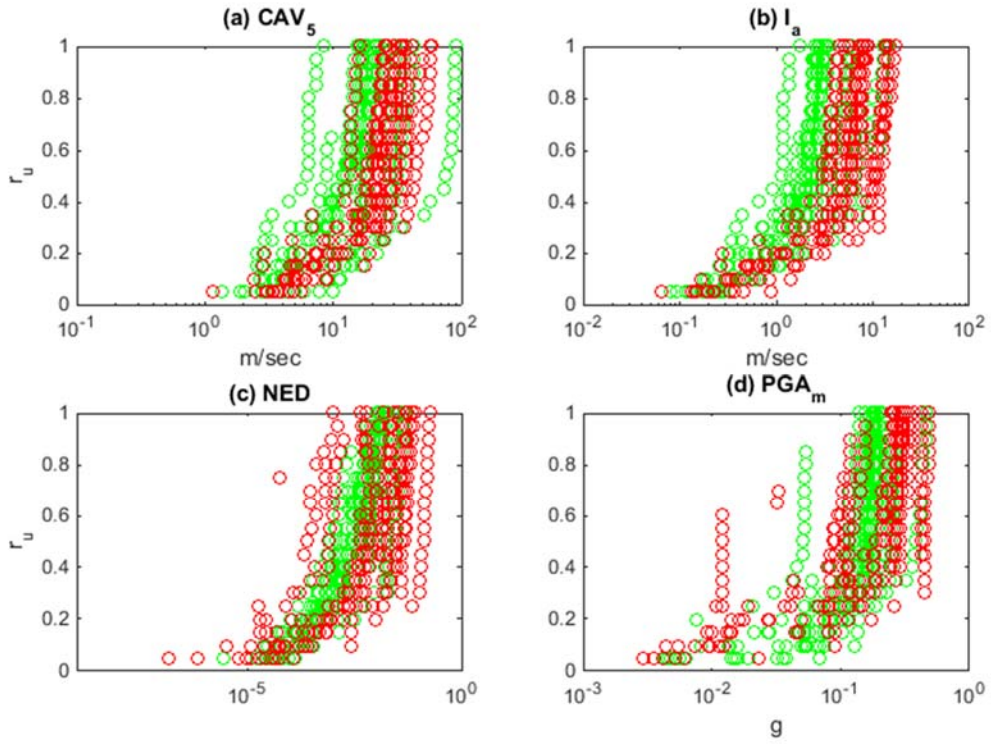

Figure 6.2: Evolutionary IMs vs. r_u. 28 Cyclic Simple Shear tests under different transient loadings. (Green dot = loose test; Red dot = dense test)

Liquefaction initiation can be defined as r_u reaching unity. Knowing the timing of r_u reaching one, each of the CSS tests in this testing program can be divided into two parts; before and after liquefaction initiation, or pre-triggering and post-triggering of liquefaction. Knowing the timing of liquefaction initiation allows us to calculate the corresponding IMs separately for pre-triggering and post-triggering, in contrast to characterizing the entire ground motion as a single cumulative value. For the rest of this dissertation, IM_{pre} is labeled as the IM corresponding to pre-triggering; whereas, IM_{post} is used for post-triggering. This chapter focus on identifying the optimum IM_{pre}; Chapter 7 focus on IM_{post}.

6.2 SITE RESPONSE ANALYSIS

Since the liquefaction evaluation procedures of CAV_5, I_a, and PGA_M require acceleration time histories, the shear stress time histories recorded in CSS tests were needed to be converted into acceleration time histories. An equivalent linear analysis program in Matlab script (Sideras 2015) was used. The script specially evaluates the response of a trial soil profile which consisting of a 6 meter layer of clean sand on top of a 1 m layer of cemented sand (Figure 6.3). The profile is simple because this research project encompasses fundamental studies of liquefiable soil responses. The profile is also consistent with the centrifuge testing at the NEES@RPI (Sideras 2015). Figure 6.4 shows an example of result from the project specific site response analysis program. Figure 6.4a is the input shear stress time history; Figure 6.4b is the output acceleration time history at a depth of 6m, and Figure 6.4c is the output acceleration time history at the ground surface.

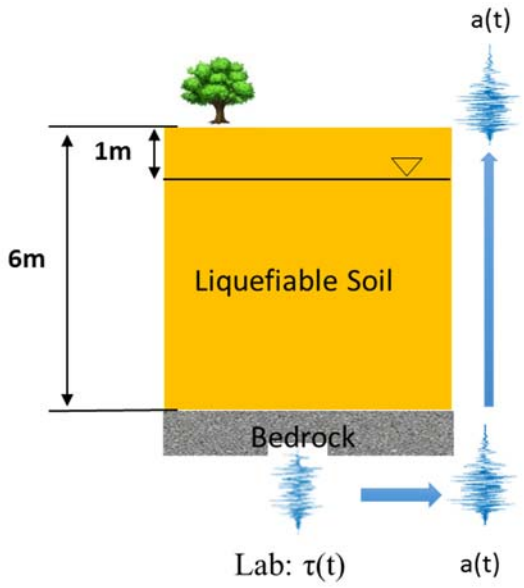

Figure 6.3: Soil profile used to generate acceleration loading histories based on CSS shear stress time histories using equivalent-linear analyses.

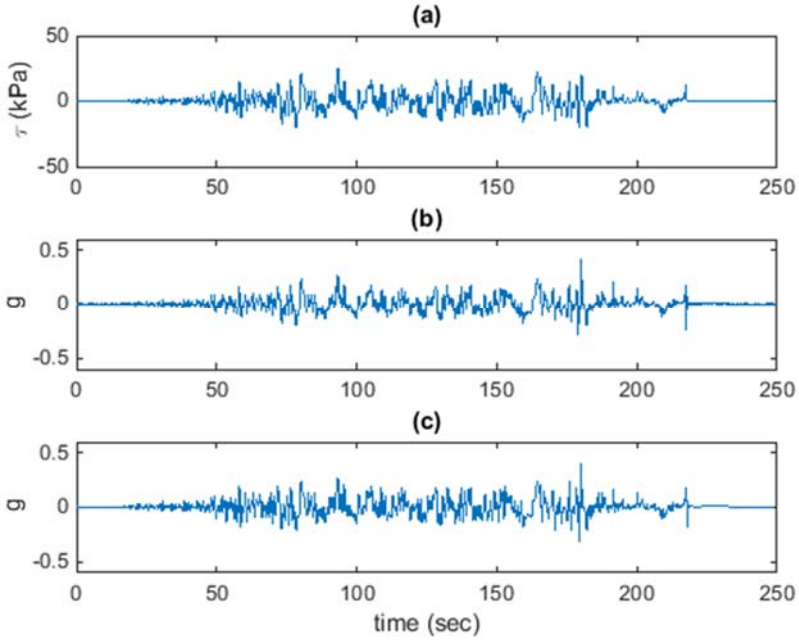

Figure 6.4: Results of the project specified site response analysis program. (a) Shear stress time history input (Test ID 130110). (b) Acceleration time history output at 6m. (c) Acceleration time history output at the ground surface.

Equivalent linear analyses are limited to total stress analysis, since the generation of excess pore pressure is not accounted for. Equivalent shear modulus and damping ratios vary with the strain level and are typically defined by the secant shear modulus from hysteresis loops of cyclic laboratory testing. The modulus and damping ratios are usually started at small strain and iterated until the strain-compatible numbers are obtained for all soil layers in a given soil profile. Nevertheless, because of the pore pressure responses under undrained conditions, the shear modulus and damping ratios vary with the loading time. Nonlinear inelastic soil models (e.g. Lee and Finn 1982) were developed as a manner of time-step by time-step; therefore, the nonlinear models are capable of simulating the changes in shear modulus and damping ratios. A few studies (e.g., Mitra 2011; Zalachoris and Rathje 2015) have compared the performance between equivalent linear and nonlinear

models, and concluded that greater discrepancy in the computed surface ground motions and response spectra were obtained when the input motion intensity was increased. A more vigorous shaking induces a higher level of strain, where the soil behaves more nonlinearly. In this study, equivalent linear analyses are used, and therefore the calculated ground surface accelerations may not be so accurate for tests that have a significant amount of phase transformation and soft responses. However, the equivalent linear analyses should give reasonably accurate responses analyses when the strains are small.

6.3 IDENTIFYING PRE- VERSUS POST-LIQUEFACTION FOR IM EVALUATION

Knowing the timing of liquefaction initiation can significantly improve the evaluation of liquefaction hazard. Abegg (2010) separated IMs into pre- and post-triggering IMs (IM_{init} and IM_{post}) by identifying the time of liquefaction initiation through numerical analyses, and searched for potential IM candidates for further experimental studies. CAV_5, I_a, NED, and PGA_M were proposed and investigated, and CAV_5 and I_a were concluded as the better performers. Figure 6.5 illustrates the four evolutionary IMs buildup over time along with the shear stress. The plots are separated into two domains, pre-triggering and post-triggering of soil liquefaction. From looking at the 4 plots, it is clear that the different IMs build up at different rates for the same stress history, implying that they will not be equally effective in assessing liquefaction. A few thousand simulations were performed in Abegg (2010), and therefore a large numerical database was established to check the effectiveness and sufficiency of each proposed IM. The finding generally agrees with previously research (Kramer and Mictchell 2006), which evaluated the

performance of the same group of IMs but considered the entire ground motion without identifying the time of liquefaction initiation.

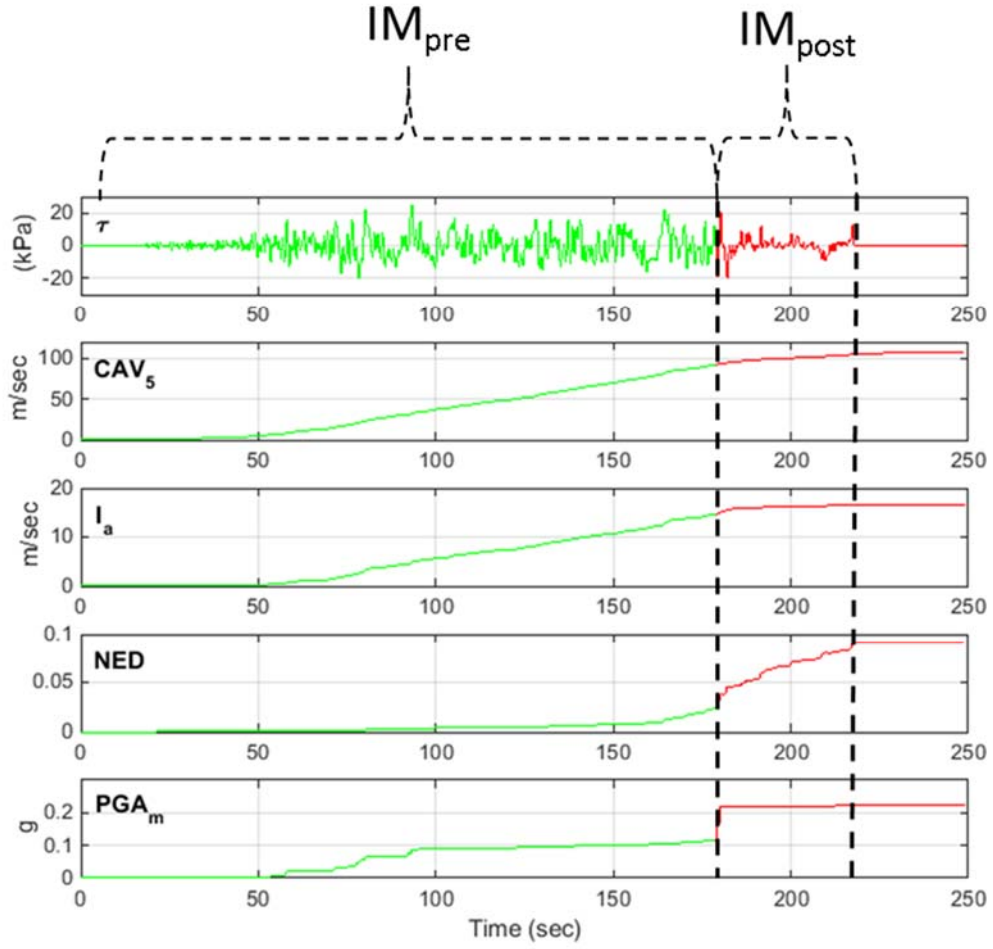

Figure 6.5: Four proposed IM candidates calculated from an acceleration time history.

One of the major purposes of this research project is to provide experimental data to evaluate the proposed IM's performance of predicting soil responses (excess pore pressure generation and shear strain development). By scaling an input motion in the CSS

testing, the time of liquefaction initiation of a sand specimen can be manipulated to occur either at an early or later part of the motion. Therefore, the liquefaction triggering ($r_u = 1.0$) time can be identified and the test records (including input shear stress, pore pressure measurement, and shear strain) can then be divided into two parts, pre-triggering and post-triggering. Figure 6.6 compares a record of r_u measurement from a CSS test under transient loading with the four calculated evolutionary IMs. The x-axis is presented as time normalized by the time of liquefaction initiation ($r_u = 1.0$); while normalizing time when presenting data from one test is not significant, this approach will be very helpful when comparing results from multiple tests (check Figure 6.1 for example). Each of the IMs values are normalized by their values at time of liquefaction initiation.

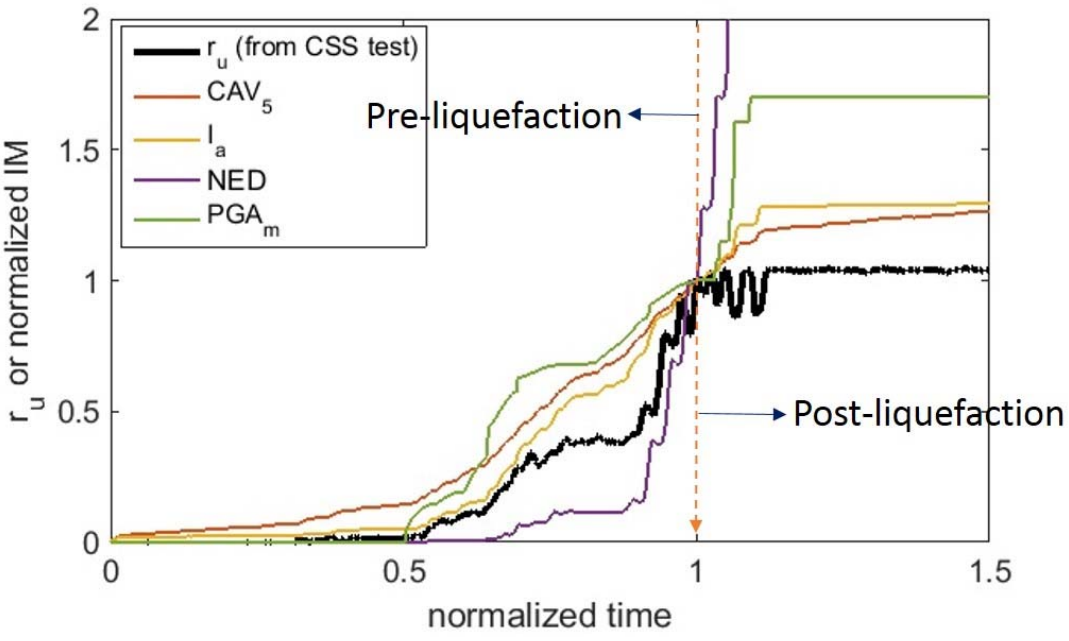

Figure 6.6: An example from a CSS test - r_u or evolutionary IM vs. normalized time.

Normalizing the IM values allows comparisons with the experimentally measured r_u values. The normalized evolutionary IMs ($N.CAV_5(t)$, $N.I_a(t)$, $N.NED(t)$ and $N.PGA_m(t)$)are calculated using the following equations:

$$N.CAV_5(t) = \frac{\int_0^t \langle\chi\rangle\,|a(t)|dt}{\int_0^{t_{liq}} \langle\chi\rangle\,|a(t)|dt} \; where\; \langle\chi\rangle = \begin{cases} 0\; for\; |a(t)| \le 5cm/sec^2 \\ 1\; for\; |a(t)| \ge 5cm/sec^2 \end{cases} \qquad [6.1]$$

$$N.I_a(t) = \frac{\int_0^t a^2(t)dt}{\int_0^{t_{liq}} a^2(t)dt} \qquad [6.2]$$

$$N.NED(t) = \frac{\sum_{i=1}^{n-1}(\tau_{i+1}+\tau_i)(\gamma_{i+1}-\gamma_i)}{\max[\sum_{i=1}^{n-1}(\tau_{i+1}+\tau_i)(\gamma_{i+1}-\gamma_i)]} \qquad [6.3]$$

$$N.PGA_m(t) = \frac{\frac{a_{max}(t)}{MSF(t)}}{\frac{a_{max}(t_{liq})}{MSF(t_{liq})}} \qquad [6.4]$$

where, t_{liq} is the timing of liquefaction initiation, n is the total number of increments up to liquefaction initialization, and other variables are as described in Chapter 2. N.NED(t) is normalized by the max value instead of the liquefaction-reaching value because the calculation of NED allows stress-strain reversals; therefore, NED(t) is not a strictly increasing function (Figure 6.7).

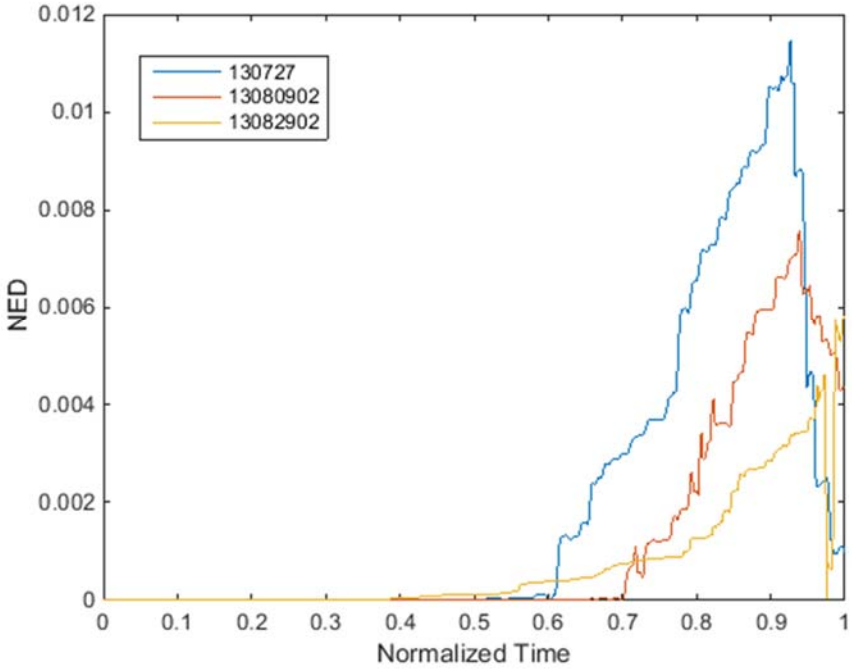

Figure 6.7. NED (t) developments from three CSS tests.

As the calculation of each IM has a cumulative formulation, such as integration of velocity or acceleration function over time, the use of evolutionary intensity measures can potentially track excess pore pressure generation and identify the timing of liquefaction. By definition, liquefaction is reached when the normalized time and normalized IM are both at unity, and the stage of post-liquefaction begins when the two axes are beyond unity. The perfect IM is setup to exactly track or predict the soil responses; therefore, the better match or correlate with the recorded r_u value, the better performance of the proposed IM. As can be seen in Figure 6.6, different IMs have different rates of buildup over the time of the loading and therefore, not all IMs are going to be as effective in predicting pore pressure buildup up to liquefaction initiation. A more in-depth assessment of IMs' efficiency is covered in section 6.4.5.

For more in-depth analyses regarding IMs, results of 28 CSS tests performed under transient loading were selected and summarized in Table 6.1. The 28 tests (15 loose and 13 dense) were selected based on two criteria: (1) no repetition of ground motion at the same density range and (2) liquefaction is triggered at the end or near the end of the applied motion. The first criterion ensures that the evaluations are not biased to any particular IM, since some ground motions are considered more frequent than others. The second criterion ensures that the most of the time-domain characteristic of the different ground motion is reflected in the collected data.

Table 6.1: Summary table of the 28 selected CSS tests.

#	Test ID	Dr (%)	motion
1	130115	43	NGA_no_1534_TCU107-N.AT2
2	130118	41	NGA_no_484_PLK-NS.AT2
3	130119	37	NGA_no_1157_CNA000.AT2
4	130209	47	NGA_no_249_L-FIS090.AT2
5	130215	50	NGA_no_695_A-RO3000.AT2
6	130215-02	47	NGA_no_1792_12543090.AT2
7	130306	40	NGA_no_527_MVH135.AT2
8	130401	37	NGA_no_107_B-OAP180.AT2
9	130628	43	NGA_no_288_A-BRZ000.AT2
10	130916	47	7030_1A
11	130921	44	6530_1B
12	130923	49	7030_2B
13	130924	41	7030_2A
14	130925	55	6530_2B
15	131001	50	6530_2A
16	130711-02	78	NGA_no_724_B-PLS135.AT2
17	130726-02	72	NGA_no_988_CCN360.AT2
18	130727	84	NGA_no_755_CYC195.AT2
19	130809-02	74	NGA_no_587_A-MAT083.AT2
20	130821	80	7030_2A
21	130826-02	89	7030_1A
22	13082702	89	6530_2A
23	130829-02	81	7030_2B
24	130905-02	86	6530_1B
25	131008	73	NGA_no_484_PLK-NS.AT2
26	131009	72	NGA_no_527_MVH135.AT2
27	131009-02	71	NGA_no_880_MCF000.AT2
28	131106-02	74	NGA_no_1157_CNA000.AT2

6.4 PRE-LIQUEFACTION IMS ASSESSMENT BASED ON EXCESS PORE PRESSURE

6.4.1 Searching for Optimum Threshold Acceleration for CAV and I_a

In addition to the four fundamental IMs (CAV_5, I_a, NED and PGA_m) that are well documented in the literature, a parametric study was conducted to evaluate the use of different threshold accelerations on the accuracy of the IMs in matching the pre pressure generation trends. The trend of over predicting the increasing rate of r_u from $CAV_5(t)$ suggests that a higher acceleration threshold may provide a better agreement with the CSS data. Threshold accelerations ranging from 2 to 200 cm/sec^2 were considered and the corresponding normalized $CAV_x(t)$ (N. $CAV_x(t)$) values were calculated (equation 6.5) and compared to the selected 28 CSS tests' r_u values (Figure 6.8).

$$N.CAV_x(t) = \frac{\int_0^t \langle\chi\rangle\,|a(t)|dt}{\int_0^{t_{liq}} \langle\chi\rangle\,|a(t)|dt} \; where \; \langle\chi\rangle = \begin{cases} 0 \; for \; |a(t)| \le x cm/sec^2 \\ 1 \; for \; |a(t)| \ge x cm/sec^2 \end{cases} \qquad [6.5]$$

$$x = [2 \; to \; 200 \, \frac{cm}{sec^2}]$$

The averaged differences of the 28 CSS tests between the calculated N. $CAV_x(t)$ and measured r_u across the normalized time are shown in Figure 6.8. The optimum threshold acceleration resulting in the smallest difference between $CAV_x(t)$ and r_u is 75 cm/sec^2 with lower threshold accelerations generating more error than higher ones. Similarly, the optimum threshold acceleration for the Arias Intensity was also investigated to best match the CSS test's r_u values. The results are depicted in Figure 6.9, and the optimum acceleration for $I_{a,x}$ is 50 cm/sec^2. The formulation for searching the optimum threshold acceleration of I_a is shown as the following:

$$N.I_{a,x}(t) = \frac{\int_0^t [\langle \chi \rangle |a(t)|]^2 dt}{\int_0^{t_{liq}} [\langle \chi \rangle |a(t)|]^2 dt} \quad where\ \langle \chi \rangle = \begin{cases} 0\ for\ |a(t)| \leq xcm/sec^2 \\ 1\ for\ |a(t)| \geq xcm/sec^2 \end{cases} \qquad [6.6]$$

$$x = [0\ to\ 200\ \frac{cm}{sec^2}]$$

Unlike the case of CAV, the improvement of matching the recorded r_u value is minor for $I_{a,x}$ after adopting a threshold acceleration. The analysis of searching optimum threshold acceleration for CAV and I_a is only based on a limited number of shear stress histories (i.e. ground motions) and a single soil profile with one sand type at two different relative densities. Therefore, these optimum threshold acceleration values should not be extrapolated to additional cases without further investigations. Also, although CAV75 and Ia,50 provide better match with the ru values, those two IMs are not necessary providing better efficiency than CAV5 and Ia.

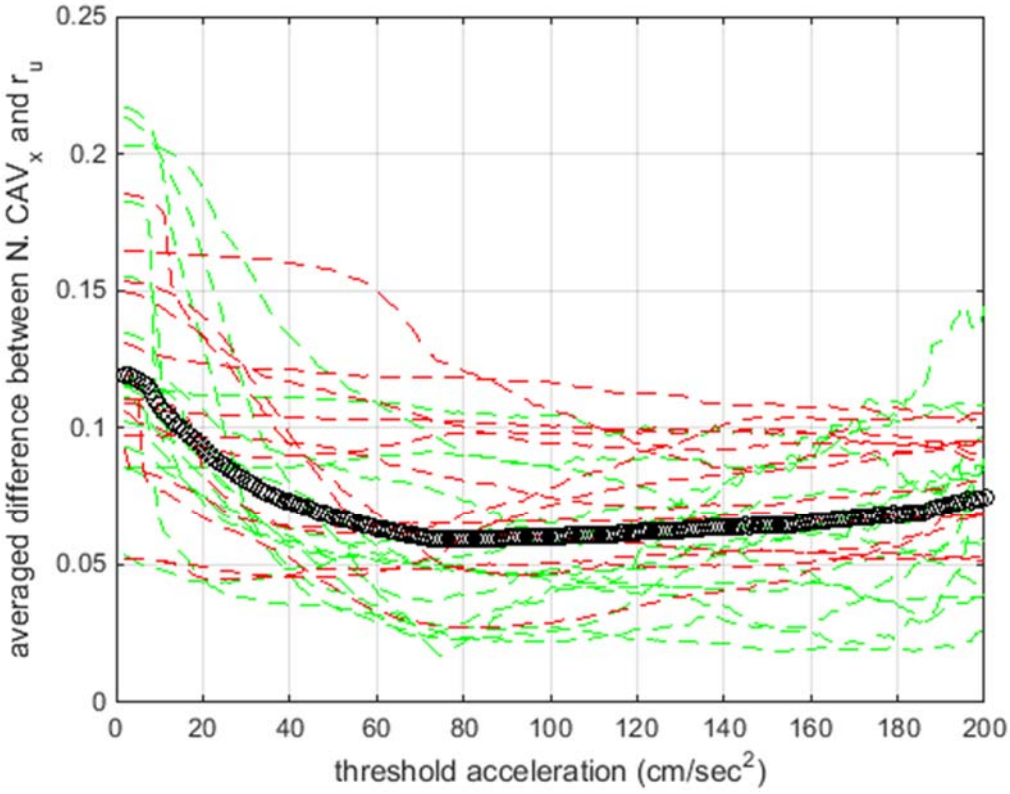

Figure 6.8: Results of searching for the threshold acceleration that gives minimum overall difference between the measured r_u values and calculated normalized CAV values. 28 CSS tests were considered in this analysis (dotted green line = loose test, dotted red line = dense test, open black circle = average of the 28 tests).

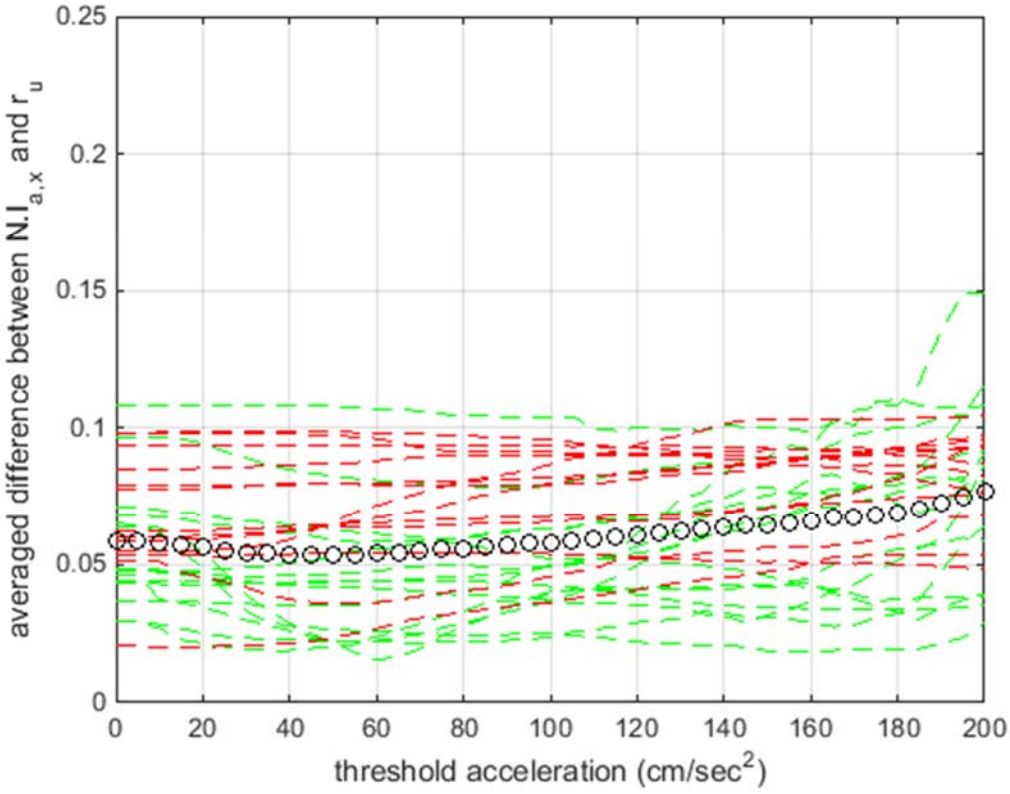

Figure 6.9: Results of searching for the threshold acceleration that gives minimum overall difference between the measured r_u values and calculated normalized I_a values. 28 CSS tests were considered in this analysis (dotted green line = loose test, dotted red line = dense test, open black circle = average of the 28 tests).

6.4.2 Predicting Rate of Excess Pore Pressure Generation

The goal of this analysis is to investigate how well the IM candidates compare with the CSS excess pore pressure generation data. Hence, the perfect IM function should evolve identically or correlate efficiently with r_u. Figures 6.10 and 6.11 display test results from 15 loose and 13 dense CSS tests loaded under different transient loadings, respectively. Each subplot illustrates how each individual calculated IM evolved with normalized time; the laboratory measured r_u values are included as well. Coordinate (0, 0) defines the beginning of loading and coordinate (1, 1) defines reaching liquefaction initiation. The smaller the difference between calculated IM and measure r_u, the better performance of the IM. The average difference between the normalized IM values and r_u are plotted at given normalized time increments (the error bars represent one standard deviation).

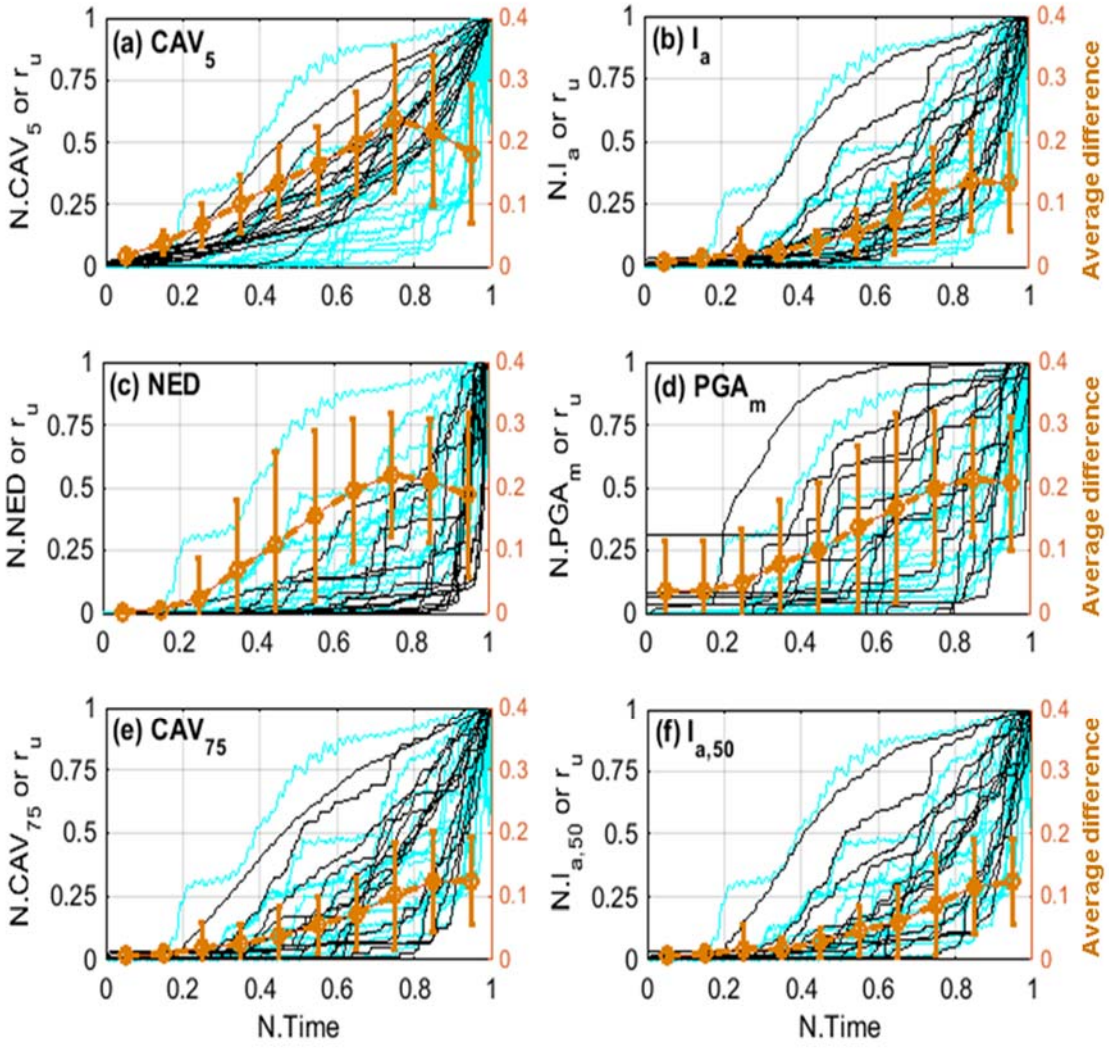

Figure 6.10: Normalized IM vs. Normalized Time. Comparison between the calculated IMs and measured r_u values from 15 loose CSS tests (Cyan = measured r_u; black = Calculated IM)

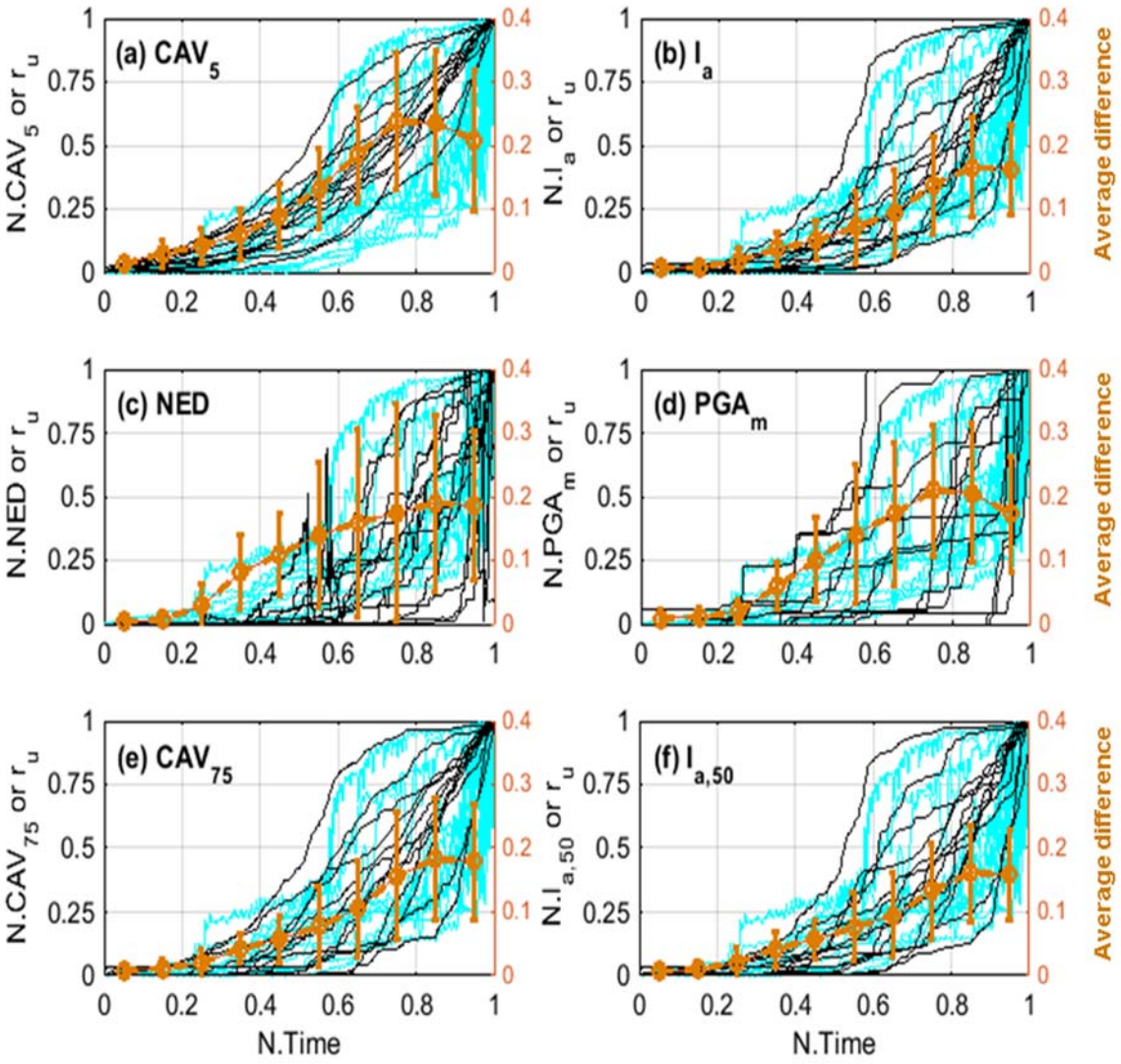

Figure 6.11: Normalized IM vs. Normalized Time. Comparison between the calculated IMs and measured r_u values from 13 dense CSS tests (Cyan = measured r_u; black = Calculated IM)

The normalized CAV_5 has a tendency of overestimating the rate of r_u generation which suggests that a higher acceleration threshold may provide a stronger correlation with the CSS data. The CAV_{75} plots have significantly improved correlation with the correspondent r_u values compared to CAV_5 (the maximum average error deceased by half for the loose sand). NED tends to under-predict excess pore pressure generation, particularly for loose sand. The NED plots for the dense sand are more irregular at lower r_u values due to the low strain measurements, leading to large noise level in the calculated NED values. PGA_m plots tend to cover the same range as the r_u plots (as reflected by the smaller standard deviation bars), but the plots are randomly spread across the range and there is no one-to-one correspondence with the r_u plots. I_a and $I_{a,50}$ plots corresponds best with the r_u plots and show consistent time and magnitude ranges. As expected from the relatively constant average error plot in Figure 6.9, the benefit from using $I_{a,50}$ instead of Ia is minimal compared to the advantage of using CAV_{75} instead of CAV_5.

Figures 6.12 and 6.13 illustrates the same normalized IMs plotted against r_u for the loose and dense sand specimens, respectively. The ideal IM would show minimal deviations meaning high efficiency. The red circles are the averaged values of the calculated IM at a given r_u value, and the error bars represent one standard deviation within the data. CAV_{75} (Figure 6.12e) provides a better one-to-one correlation than CAV_5 (Figure 6.12a). For PGA_m, the calculated values increase in a stepwise manner rather than in a transient manner as observed in the laboratory and field records (the calculated PGA_m value increase at each peak value only). Table 6.2 summaries the overall difference and average of CoV values for the 28 CSS tests throughout all the loading time. From the six investigated IMs (CAV_5, I_a, NED, PGA_m, CAV_{75}, and $I_{a,50}$), I_a, $I_{a,50}$ and CAV_{75} give the smallest differences and CoV values, while NED and PGA_m give significant higher standard deviation (weakest correlations) and differences.

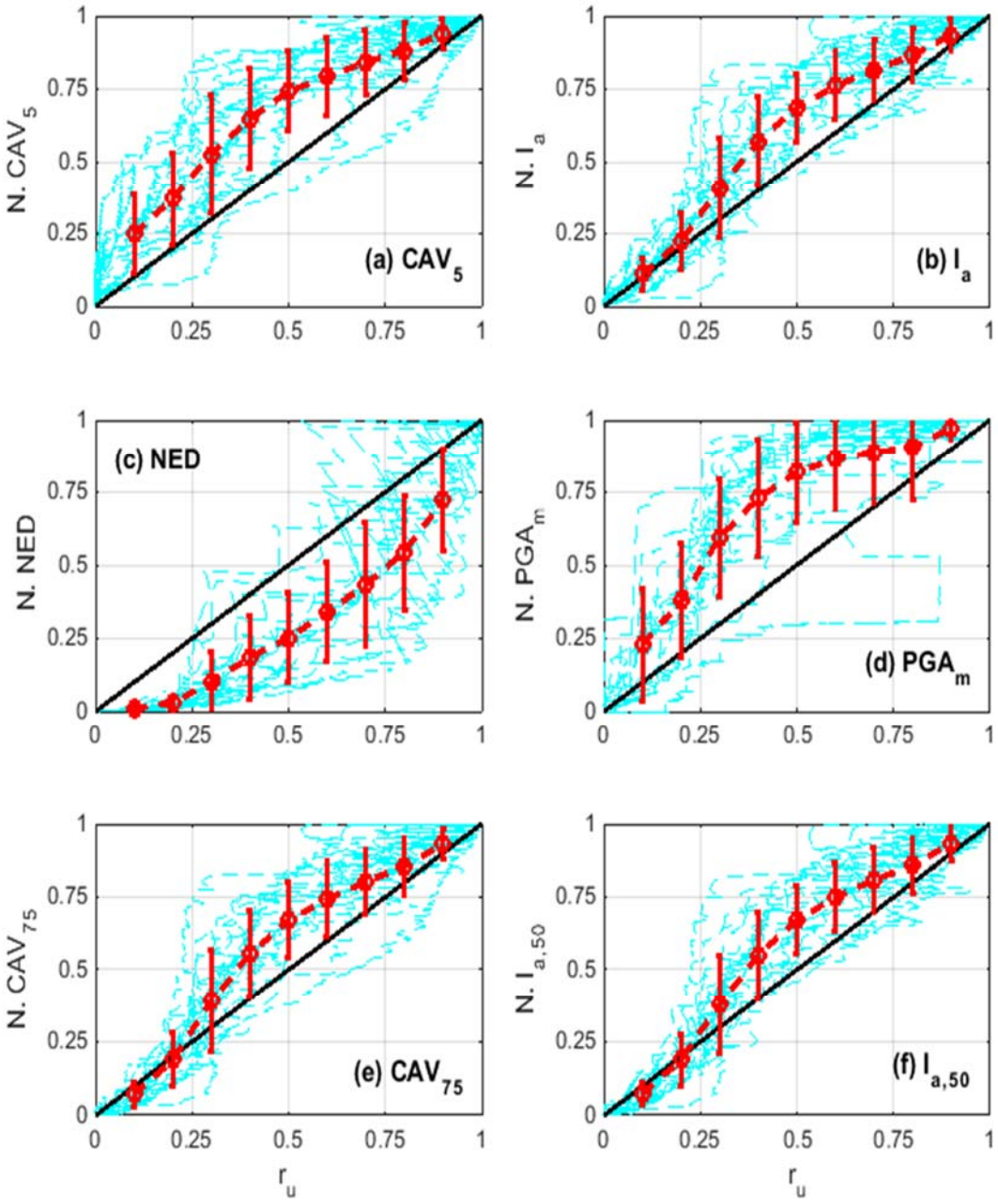

Figure 6.12: Normalized IM vs. r_u. 15 loose CSS tests.

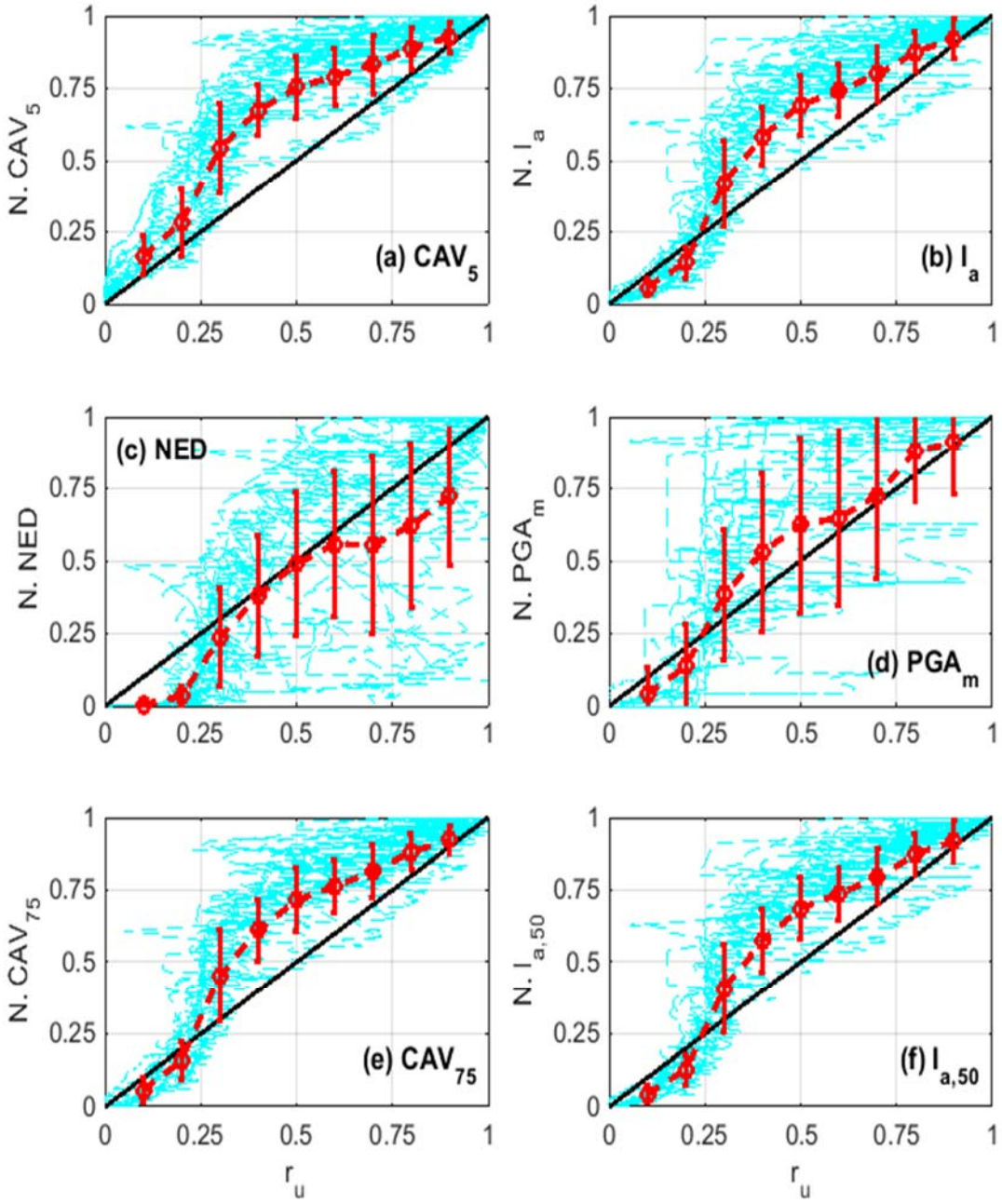

Figure 6.13: Normalized IM vs. r_u. 13 dense CSS tests.

Table 6.2: The overall differences for each IM vs. r_u.

IMs	Overall Average Difference (%)	Overall Average CoV
CAV_5	12.37	0.22
I_a	6.21	0.30
NED	10.68	0.60
PGA_m	10.98	0.50
CAV_{75}	6.38	0.26
$I_{a,50}$	5.71	0.25

6.4.3 Predicting the Time of Liquefaction Initiation (r_u)

The increase in calculated I_a and CAV in general provides best match for the rate of excess pore pressure buildup when the time of liquefaction is pre-identified. However, the optimal IM should be able to identify the time of liquefaction as well as rate of excess pore pressure generation. Figures 6.14 and 6.15 show the IM buildup versus r_u up to r_u equal to one for the loose and dense specimens, respectively. The average values of each IM at given r_u increments are included as well along with the 1-standard deviation bars (red color). Since all the tests were performed on the same sand at similar relative densities and following same specimen preparation technique, an ideal IM should result in all plots for the different ground motions clustered in a tight band and reaching liquefaction at comparable IM values. However, the experimental results show a large scatter in the plots for all IMs, with some tests reaching liquefaction at IM values significantly higher than others.

Tables 6.3 and 6.4 summarize the different IM values for all tests at time of liquefaction for the loose and dense specimens, respectively. All IMs show a lower value at liquefaction for loose sand compared to dense sand, although the ratio of dense to loose varied from 1.3 (CAV_5) to 2.4 (NED). The Standard Deviation values for both loose and dense are relatively similar, leading to a lower Coefficient of Variation (CoV) for the dense

specimen results (except for NED for which the SD value increased 5 times). Based on CoV, PGA_m is the best indicator of liquefaction initiation with a CoV of 0.4 and 0.2 for the loose and dense specimens, respectively. NED has the second lowest CoV for the loose sand but has a CoV of 1.2 for the dense sand. These results disagree with prior numerical studies (Abegg 2010; Kramer and Mitchell 2006) which concluded that CAV_5 and I_a are the most efficient IMs and PGA_m is the least efficient.

It should be noted that the Mean, SD and CoV values are all biased by one or more outlier results for each of the IMs. Table 6.3 shows that the outlier plot for CAV_5 in Figure 6.14 is for Test # 1 and 6, while the outliers for CAV_{75}, I_a and $I_{a,50}$ are Tests # 1 and 8. Similarly, the outlier plots for PGA_m and NED are for Test 8 and for Tests 15 and 12, respectively. These results indicate that the ability of using the different IMs to predict liquefaction initiation can be biased by the ground motion characteristics. Figure 6.16 shows the applied loading up to liquefaction (X-axis normalized by time of liquefaction) for the two tests that generated most high IM values (Tests #1 and #8) and most low IM values (Test #9 and #11) for the loose sand specimens. The plots indicate that when the loading consists of relatively uniform loading cycles, the resulting IM values at liquefaction are higher compared to the IM value at liquefaction when there are some distinct higher peaks in the pre-liquefaction loading.

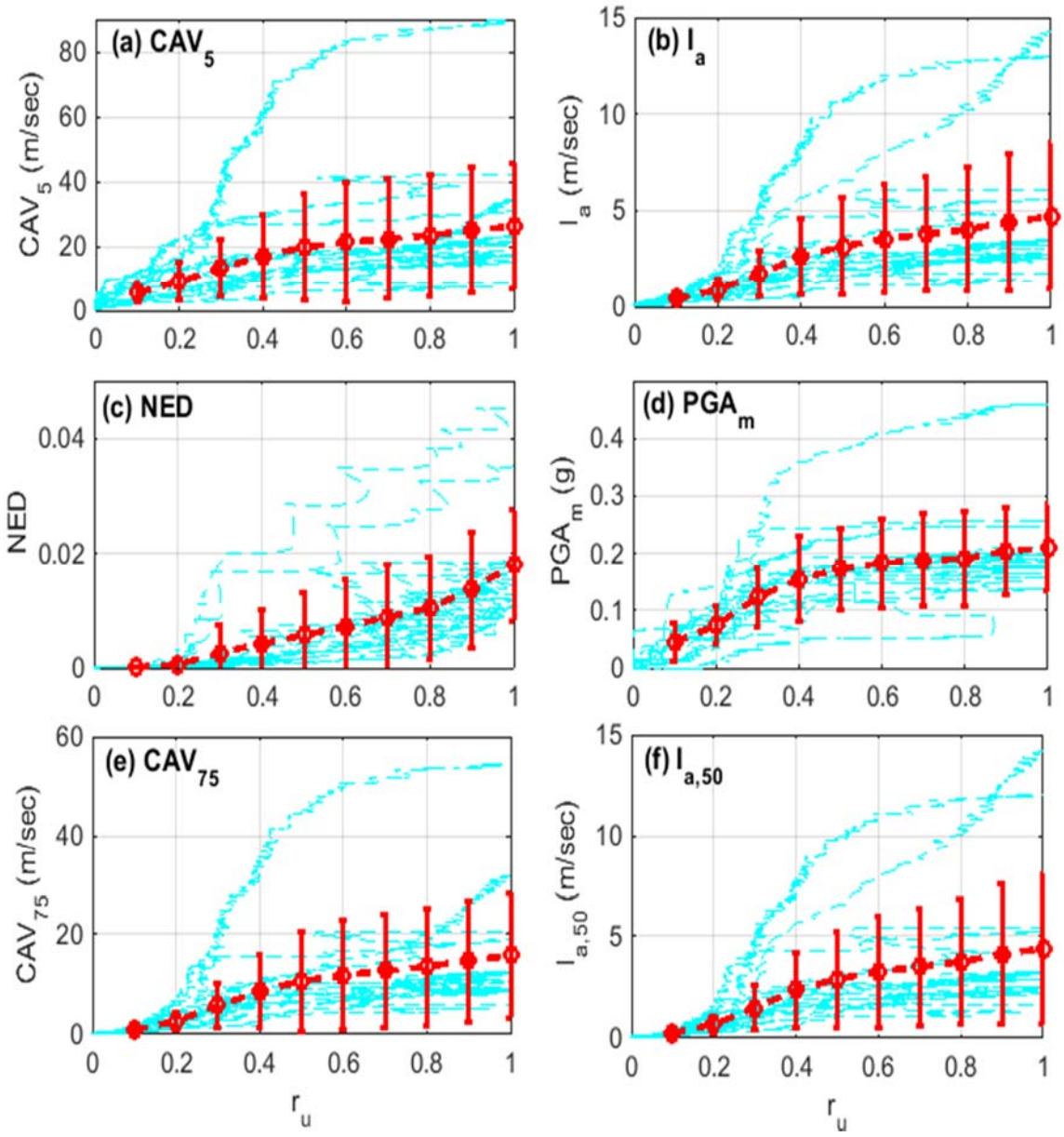

Figure 6.14. Normalized Evolutionary IMs vs measured r_u – loose sand

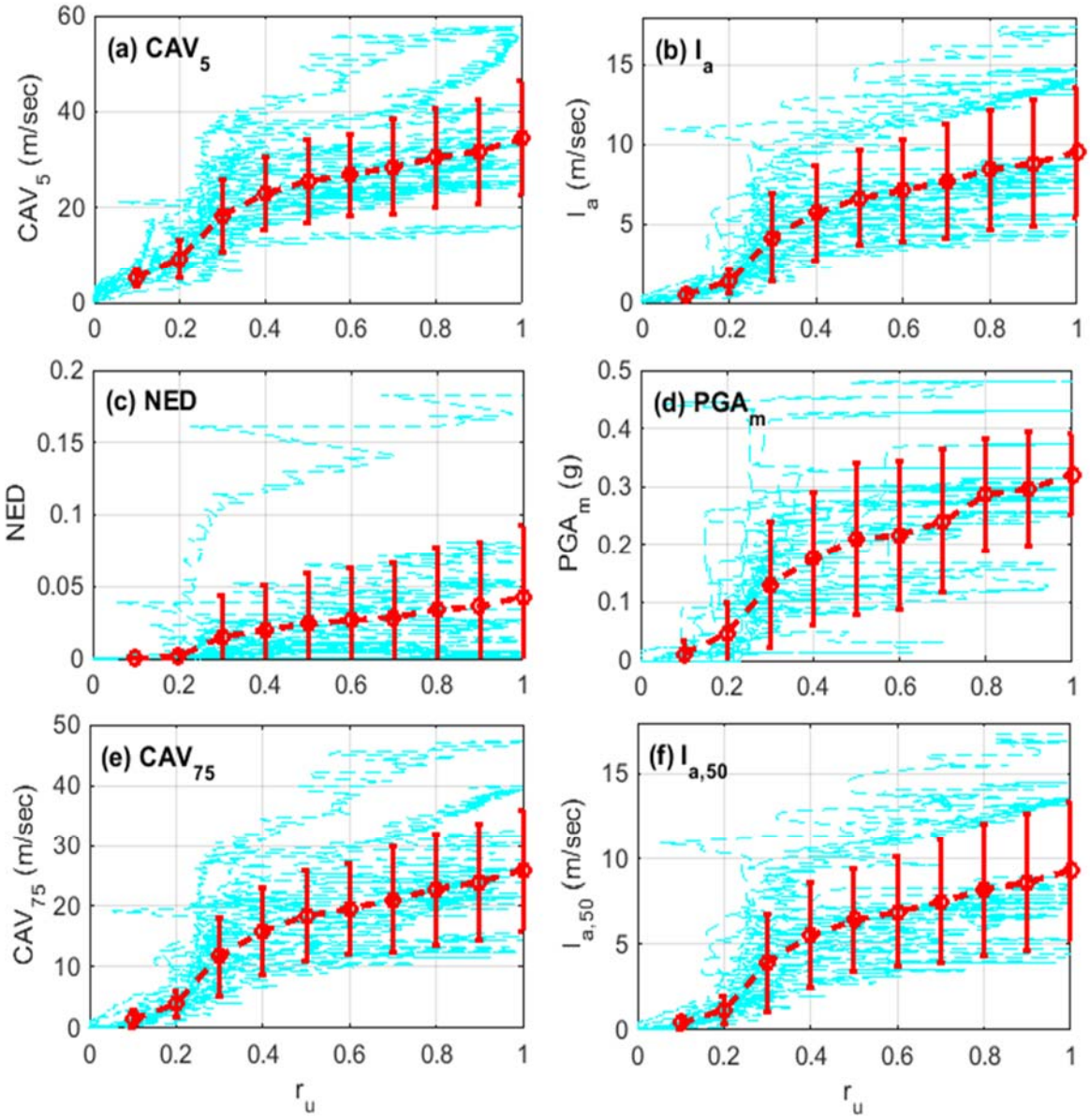

Figure 6.15: Evolutionary IMs vs measured r_u – dense sand

Table 6.3: IM values at liquefaction for loose specimens (bold numbers indicate highest 2 values, light color indicate lowest 2 values)

Test #	**CAV_5** m/sec	**I_a** m/sec	**NED** (x 10^{-3})	**PGAm** (x 10^{-2}) g	**CAV_{75}** m/sec	**$I_{a,50}$** m/sec
1	**89.8**	**13.0**	10.7	24.8	**54.5**	**12.0**
2	15.2	3.2	10.3	20.1	11.9	3.1
3	21.0	2.8	18.0	19.0	9.5	2.5
4	15.8	2.7	17.4	15.7	10.1	2.5
5	17.2	3.0	10.4	18.3	10.4	2.9
6	**41.9**	6.1	16.7	17.5	20.7	5.5
7	17.2	3.4	15.5	13.8	12.5	3.3
8	34.4	**14.2**	12.6	**46.0**	**31.8**	**14.2**
9	18.6	2.6	11.8	18.6	8.5	2.3
10	23.2	3.5	18.6	19.6	12.6	3.2
11	8.4	1.8	18.3	19.0	6.1	1.7
12	30.7	5.6	**35.1**	**25.7**	18.9	5.3
13	17.3	2.6	12.1	21.0	9.2	2.3
14	21.5	3.3	16.3	17.3	11.1	3.0
15	20.8	2.7	**45.2**	17.9	8.9	2.4
Mean	26.2	4.7	17.9	21.0	15.8	4.4
S.D.	19.5	3.8	9.7	7.6	12.5	3.7
C.o.V.	0.74	0.8	0.5	0.4	0.8	0.8

Table 6.4: IM values at liquefaction for dense specimens (bold numbers indicate highest 2 values, light color indicate lowest 2 values)

Test #	**CAV_5** m/sec	**I_a** m/sec	**NED** ($\times 10^{-3}$)	**PGAm** ($\times 10^{-2}$) g	**CAV_{75}** m/sec	**$I_{a,50}$** m/sec
16	**57.8**	**14.8**	54.6	37.3	**47.3**	**14.5**
17	29.7	7.3	**182.1**	29.5	22.2	7.1
18	26.4	7.9	1.0	31.4	21.2	7.7
19	29.0	7.8	4.3	30.0	22.1	7.6
20	**56.8**	14.1	1.0	**42.9**	**39.8**	13.6
21	34.7	9.1	15.1	28.0	27.4	8.9
22	25.5	5.6	52.4	29.6	15.5	5.4
23	33.1	8.2	5.8	33.1	24.0	7.9
24	34.1	**17.4**	**81.1**	**48.2**	31.6	**17.4**
25	16.2	4.5	72.6	25.4	12.8	4.4
26	36.8	13.5	26.6	25.7	32.4	13.4
27	25.3	5.0	33.6	24.7	14.5	4.7
28	41.5	8.7	27.0	31.4	25.8	8.2
Mean	34.4	9.5	42.9	32.1	25.9	9.3
S.D.	12.0	4.1	49.7	7.0	10.0	4.1
C.o.V.	0.35	0.4	1.2	0.2	0.4	0.4

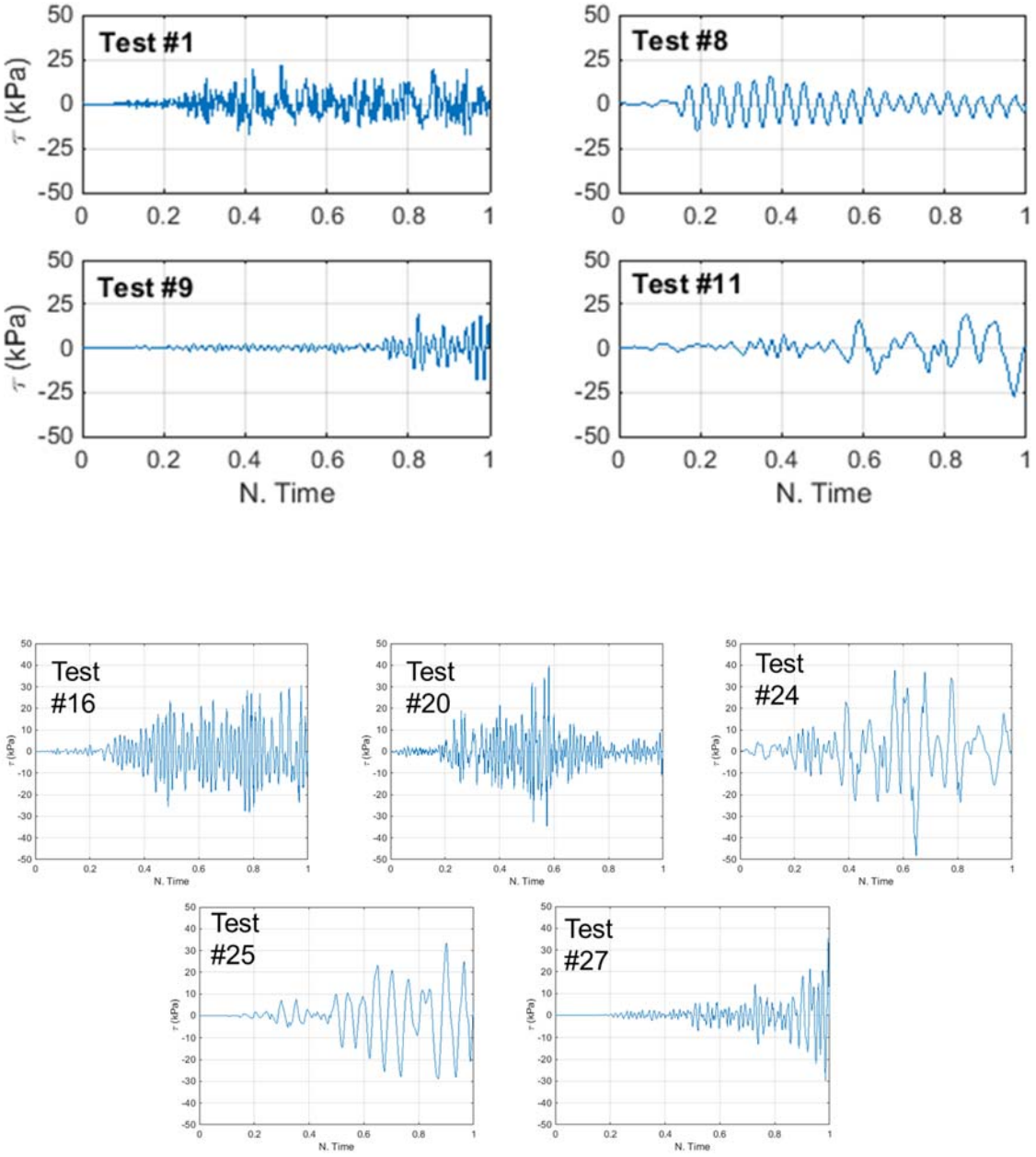

Figure 6.16: Loading up to liquefaction for tests with high IM (Test #1, 8, 16, 20 and 24) and low IM (Test #9 11, 25 and 27) values at liquefaction

6.4.5 Efficiency Evaluation

The purpose of this section is to evaluate the performance of each proposed IM for predicting excess pore pressure generation at different levels. In addition to matching the generation of excess pore pressure from each CSS test, the performance in the aspect of "correlation" between IMs and pore pressure development can be accessed by the efficiency of IMs (Abegg 2010). Efficiency is a measure of the uncertainty that the engineering demand parameter (EDP) can be correlated with a proposed parameter. If the EDP is closely related to the proposed parameter, the proposed parameter is an efficient parameter. The effectiveness of 'correlation' is assessed by standard deviation (EDP | Parameter). In this study, the EDP is r_u and the proposed parameter is a given IM. The most effective IM should provide the smallest standard deviation at a given r_u level, and therefore the best predictor of r_u value. In this section, the analysis is performed to correlate the proposed IMs to r_u values, and efficiency is based on the standard deviation of r_u | IM, a measure of the uncertainty with which the IM can be estimated for a given r_u value. The values of the four IM_{pre} candidates corresponding to specific values of r_u (0.1, 0.2, 0.3… 1.0) are calculated and checked with the standard deviation at each r_u level. The overall efficiency of each IM candidate is characterized by the averaged standard deviation of IM | r_u over all r_u levels. Therefore, the most efficient IM is the one with the lowest average standard deviation value. A perfect IM would have zero standard deviation, representing a perfect relationship with r_u.

There are two sets of data in accessing the efficiency of IMs. The first set of data is maximizing the number of tests. On the other hand, the second set of data is utilizing the variety in ground motion loadings. The first set includes all 79 transient loading CSS-tests, which soil specimens did or did not liquefy. The second set includes 28 CSS tests, where soil specimens reached liquefaction at the end of loaded motion. Also, none of the ground

motions used was repeated at the similar density range in the second set. Each set of data is further separated into two different groups, loose and dense, based on the relative density of each CSS test.

Figure 6.17 demonstrates the coefficients of variation (CoV) for each IM at different r_u values and data groups, and Table 6.5 summarizes the overall results. While NED is showing the highest values of CoV (least efficiency), PGA_m is yielding the lowest values of CoV (highest efficiency). The results disagree with prior numerical studies (Abegg 2010; Kramer and Mitchell 2006), which CAV_5 and I_a are the most efficient IMs and PGA_m was found to be the least efficient. It should be noted though that the CSS experimental database generated in this research project may not be as large as those for previous numerical studies. There are only 23 ground motions included in the CSS database, but previous numerical studies had considered thousands of different ground motions.

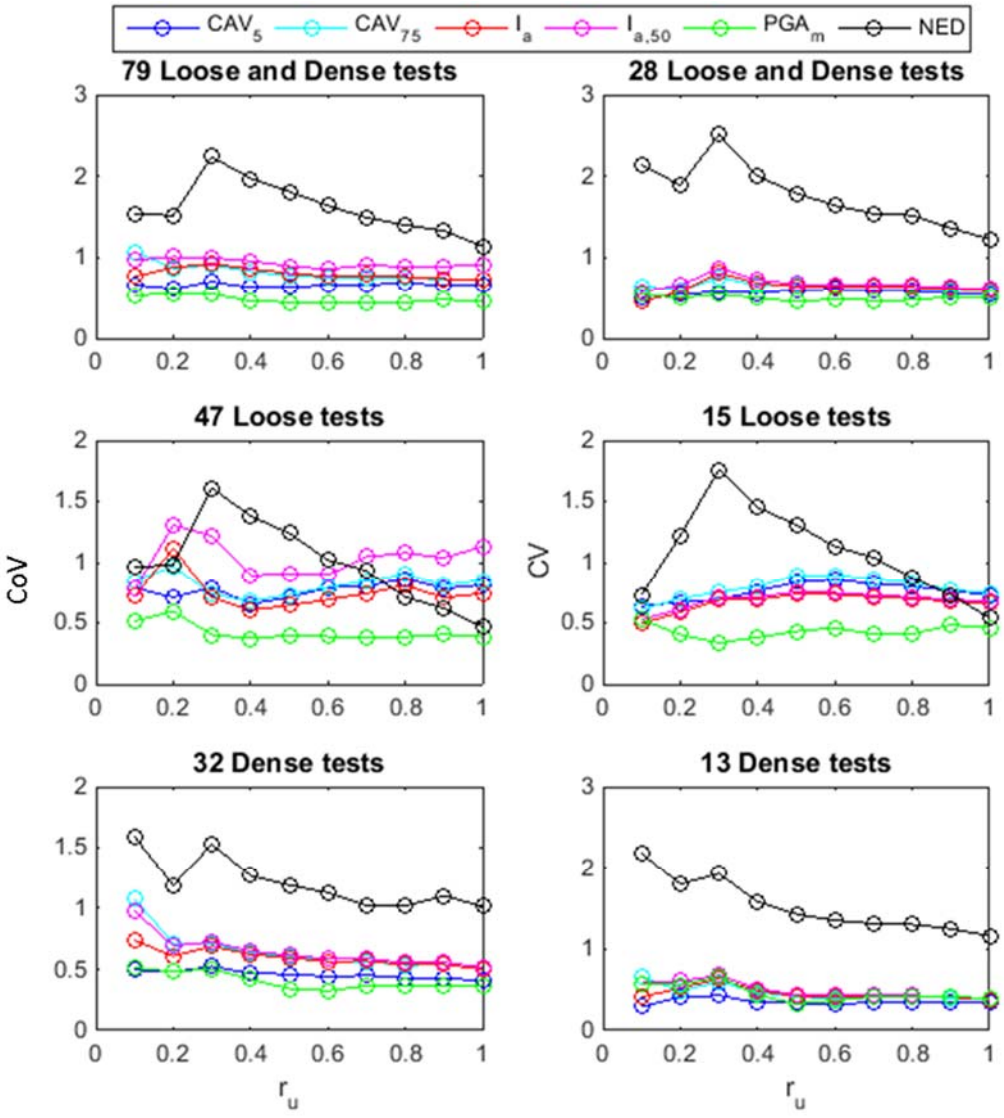

Figure 6.17: Coefficient of Variation (CoV) for the four proposed IMs.

Table 6.5: Averaged CoV for the four proposed IMs.

		79 tests	28 tests
Combined Loose and Dense	CAV_5	0.656	0.568
	CAV_{75}	0.817	0.642
	I_a	0.802	0.626
	$I_{a,50}$	0.928	0.670
	PGA_m	0.476	0.496
	NED	1.608	1.764
Loose	CAV_5	0.770	0.757
	CAV_{75}	0.816	0.786
	I_a	0.748	0.668
	$I_{a,50}$	1.028	0.687
	PGA_m	0.422	0.430
	NED	0.992	1.079
Dense	CAV_5	0.458	0.350
	CAV_{75}	0.645	0.461
	I_a	0.596	0.452
	$I_{a,50}$	0.646	0.492
	PGA_m	0.405	0.456
	NED	1.207	1.529

An ideal IM_{pre} candidate should not only able to predict the excess pore pressure generation, but also the effect of the soil density. This being said, a higher IM value is required to generate the same amount of excess pore pressure in a denser than a looser specimen. Figure 6.18 demonstrates a conceptive contour plot on how the evolution of IM is correlated with both r_u and relative density, D_r. Figures 6.19 and 6.20 show the IM values obtained from CSS test result at different r_u values based on each specimen's D_r.

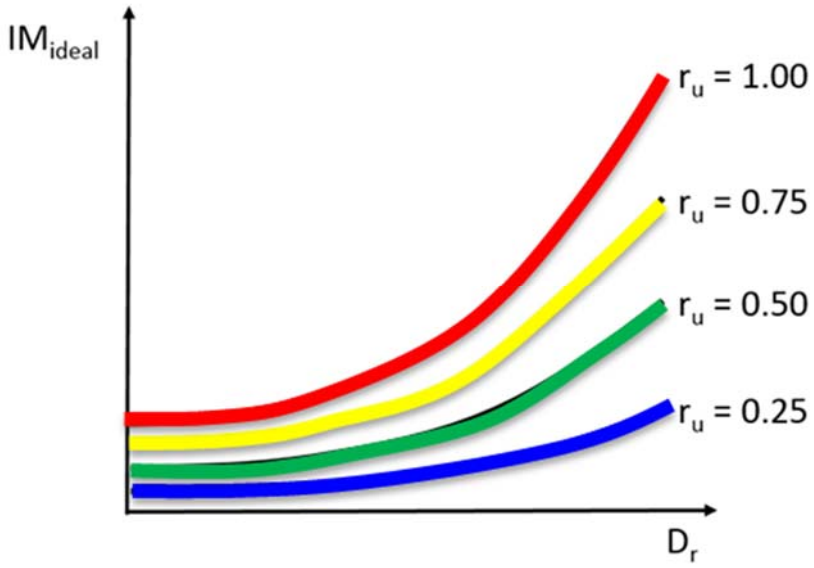

Figure 6.18: Conceptive contour plot showing the evolution of IM correlating with r_u and D_r values.

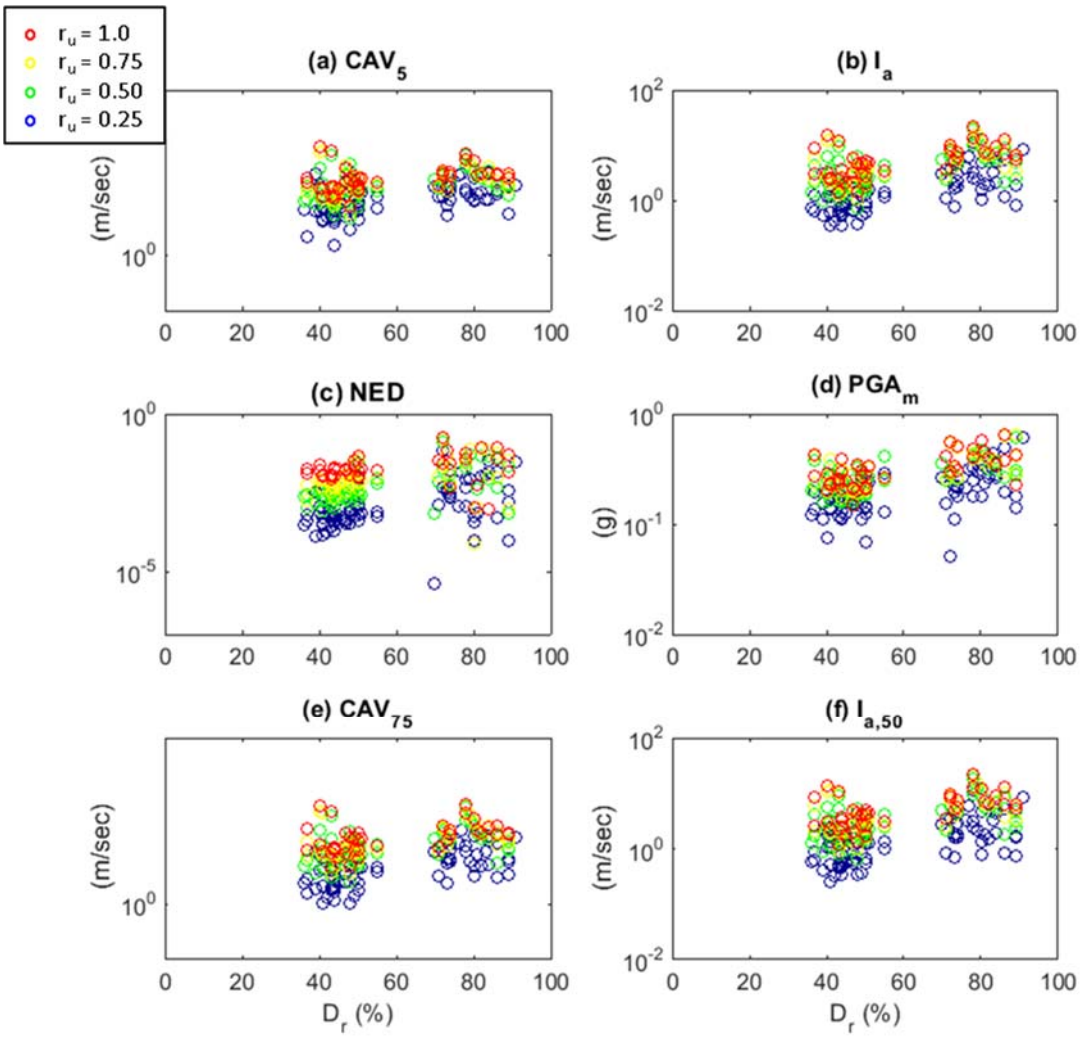

Figure 6.19: Color coded contours of constant r_u as function of each IM and density. 79 tests included.

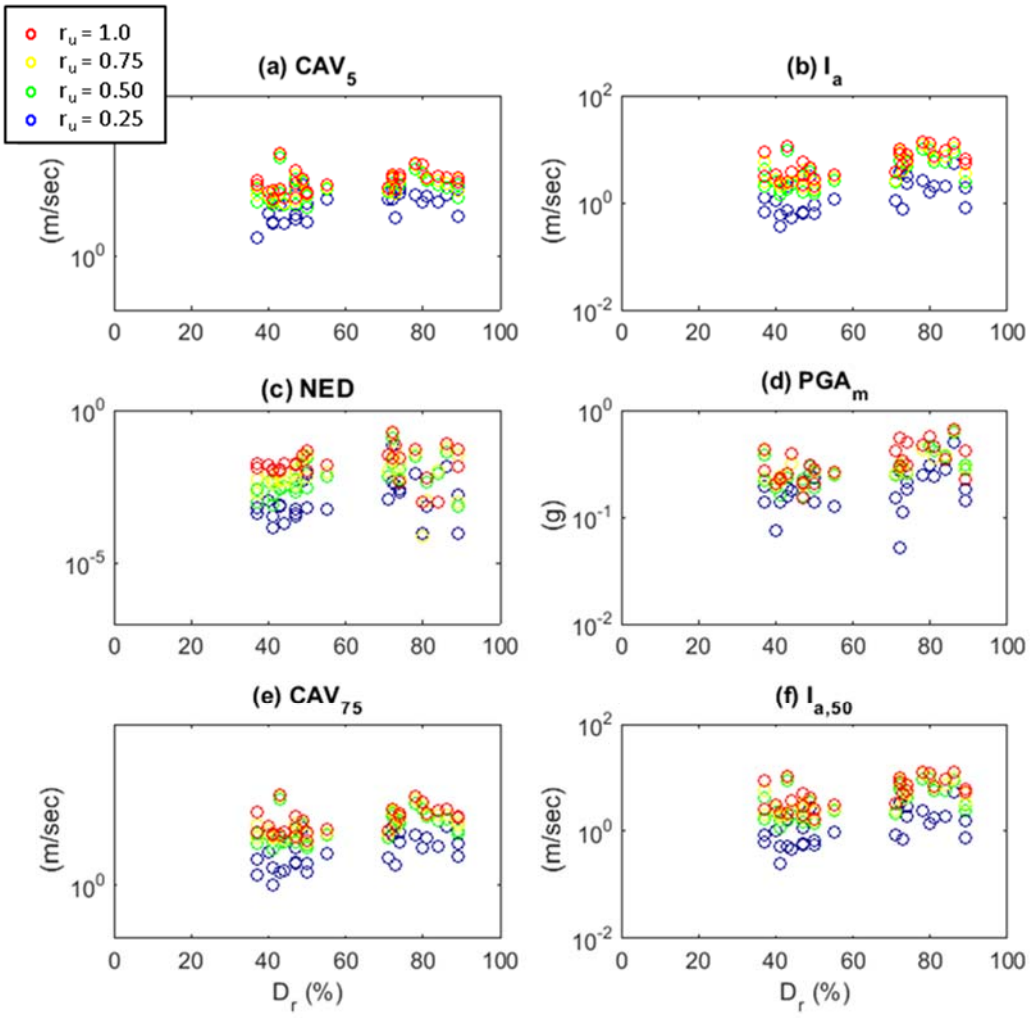

Figure 6.20: Color coded contours of constant r_u as function of each IM and density. 28 tests included.

6.5 LIQUEFACTION ASSESSMENT BASED ON SHEAR STRAIN

Using shear strain (or deformation), instead of excess pore pressure, as the parameter for liquefaction evaluation can reflect or access the seismic performance of liquefiable soils. The seismic performances of most structures and buildings are strongly dependent on the performance of the foundation soil that they were built upon. Hence, establishing a strain-based definition can potentially yield a performance assessment of the structure that is built on top of it. Liquefaction in loose sand immediately develops a severely large amount of shear strain; nevertheless, liquefaction in dense sand generate relatively limited amount of shear strain even though high r_u values are reached, because of the strong dilative behavior upon continuous shear deformation. Therefore, using pore pressure parameter solely provide limited information regarding the performance of ground surface structures. While the shear strain criterion sounds very ideal in the experimental setting, it is not as easily transferable to field applications. Deformations induced by a seismic event in the field are multidirectional and depends on many factors, such as shearing mechanism, soil fine content and initial shear stress condition. For this research project, the criteria are limited to uni-directional simple shear, clean Nevada sand and level ground condition.

Dobry et al. (1982) showed that there is a strong correlation between cyclic shear strain and excess pore pressure (Figure 6.21), and many other research projects had provided experimental data substantiating this correlation. However, the existing evidences from cyclic triaxial or simple shear testing program (stain or stress controlled) are limited to uniform harmonic motion loadings, for which the shear strain is relatively uniform, compared to the shear strain induced from transient loadings. The correlation between shear strain and excess pore pressure generated from transient loading database is expected to be much weaker than the one established from harmonic motion loadings. Figure 6.22

illustrates the correlation between cyclic shear strain and excess pore pressure that is obtained from the CSS tests under transient loading. The correlation is much weaker than the one reported by Dobry et al. (1982) and is dependent to the relative density. Nonetheless, the data clearly agrees with the results presented by Dobry et al. (1982) in terms of the shear strains as which excess pore pressures start generating. After r_u reaching 0.6, the correlation that is established from the transient loading data starts to be diverged from the one reported by Dobry et al. (1982). The correlation curve is very stiff, as opposed to be leveling out (Figures 6.22 and 6.23). The difference can be explained in Figure 6.23a-c. Under transient loading, there are loading pulses that are not large enough to induce maximum shear strain but generate excess pore pressure. On the other hand, after r_u is greater than 0.6, generally the harmonic loading would introduce maximum shear strain and generate excess pore pressure after each loading cycle.

After liquefaction is triggered, significantly more amount of shear strain is generated in loose sand than dense. The detail of post-liquefaction deformation is discussed in Chapter 7. To mimic the cyclic shear strains induced by harmonic loading, the shear strain induced by transient loading is represent by the absolute maximum value. Figure 6.23 illustrates an example. Figure 6.23a shows the r_u development of a CSS test under transient loading and Figure 6.23b reflects the shear strain response. The absolute values of shear strain are taken, in order to count both positive and negative magnitudes. At a given r_u value, the corresponding maximum value can be found (Figure 6.23c). Soil liquefaction is a time evolutionary process in which the damage builds up with time. r_u servers well as an engineering demand parameter in the framework of performance based earthquake engineering, as described in previous sections. In fact, shear strain can also be used to depict the seismic damage build-up. A new parameter, absolute cumulative shear strain, $\Sigma|\gamma(t)|$, is proposed:

$$\Sigma|\gamma(t)| = \int_0^t |\gamma(t)|dt \qquad [6.7]$$

Figure 6.23d shows an example of $\Sigma|\gamma(t)|$. It is an evolutionary function with loading time, like r_u, and contains both elastic and plastic strain components. Based on harmonic loading test data, there are two threshold cyclic shear strain level criteria (Figures 6.21 and 6.22) to describe the liquefaction phenomenon: 1) shear strain level that r_u starts to build up, and 2) shear strain level of liquefaction triggering, followed by a flow type deformation.

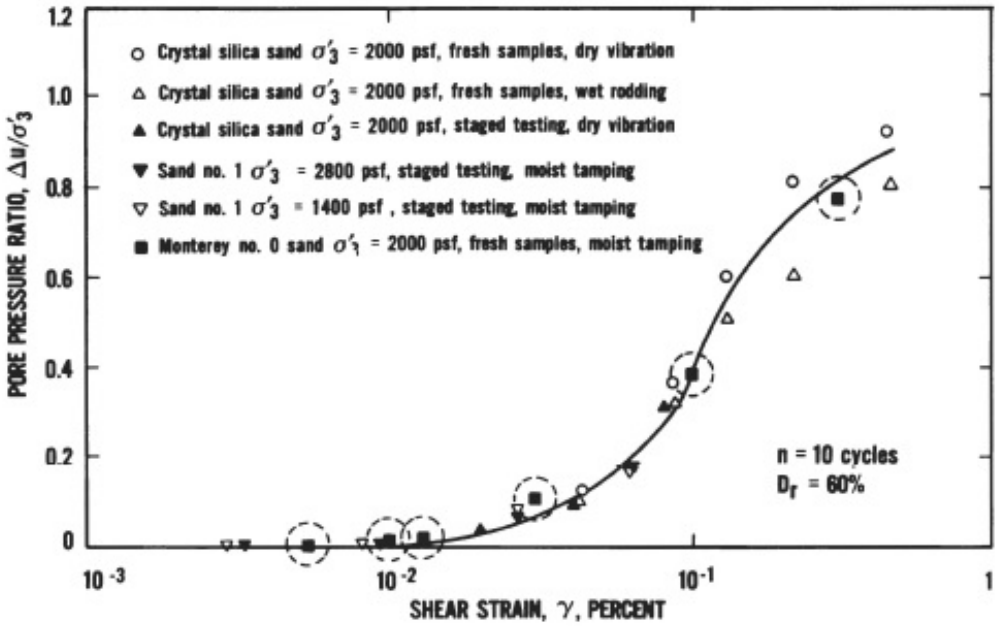

Figure 6.21: Dobry et al. (1982) Pore water pressure buildup in cyclic triaxial strain-controlled tests after ten loading cycles. (Dr = 60% saturated sand)

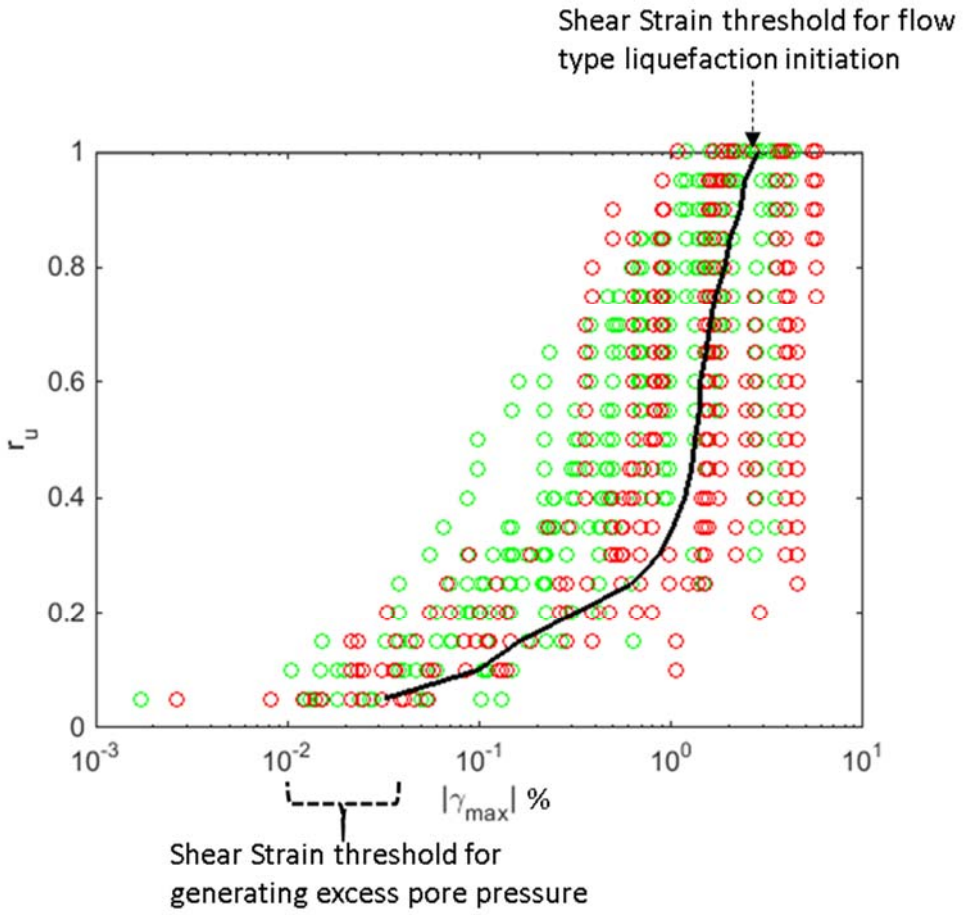

Figure 6.22: Correlation between excess pore pressure and cyclic shear strain under transient loadings (green dots = loose tests; red dots = dense tests; solid back line = overall average)

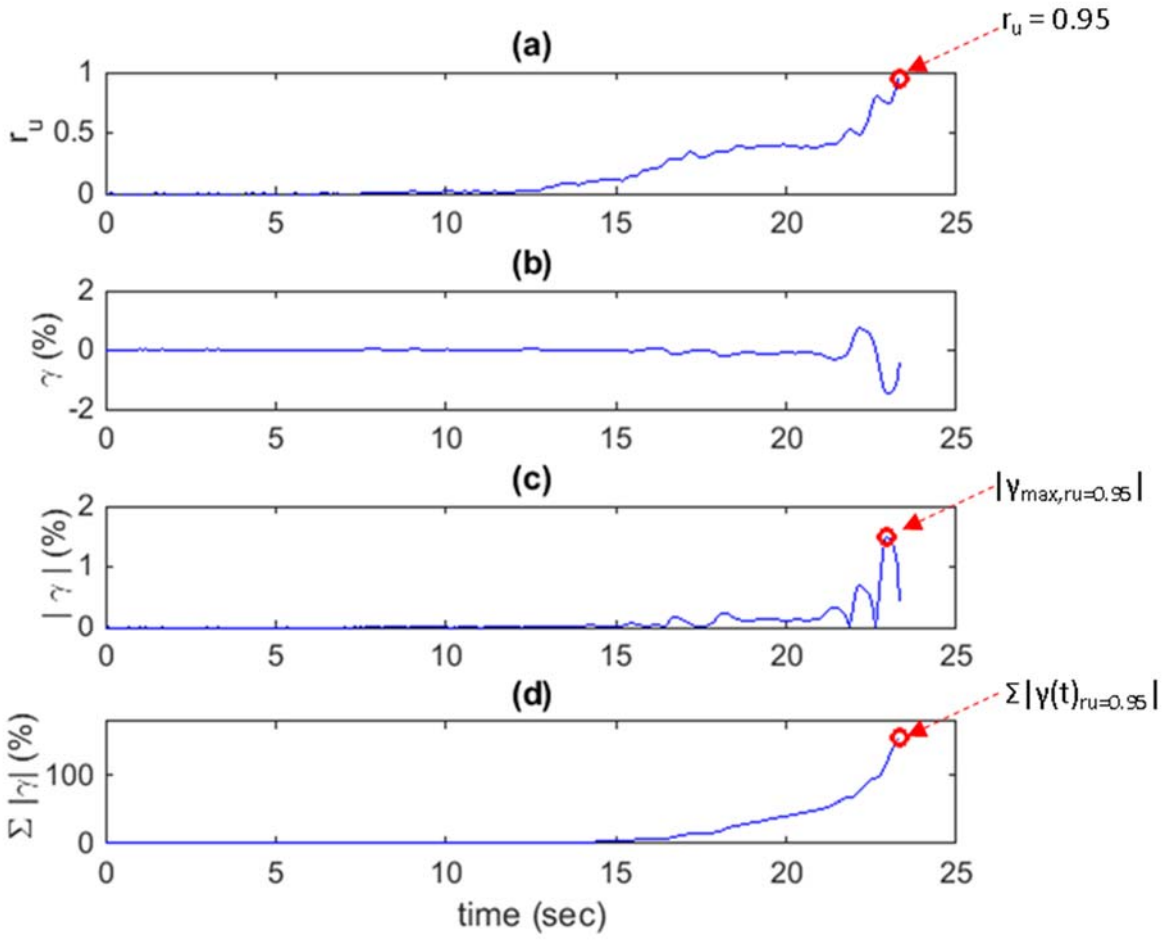

Figure 6.23: Example on calculation of $\Sigma|\gamma(t)|$ at $r_u = 0.95$. (a) r_u vs. time. (b) shear strain vs. time. (c) absolute value of shear strain vs. time (d) absolute cumulative value of shear strain vs. time

6.5.1 Threshold Shear Strain for Initiation of r_u Generation

It is a well-accepted fact that the process of liquefaction phenomena is more closely related to cyclic strains than cyclic stresses. It is logical to expect that liquefaction hazard can be evaluated by cyclic strains. Drnevich and Richart (1970) and Youd (1972) experimentally proves that there is a threshold cyclic shear strain of 10^{-2} %, below which

no sand densification or excess pore pressure generation. Dobry (1982) suggested a threshold cyclic shear strain range of $1x10^{-2}$ to $4x10^{-2}$. Figure 6.24 illustrates the correlation between shear strain and excess pore pressure generation at small r_u values. The accuracy of the UTCSS pore pressure sensor is 0.35kPa ($r_u \sim 0.0035$) and the resolution with 95% confidence of the horizontal internal LVDT is 0.0026 mm (10^{-2} % shear strain). The correlation in Figure 6.24 indicates that the excess pore pressure generally picked up at a strain level between $10^{-3}$and 10^{-2}which is consistent with previous studies.

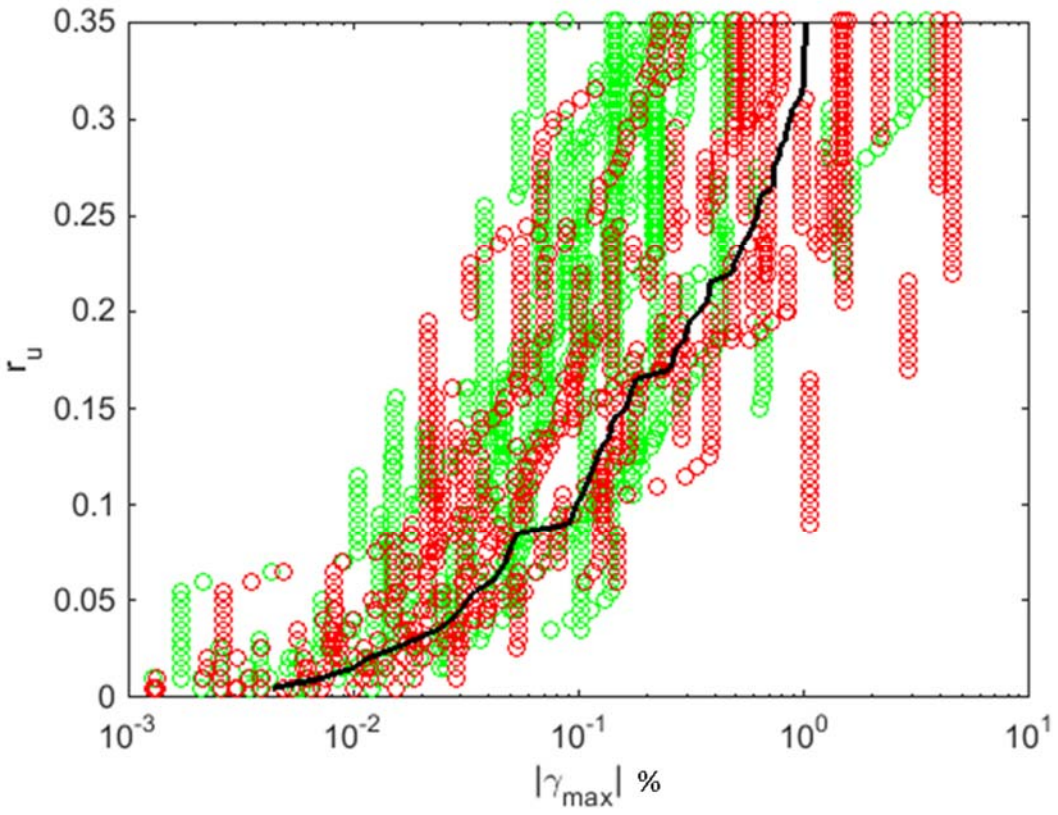

Figure 6.24: Correlation between r_u values and shear strain at smaller r_u range.

6.5.2 Threshold Shear Strain for Flow Type Liquefaction Initiation

Onset of flow-type deformation in liquefied sand is triggered when the soil loses most of its effective confining stress, associating with a high r_u value (> 0.9) and certain level of shear strain. Alternatively, the flow-type liquefaction initiation can be defined by a shear strain threshold as the liquefaction triggering criteria. In the past, different values of threshold were established, based on testing program of cyclic triaxial or simple shear under uniform harmonic sinusoidal loading. Typically, the triggering threshold criteria is selected as the first occurrence of either certain amount of double amplitude (DA) or single amplitude (SA).

First, the 28 CSS transient loading test results are compared with the 12 harmonic loading test results. All tests were conducted with Nevada Sand. The shear strains criteria is selected as the absolute maximum value occur before or at $r_u = 0.95$, and the averaged results were summarized in Table 6.6. Under harmonic and transient loadings, the threshold shear strains for the loose specimens are similar. However, the threshold value is much higher for dense sand under transient loading than under harmonic loading. When the loading is uniform, it's a well-accepted fact that limited shear strain is induced at a high level of r_u, because the sand is dense. However, for the tests on dense sand under transient loading, in order to liquefy the specimen, relatively large amplitudes of loading are required at the few dominant pulses and that created one or a few maximum shear strain amplitudes that resulted in high plastic deformations even when r_u values didn't approach unity yet. The aspect of high loading pulses may not be well captured in the harmonic loading tests.

Wu et al (2004) tested with Monterey #0/30 sand, suggested 6% SA or DA, and Ishihara (1993) recommend 3% to 3.5% SA shear strain and 5% DA axial strain. This research project provides a systematic database reflecting shear strain level at liquefaction

triggering (r_u = 0.95) under different transient loadings (Figures 6.22 and 6.23). The averaged SA $|\gamma_{max}|$ threshold value for the transient loading CSS tests is 2.4%. The averaged values of $\Sigma|\gamma|$ required to trigger liquefaction are also included. The obtained threshold values from this research in general agree with previous studies that were based on uniform loading.

Table 6.6: Different shear strain threshold values from different CSS tests in Nevada Sand.

$\|\gamma_{max}\|$ (%)	Harmonic		Transient	
	Loose	Dense	Loose	Dense
This study	2.34	1.74	2.13	2.73
Wu	3		NA	
Ishihara	3 to 3.5			
This study:$\sum\|\gamma\|$	2238	1021	468	1167

6.5.3 Identifying Optimum IM based on Shear Strain

Shear strain can also serve an engineering demand parameter to determine the effectiveness of proposed IMs. In order to translate shear strain into an evolutionary manner, summation is taken (Equation 6.7). Same as Section 6.3, only CSS data of before liquefaction initiation (r_u < 1.0) is considered, and all data after liquefaction triggering is ignored. For comparing the effectiveness of the different IMs in predicting the development of shear strain, the time and all IMs values are normalized by their value at the timing of liquefaction initiation (r_u = 1.0). The normalized cumulative absolute shear strain is calculated as the following:

$$N.\Sigma|\gamma(t)| = \frac{\int_0^t |\gamma(t)|dt}{\int_0^{t_{liq}} |\gamma(t)|dt} \qquad [6.8]$$

Like Section 6.3, parametric studies were performed to evaluate the optimum threshold accelerations on the accuracy of CAV_x and $I_{a,x}$ in matching the development of shear strain. The formulation for searching the optimum threshold acceleration of CAV and I_a are shown in Equations 6.5 and 6.6. Threshold accelerations ranging 0 to 200 cm/sec^2 were evaluated and the corresponding normalized CAV_x and $I_{a,x}$ values were calculated and compared to $N.\Sigma|\gamma(t)|$ values from 28 CSS tests. The averaged differences between the calculated IM_x and measured $N.\Sigma|\gamma(t)|$are shown in Figures 6.25 and 6.26. The optimum threshold acceleration, based on shear strain development, for CAV is 177 cm/sec^2, and for I_a is 180 cm/sec^2. The two threshold accelerations are significantly higher than those determined based on matching of r_u (75 and 50 cm/sec^2, respectively), because both elastic and plastic strain components are considered

Figures 6.27 and 6.28 are very similar to Figures 6.10 and 6.11, except the yellow lines are showing the $N.\Sigma|\gamma(t)|$ instead of r_u. The perfect IM should evolve identically with with the shear strain development; therefore, the smaller the difference or better correlation between calculated IM and measured r_u, the better the IM is. The average error between the normalized IM values and $N.\Sigma|\gamma(t)|$ are plotted in orange color and the bars represent one standard deviation. The normalized CAV_5 and I_a have a tendency of overestimating the shear strain developments, and therefore applying higher acceleration threshold provides better matches with the CSS data. The CAV_{177} and $I_{a,180}$ plots show significantly improved correlations with the correspondent shear strain developments. Since the threshold accelerations are high, the calculated values increase in a stepwise manner. Overall, NED provides the best matches with the $N.\Sigma|\gamma(t)|$ values. This finding is no surprise because the shear strain values are used to calculate the NED values.

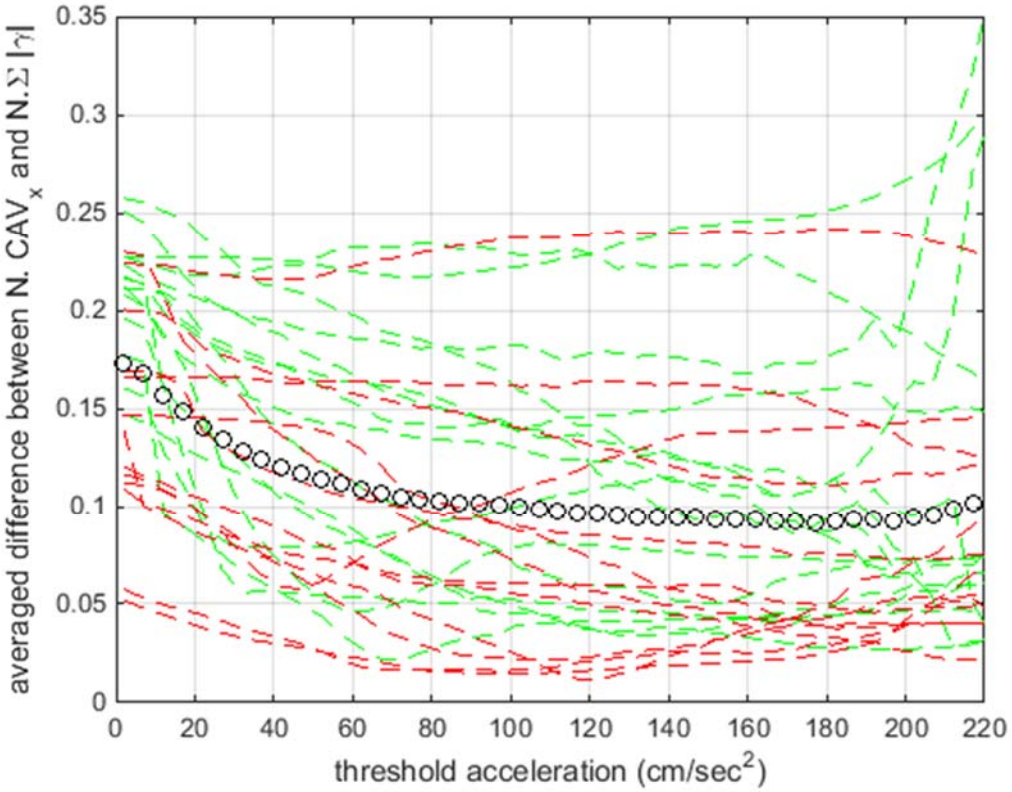

Figure 6.25. Results of searching for the threshold acceleration that gives minimum overall difference between the measured shear strain values and calculated normalized CAV values. 28 CSS tests were considered in this analysis (dotted green line = loose test, dotted red line = dense test, open black circle = average of the 28 tests). Smallest different at 177 cm/sec.

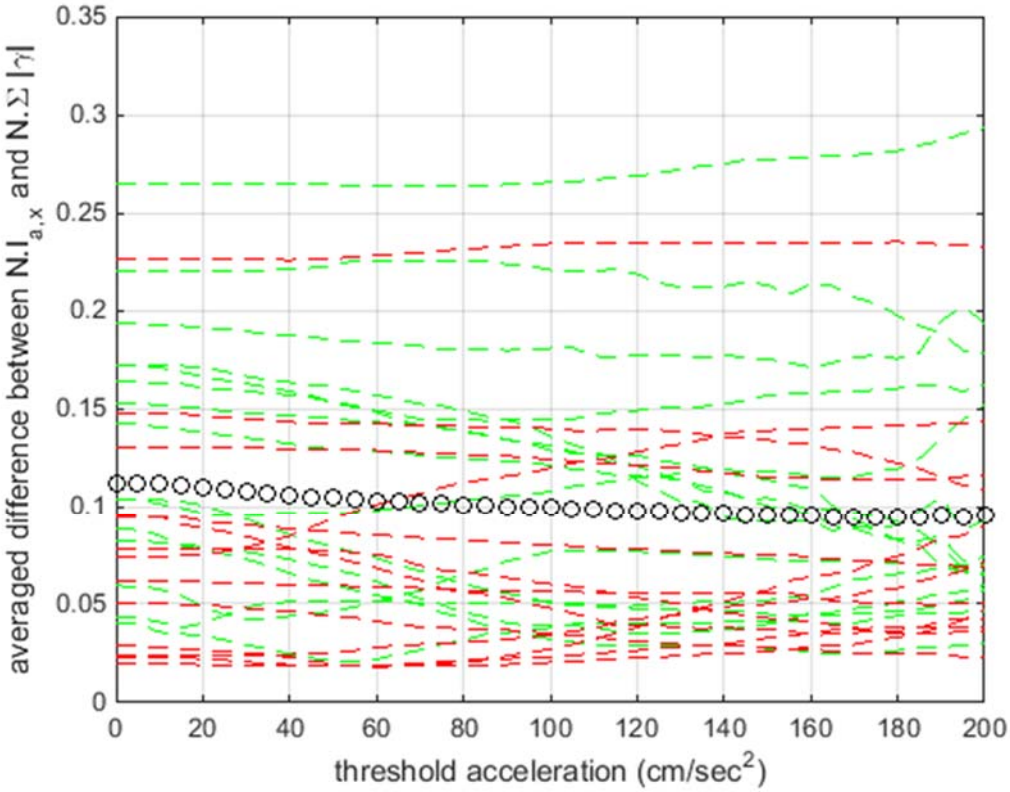

Figure 6.26. Results of searching for the threshold acceleration that gives minimum overall difference between the measured shear strain values and calculated normalized I_a values. 28 CSS tests were considered in this analysis (dotted green line = loose test, dotted red line = dense test, open black circle = average of the 28 tests).

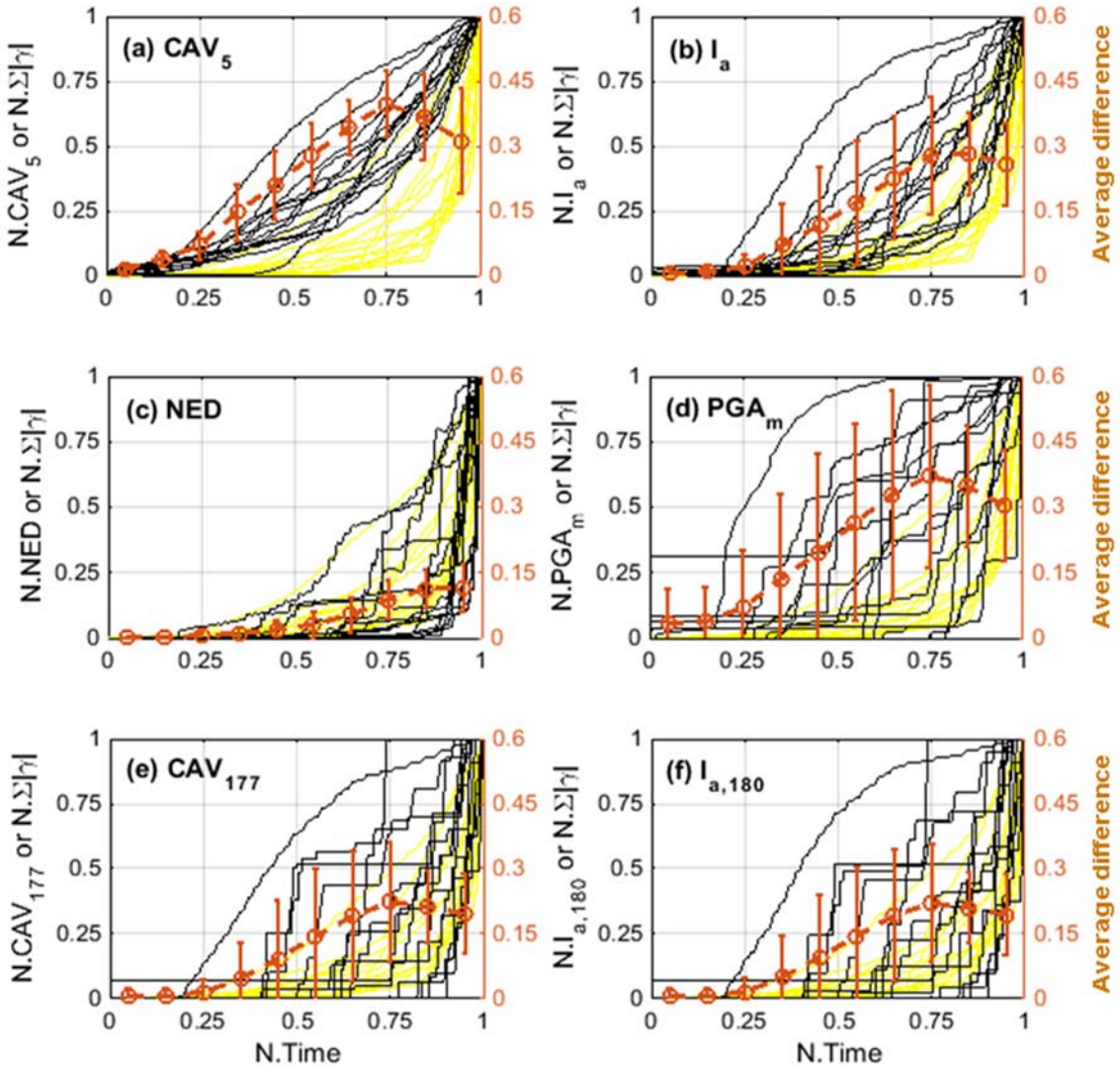

Figure 6.27: Normalized IM vs. Normalized Time. Comparison between the calculated IMs and shear strain development from 15 loose CSS tests (yellow = $N.\Sigma|\gamma(t)|$; black = calculated IM)

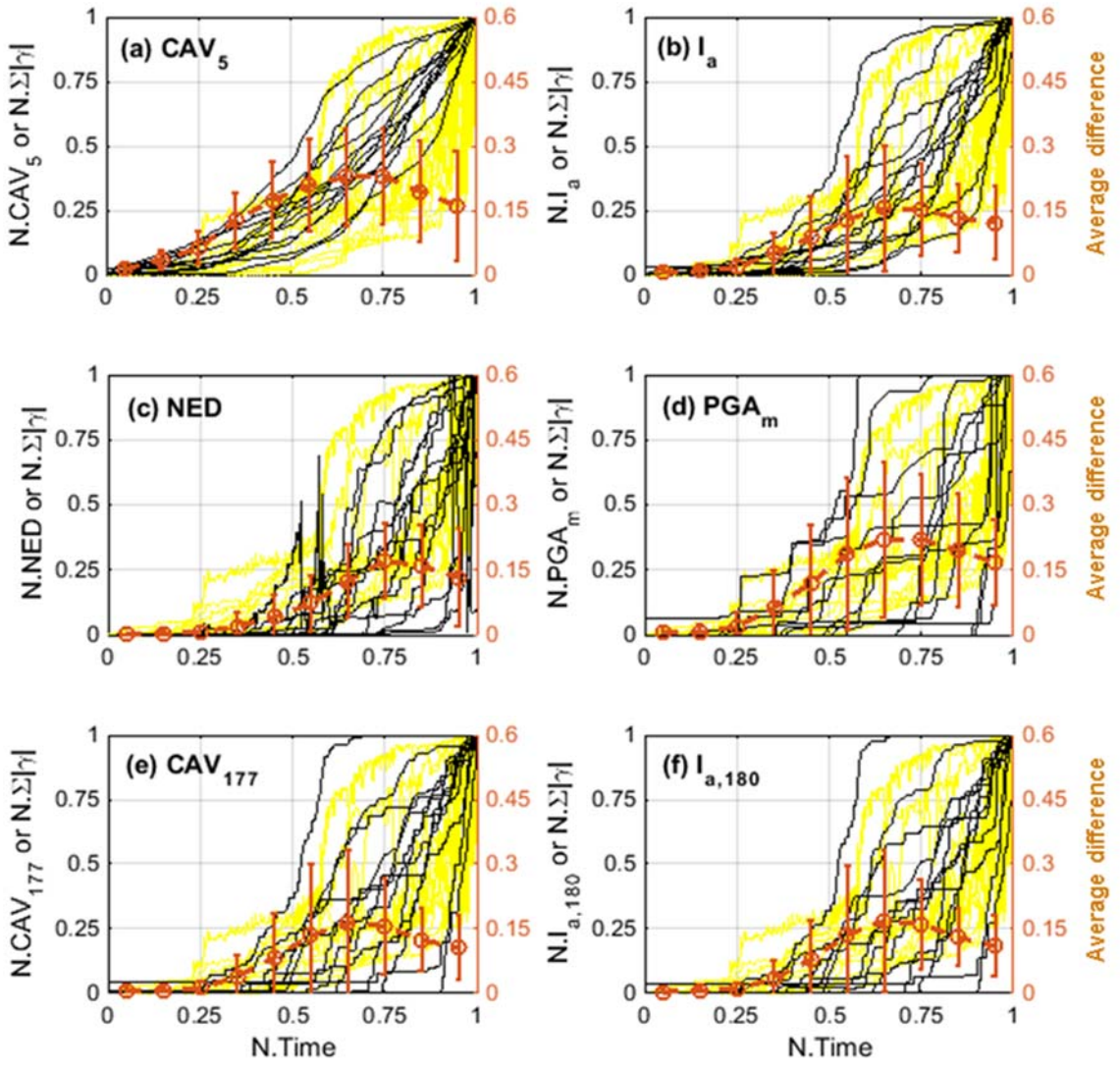

Figure 6.28: Normalized IM vs. Normalized Time. Comparison between the calculated IMs and shear strain development from 13 dense CSS tests (yellow = $N.\Sigma|\gamma(t)|$; black = calculated IM)

Figures 6.29 to 6.30 compare the normalized IM values with the normalized shear strain values. The perfect IM should provide minimal deviation when compares with N.Σ|γ| values, which graphically, the smallest error bars in Figures 6.29 and 6.30. Figures 6.31 and 6.32 illustrates the absolute values of the Σ |γ| and IMs along the normalized time.

Table 6.7 summarizes the overall averaged differences between the normalized shear strains and calculated IMs from the 28 CSS tests under transient loadings. NED provides the smallest differences on matching the values of Σ |γ|, but gives relatively large standard deviation (low efficiency). Implementing a larger threshold acceleration for CAV, 177 instead of 5 cm/sec^2 makes a significant improvement in matching the shear strain values (17.62 to 6.4%). For I_a, adopting a threshold acceleration only make a slight improvement, 10.9 to 9.35%. However, the efficiency of CAV_{177} and $I_{a,180}$ decreased significantly (higher CoV values), and suggested that CAV_5 and I_a are the better performers.

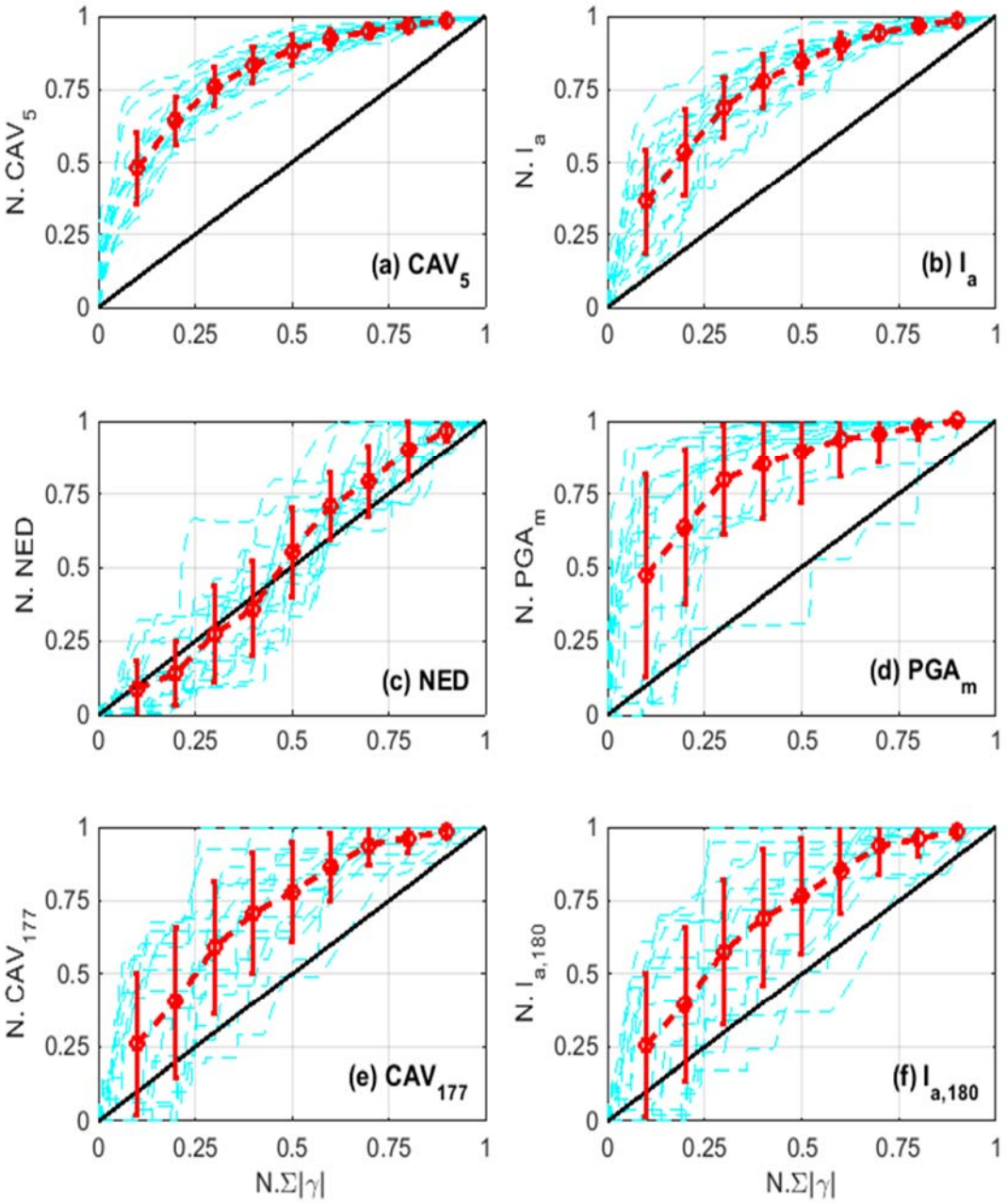

Figure 6.29: Normalized IM vs. $N.\Sigma|\gamma(t)|$, 15 loose CSS tests.

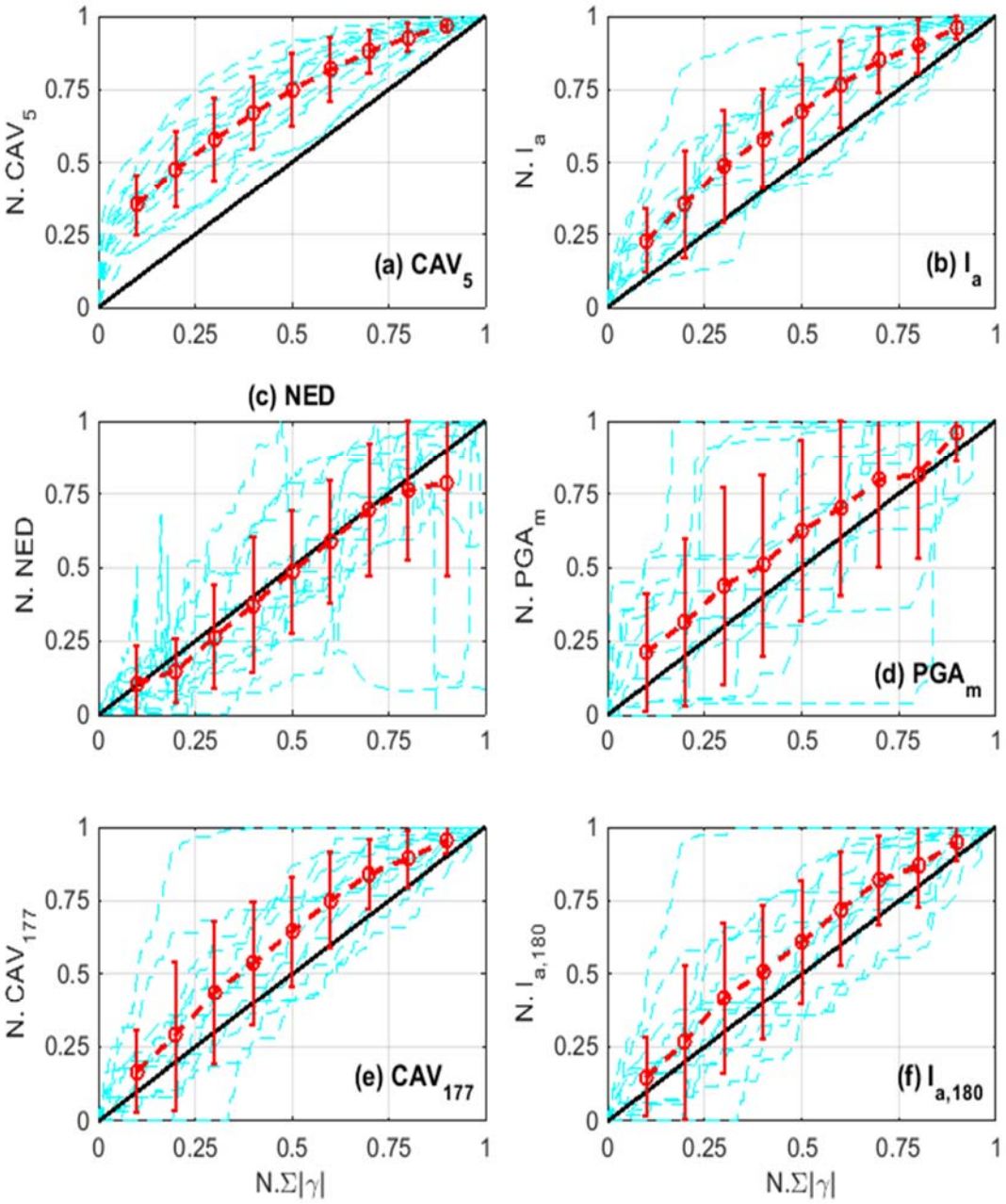

Figure 6.30: Normalized IM vs. $N.\Sigma|\gamma(t)|$, 13 dense CSS tests.

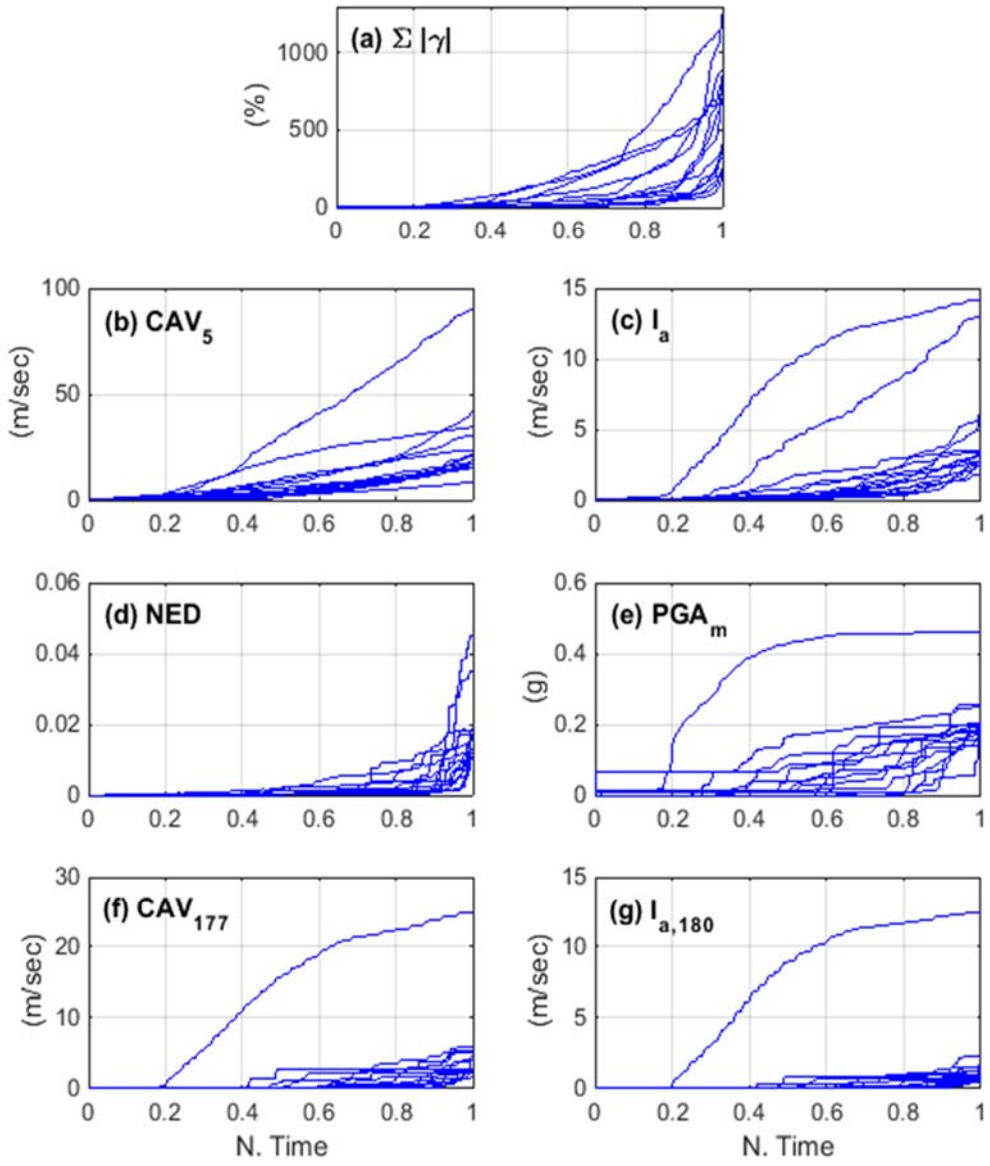

Figure 6.31: (a) Absolute values of Σ |γ| vs. normalized time. (b-g) Absolute values of different IMs vs. normalized time. 15 loose CSS tests include.

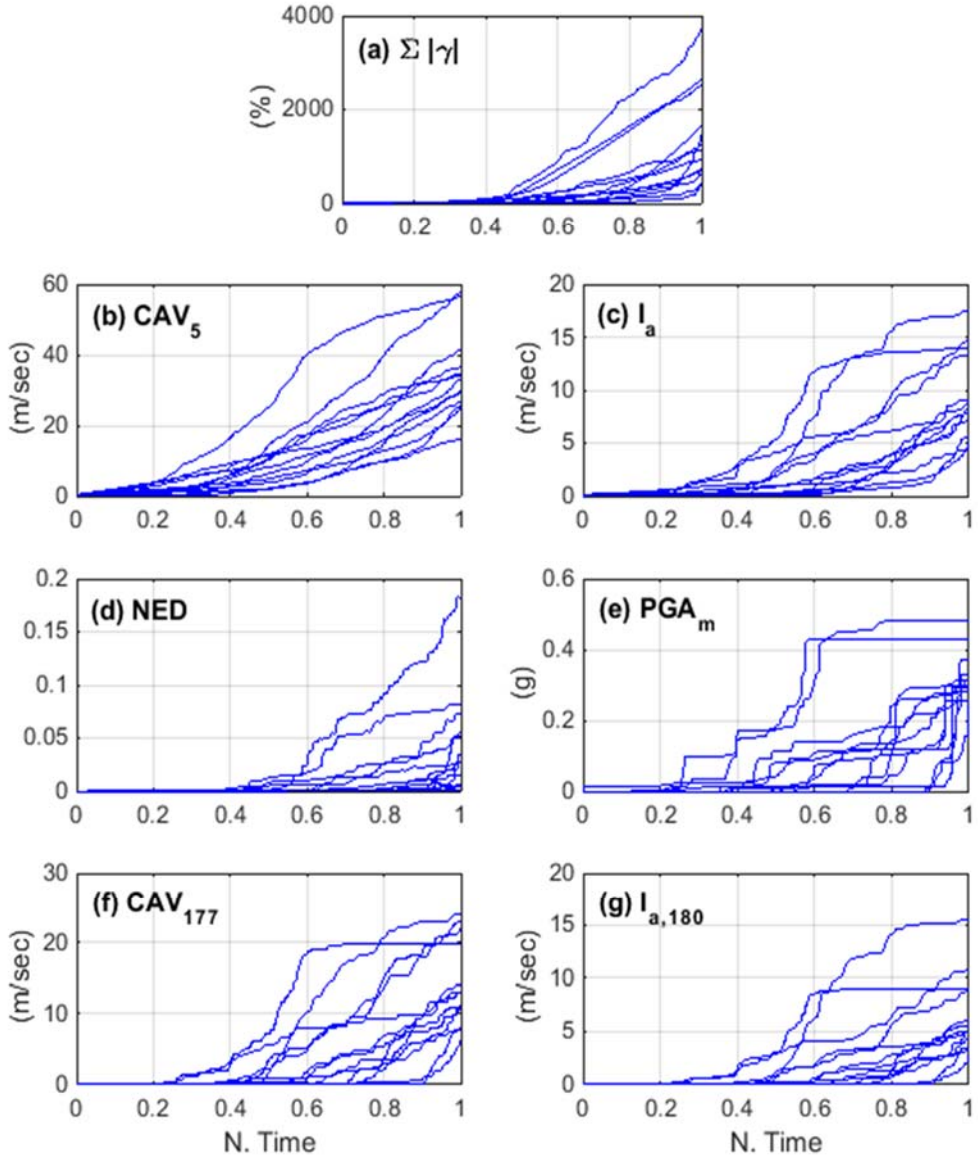

Figure 6.32: (a) Absolute values of Σ |γ| vs. normalized time. (b-g) Absolute values of different IMs vs. normalized time. 13 dense CSS tests include.

Table 6.7: The overall differences for each IM and normalized shear strain.

IMs	Overall Average Difference (%)	Overall Average CoV
CAV_5	17.62	0.12
I_a	10.90	0.20
NED	5.17	0.48
PGA_m	15.95	0.39
CAV_{177}	6.40	0.34
$I_{a,180}$	9.35	0.39

6.6 CONCLUSION AND DISCUSSION

This chapter presents an evaluation of the use of Intensity Measures (IMs) for characterization of earthquake loadings and determining liquefaction potential. The study mainly analyzed results of 28 cyclic simple shear tests under 19 different ground motions on loose and dense sand specimens. The assessments were mainly based on how well the calculated IM values matching and/or correlating with the measured damage in the form of excess pore pressure (r_u) and shear strain ($N.\Sigma|\gamma(t)|$). In addition to the four basic IMs (CAV_5, I_a, NED and PGA_m), parametric studies were performed and found that a greater threshold accelerations on CAV and I_a gave significantly better matches to the experimental data, CAV_{75} for r_u and CAV_{177} and $I_{a,180}$ for $N.\Sigma|\gamma(t)|$, but not necessary better correlations. Overall, CAV_5 and I_a are identified as the optimum IMs under the comparison with r_u and $N.\Sigma|\gamma(t)|$, because of the better efficiency (lower overall CoV values). NED provides the best matches with the shear strain development, but gives relatively weak correlation with r_u and $N.\Sigma|\gamma(t)|$. In fact, there is an argument of selecting the better engineering demand parameter, r_u or $N.\Sigma|\gamma(t)|$. For this analysis, r_u could be a better engineering demand parameter than the $N.\Sigma|\gamma(t)|$) for two reasons. First, there is no no consensus on the strain-based liquefaction triggering criteria. The cut-off of data for

liquefaction initiation is based on r_u, which lead to very different triggering strain-levels ranging from 1% to 6% shear strain as shown in Figure 6.22. Secondly, the resolution of the internal horizontal LVDT may not be high enough to capture the very small strains ($<10^{-2}$ %), which shear deformation may have already been mobilized for excess pore pressure generation. This limitation should be magnified in loose specimen, since excess pore pressures might be generating at lower shear strains. From Figure 6.26, the calculated IMs (CAV_5, I_a and PGA_m) have tendencies of overestimating the $N.\Sigma|\gamma(t)|$ values, which could be due to limitation of the LVDT resolution. Results from this study indicate that r_u is a better indicator of liquefaction initiation than $N.\Sigma|\gamma(t)|$ as the engineering demand parameter when using IMs, not because of its superiority, but rather the limitations of current knowledge and instrumentation that affecting the use of shear strain. In fact, those limitations open the door of future research.

Chapter 7: Post-liquefaction Soil Responses

7.1 INTRODUCTION

Liquefaction of saturated sand is a well-recognized devastating hazard that has caused catastrophic losses in the past. During a liquefaction event, landslides are often triggered because the shear strength of the soil is significantly reduced due to excess pore pressure generation and decrease of effective stress. Although much research has been devoted in the past few decades to evaluating or improving the soil resistance during undrained loadings, very limited attention has been given to post-liquefaction soil responses. In fact, it is of equal importance to gain insight into the characteristics and effects of liquefied soil. In laboratory modeling, there are two approaches to study liquefied soils. First, investigating the stress-strain behavior by applying monotonic loading after liquefaction initiation. Second, studying the effects of soil liquefaction from cyclic testing by identifying the triggering time.

In terms of stress-strain behavior of liquefied soil, there is a general agreement that a flat, low stiffness phase of the stress-strain plot appears before the beginning of a dilation phase when monotonic loading is applied (Figure 2.13). A limited amount of post-liquefaction monotonic test results under the CSS setup are documented in this chapter. The data shows a great variation in the strain levels needed to transition between the low-stiffness phase and the dilation phase. A better knowledge of the stress-strain behavior of liquefied soil can benefit the evaluation of liquefaction in many ways, especially in advancement of constitutive modeling. However, the response of liquefied soils depends on many factors, such as density, stress level and fines content. More importantly, the effects of irregular pre-liquefaction loading to responses of post-liquefaction has not been

well explored. Kwan et al. (2015) has shown pre-liquefaction irregular loadings affect the post-liquefaction responses, using a triaxial setup. Further research is needed in this topic for adopting systematic transient loading, and, preferably, in a simple shear setup.

Succeeded from Chapter six, using IMs to analyze the CSS post-liquefaction data can provide valuable insight of liquefaction effects. In fact, the IM that works well for predicting liquefaction initiation does not guarantee working equally well for estimating liquefaction effects. The two ideal IMs (IM_{pre} and IM_{post}) are likely to be mutually exclusive, because the properties of sand change dramatically before and after the initiation of liquefaction. The effects of liquefaction are predominantly driven by the earthquake loading that occurs after liquefaction has been triggered. If the remaining seismic loading is strong and the duration is long, the damage is expected to be severe, possibly resulting in total collapse of above-ground structures. On the other hand, if the remaining loading is weak and the duration is short, the damage, perhaps, is tolerable and the above-ground structures can be sustained. However, the current stress-based liquefaction evaluation procedure provides no information about the expected damage after liquefaction has initiated. Chapter 6 experimentally identifies the IM that best correlate with soil response up to liquefaction initiation. This chapter focuses on experimentally identifying the best IM that can predict seismic damage after liquefaction is triggered. The prime goal is to identify the optimum IM for predicting lateral spreading from a given ground motion.

7.2 POST-LIQUEFACTION MONOTONIC BEHAVIOR

Twelve tests (Table 7.1) were sheared under monotonic loading after liquefaction initiation to investigate the stress-strain behavior of liquefied sand. Those data is considered to be preliminary, because excessive tilting may occur under the current UTCSS

configuration, especially the application of displacement control. Even though the tilting problem has been significantly improved after the installation of the aluminum bracket (Figure 3.12), the overall stiffness of the apparatus may not be high enough to provide the necessary rigidity to prevent tilting when the specimen is monotonically loaded to a high strain level. The problem of tilting or rocking is dominant when the sand specimen is stiff (sand dilation after liquefaction initiation) and loaded to large strains. For the stress controlled cyclic tests up to liquefaction, the rocking problem is not as significant as in the post-liquefaction monotonic shear tests.

The post-liquefaction monotonic tests were performed under undrained condition at a shear rate of 0.1 % shear strain per minute. Four tests were done on loose specimens, and eight tests on dense specimens. All test results are documented in appendix A.7. Figure 7.1 depicts an example of the post-liquefaction monotonic test results. As seen in Figure 7.1a, like previous studies (Vaid and Thomas 1995; Sivathayalan and Yazdi 2013; Dahl et al. 2014) on this topic, a flat, low stiffness, part appears in the plot before the beginning of dilation.

For this project, a special strain level, $\gamma_{post,T}$, is set up to describe the transition from the low stiffness phase to the dilative phase in a post-liquefaction stress-strain curve. $\gamma_{post,T}$ is defined by the conjunction point of two tangent lines that represent two different phases, as shown in Figure 7.1b. It should be noted that $\gamma_{post,T}$ can be determined only when both phases (low stiffness and dilative) exist. There are tests that either were terminated before reaching the dilative phase (Test IDs: 20130815 and 20130816) or the dilative phase was initiated once the monotonic shearing started (Test ID: 20130821). The $\gamma_{post,T}$ value for each test is summarized in Table 7.1. It is interesting to observe that the $\gamma_{post,T}$ values are ranging from zero to over twenty percent. The variation in $\gamma_{post,T}$ values is attributed to the differences in particle rearrangement or change of fabric during liquefaction under different

type of pre-liquefaction loading motions. However, the test results developed in this research project are not sufficient to draw conclusive findings on the effect of pre-liquefaction loading into post-liquefaction responses.

Table 7.1: Summary table for post-liquefaction monotonic tests

ID	Pre-liquefaction loading histories	Vert. Stress (kPa)	D_r (%)	$\gamma_{post,T}$ %
20130813	Modulated_down_n=0.1	100	86	8.1
20130815	Harmonic	50	49	NA
20130816	Harmonic	50	43	NA
20130821	7030_2A	100	89	NA
20130827	6530_2A	100	97	5.3
20130904	6530_1B + Stage 2 taper up	100	94	4.5
20130919	6530_1B + Stage 2 taper up	100	62	6.0
20131001	6530_2A	100	65	15.0
20131007	NGA_no_1157_CNA000	100	91	26.0
20131008	NGA_no_484_PLK-NS	100	83	10.9
20131024	NGA_no_1157_CNA000 + Stage 2 taper up	100	90	6.7
20131104	NGA_no_880_MCF000 + Stage 2 taper up	100	97	2.3

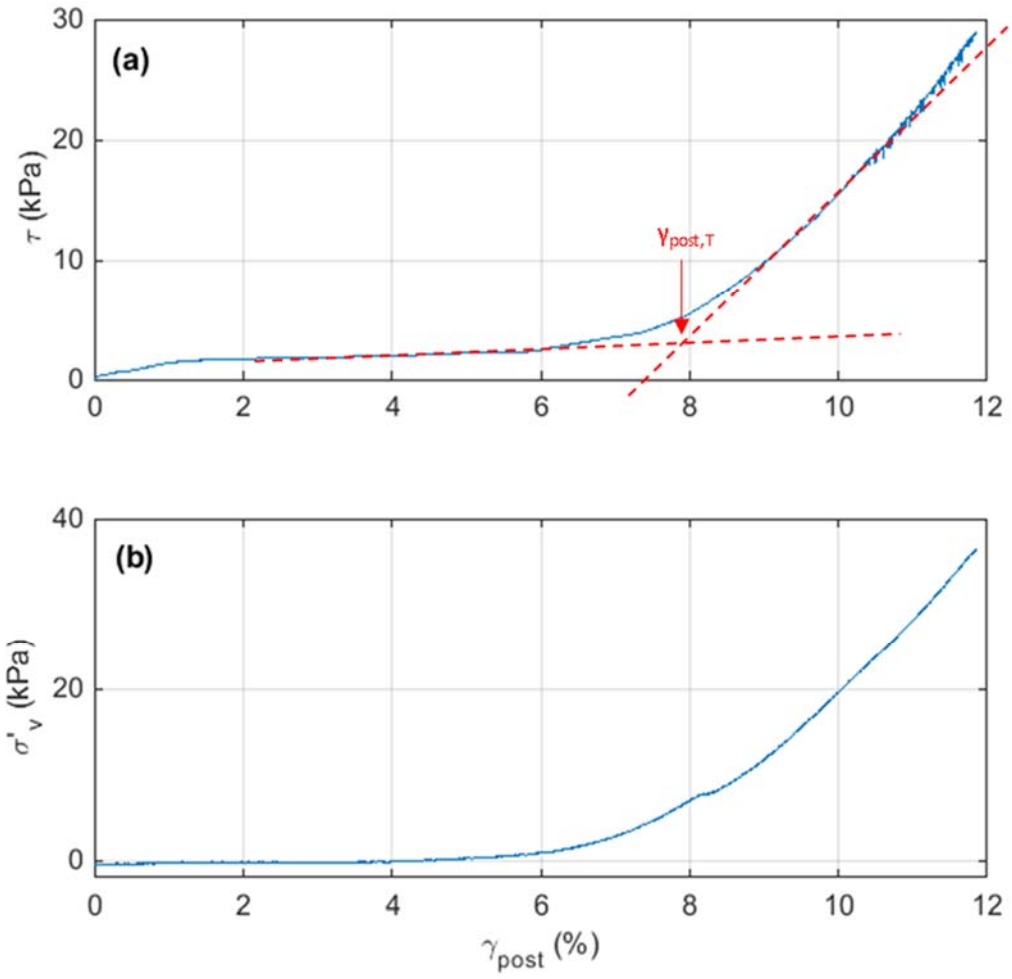

Figure 7.1: A typical result of post-liquefaction monotonic loading (Test ID: 20130813P). (a) stress-strain plot. (b) change in vertical effective stress.

7.3 EXPERIMENTAL RESULTS FROM TRANSIENT LOADING

The CSS test results used for analysis in this chapter is the same as the one used in Chapter 6, but only the post-liquefaction part of data is used in which the timing starts from r_u reaching unity and ends with the last zero crossing point of shear strain (Figure 7.2).

There are two tests (ID: 130925 and 130821) in which the post initiation shear strains (γ_{post}) do not cross the zero axis; therefore, the end points were picked at the absolute maximum value of γ_{post}. Imposing an end point of the post-liquefaction data avoids counting the bias of residual shear strain when the loading ends.

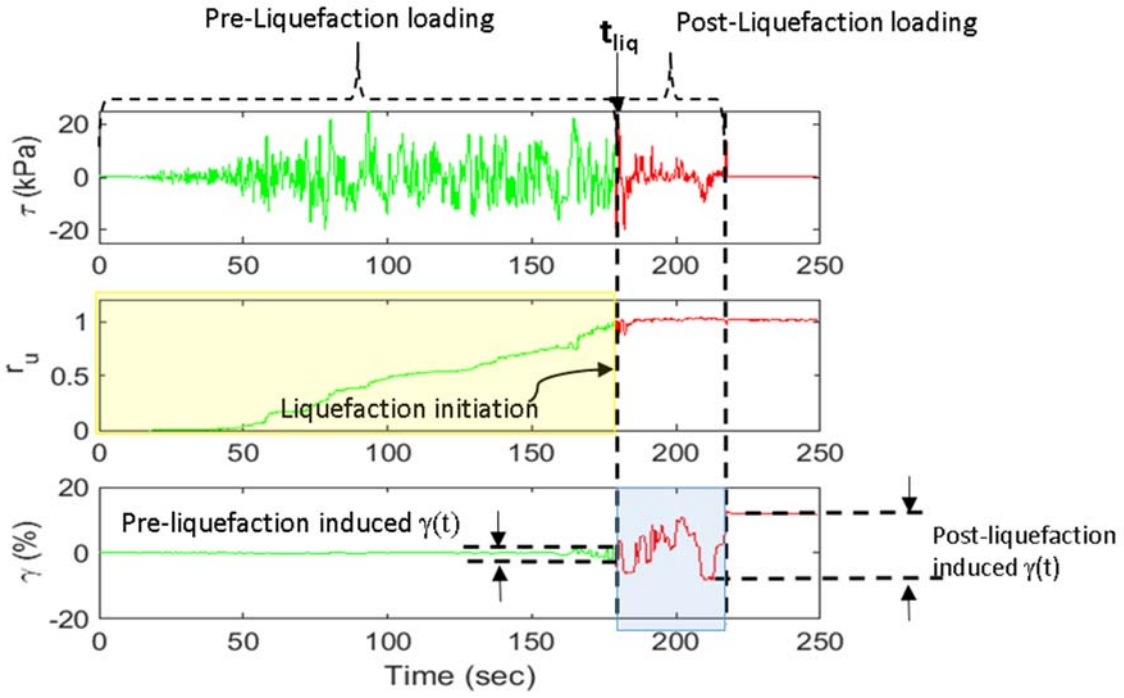

Figure 7.2: Separating post-liquefaction loading and soil response from the entire motion

Instead of 28 CSS tests, 43 CSS tests (27 loose and 16 dense) under transient loadings that have loaded beyond liquefaction initiation are used for analysis in this chapter. This means that some ground motions are repeated in the 43 CSS tests database. For two CSS tests that are loaded under the same shear stress time histories but with

different amplitude (i.e., different liquefaction initiation time), unlike the pre-liquefaction responses (shear stress and corresponding acceleration time histories), the post-liquefaction responses can be very different. Figure 7.3 illustrates four acceleration time histories that were converted from two different CSS shear stress post-liquefaction time histories. Since different amplitudes of shear stress time histories were imposed on the 'identical' soil specimens, liquefaction was triggered at different times and yielded distinctive post-liquefaction temporal responses.

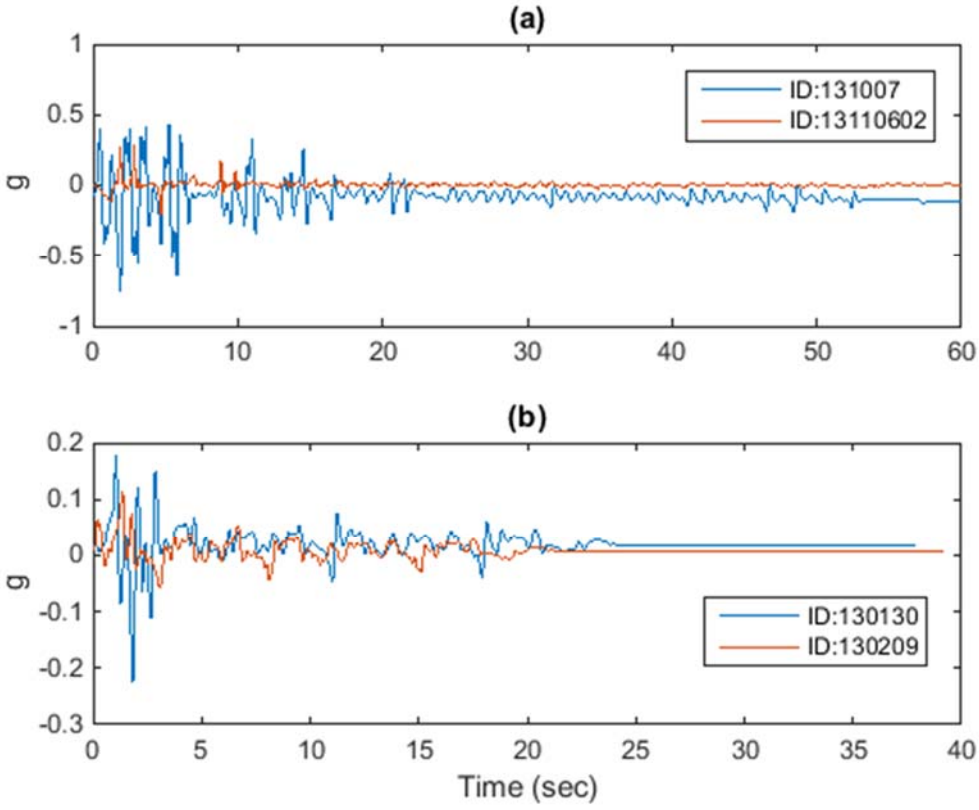

Figure 7.3: Post-initiation acceleration time histories from identical ground motions. (a) KOCAELI CNA000 h2. (b) PALMSPRMVH135

Intensity Measures, particularly IM_{post}, has potential of tracking earthquake induced lateral deformation, which is quantified by shear strain in this study. Since the liquefaction initiation time can be identified in a CSS test, post-liquefaction shear strain (γ_{post}) can be separated from the entire course of shear strain (γ). γ_{post} is transformed into an evolutionary manner, ($\Sigma|\gamma_{post}(t)|$), like Chapter 6.

$$\Sigma\left|\gamma_{post}(t)\right| = \int_{t_{liq}}^{t_{end}}\left|\gamma_{post}(t)\right|dt \qquad [7.1]$$

where t_{liq} is the timing of liquefaction initiation and t_{end} is the last zero-crossing of shear strain. The prime goal of this analysis is to identify the optimum IM that can correlate with seismic induced damage. The analysis considered the same four IMs, CAV_5, I_a, NED and PGA_m. Additional IMs are sought by examining the threshold acceleration of CAV and I_a. Figure 7.4 illustrates the evolution of different IM_{post} (calculated from CSS measured shear stress time histories) with the corresponding $\Sigma|\gamma_{post}(t)|$. Like Chapter 6, the optimum IM_{post} is experimentally identified by the smallest difference between and/or most effectively correlate with the earthquake loading (IM_{post}) and damage ($\sum\left|\gamma_{post}(t)\right|$).

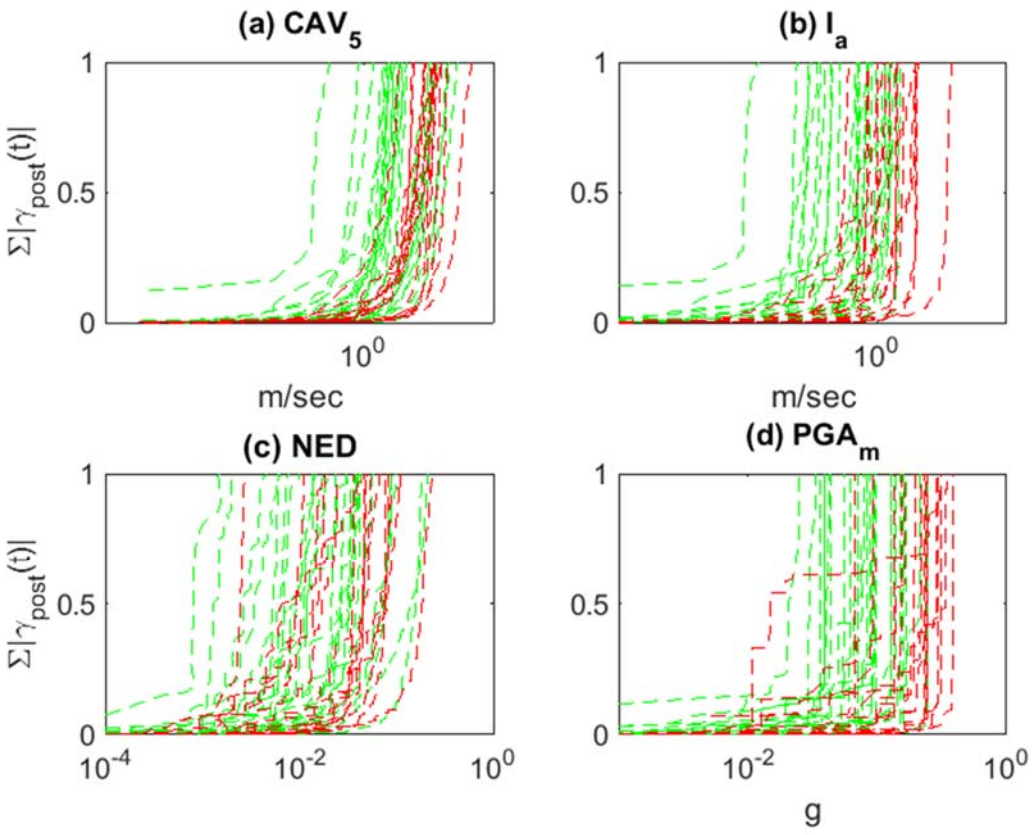

Figure 7.4: Evolutionary IMs vs. post-liquefaction normalized shear strain. 43 Cyclic Simple Shear tests under different transient loadings are included (green dot line = loose tests; Red dot line = dense tests).

7.4 IDENTIFYING OPTIMUM EVOLUTIONARY POST-LIQUEFACTION IM

Figures 7.5 to 7.8 illustrate the development of each IM_{post} function and compare it with the N. $\Sigma|\gamma_{post}(t)|$ values from the 43 CSS tests. Both the x- and y- axes are normalized, in the way that coordinate (0, 0) represents liquefaction initiation and coordinate (1, 1) represents the end of post-liquefaction loading. One of the main goals of this analysis is to investigate how well the IM_{post} candidates compare to the CSS data. Hence, the perfect IM_{post} function should evolve identically and/or perfectly correlate with the shear strain

development, which show minimal deviation in Figures 7.7 and 7.8 between the N. IM_{post} and N.$\Sigma|\gamma_{post}(t)|$. For Figures 7.5 and 7.6, the average error between the normalized IM values and $\Sigma|\gamma_{post}(t)|$ values plotted at given time increments (the error bars present one standard deviation). By inspection, $CAV_5(t)$, $I_a(t)$, NED(t) and $PGA_m(t)$ are all over predicting the shear strain developments. While $CAV_5(t)$ provides the best matches, PGA_m is overwhelmingly overestimating the corresponding shear strain.

Based on the CSS data, alternative optimum IM_{post} were searched by refining the threshold accelerations of CAV and I_a. The calculation detail can be found in Chapter 6. Figures 7.9 and 7.10 show the results. For both cases, the smallest differences are found when no threshold acceleration is applied, which implies that the pulses with very small amplitudes cannot be neglected because liquefied soil is so weak. Therefore, CAV could be a better IM_{post} than CAV_5 for the characterization of post-liquefaction loading. Table 7.2 summarizes the overall differences between the normalized IM_{post} and $\Sigma|\gamma_{post}(t)|$ of 43 CSS tests under transient loading. In general, CAV is slightly better than CAV_5, with the smallest difference, and provide satisfied efficiency. PGA_m provides the worst matchings of shear strain developments. Even though PGA_m gives the smallest overall CoV value, but the CoV values of PGA_m could be bias in this analysis because of the normalizations. As indicated in Figures 7.7 and 7.8, the N.PGA_m values averagely almost reach 1.0 after $\Sigma|\gamma_{post}(t)|$ is greater than 0.5. This finding implies that using PGA_m to predict the effects of soil liquefaction can be misleading. Therefore, it is not recommended to use PGA_m to characterize earthquake loading after liquefaction initiation. In order to predict liquefaction effects, a new parameter is needed.

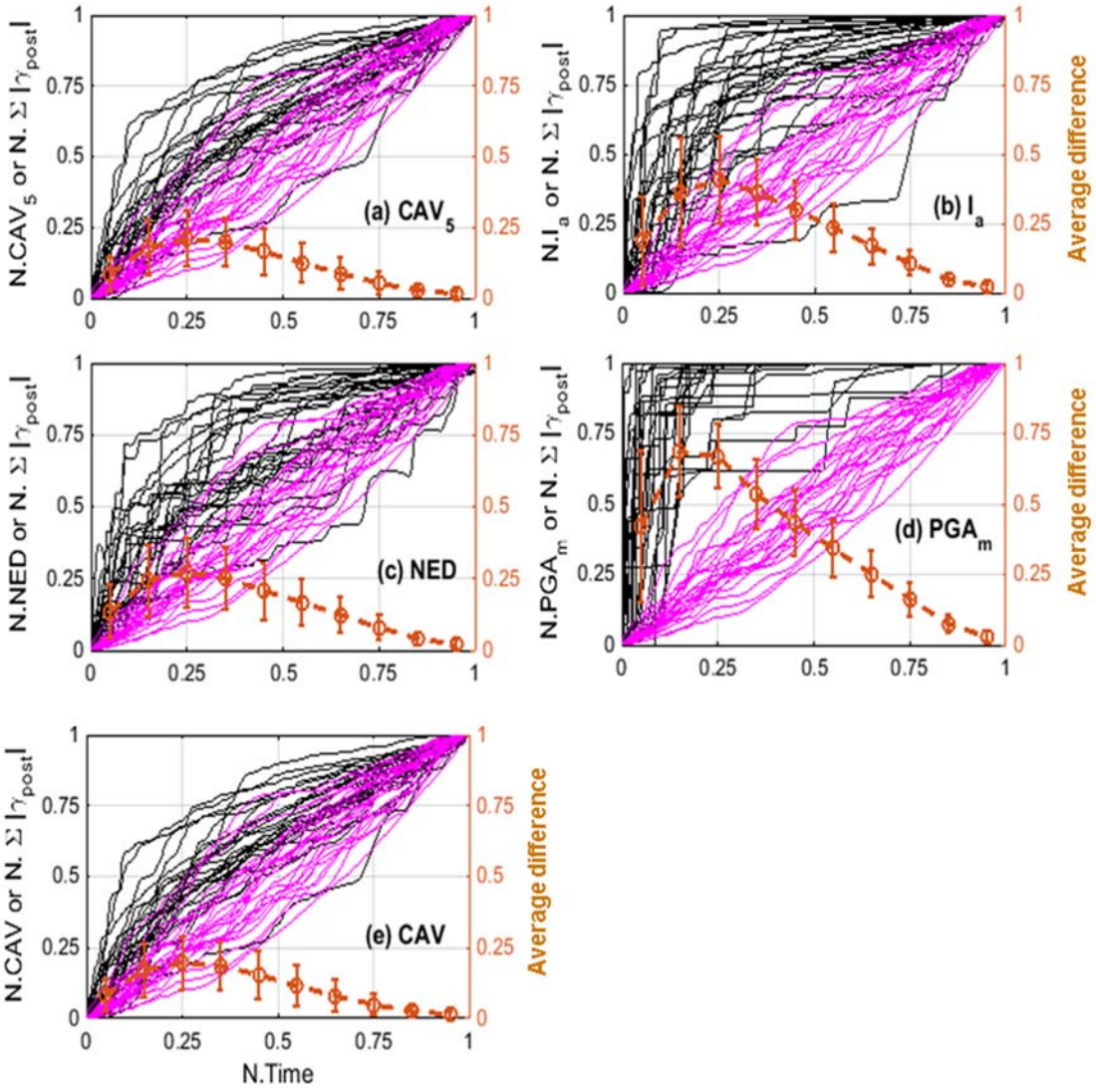

Figure 7.5: Comparison between the calculated post-liquefaction IMs and measured shear strain from 27 loose CSS tests (Pink = measured shear strain; black = calculated IM_{post}).

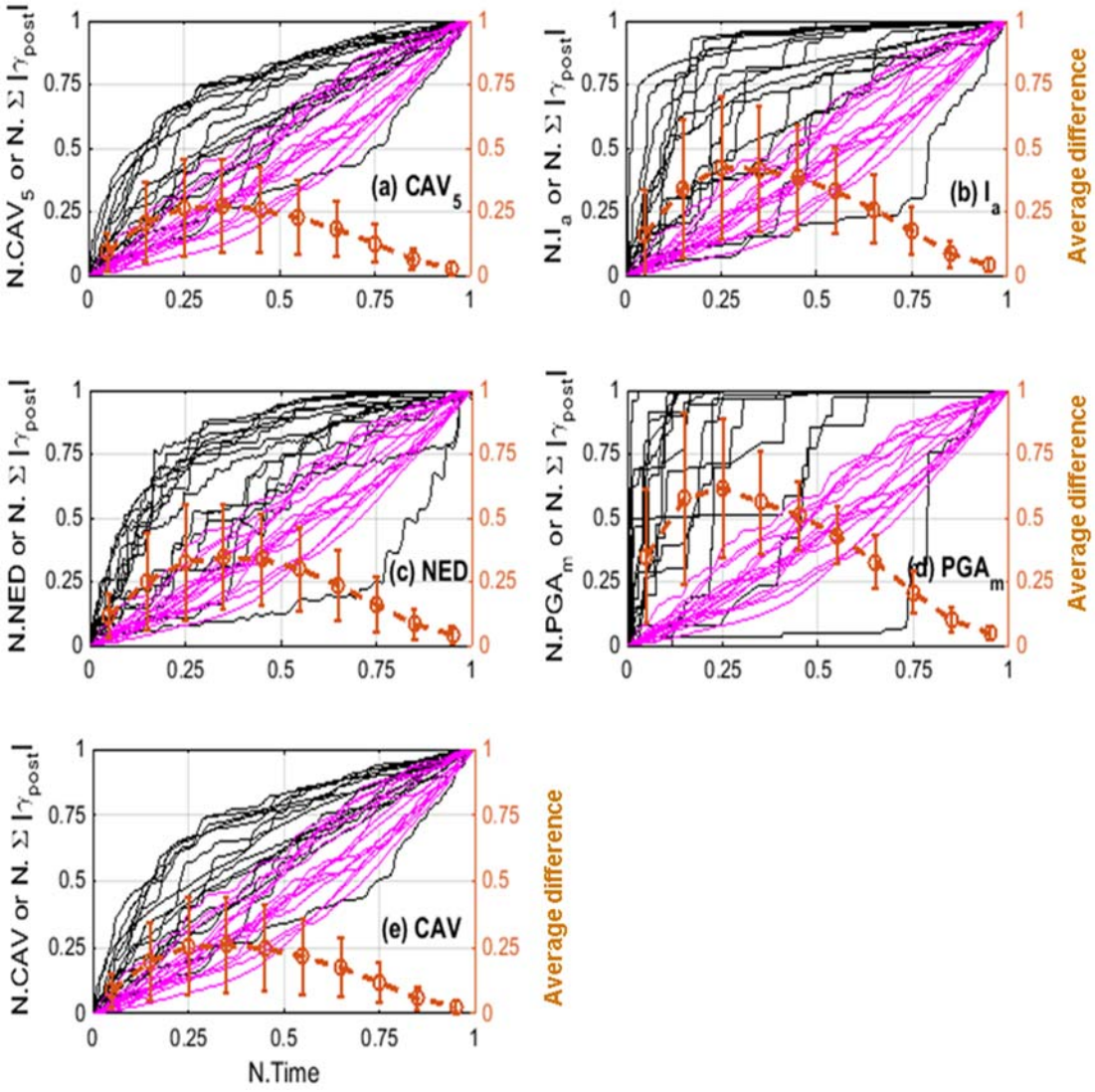

Figure 7.6: Comparison between the calculated post-liquefaction IMs and measured shear strain from 16 dense CSS tests (Pink = measured shear strain; black = calculated IM_{post}).

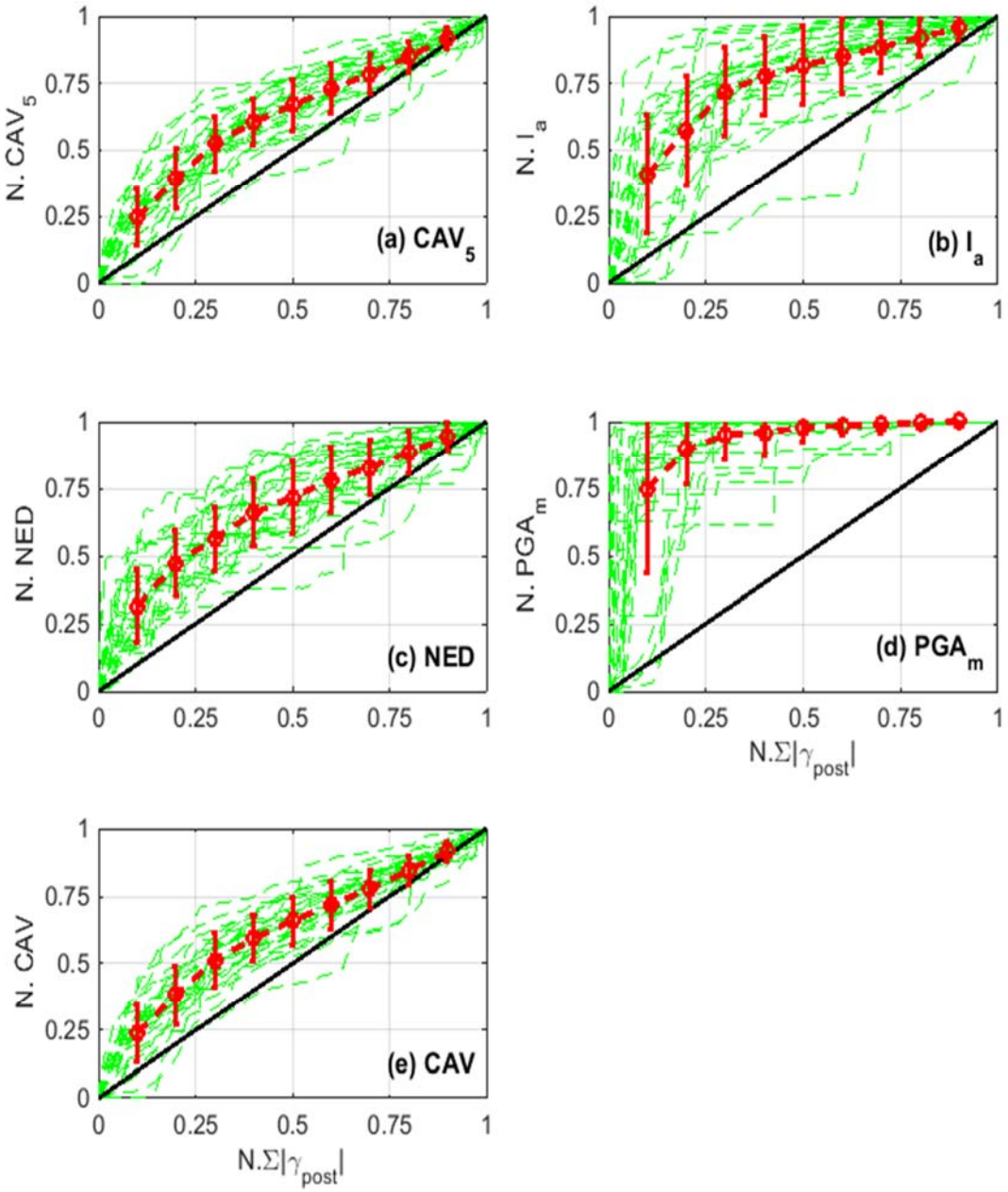

Figure 7.7: Normalized IMs vs. Normalized Post-liquefaction Shear Strain. 27 loose CSS tests included.

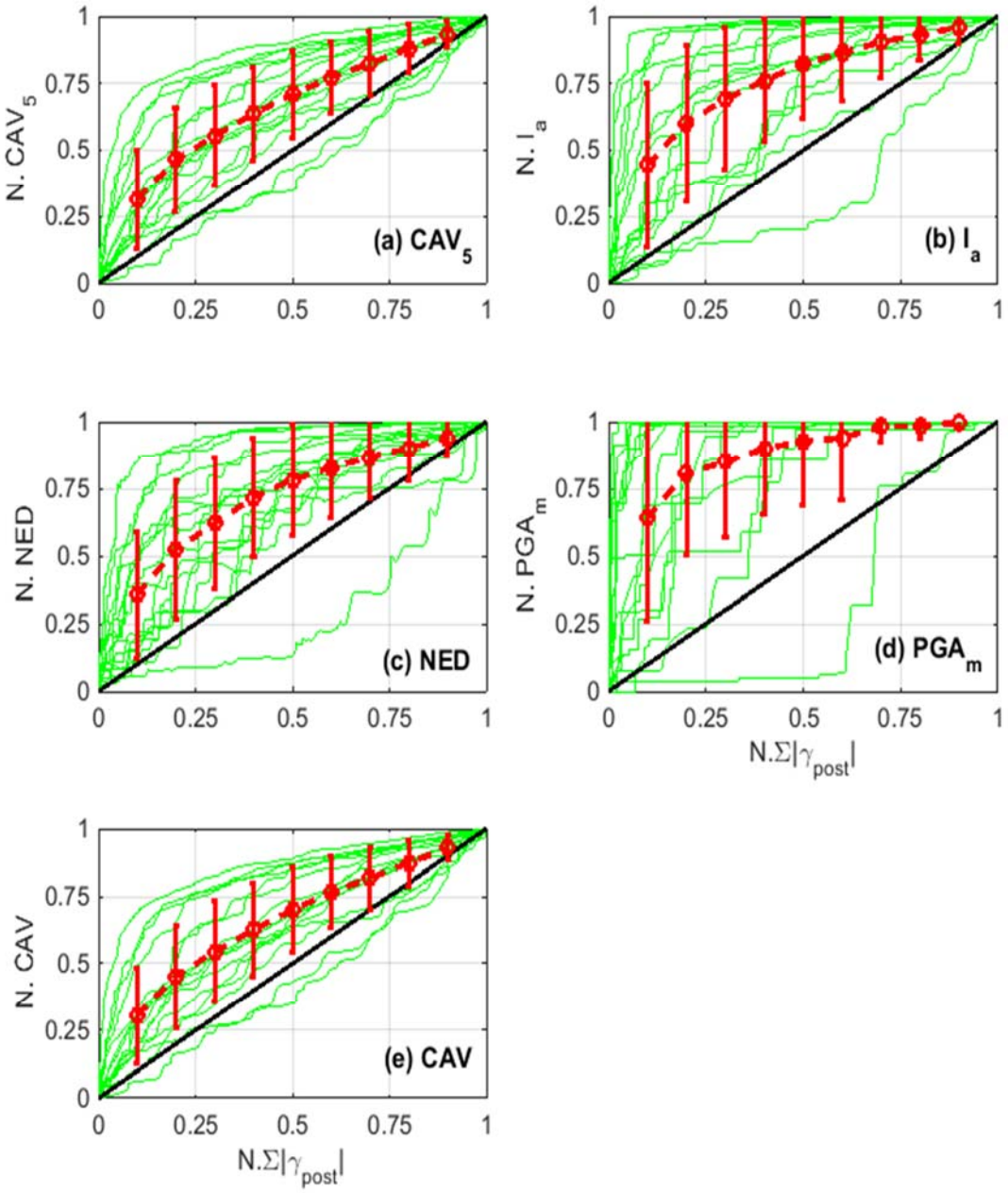

Figure 7.8: Normalized IMs vs. Normalized Post-liquefaction Shear Strain. 16 dense CSS tests included.

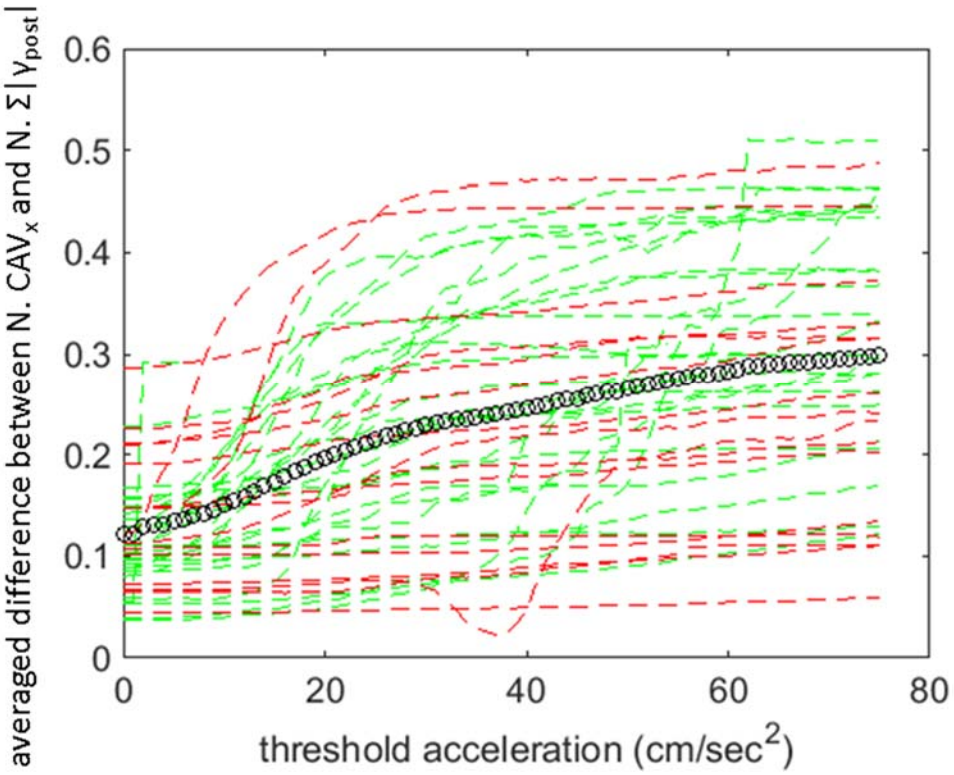

Figure 7.9: Results of searching for the threshold acceleration that gives minimum overall difference between the measured $N.\Sigma|\gamma_{post}(t)|$ values and calculated normalized CAV values. 43 CSS tests were considered in this analysis (dotted green line = loose test, dotted red line = dense test, open black circle = average of the 43 tests).

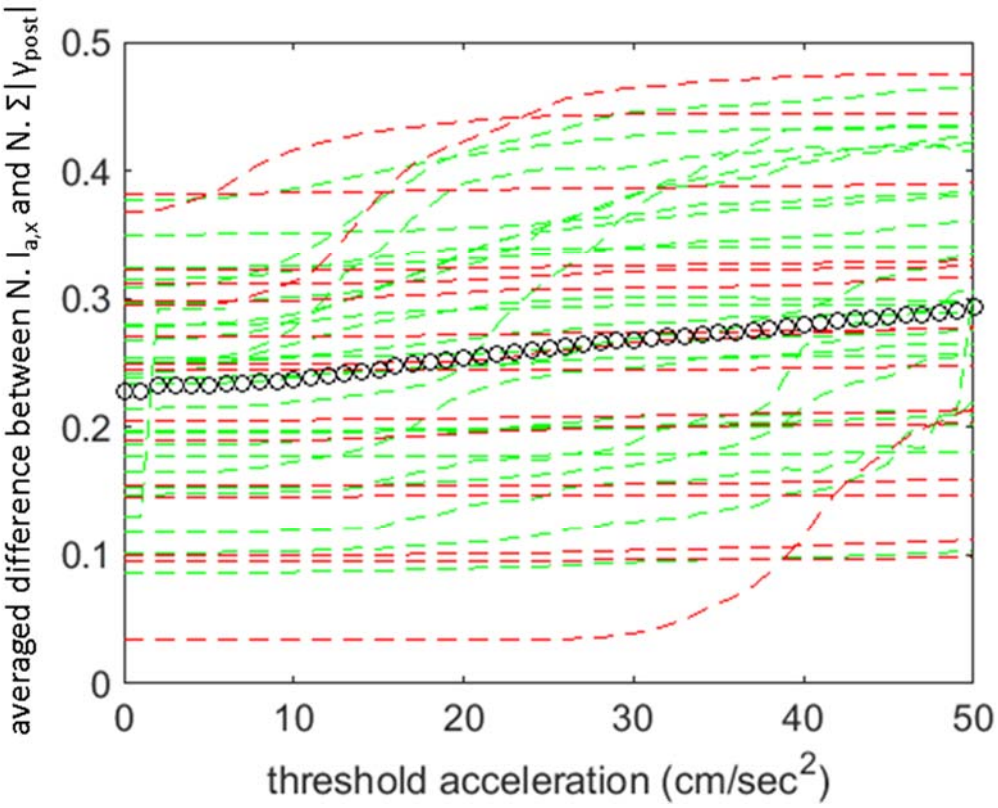

Figure 7.10: Results of searching for the threshold acceleration that gives minimum overall difference between the measured $N.\Sigma|\gamma_{post}(t)|$ values and calculated normalized I_a values. 43 CSS tests were considered in this analysis (dotted green line = loose test, dotted red line = dense test, open black circle = average of the 43 tests).

Table 7.2: The overall difference for the different normalized IM_{post} vs. $\Sigma|\gamma_{post}(t)|$.

IM_{post}	**Overall Difference (%)**	**Overall Average CoV**
CAV_5	14.78	0.22
I_a	25.45	0.25
NED	19.29	0.25
PGA_m	39.58	0.17
CAV	14.03	0.21

7.5 PREDICTABILITY OF LIQUEFACTION EFFECTS

Beside individually matching the development of shear strain for each CSS test, an ideal IM_{post} should also provide a good correlation between the end values (at the end of loading) of IM_{post} and $\Sigma|\gamma_{post}(t)|$. Such a correlation can then be used to predict earthquake induced lateral displacement. Figures 7.11 to 7.14 illustrate the correlations of each proposed IM_{post} (CAV_5, I_a, NED, PGA_m and CAV) at different soil relative density ranges (loose, dense and combined). Each point represents a CSS test and their cumulative values of IM_{post} and absolute cumulative shear strain from the beginning to the end of post-liquefaction loading. Overall, the correlations obtained from loose CSS test results (Figure 7.11) are better than those obtained from dense CSS test results (Figure 7.12). Liquefaction effects are more severe in loose sand than dense sand, so it is more important to build a framework of predicting lateral spreading in loose soil. Figure 7.11 shows that CAV is the best IM, providing a coefficient of determination of 0.84, whereas PGA_m yields the lowest coefficient of determination of 0.2.

A major advancement of this research project is that, for each of the CSS transient loading tests, the timing of liquefaction was experimentally identified. Therefore, the correlation between an IM and lateral spreading can be made based on post-liquefaction data. There is a need in considering the pre- and post-liquefaction motions separately so that analyses can account for the drastic changes in soil properties. This hypothesis can be proven with the CSS data. Figure 7.14 illustrates the correlations of loose CSS tests between the end values of cumulative IM and absolute shear strain that considers both the pre- and post-liquefaction motions. It is clear that the coefficients of determination drop significantly for all IMs, expect NED. It appears that there is no significant advantages of separating the motion for NED.

The performance-based earthquake engineering (PEBB) framework requires probabilistic characterization of earthquake loading, which can be significantly improved by adopting a more accurate predictor to reduce the epistemic uncertainties. Therefore, the factor of safety from evaluation can be increased at the same hazard level. While the post-liquefaction data has shown that PGA_m provides the worst correlation with lateral deformations, CAV gives the best correlations. The use of PGA works well in stress-based evaluation for liquefaction initiation; however, it should not be used for assessing the possible damage resulting from liquefaction.

It should also be noted that equivalent linear analysis was used to calculate the acceleration time histories from shear stress time histories; therefore, calculated ground surface accelerations from post-liquefaction data may not be as accurate as those from pre-liquefaction data. A fully nonlinear analysis that accounts for changes in shear modulus and damping ratios would provide better representations of acceleration time histories after liquefaction initiation at larger strain level. Such analyses can potentially improving the CAV and I_a's predictability of liquefaction effects. This is an area that requires further research efforts. Also, the CSS post-liquefaction database provides valuable data for searching new IMs that can give better predictability to liquefaction effects.

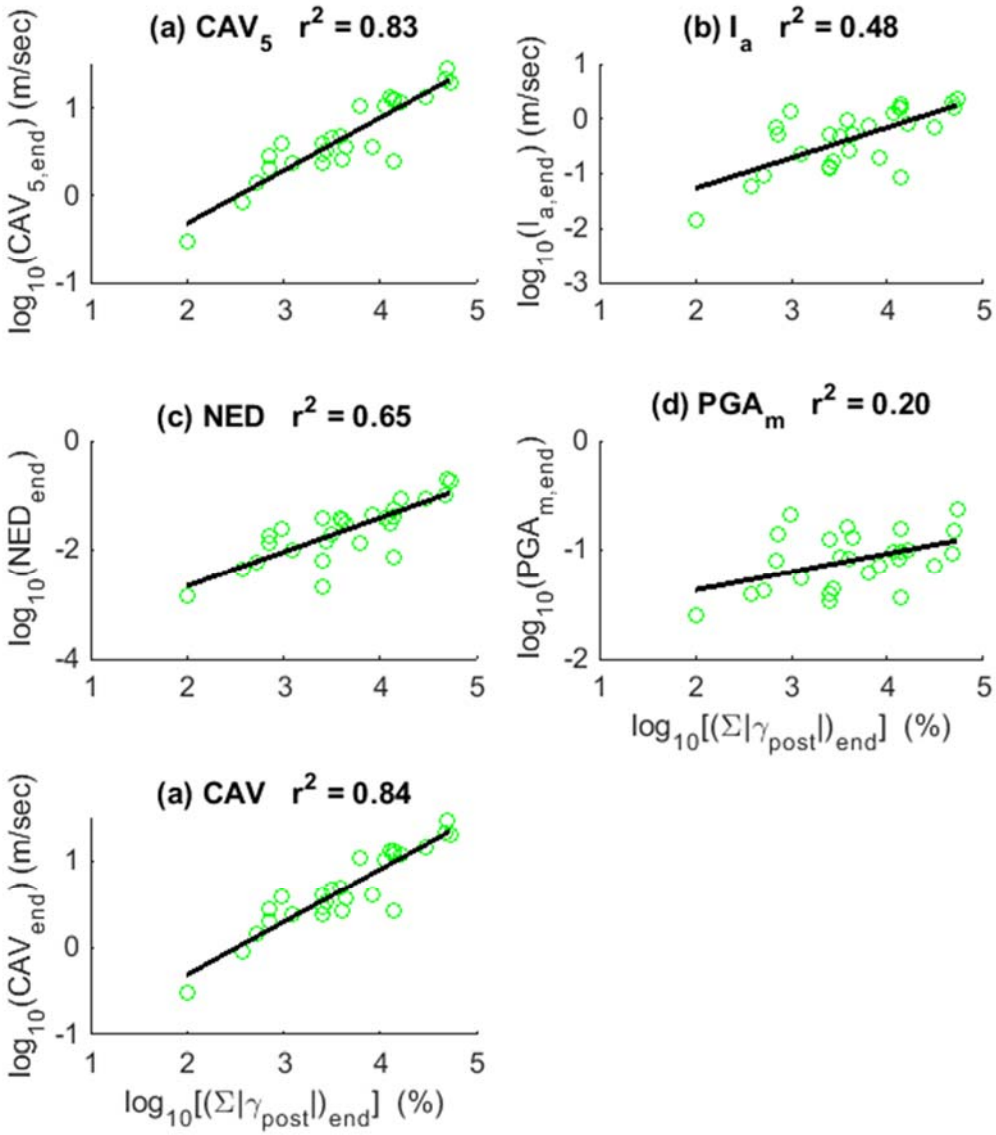

Figure 7.11: Correlation between the final IM_{post} values and the final cumulative absolute shear strain value. Only the post-liquefaction portion of data was considered. 27 loose CSS tests included.

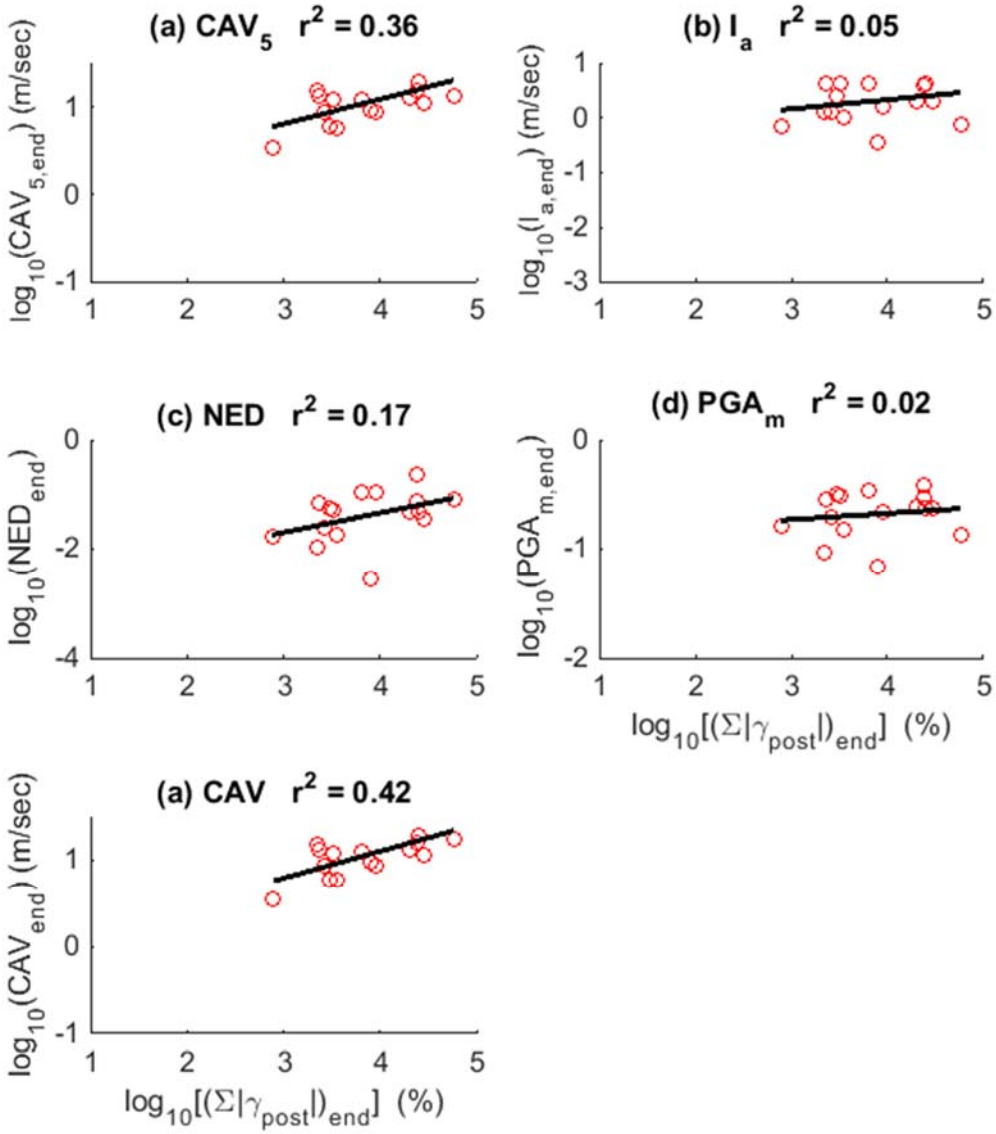

Figure 7.12: Correlation between the final IM_{post} values and the final cumulative absolute shear strain value. Only the post-liquefaction portion of data was considered. 16 dense CSS tests included.

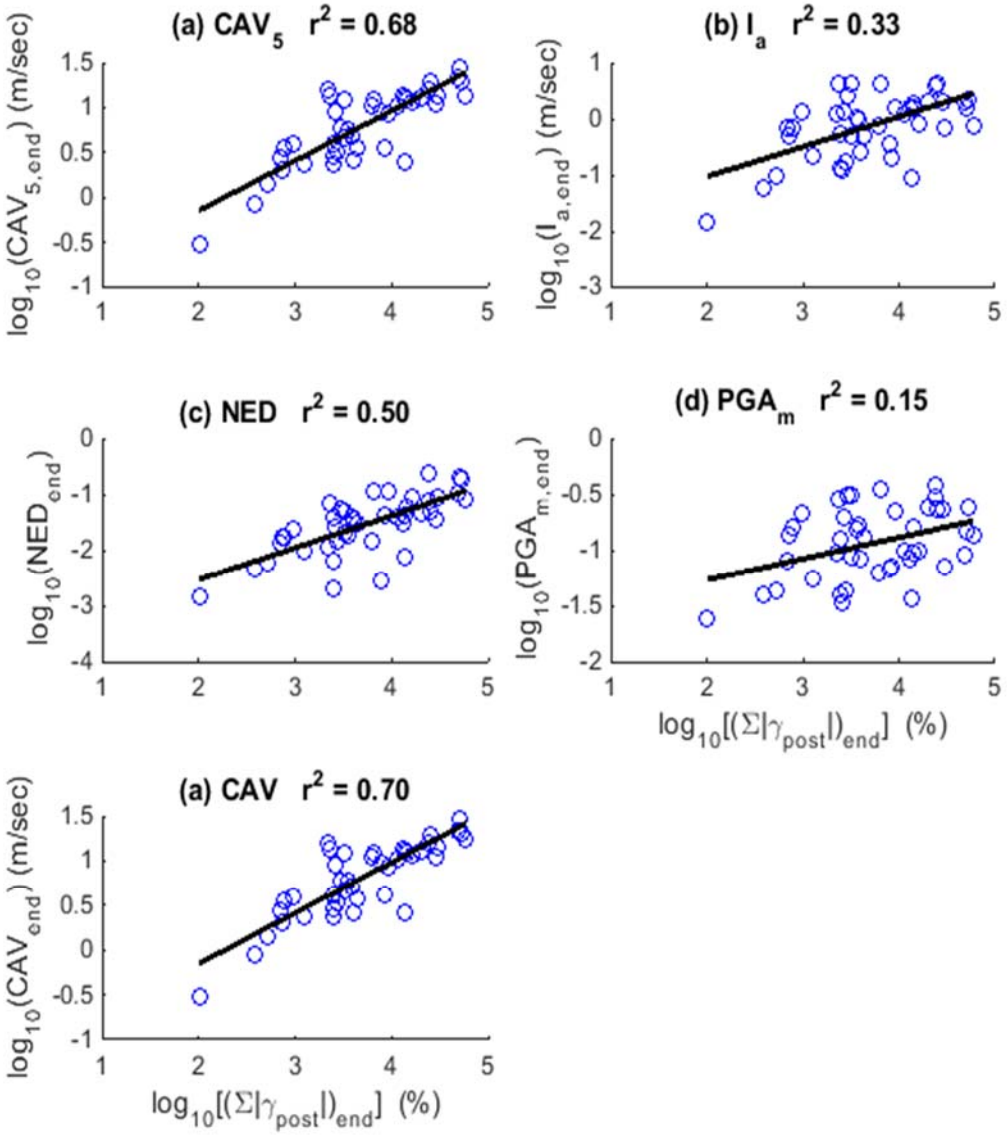

Figure 7.13: Correlation between the final IM_{post} values and the final cumulative absolute shear strain value. Only the post-liquefaction portion of data was considered. 43 loose and dense CSS tests included.

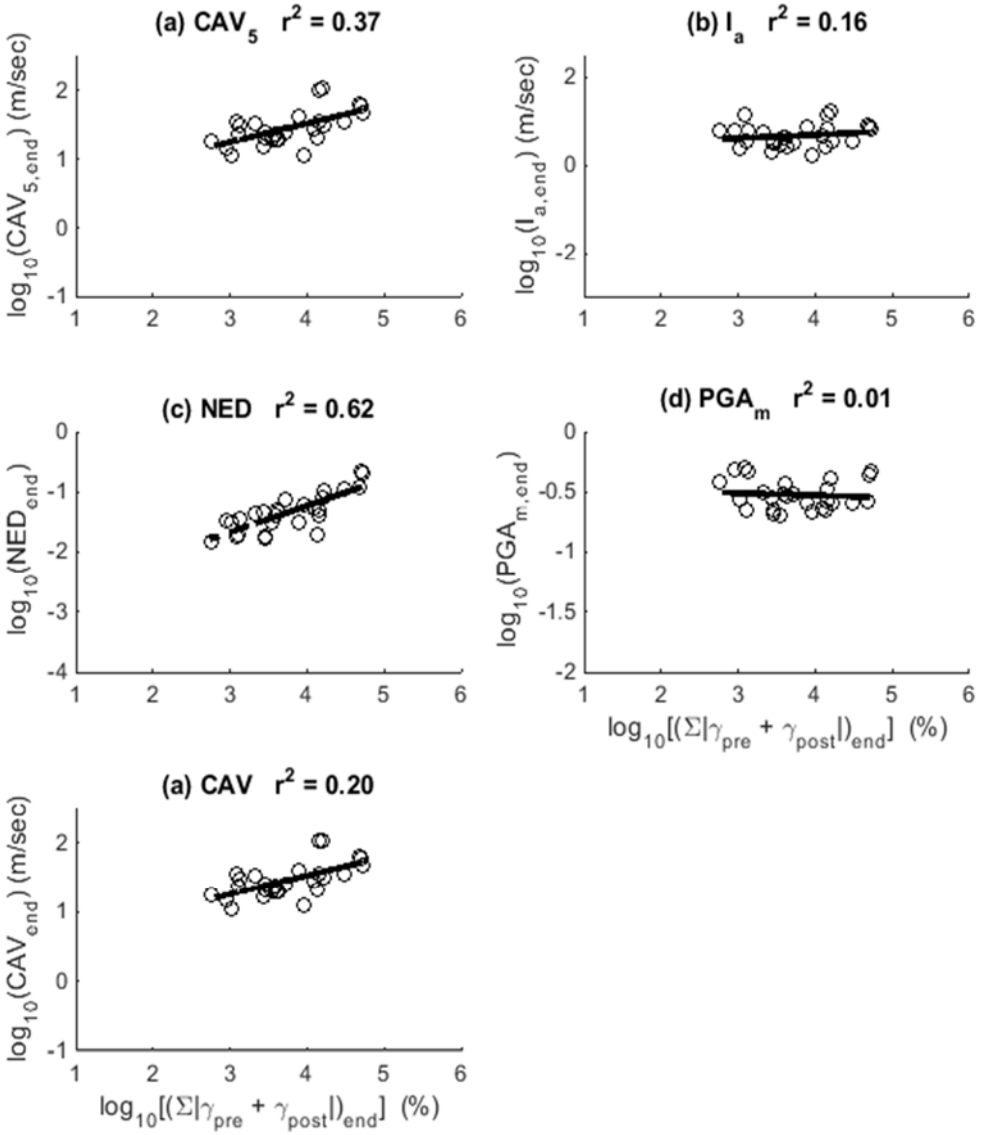

Figure 7.14: Correlation between the final IM values and the final cumulative absolute shear strain value. Both pre- and post-liquefaction data was considered. 27 loose CSS tests included.

7.6 CONCLUSION AND DISCUSSION

The testing results presented in this chapter provide many insights into the liquefied soil under monotonic and transient loadings. The data generated from this research project provides unprecedented and valuable information for the development of new methods for liquefaction evaluation and constitutive modeling. Twelve monotonic post-liquefaction tests were conducted, and a great variation of post-liquefaction responses were recorded. This chapter also evaluates the performance of five IMs (CAV5, I_a, NED, PGA_m and CAV) based on the comparison of 43 CSS tests under different transient loadings on both loose and dense sand. Like Chapter 6, the assessments were mainly based on how well the calculated IM values matched and/or correlate with the post-liquefaction shear strain development.

The findings are concluded as follows:

1. The stress-strain behavior of liquefied sand is depends on the corresponding pre-liquefaction loading history.
2. Threshold accelerations are not needed for CAV and I_a when assessing post liquefaction damage as all accelerations, even the small amplitude ones, will contribute to the final strains due to the low soil stiffness.
3. There is a need to identify the timing of liquefaction initiation to allow separating post-liquefaction loading from the entire course of loading. Experimental data has proven that the correlations between the IMs and measured shear strain are much better if only the post-liquefaction data is considered (i.e. reducing uncertainty in earthquake loading characterization).

4. CAV is identified as the best performer among the investigated post-liquefaction IM, which provides the best matches and satisfied correlations with the CSS post-liquefaction results.
5. CAV provides the best predictability on liquefaction induced lateral spreading in loose specimens.
6. It is the author's opinion that this IM should be avoided for the characterization of post-liquefaction earthquake loading.

Chapter 8: Summary, Conclusion and Future Research

8.1 SUMMARY

In laboratory modeling of soil liquefaction, previous testing has almost exclusively relied on using uniform harmonic motions to represent earthquake loadings. This research project is the first that systematically reveals the liquefiable soil responses under transient loadings in a simple shear set up and the obtained data indicate that the phenomenon of soil liquefaction is far more complex than previously explored. This study was carried in three stages: A) CSS apparatus optimization and validation, B) generate a CSS database that is virtually non-existent, and C) identify the optimum IMs for predicting liquefaction initiation and post-liquefaction strains. At each stage, the accomplishments can be summarized as follows:

A1. The performance of the UTCSS apparatus was optimized and the issues and limitation of the original GCTS setup were studied and addressed.

A2. The feasibility of using stacked rings to replace wire reinforced membrane was validated, albeit through a limited study.

A3. Two different specimen reconstitution methods are established, one for loose and one for dense. The final specimen preparation methods were found to prepare consistent uniform specimens.

B1. A preliminary database is established, encompassing CSS results of irregular sinusoid loadings and post-liquefaction monotonic loading.

B2. A high quality database is established, including CSS results from traditional harmonic motions and the new modulated sinusoid loadings.

B3. A high quality CSS database of transient loading is generated, including 47 loose and 32 dense tests.

C1. For pre-liquefaction, CAV_{75} and I_a are experimentally identified as the optimum evolutionary IMs to predict excess pore pressure generation.

C2. For pre-liquefaction, CAV_5 and I_a are experimentally identified as the best performer among the investigated IMs to predict sustained shear strains.

C3. For post-liquefaction, analyzes have shown that the CAV values provides the best correlation with induced deformations.

8.2 CONCLUSION

Cyclic simple shear (CSS) has long been used to physically model a soil element under seismic loadings because of its superior capability of reproducing the seismic loading conditions. Nevertheless, the CSS test is not easy to run, and the main difficulty comes from the requirement of high apparatus rigidity. This study provides a method to improve the rigidity of an existing CSS apparatus at the University of Texas and a design of a new CSS set up. After apparatus optimization, the generated CSS data is considered to be high quality. Reconstituting soil specimens with uniform density is also equally important. This study documents two procedures of producing high quality sand specimen, one loose and one dense.

Using a simplified harmonic loading to represent transient loading is too crude. Experimental data from this project has shown that the rate of excess pore pressure generation is not constant when a soil specimen is subjected to irregular sinusoid or transient loadings. Similarly, the induced shear strains are no longer in a symmetric pattern with exponential increase in magnitude as r_u approaches unity and exceeds it, but rather

vary in an irregular format that strongly depends on imposed shear stress histories. In fact, there is a general observation that the soil responses are dictated by a few dominated pulses that can be located at any part of a ground motion. From those irregular and modulated sinusoid loadings, the test results indicate that the order of stress cycle matters, even though the amplitudes of loading cycles are identical. More severe damages (higher r_u and shear strain) are found when the dominated loading pulse is located at the earlier part of motion rather than later. Likewise, a taper up motion produces more damage than an equal-amplitude taper down loading. However, since those irregular and modulated sinusoid histories contain identical maximum amplitude, the loading is characterized equally, according to the current stress-based liquefaction evaluation procedure.

The experimental data generated in this project has clearly shown that it is an over simplification to represent an earthquake loading by the current stress based procedure with PGA and MSF only. The method works well in the worst-case-scenario-type-of analysis, but would create great uncertainty in the framework of PBEE. The increased popularity of using PBEE for liquefaction evaluation has driven the use of intensity measures (IMs) to characterize earthquake loadings. In addition to PGA_m, this study particularly investigates IMs of CAV_5, I_a, and NED, which have been numerically proven to be relatively efficient based on previous numerical studies. Those IMs are obtained by integrating the entire ground motion (acceleration or energy over time) into one parameter, and therefore, they show how the seismic loading builds up with time, and potentially reveal the timing of liquefaction initiation. The performances of each IM are assessed by how well the normalized IM values match and/or correlate with excess pore pressure generation and shear strain development. Moreover, CAV and I_a are refined by examining the optimum threshold acceleration that allows the best matching with developments of r_u or $N.\Sigma|\gamma(t)|$.

Table 8.1 summarizes the optimum threshold accelerations found based on the two criteria (r_u or $N.\Sigma|\gamma(t)|$):

Table 8.1: Summary of the optimum threshold accelerations for CAV and I_a.

optimum threshold acceleration	CAV	I_a
	(cm/sec^2)	
r_u	75	50
$N.\Sigma\|\gamma(t)\|$	177	180

In fact, modifying the threshold acceleration has a larger impact on CAV than I_a. There are almost no improvements on matching the CSS data by adding a threshold acceleration for I_a. It is noted that good matches between the IMs and engineering demand parameter(s) doesn't mean effective correlations. Overall, the best and worst performers based on matching and/or correlating the CSS data (up to liquefaction initiation) are summarized in Table 8.2. The assessments are based on both how well the IMs match and/or correlate with the r_u and $N.\Sigma|\gamma(t)|$.

This research project proves that knowing (or being able to predict) the time of liquefaction initiation is very important for advancing the liquefaction evaluation procedure, because separating the pre and post-triggering loading, or intensity measure from an entire ground motion can potentially give a much better prediction on the expected damage (lateral spreading) due to soil liquefaction. The CSS data shows that the correlation of coefficients is significantly improved when only the post-triggering part of data is analyzed separately when estimating final shear strains. Since the soil properties change drastically after liquefaction initiation, it is necessary to have two separated IMs to address the design for earthquake loading: before and after liquefaction initiation. The CSS data

obtained in this project allows to experimentally identifying the time of liquefaction initiation (r_u =1.0); therefore, post-triggering data can be separated. An analysis of finding optimum post-liquefaction IM is performed based on post-liquefaction portion of the data. An optimum post-liquefaction IM is identified as best matching of cumulative shear strain development. Table 8.2 summarizes the best and worst IMs based on different criteria and stages. The evaluation of IM_{post} mainly based on how the IM_{post}'s predictability on liquefaction effect (cumulative shear strain).

Table 8.2: Summary of performance of investigated IMs

	Criteria	Intensity Measures	
		Best	Worst
Pre-triggering	r_u	I_a / $I_{a,50}$ and CAV_{75}	NED and PGA_m
	$N.\Sigma\|\gamma(t)\|$	CAV_5 and I_a	PGA_m
Post-triggering	$N.\Sigma\|\gamma(t)\|$	CAV	PGA_m

8.3 FUTURE RESEARCH

The main motivation of this research project is to develop a more accurate and informative liquefaction hazard evaluation procedure. While this dissertation has shown the importance of identifying the timing of liquefaction initiation, and the optimal intensity measures, the following research topics require future attention in order to develop a more sophisticated liquefaction hazard evaluation framework. The advanced procedure should be compatible with the PBEE frameworks, and hence be able to probabilistically predict the effects of soil liquefaction. The following topics for future research arise from this dissertation and require further attention:

8.3.1 New Intensity Measure(s)

This research project examined four basic IMs (CAV_5, I_a, NED and PGA_m), and further investigated CAV and I_a by alternating the threshold accelerations. In fact, CAV and I_a can be modified by changing its power, and could potentially become more efficient when compared against the experimental data. In fact, with more experimental and field data available in the future, new forms of IM, both before and after liquefaction initiation, could be developed based on statistical analyses. The new IM should be able to provide a reasonable threshold value that corresponds to liquefaction initiation for a given soil type and relative density (or critical state parameter). This step is crucial, because the time when the IM reaches this threshold value represents the time of liquefaction initiation.

8.3.2 New CSS Apparatus

Chapter four documents a new CSS apparatus design at the University of Texas, which features a pair of shear walls that can significantly improve the apparatus' overall rigidity. The importance of rocking has been well documented for generating high quality data, and should be well addressed in the new design. Higher rigidity is needed for conducting monotonic tests, especially those which need to get into high strain ranges and the specimen is in a dilation phase. Moreover, previous studies have shown that bi-directional apparatus provides more accurate simulations of seismic events. Nevertheless, those bi-directional testing programs are limited to application of harmonic loadings. The most ideal simulation is to apply two recorded actual time histories simultaneously in perpendicular directions. Furthermore, bi-directional loading allows simulation of sloped ground conditions.

8.3.3 Effects of Pre-liquefaction Loading on Post-liquefaction Responses

The stress strain behavior of liquefied sand is a topic that has not yet been comprehensively explored, although extensive research projects have invested in studying or improving the soil resistance to liquefaction. In fact, it is also important to gain insight into the liquefied soil responses for liquefaction damage assessment. In practice, the seismic loading induced deformation is correlated with field testing indexes (SPT or CPT), which is typically very uncertain and conservative. Laboratory studies, based on pre-liquefaction harmonic loadings, have shown that there is a flat, low-stiffness, portion of stress-strain phase following with a dilation phase. The critical low-stiffness phase depends on many factors: soil density, pre-liquefaction harmonic amplitude, particle angularity, etc. Nevertheless, there is no investigation into how the irregular pre-liquefaction loading would affect the post-liquefaction responses. The phase transformation from low-stiffness to dilation is due to particle rearrangement, which is strongly influenced by pre-liquefaction history. In this research project, the pre-liquefaction loadings are characterized as IM_{pre}, and the post-liquefaction consequences are quantified as $\Sigma|\gamma_{post}|$. Future research should look into the possible correlation between IM_{pre} and $\Sigma|\gamma_{post}|$. Moreover, a better understanding in the liquefied soil stress-strain relationship allows calibration of existing constitutive models, which performs relatively poor at larger strain after the soils are fully softened.

8.3.4 Nonlinear Site Response Analysis

Equivalent linear analysis is used to obtain acceleration time histories from experimental recorded shear stress time histories. The method works well at small strain when the soil behavior linearly, but relatively poor at larger strain when there are a significant amount of phase transformation and softening responses. Therefore, nonlinear

site response models may provide more accurate simulations of acceleration time histories after liquefaction initiation. The improved time histories may yield better (or worse) predictions of later deformation from calculated IMs (e.g. CAV_5 or I_a).

8.3.5 Examination of Strain-based Liquefaction Triggering Criteria

Single or double peak strain amplitudes are used to define liquefaction triggering. For example, Wu et al. (2002) defines that liquefaction is triggered once the double amplitude of shear strain has reached a threshold of six percent. However, there is no consensus on a particular value corresponding to liquefaction initiation. In fact, using cumulative plastic strain, instead of peak amplitude, could be a better representation of seismic loading induced damages. Using peak amplitude to describe liquefaction triggering works fine for harmonic loading, but not transient. With more experimental and field data (under transient loading) available in the future, there is a need of inquiring into a better strain approach of liquefaction triggering criteria.

Appendix A CSS Data

A.1. PRELIMINARY CSS DATA: IRREGULAR SINUSOID LOADING

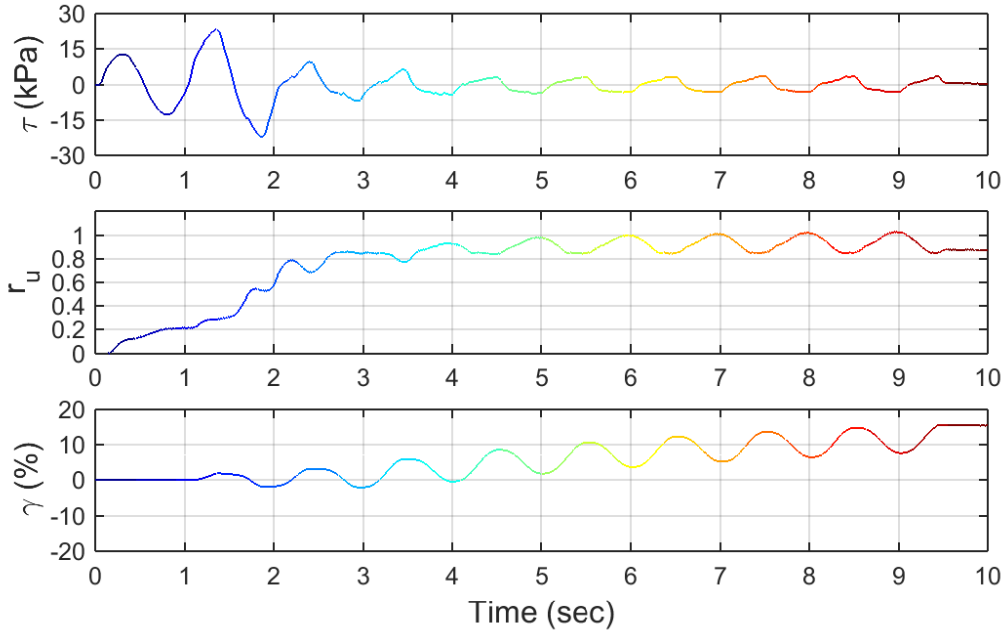

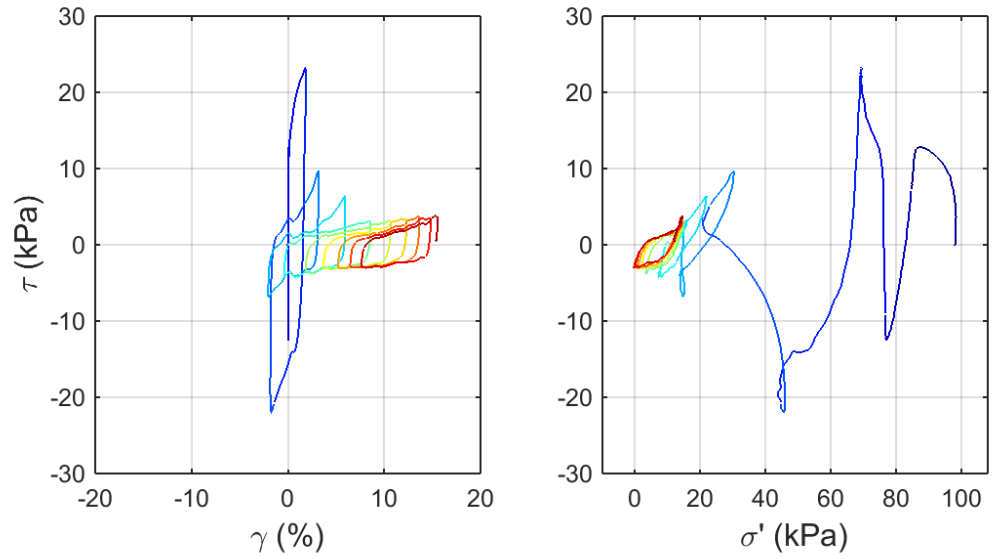

Test ID: 2012042302
Nevada Sand
D_r = 64%
Motion: Irregular sine peaking at the 2nd cycle
CSR = 0.25 (determined from the largest loading cycle)

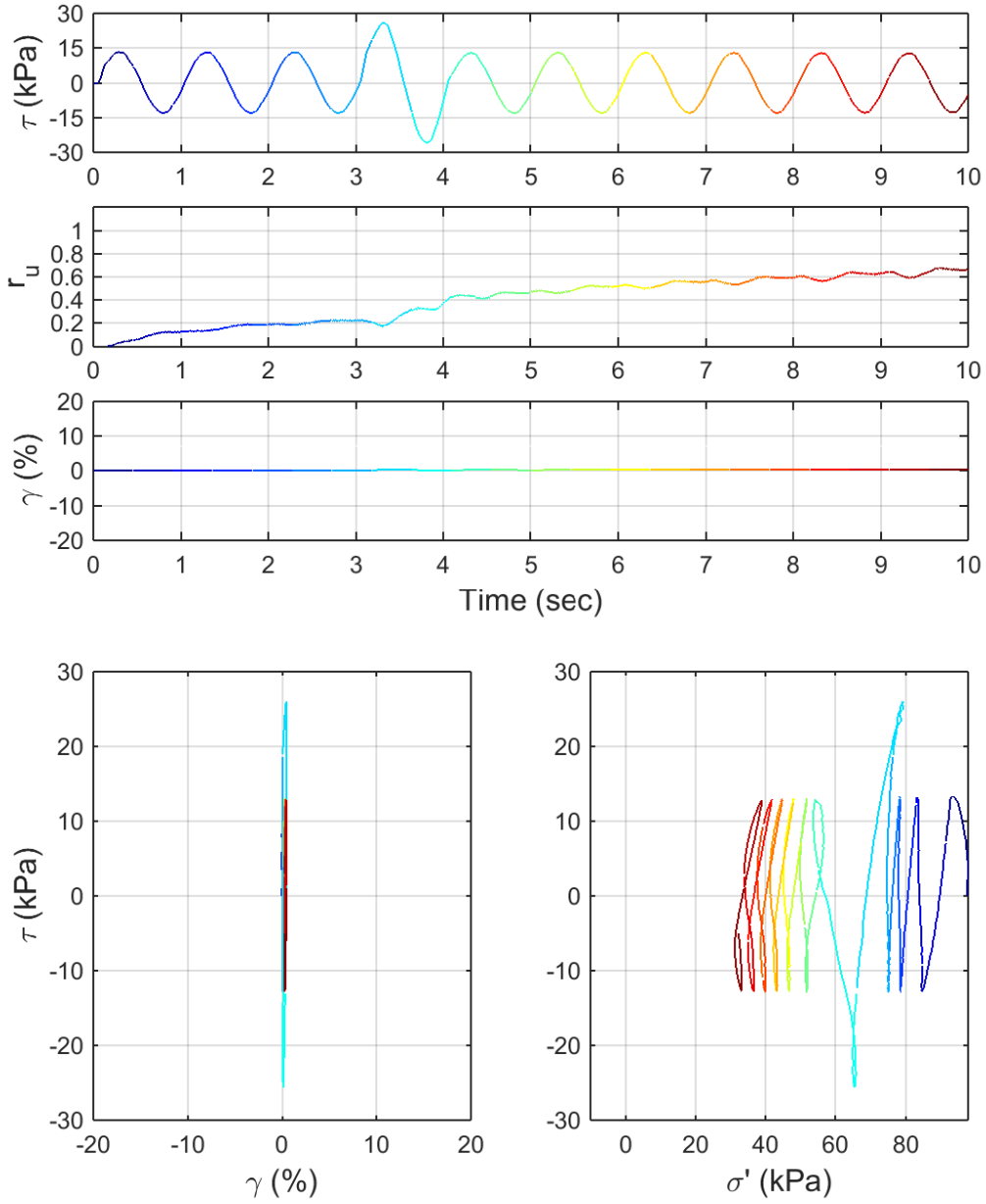

Test ID: 20120429
Nevada Sand
D_r = 71%
Motion: Irregular sine peaking at the 4th cycle
CSR = 0.25 (determined from the largest loading cycle)

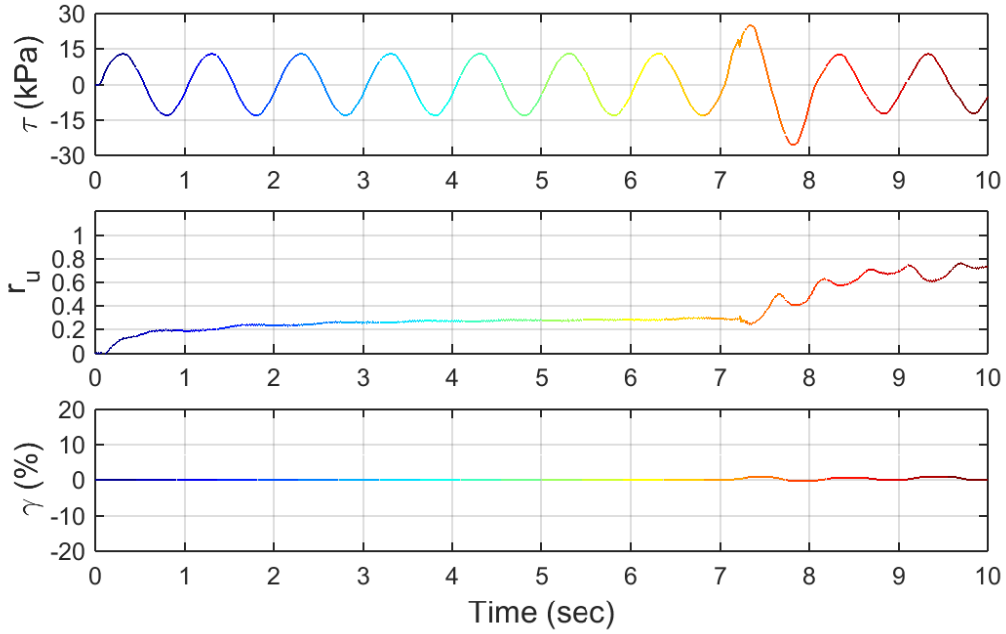

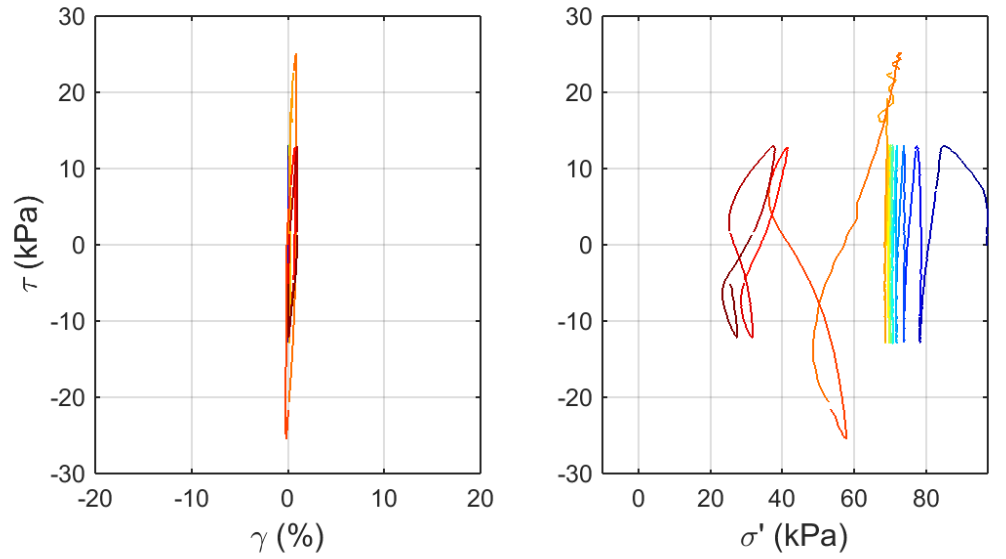

Test ID: 20120430
Nevada Sand
D_r = 72%
Motion: Irregular sine peaking at the 8th cycle
CSR = 0.25 (determined from the largest loading cycle)

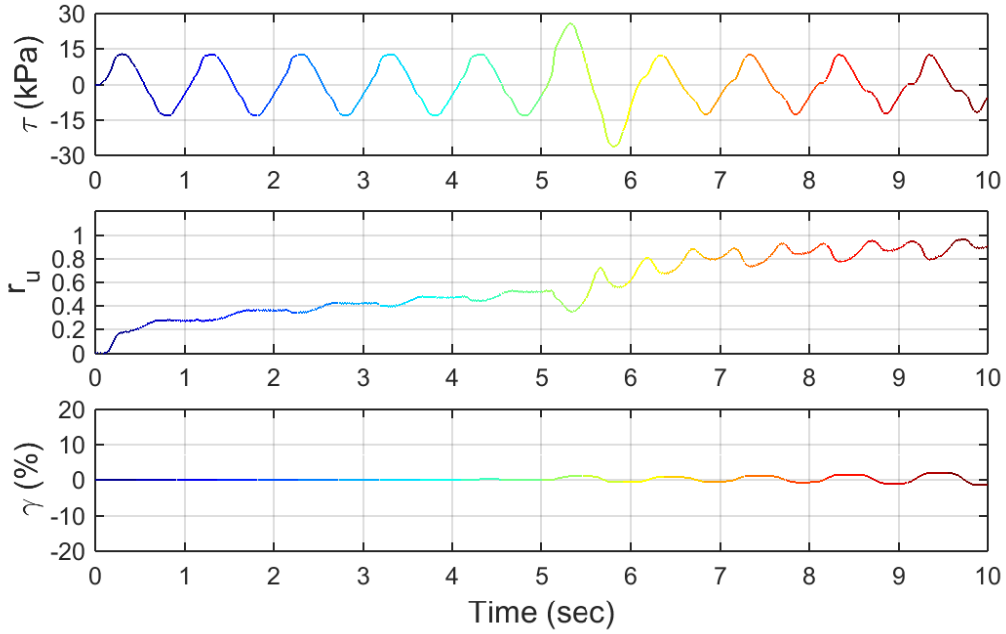

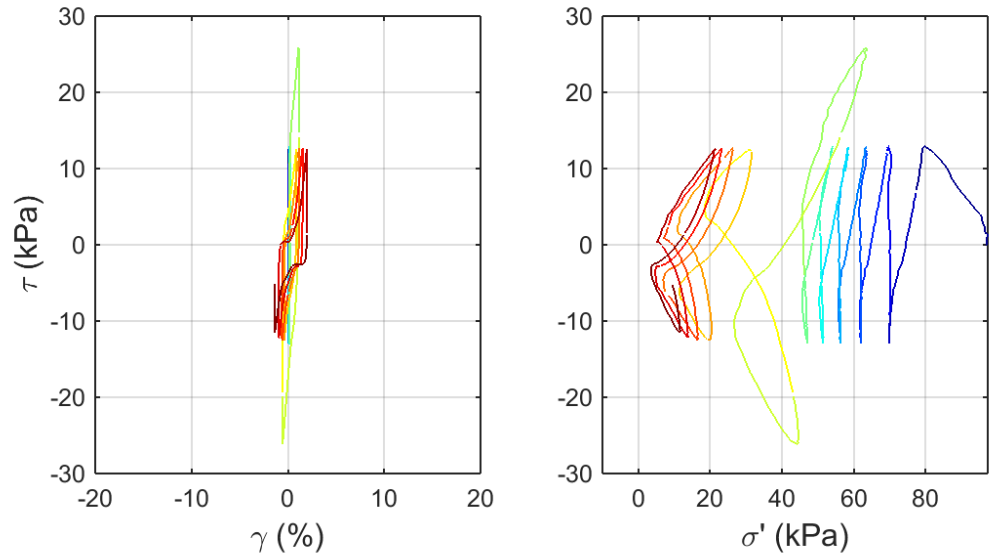

Test ID: 20120501
Nevada Sand
D_r = 66%
Motion: Irregular sine peaking at the 6th cycle
CSR = 0.25 (determined from the largest loading cycle)

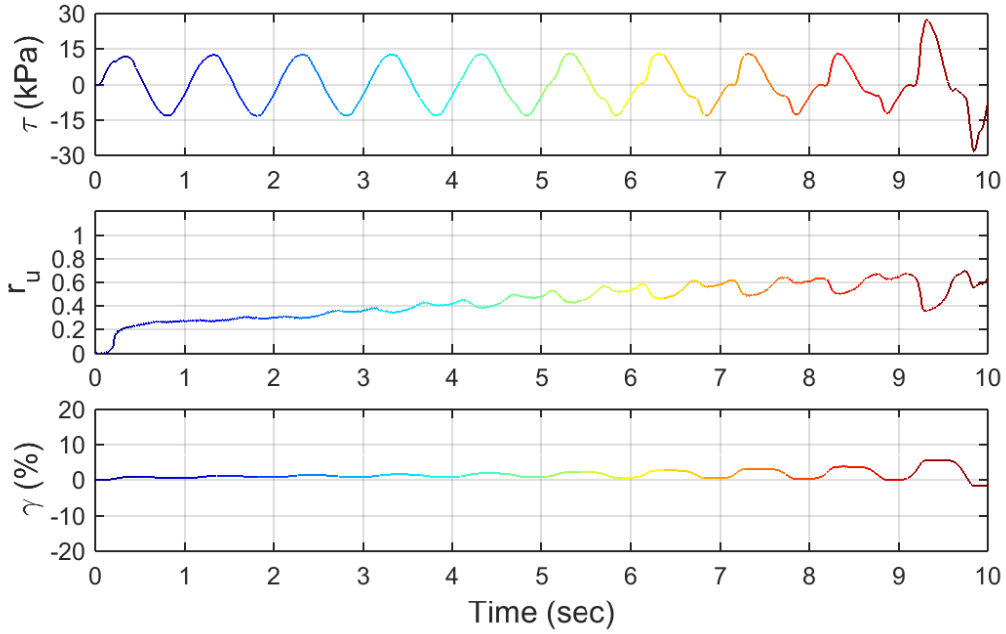

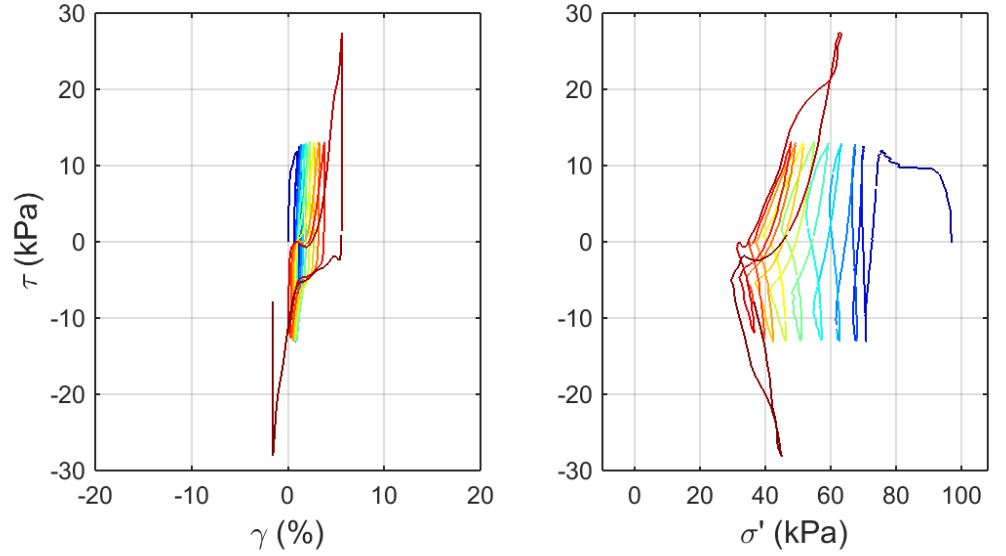

Test ID: 20120509
Nevada Sand
D_r = 71%
Motion: Irregular sine peaking at the 10th cycle
CSR = 0.25 (determined from the largest loading cycle)

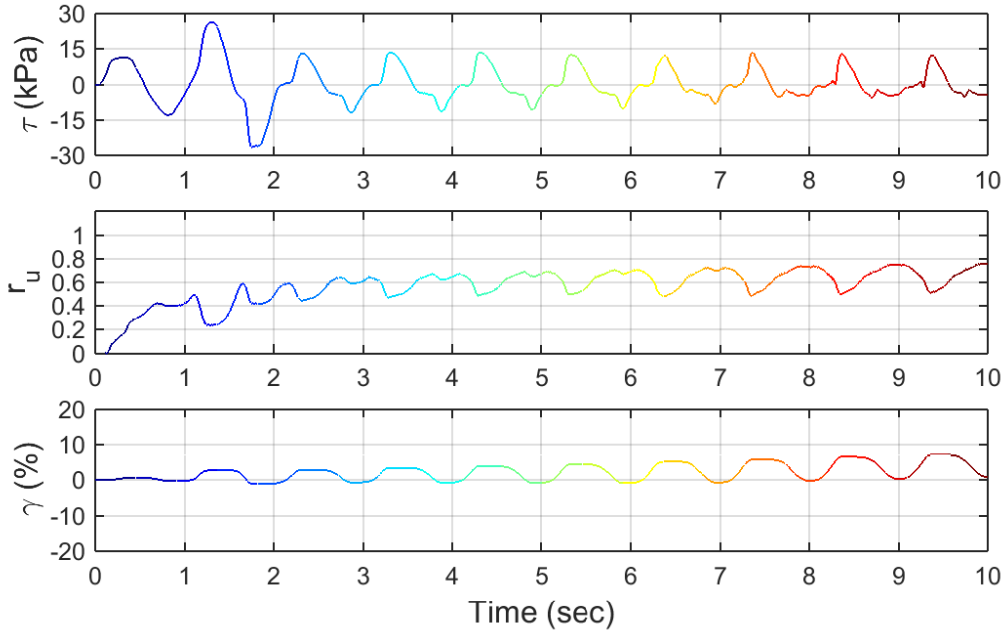

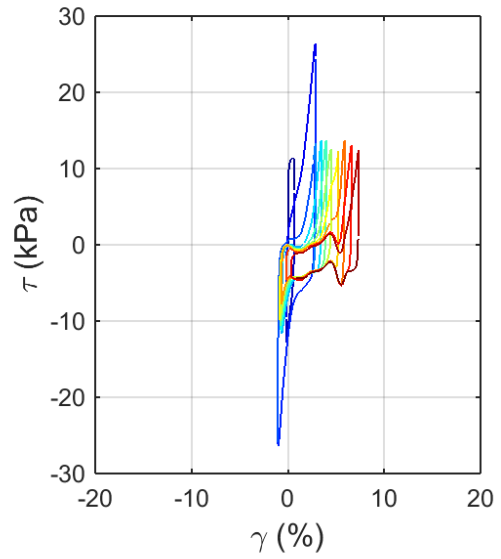

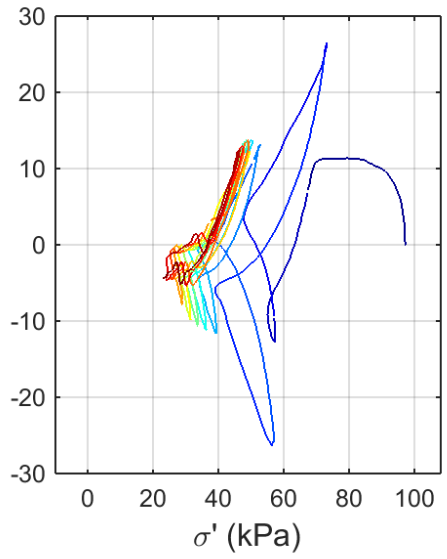

Test ID: 20120509_02
Nevada Sand
D_r = 78%
Motion: Irregular sine peaking at the 2nd cycle (2nd round of loading)
CSR = 0.25 (determined from the largest loading cycle)

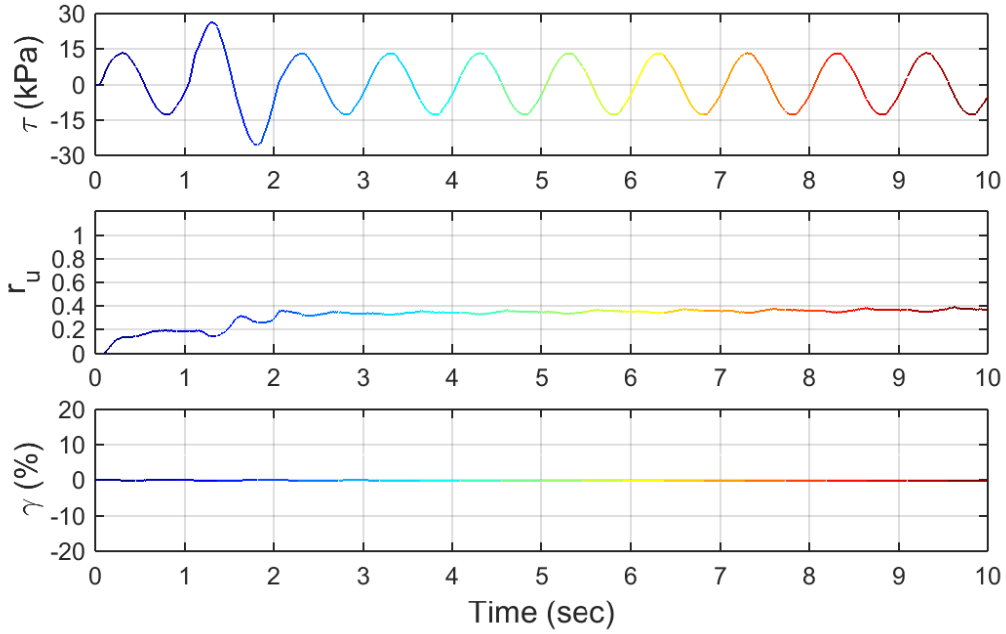

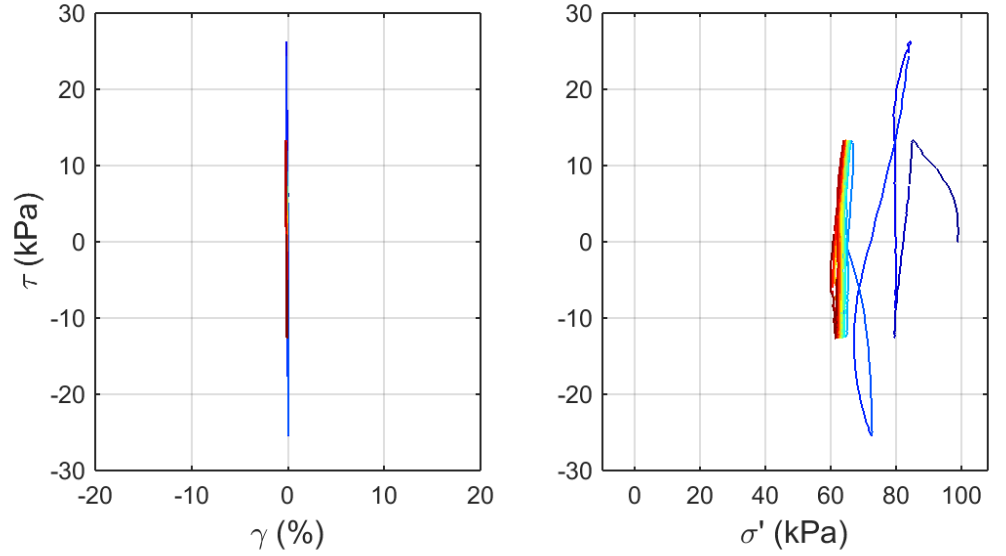

Test ID: 20120425_03
Nevada Sand
D_r = 75%
Motion: Irregular sine peaking at the 2nd cycle (3rd round of loading)
CSR = 0.25 (determined from the largest loading cycle)

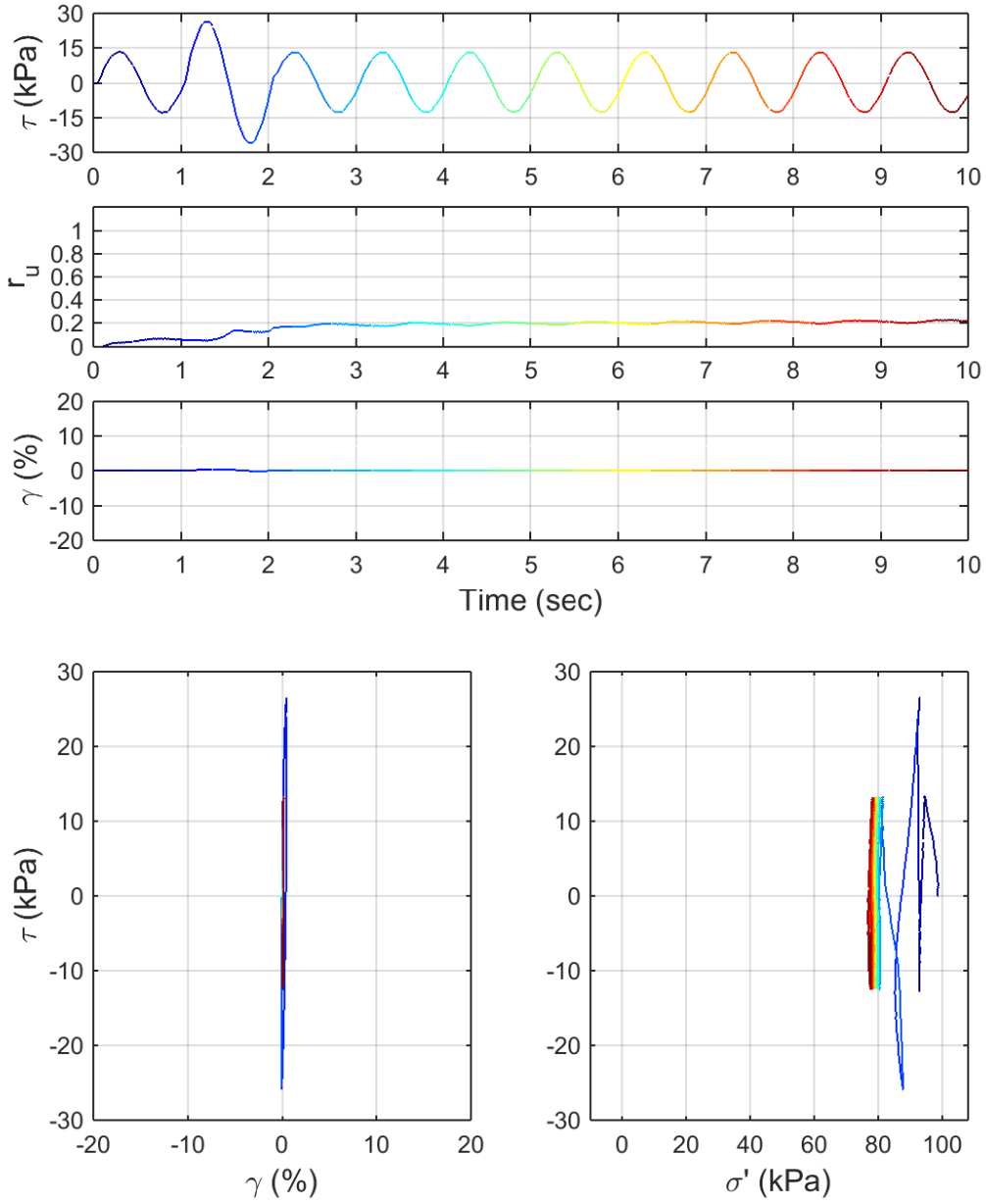

Test ID: 20120424_04
Nevada Sand
D_r = 76%
Motion: Irregular sine peaking at the 2nd cycle (4th round of loading)
CSR = 0.25 (determined from the largest loading cycle)

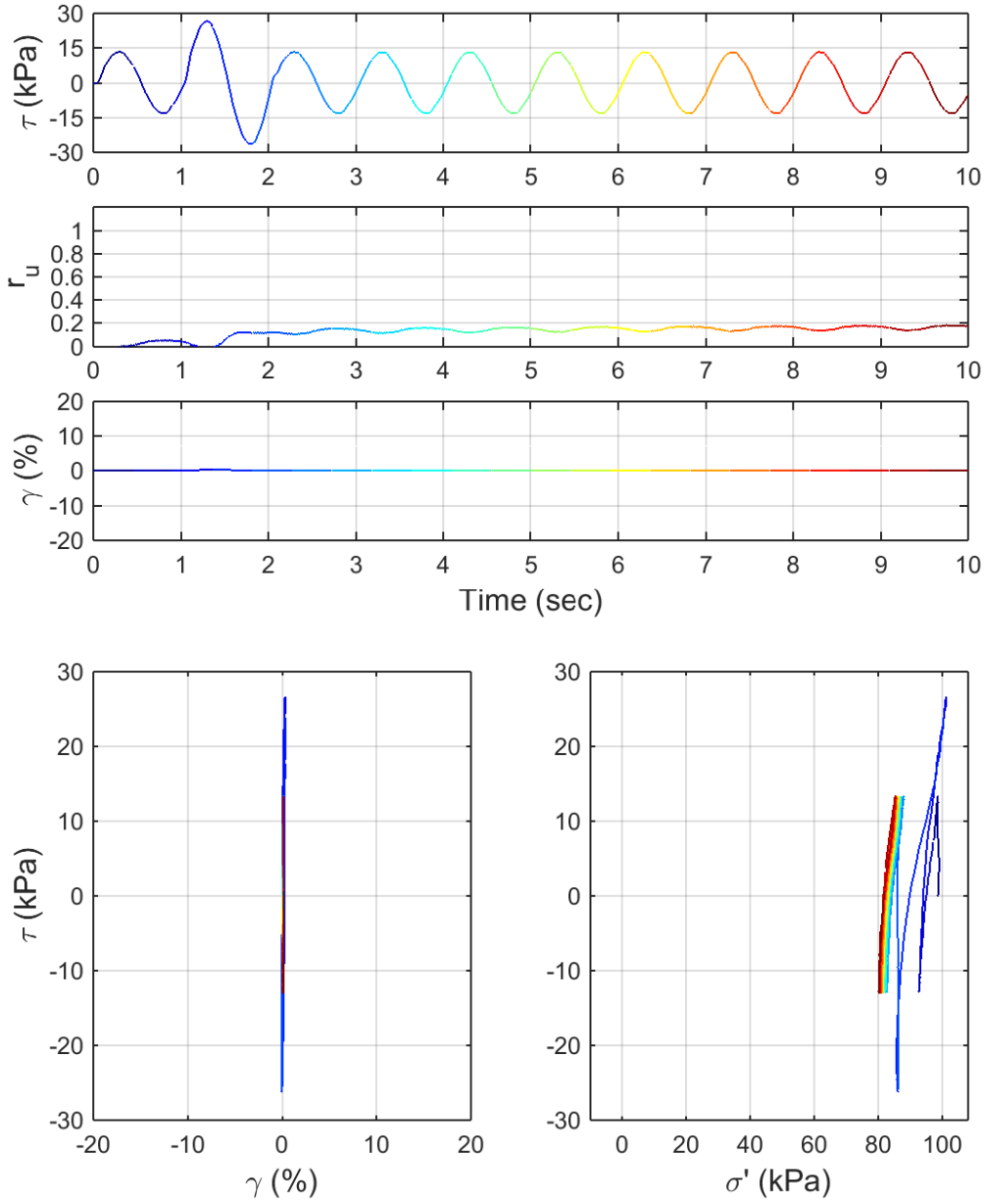

Test ID: 2012042502_05
Nevada Sand
D_r = 82%
Motion: Irregular sine peaking at the 2nd cycle (5th round of loading)
CSR = 0.25 (determined from the largest loading cycle)

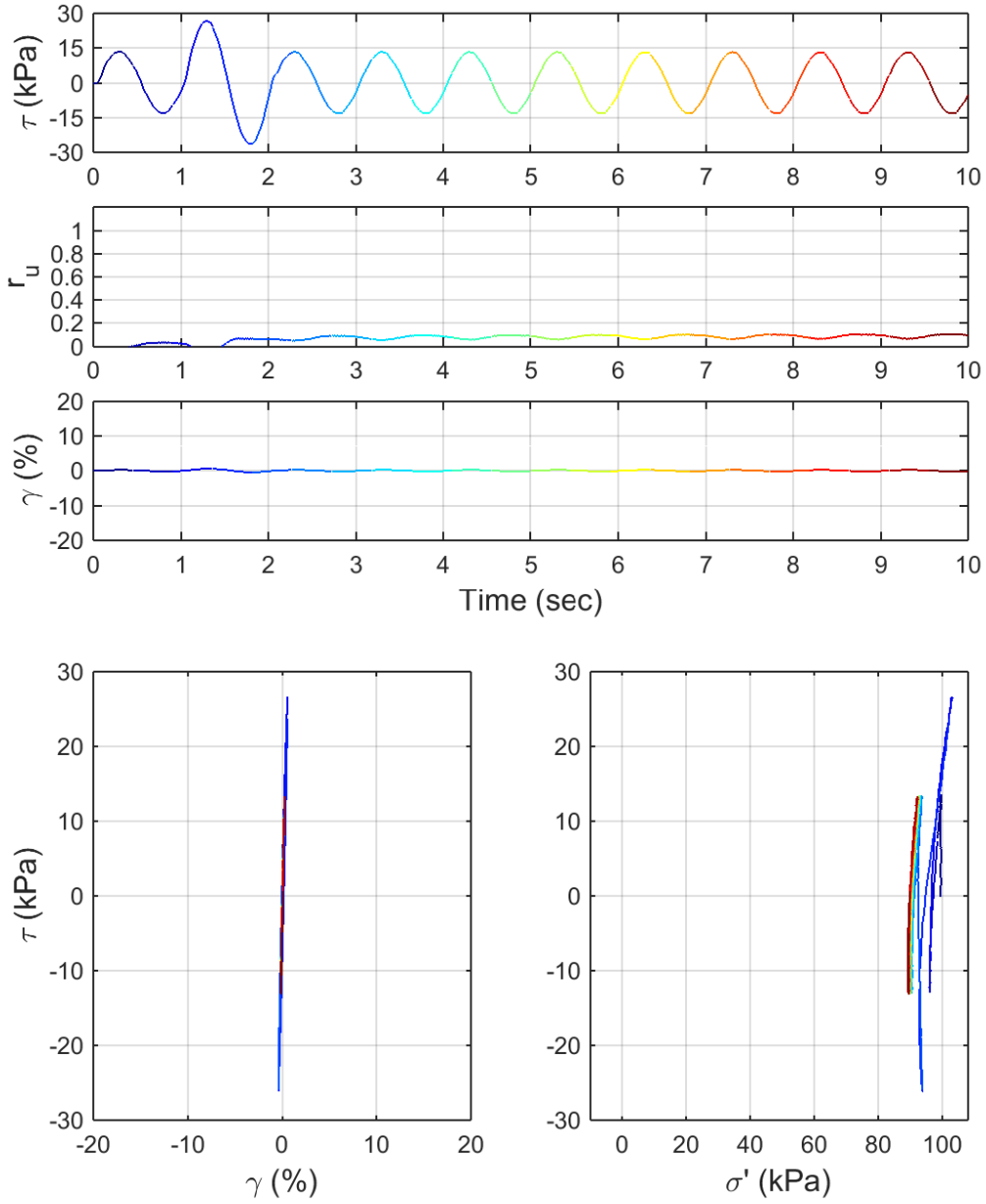

Test ID: 20120428_06
Nevada Sand
D_r = 71%
Motion: Irregular sine peaking at the 2nd cycle (6th round of loading)
CSR = 0.25 (determined from the largest loading cycle)

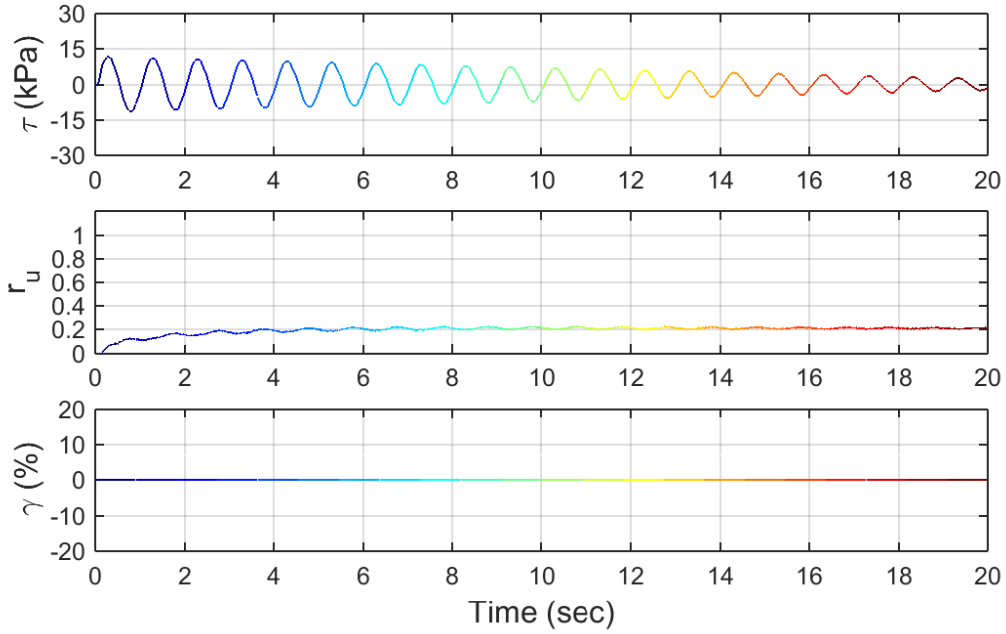

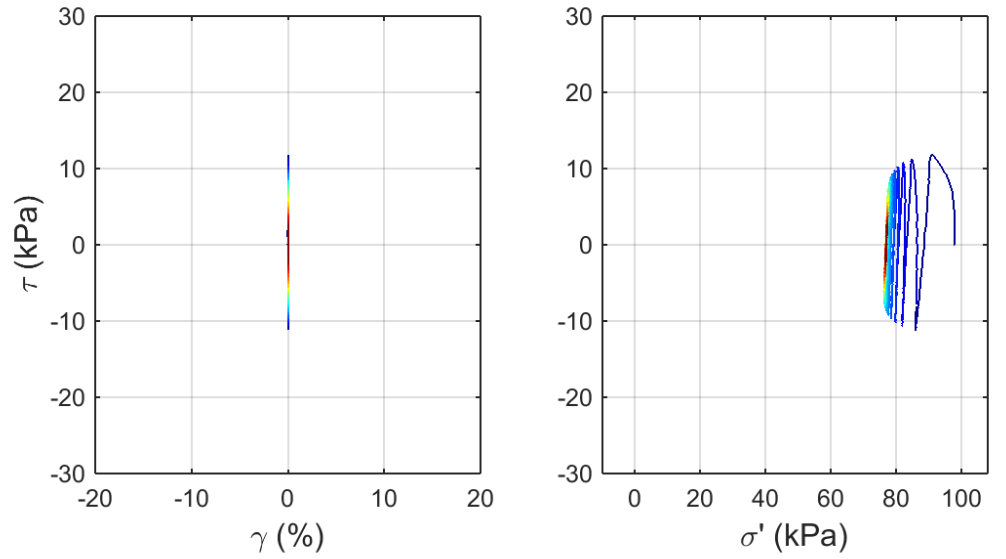

Test ID: 20120512
Nevada Sand
D_r = 66%
Motion: Taper Down (Low)
CSR = 0.1 (determined from the largest loading cycle)

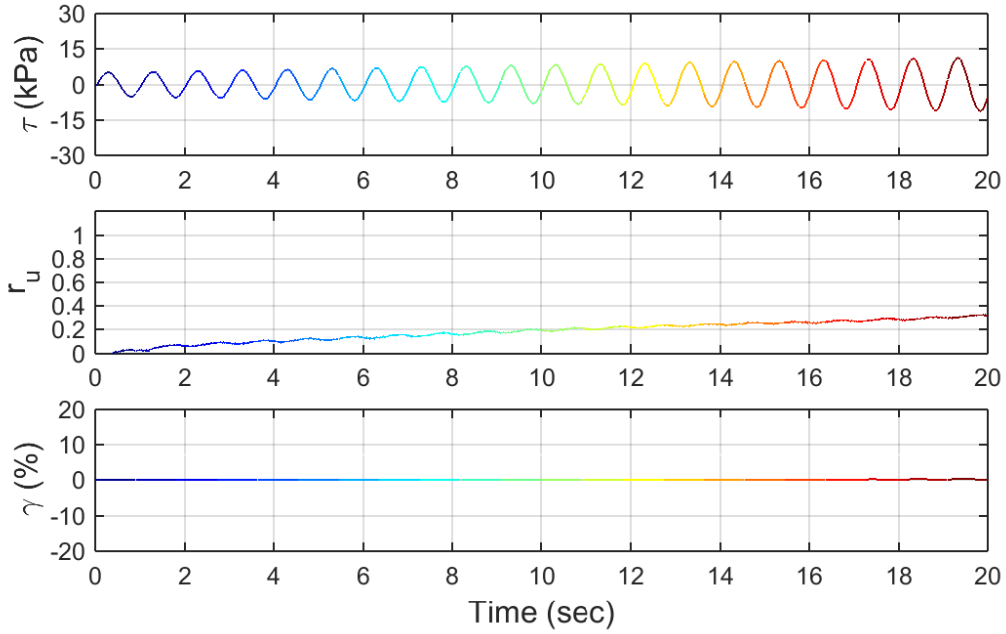

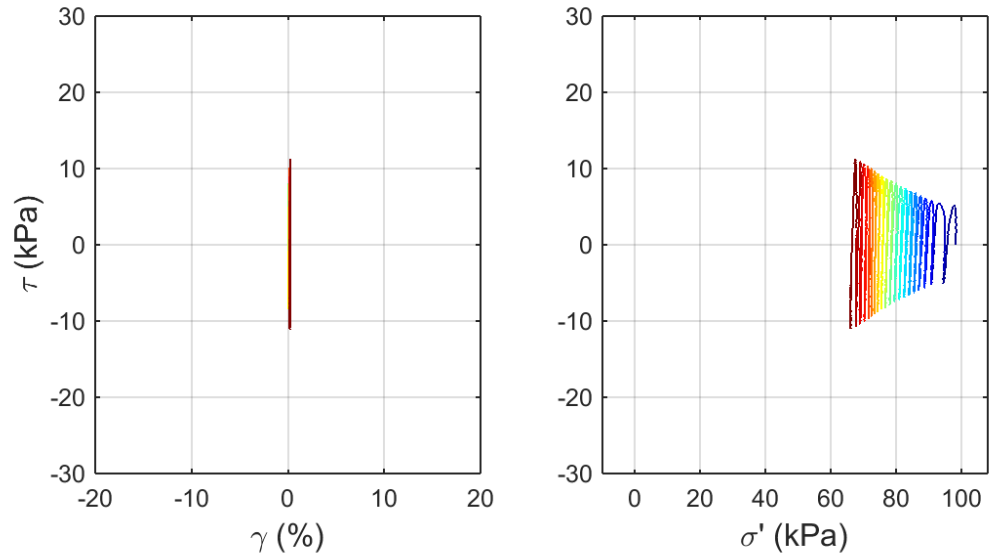

Test ID: 20120513
Nevada Sand
D_r = 68%
Motion: Taper Up (High)
CSR = 0.1 (determined from the largest loading cycle)

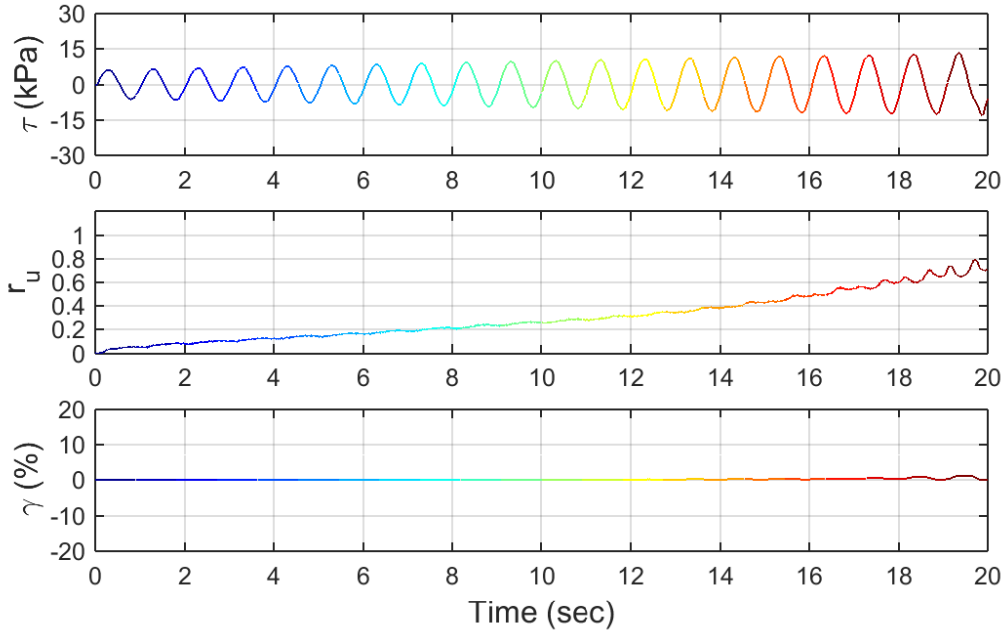

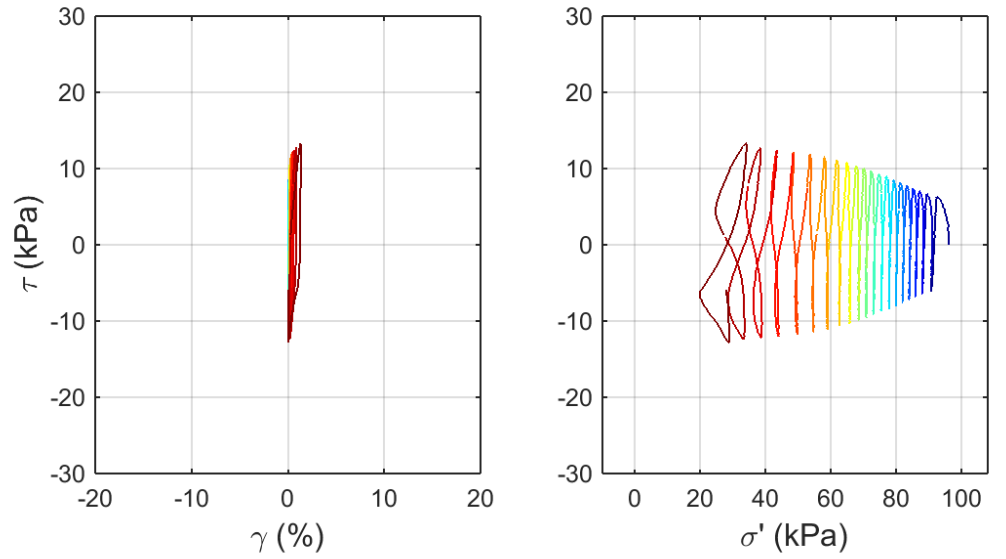

Test ID: 20120514
Nevada Sand
D_r = 54 %
Motion: Taper Up (High)
CSR = 0.125 (determined from the largest loading cycle)

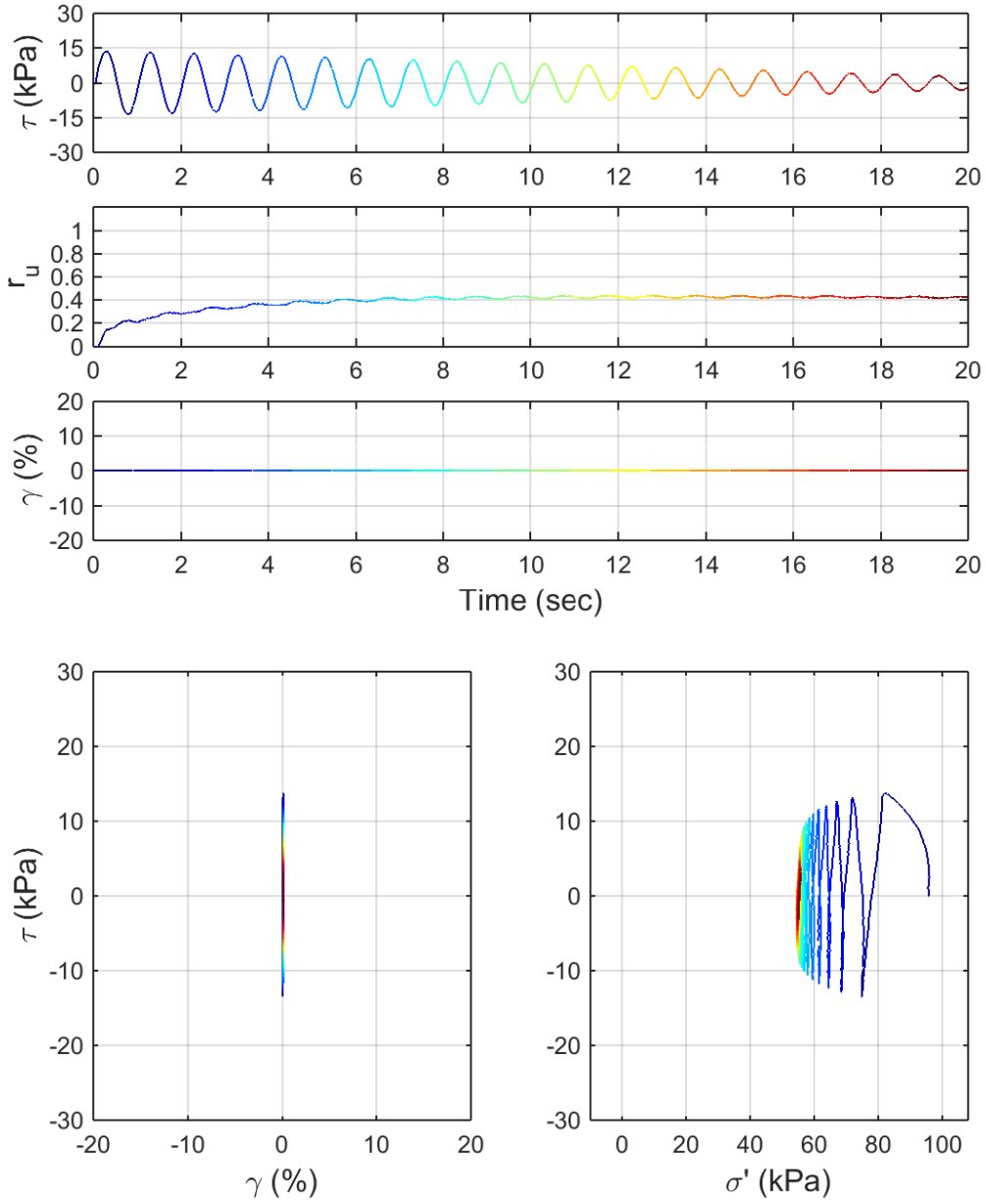

Test ID: 20120515
Nevada Sand
D_r = 57 %
Motion: Taper Down (Low)
CSR = 0.125 (determined from the largest loading cycle)

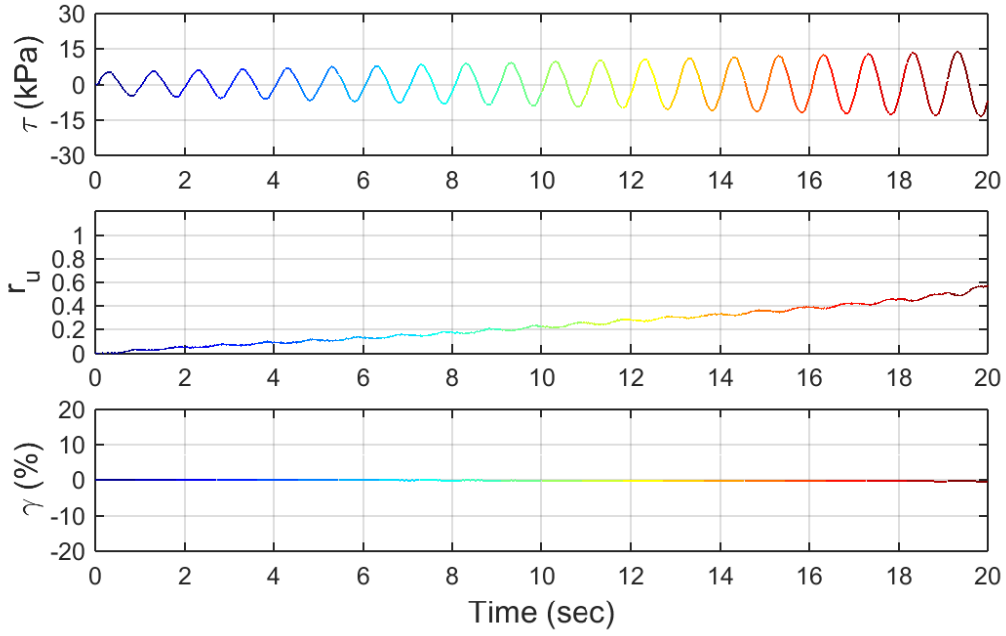

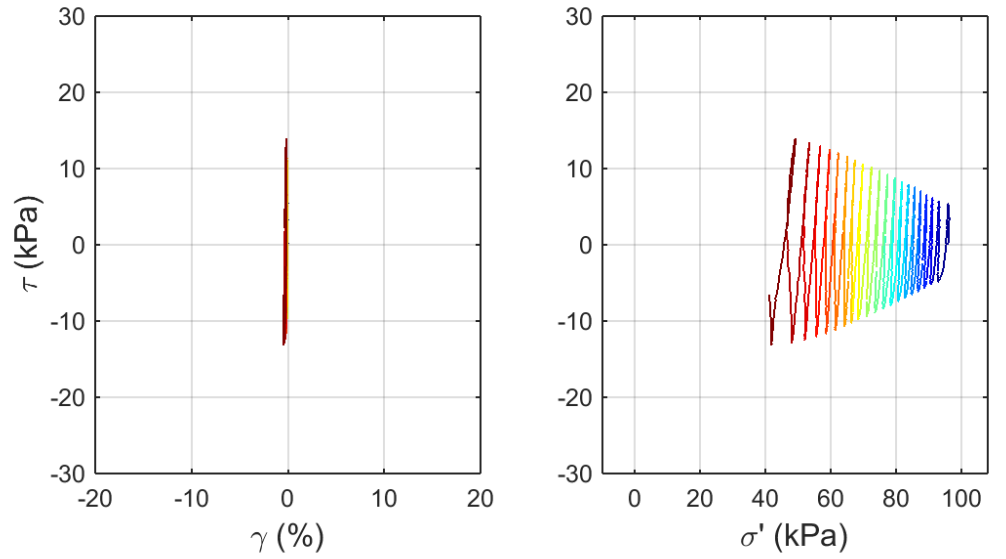

Test ID: 2012051502
Nevada Sand
D_r = 69 %
Motion: Taper Up (Low)
CSR = 0.125 (determined from the largest loading cycle)

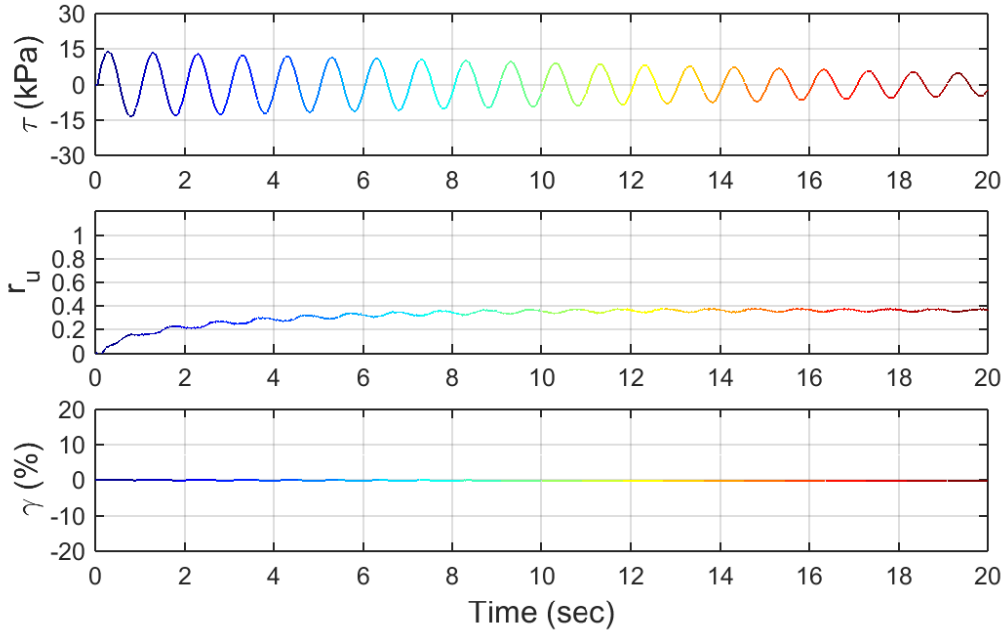

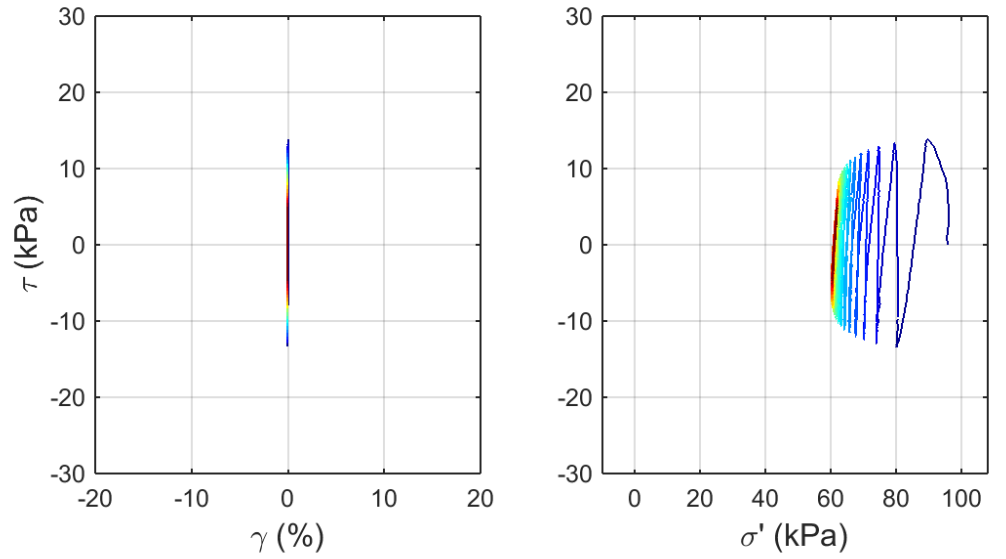

Test ID: 20120516
Nevada Sand
D_r = 54 %
Motion: Taper Down (High)
CSR = 0.125 (determined from the largest loading cycle)

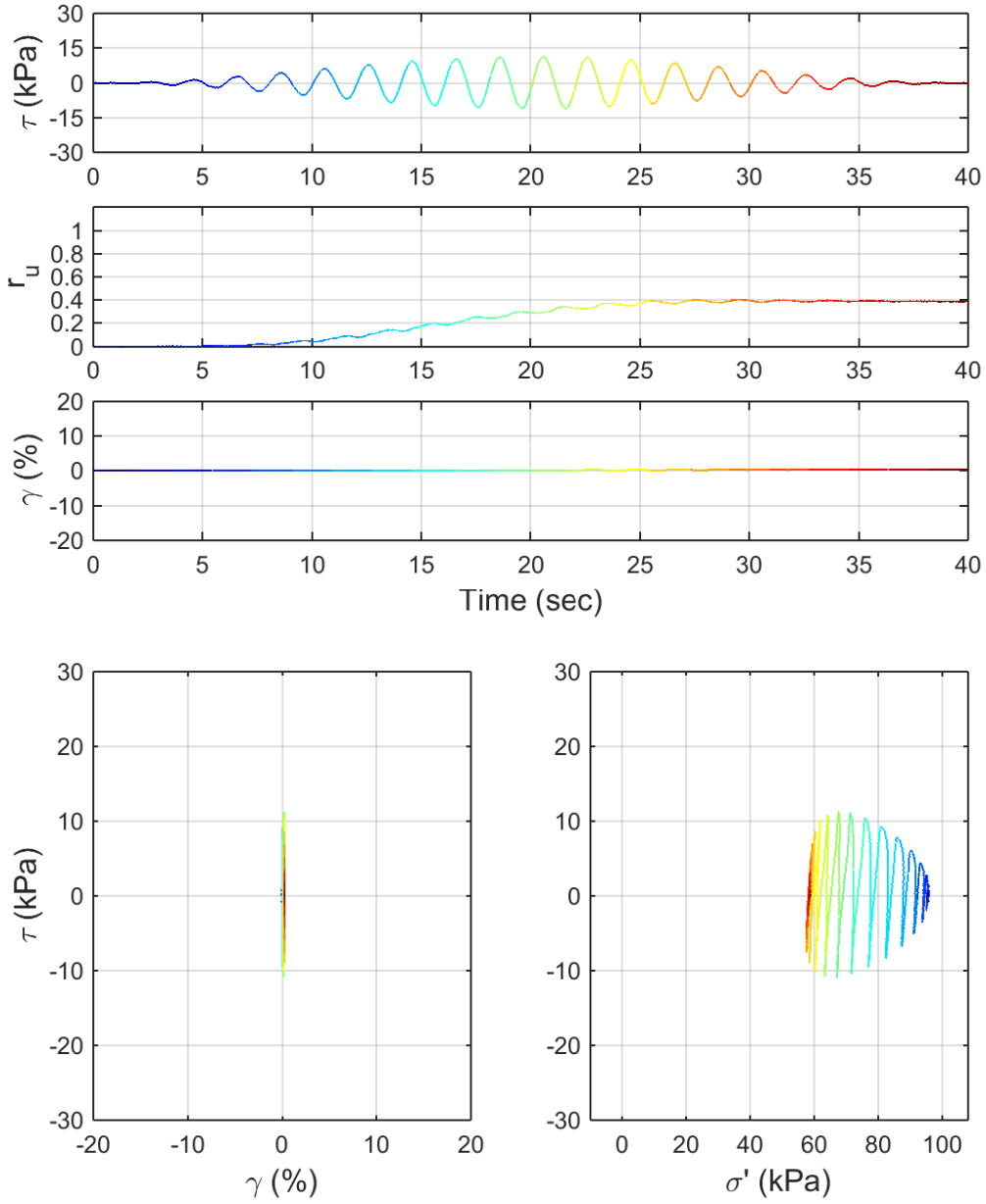

Test ID: 20120517
Nevada Sand
D_r = 55 %
Motion: Modulated
CSR = 0.1 (determined from the largest loading cycle)

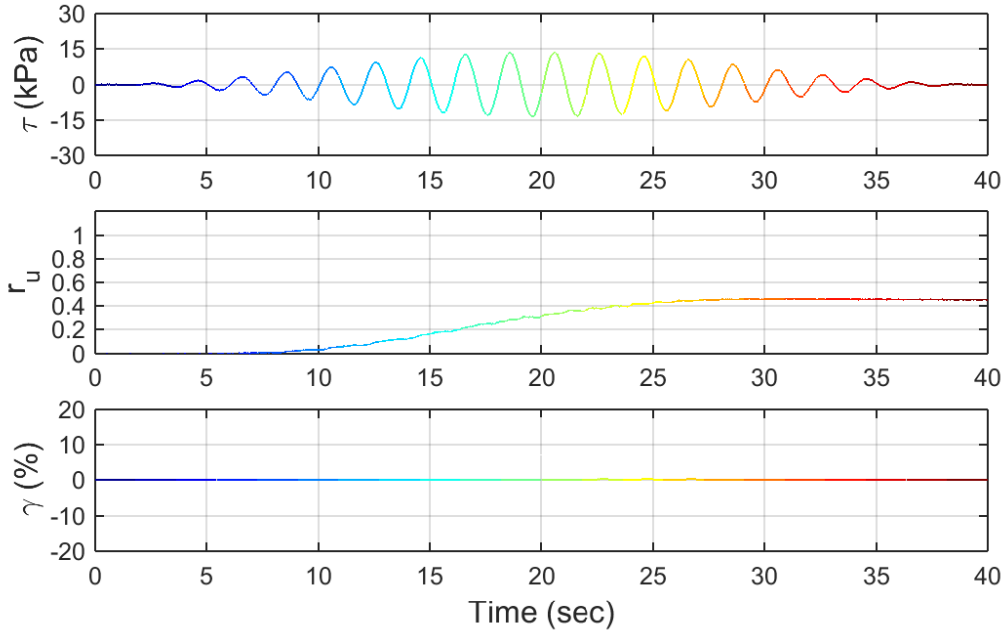

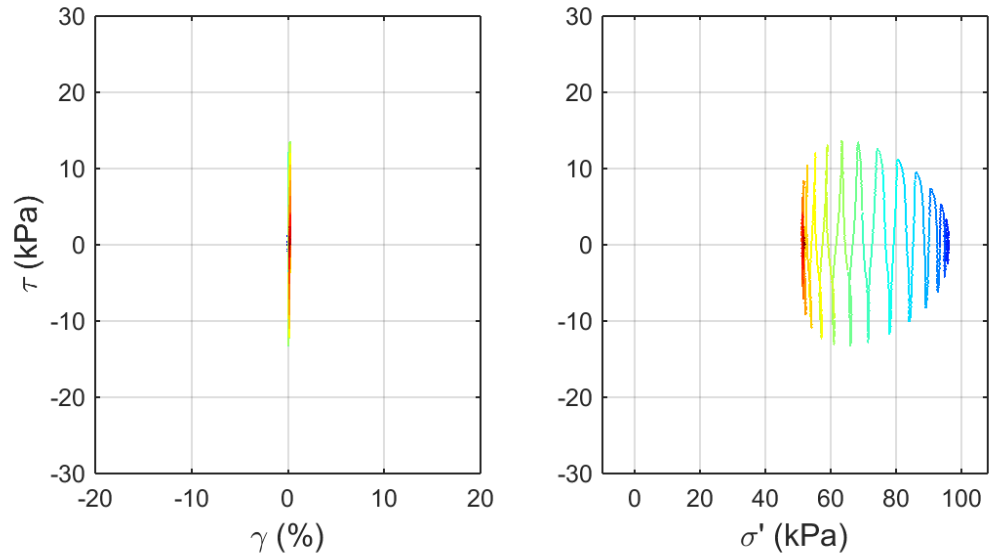

Test ID: 20120518
Nevada Sand
D_r = 57 %
Motion: Modulated
CSR = 0.125 (determined from the largest loading cycle)

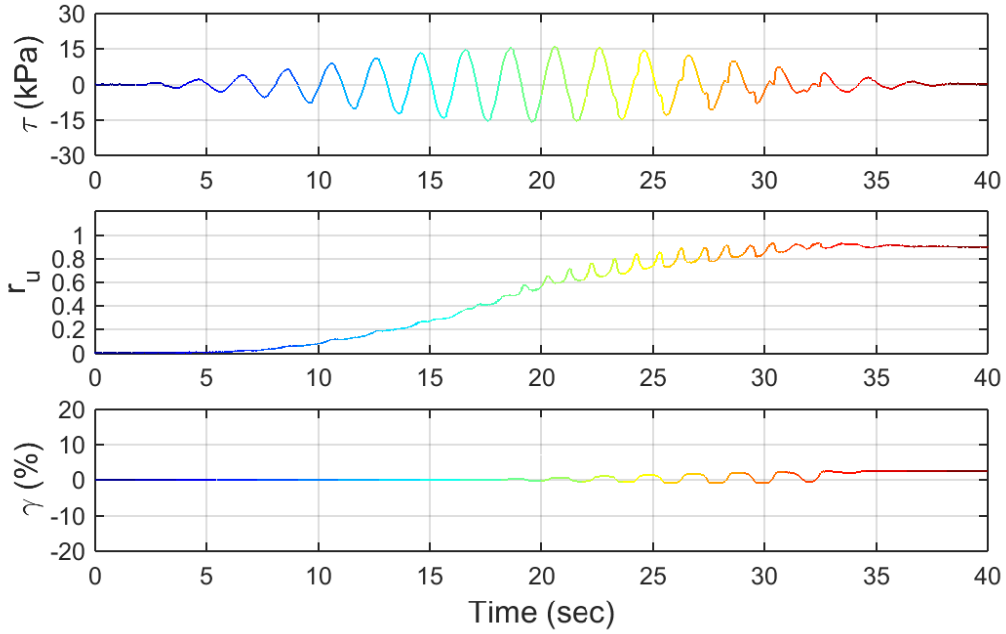

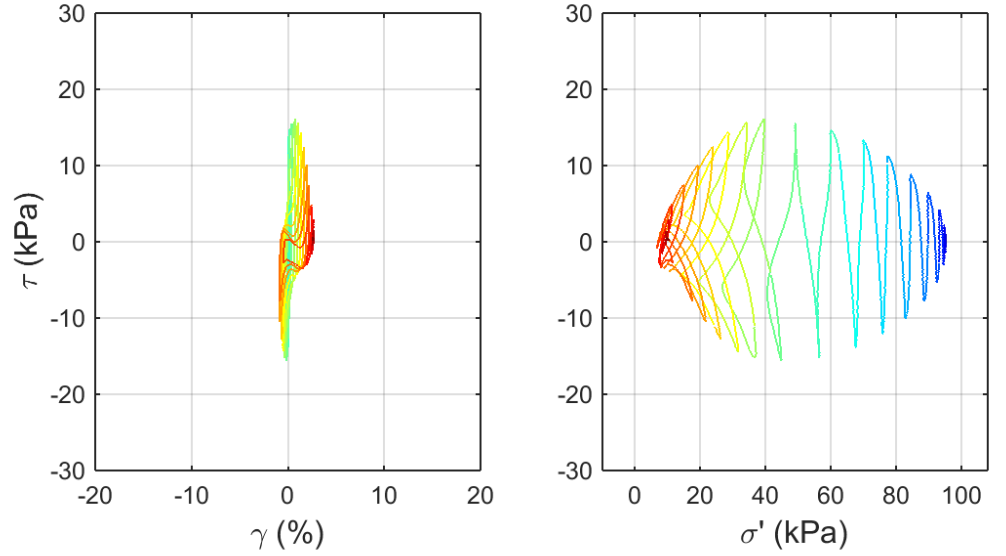

Test ID: 20120519
Nevada Sand
D_r = 62 %
Motion: Modulated
CSR = 0.15 (determined from the largest loading cycle)

APPENDIX A.2. CSS DATA: HARMONIC LOADING

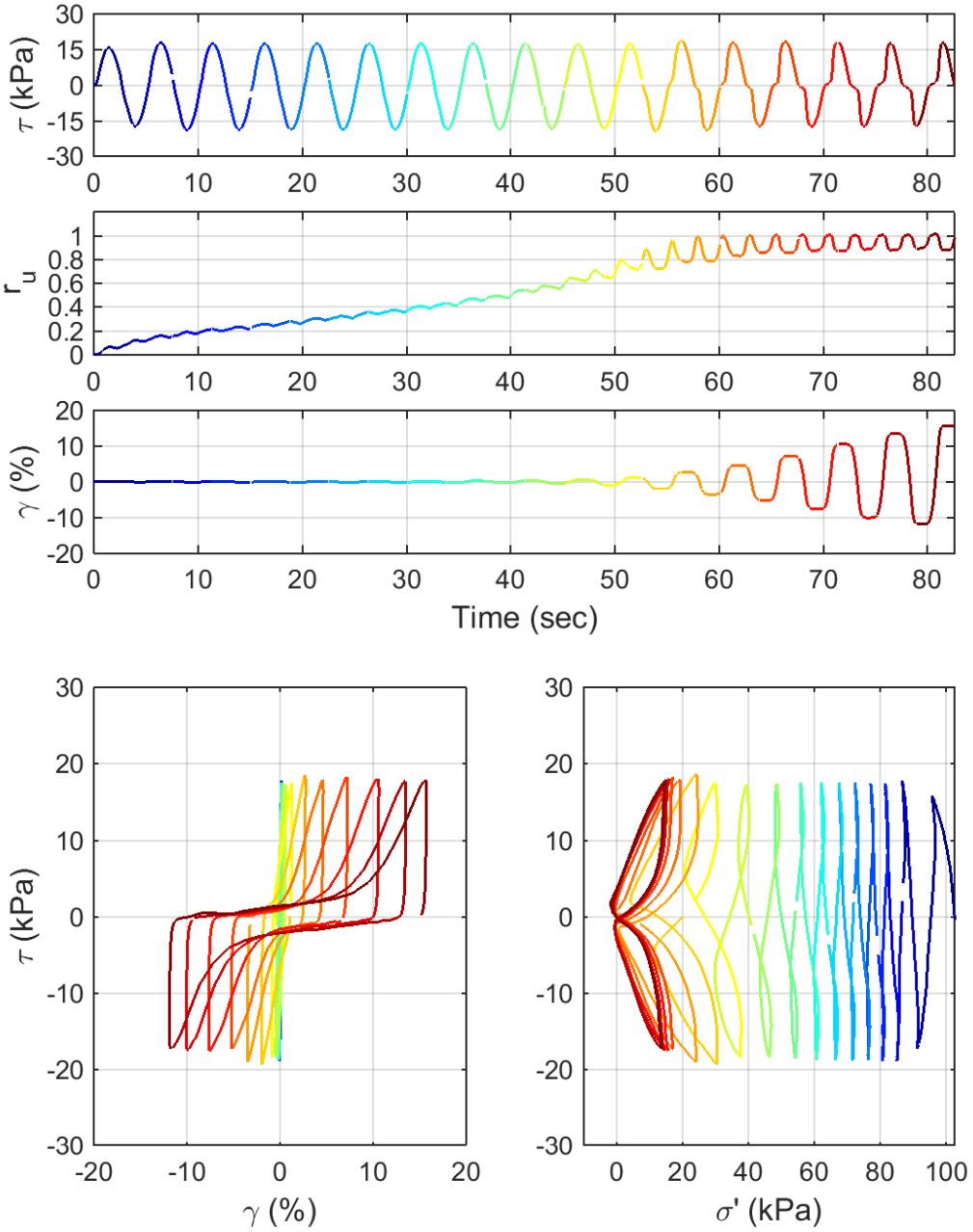

Test ID: 20130327
Nevada Sand
D_r = 49%
CSR = 0.175

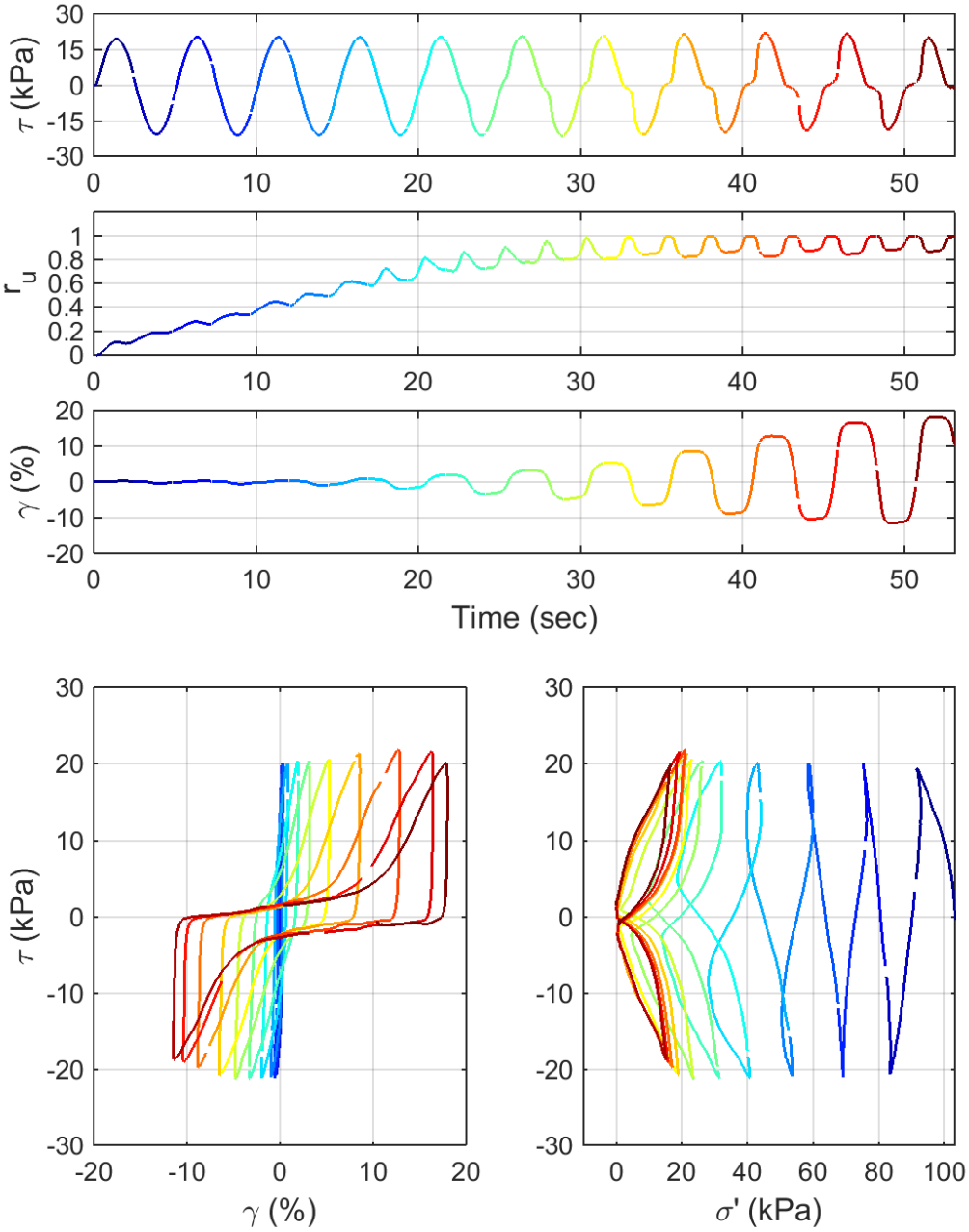

Test ID: 2013032902
Nevada Sand
D_r = 39%
CSR = 0.200

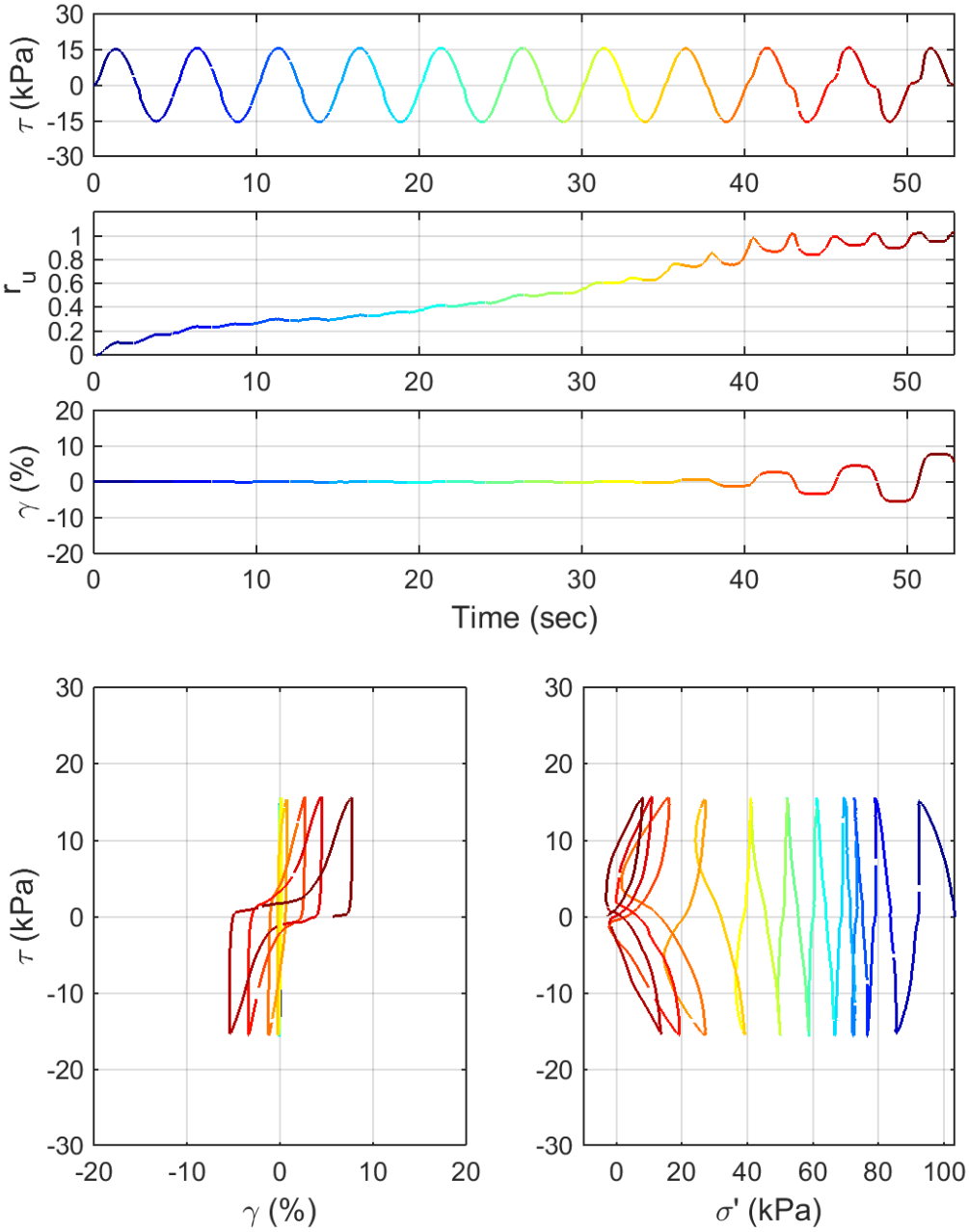

Test ID: 2013040102
Nevada Sand
D_r = 34%
CSR = 0.150

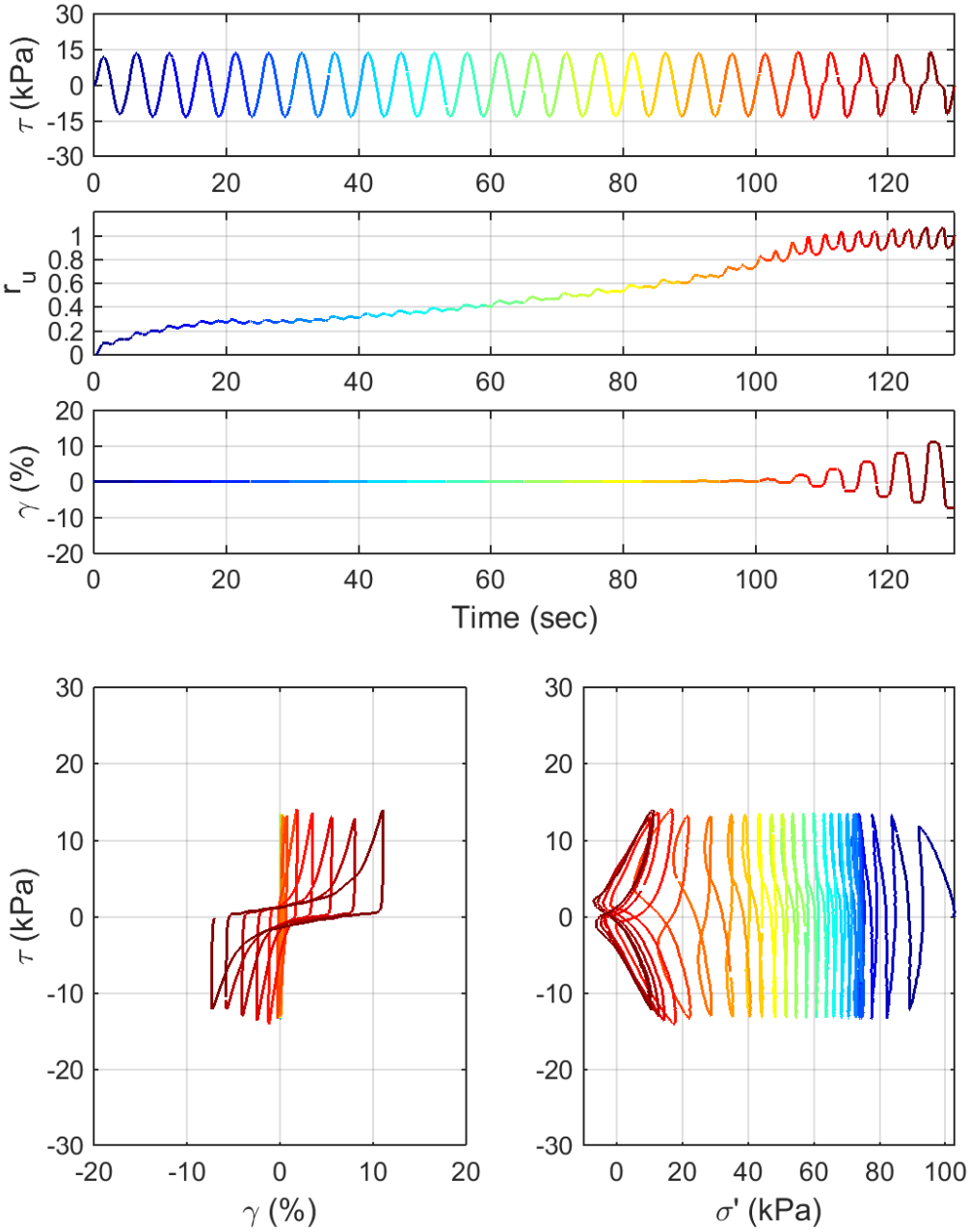

Test ID: 20130404
Nevada Sand
D_r = 51%
CSR = 0.125

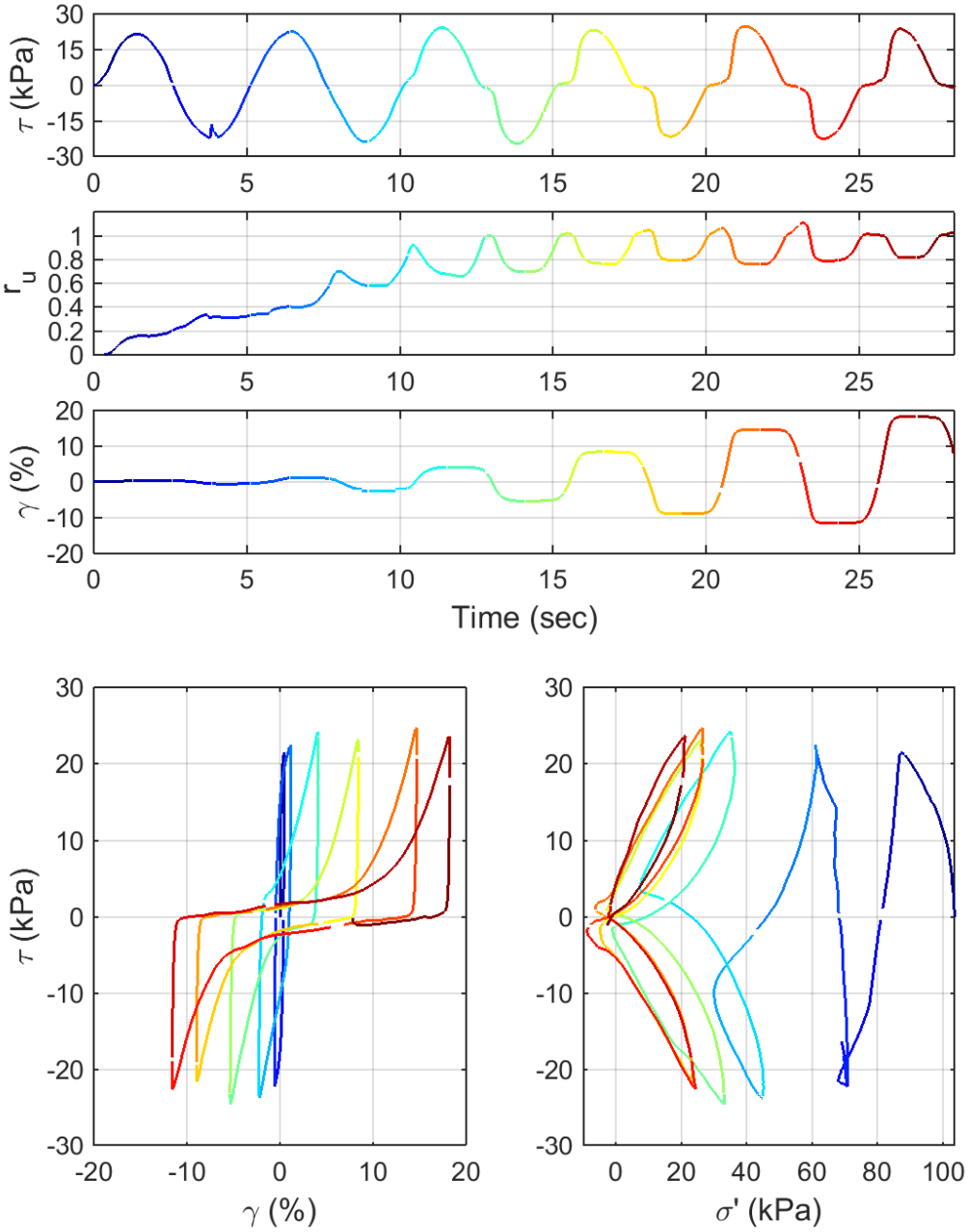

Test ID: 20130406
Nevada Sand
$D_r = 41\%$
CSR = 0.225

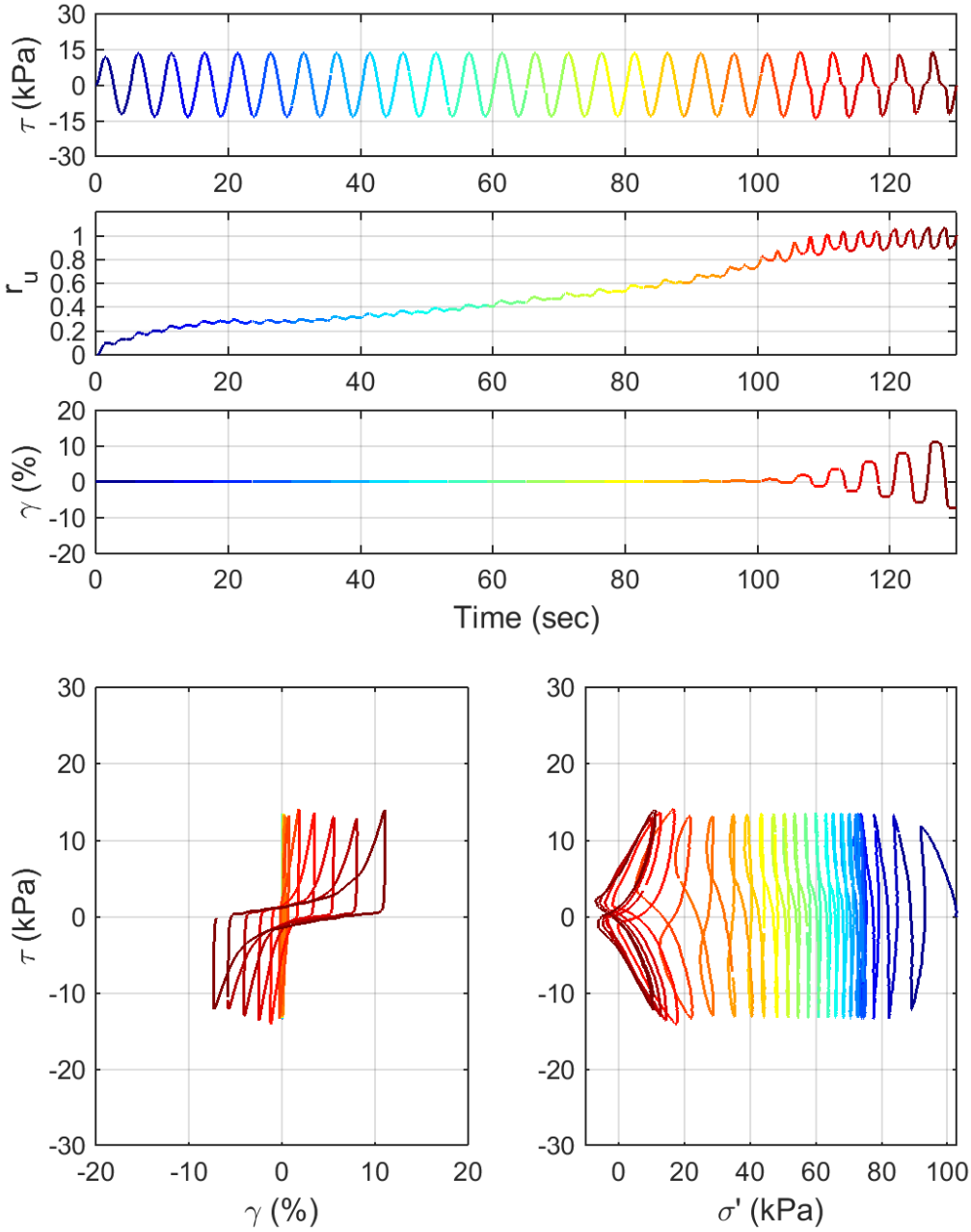

Test ID: 20130412
Nevada Sand
D_r = 81%
CSR = 0.125

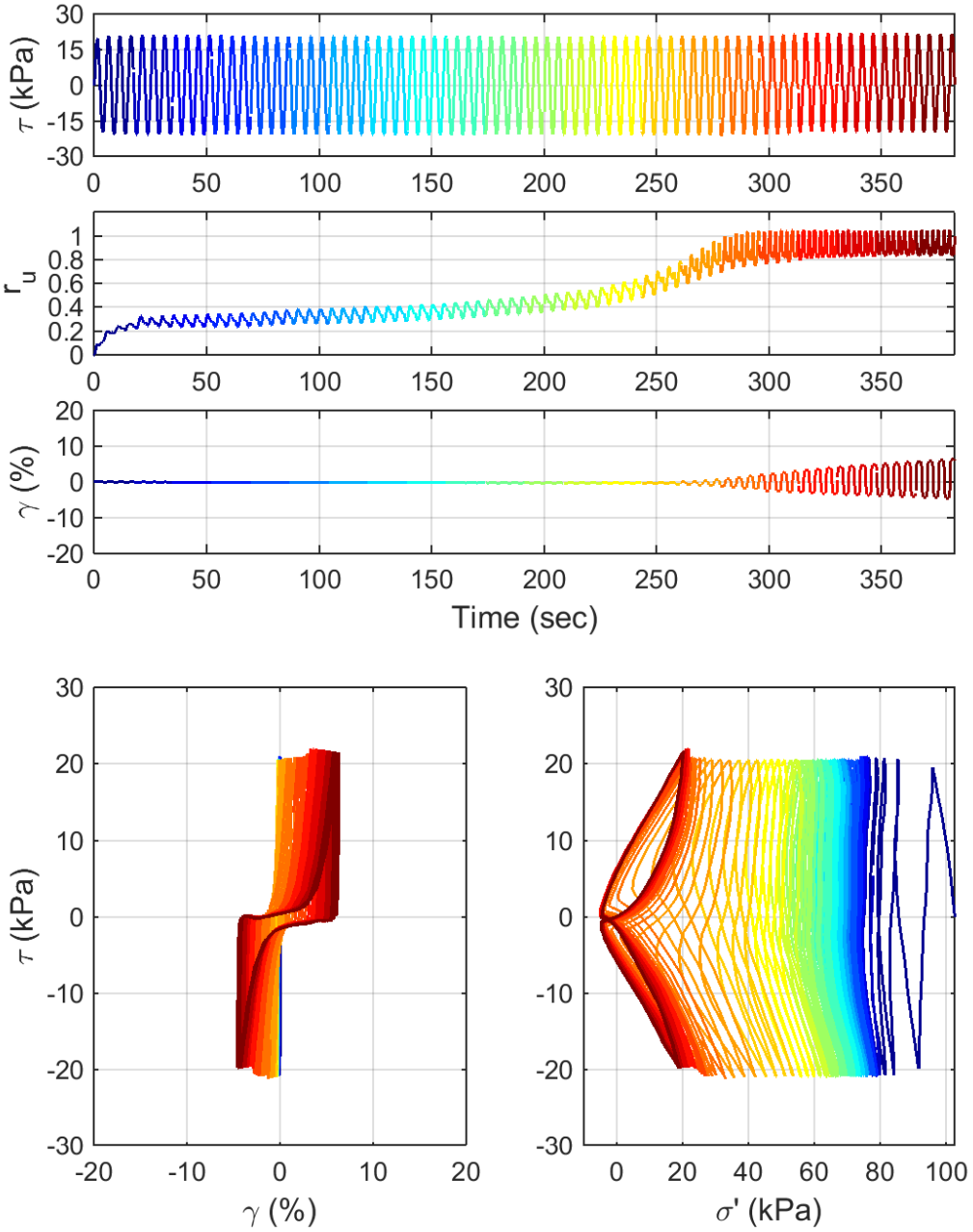

Test ID: 20130423
Nevada Sand
D_r = 66%
CSR = 0.200

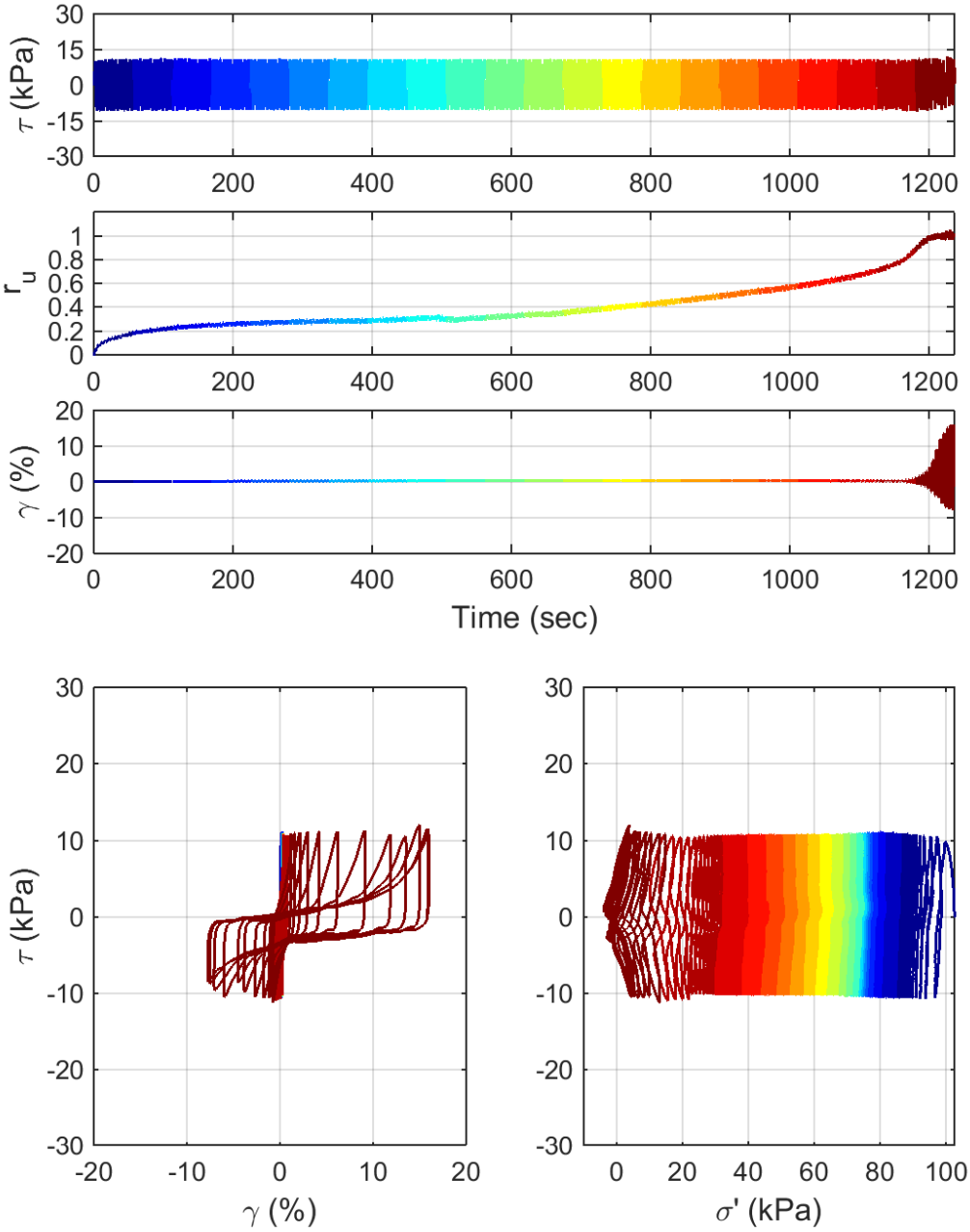

Test ID: 20130424
Nevada Sand
D_r = 44%
CSR = 0.100

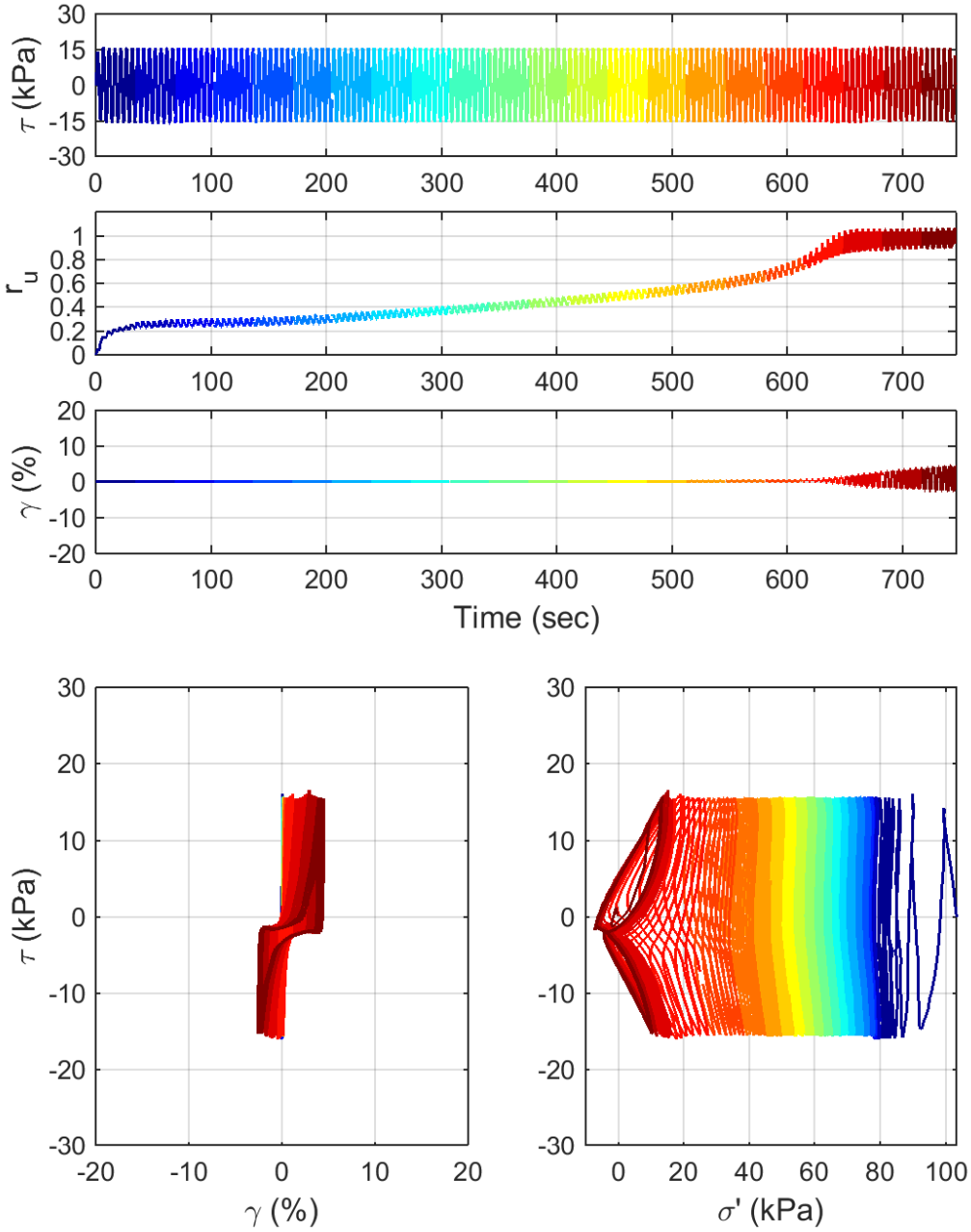

Test ID: 2013051502
Nevada Sand
D_r = 85%
CSR = 0.15

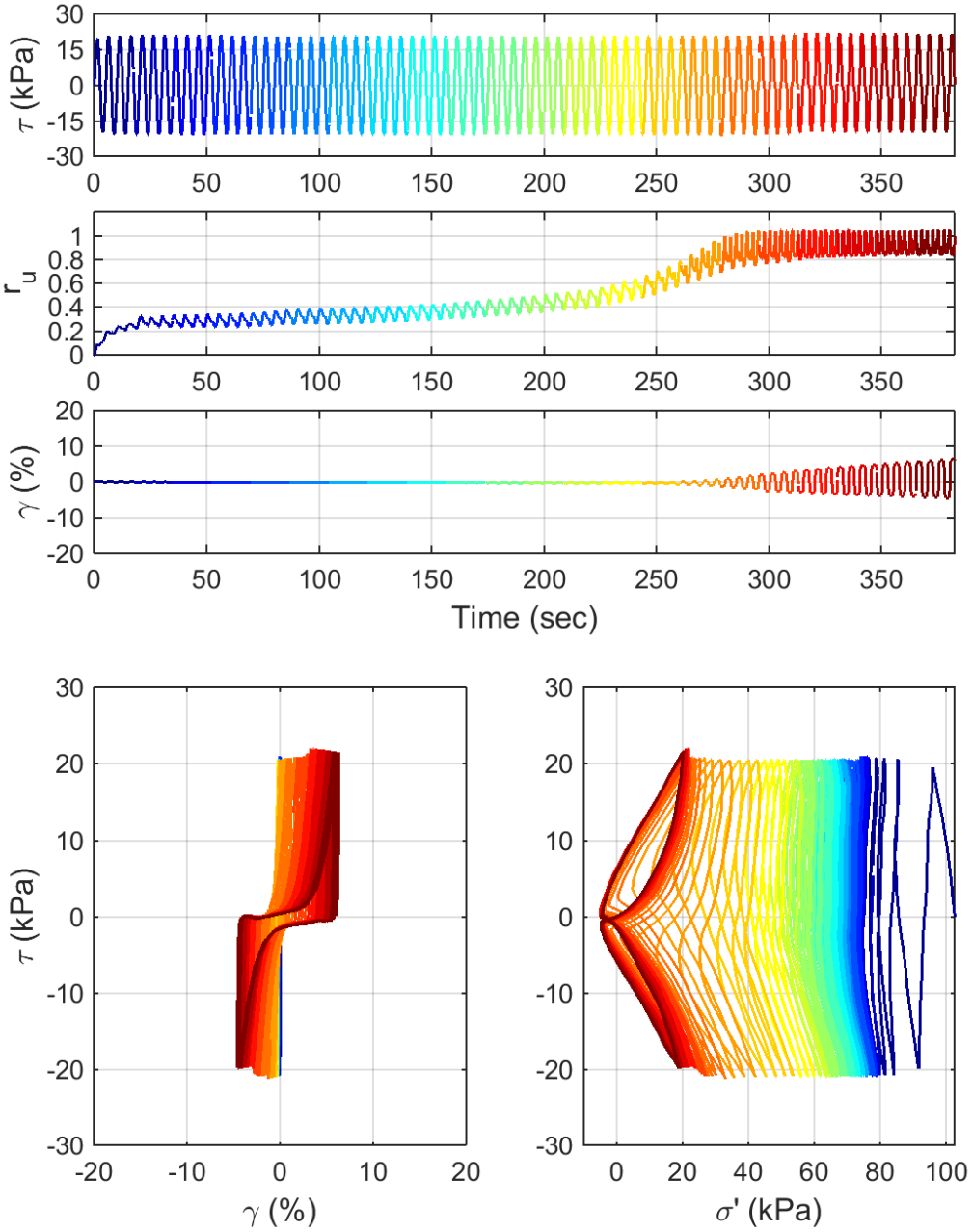

Test ID: 20130516
Nevada Sand
D_r = 85%
CSR = 0.2

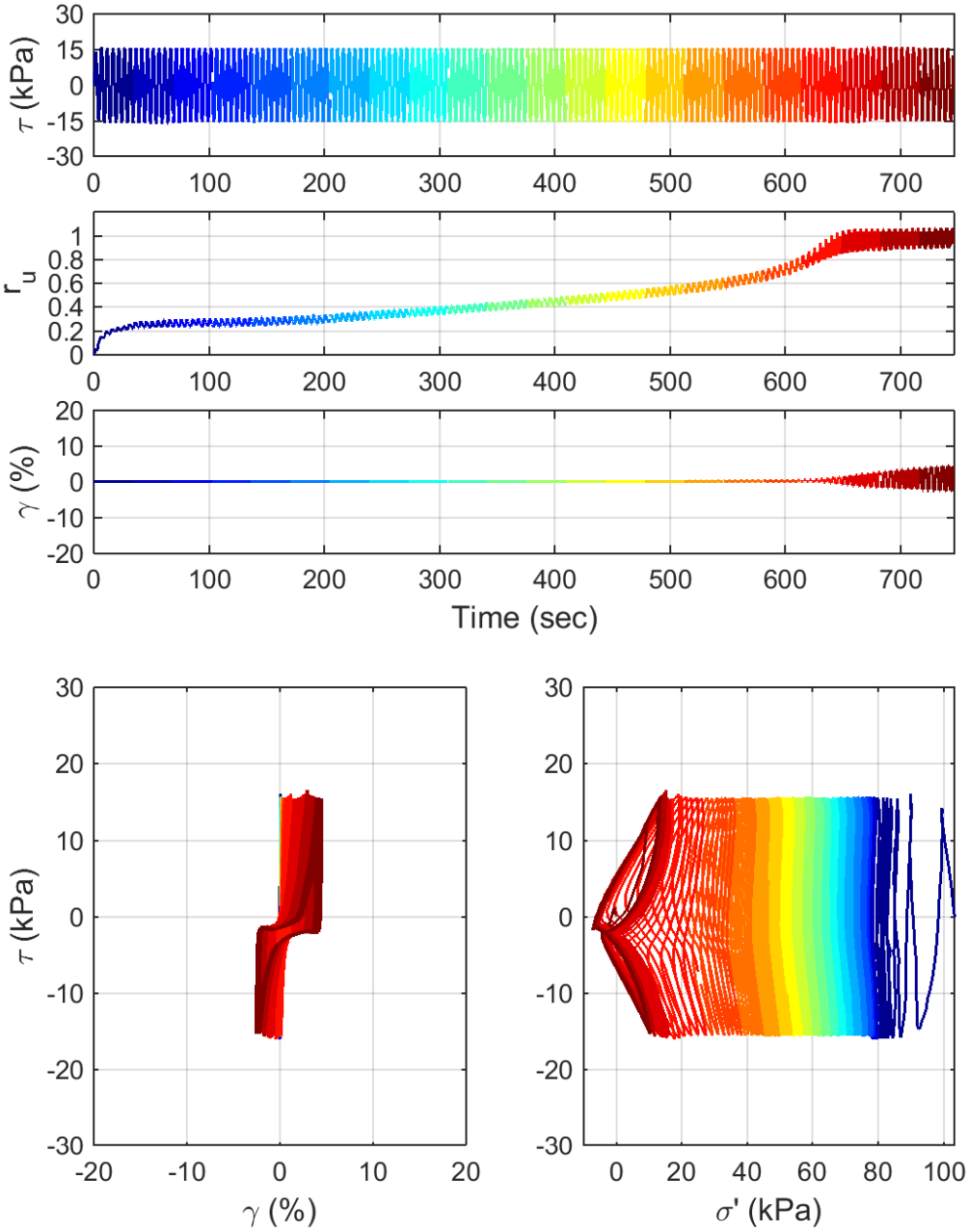

Test ID: 2013051602
Nevada Sand
D_r = 74%
CSR = 0.15

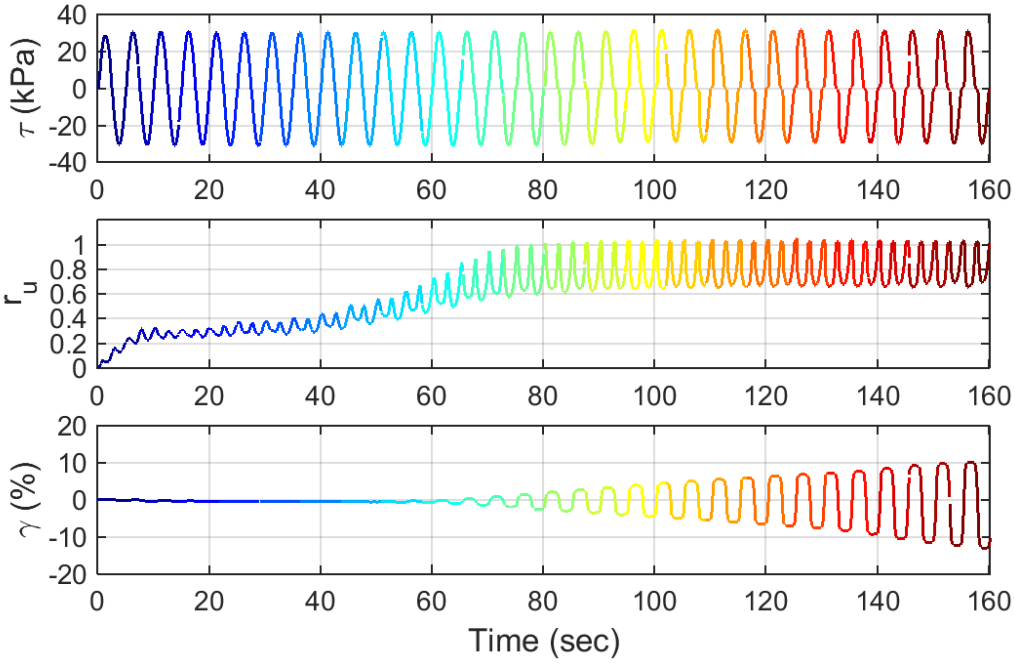

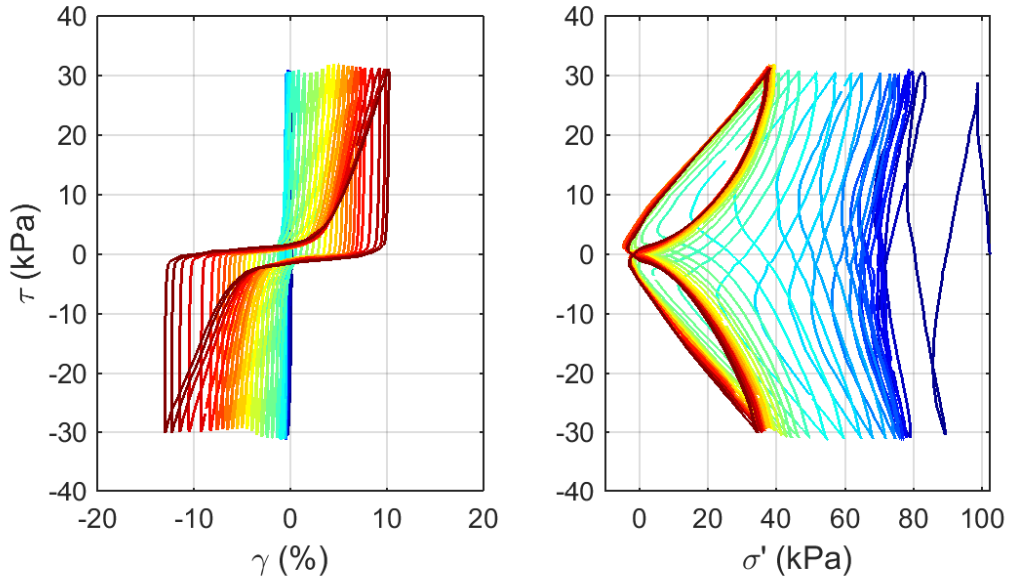

Test ID: 20130517
Nevada Sand
D_r = 79%
CSR = 0.300

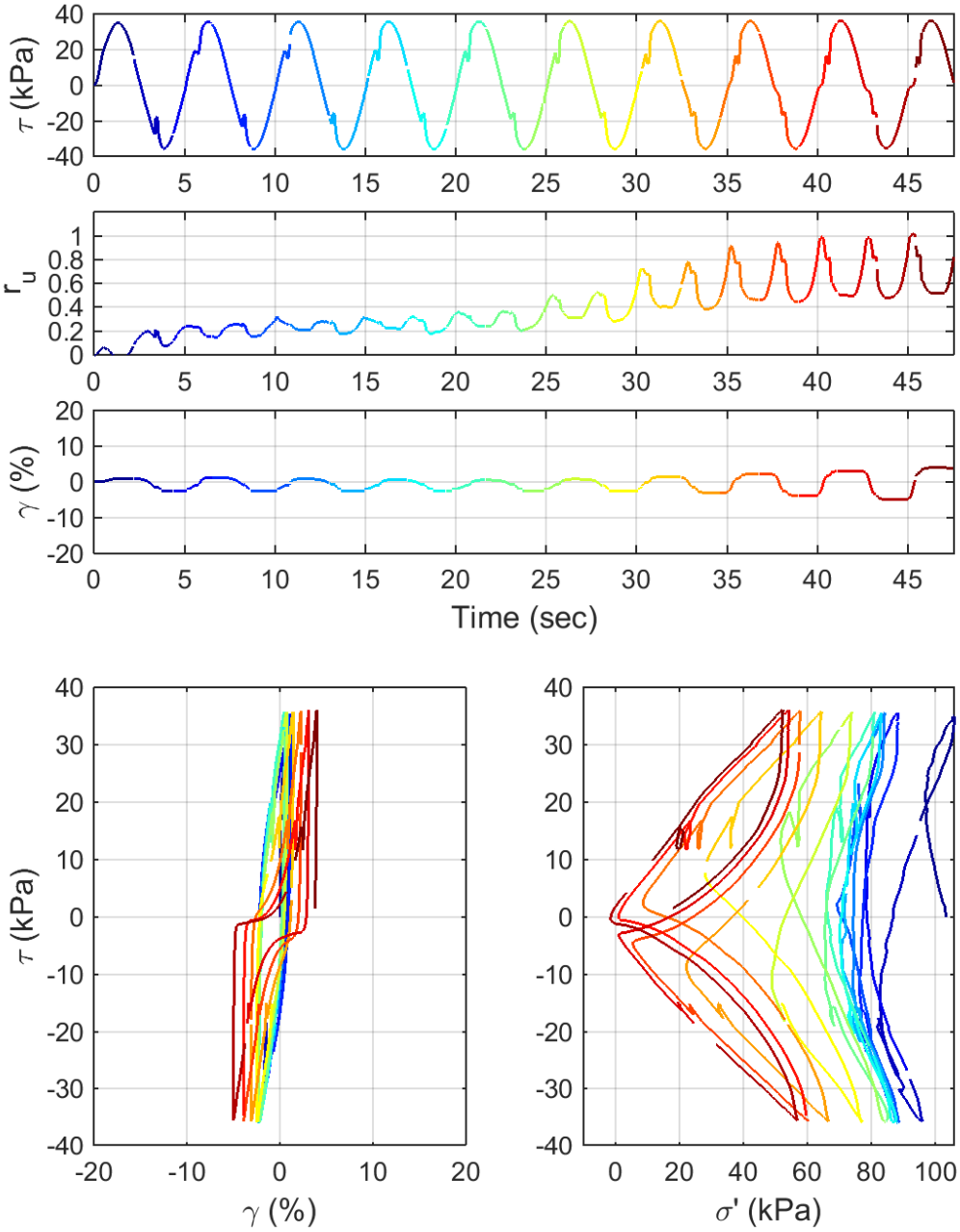

Test ID: 20130711
Nevada Sand
D_r = 78%
CSR = 0.350

APPENDIX A.3. CSS DATA: MODULATED SINUSOID LOADING

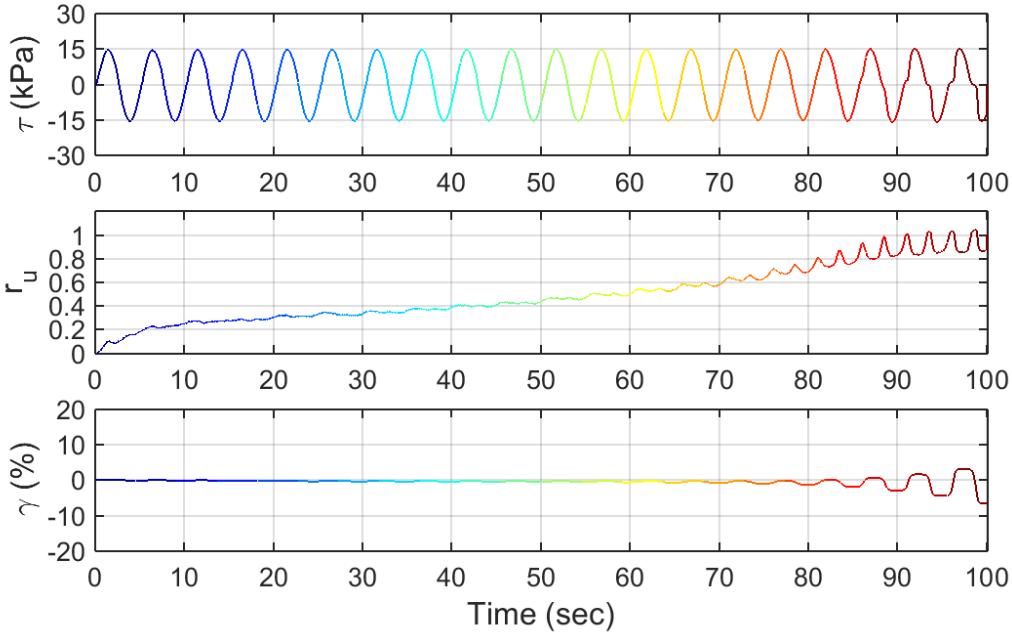

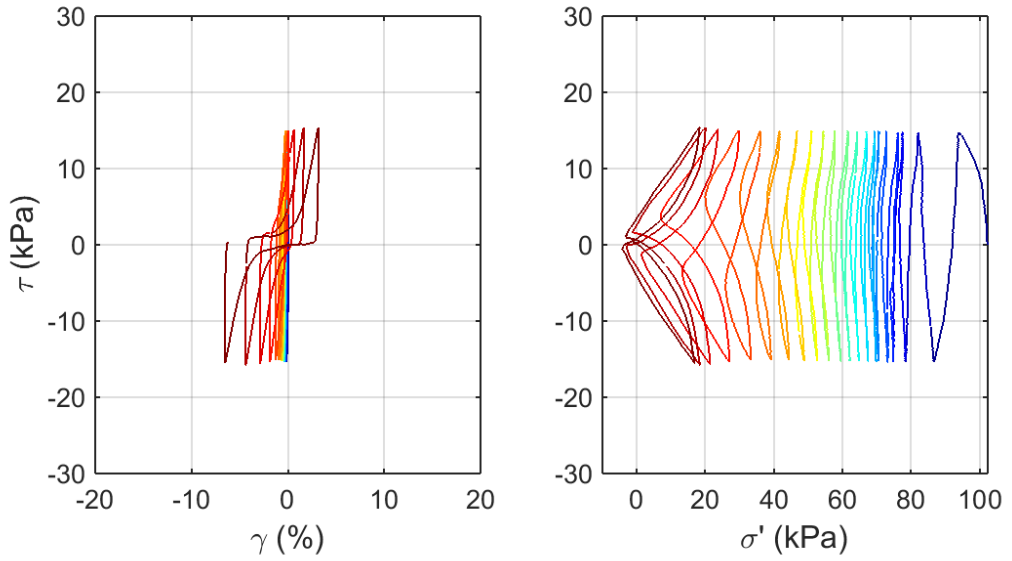

Test ID: 20130524
Nevada Sand
D_r = 55%
Motion: Baseline

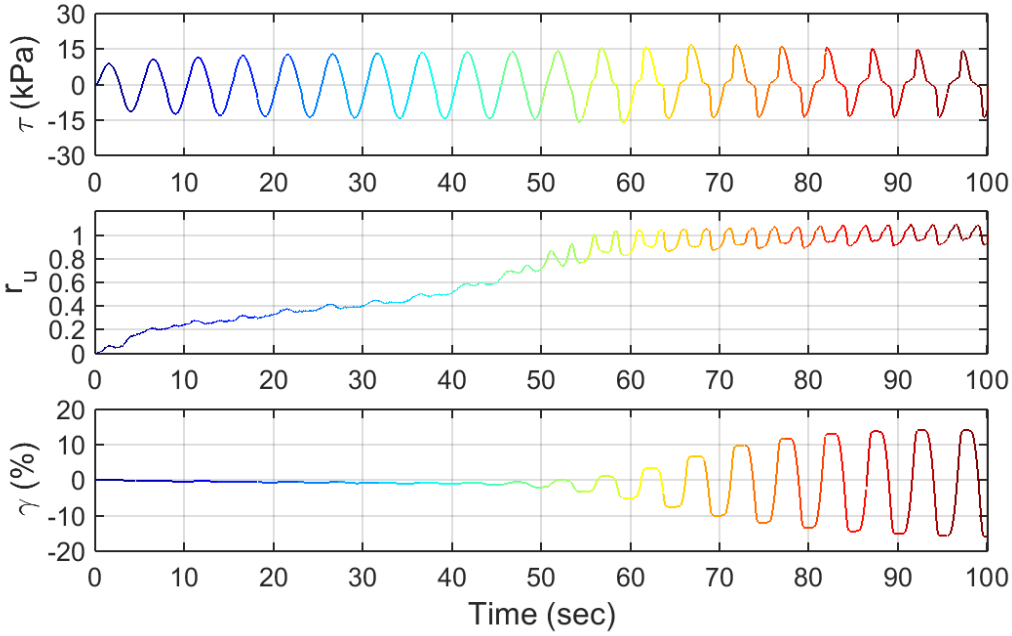

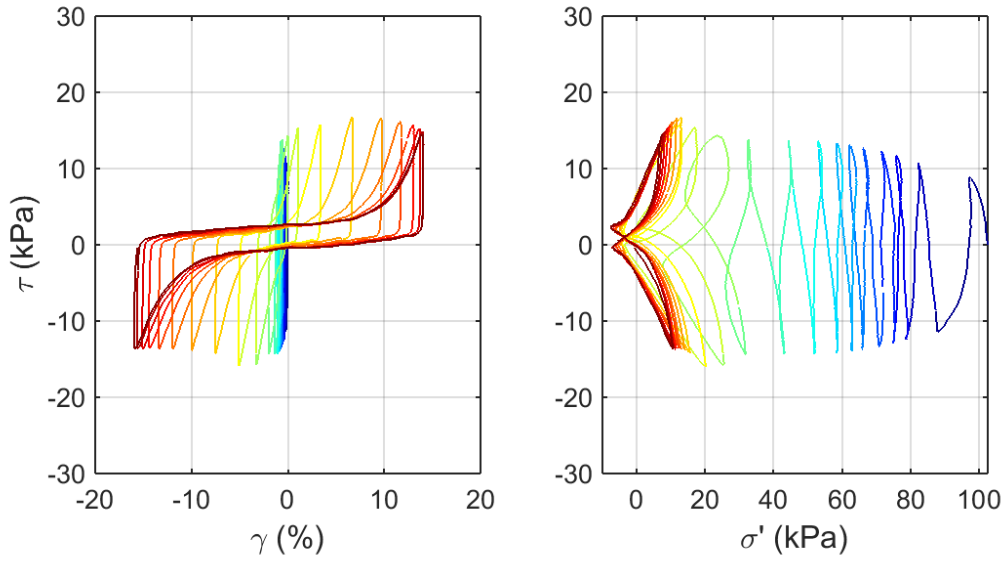

Test ID: 20130527
Nevada Sand
D_r = 54%
Motion: New_Modulated_up_n=0.1

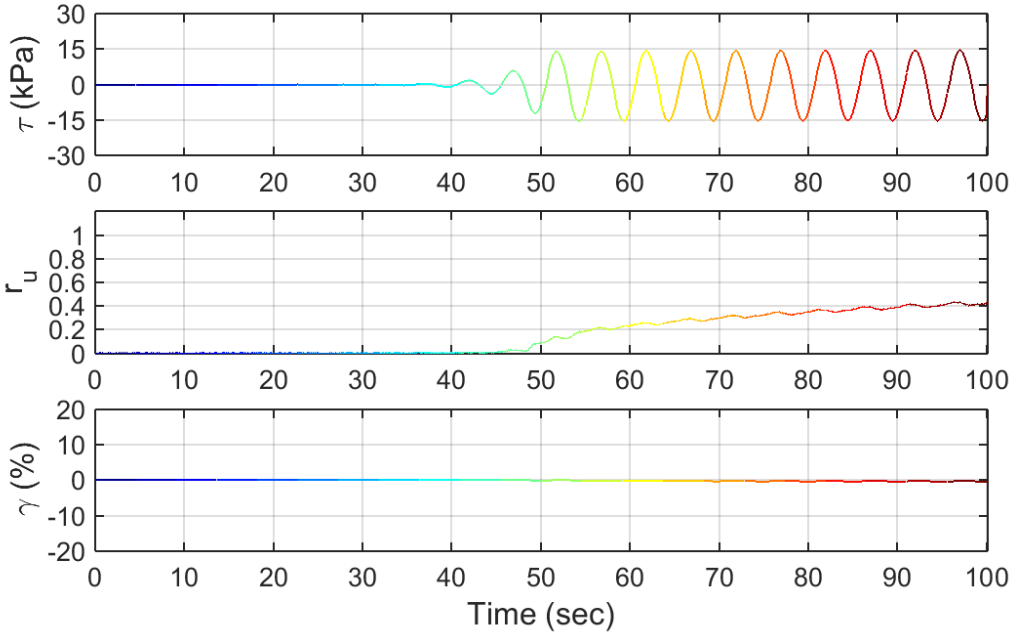

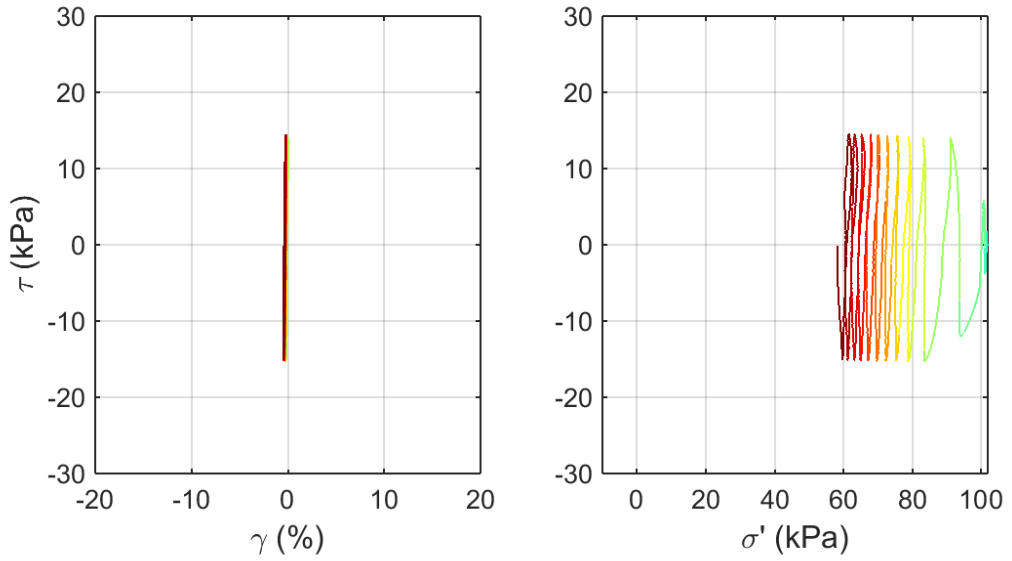

Test ID: 20130528
Nevada Sand
D_r = 47 %
Motion: New_Modulated_up_n=10

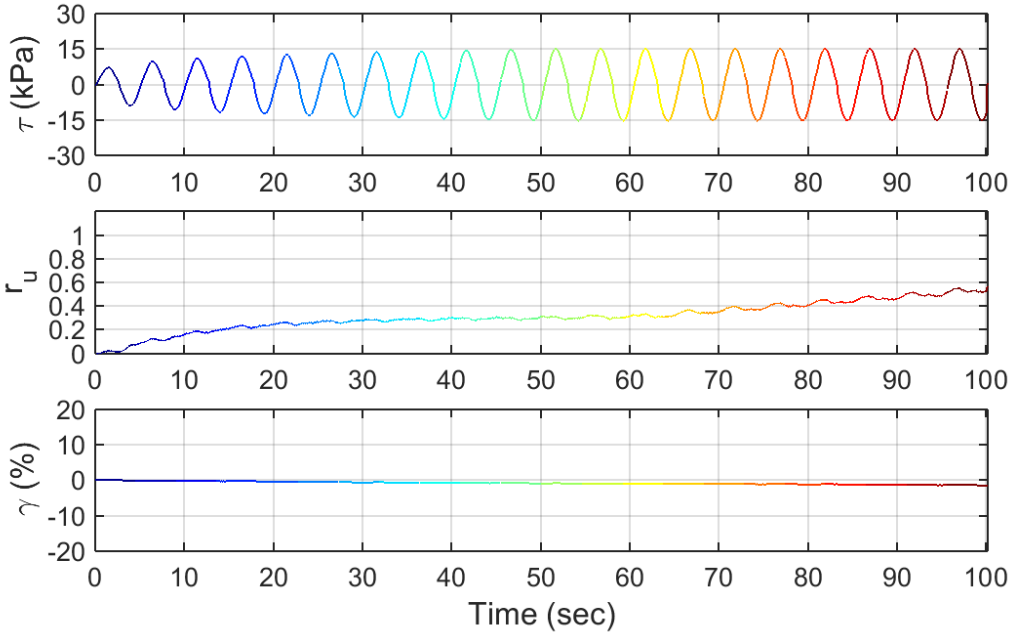

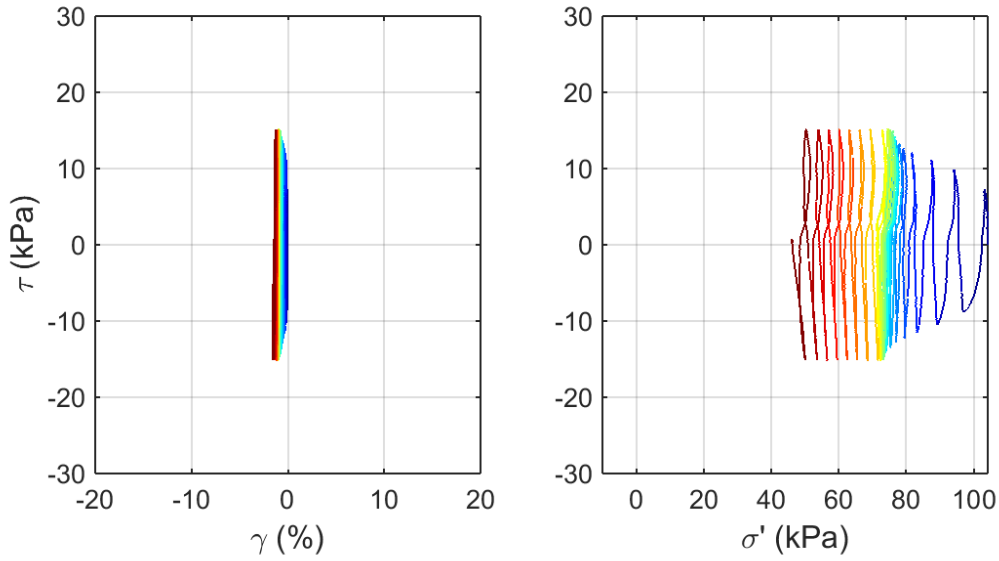

Test ID: 20130531
Nevada Sand
D_r = 56 %
Motion: New_Modulated_up_n=0.2

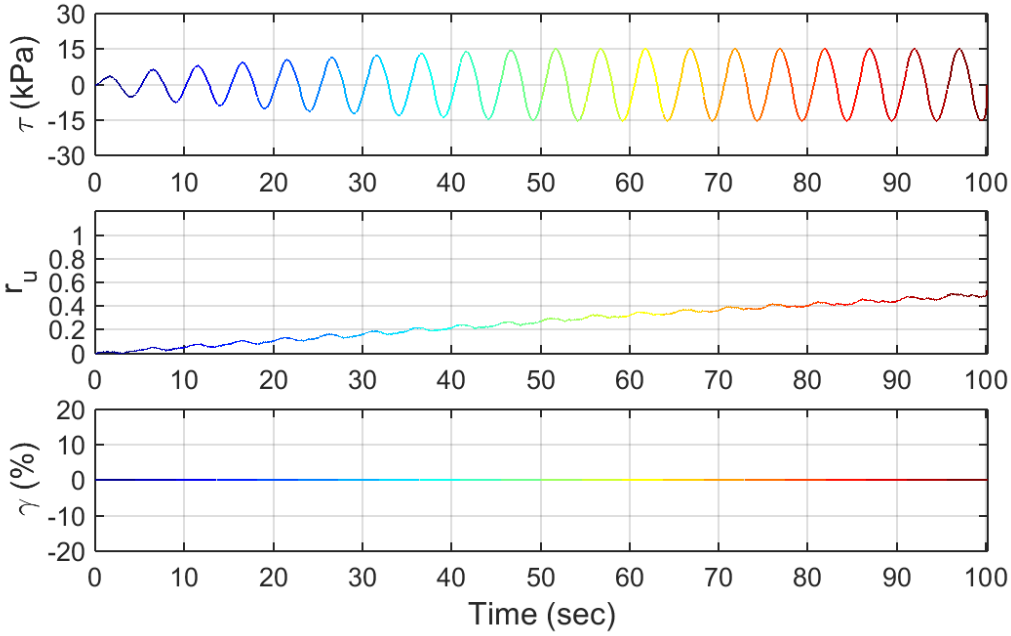

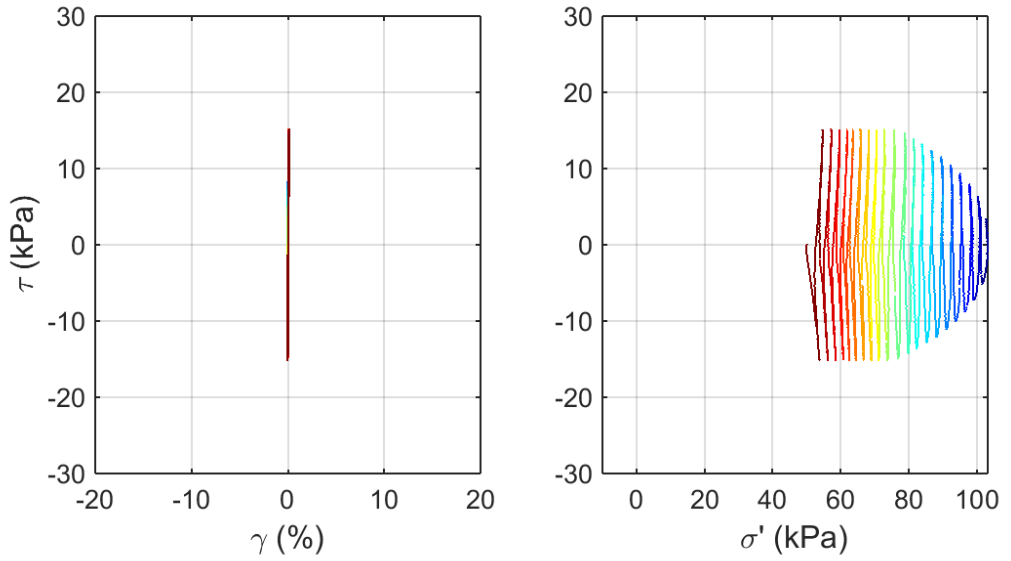

Test ID: 20130603
Nevada Sand
D_r = 52 %
Motion: New_Modulated_up_n=0.4

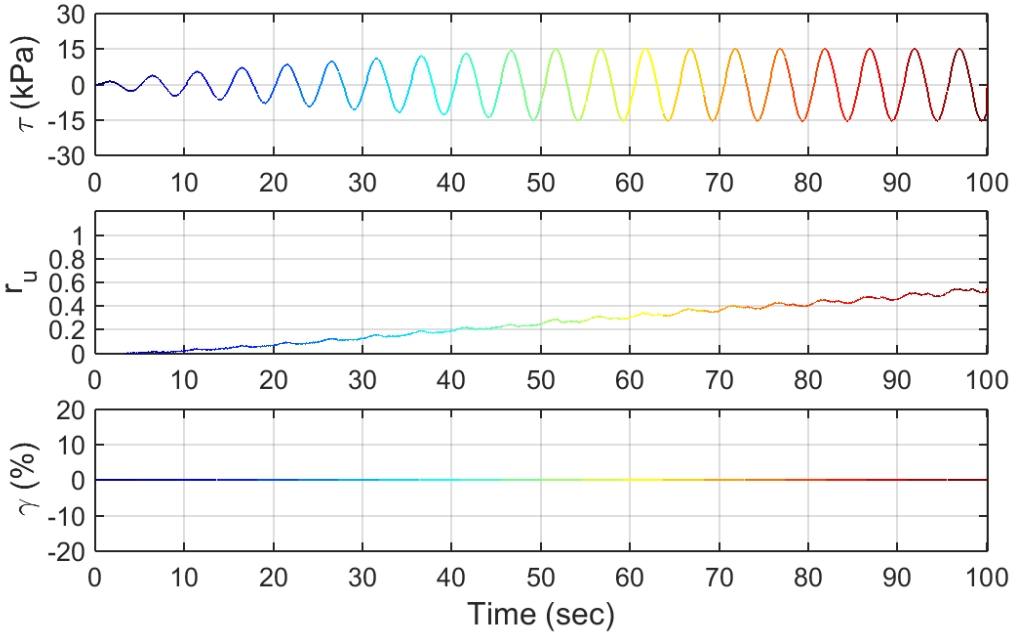

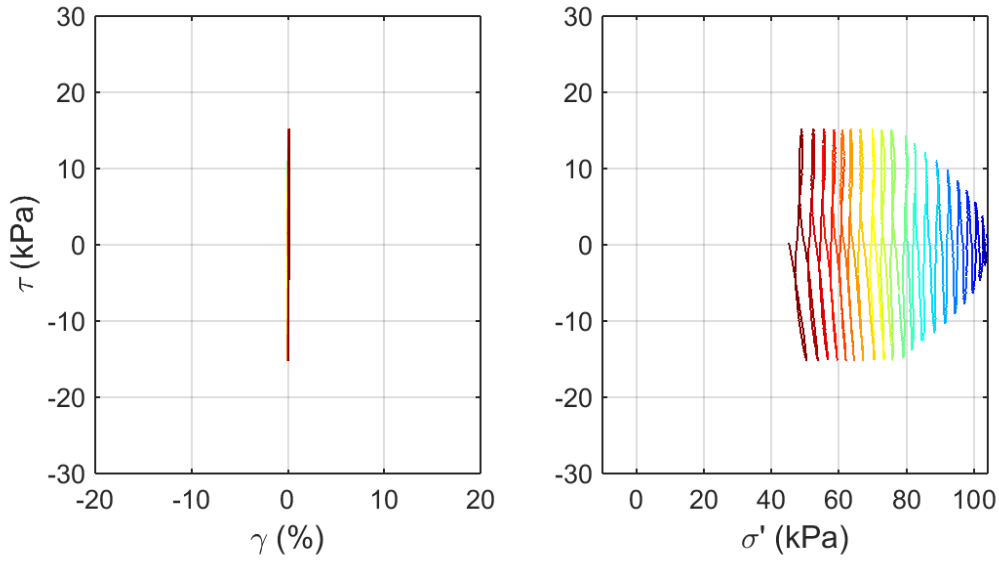

Test ID: 20130618
Nevada Sand
D_r = 52 %
Motion: New_Modulated_up_n=0.67

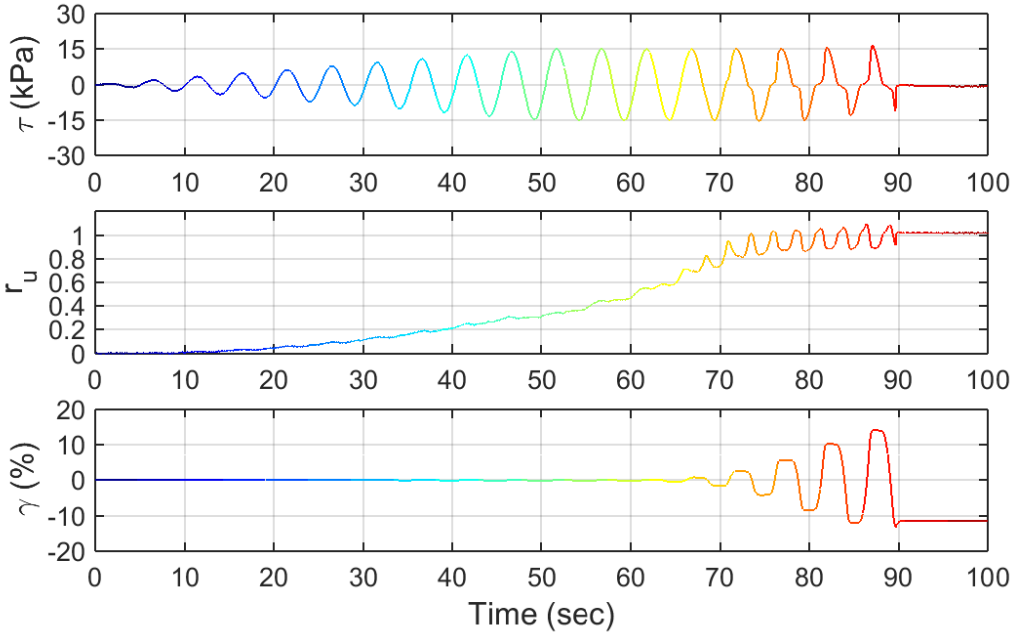

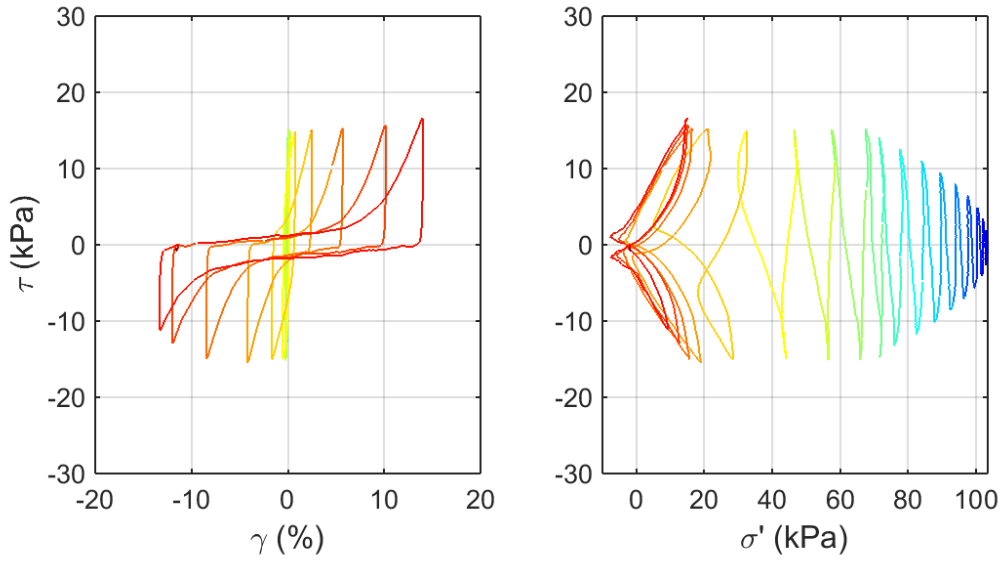

Test ID: 20130619
Nevada Sand
D_r = 39 %
Motion: New_Modulated_up_n=1.0

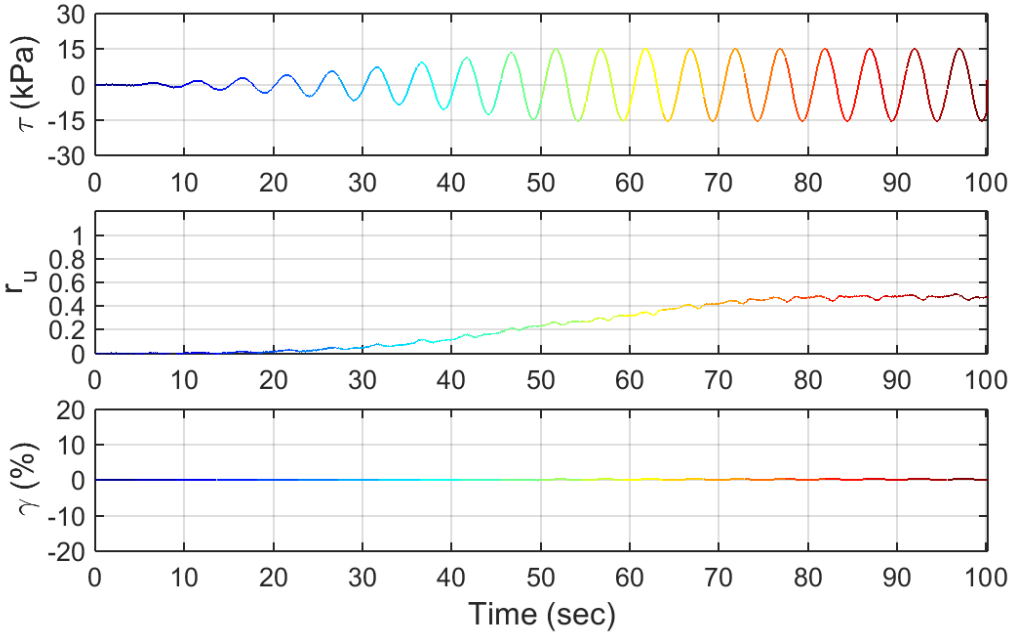

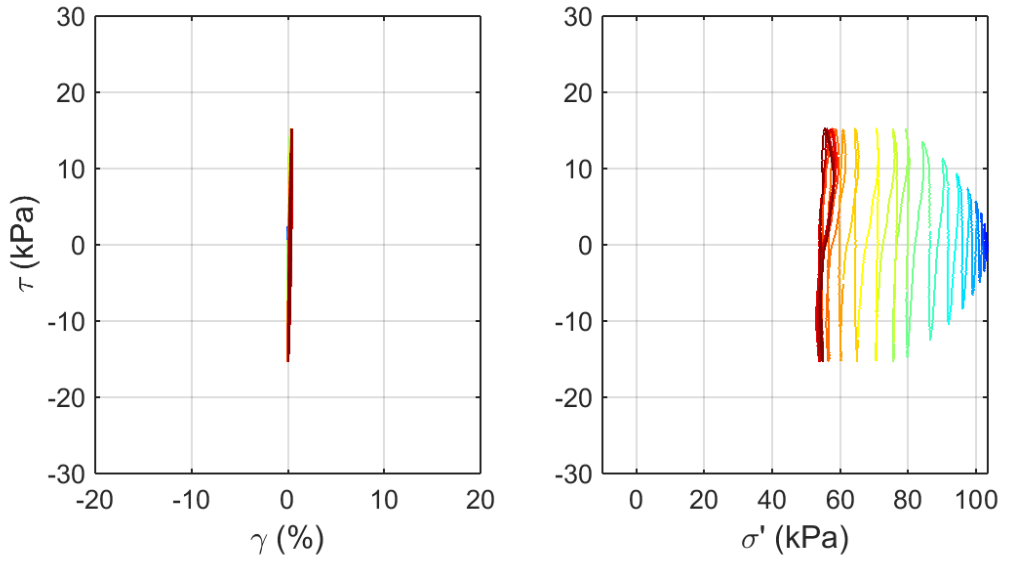

Test ID: 2013061902
Nevada Sand
D_r = 52 %
Motion: New_Modulated_up_n=1.5

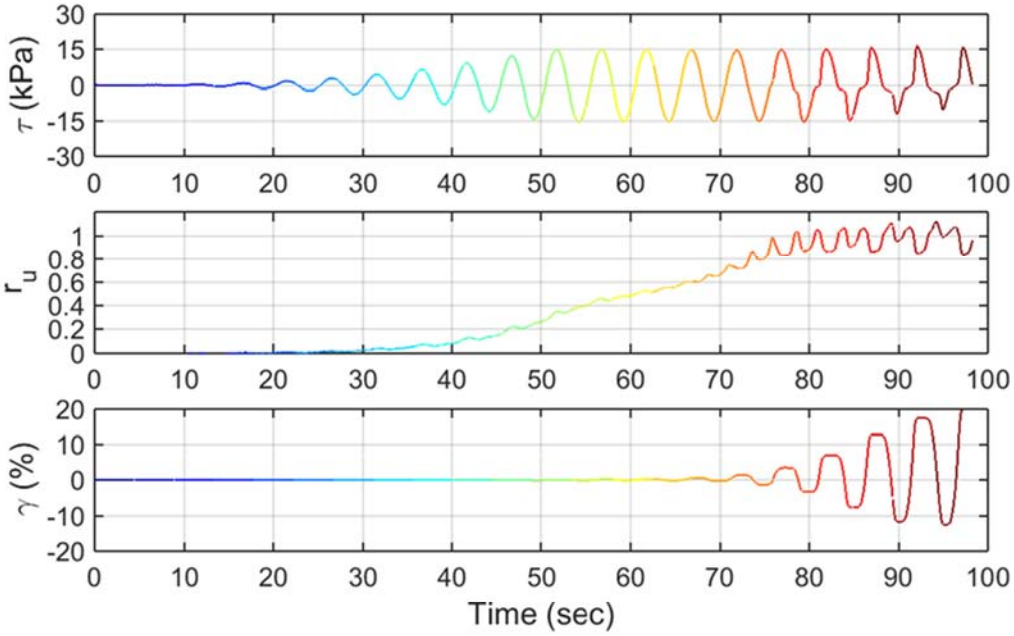

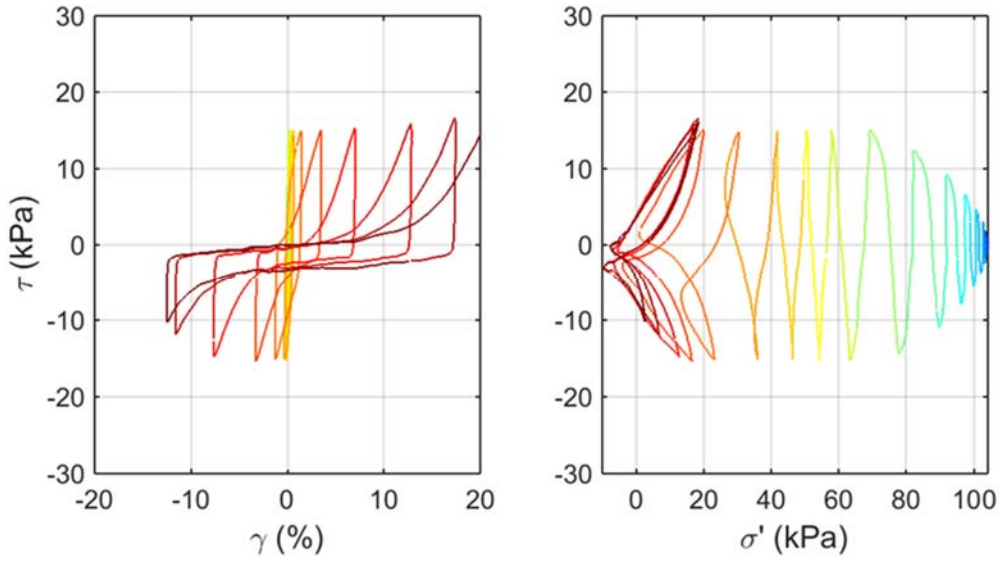

Test ID: 20130620
Nevada Sand
D_r = 41 %
Motion: New_Modulated_up_n=2.5

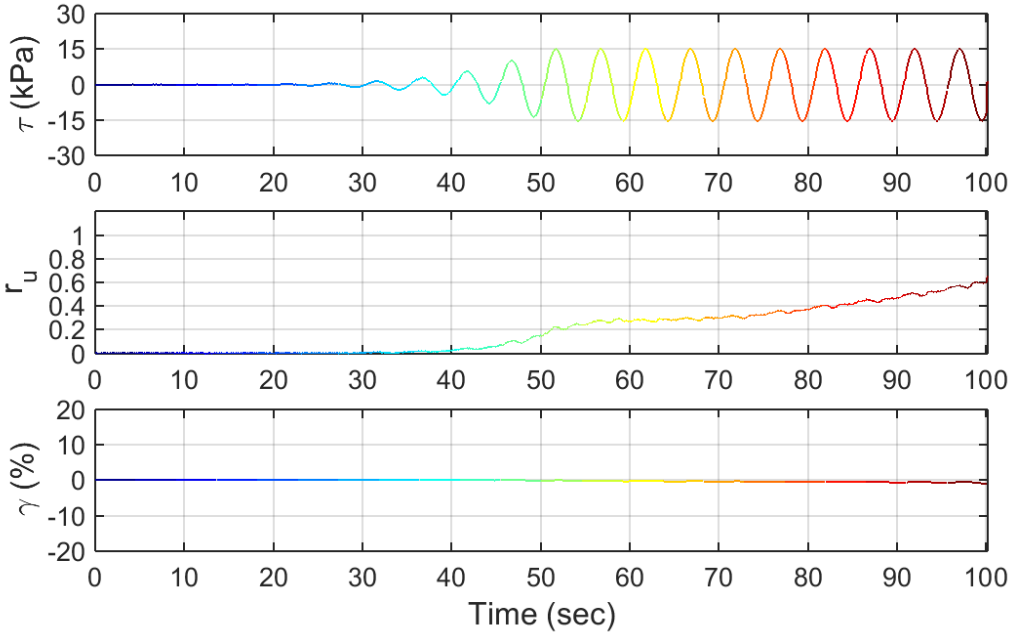

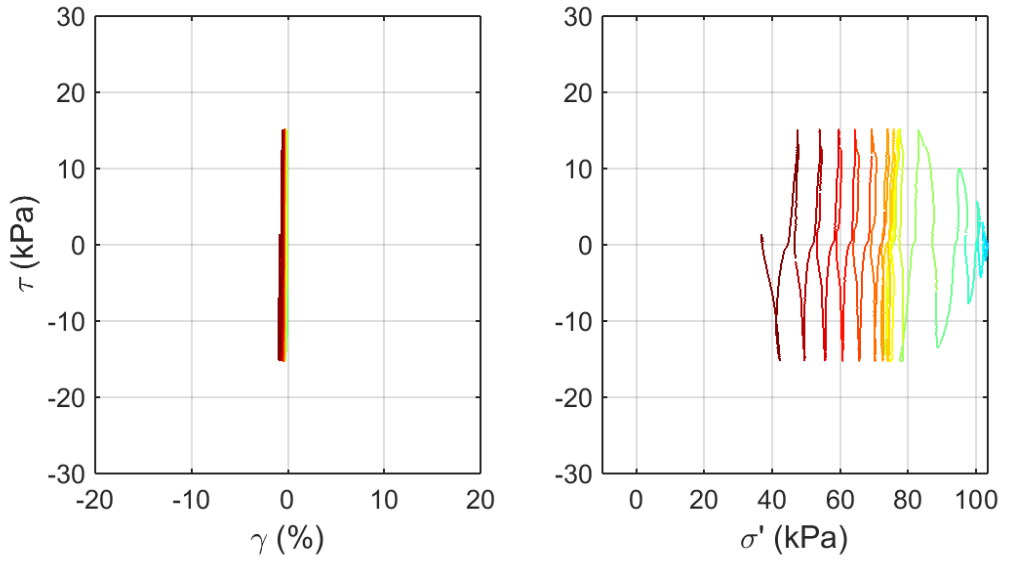

Test ID: 20130621
Nevada Sand
D_r = 43 %
Motion: New_Modulated_up_n=5

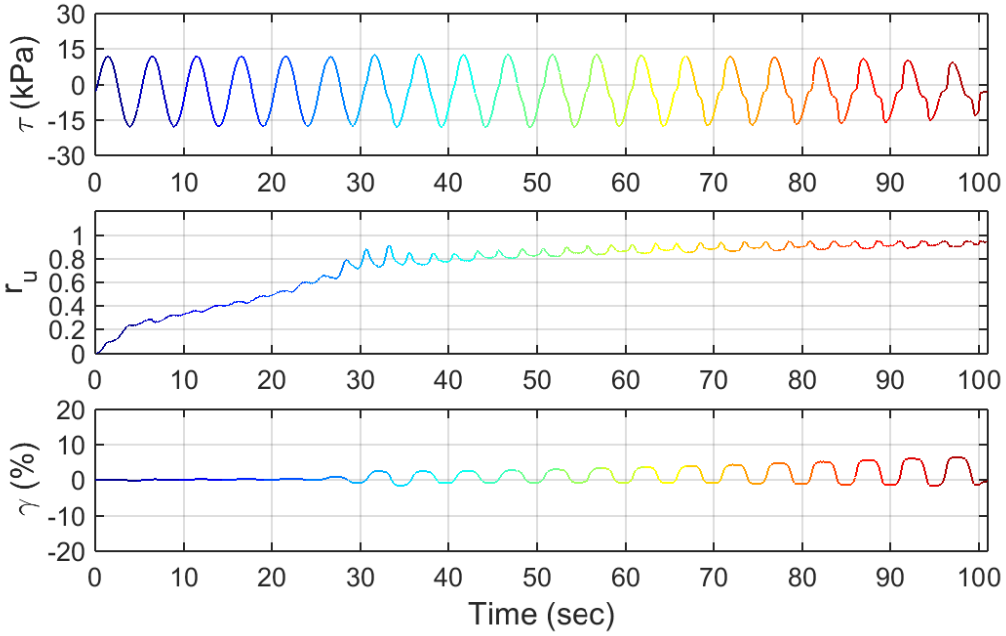

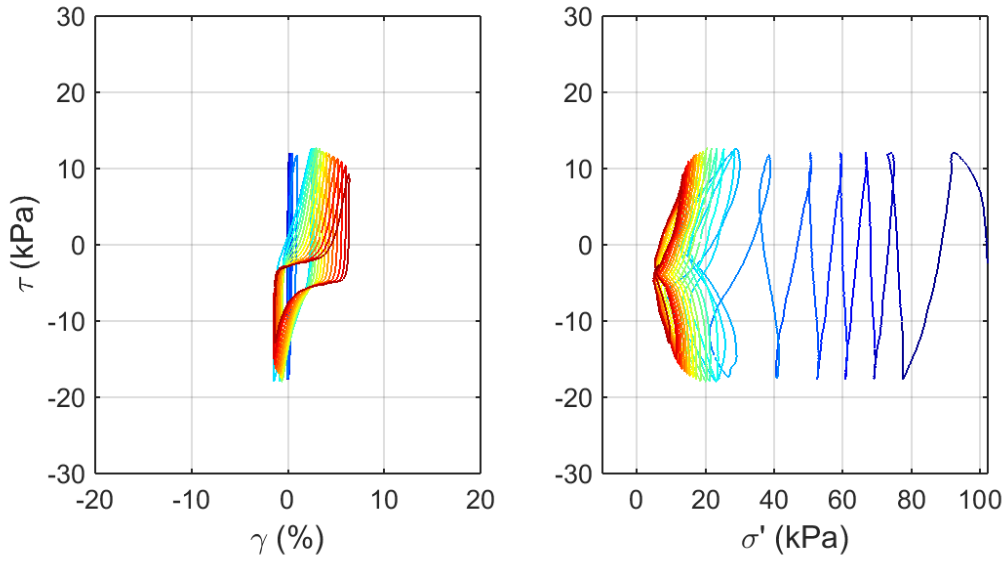

Test ID: 20130715
Nevada Sand
D_r = 39 %
Motion: New_Moduated_down_n=0.1

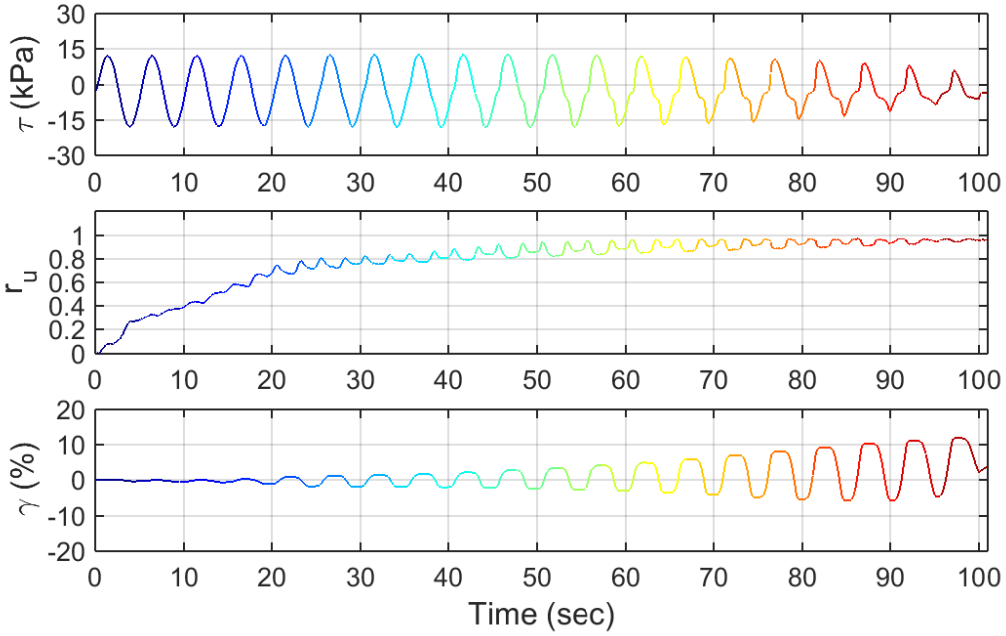

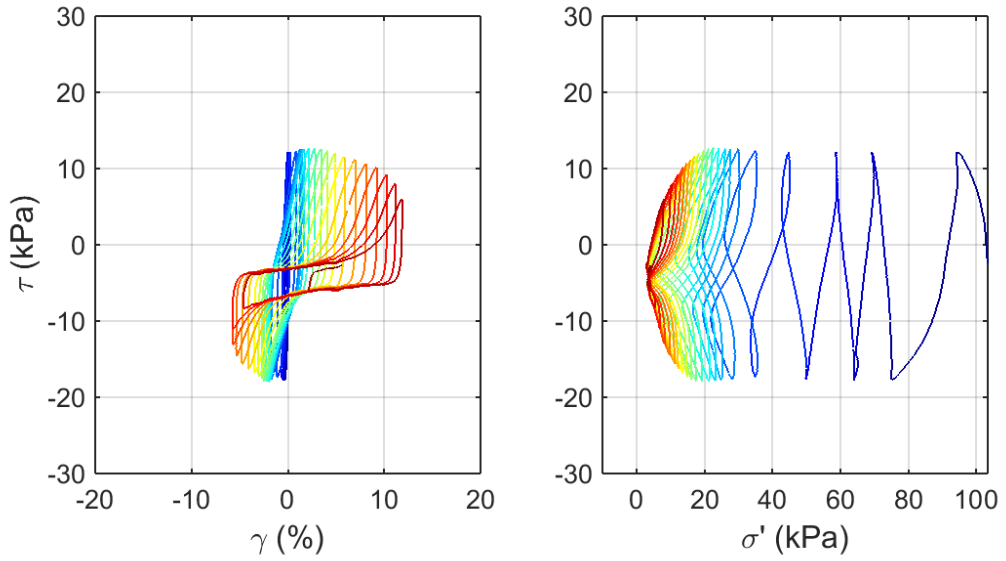

Test ID: 20130716
Nevada Sand
D_r = 39 %
Motion: New_Moduated_down_n=0.2

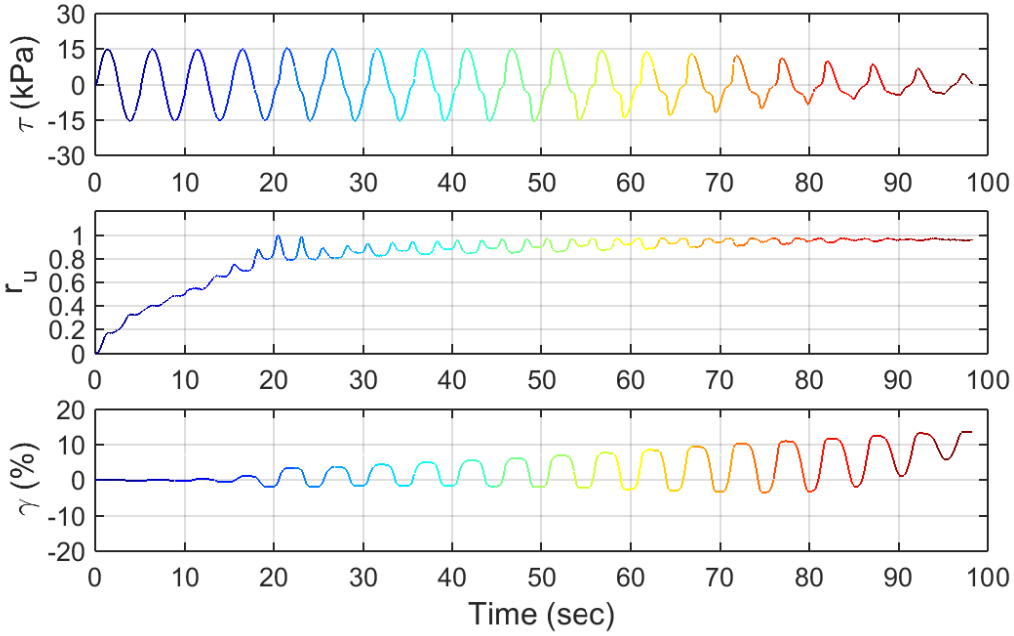

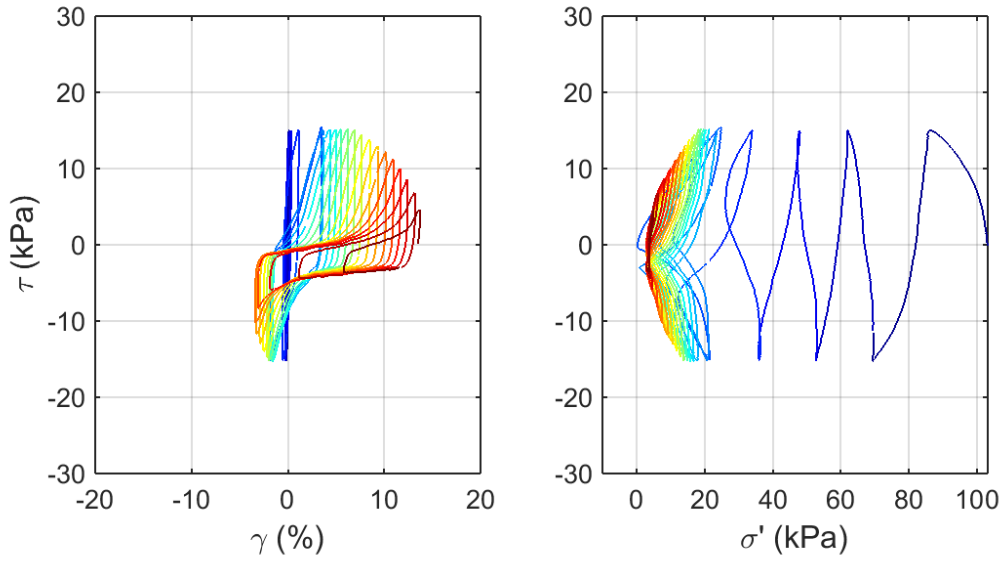

Test ID: 2013071602
Nevada Sand
D_r = 33 %
Motion: New_Moduated_down_n=0.4

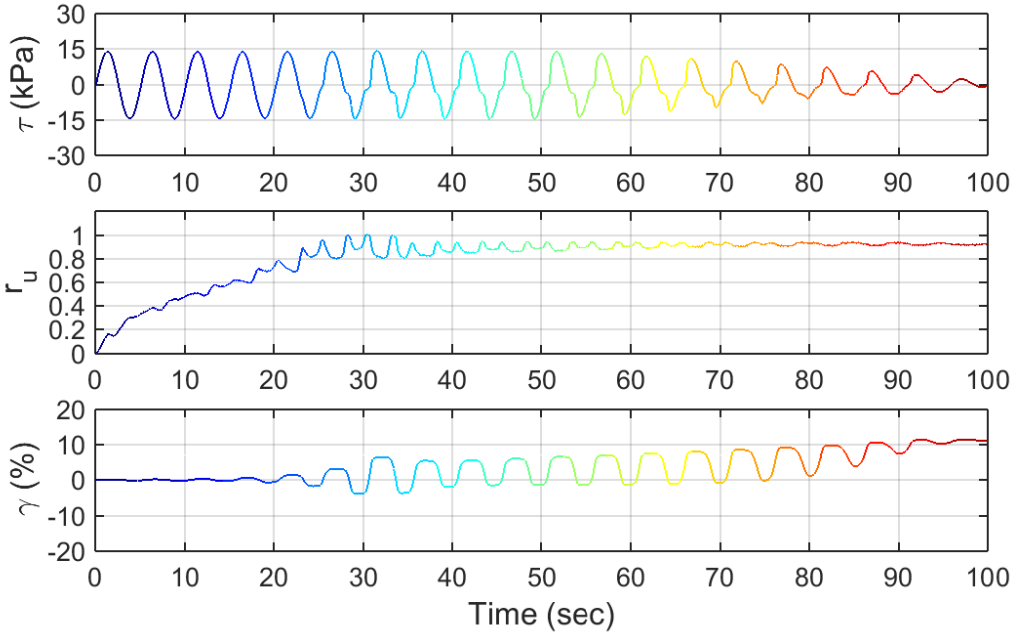

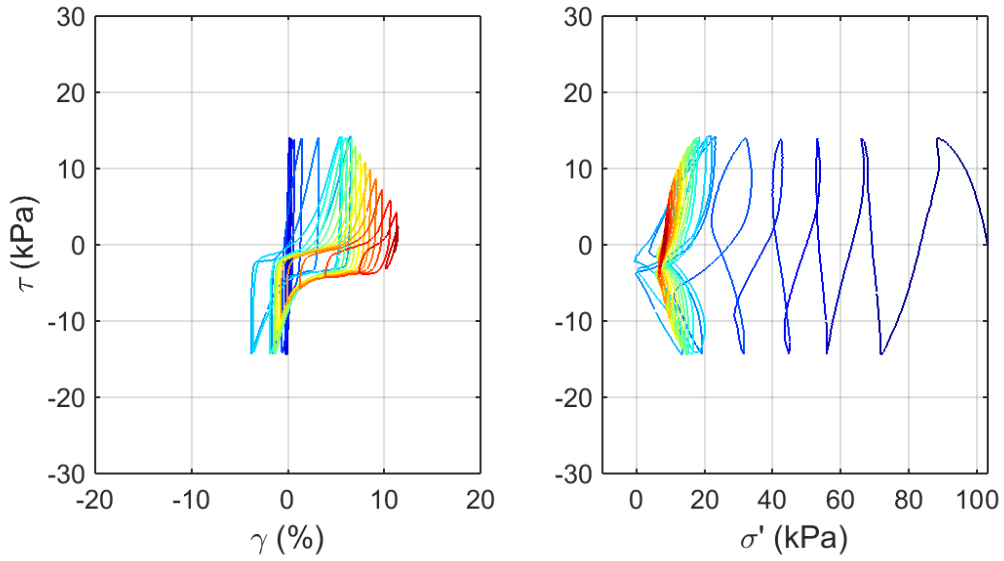

Test ID: 2013071603
Nevada Sand
D_r = 35 %
Motion: New_Moduated_down_n=0.67

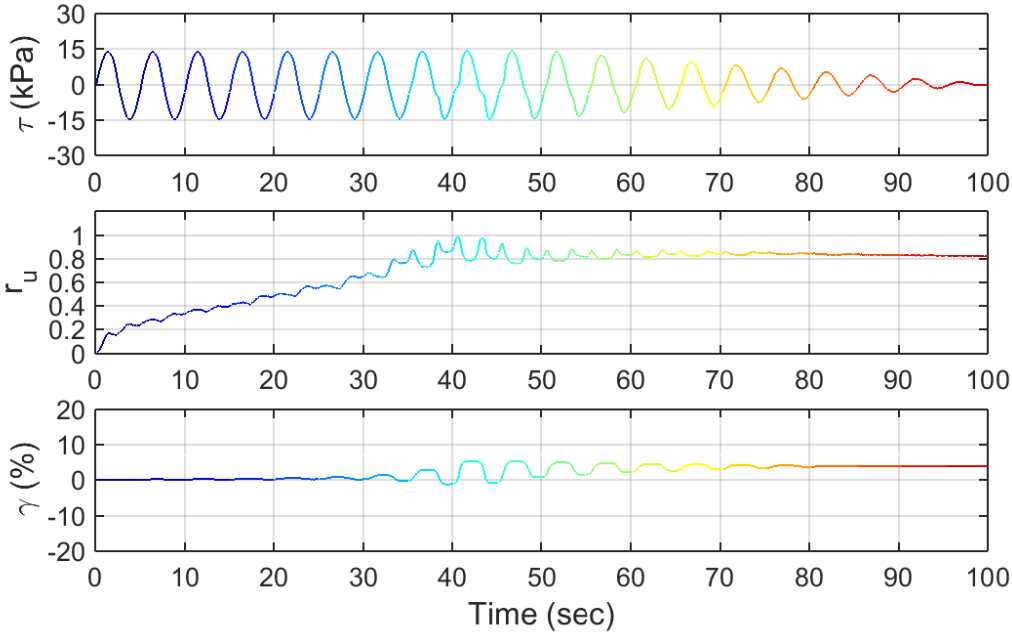

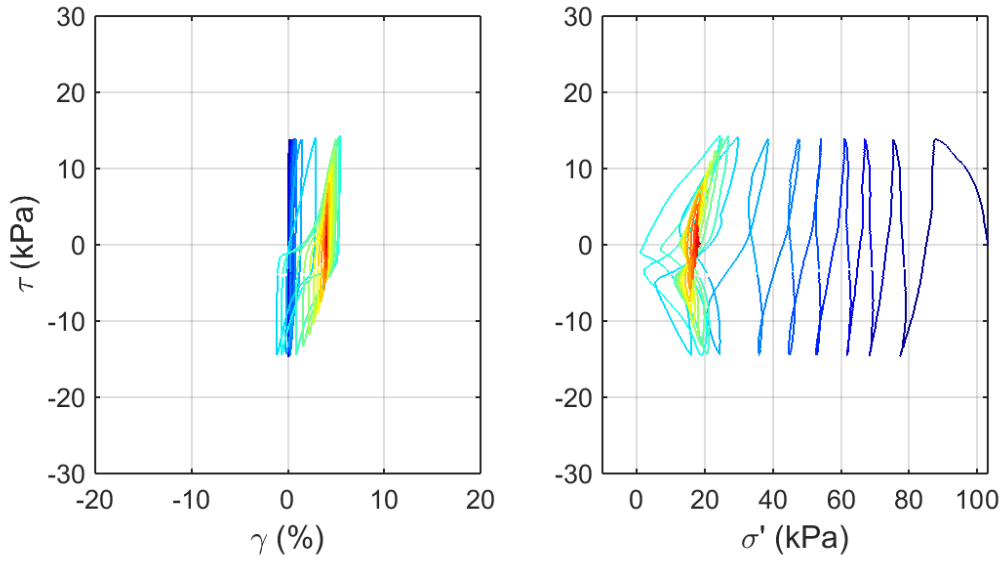

Test ID: 20130717
Nevada Sand
D_r = 43 %
Motion: New_Moduated_down_n=1

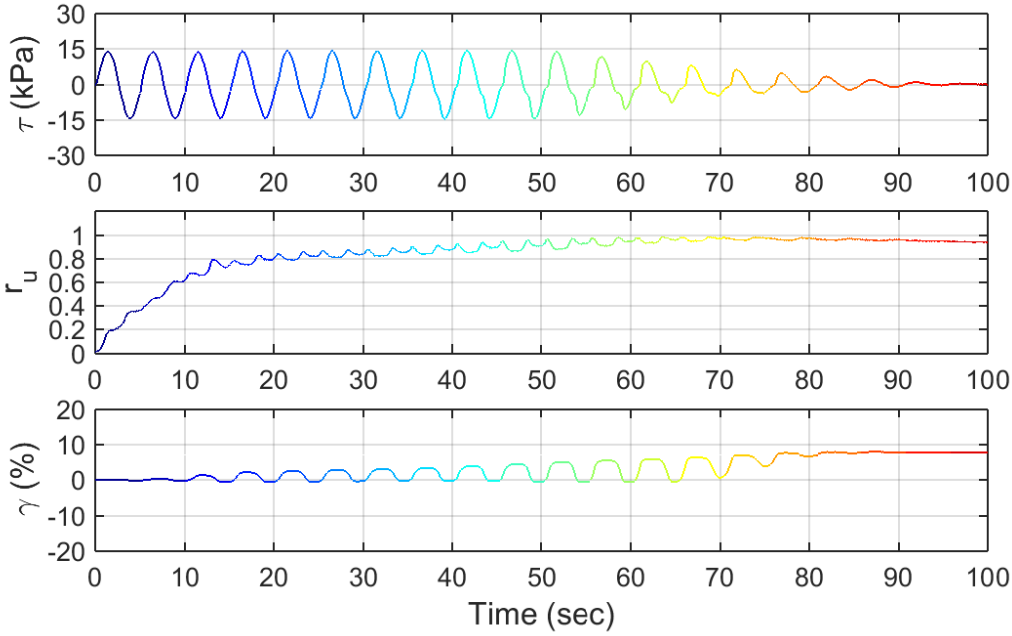

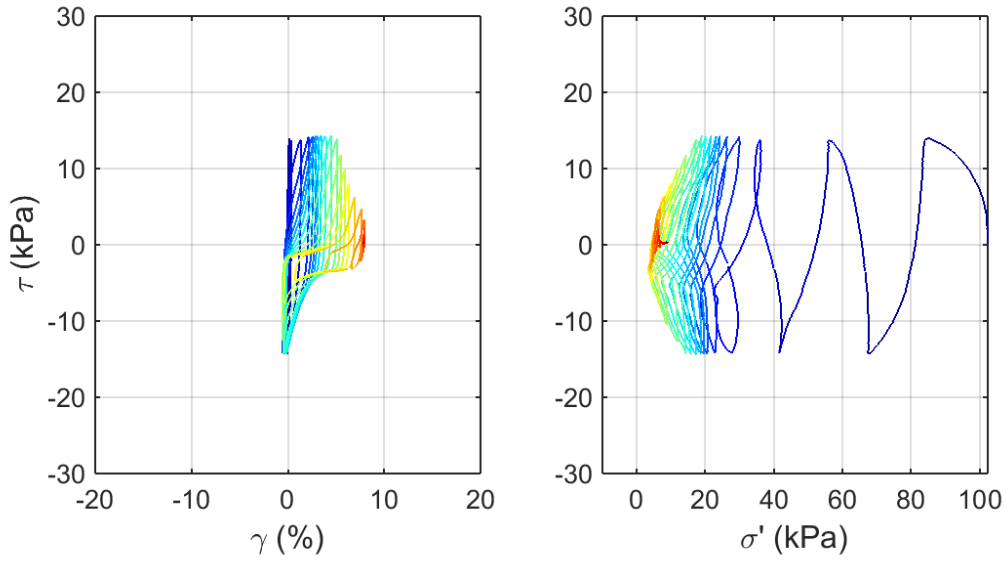

Test ID: 20130718
Nevada Sand
D_r = 35 %
Motion: New_Moduated_down_n=1.5

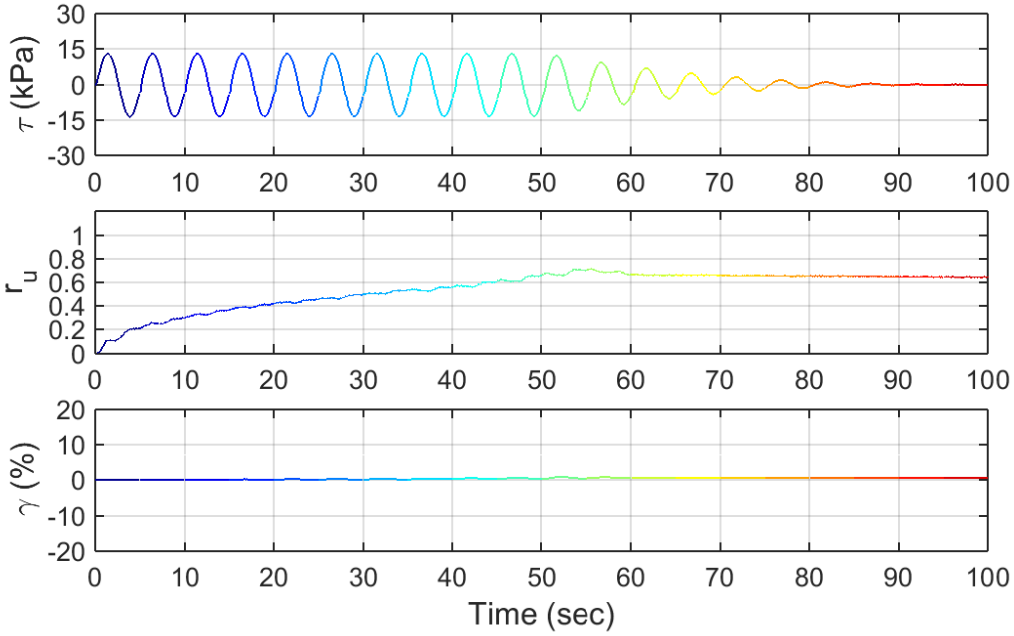

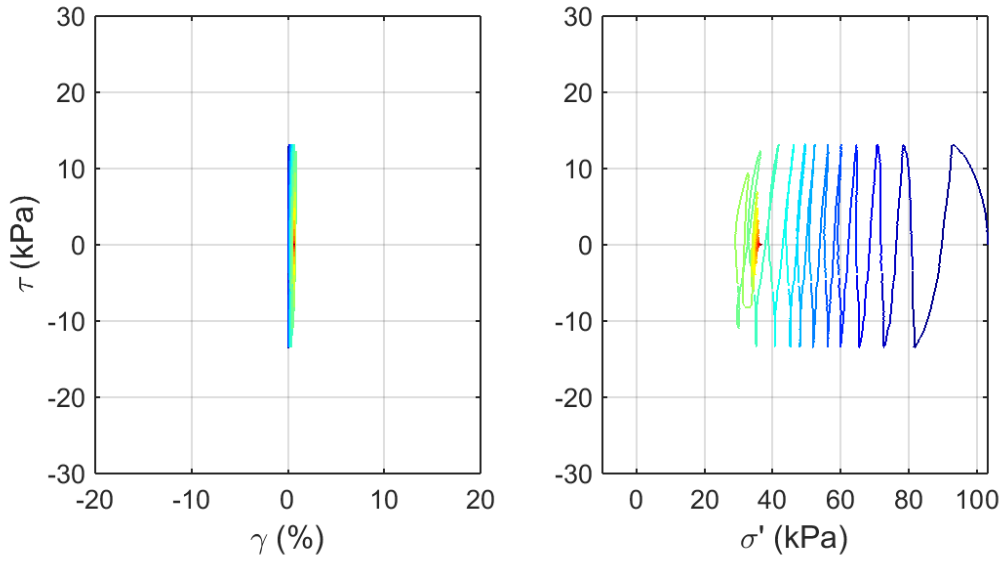

Test ID: 2013071802
Nevada Sand
D_r = 41 %
Motion: New_Moduated_down_n=2.5

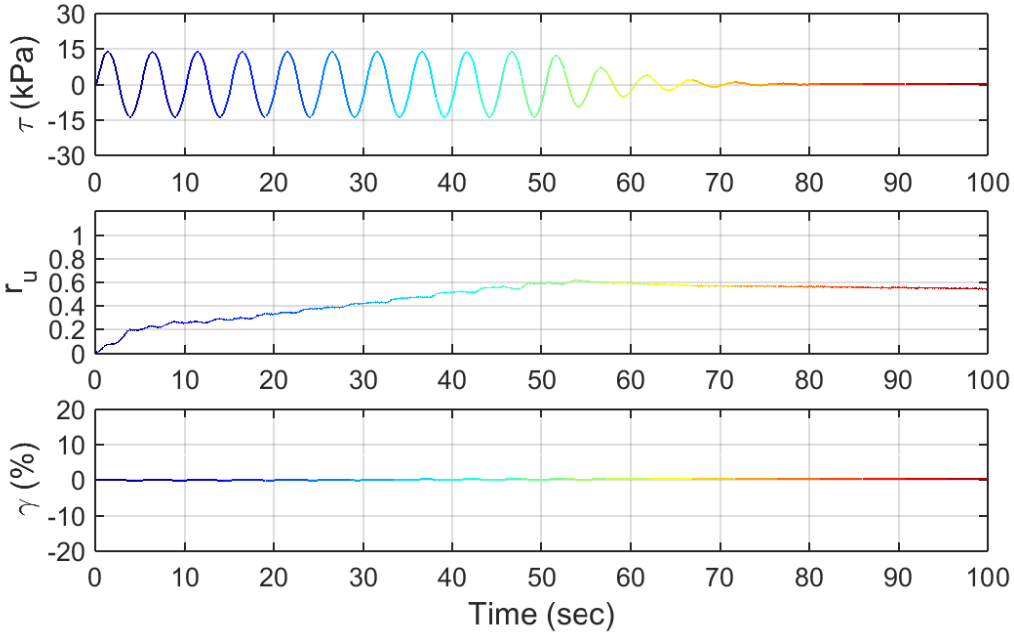

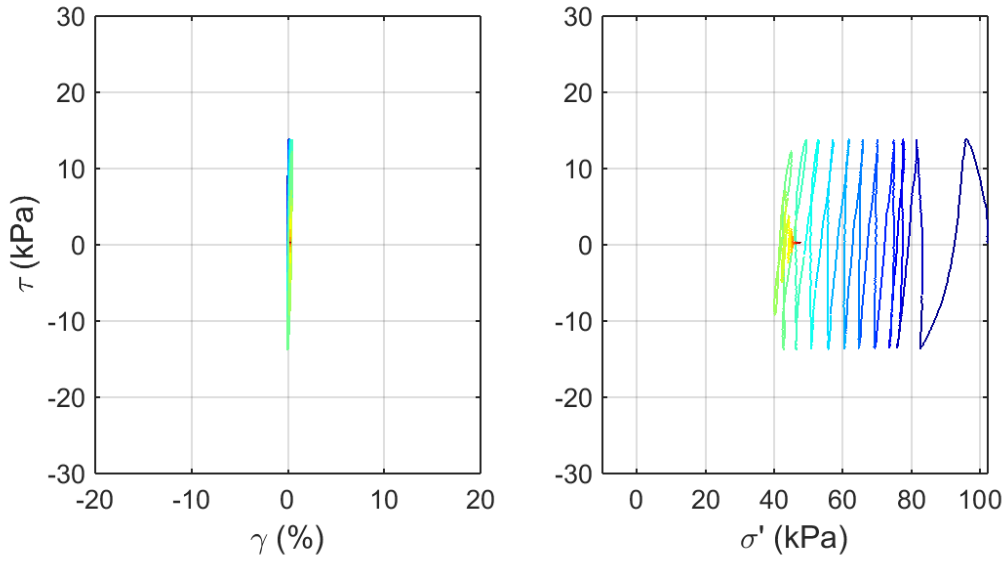

Test ID: 20130719
Nevada Sand
D_r = 44 %
Motion: New_Moduated_down_n=5

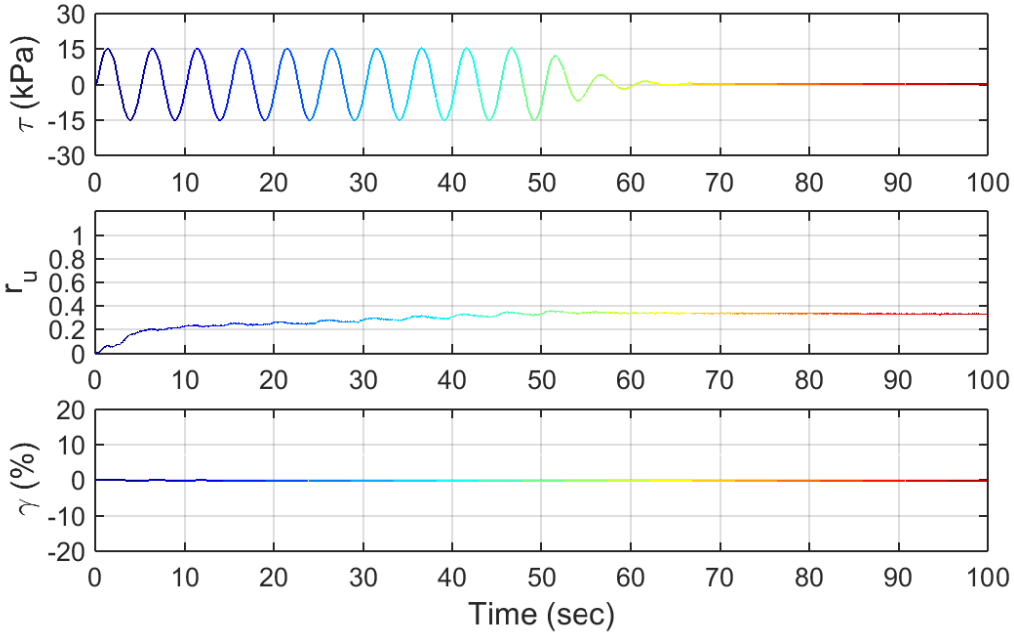

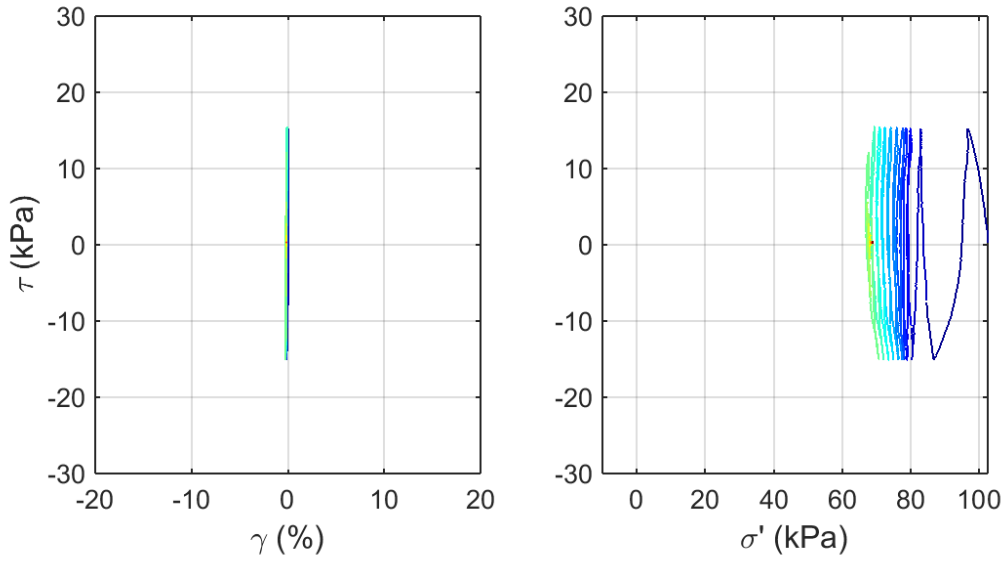

Test ID: 20130724
Nevada Sand
D_r = 53 %
Motion: New_Moduated_down_n=10

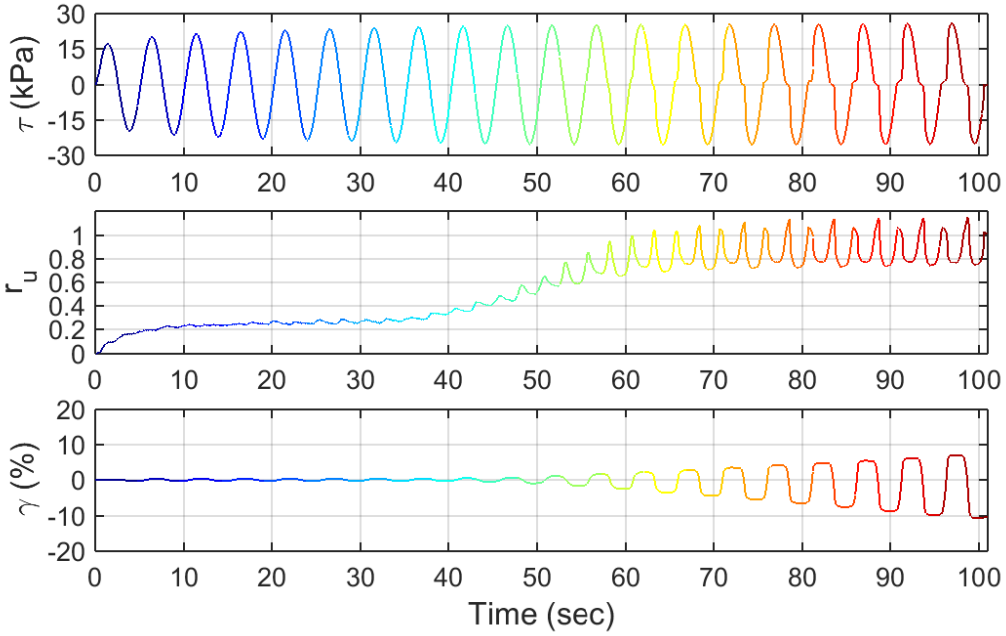

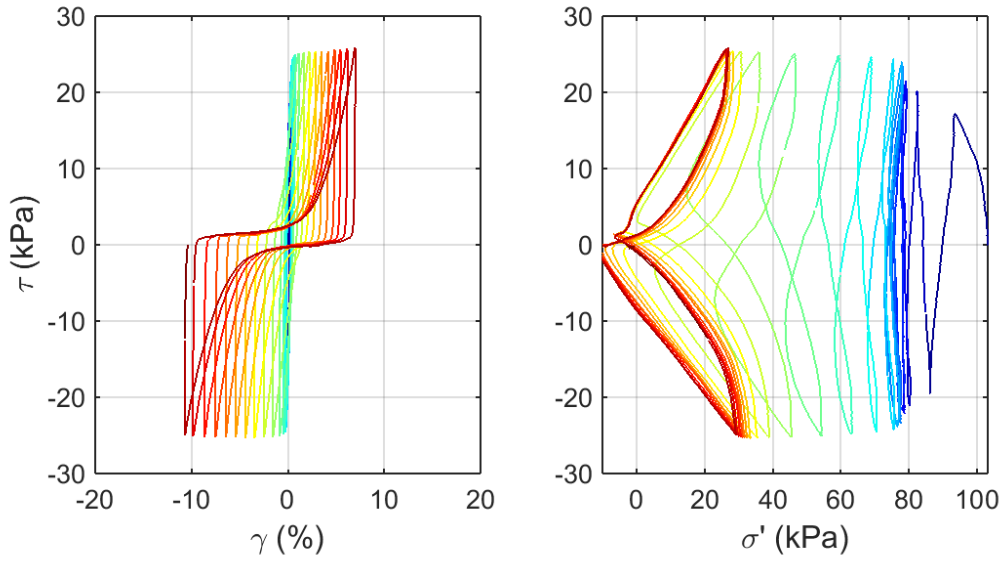

Test ID: 20130731
Nevada Sand
D_r = 76 %
Motion: New_Modulated_up_n=0.1

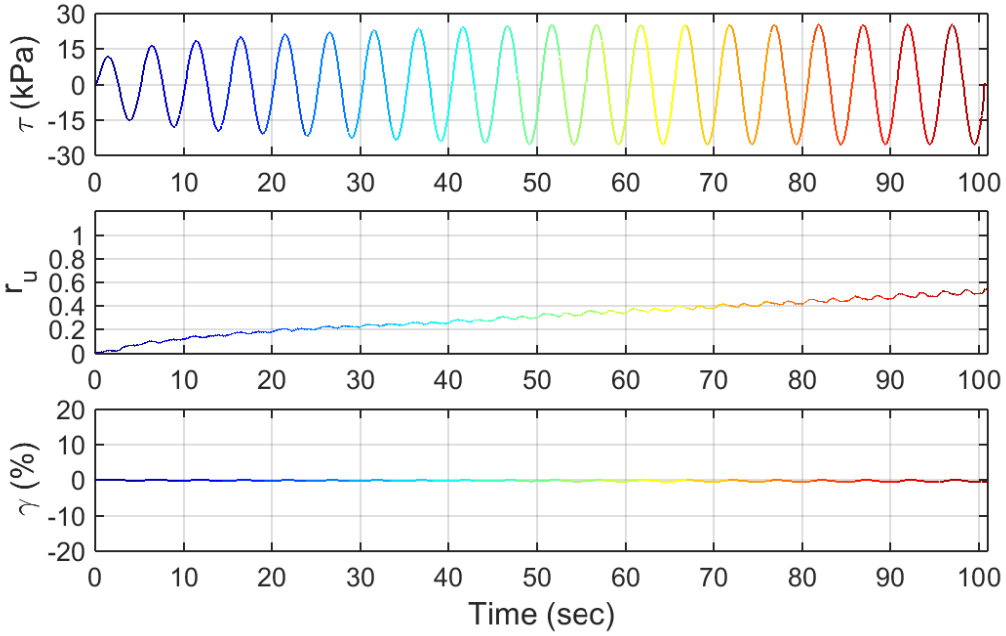

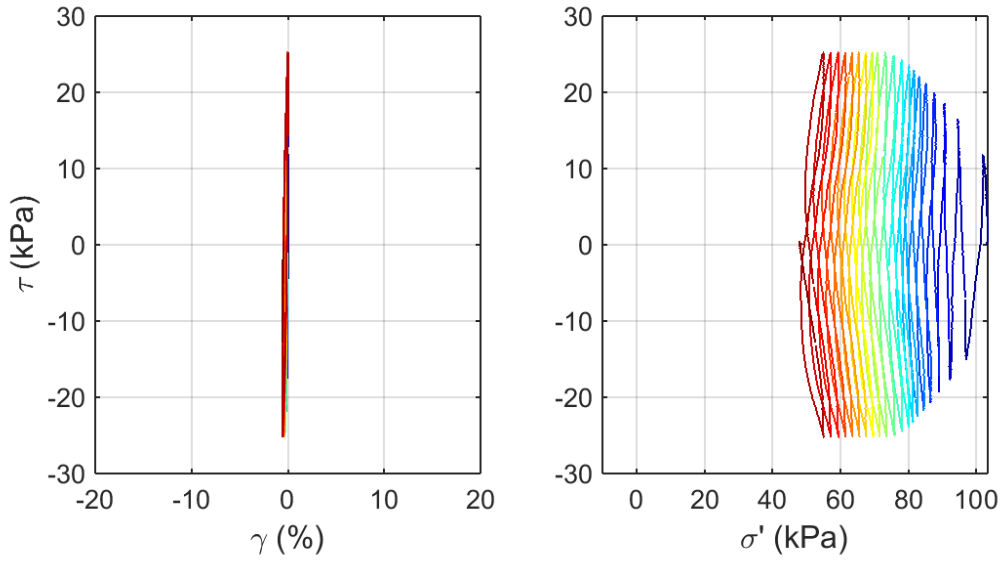

Test ID: 20130802
Nevada Sand
D_r = 94 %
Motion: New_Modulated_up_n=0.2

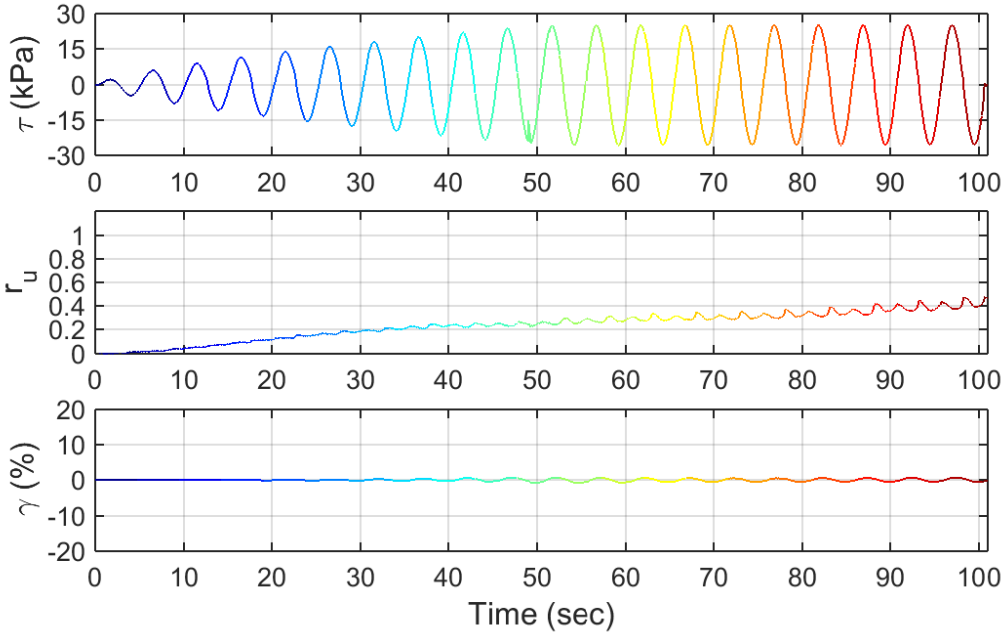

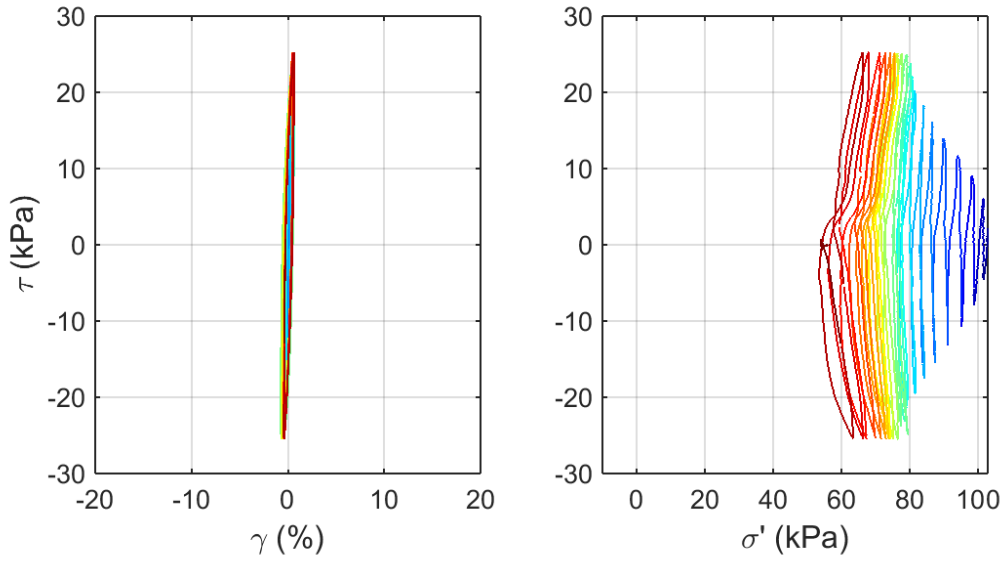

Test ID: 20130805
Nevada Sand
D_r = 77 %
Motion: New_Modulated_up_n=0.67

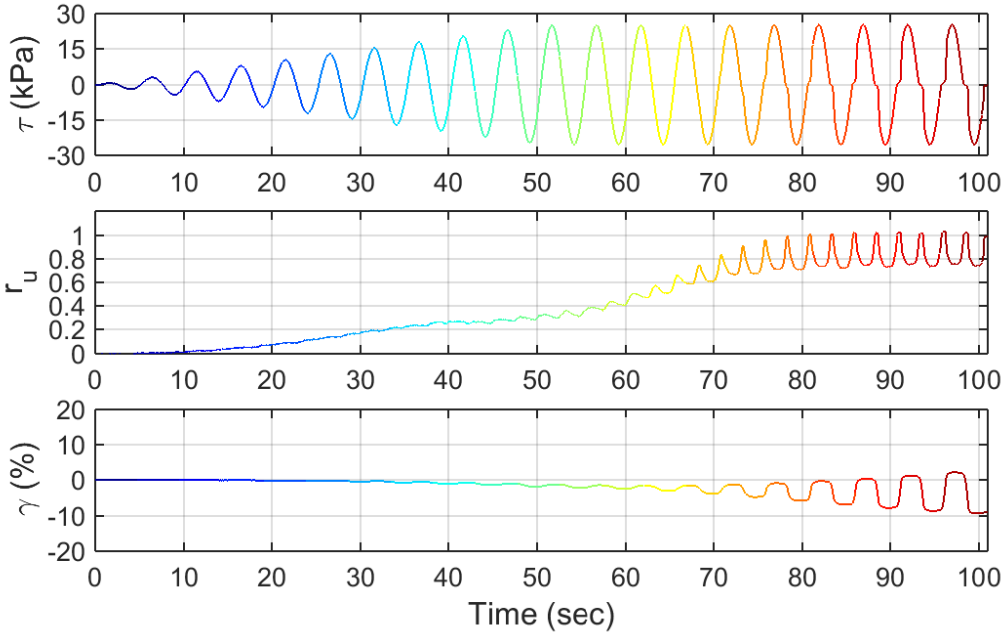

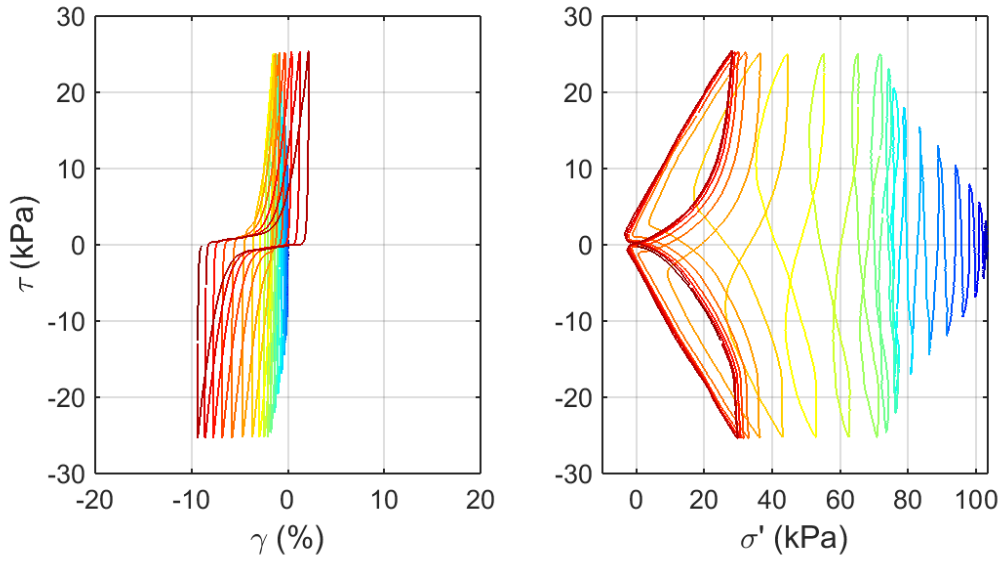

Test ID: 2013080502
Nevada Sand
D_r = 72 %
Motion: New_Modulated_up_n=1.0

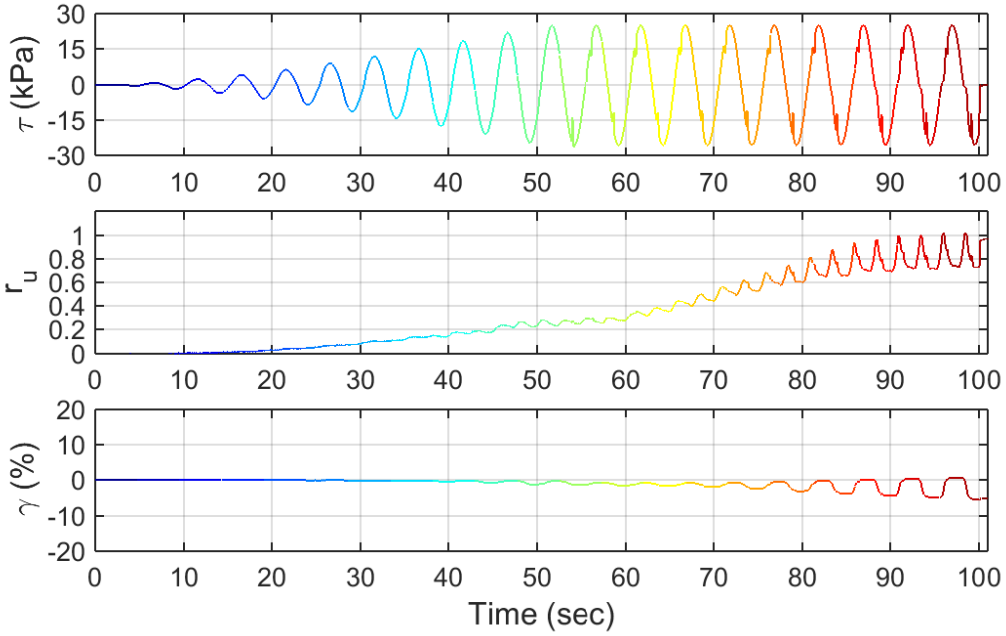

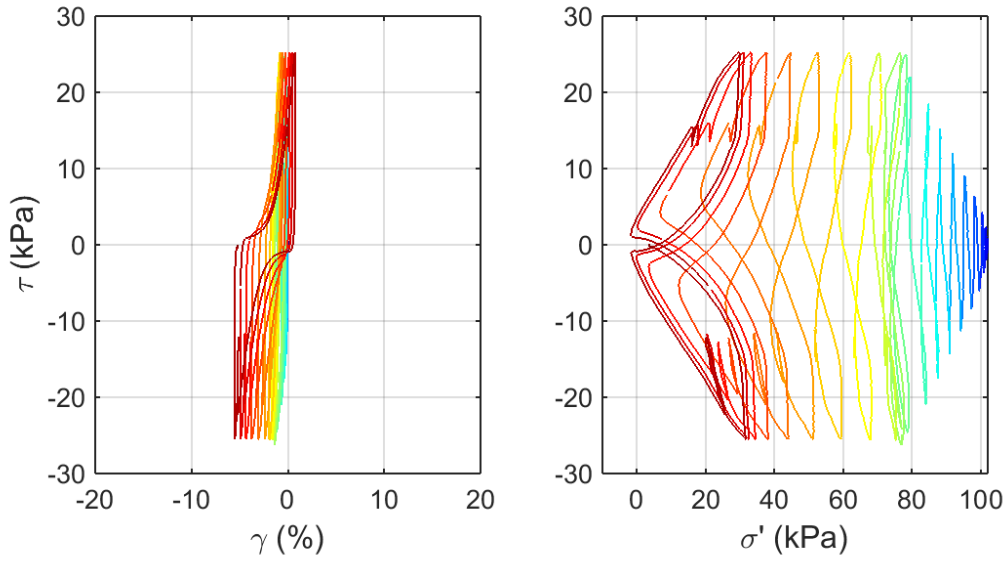

Test ID: 2013080602
Nevada Sand
D_r = 73 %
Motion: New_Modulated_up_n=1.5

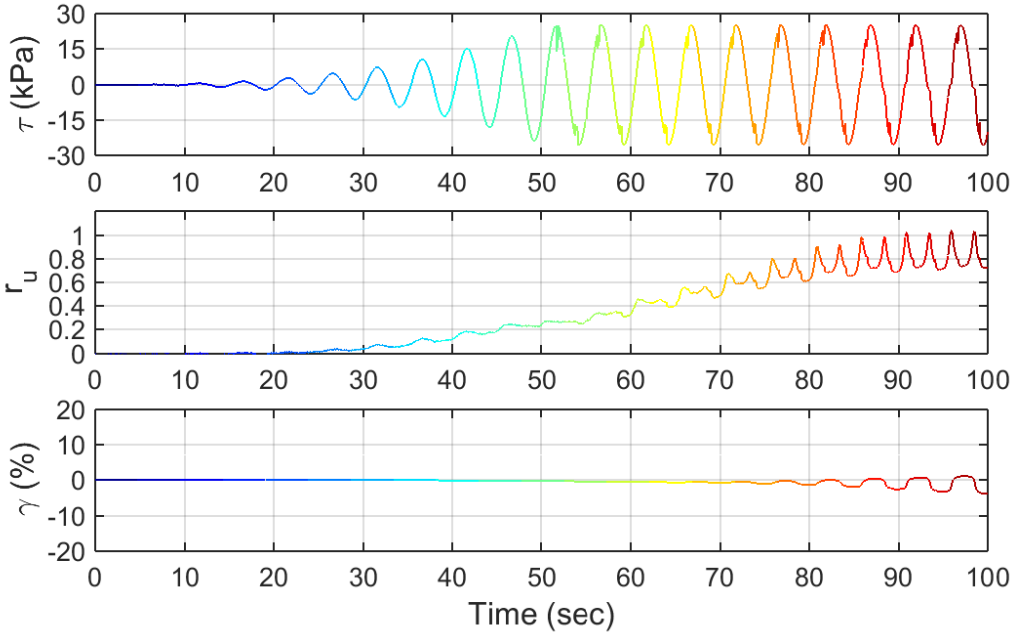

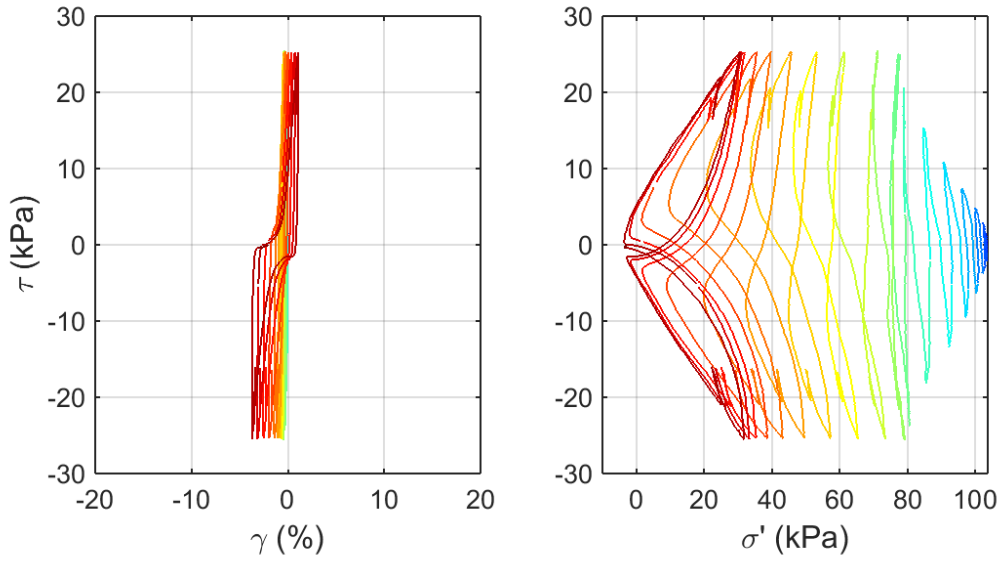

Test ID: 20130807
Nevada Sand
D_r = 85 %
Motion: New_Modulated_up_n=2.5

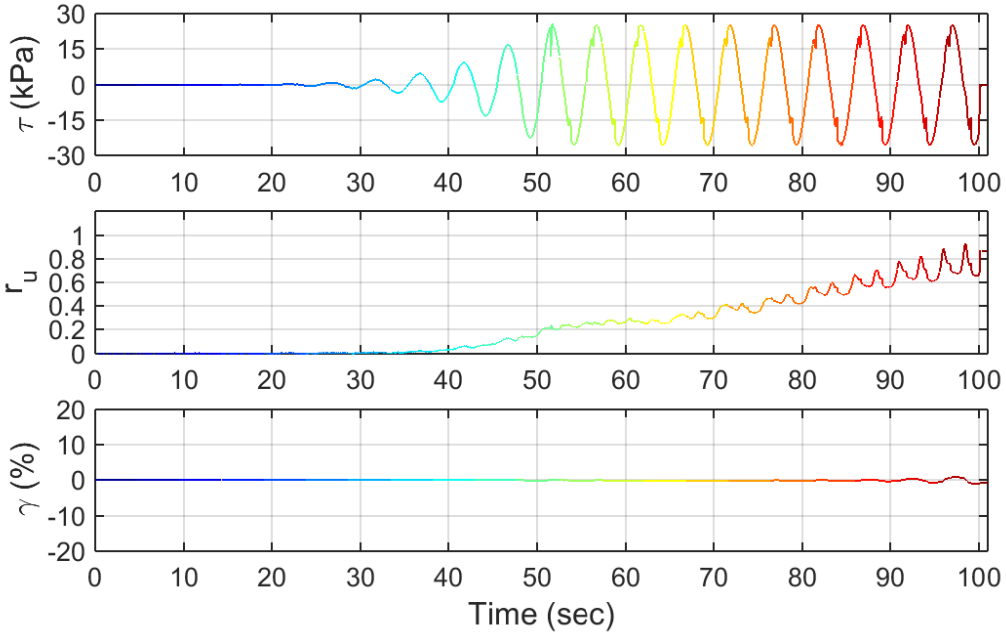

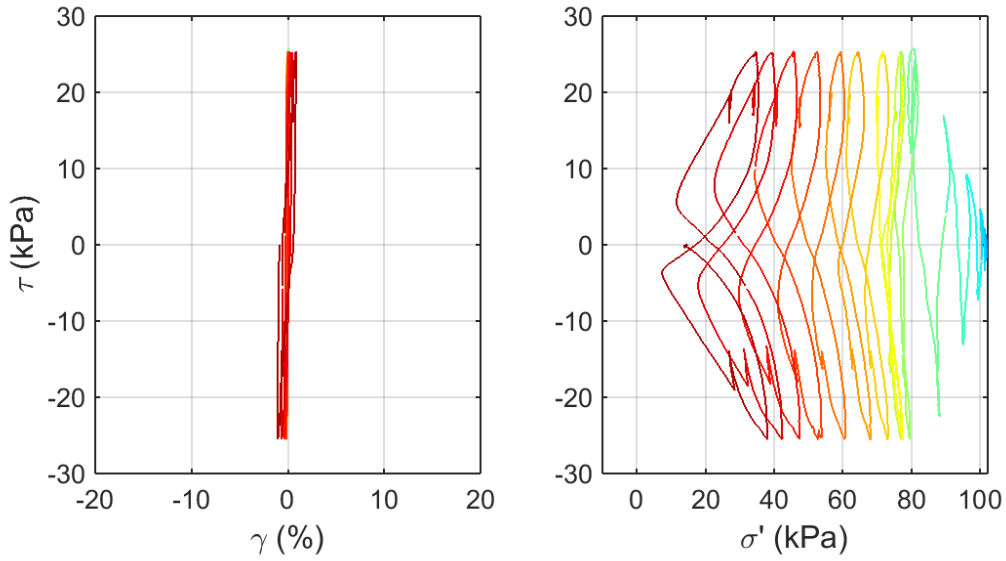

Test ID: 2013080702
Nevada Sand
D_r = 88 %
Motion: New_Modulated_up_n=5

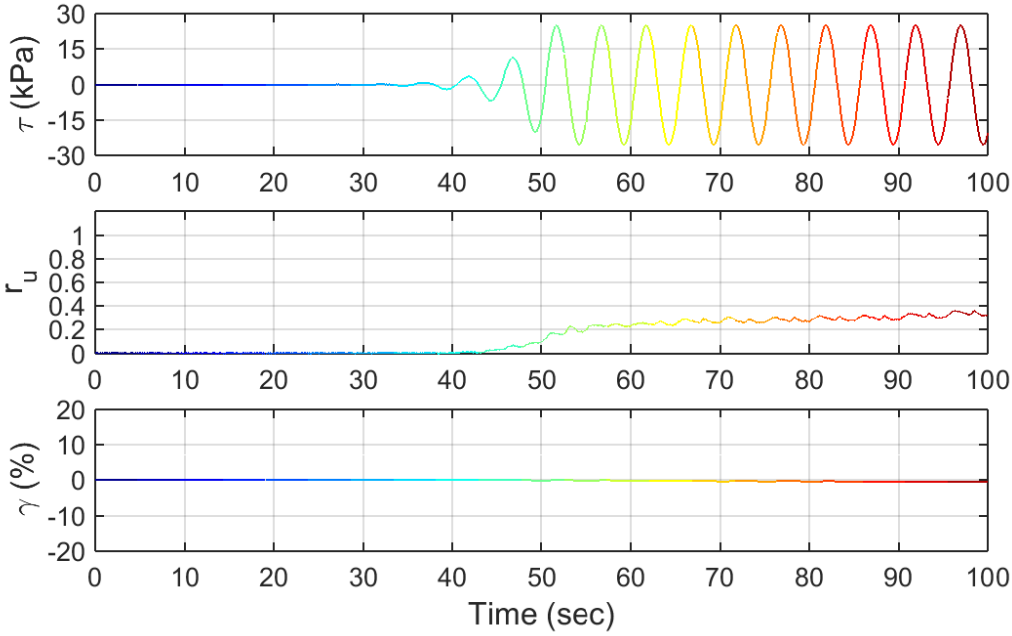

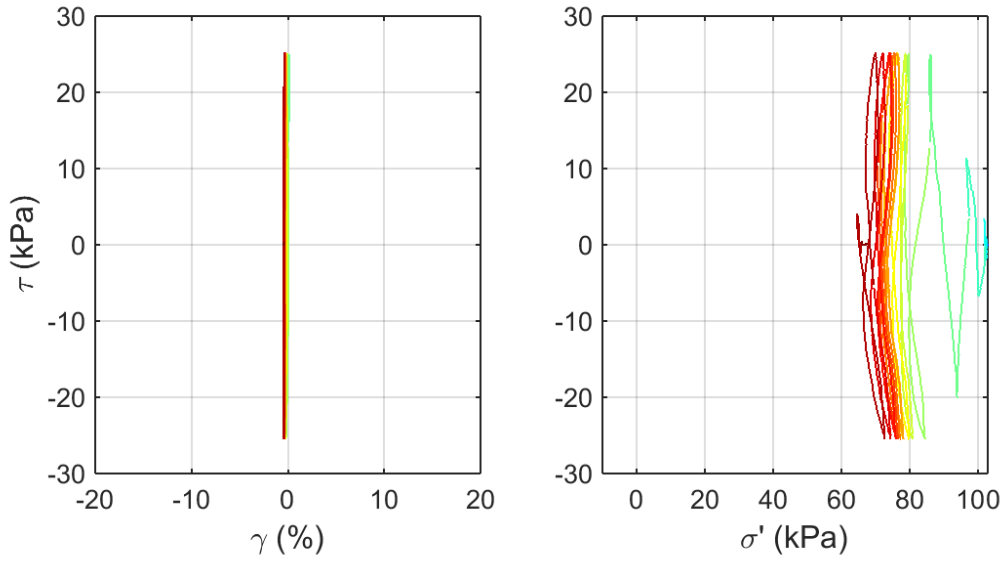

Test ID: 20130809
Nevada Sand
D_r = 90 %
Motion: New_Modulated_up_n=10

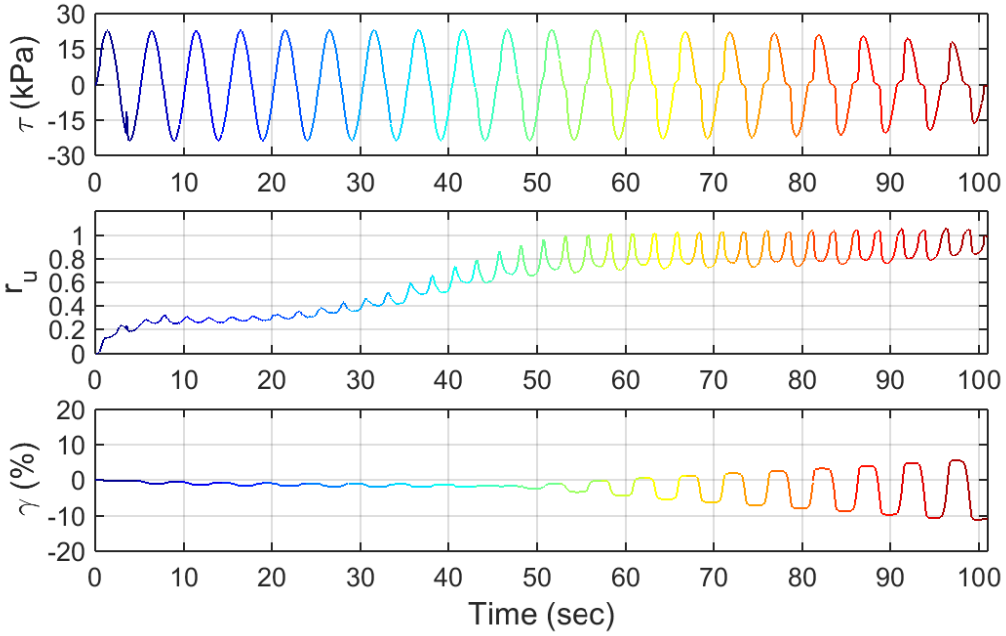

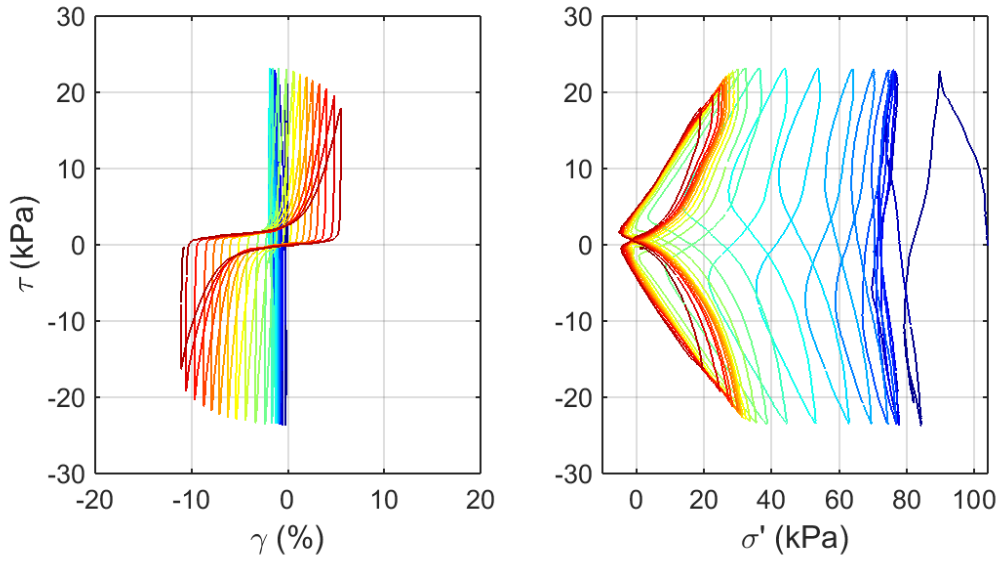

Test ID: 20130813
Nevada Sand
D_r = 73 %
Motion: New_Modulated_down_n=0.1

APPENDIX A.4. CSS DATA: TRANSIENT LOADING (D_R = 36 TO 55%)

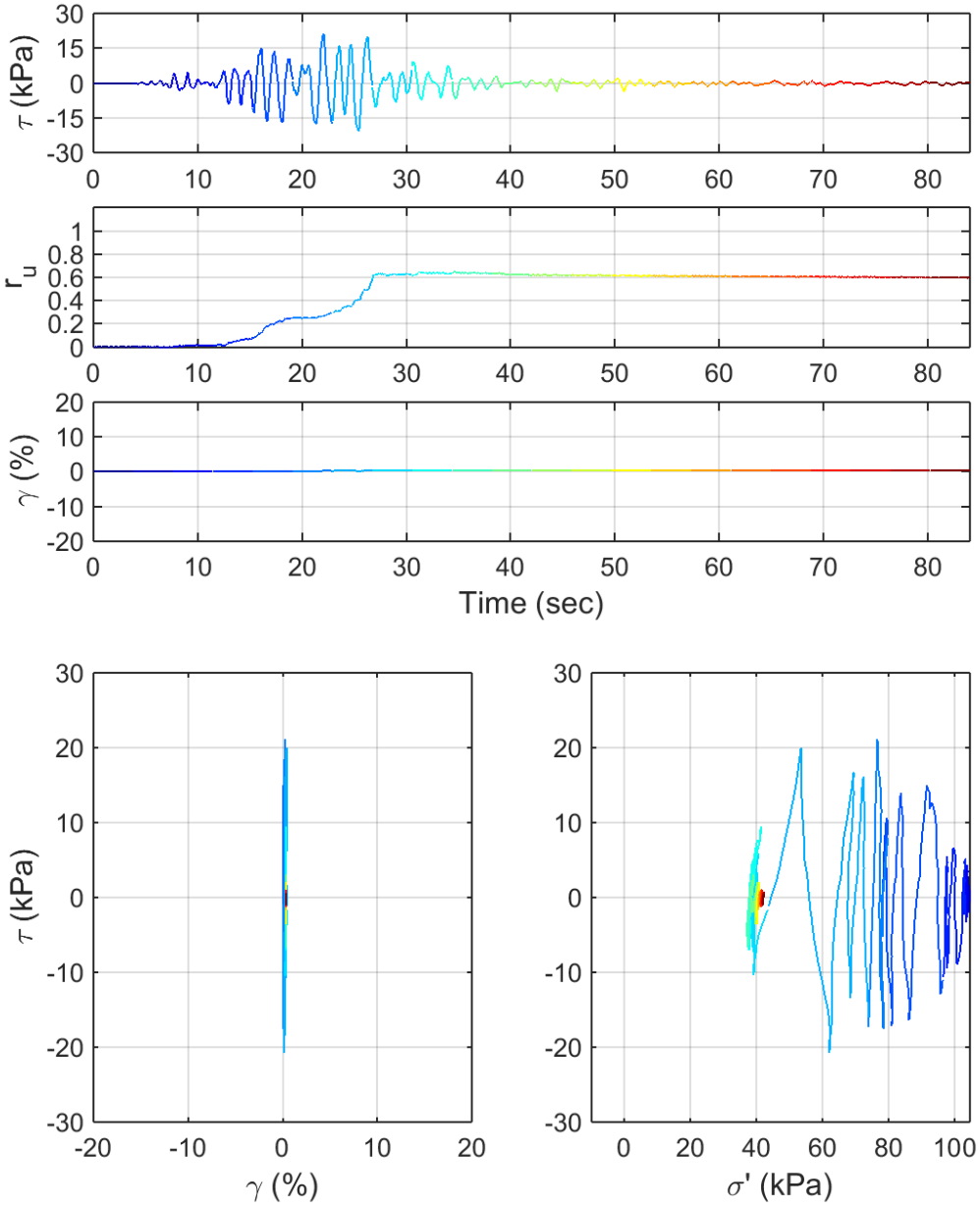

Test ID: 20121227
Nevada Sand
D_r = 41 %
Motion: NGA_no_484_PLK-NS.AT2

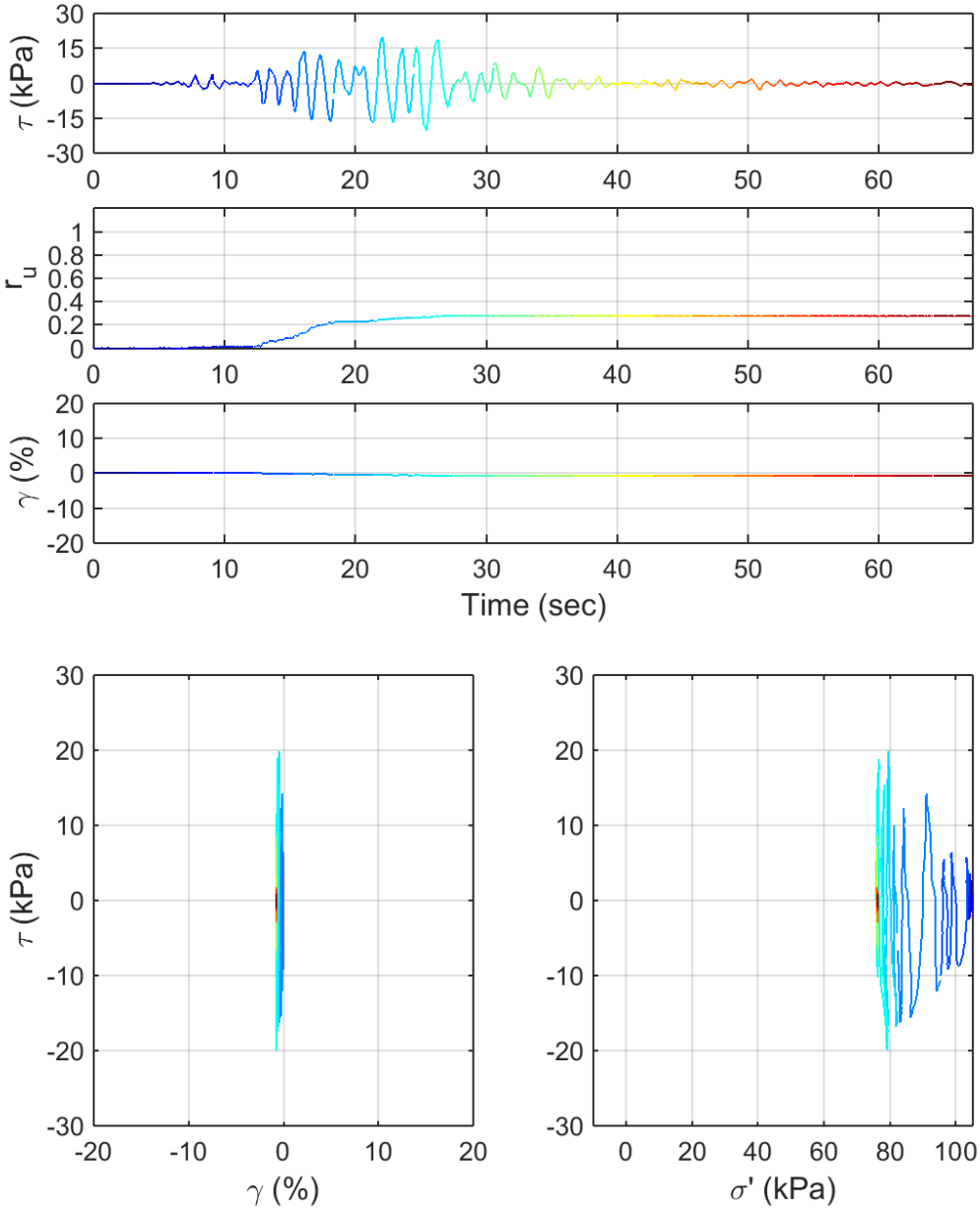

Test ID: 20121228
Nevada Sand
D_r = 47 %
Motion: NGA_no_484_PLK-NS.AT2

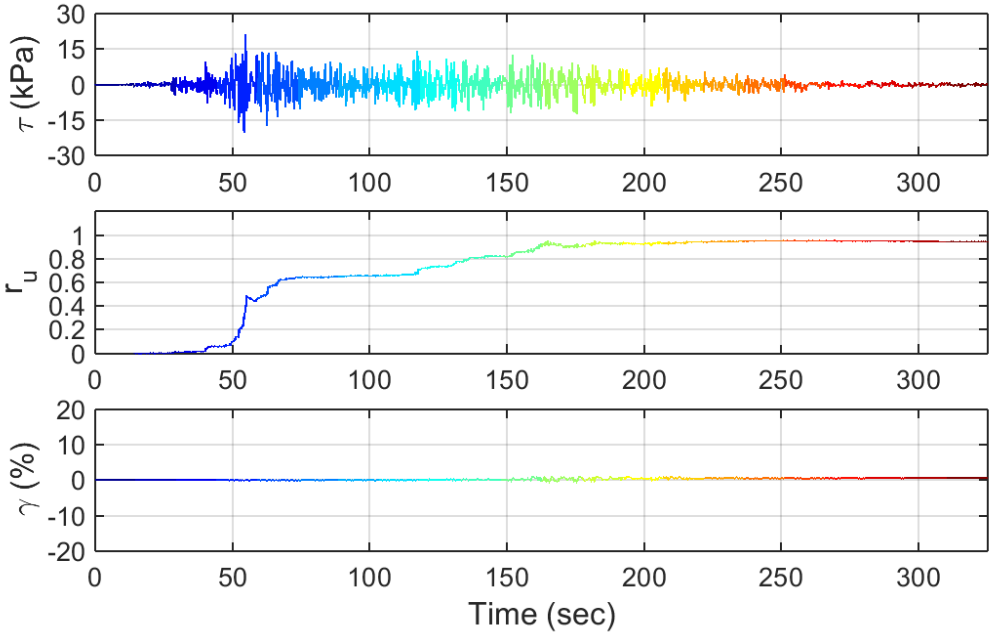

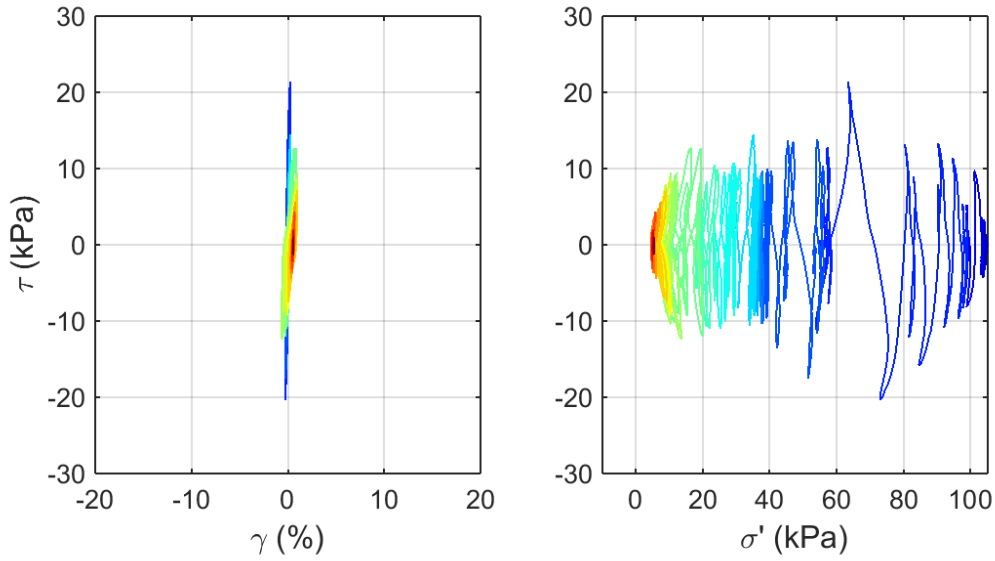

Test ID: 20121231
Nevada Sand
D_r = 47 %
Motion: NGA_no_880_MCF000.AT2

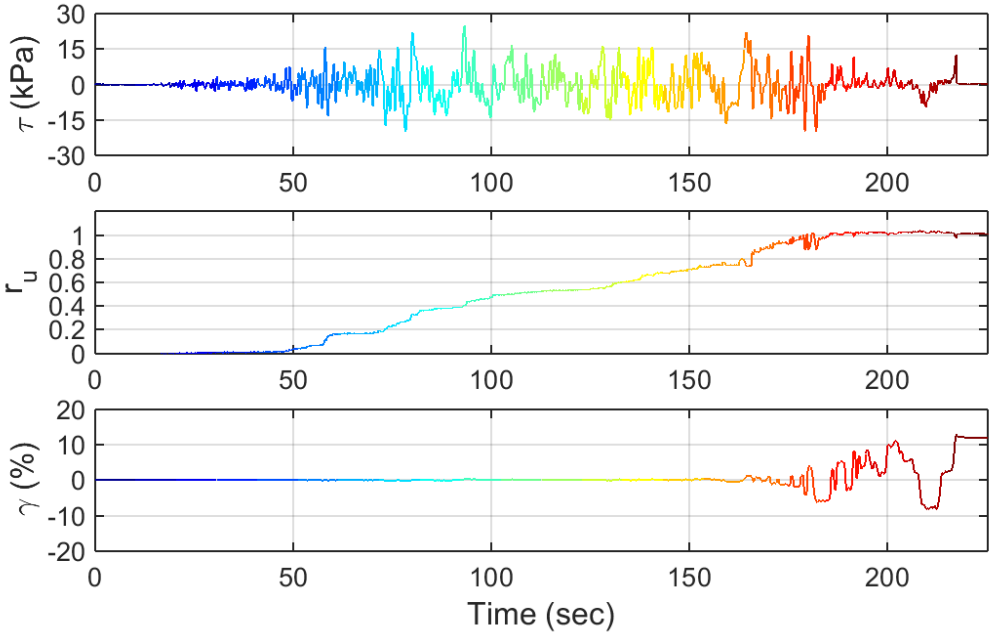

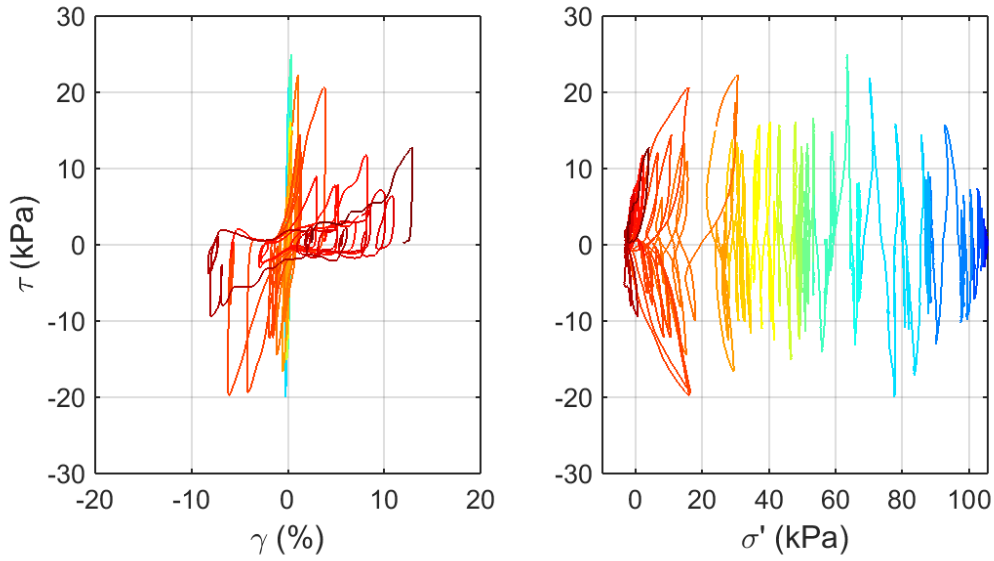

Test ID: 20130110
Nevada Sand
D_r = 40 %
Motion: NGA_no_1534_TCU107-N.AT2

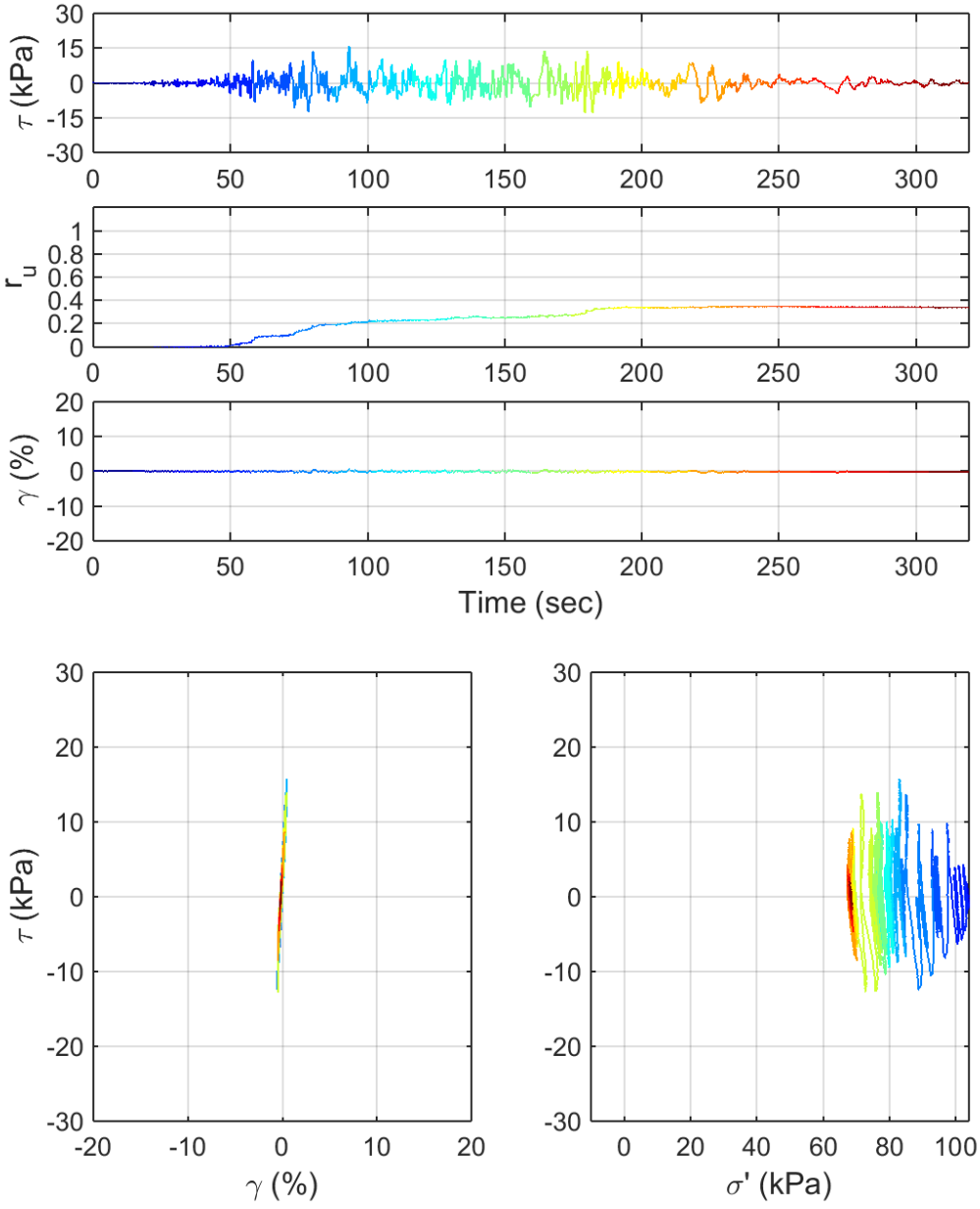

Test ID: 20130113
Nevada Sand
D_r = 39 %
Motion: NGA_no_1534_TCU107-N.AT2

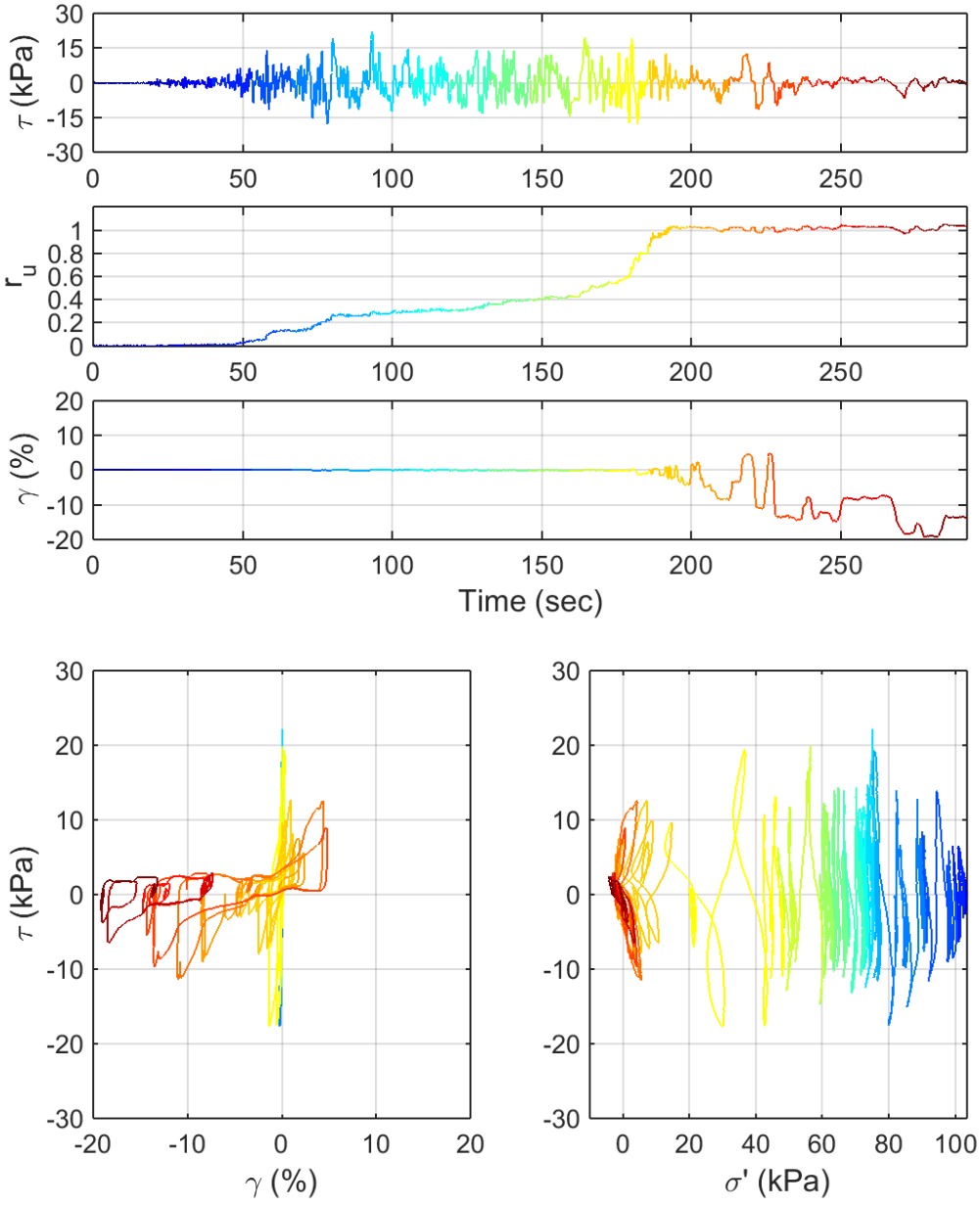

Test ID: 20130115
Nevada Sand
D_r = 43 %
Motion: NGA_no_1534_TCU107-N.AT2

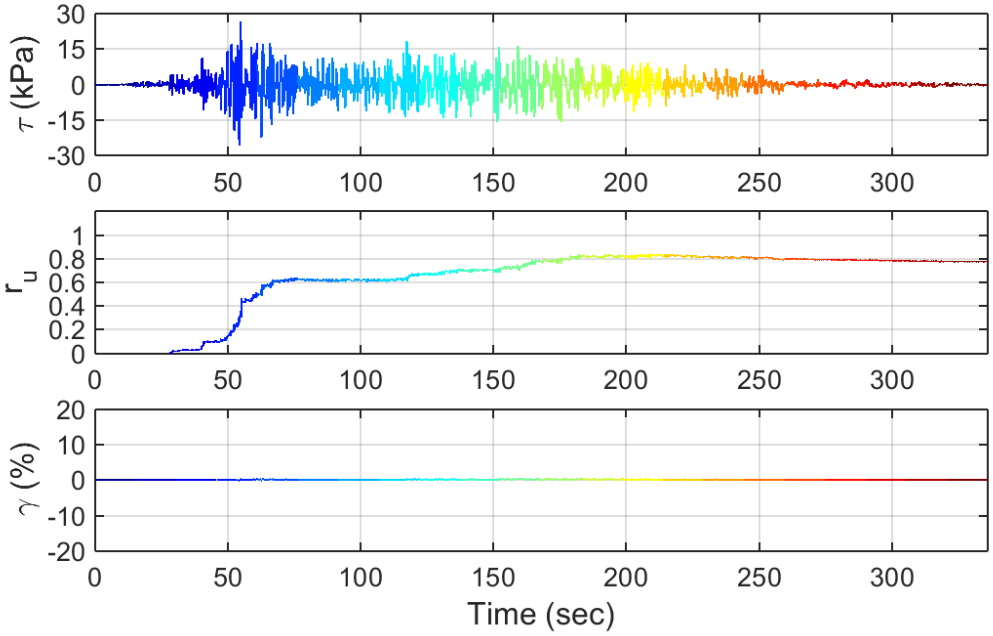

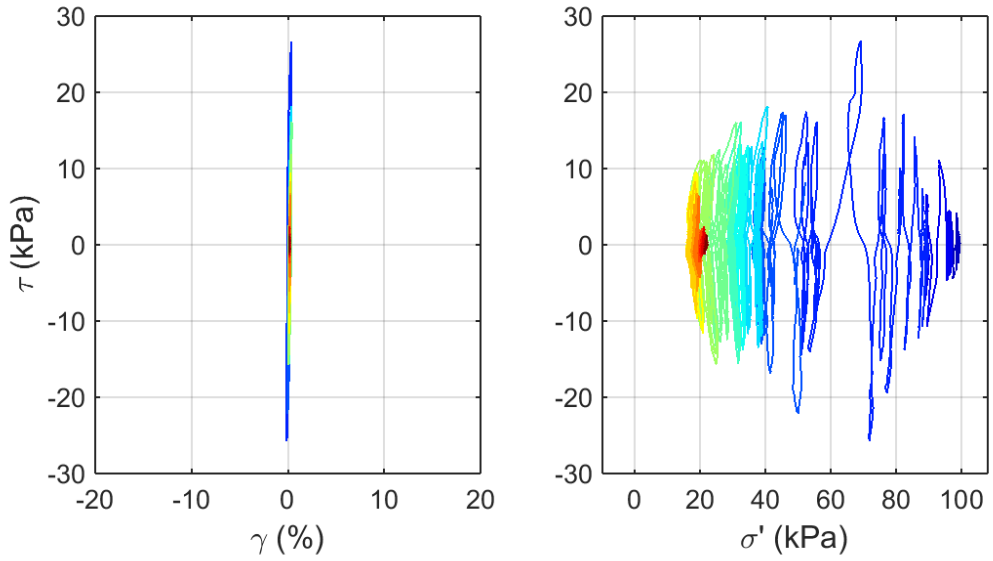

Test ID: 20130116
Nevada Sand
$D_r = 41$ %
Motion: NGA_no_880_MCF000.AT2

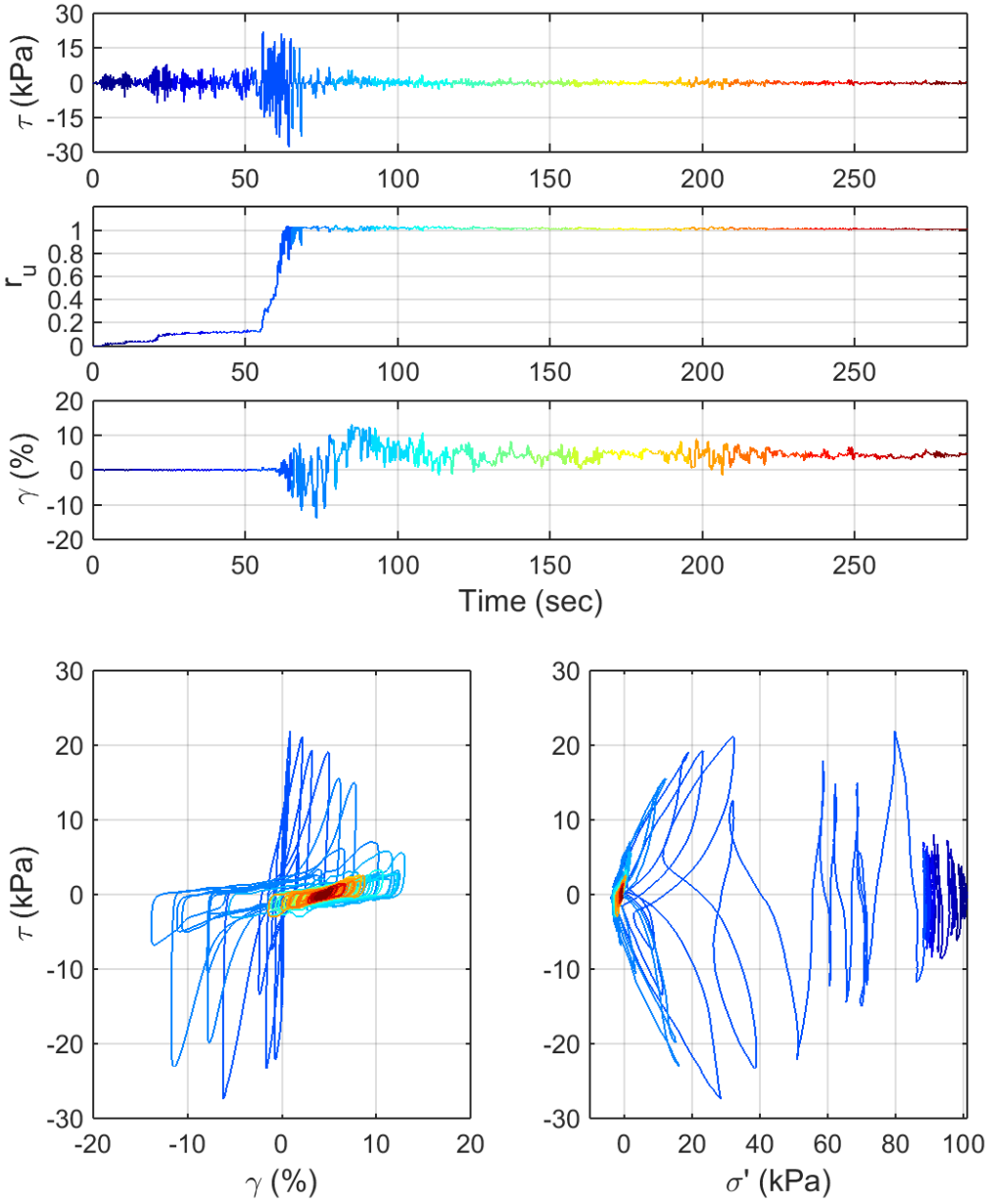

Test ID: 20130117
Nevada Sand
D_r = 49 %
Motion: NGA_no_1157_CNA000.AT2

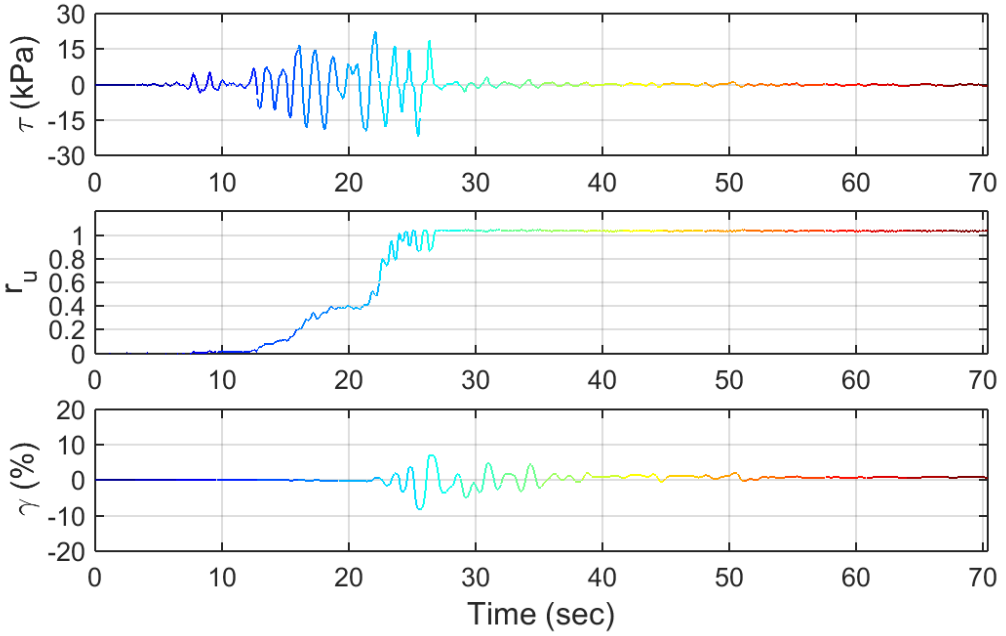

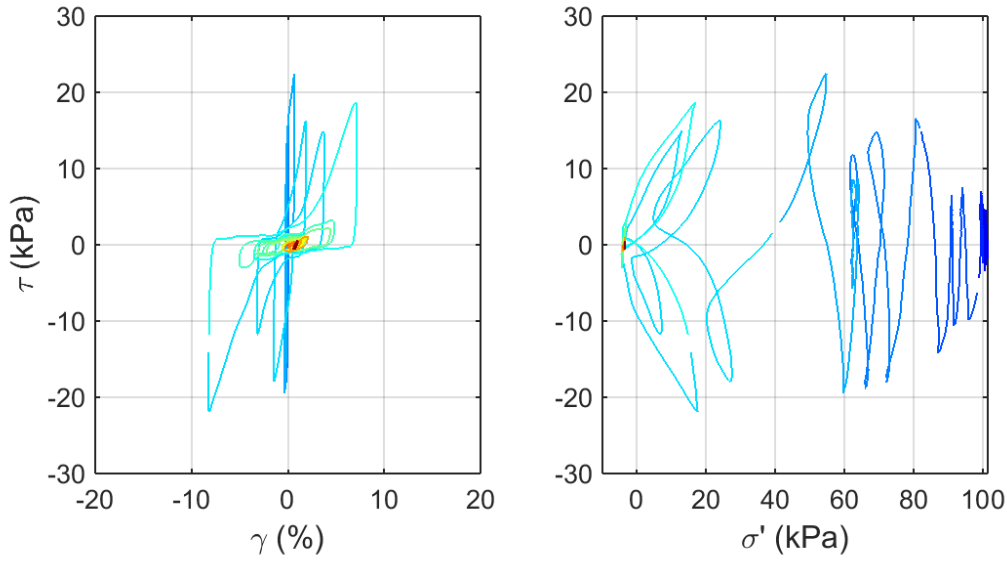

Test ID: 20130118
Nevada Sand
$D_r = 41$ %
Motion: NGA_no_484_PLK-NS.AT2

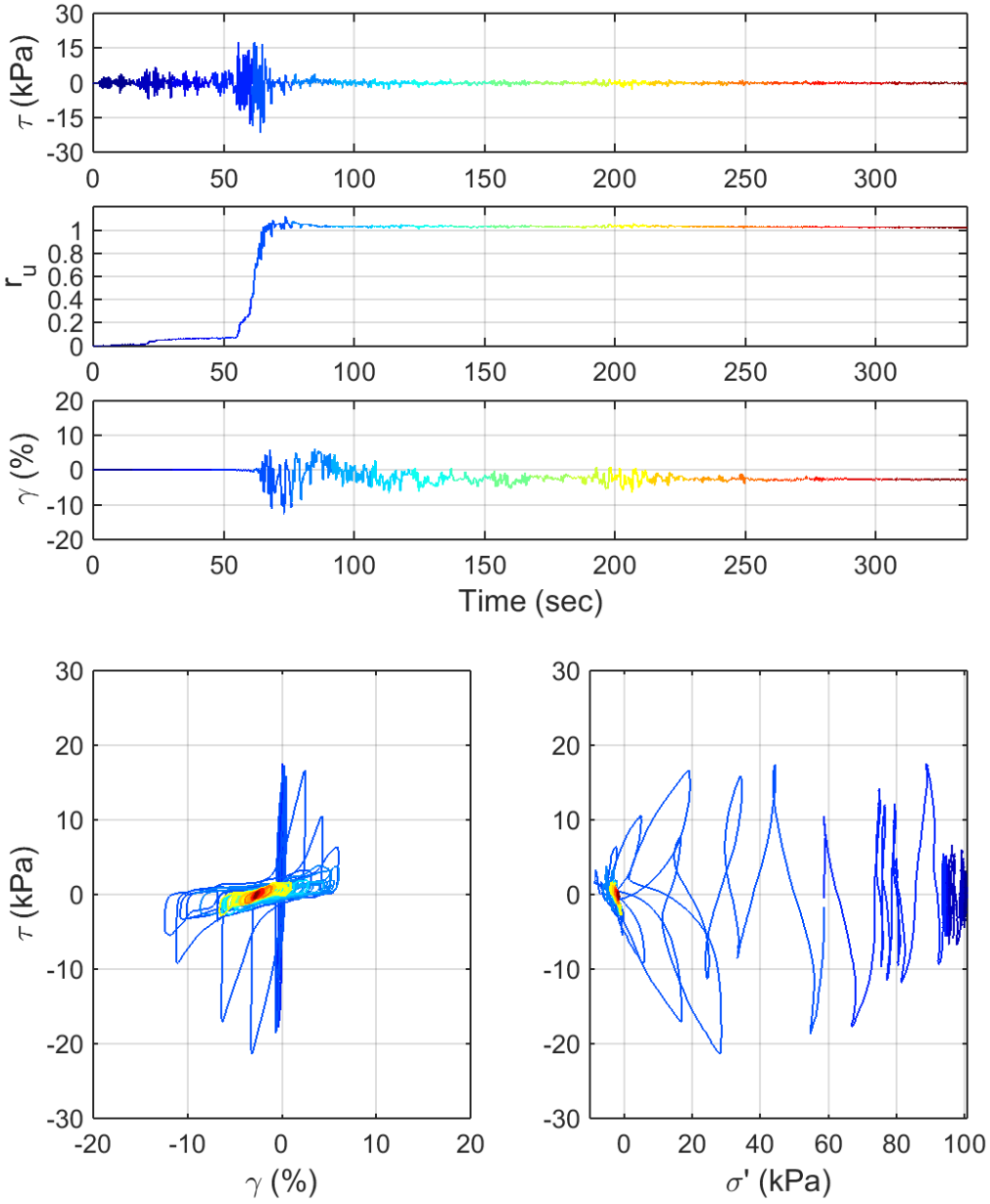

Test ID: 20130119
Nevada Sand
D_r = 37 %
Motion: NGA_no_1157_CNA000.AT2

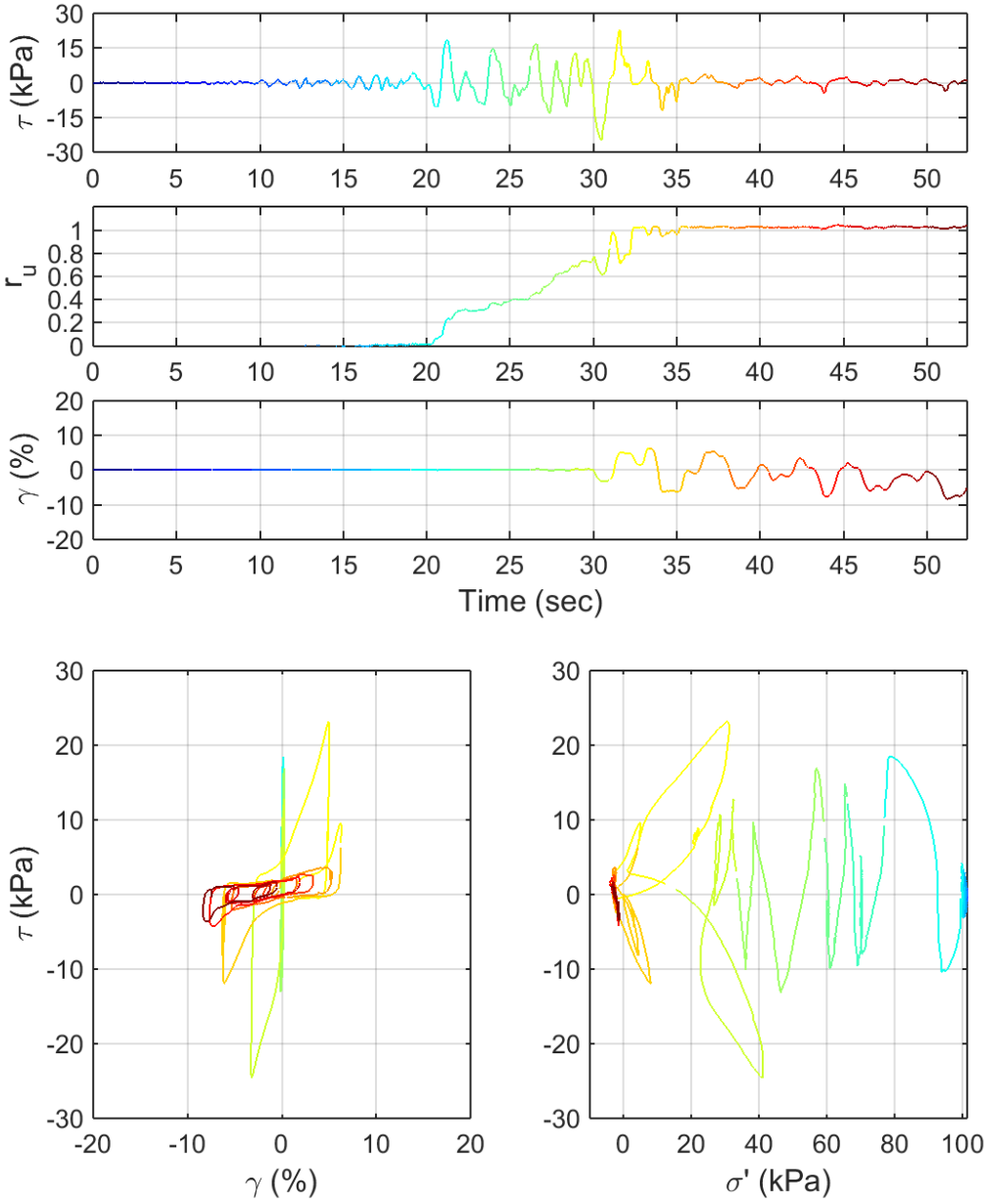

Test ID: 20130130
Nevada Sand
D_r = 44 %
Motion: NGA_no_249_L-FIS090.AT2

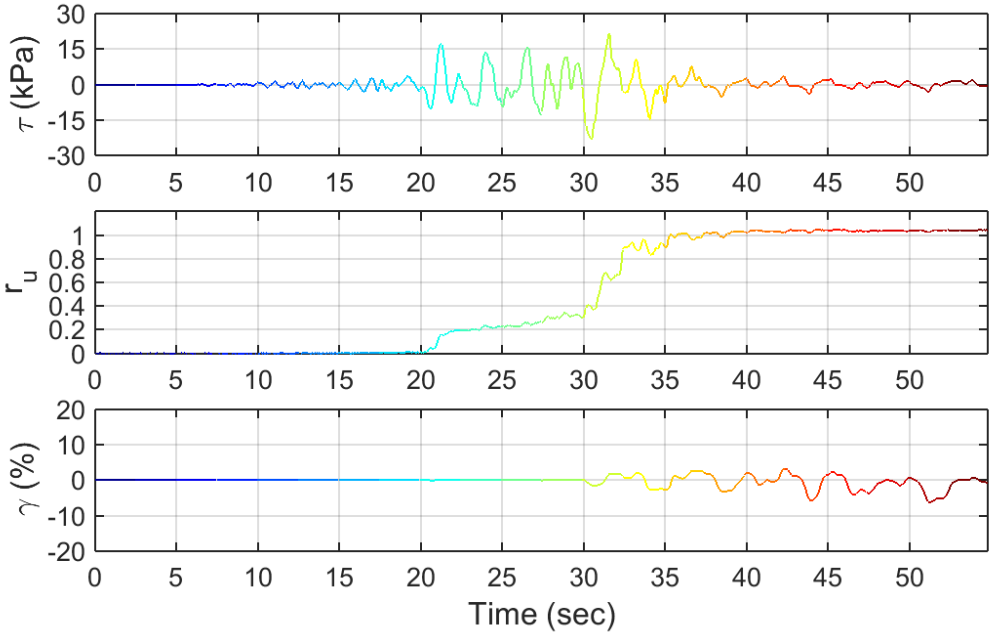

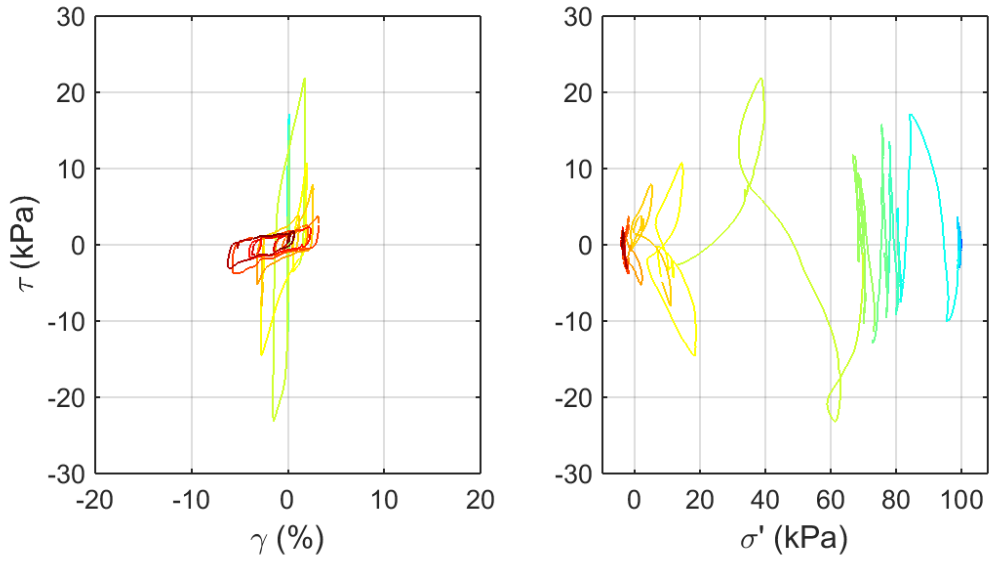

Test ID: 20130209
Nevada Sand
D_r = 47 %
Motion: NGA_no_249_L-FIS090.AT2

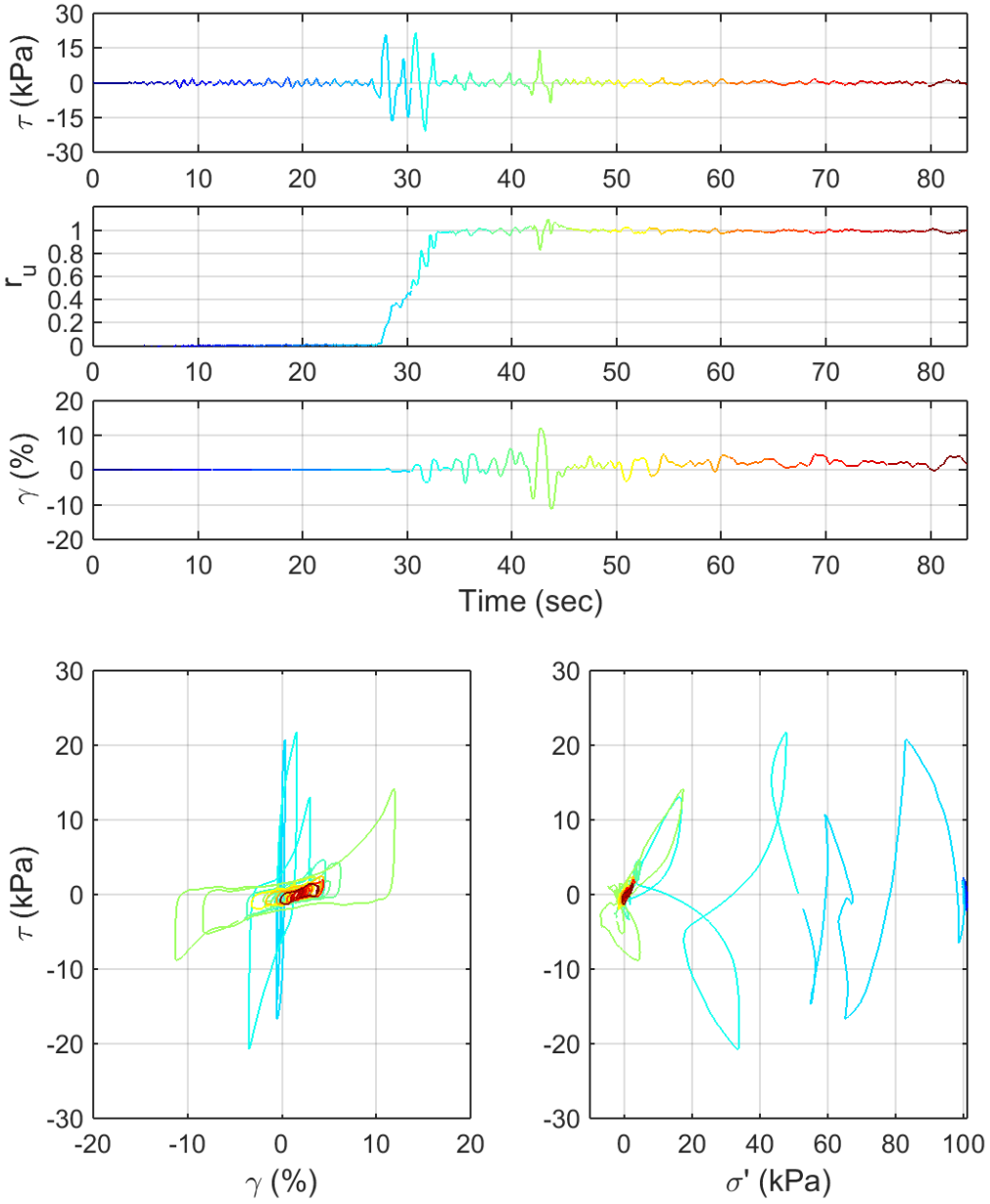

Test ID: 20130213
Nevada Sand
D_r = 48 %
Motion: NGA_no_695_A-RO3000.AT2

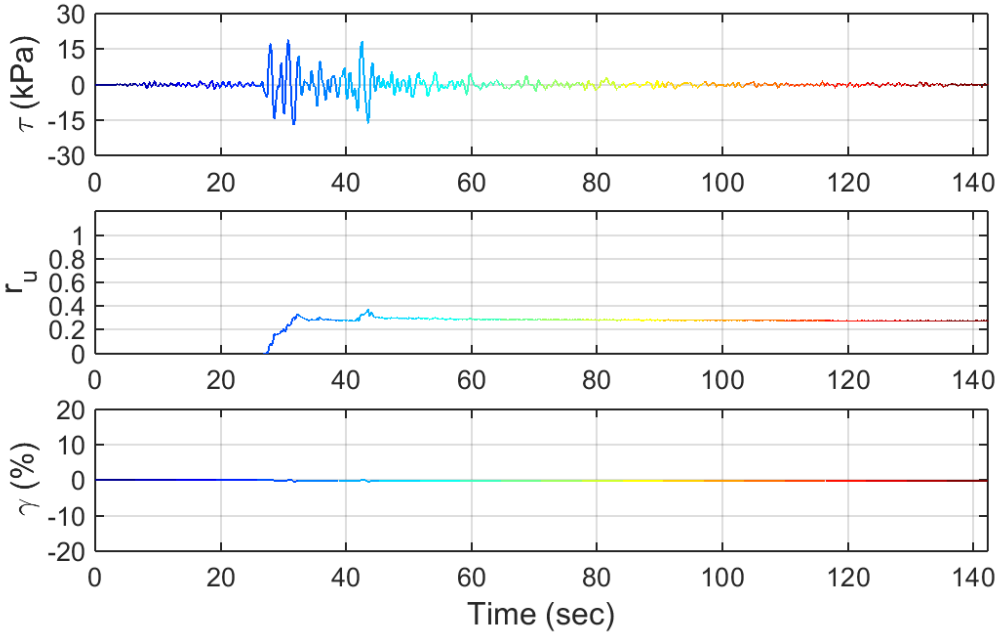

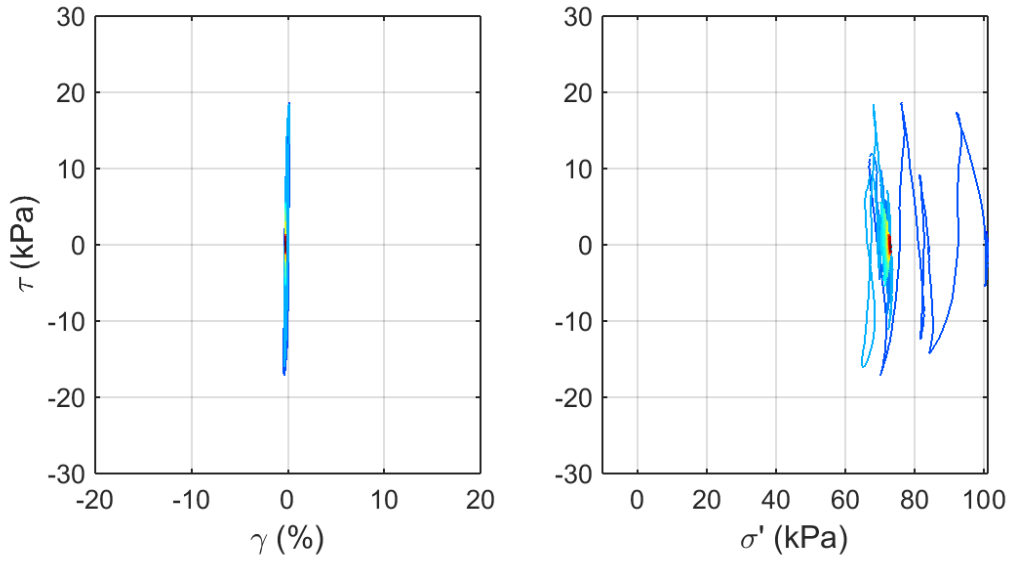

Test ID: 20130214
Nevada Sand
D_r = 44 %
Motion: NGA_no_695_A-RO3000.AT2

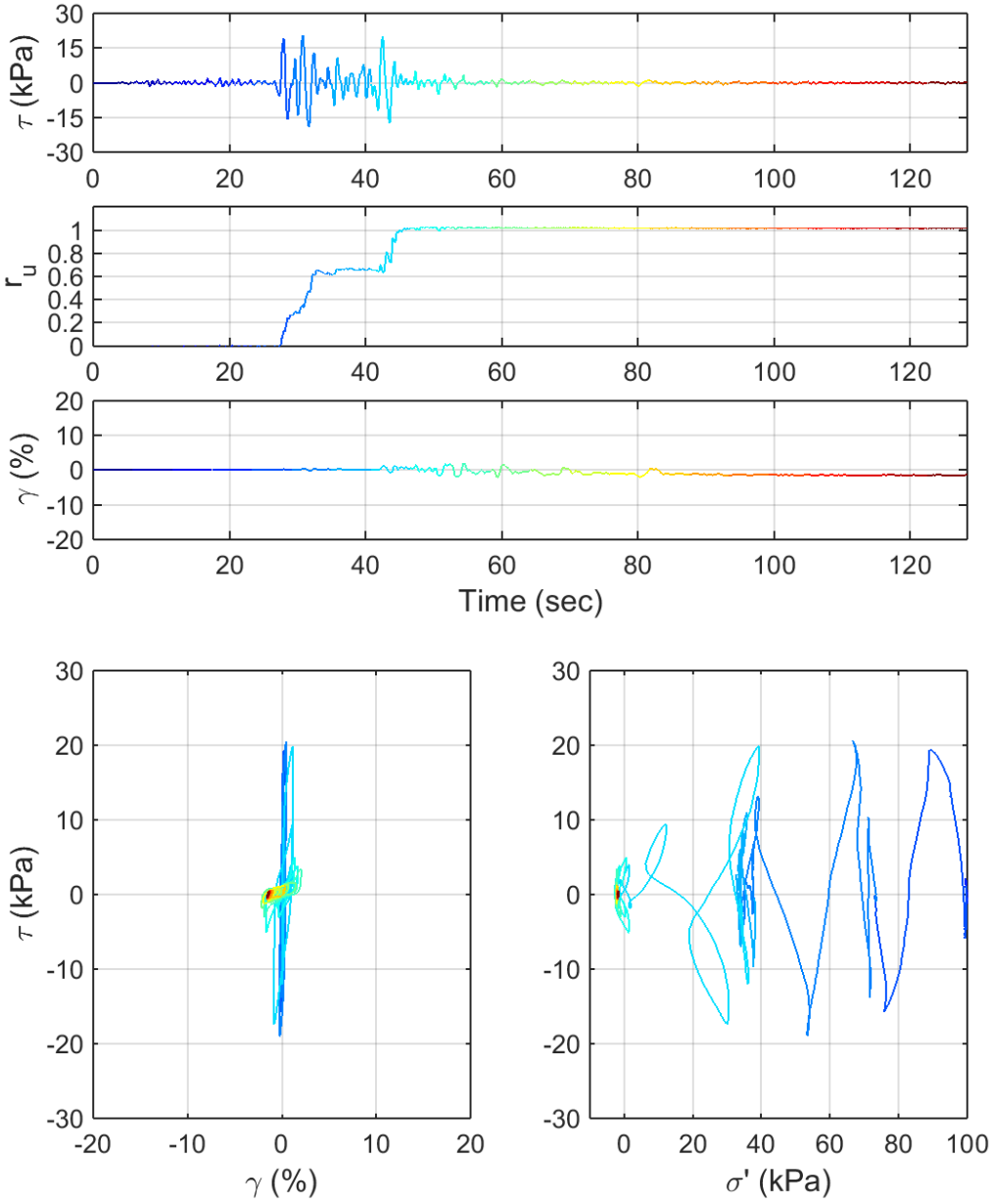

Test ID: 20130215
Nevada Sand
D_r = 50 %
Motion: NGA_no_695_A-RO3000.AT2

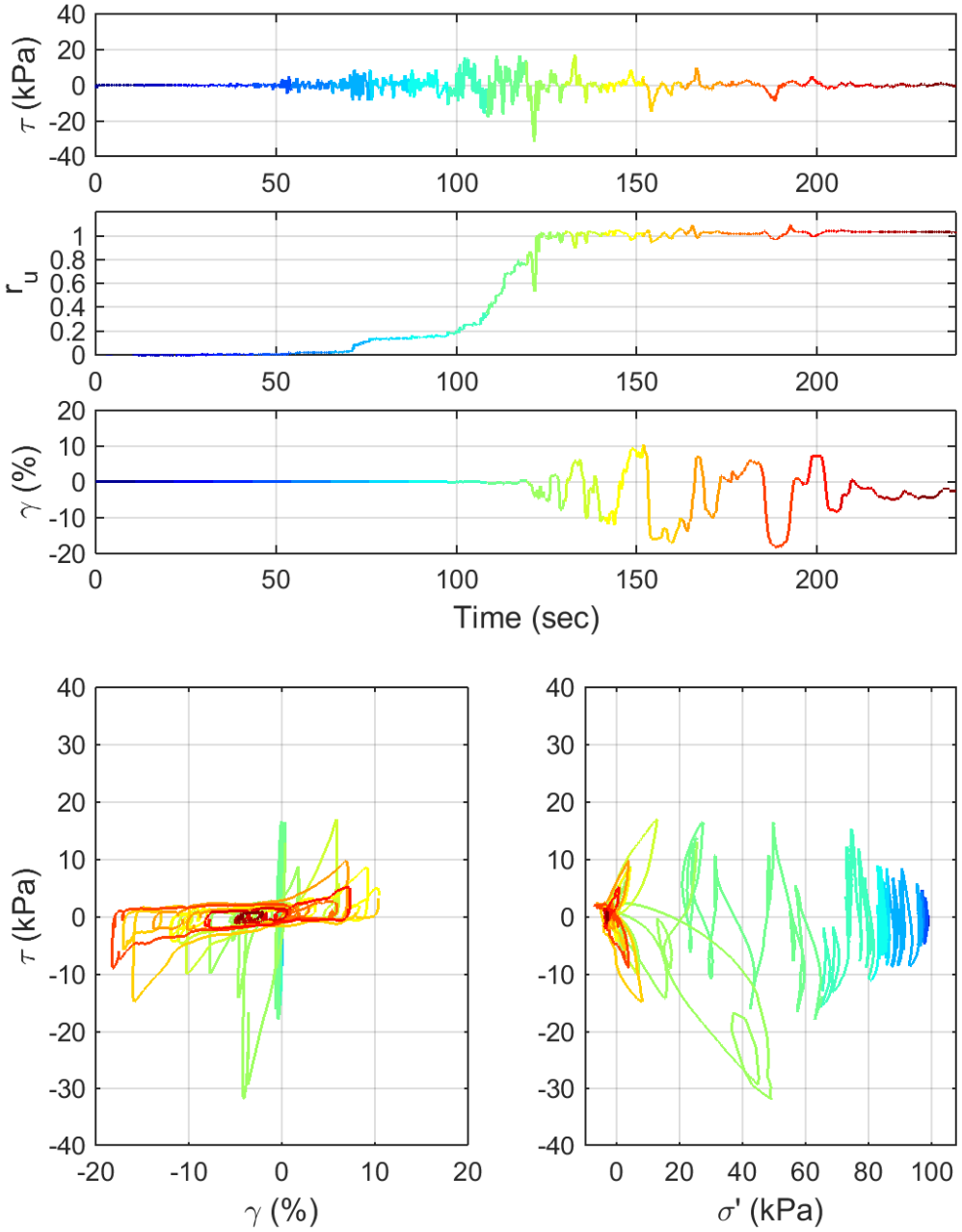

Test ID: 2013021502
Nevada Sand
$D_r = 47$ %
Motion: NGA_no_695_A-RO3000.AT2

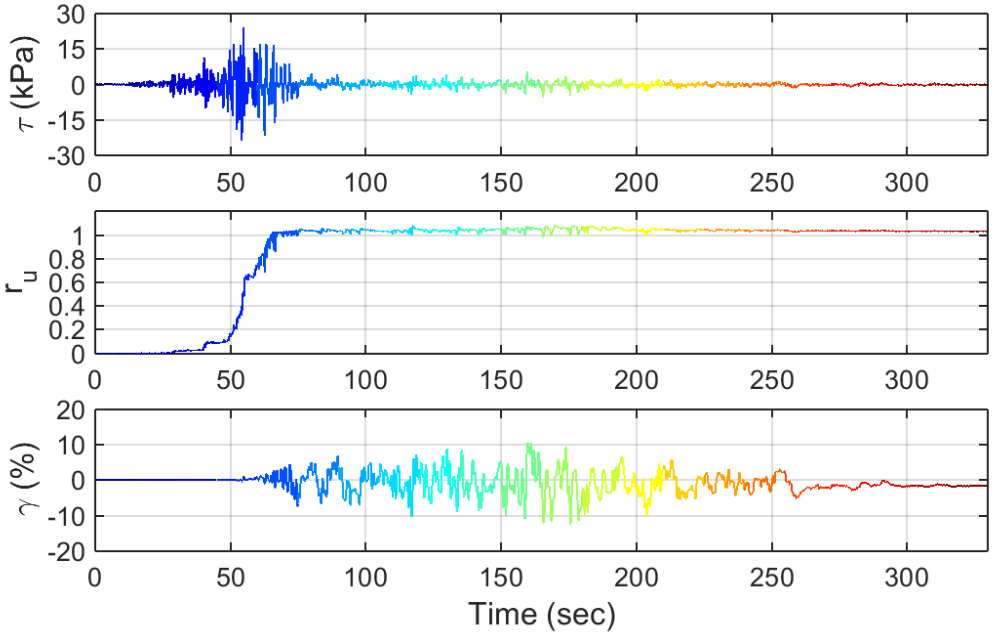

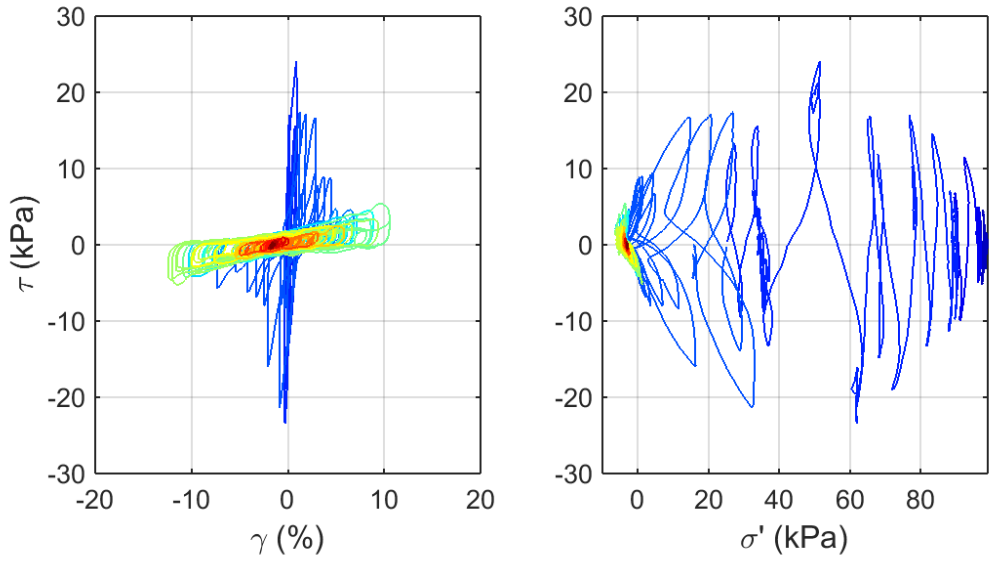

Test ID: 20130216
Nevada Sand
D_r = 51 %
Motion: NGA_no_880_MCF000.AT2

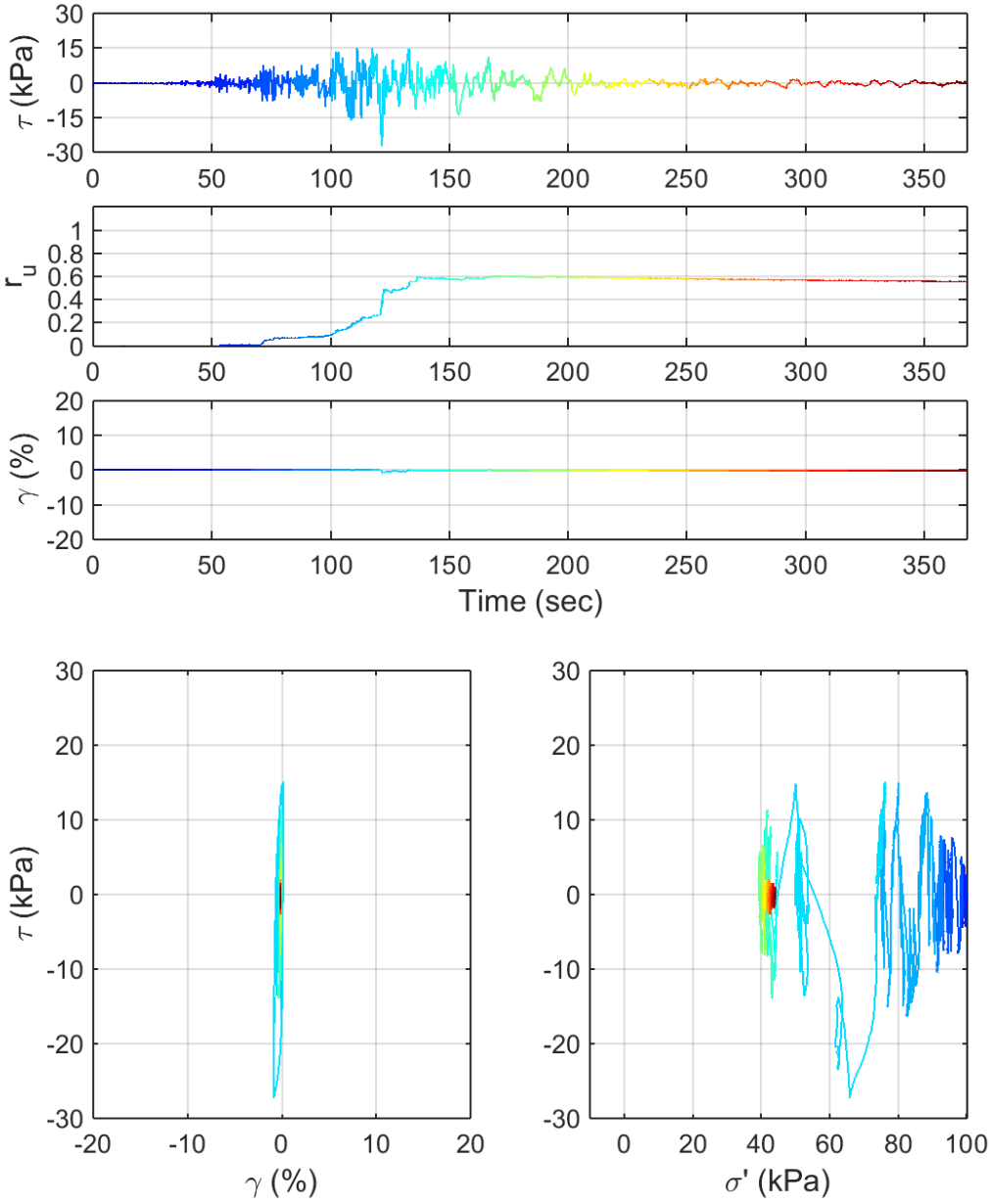

Test ID: 20130222
Nevada Sand
D_r = 48 %
Motion: NGA_no_1792_12543090.AT2

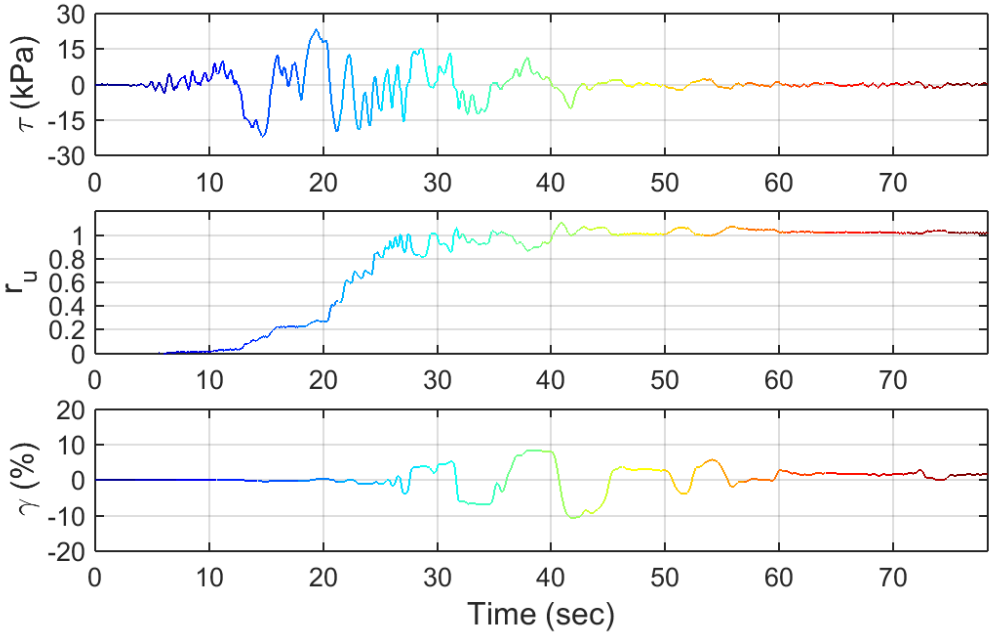

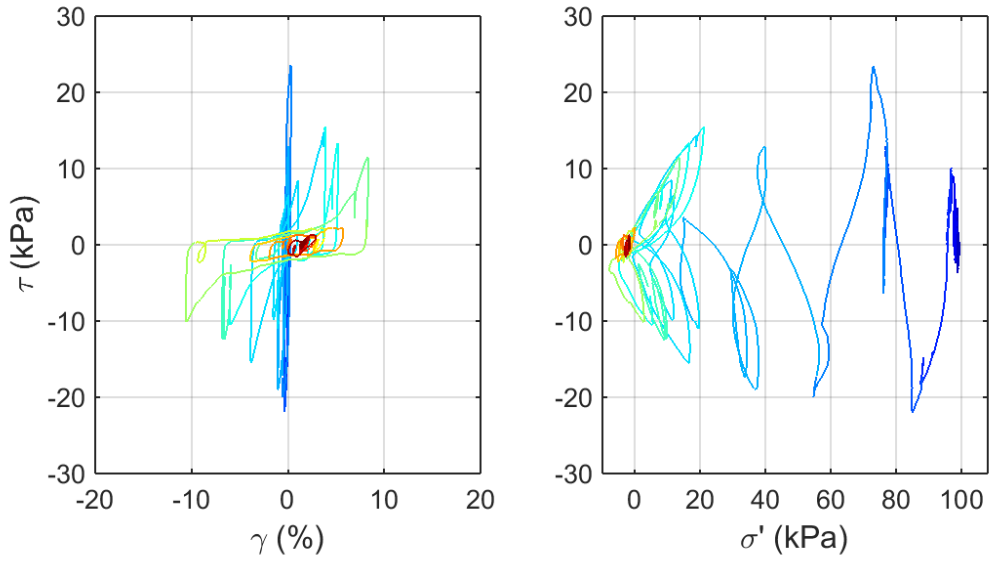

Test ID: 20130228
Nevada Sand
D_r = 50 %
Motion: NGA_no_527_MVH135.AT2

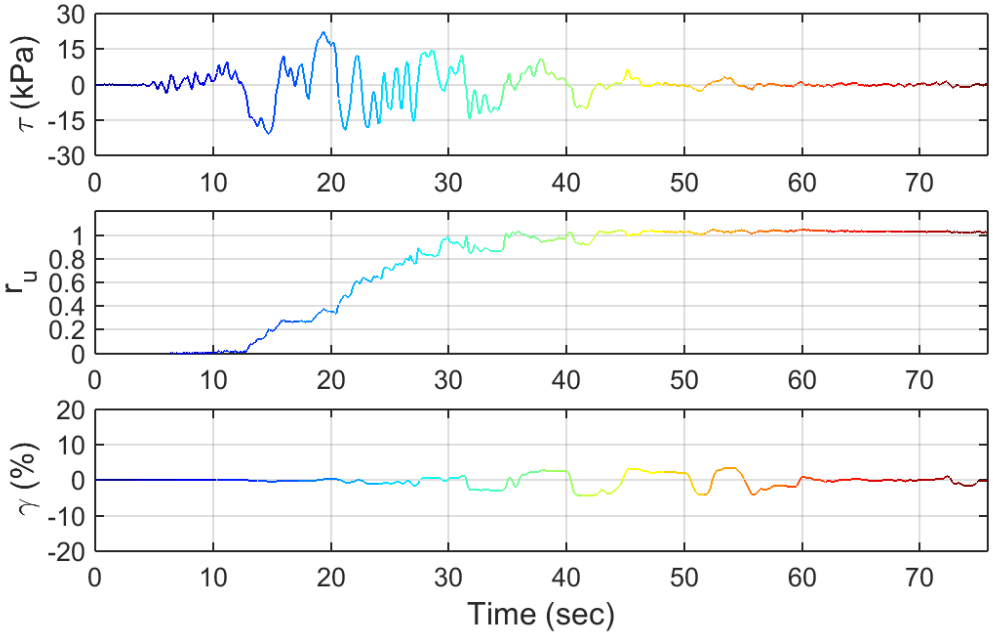

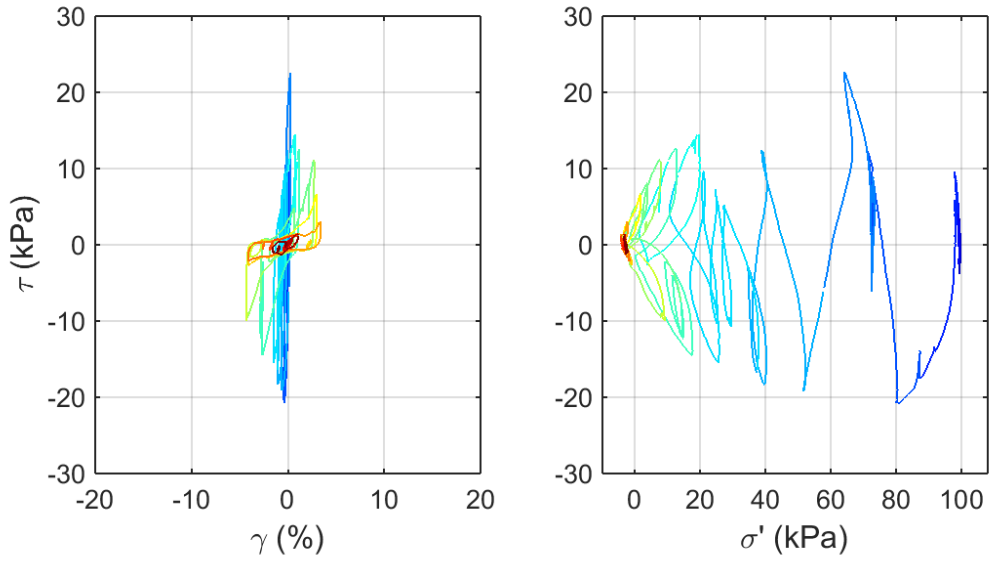

Test ID: 20130303
Nevada Sand
D_r = 50 %
Motion: NGA_no_527_MVH135.AT2

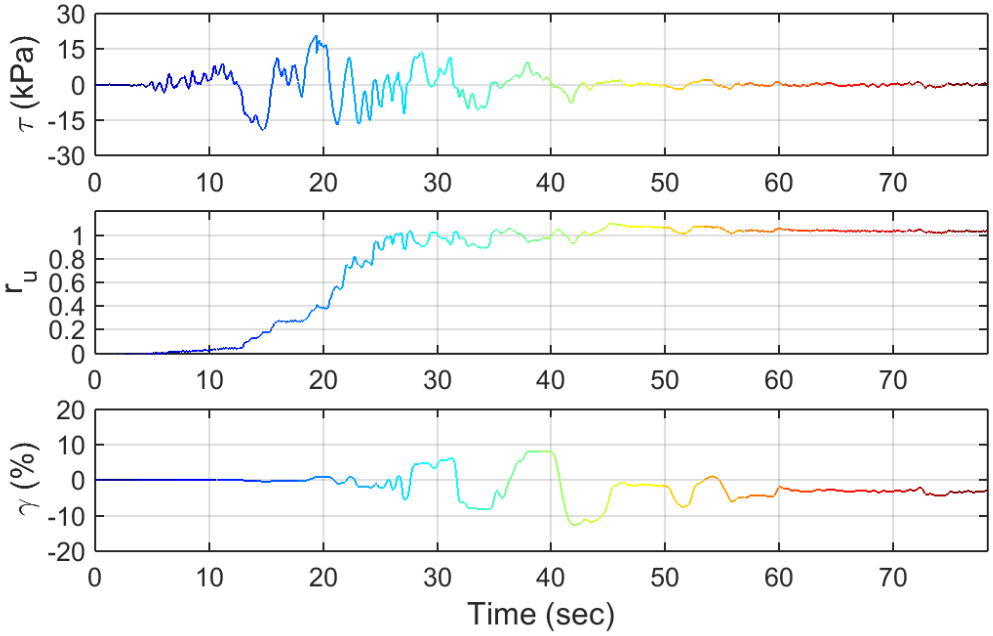

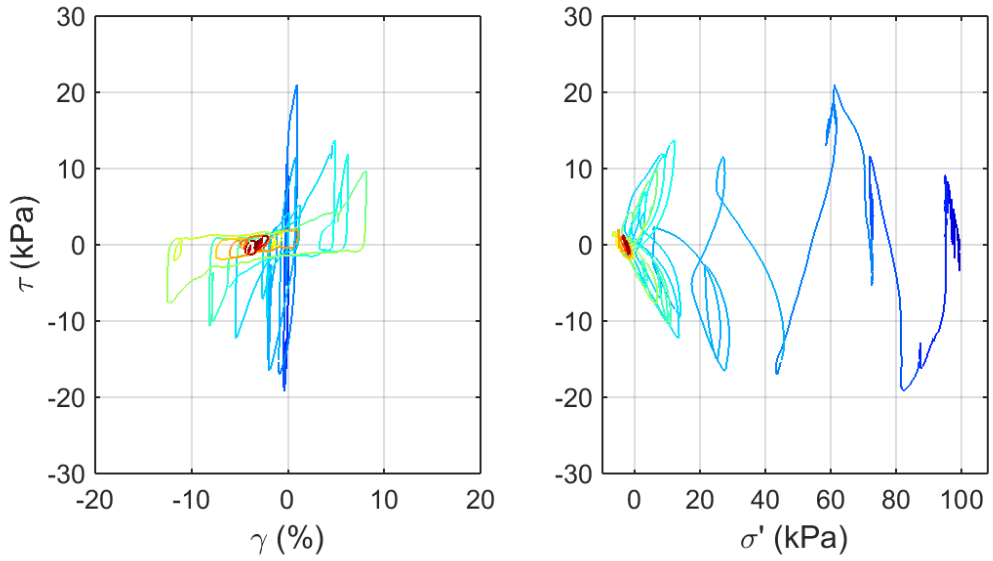

Test ID: 20130306
Nevada Sand
D_r = 40 %
Motion: NGA_no_527_MVH135.AT2

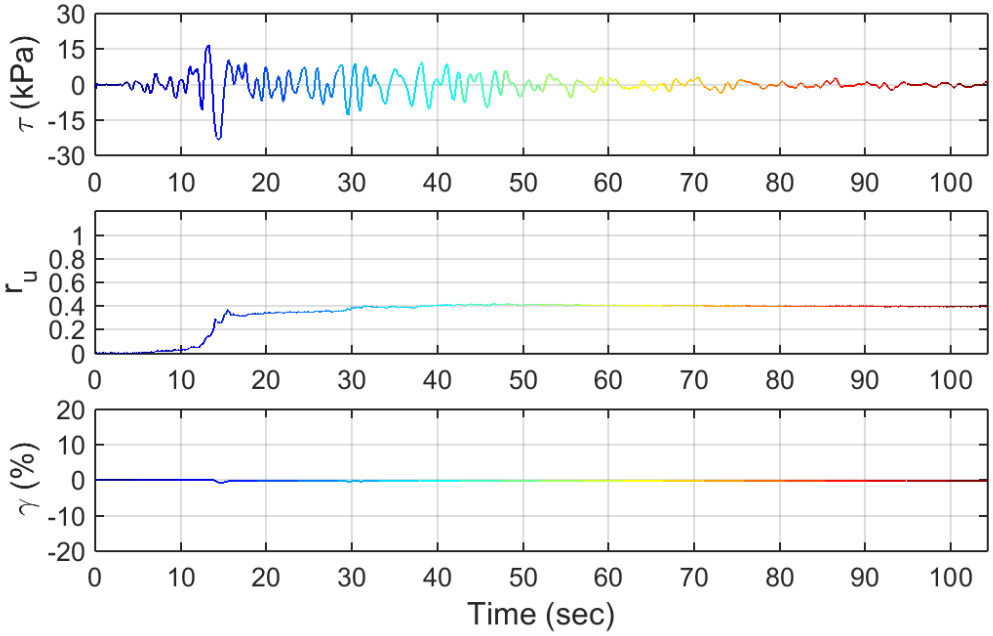

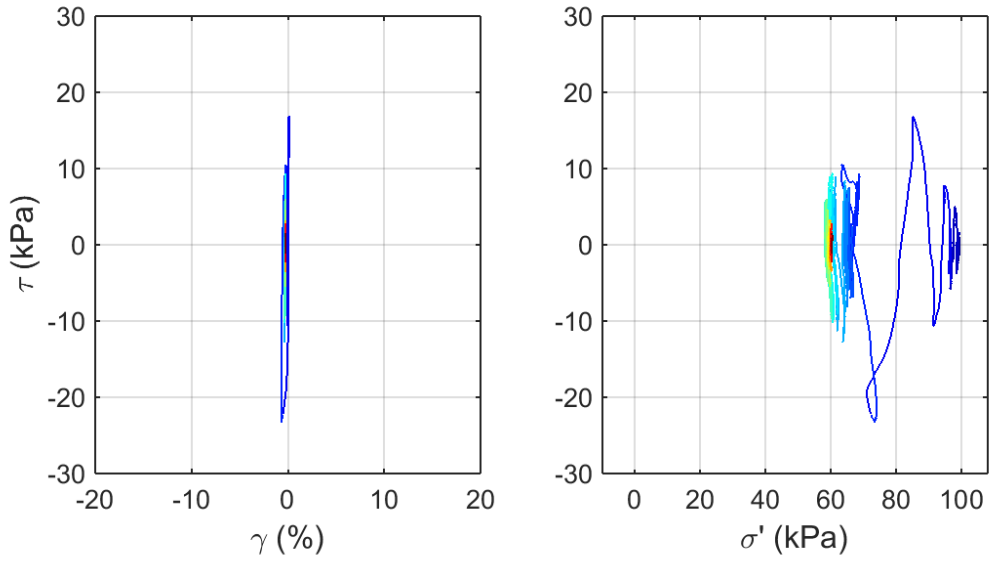

Test ID: 20130307
Nevada Sand
D_r = 44 %
Motion: NGA_no_149_G04360.AT2

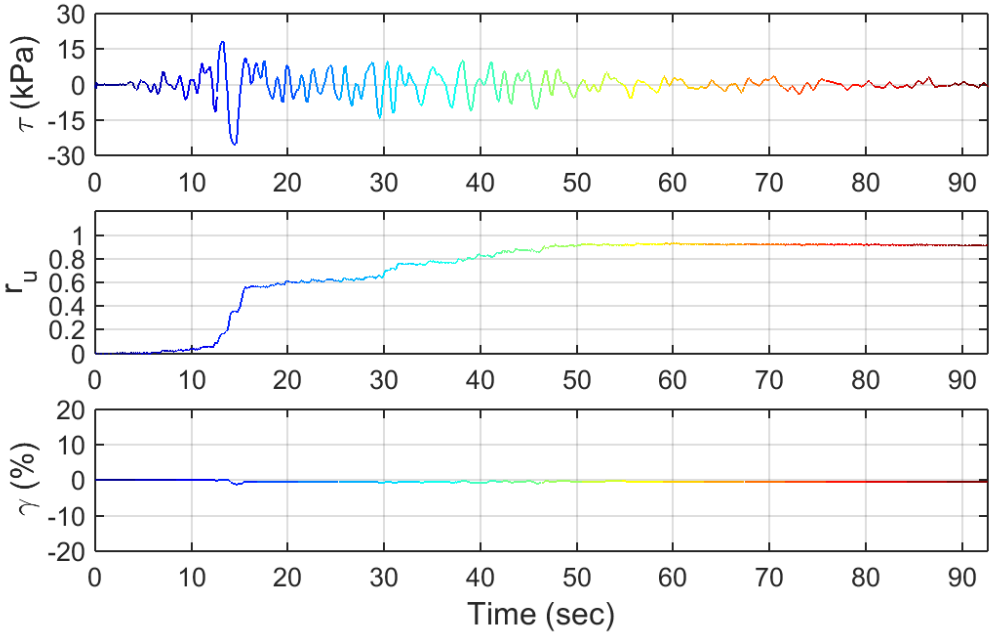

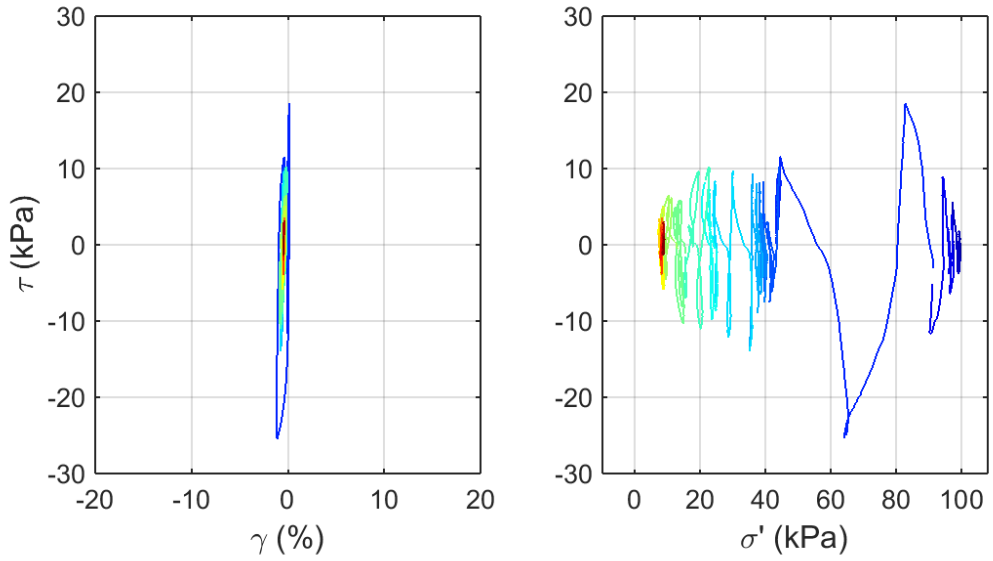

Test ID: 2013030702
Nevada Sand
D_r = 44 %
Motion: NGA_no_149_G04360.AT2

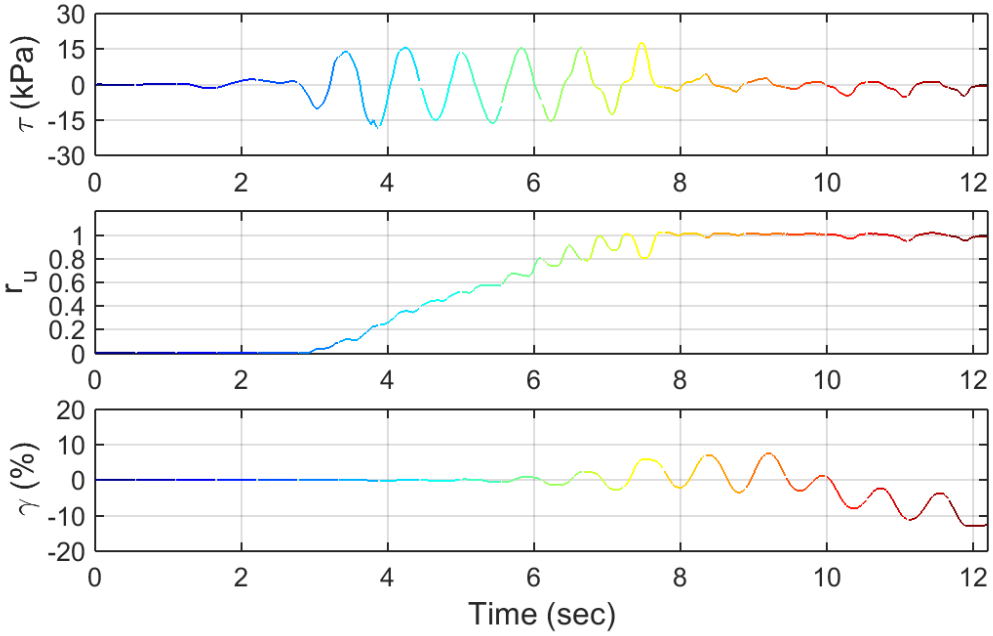

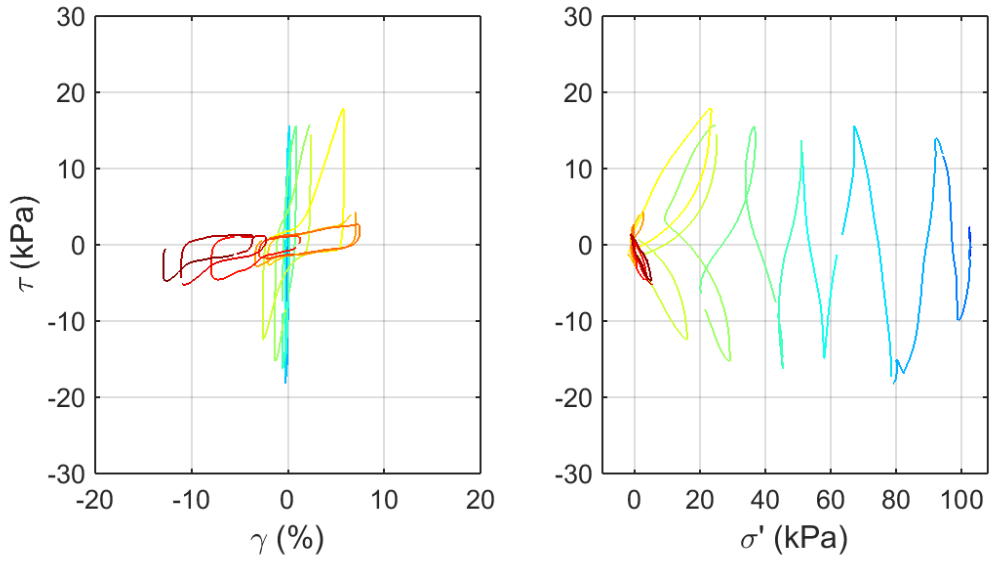

Test ID: 20130322
Nevada Sand
D_r = 41 %
Motion: NGA_no_107_B-OAP180.AT2

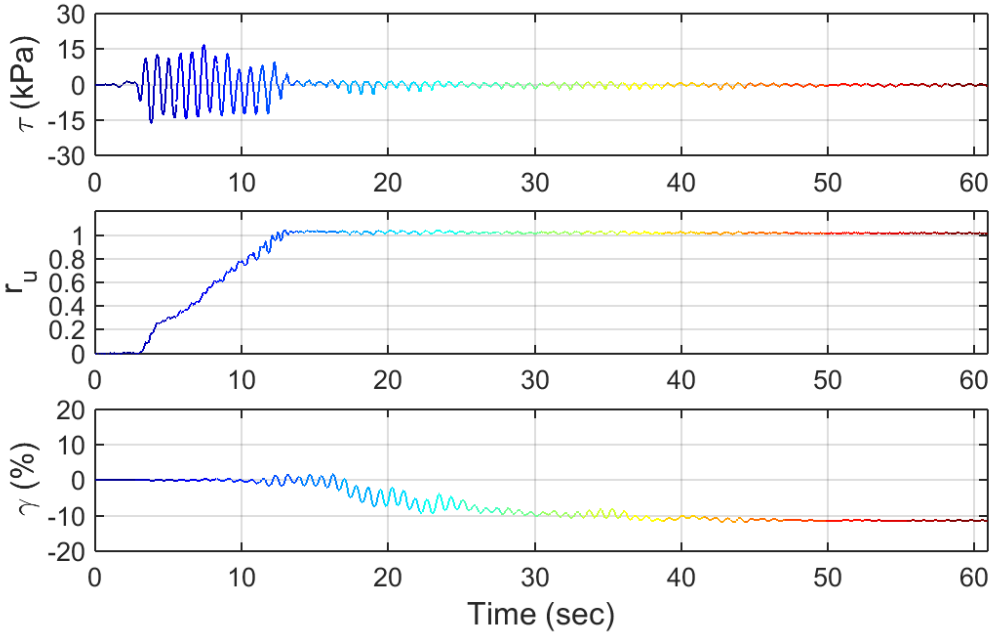

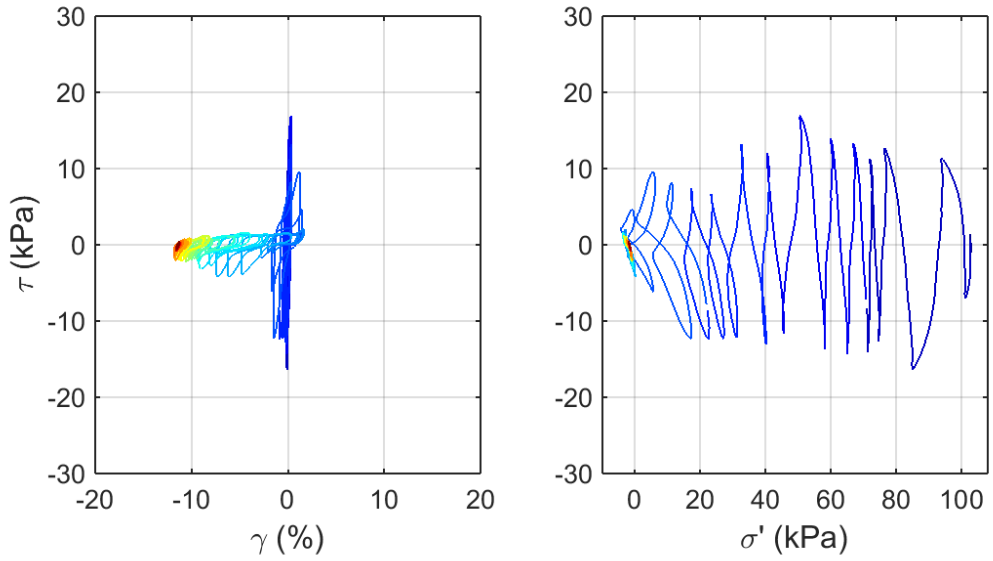

Test ID: 20130324
Nevada Sand
D_r = 44 %
Motion: NGA_no_107_B-OAP180.AT2

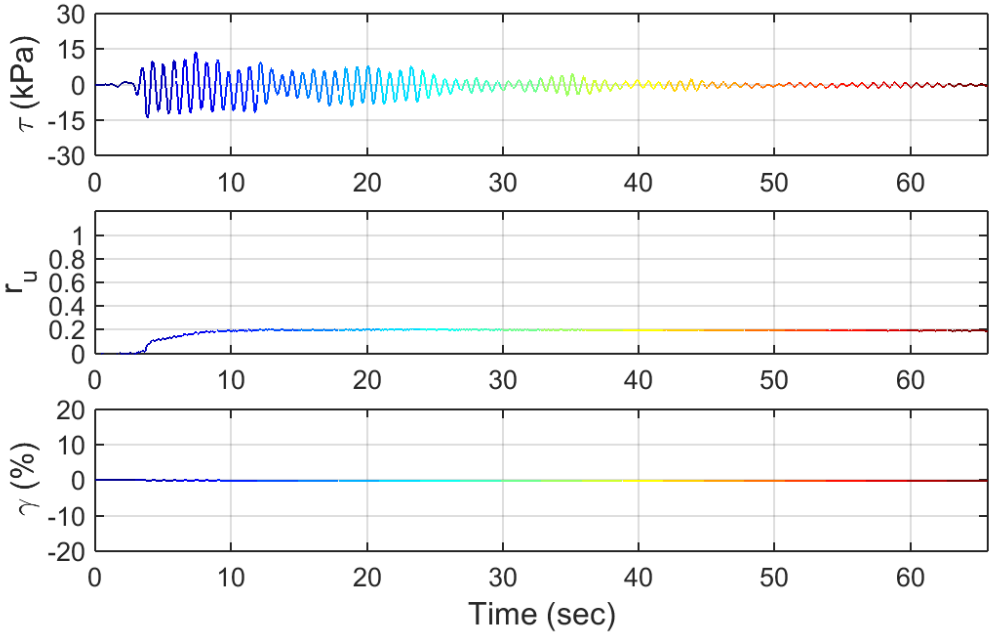

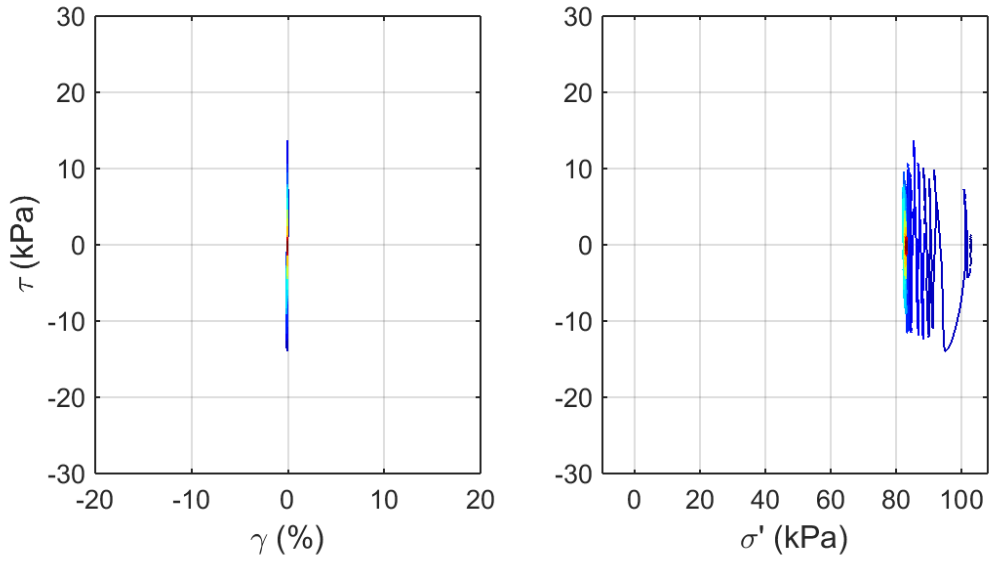

Test ID: 20130326
Nevada Sand
D_r = 43 %
Motion: NGA_no_107_B-OAP180.AT2

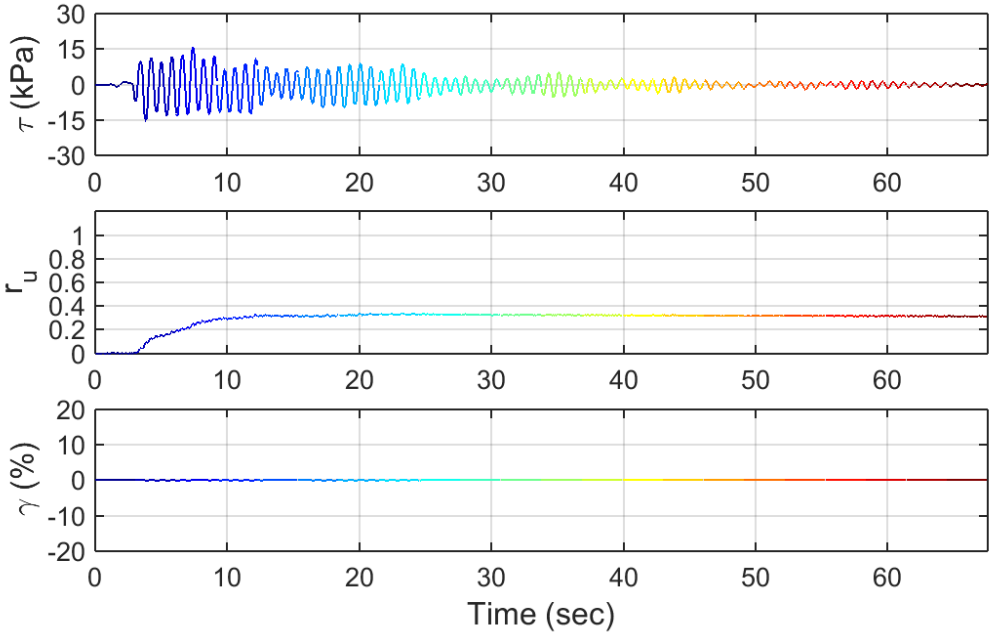

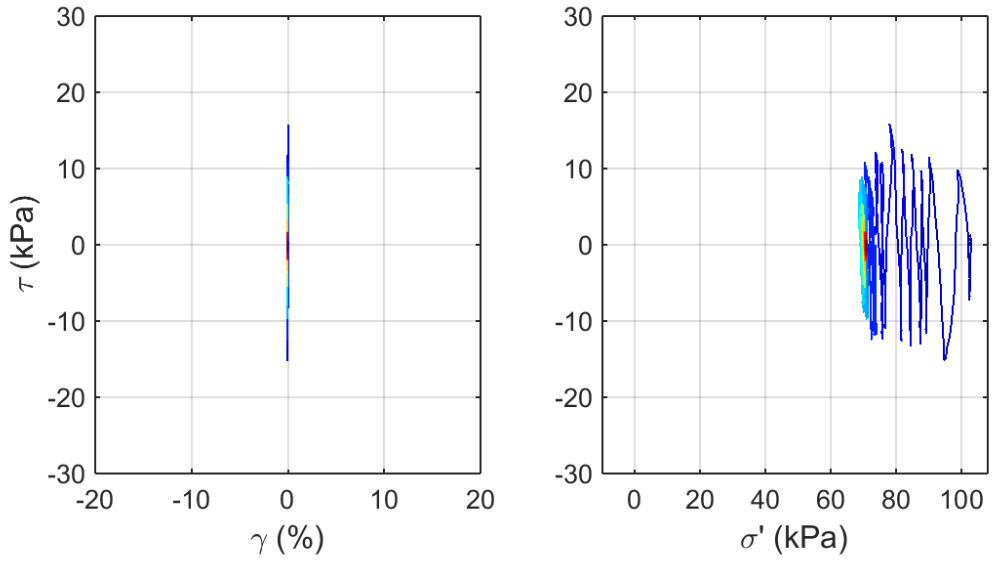

Test ID: 20130322602
Nevada Sand
$D_r = 41$ %
Motion: NGA_no_107_B-OAP180.AT2

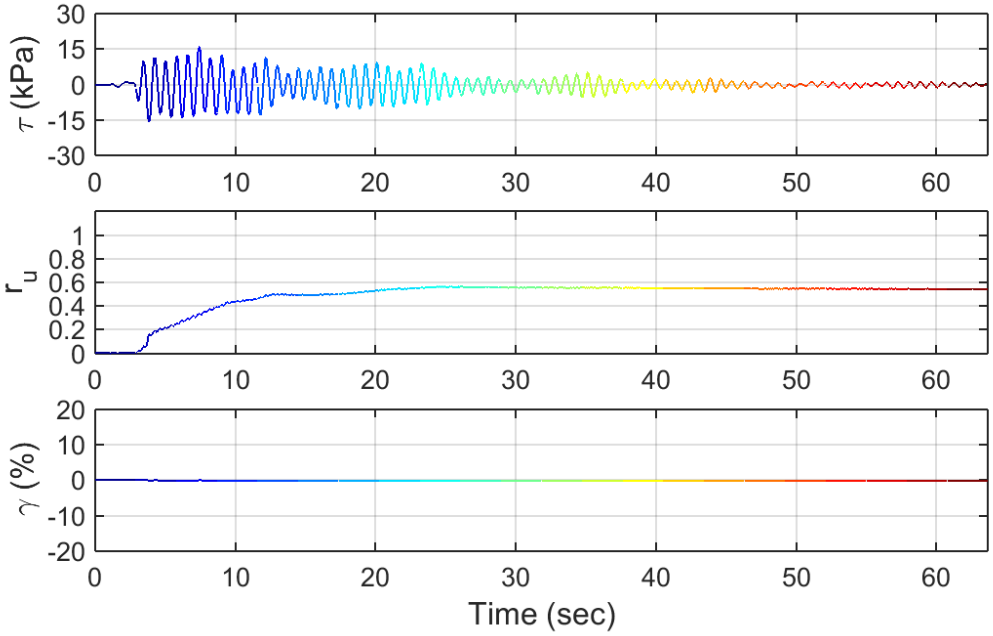

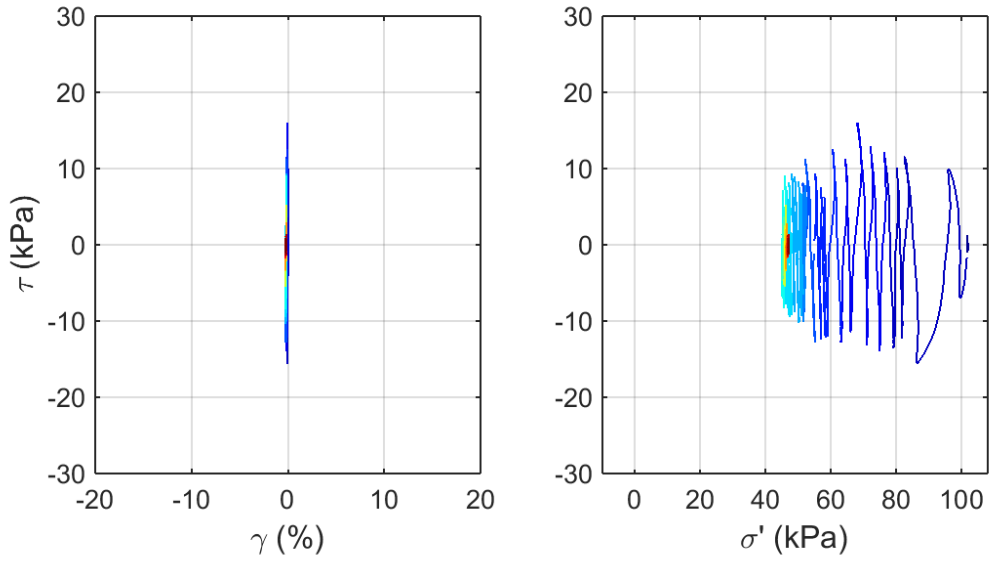

Test ID: 20130329
Nevada Sand
D_r = 43 %
Motion: NGA_no_107_B-OAP180.AT2

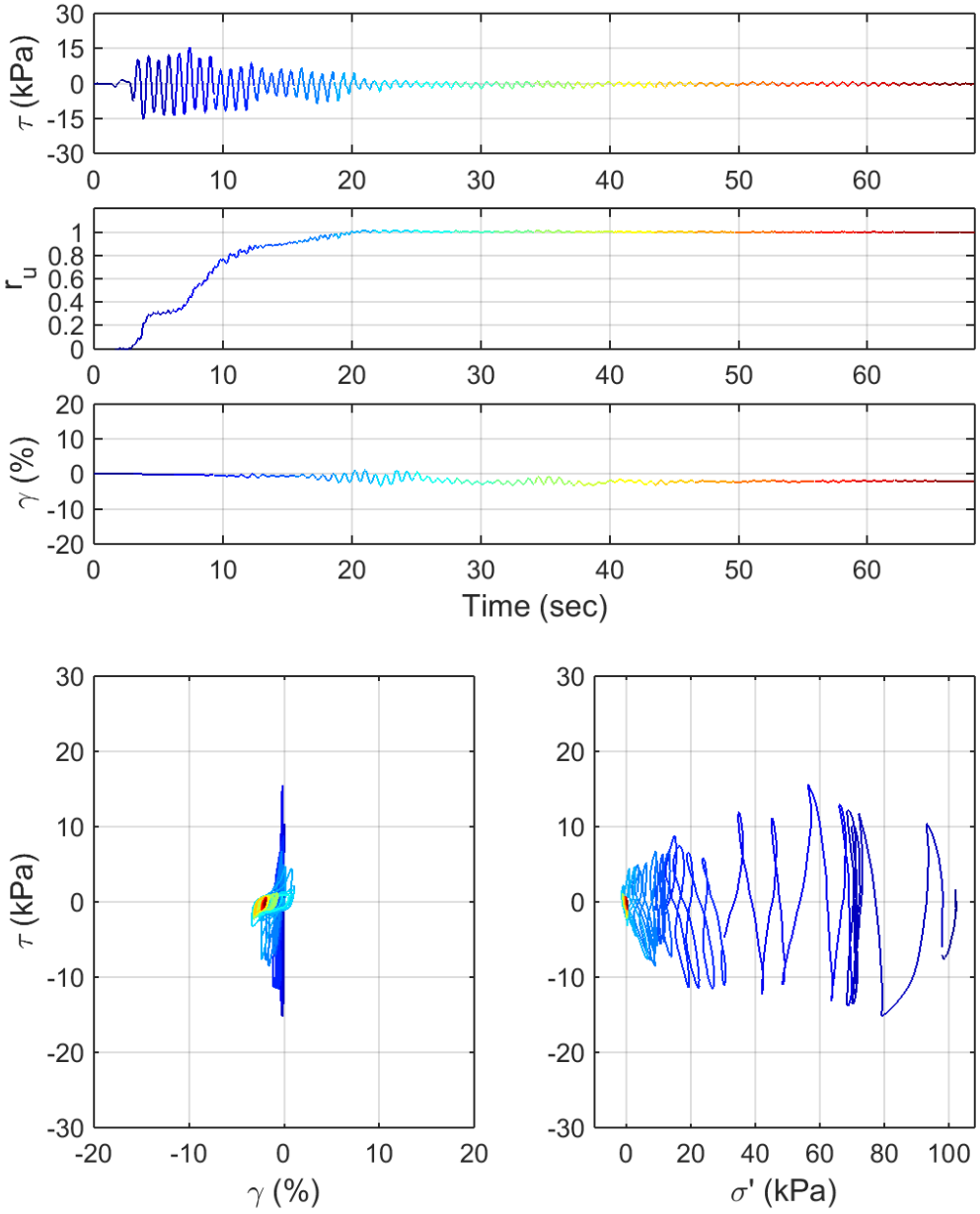

Test ID: 20130401
Nevada Sand
D_r = 37 %
Motion: NGA_no_107_B-OAP180.AT2

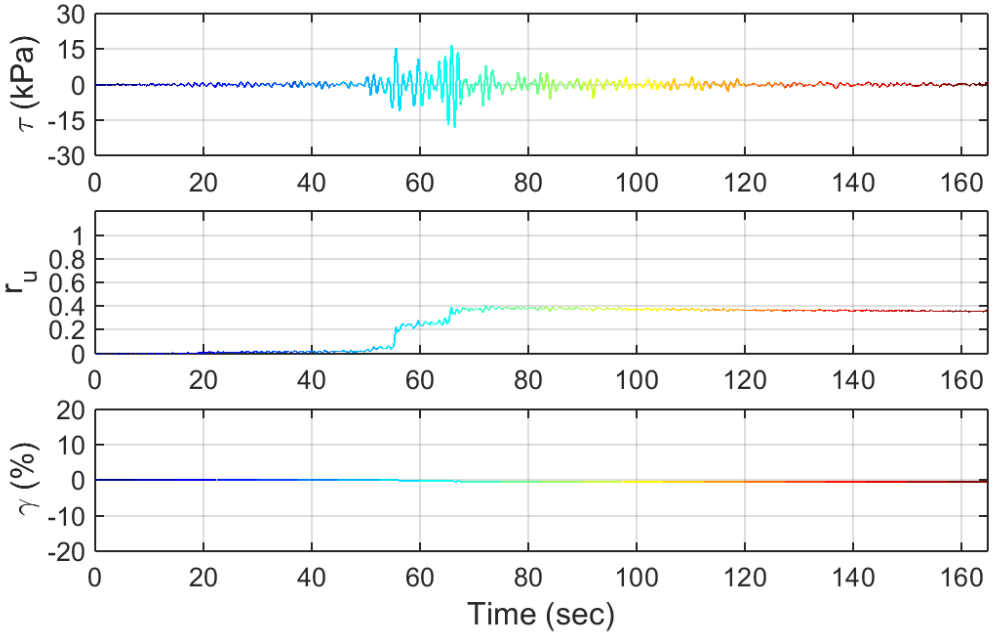

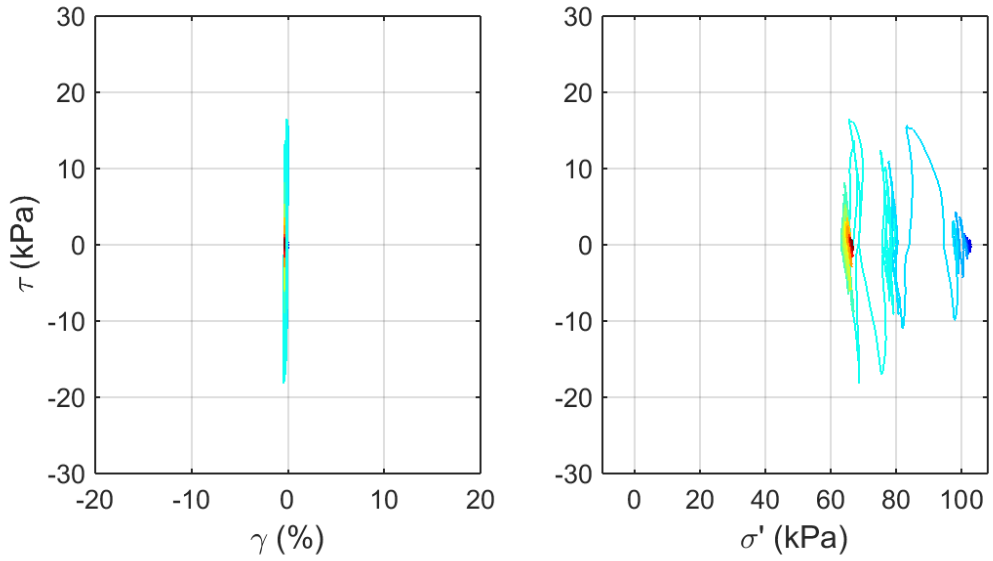

Test ID: 20130521
Nevada Sand
D_r = 42 %
Motion: NGA288_ABRZ000.AT2

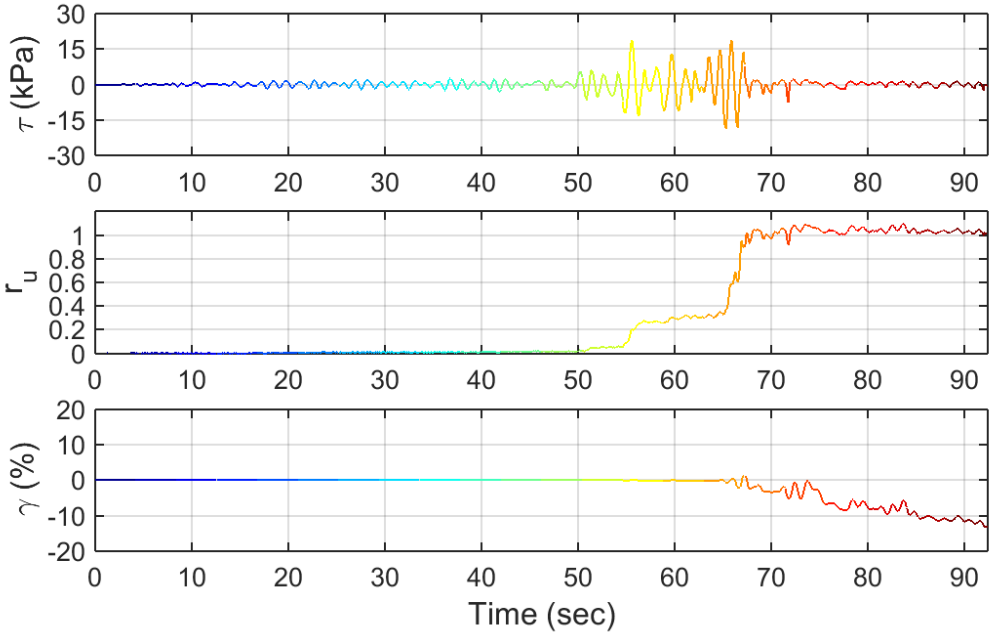

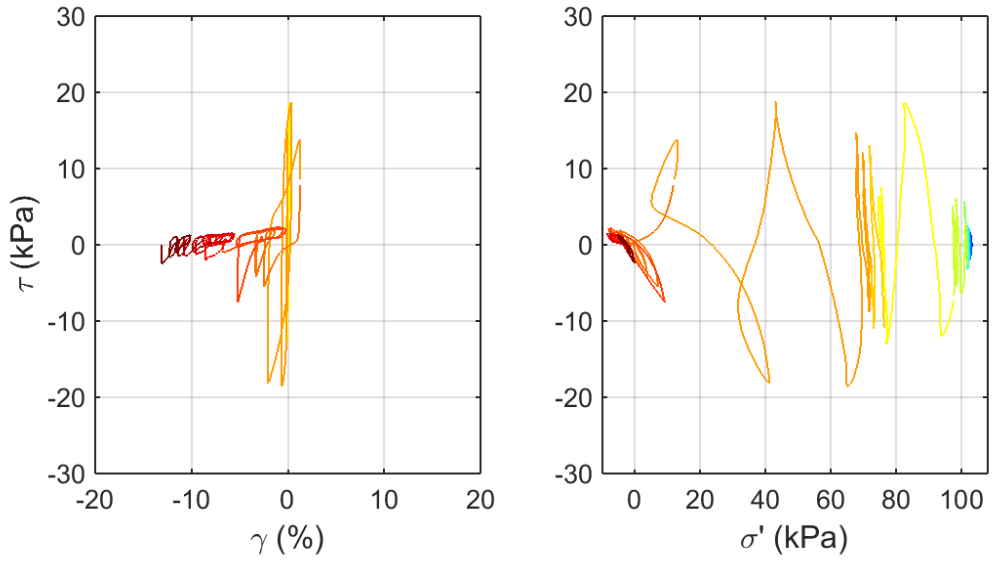

Test ID: 20130628
Nevada Sand
Dr = 43 %
Motion: NGA288_ABRZ000.AT2

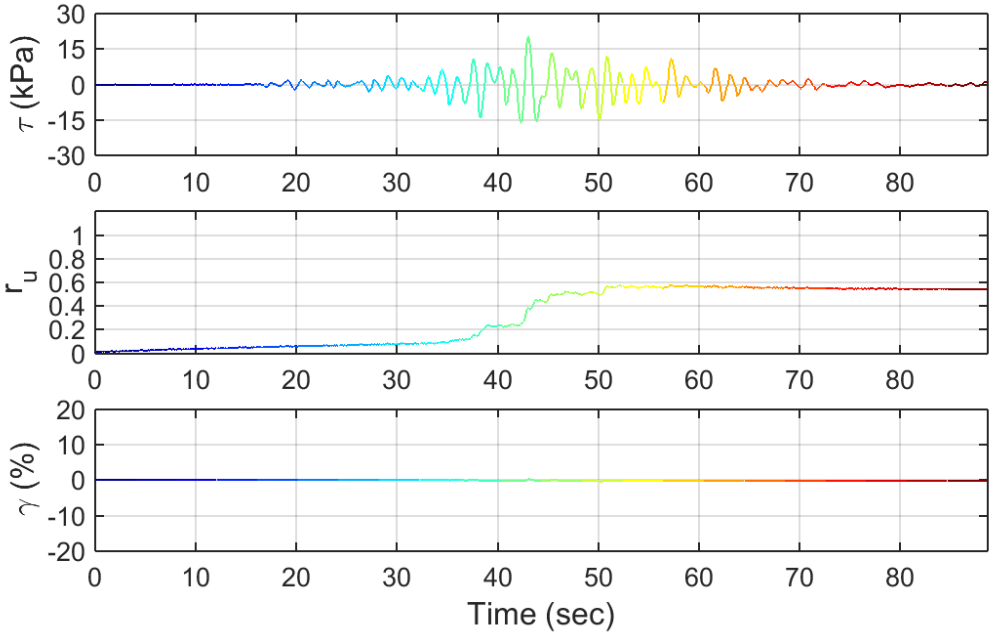

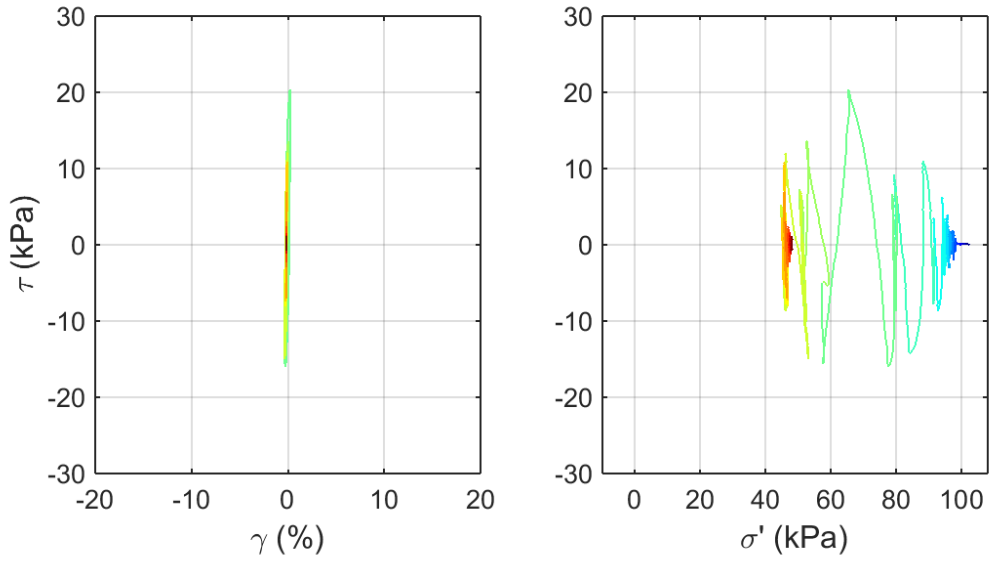

Test ID: 20130701
Nevada Sand
D_r = 36 %
Motion: NGA587_AMAT083.AT2

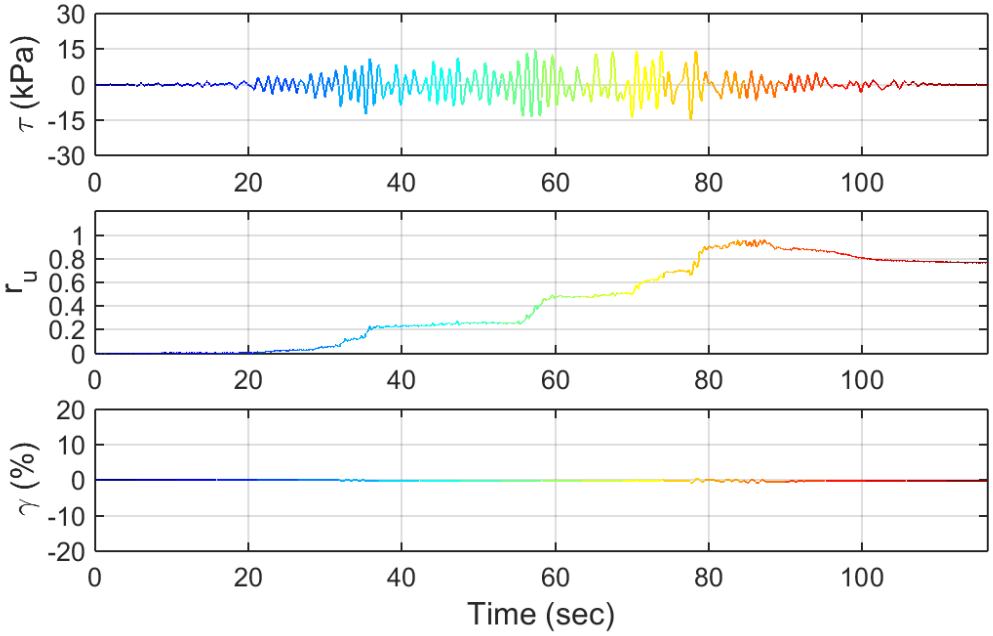

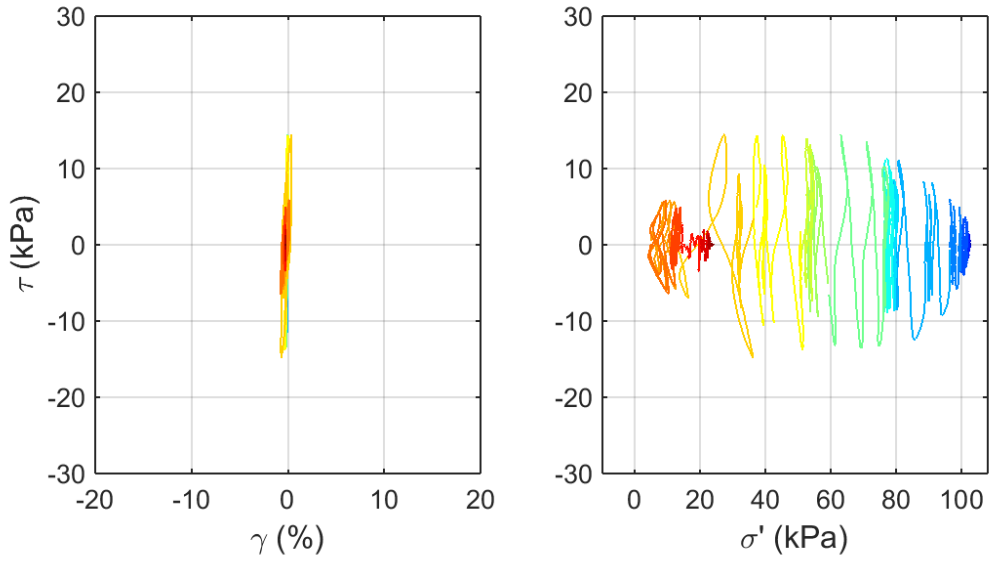

Test ID: 20130702
Nevada Sand
D_r = 50 %
Motion: NGA724_BPLS135.AT2

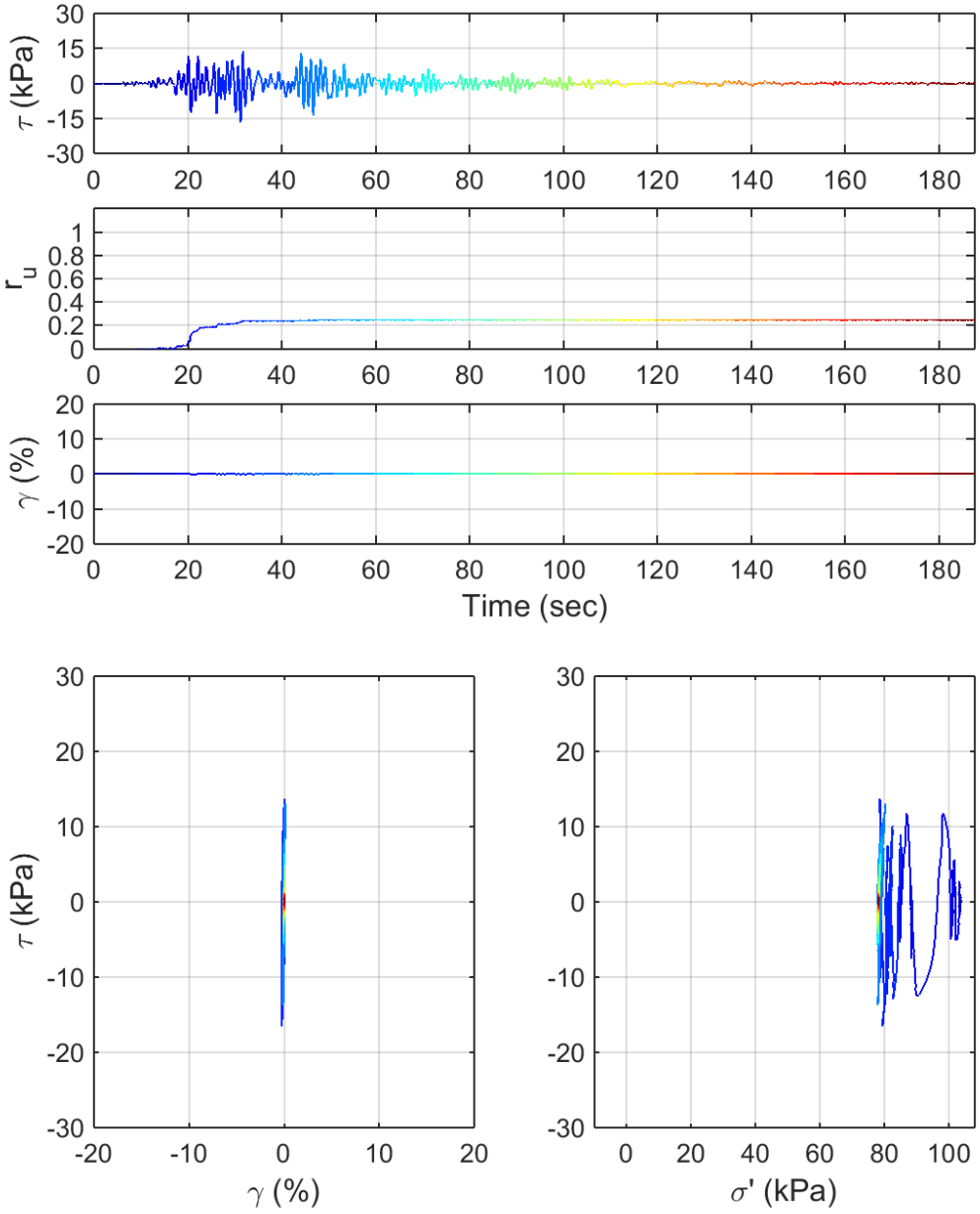

Test ID: 20130704
Nevada Sand
D_r = 42 %
Motion: NGA755_CYC195.AT2

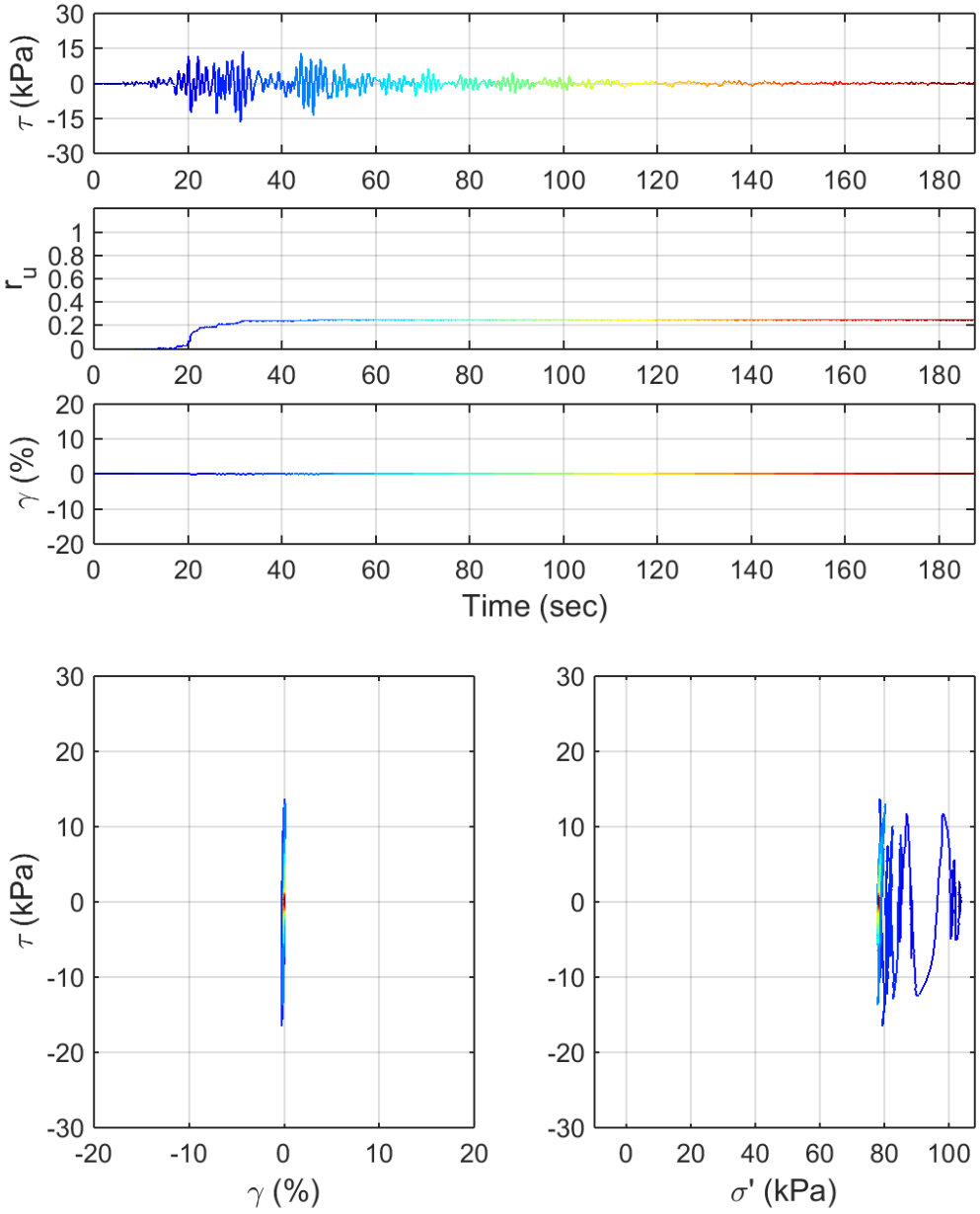

Test ID: 20130705
Nevada Sand
D_r = 45 %
Motion: NGA755_CYC195.AT2

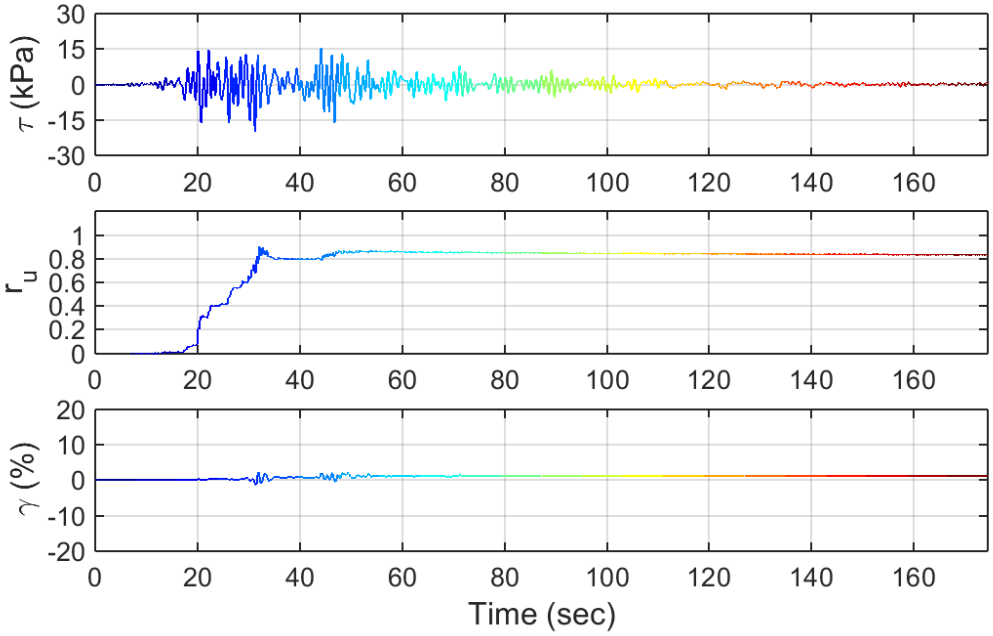

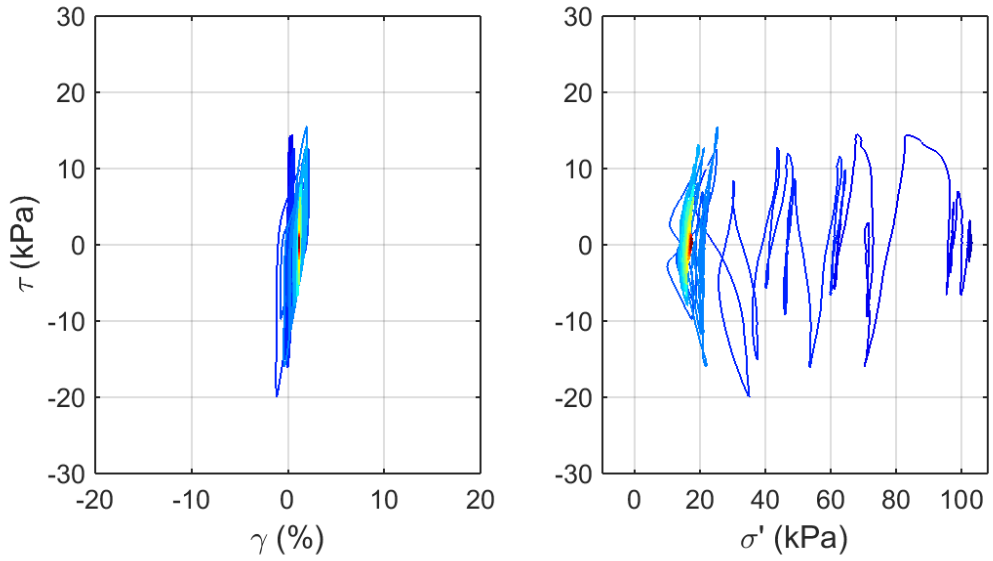

Test ID: 20130706
Nevada Sand
D_r = 49 %
Motion: NGA755_CYC195.AT2

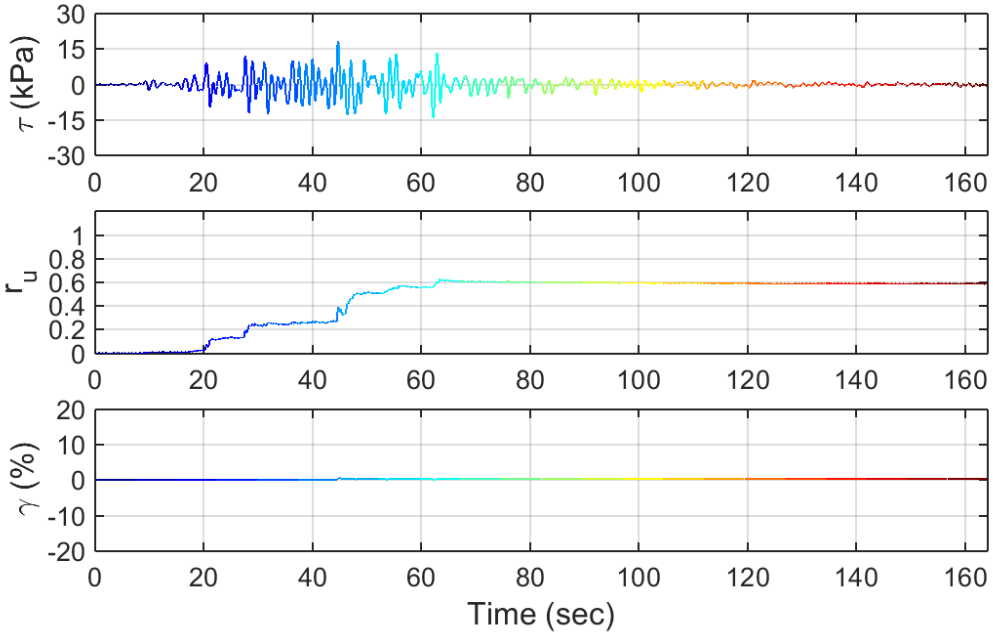

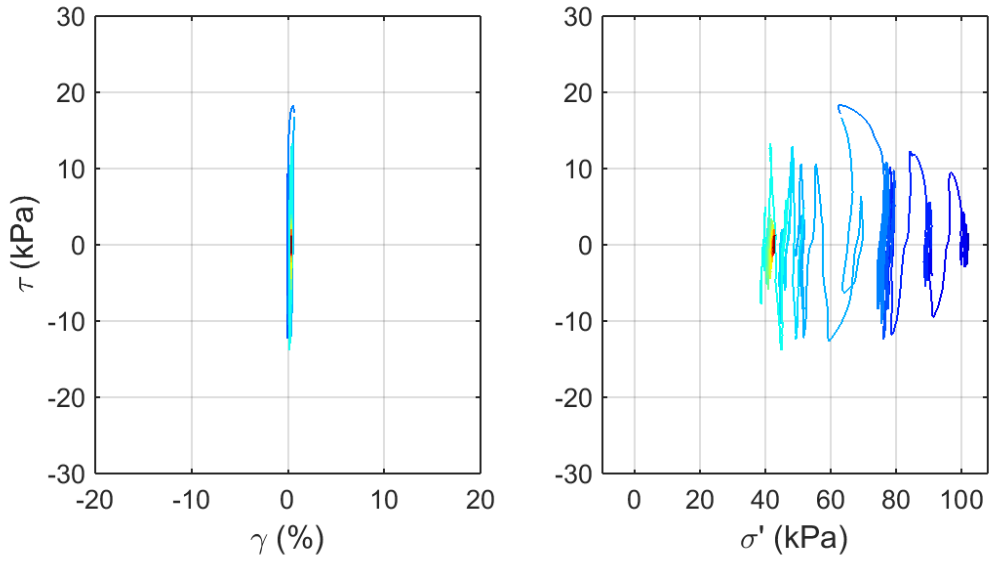

Test ID: 20130708
Nevada Sand
D_r = 43 %
Motion: NGA988_CCN360.AT2

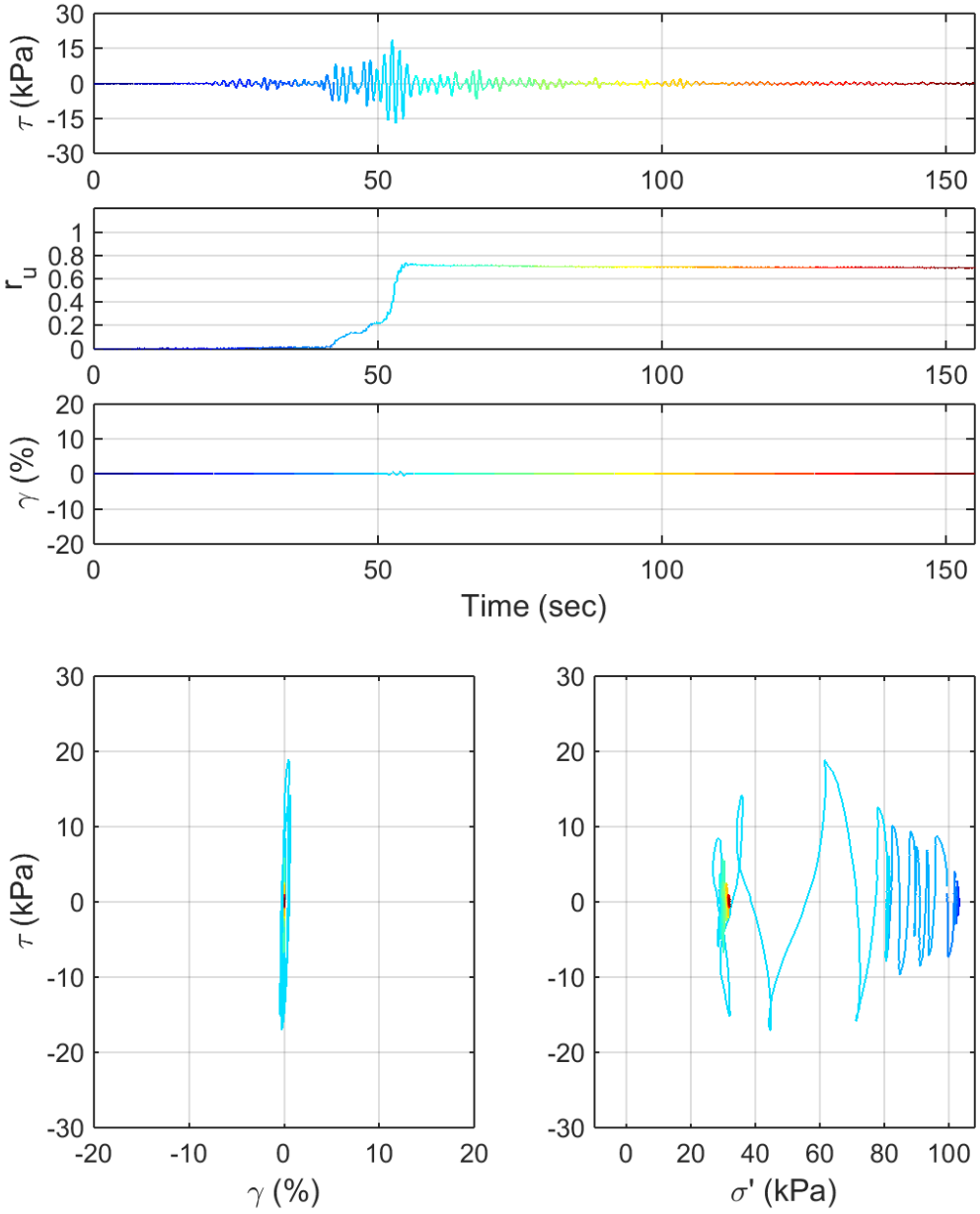

Test ID: 20130709
Nevada Sand
D_r = 39 %
Motion: NGA1020_H12090.AT2

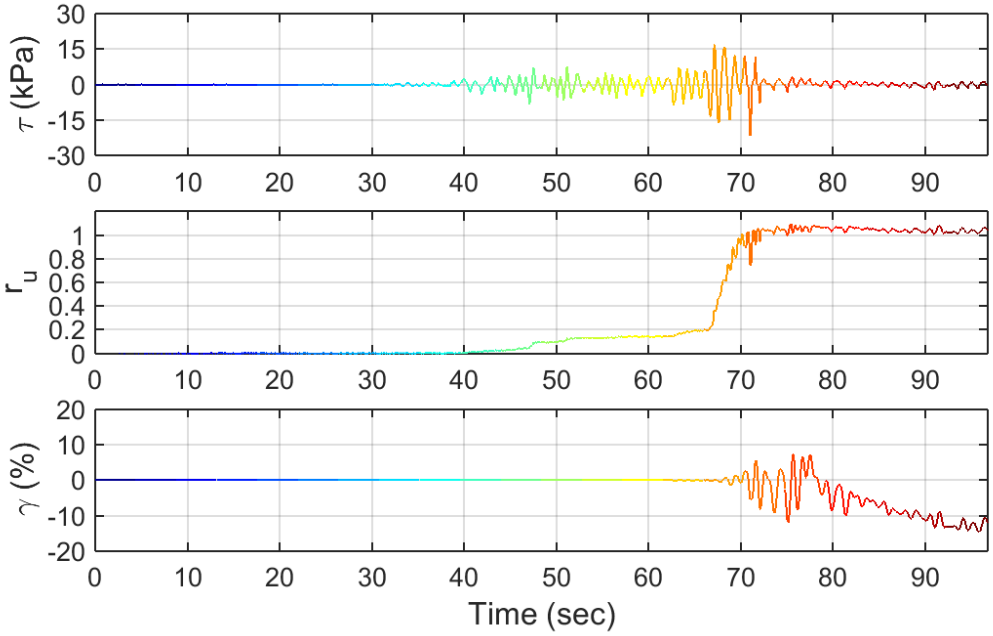

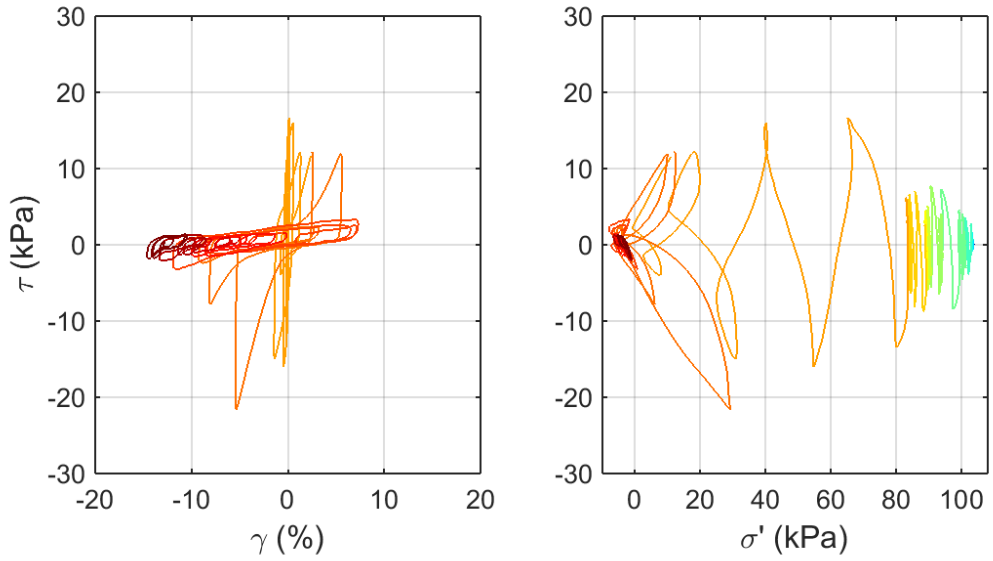

Test ID: 20130815
Nevada Sand
D_r = 43 %
Motion: 6530_2A

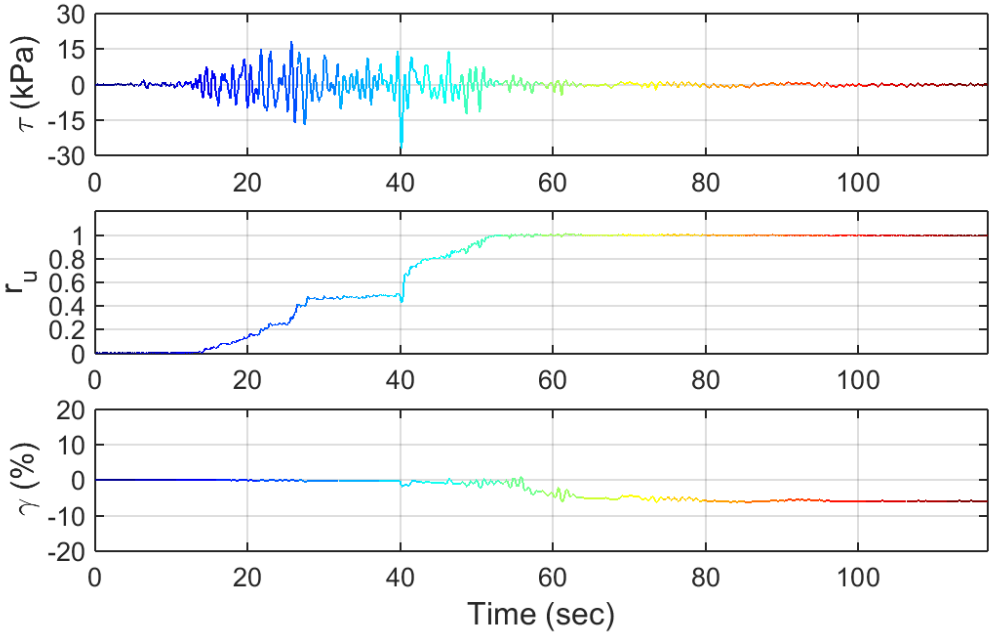

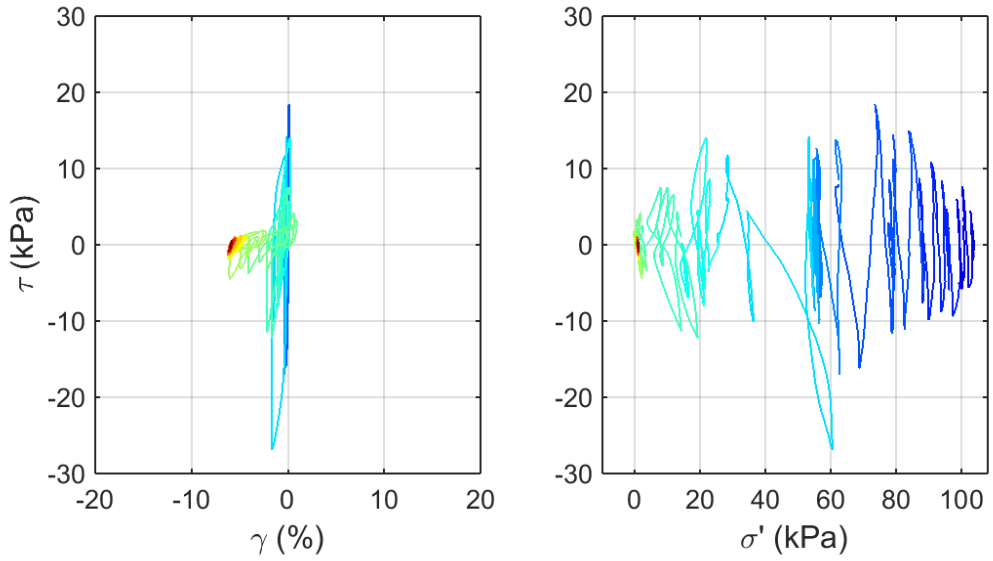

Test ID: 20130916
Nevada Sand
D_r = 47 %
Motion: 7030_1A

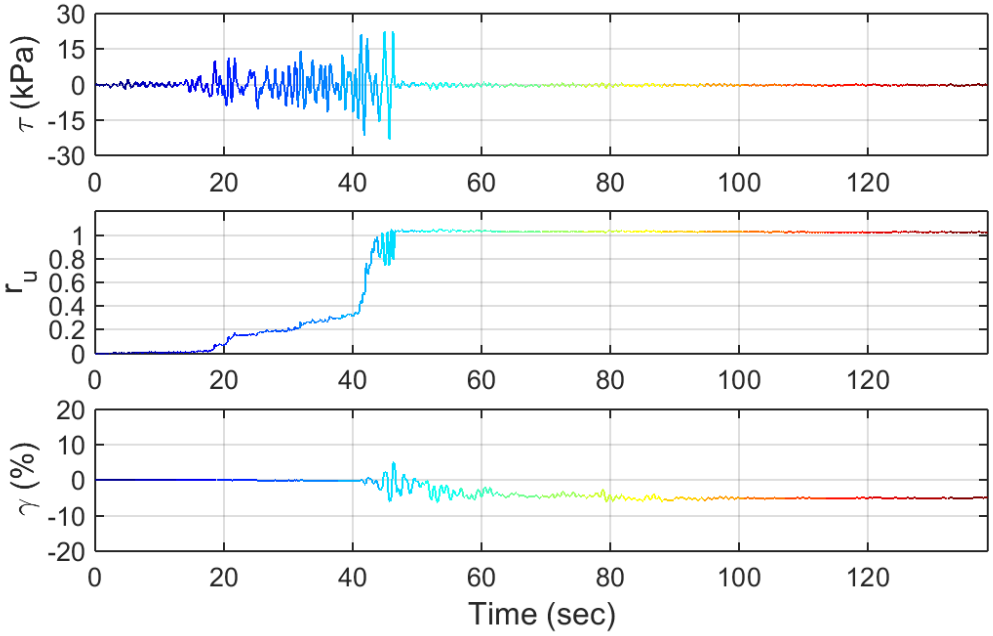

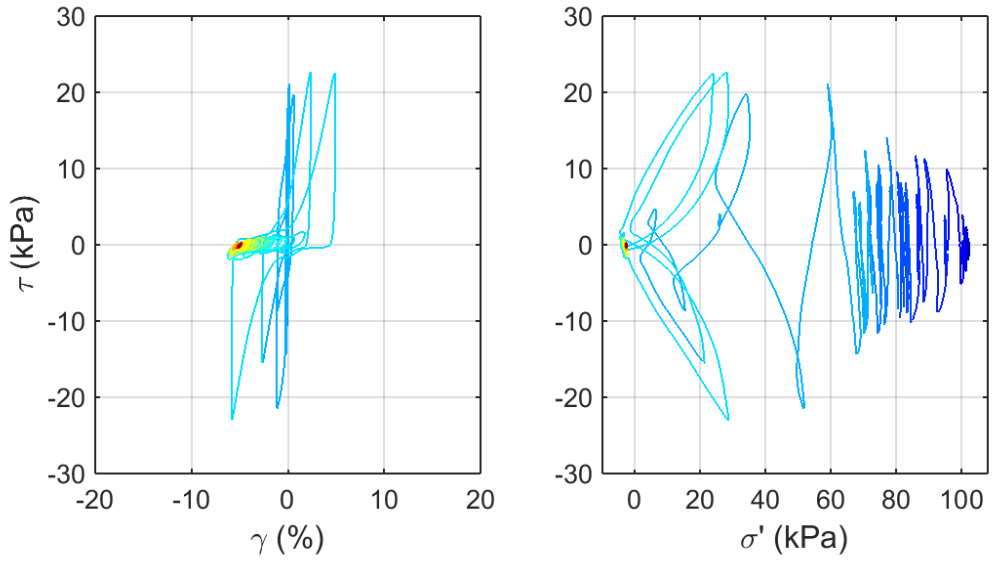

Test ID: 20130918
Nevada Sand
D_r = 48 %
Motion: 7030_2A

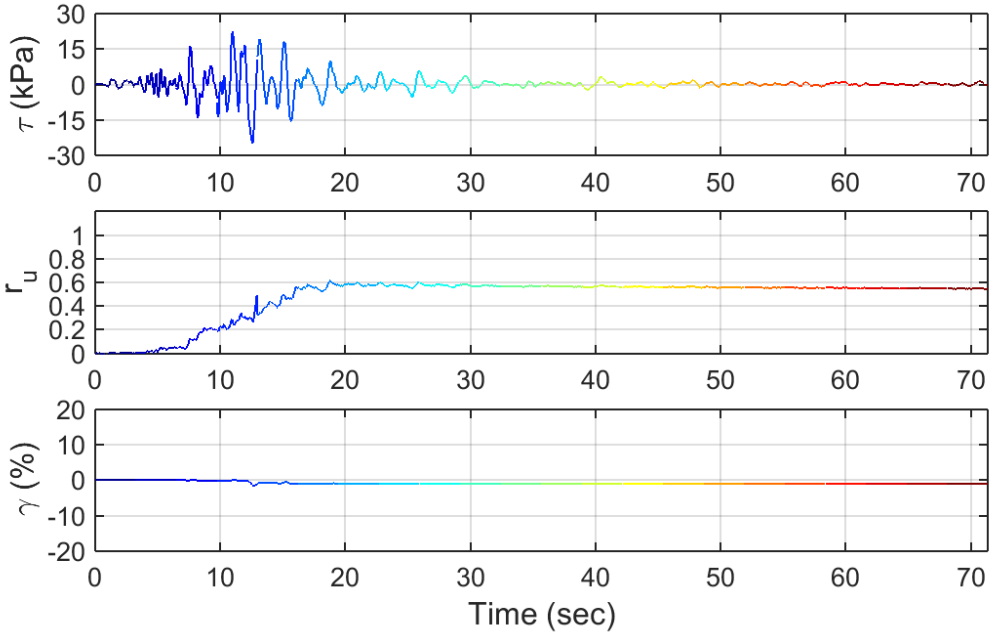

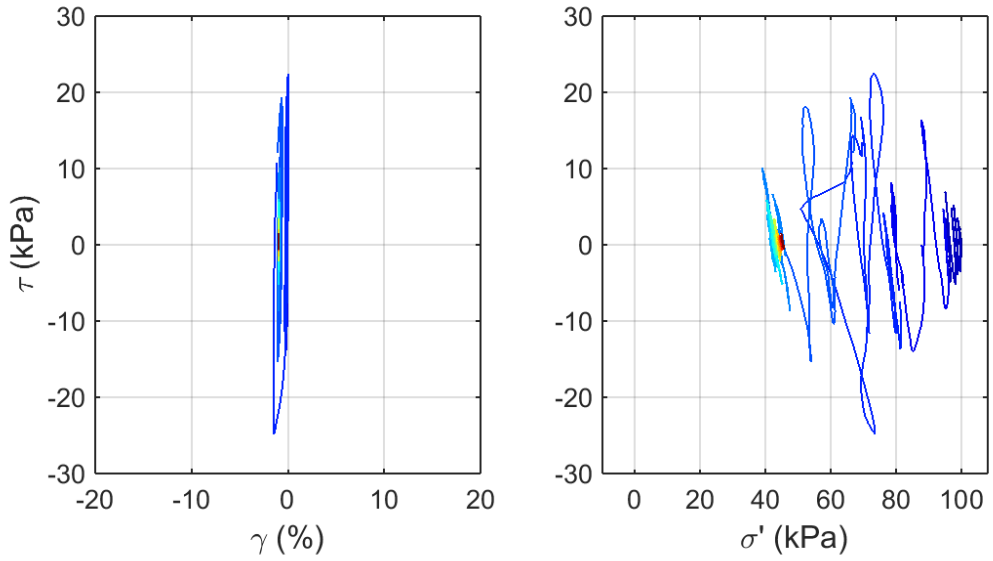

Test ID: 20130919
Nevada Sand
D_r = 55 %
Motion: 6530_1B

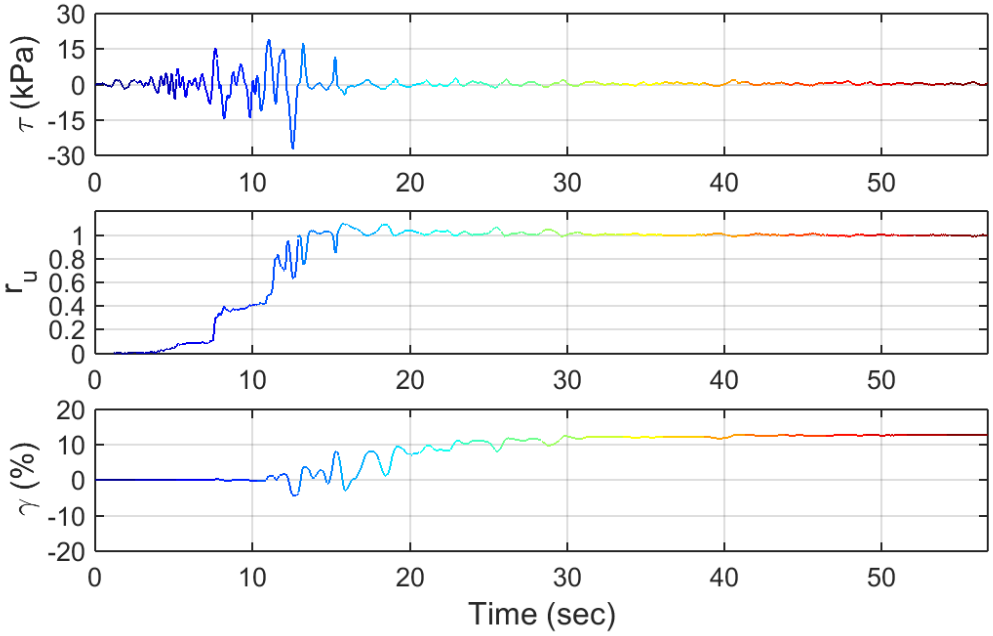

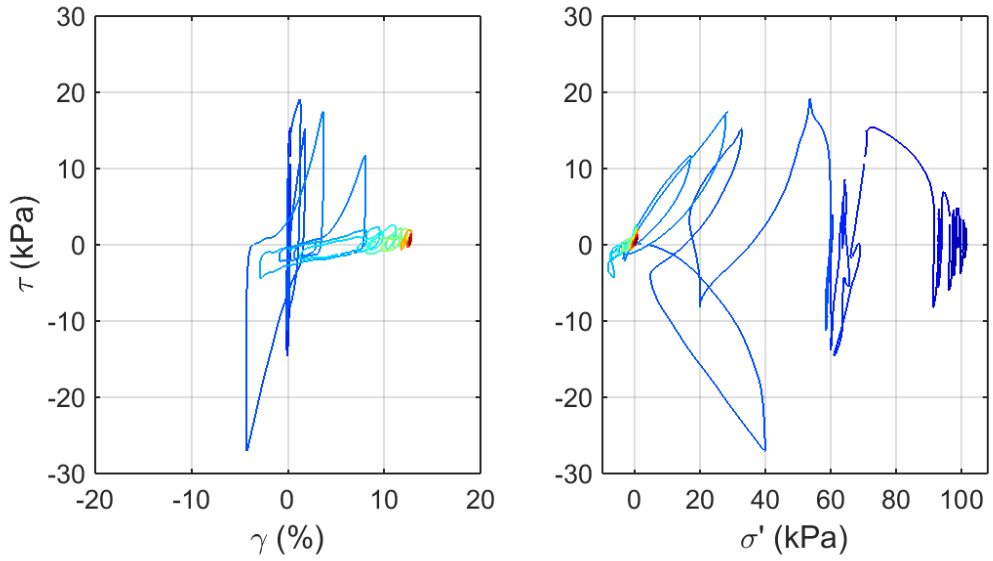

Test ID: 20130921
Nevada Sand
D_r = 44 %
Motion: 6530_1B

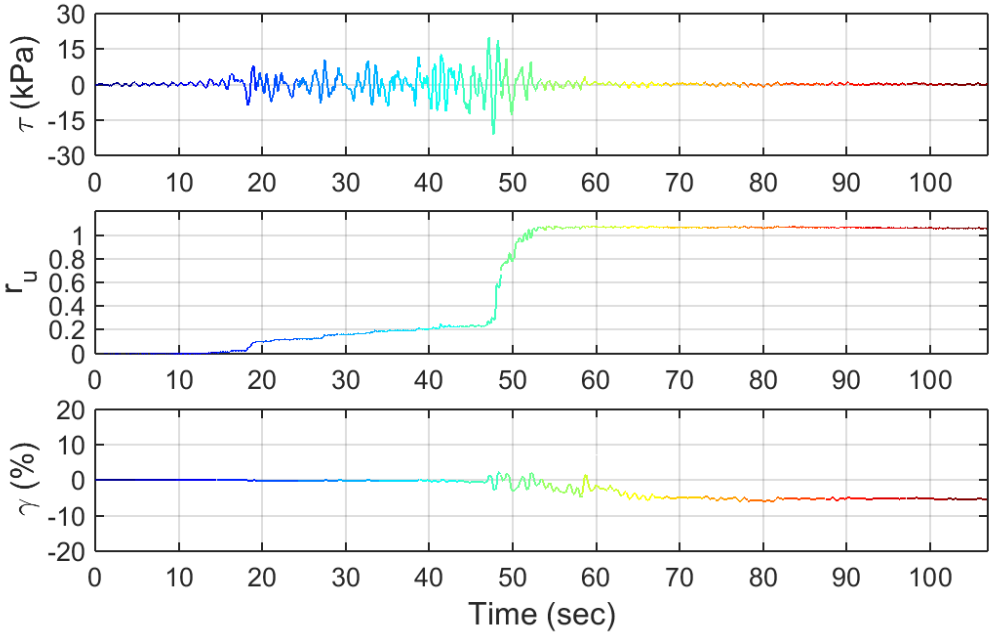

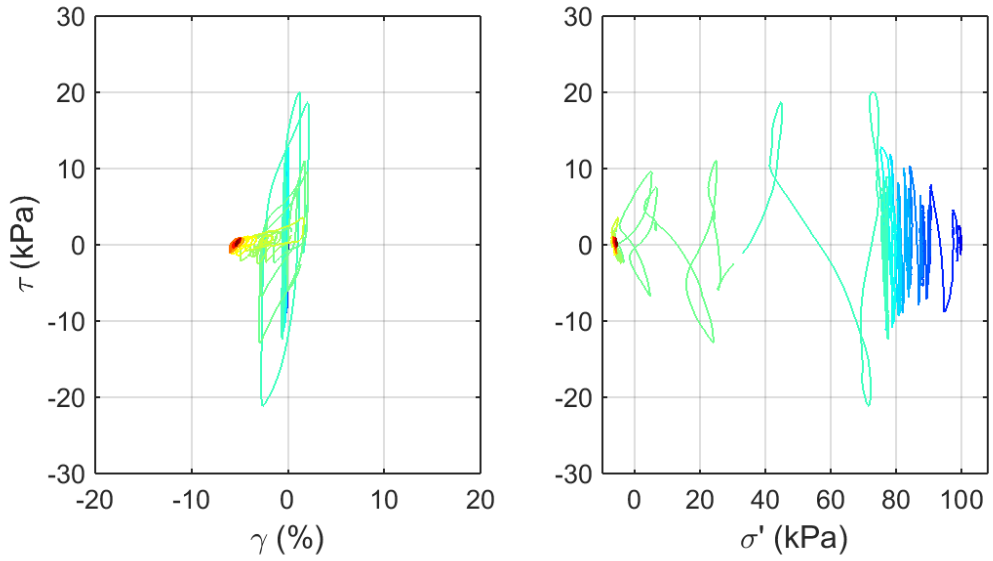

Test ID: 20130923
Nevada Sand
D_r = 49 %
Motion: 7030_2B

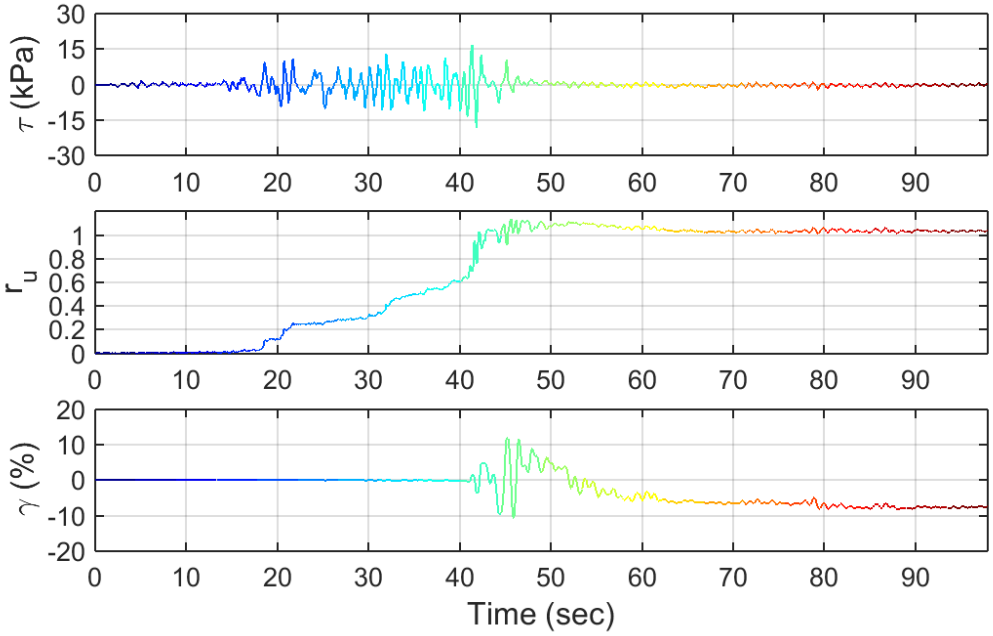

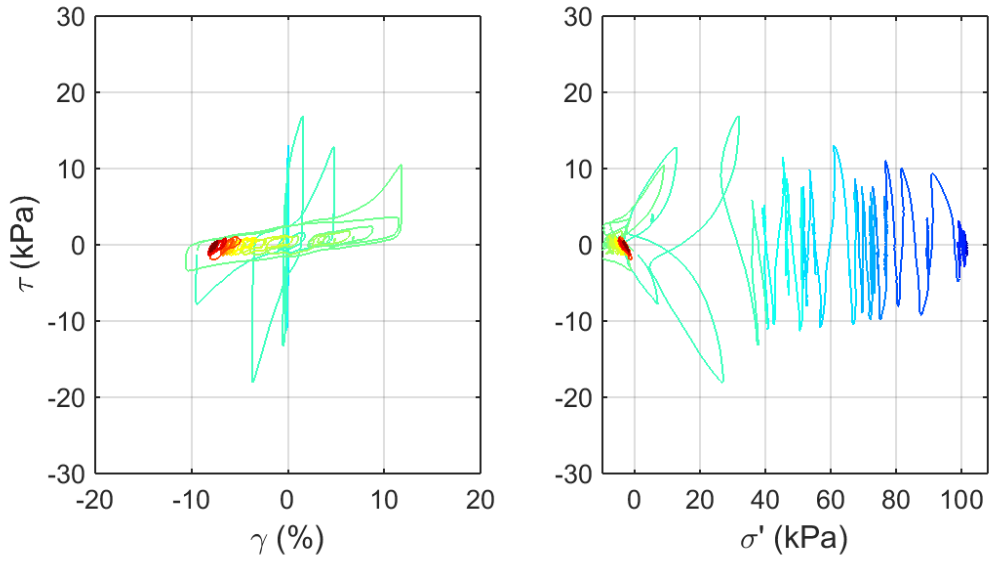

Test ID: 20130924
Nevada Sand
$D_r = 41$ %
Motion: 7030_2A

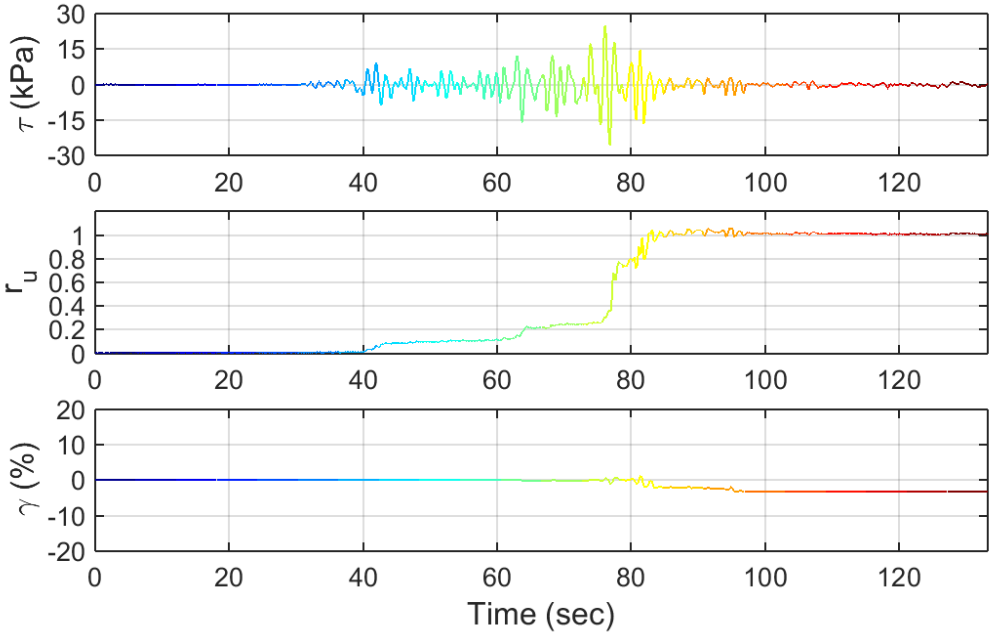

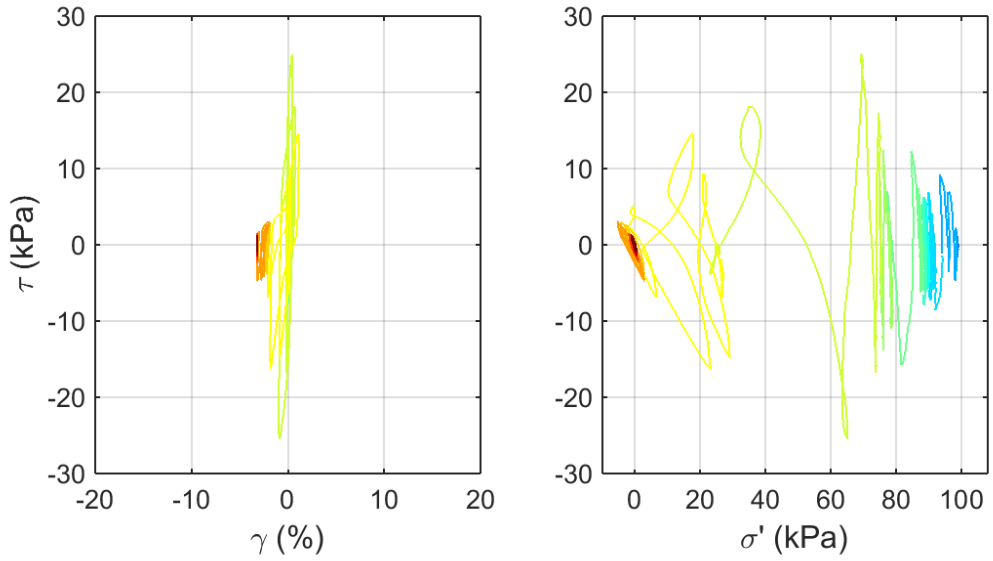

Test ID: 20130925
Nevada Sand
D_r = 55 %
Motion: 6530_2B

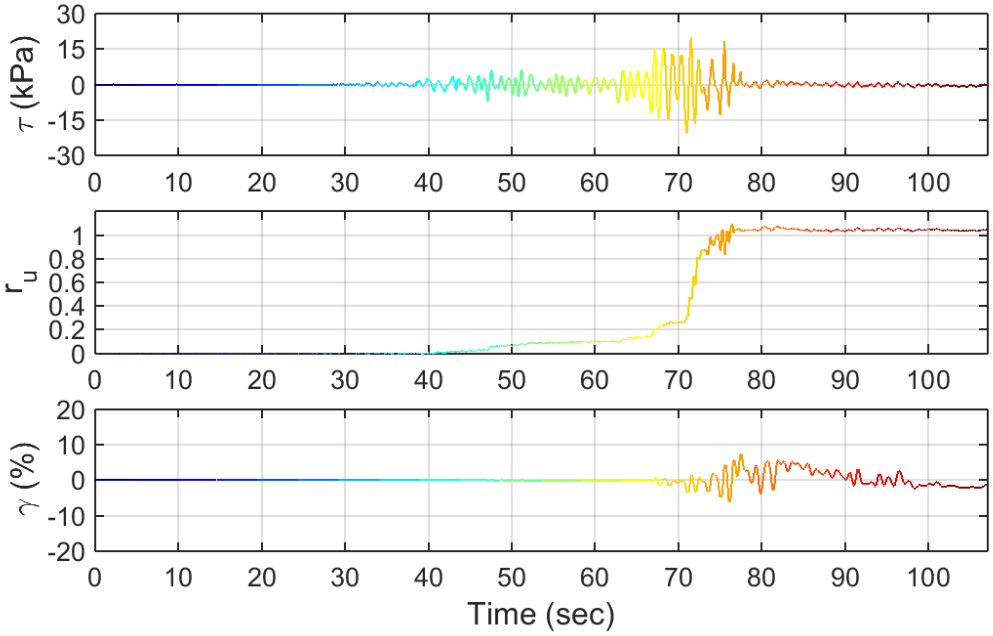

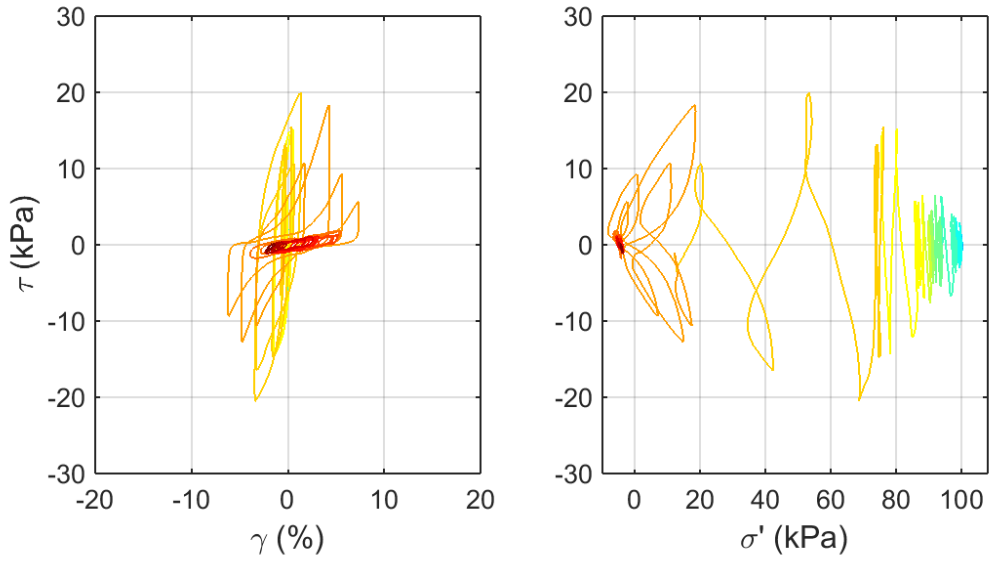

Test ID: 20131001
Nevada Sand
D_r = 50 %
Motion: 6530_2A

APPENDIX A.5. CSS DATA: TRANSIENT LOADING (D_R = 70 TO 91%)

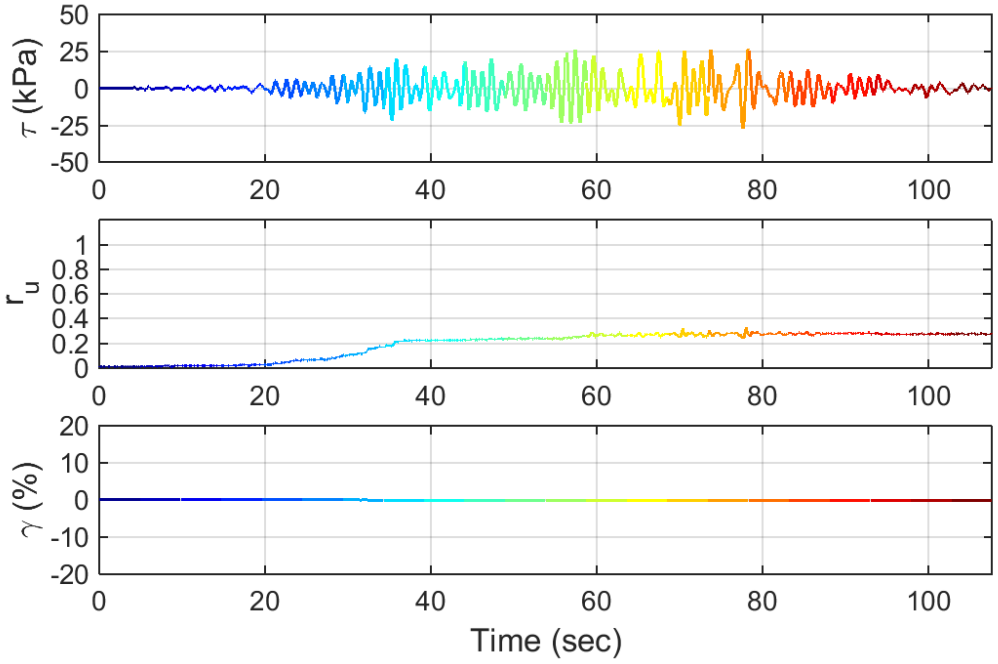

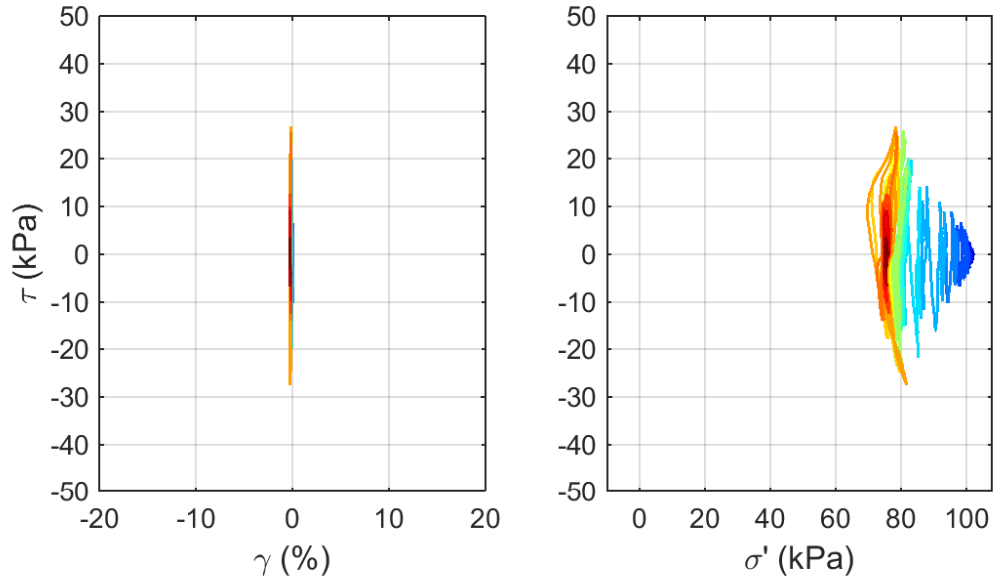

Test ID: 20130710
Nevada Sand
D_r = 80 %
Motion: NGA724_BPLS135.AT2

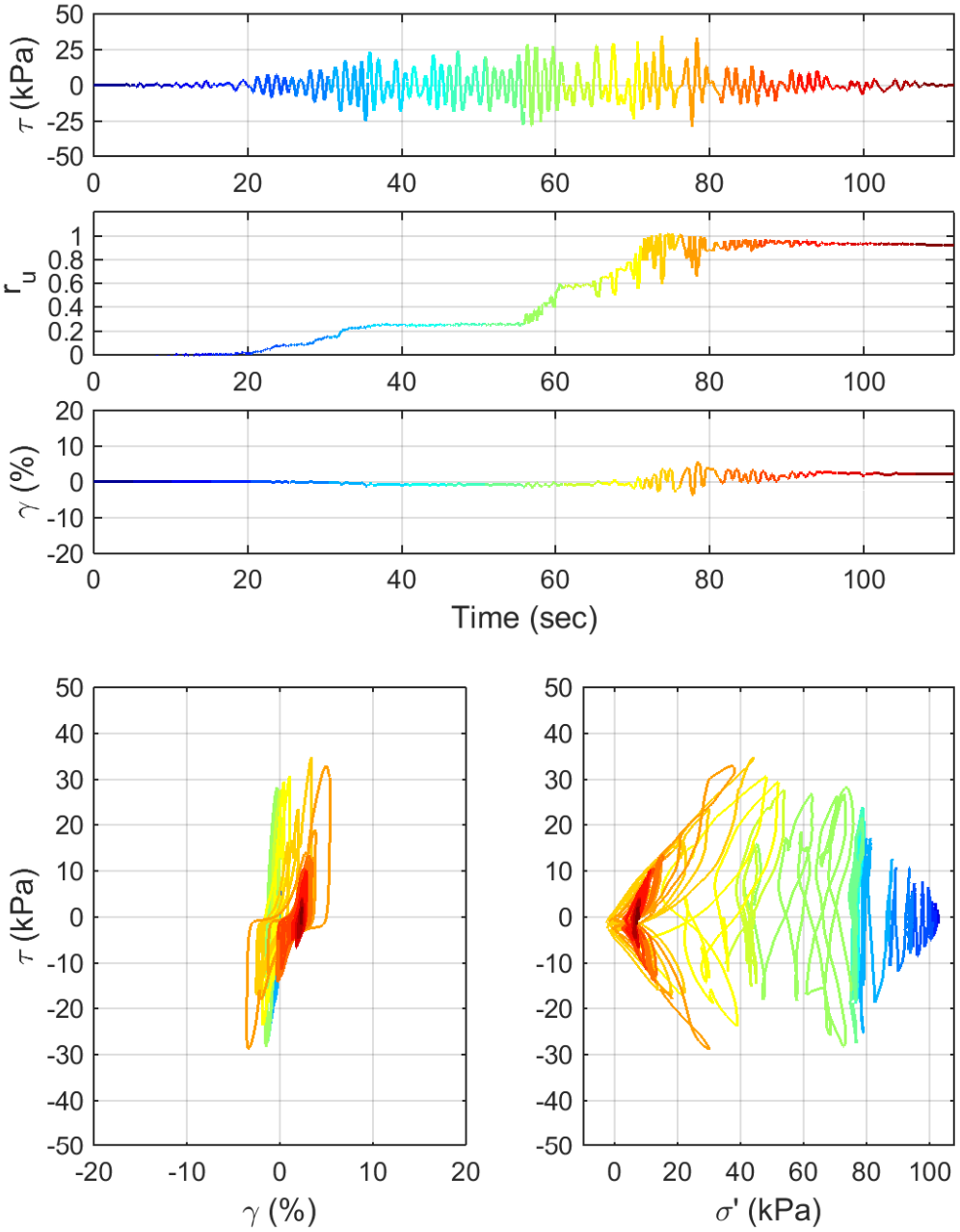

Test ID: 2013071102
Nevada Sand
D_r = 78 %
Motion: NGA724_BPLS135.AT2

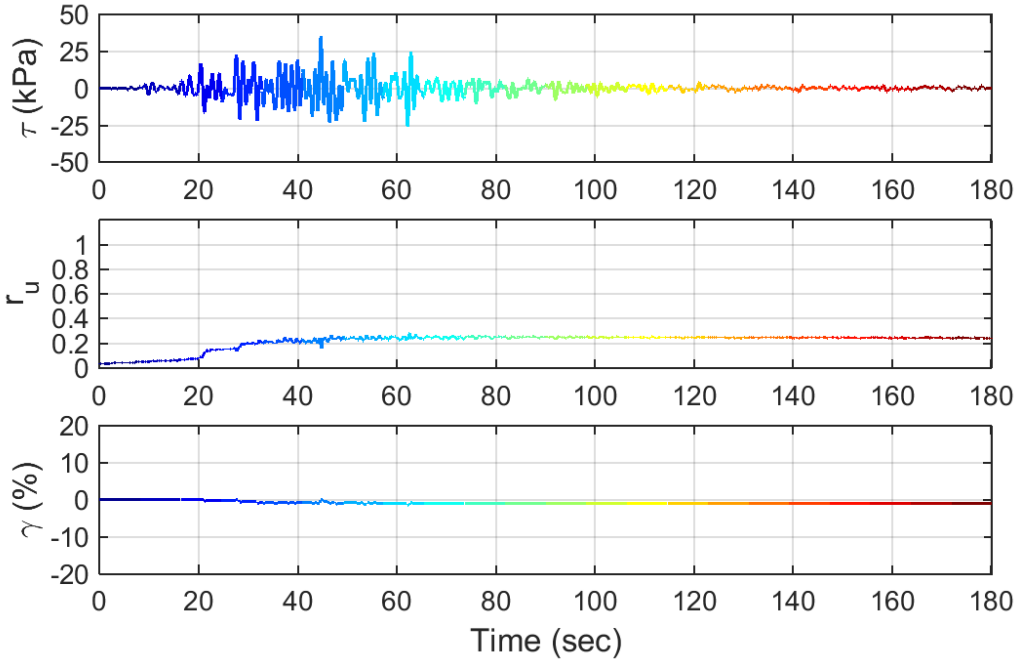

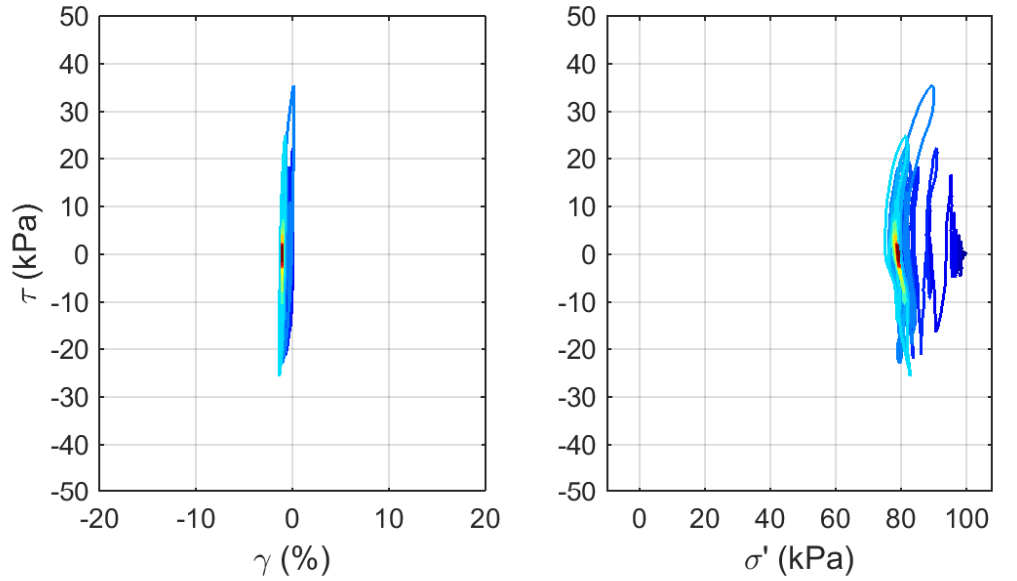

Test ID: 20130712
Nevada Sand
D_r = 77 %
Motion: NGA988_CCN360.AT2

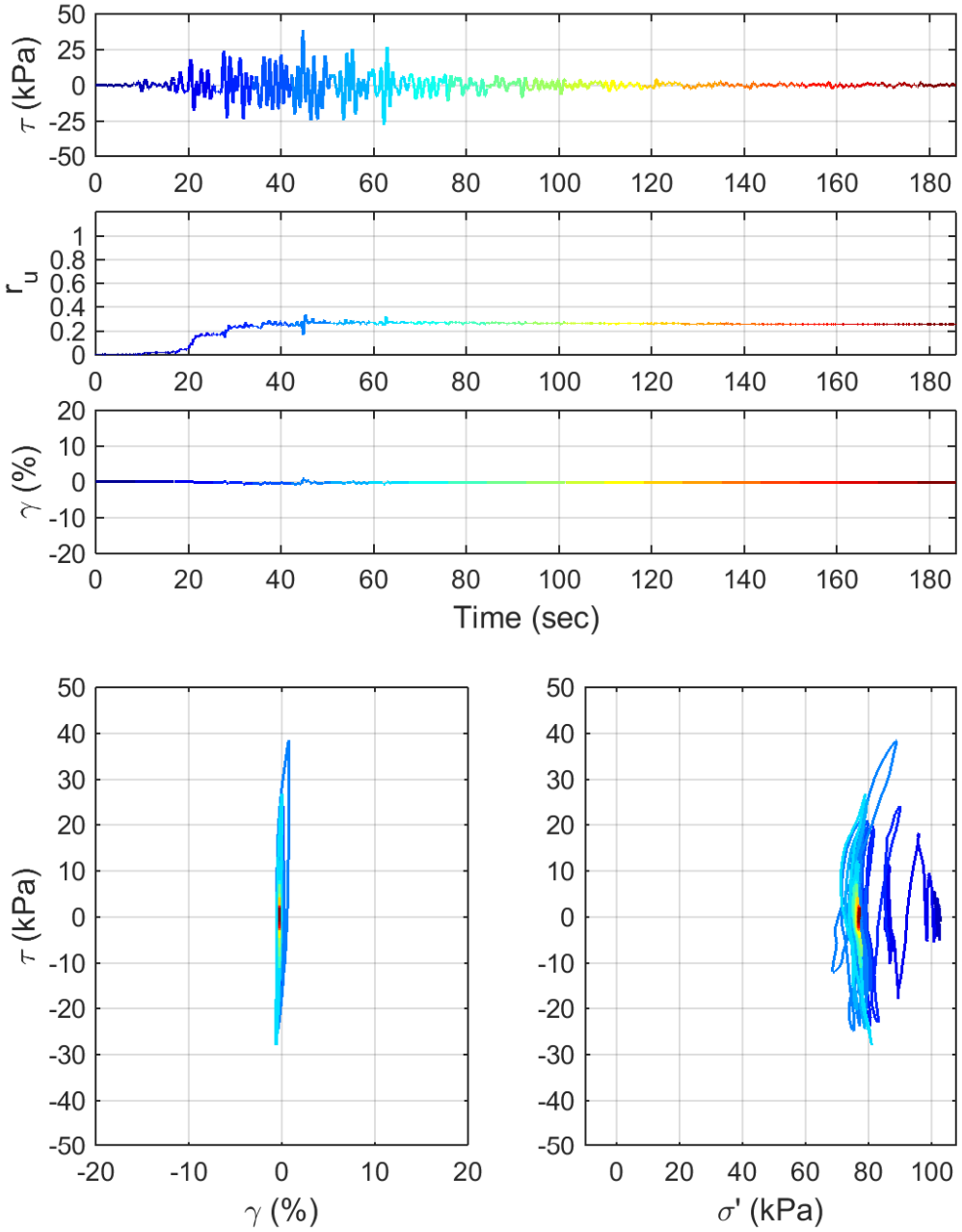

Test ID: 20130726
Nevada Sand
D_r = 74 %
Motion: NGA988_CCN360.AT2

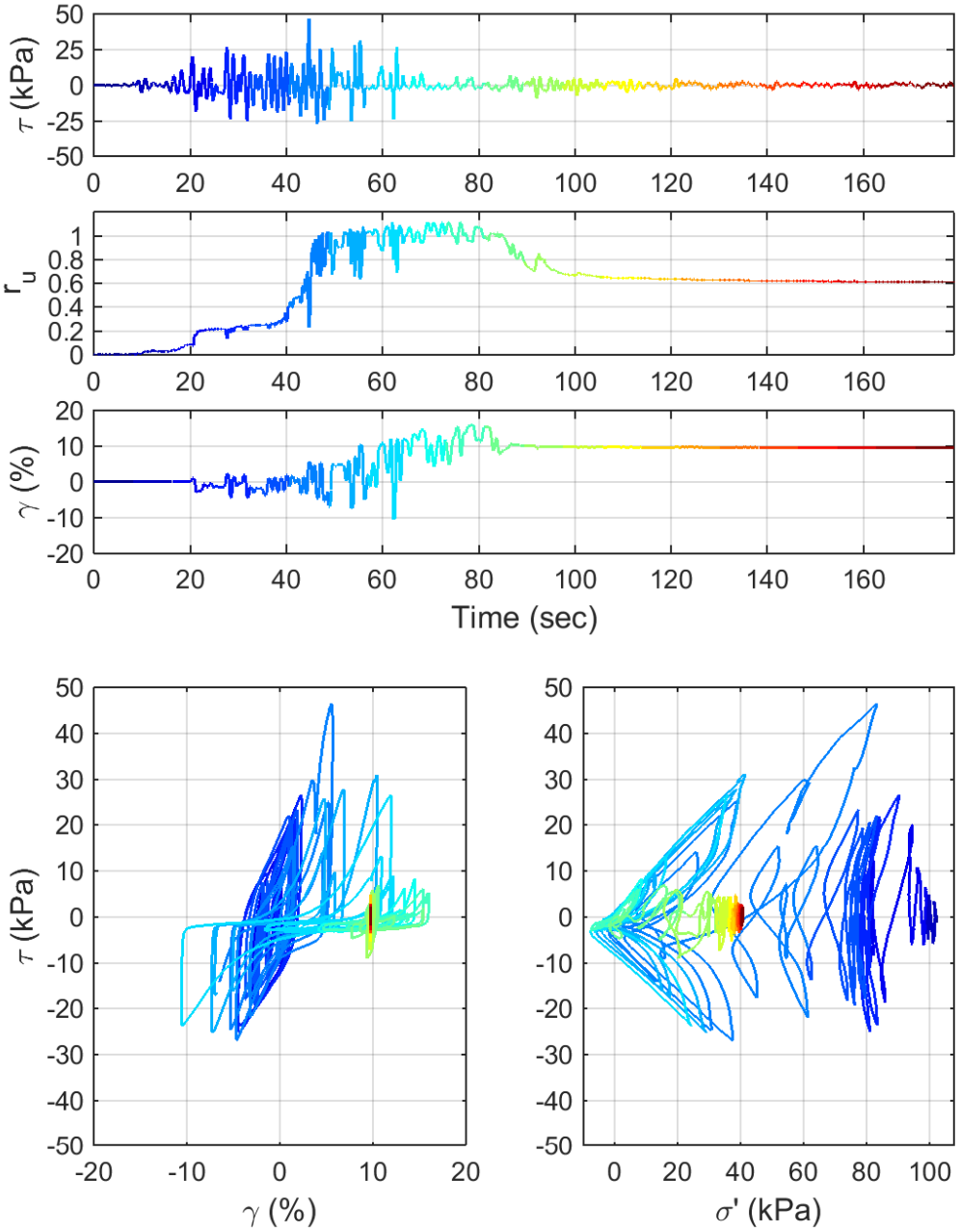

Test ID: 2013072602
Nevada Sand
D_r = 72 %
Motion: NGA988_CCN360.AT2

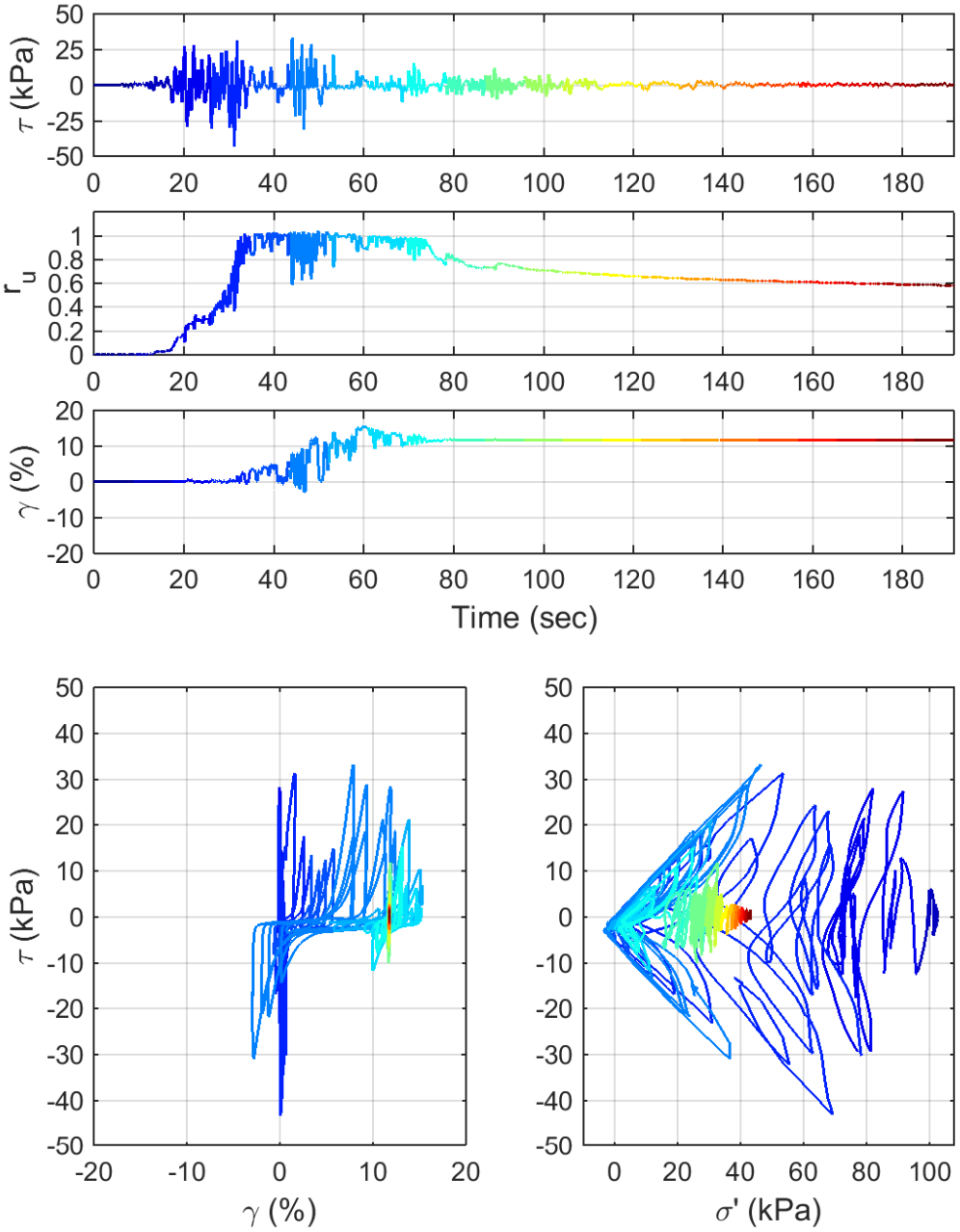

Test ID: 20130727
Nevada Sand
D_r = 84 %
Motion: NGA755_CYC195.AT2

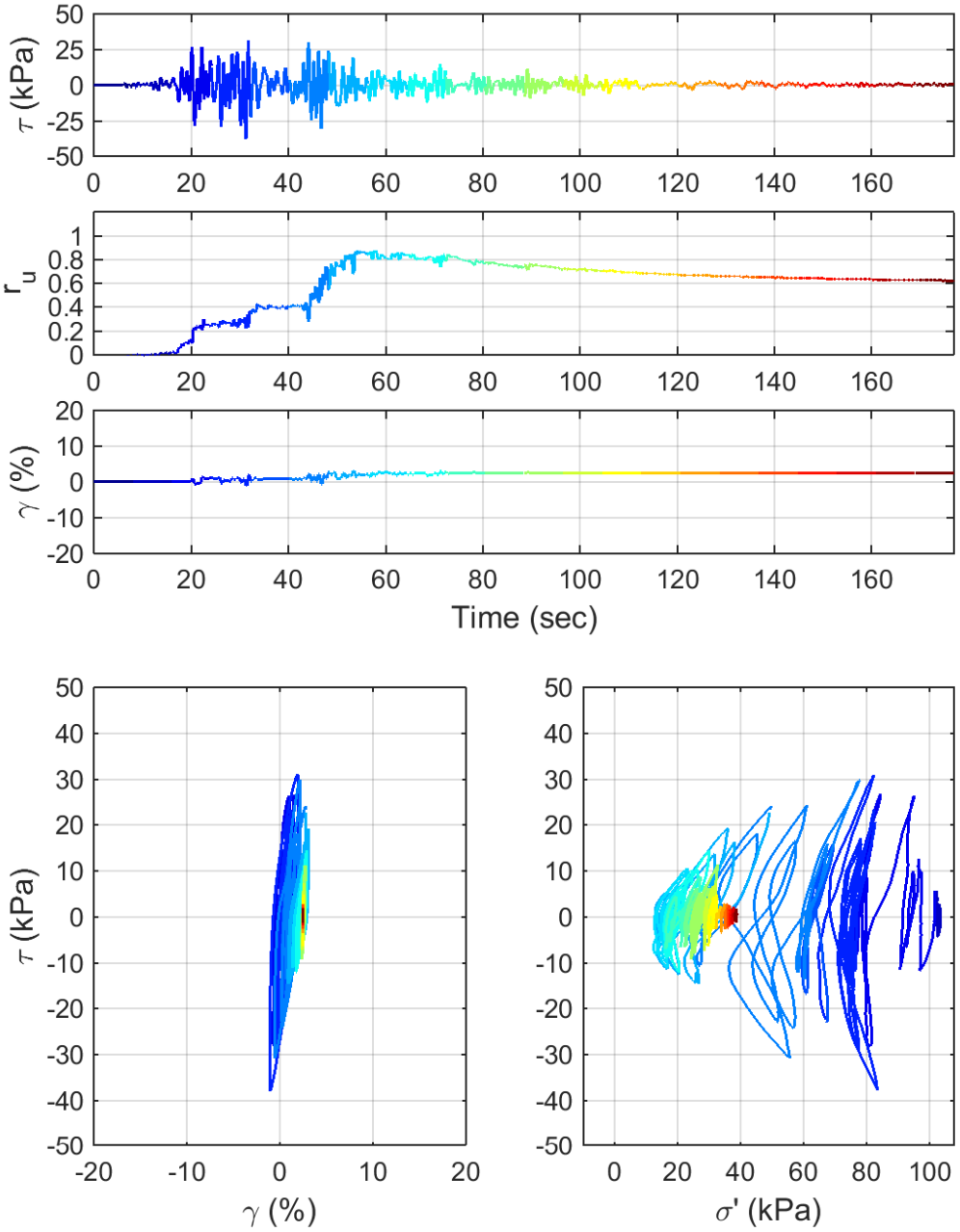

Test ID: 20130728
Nevada Sand
D_r = 79 %
Motion: NGA755_CYC195.AT2

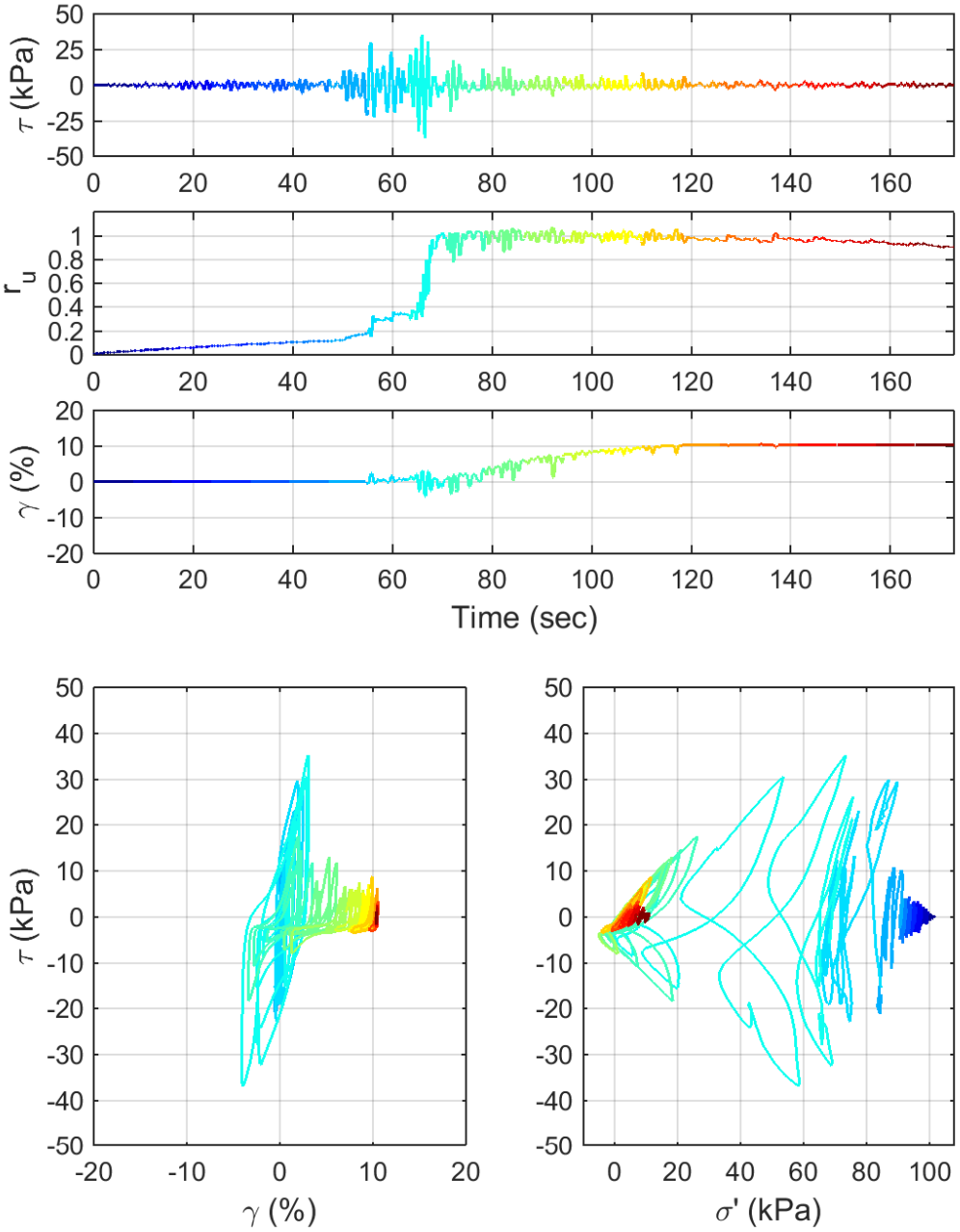

Test ID: 20130729
Nevada Sand
D_r = 82 %
Motion: NGA288_ABRZ000.AT2

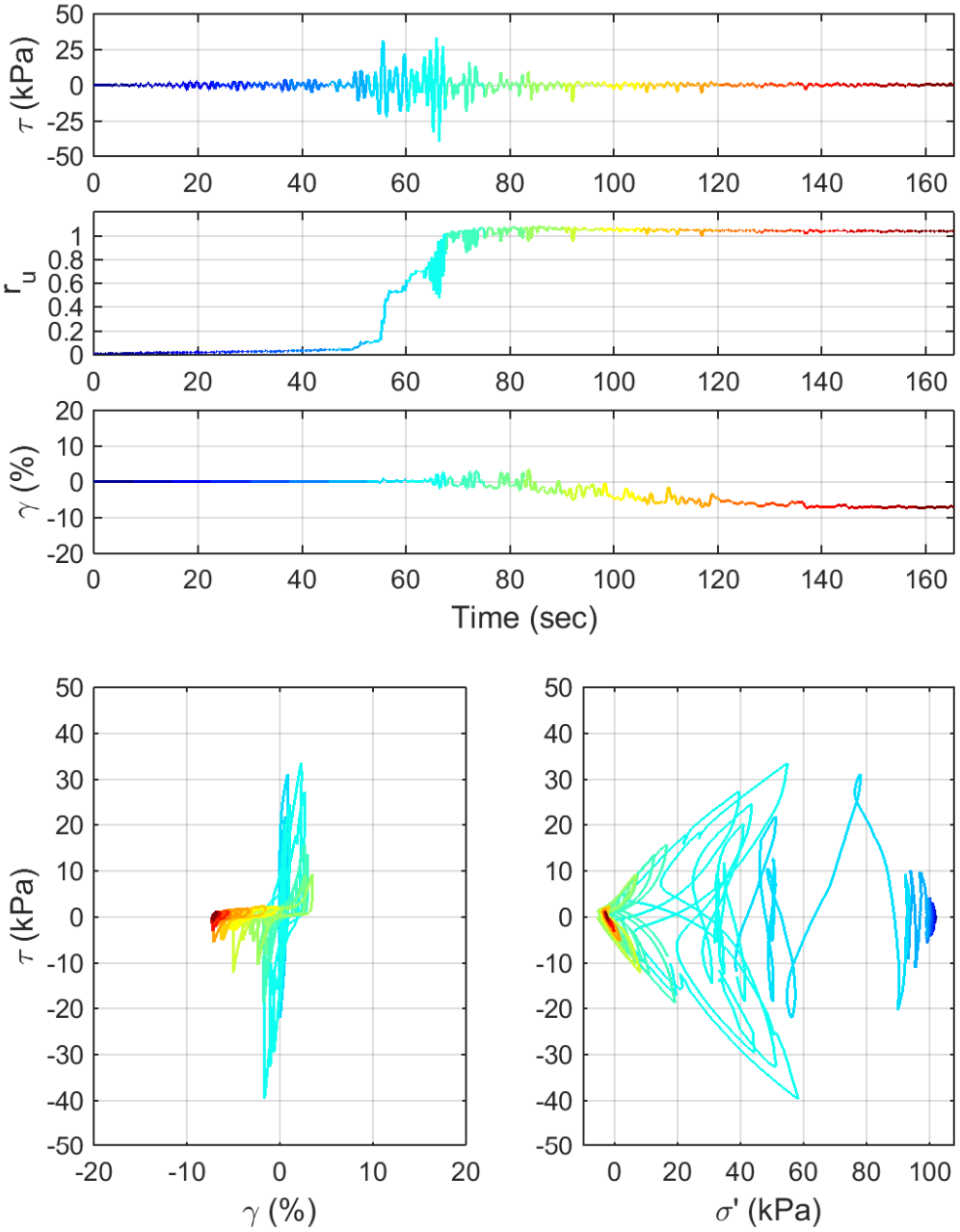

Test ID: 20130730
Nevada Sand
D_r = 86 %
Motion: NGA288_ABRZ000.AT2

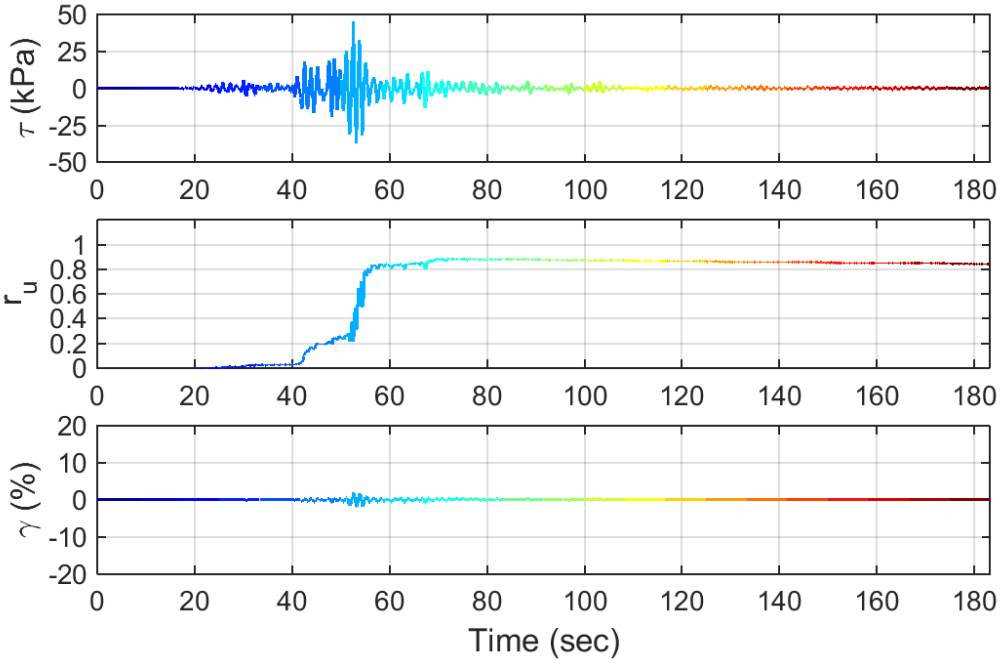

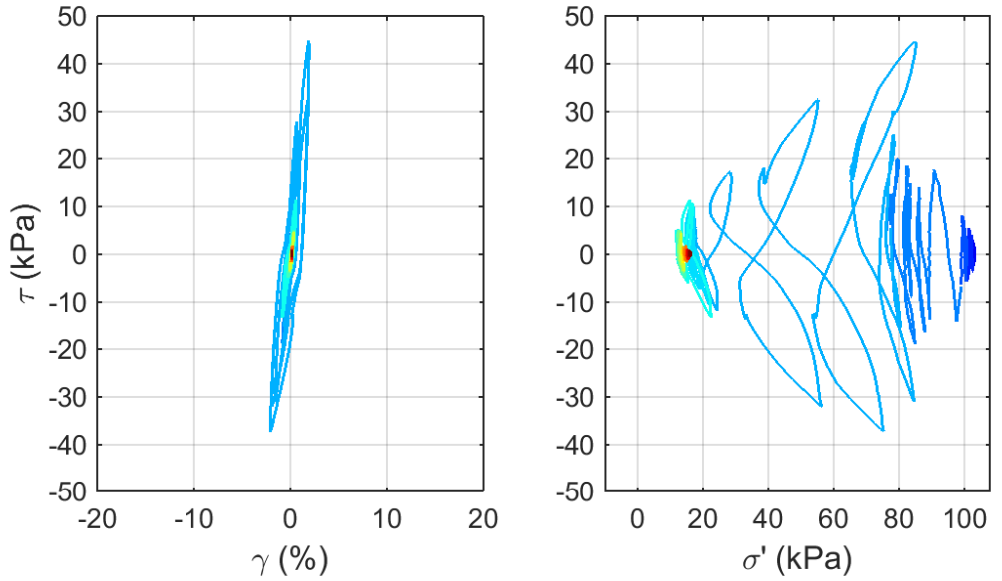

Test ID: 20130806
Nevada Sand
D_r = 89 %
Motion: NGA1020_H12090.AT2

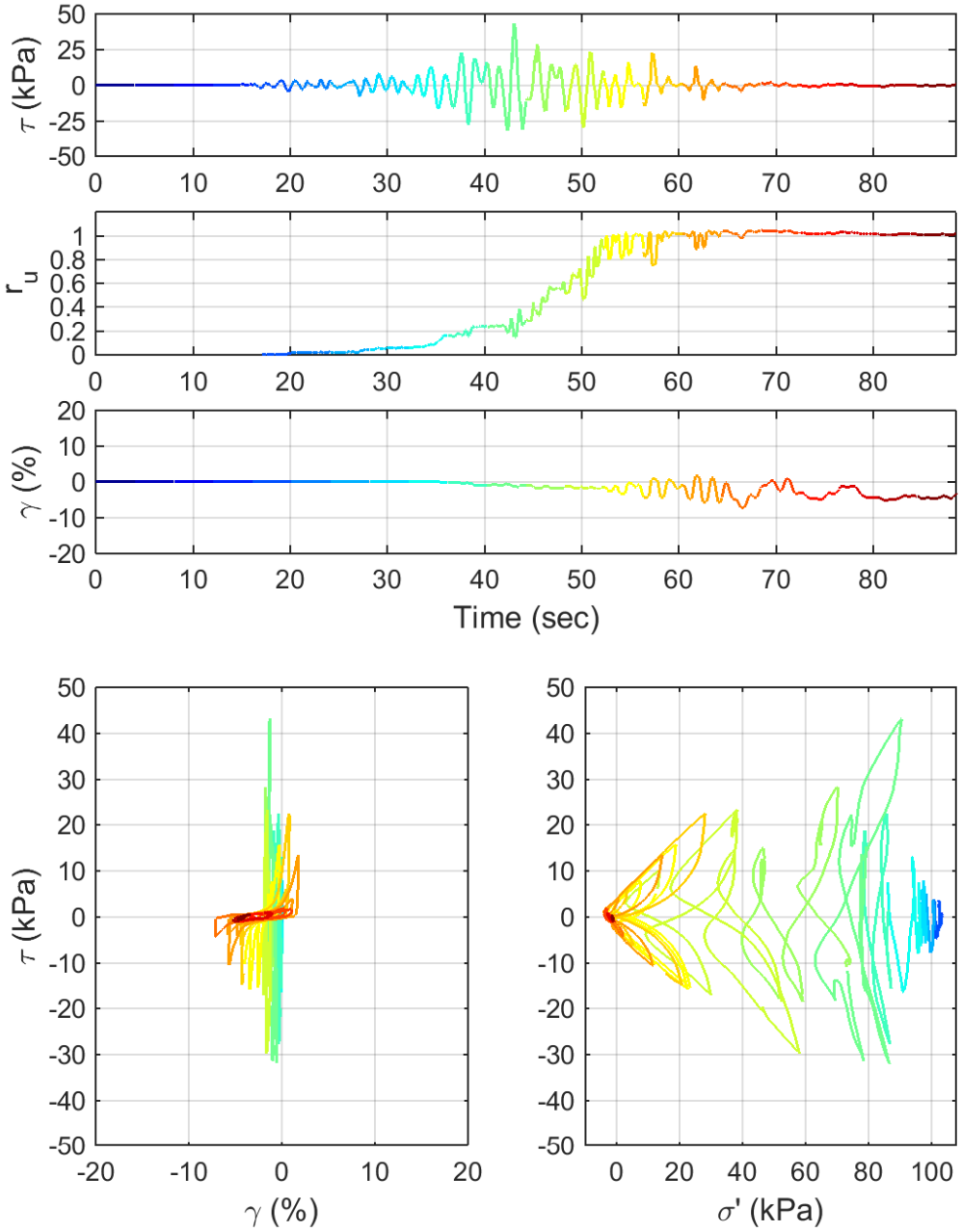

Test ID: 2013080902
Nevada Sand
D_r = 74 %
Motion: NGA587_AMAT083.AT2

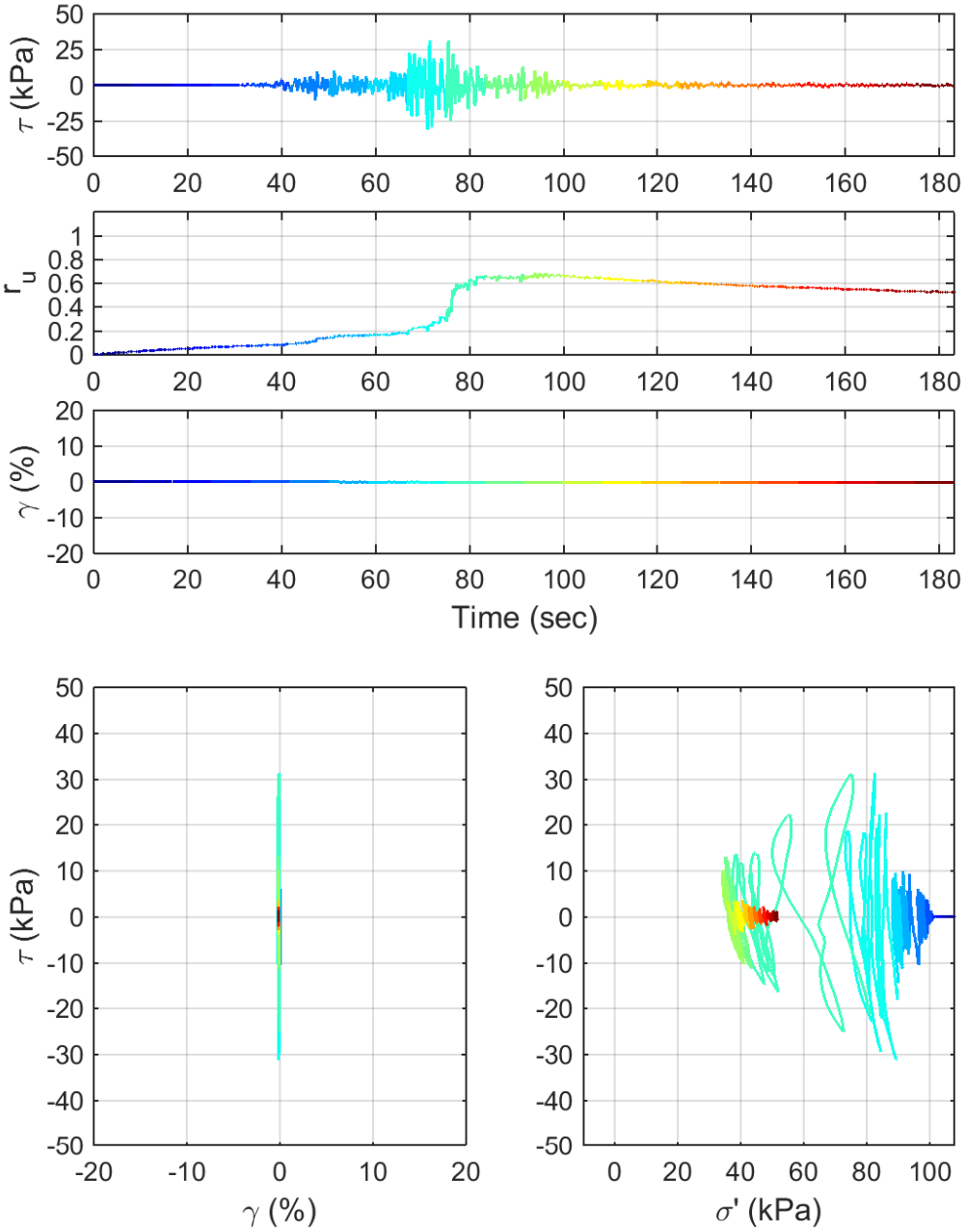

Test ID: 20130819
Nevada Sand
D_r = 70 %
Motion: 6530_2A

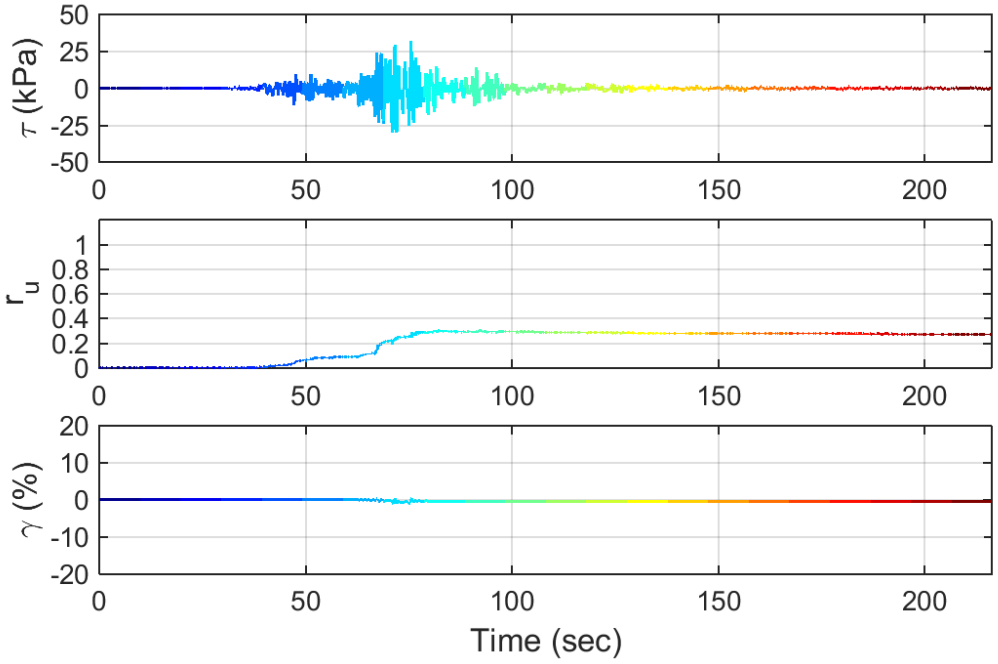

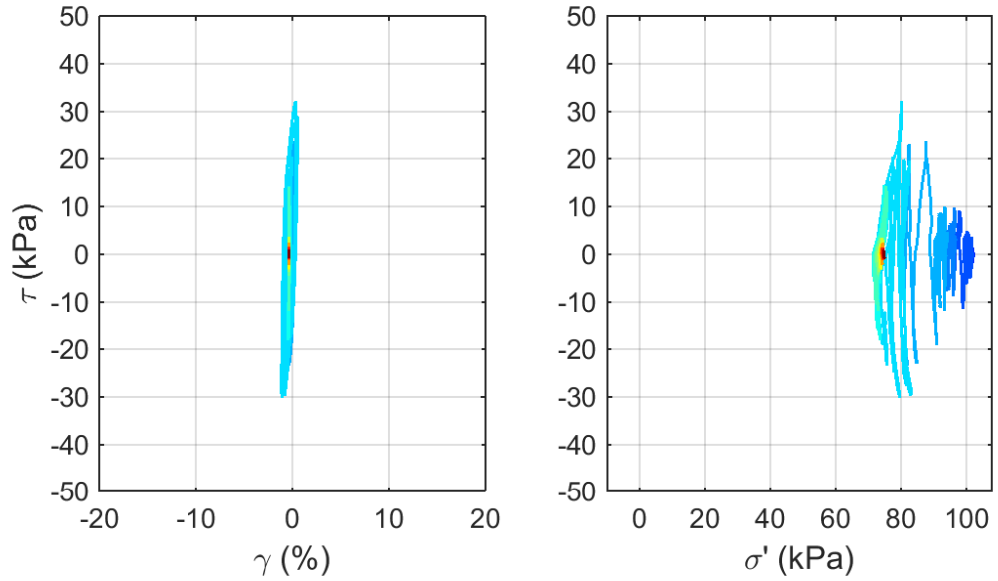

Test ID: 20130820
Nevada Sand
D_r = 74 %
Motion: 6530_2A

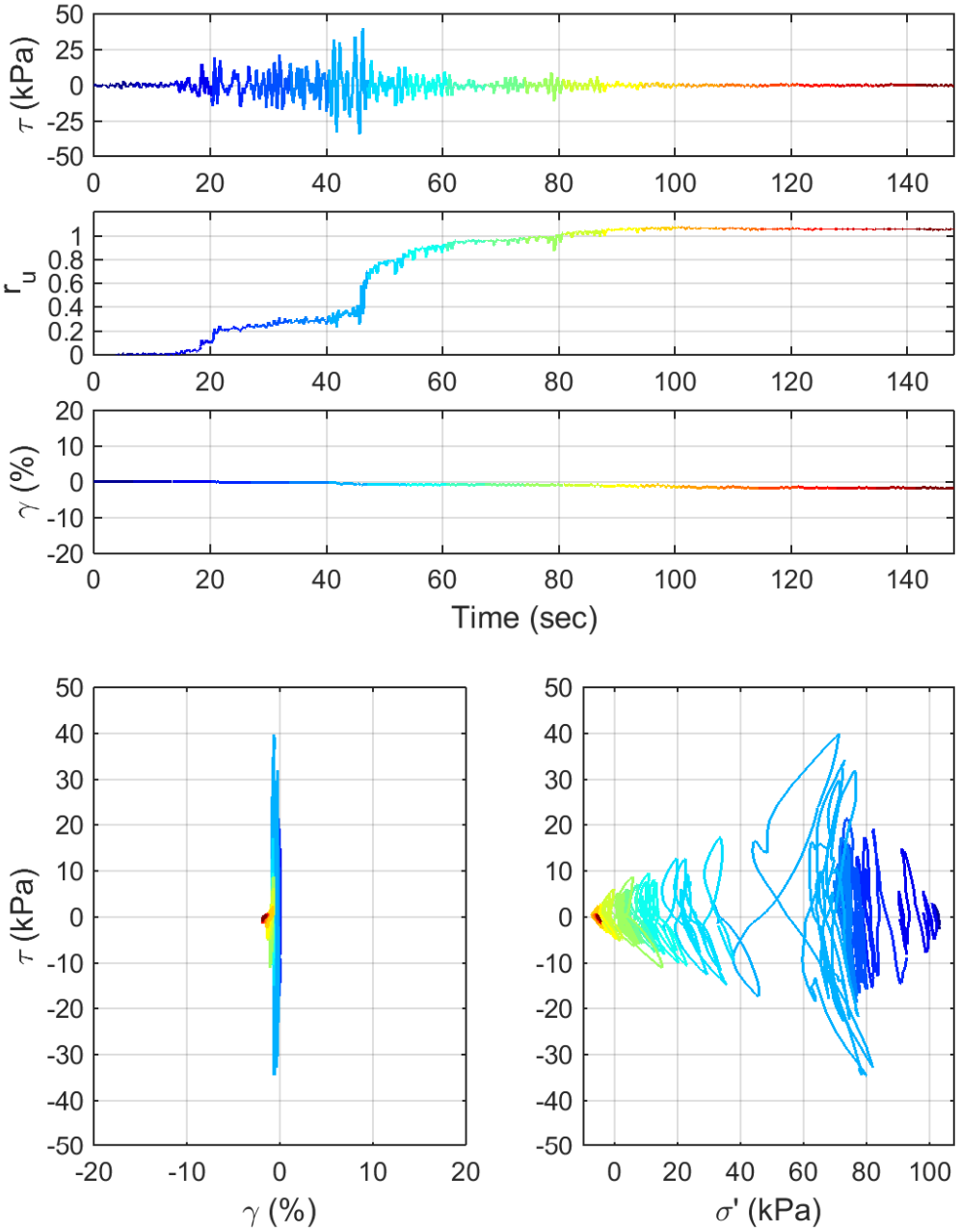

Test ID: 20130821
Nevada Sand
D_r = 80 %
Motion: 7030_2A

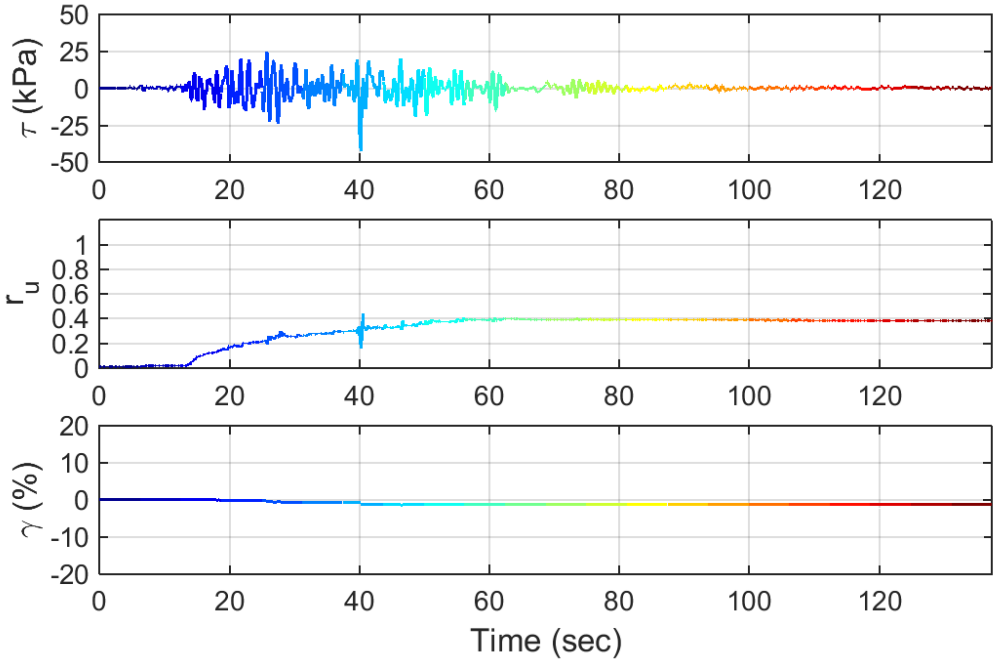

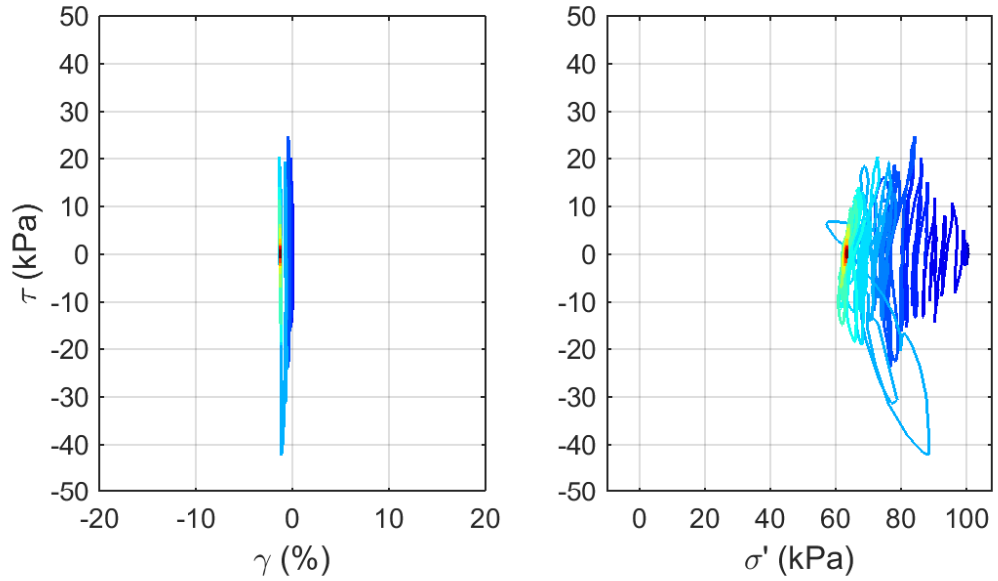

Test ID: 20130822
Nevada Sand
D_r = 78 %
Motion: 7030_1A

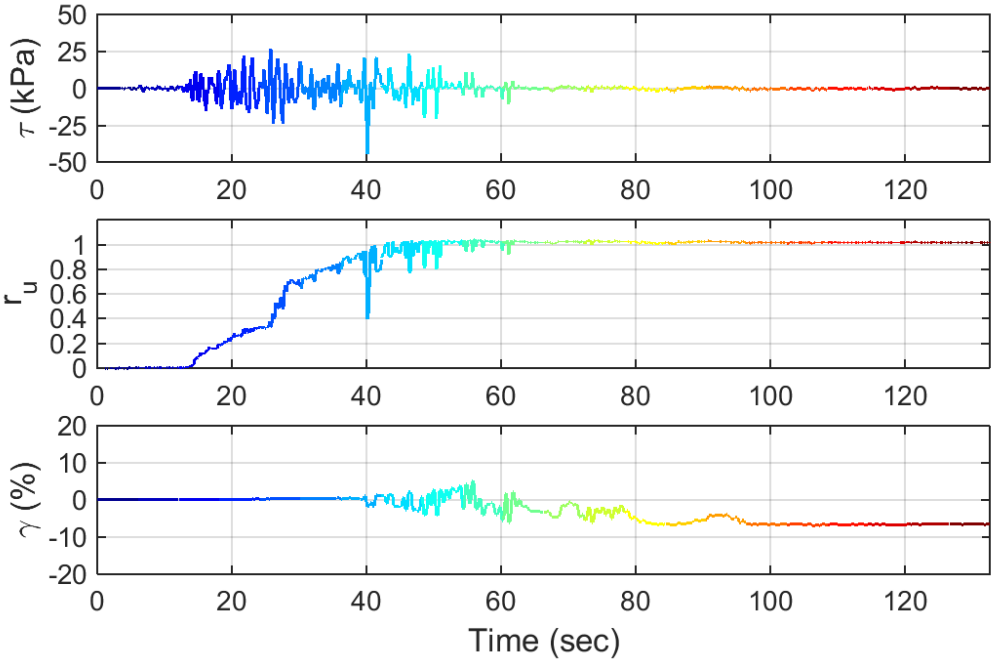

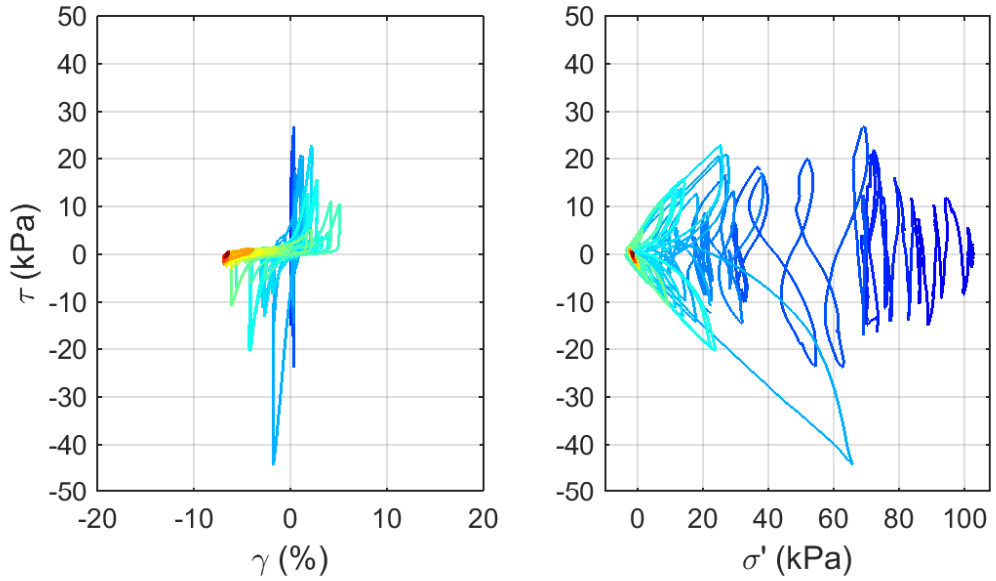

Test ID: 2013082602
Nevada Sand
D_r = 89 %
Motion: 7030_1A

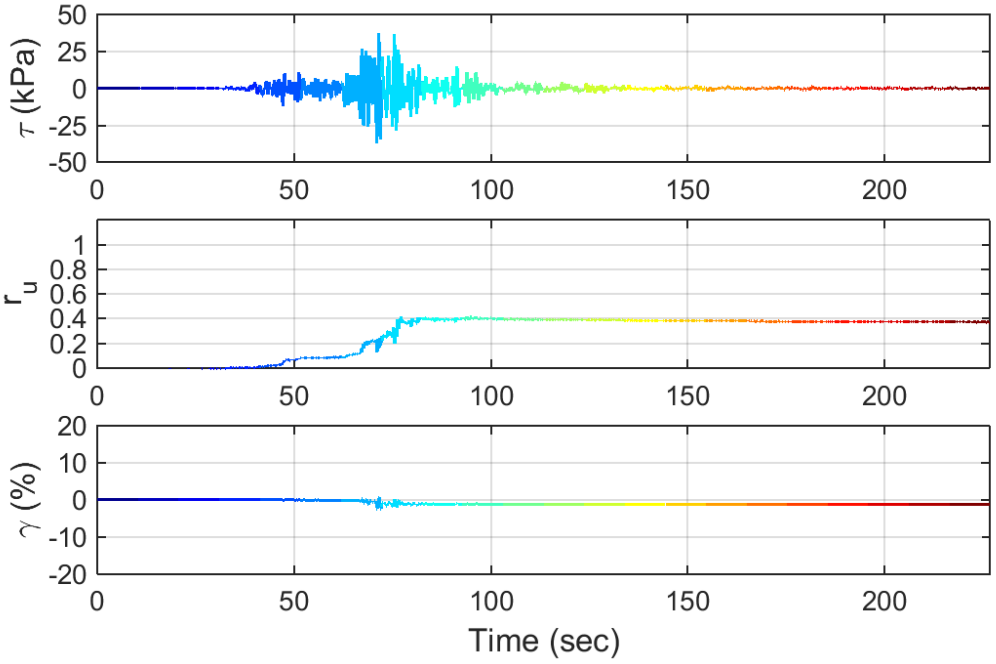

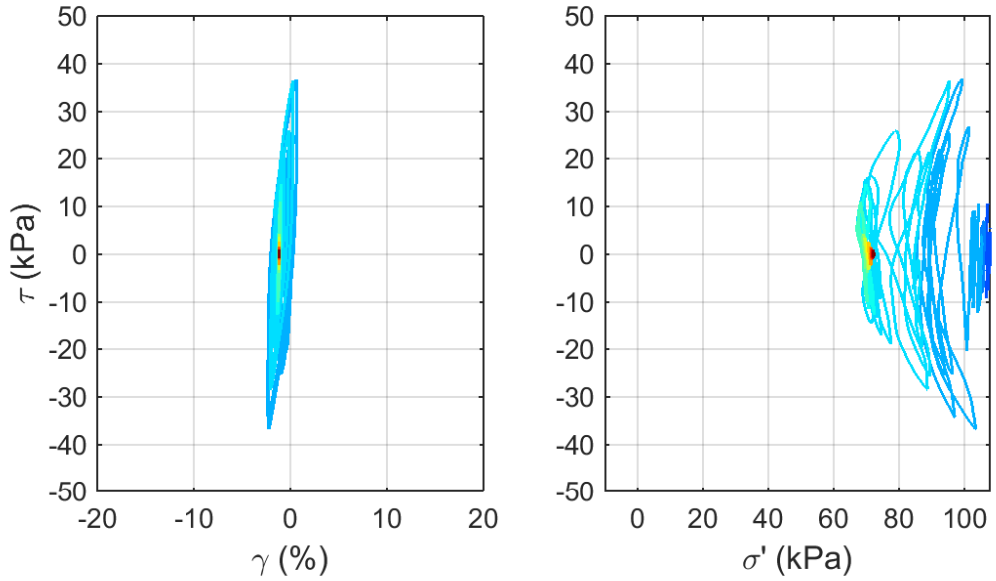

Test ID: 20130827
Nevada Sand
D_r = 84 %
Motion: 6530_2A

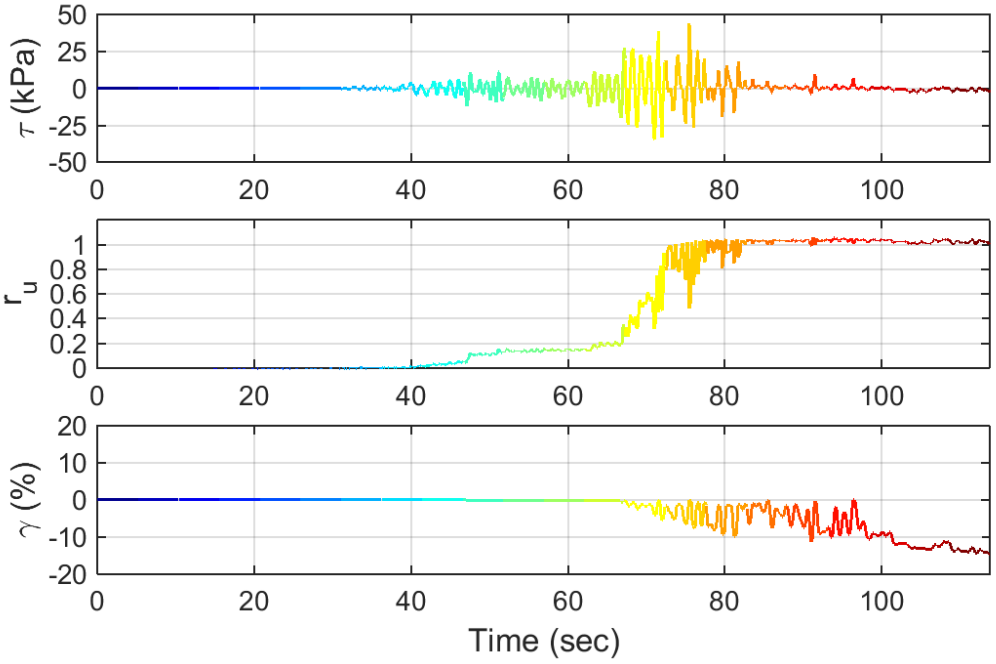

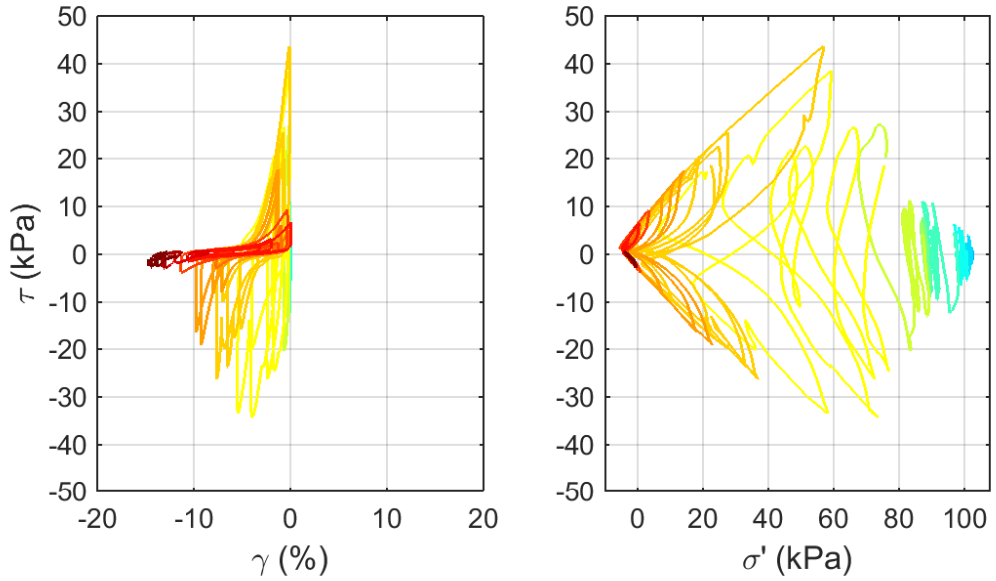

Test ID: 2013082702
Nevada Sand
D_r = 89 %
Motion: 6530_2A

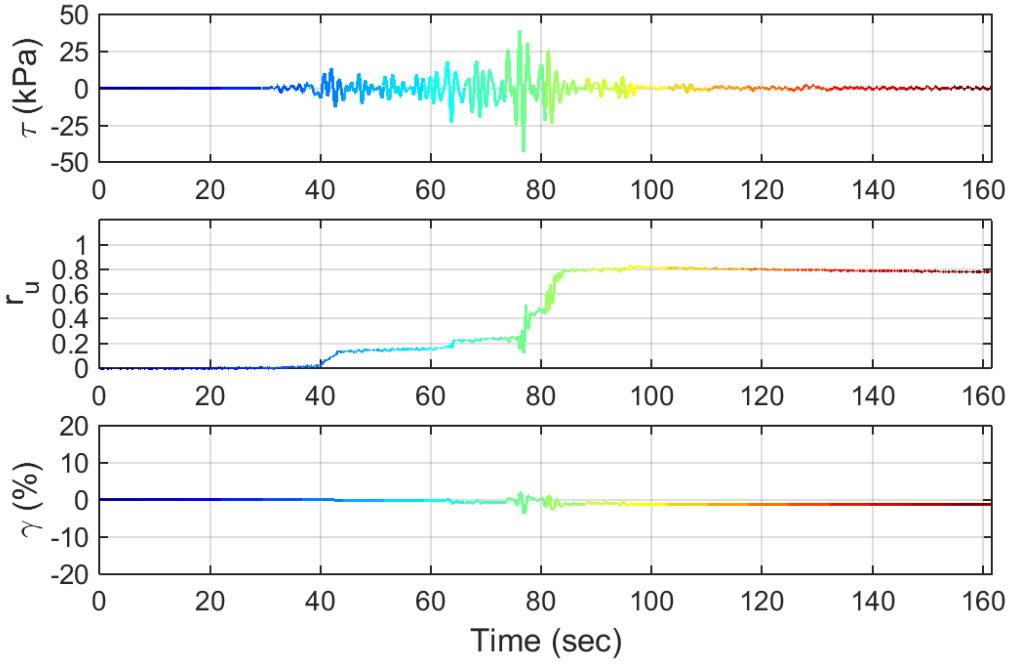

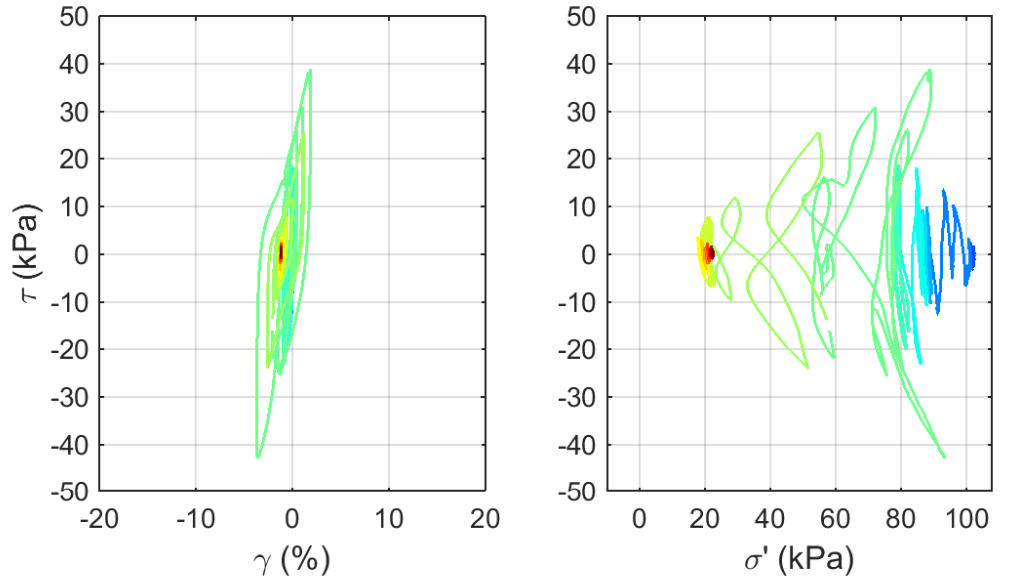

Test ID: 20130829
Nevada Sand
D_r = 84 %
Motion: 6530_2B

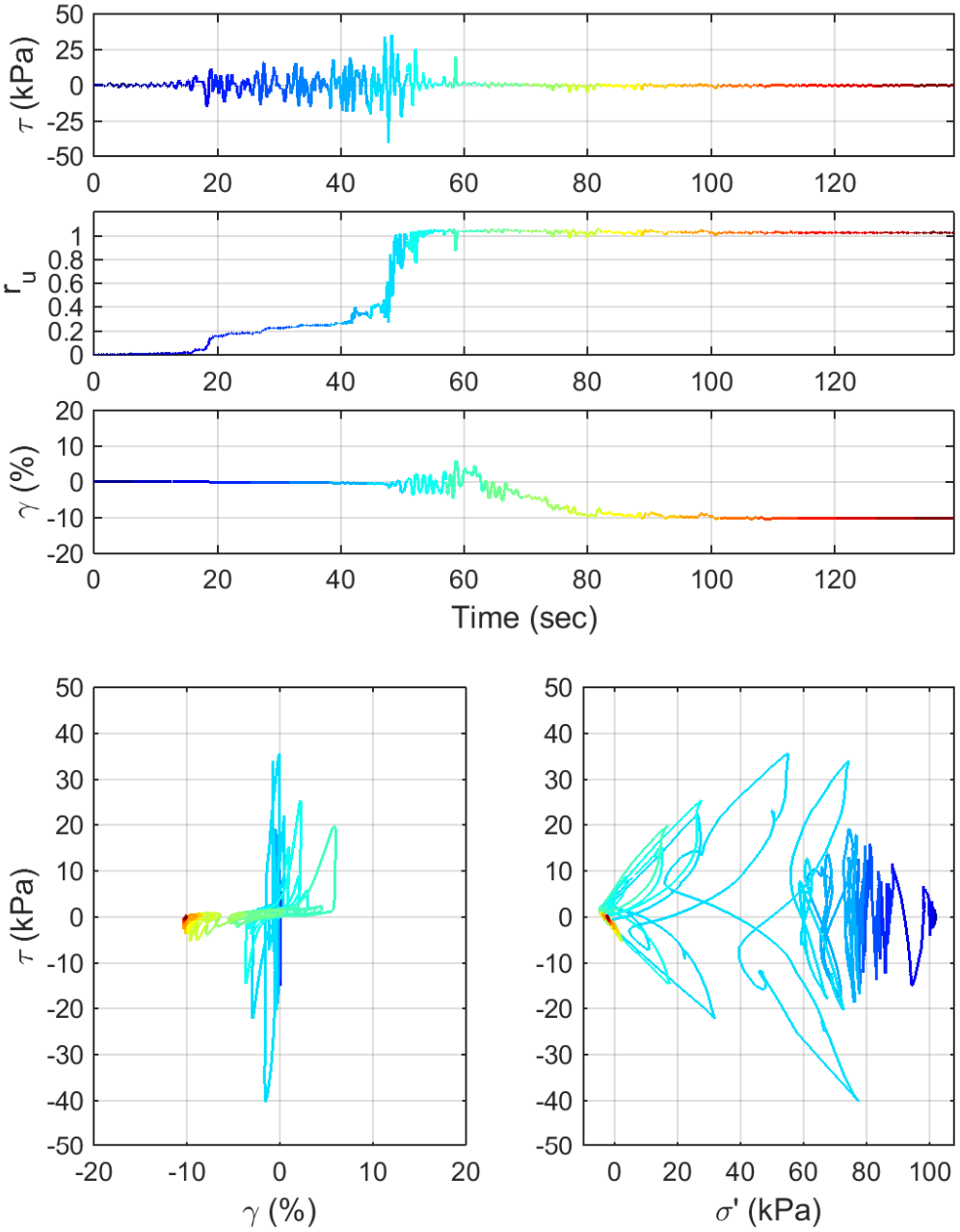

Test ID: 2013082902
Nevada Sand
D_r = 81 %
Motion: 7030_2B

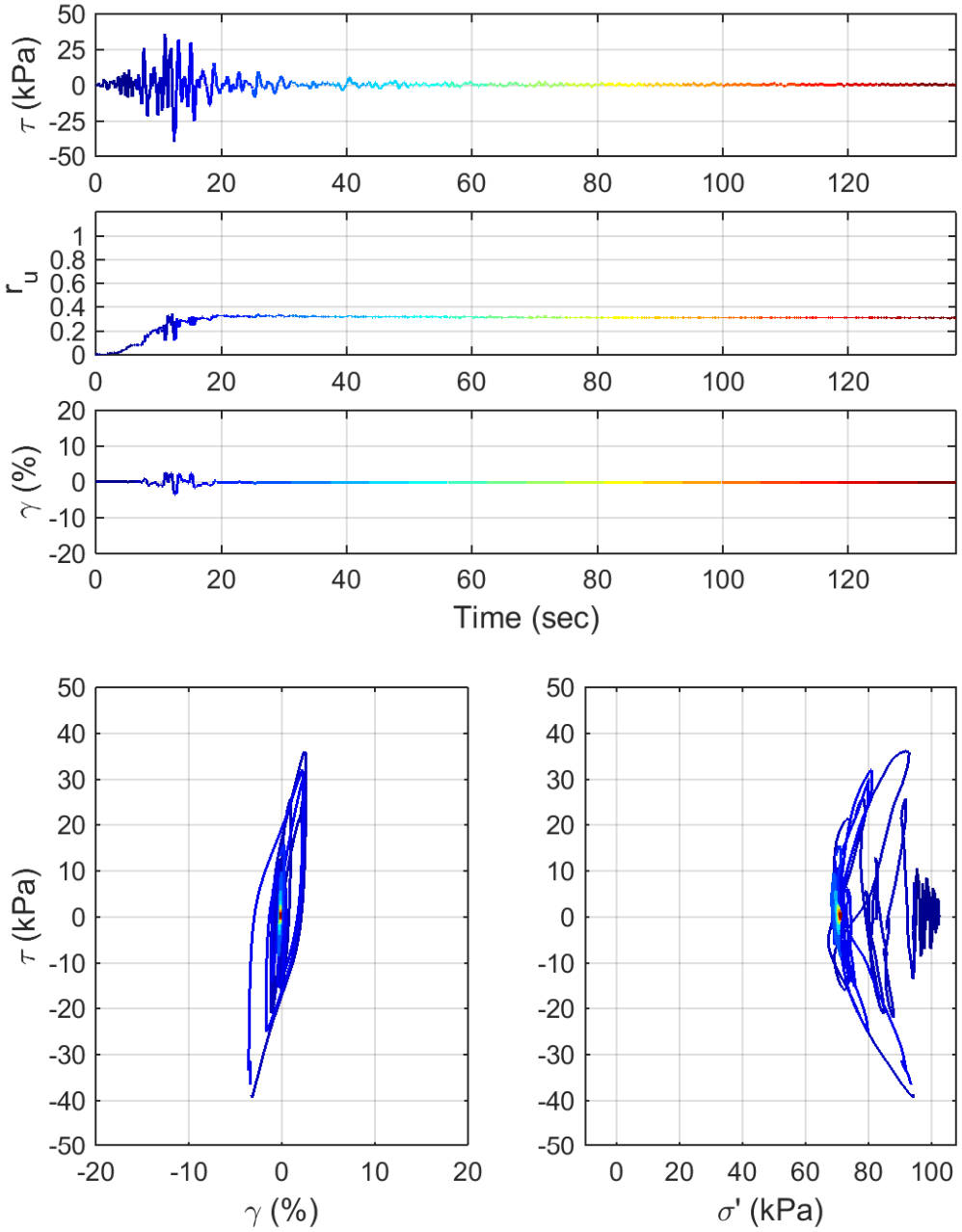

Test ID: 20130904
Nevada Sand
D_r = 83 %
Motion: 6530_1B

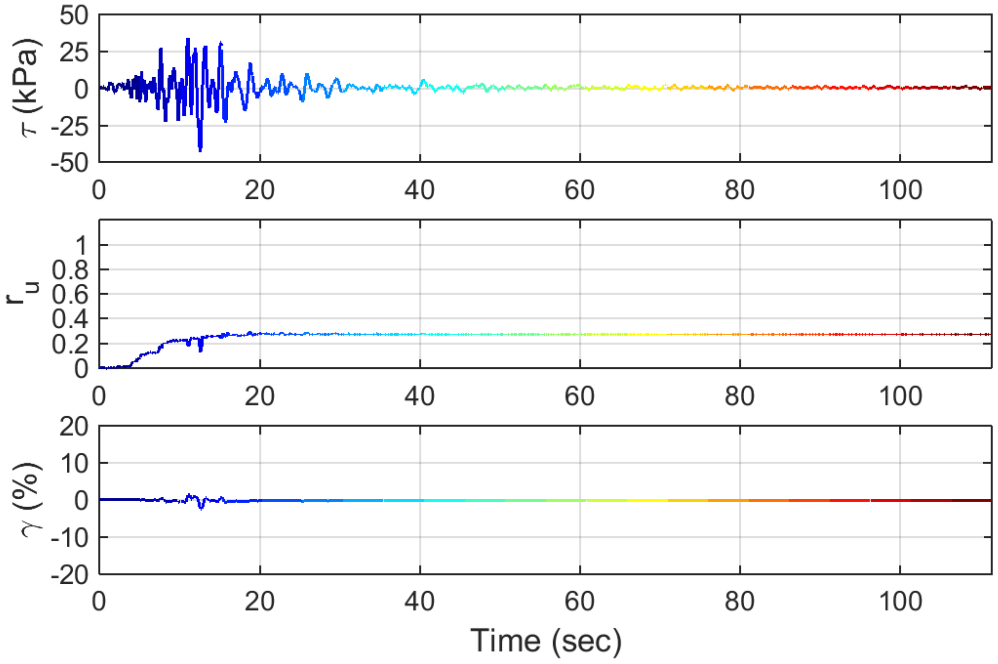

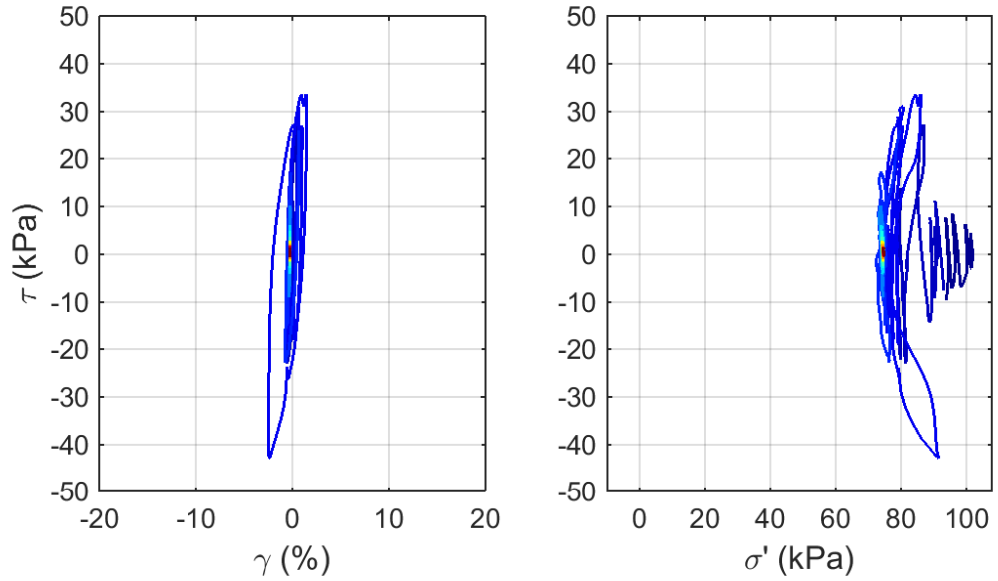

Test ID: 20130905
Nevada Sand
D_r = 91 %
Motion: 6530_1B

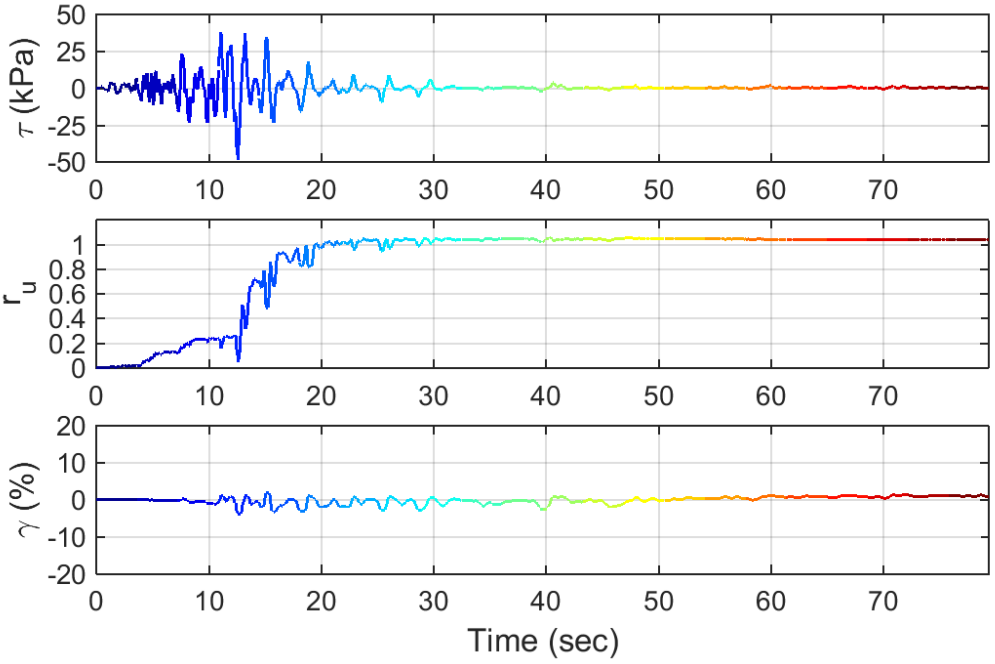

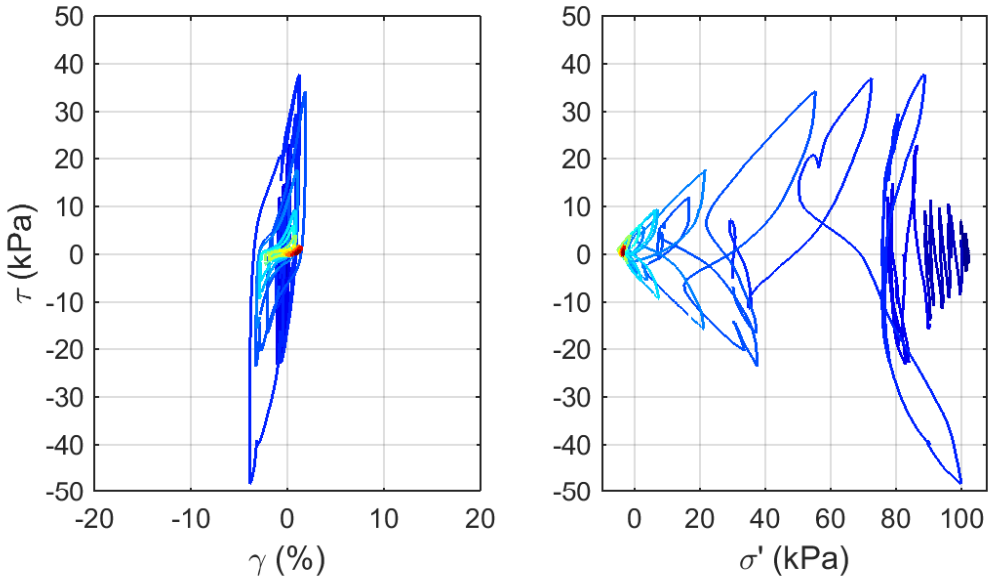

Test ID: 2013090502
Nevada Sand
D_r = 86 %
Motion: 6530_1B

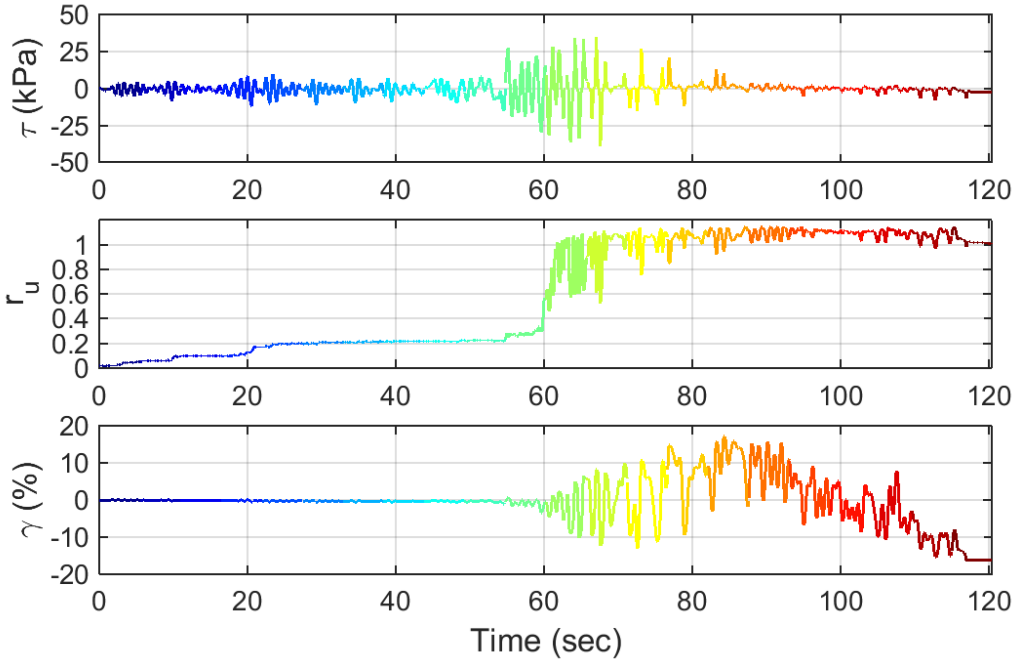

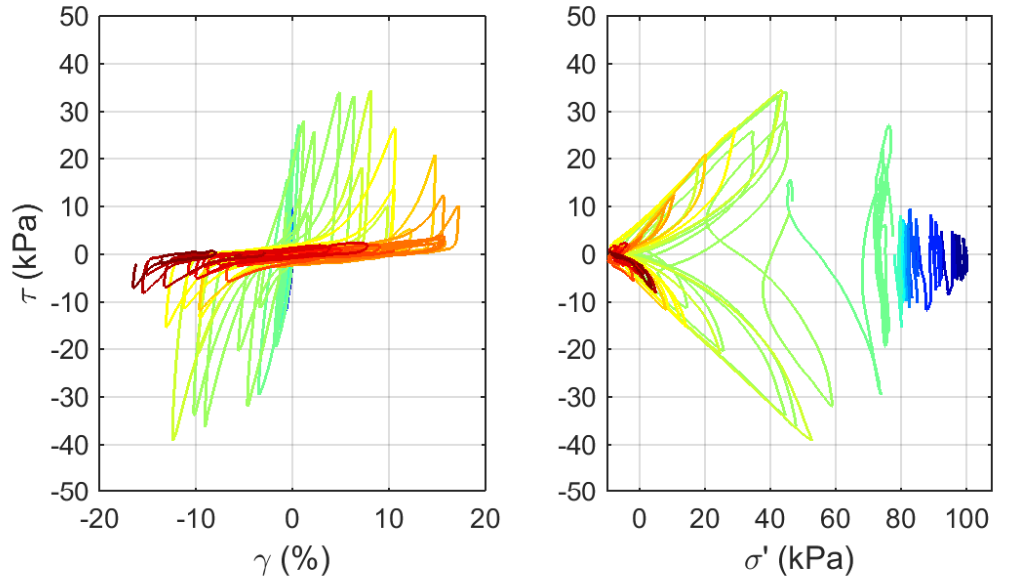

Test ID: 20131007
Nevada Sand
D_r = 78 %
Motion: NGA_no_1157_CNA000.AT2

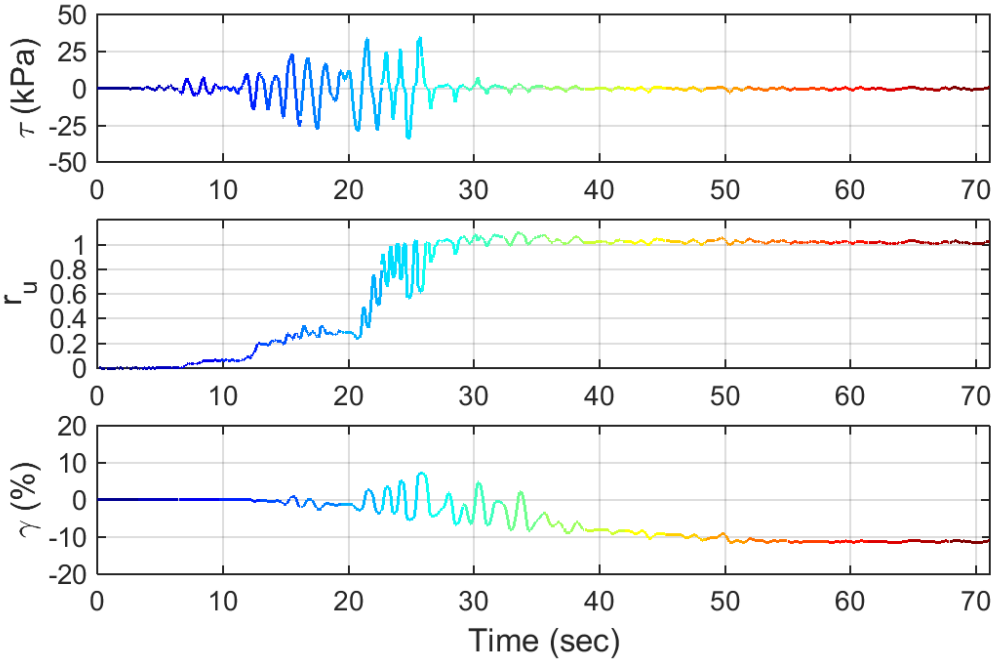

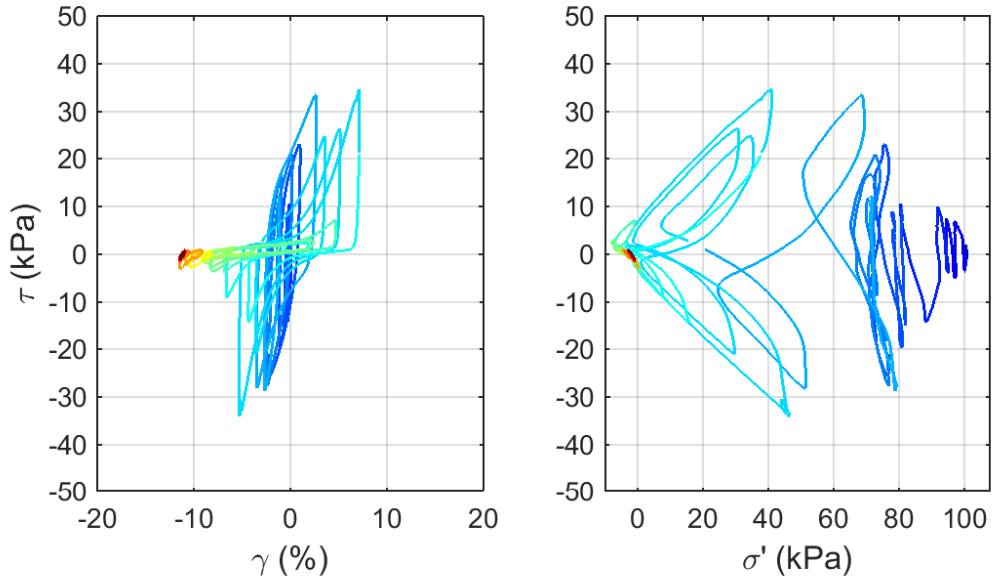

Test ID: 20131008
Nevada Sand
D_r = 73 %
Motion: NGA_no_484_PLK-NS.AT2

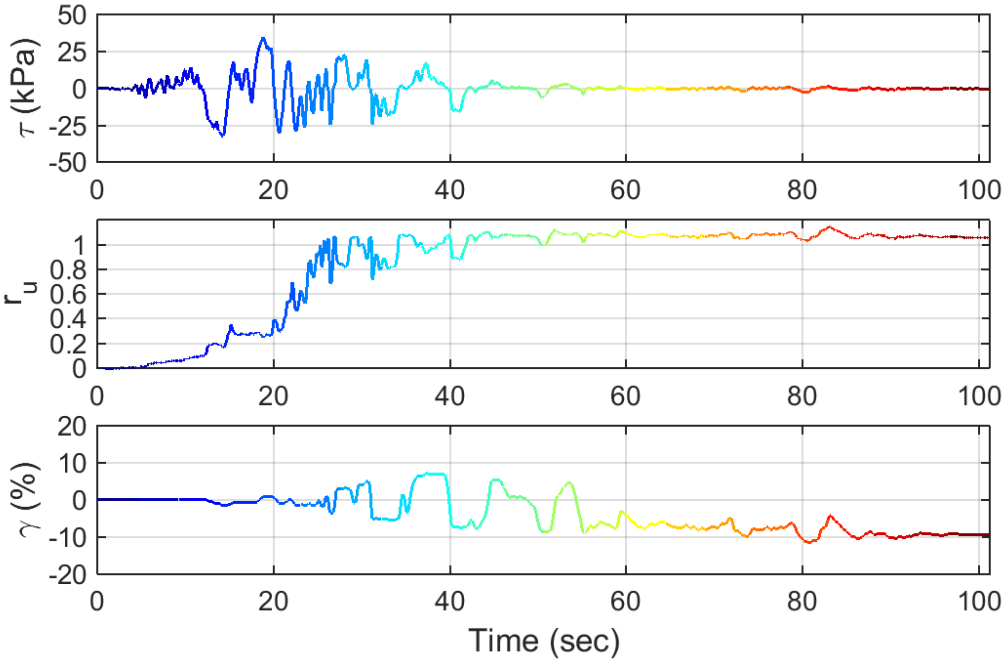

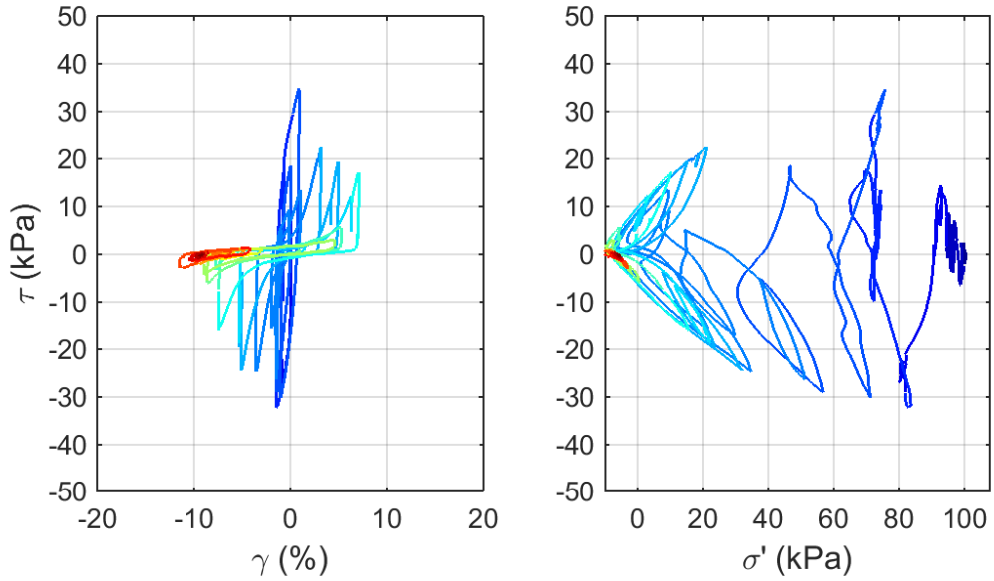

Test ID: 20131009
Nevada Sand
D_r = 72 %
Motion: NGA_no_527_MVH135.AT2

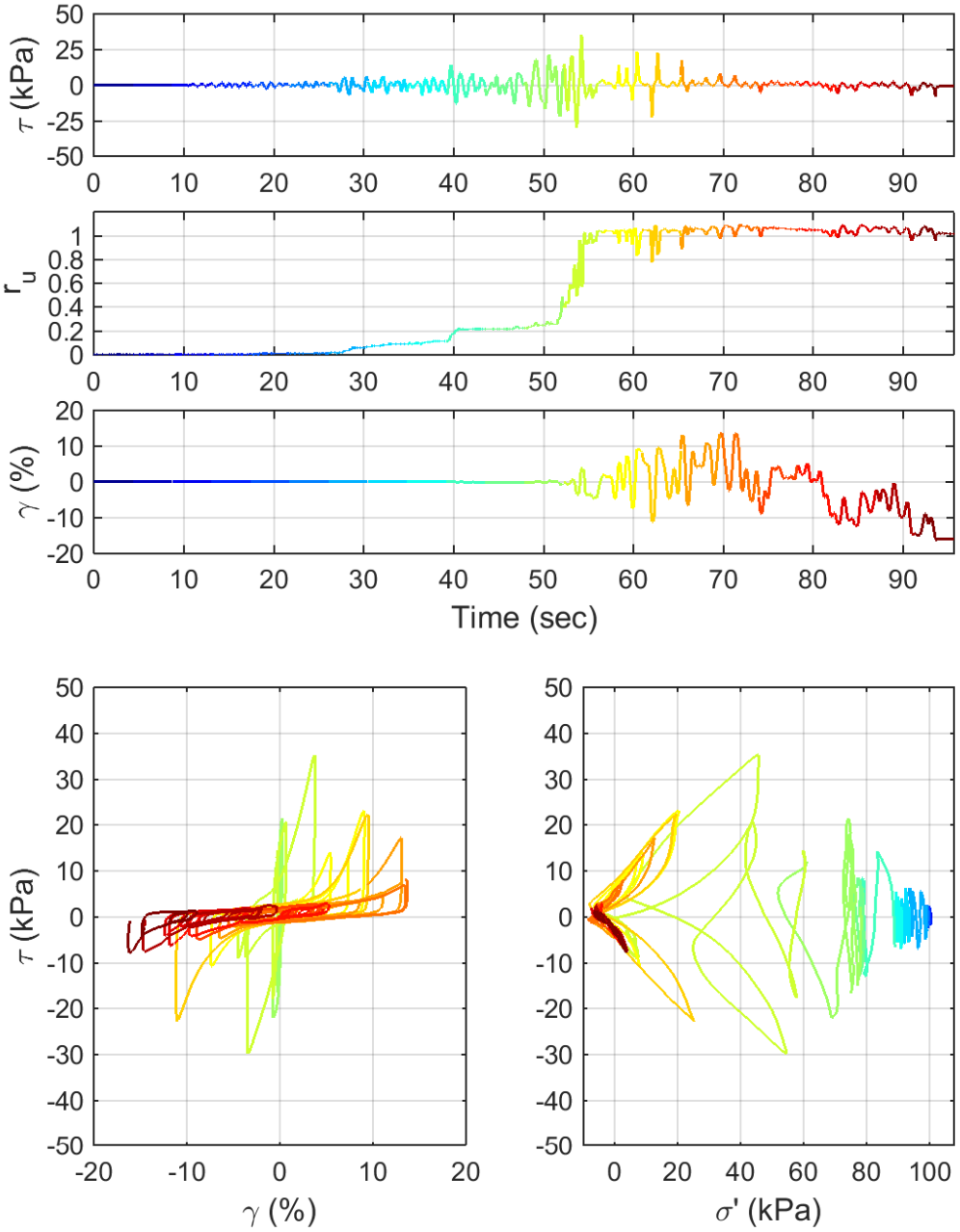

Test ID: 2013100902
Nevada Sand
D_r = 71 %
Motion: NGA_no_880_MCF000.AT2

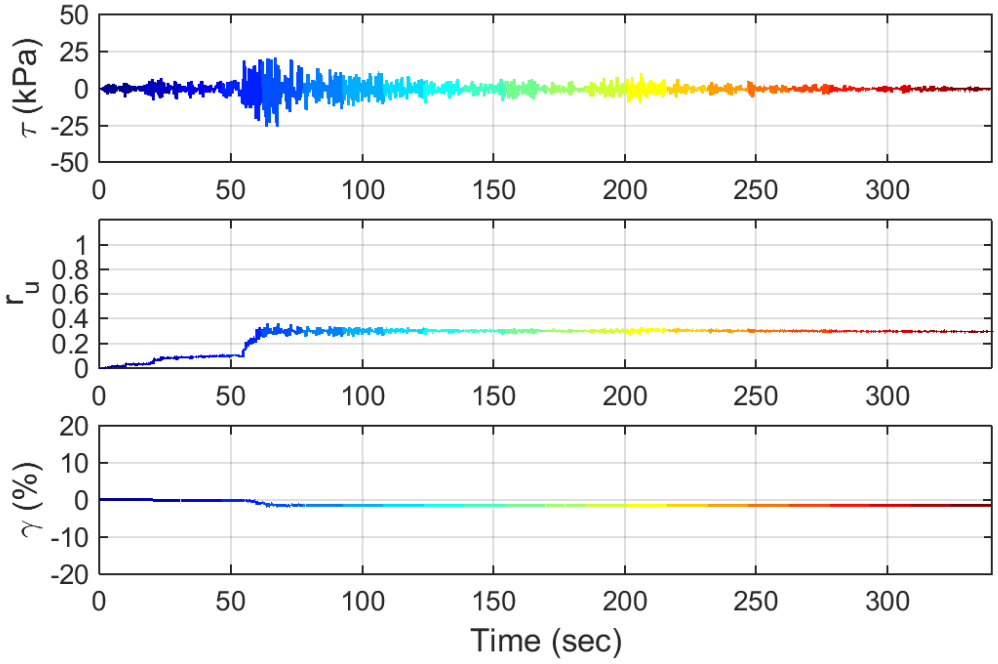

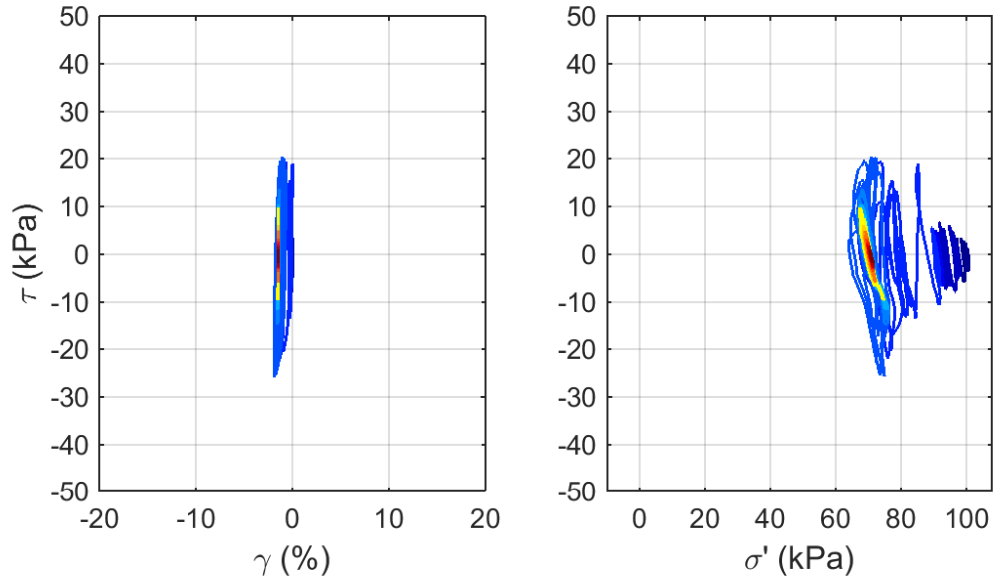

Test ID: 20131024
Nevada Sand
D_r = 76 %
Motion: NGA_no_1157_CNA000.AT2

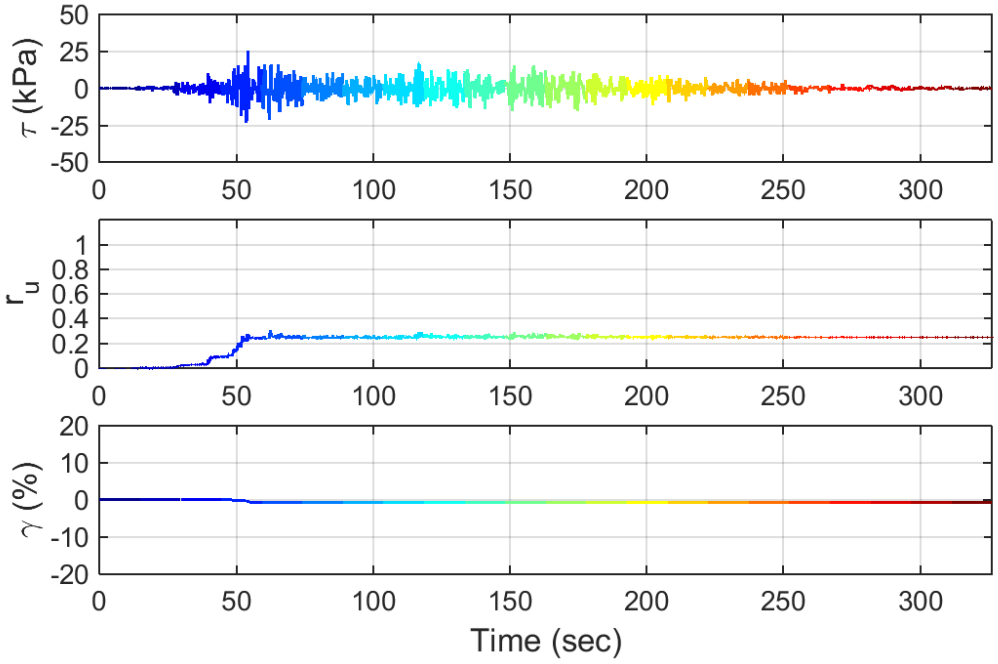

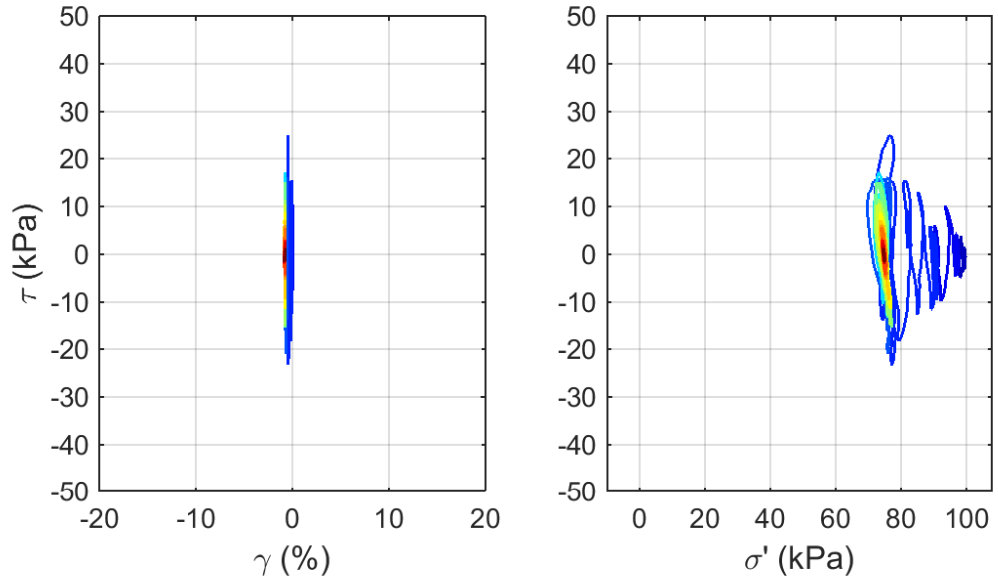

Test ID: 20131104
Nevada Sand
D_r = 80 %
Motion: NGA_no_880_MCF000.AT2

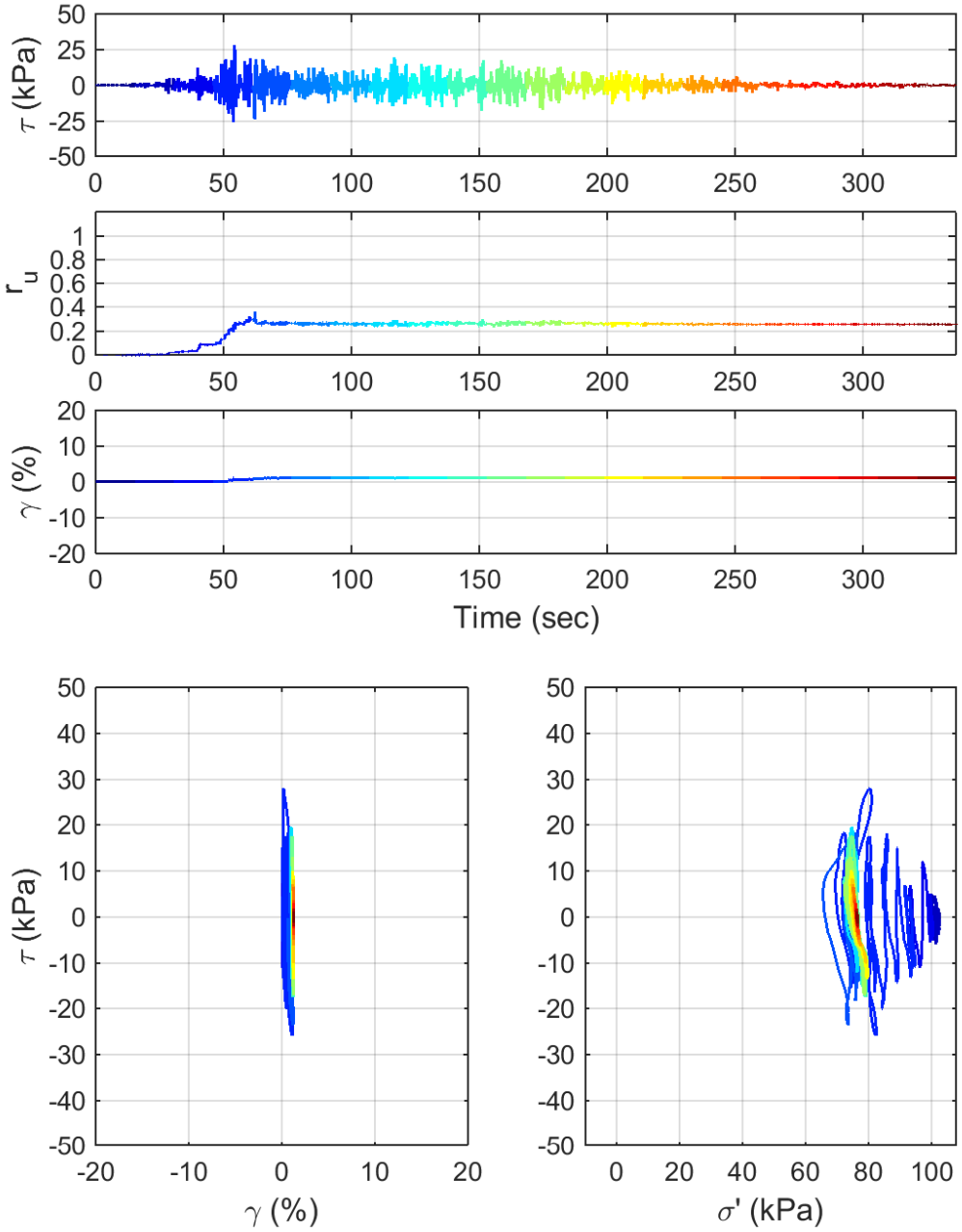

Test ID: 20131105
Nevada Sand
D_r = 73 %
Motion: NGA_no_880_MCF000.AT2

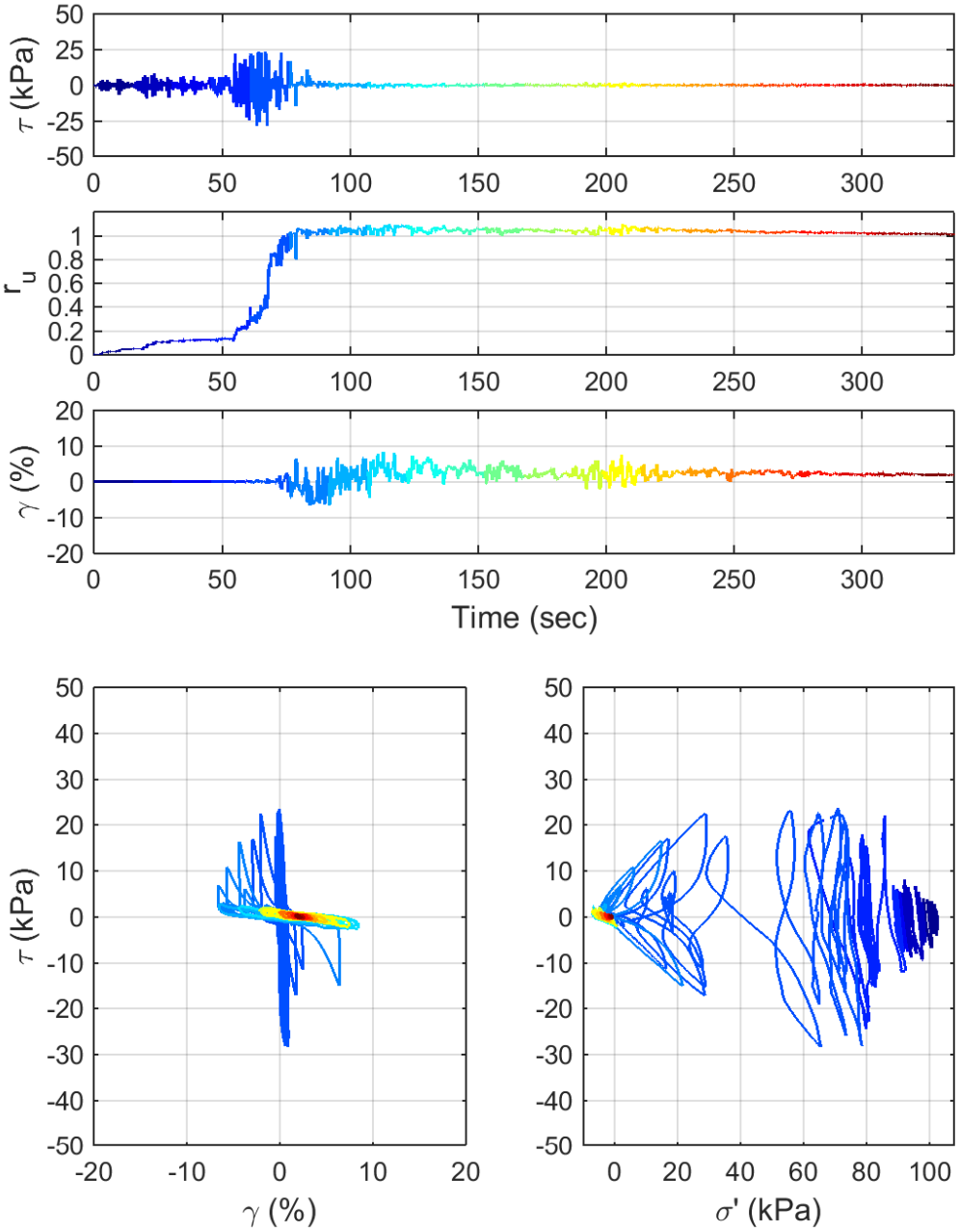

Test ID: 2013110602
Nevada Sand
D_r = 74 %
Motion: NGA_no_1157_CNA000.AT2

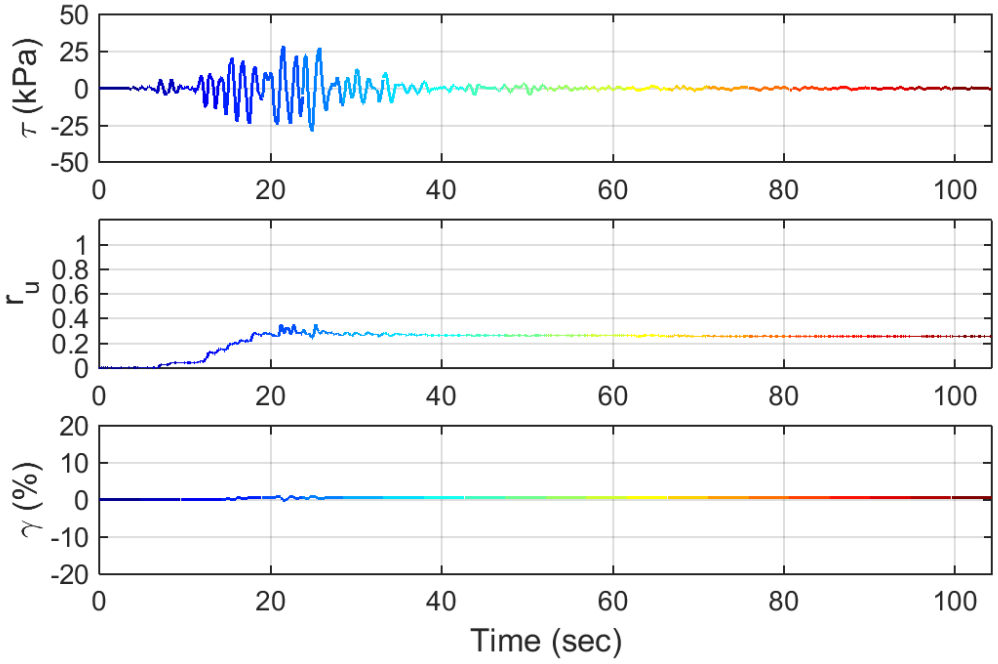

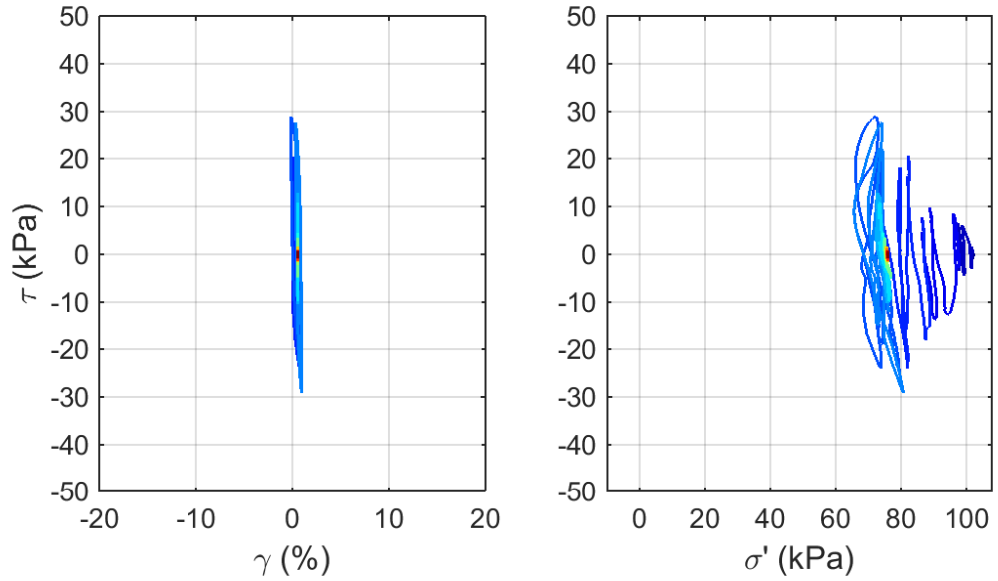

Test ID: 2013110603
Nevada Sand
D_r = 73 %
Motion: NGA_no_484_PLK-NS.AT2

APPENDIX A.6. CSS DATA: STAGE TWO TAPER UP LOADING

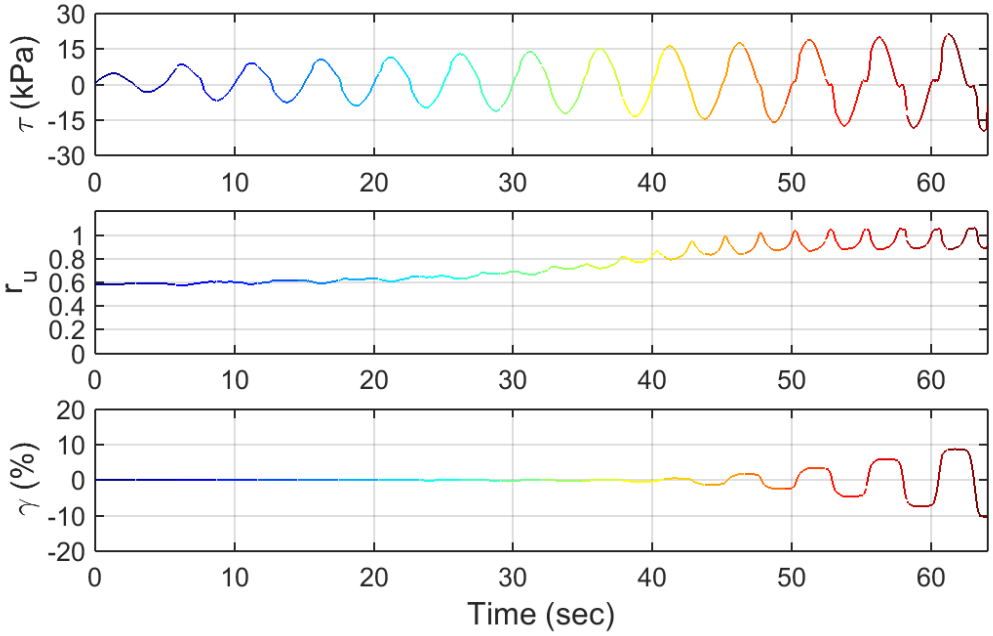

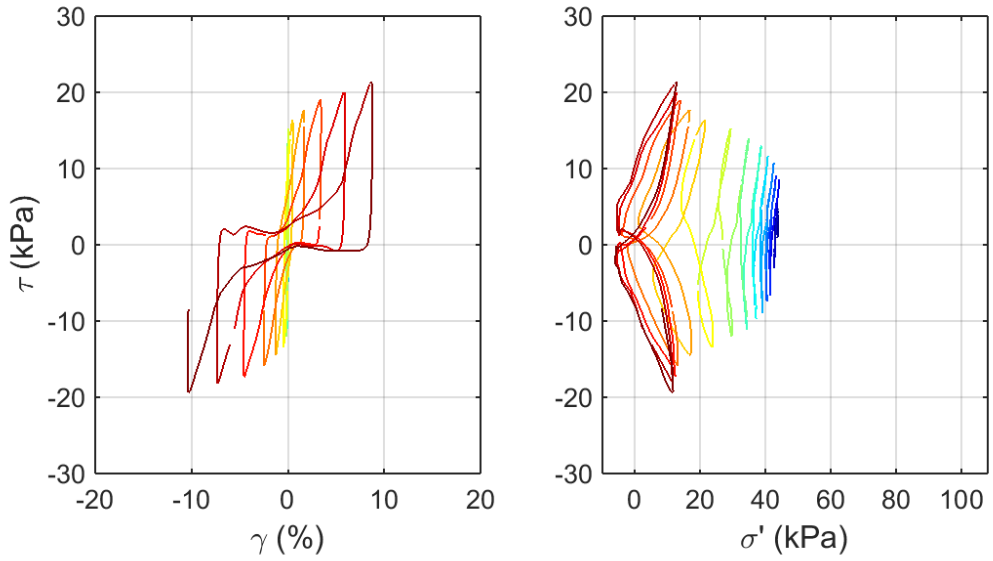

Test ID: 20121227S2
Nevada Sand
$D_r = 41$ %
Motion: Taper-up

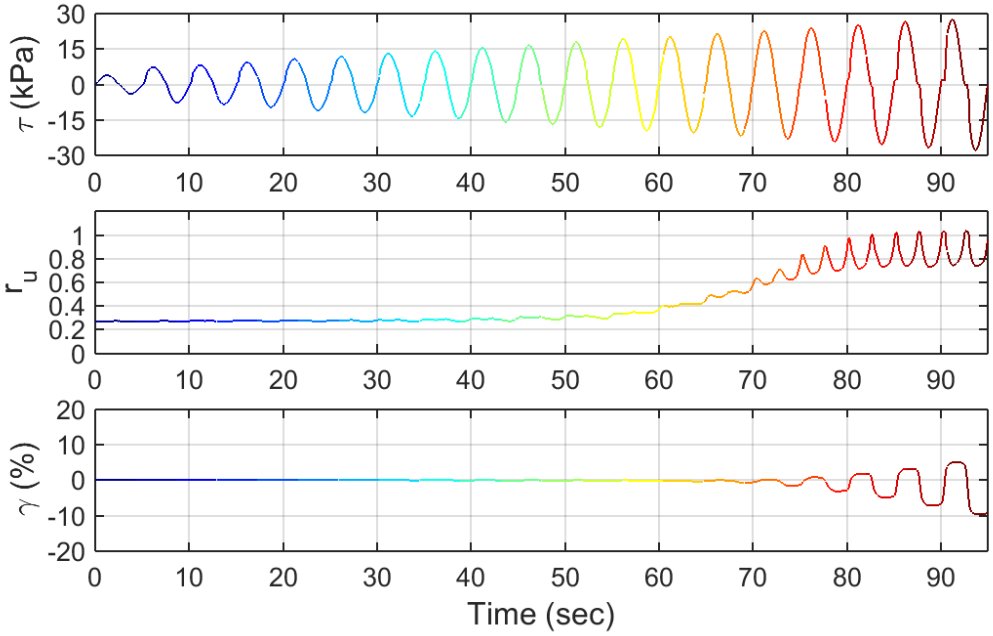

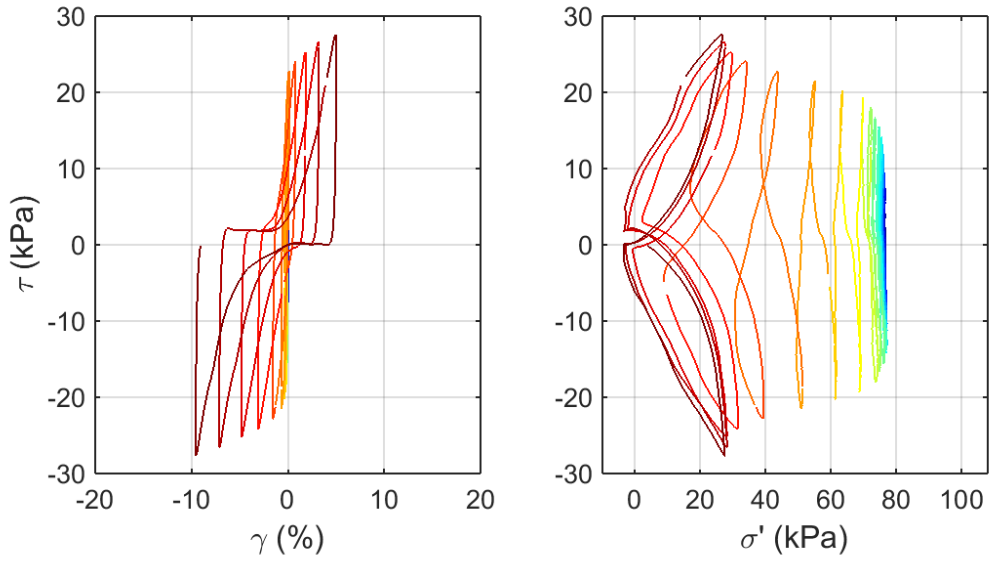

Test ID: 20121228S2
Nevada Sand
D_r = 47 %
Motion: Taper-up

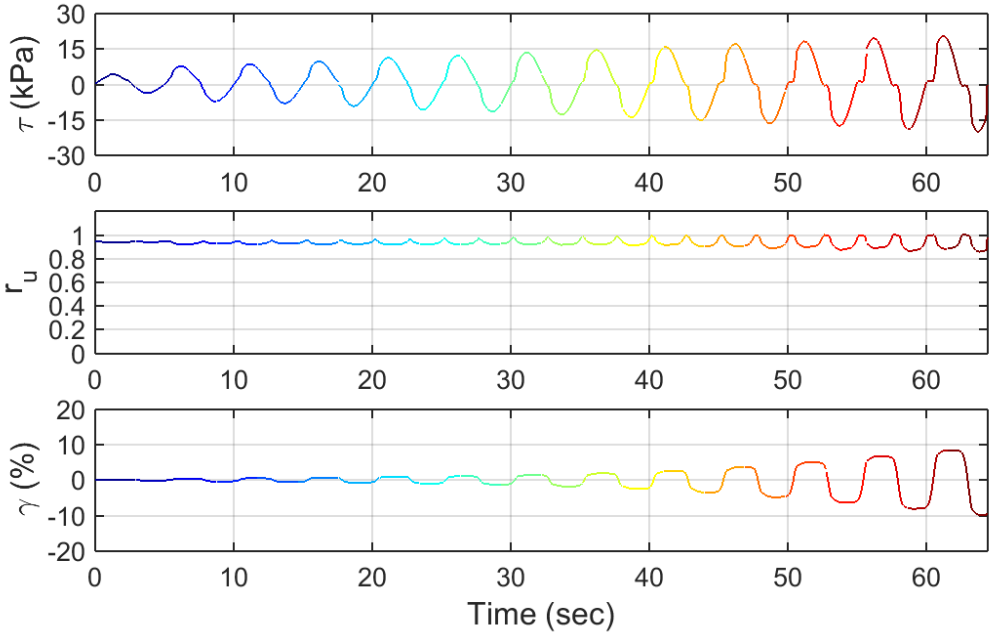

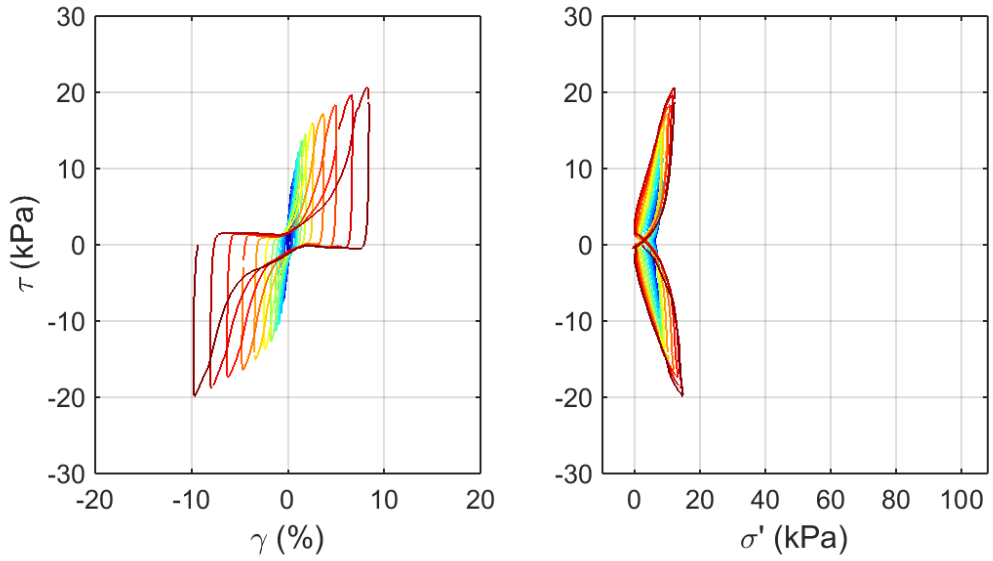

Test ID: 20121231S2
Nevada Sand
D_r = 47 %
Motion: Taper-up

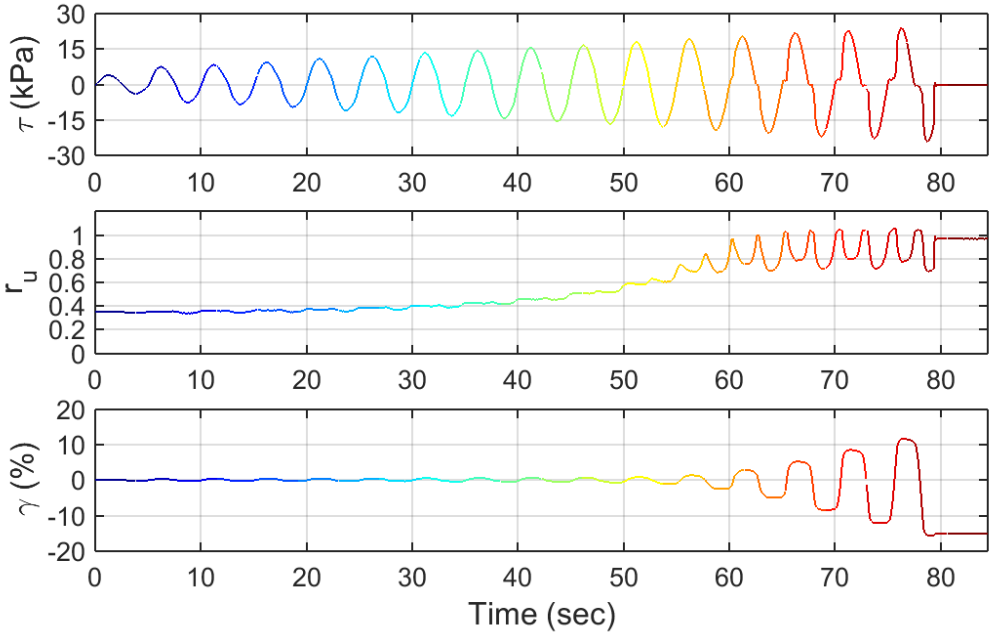

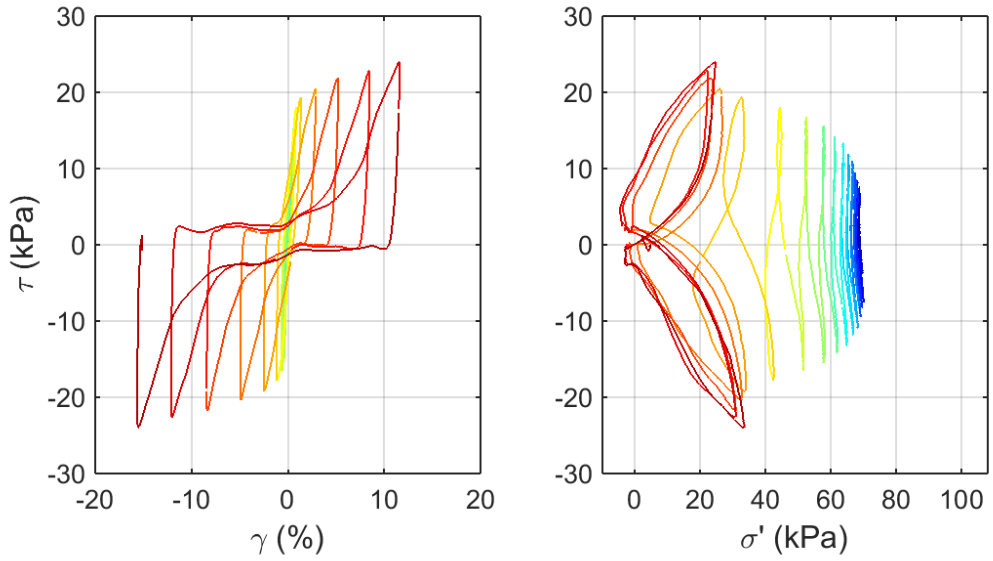

Test ID: 20130113S2
Nevada Sand
D_r = 39 %
Motion: Taper-up

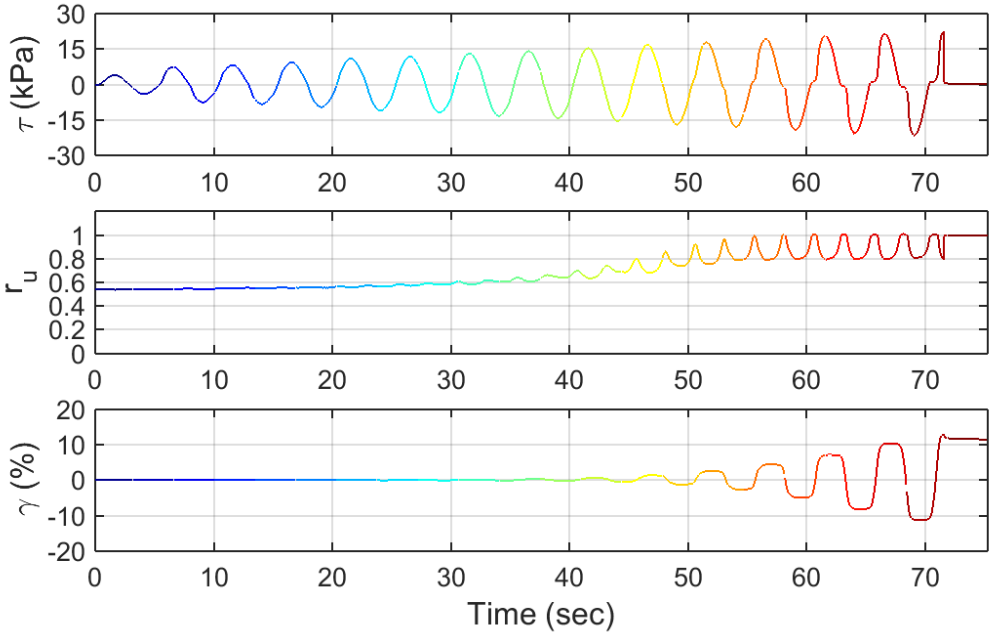

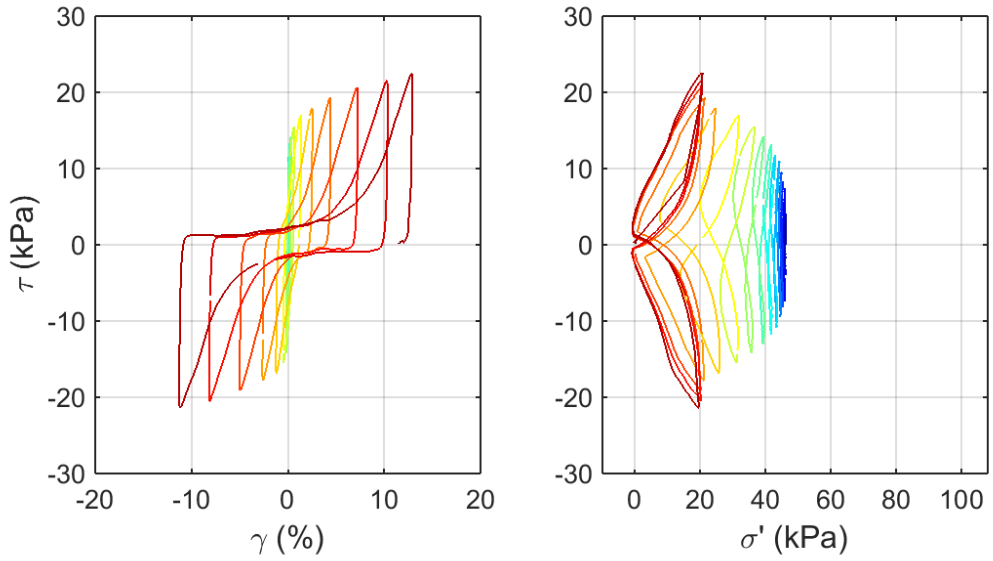

Test ID: 20130222S2
Nevada Sand
D_r = 48 %
Motion: Taper-up

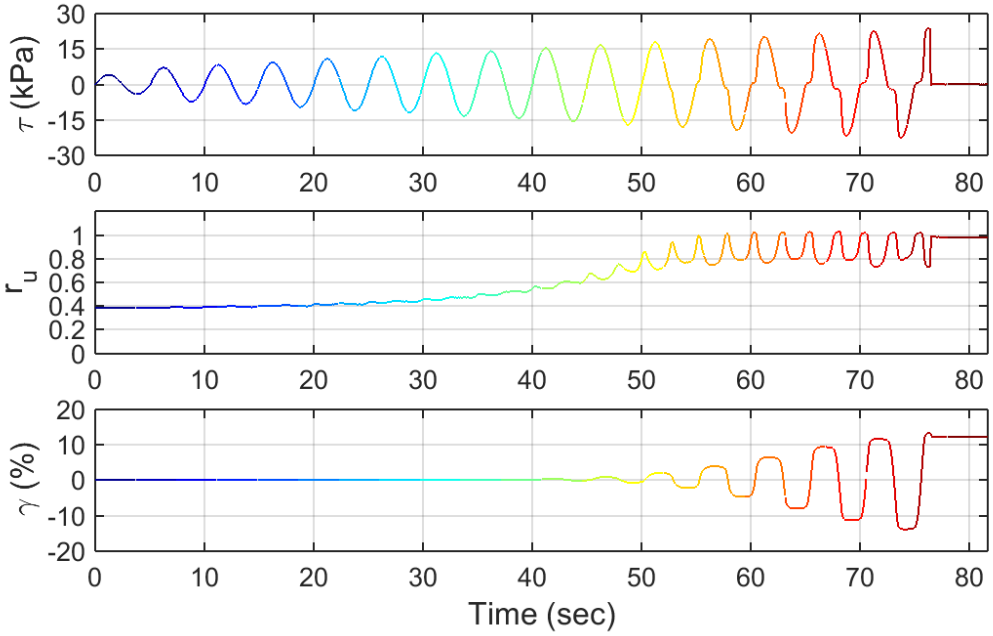

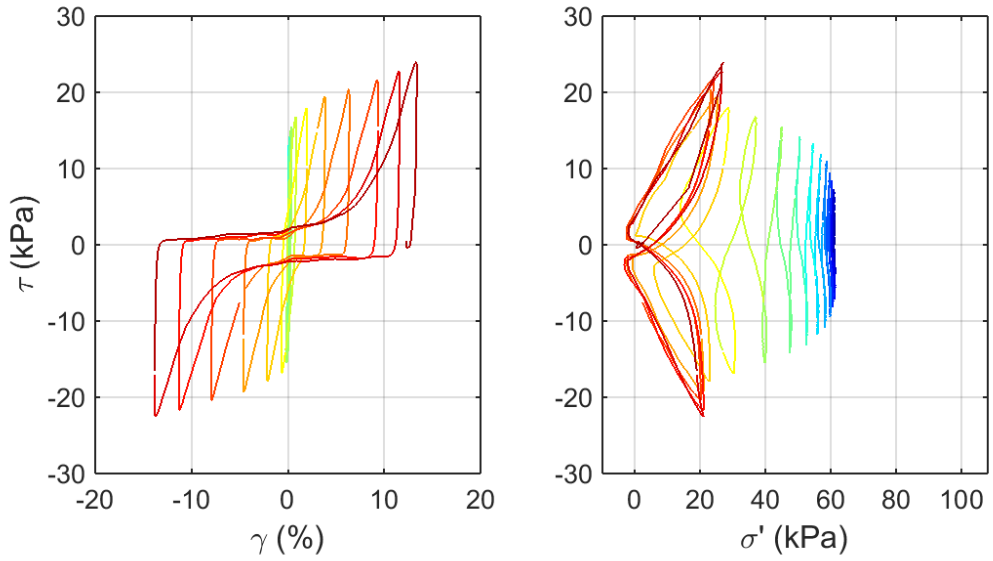

Test ID: 20130307S2
Nevada Sand
D_r = 44 %
Motion: Taper-up

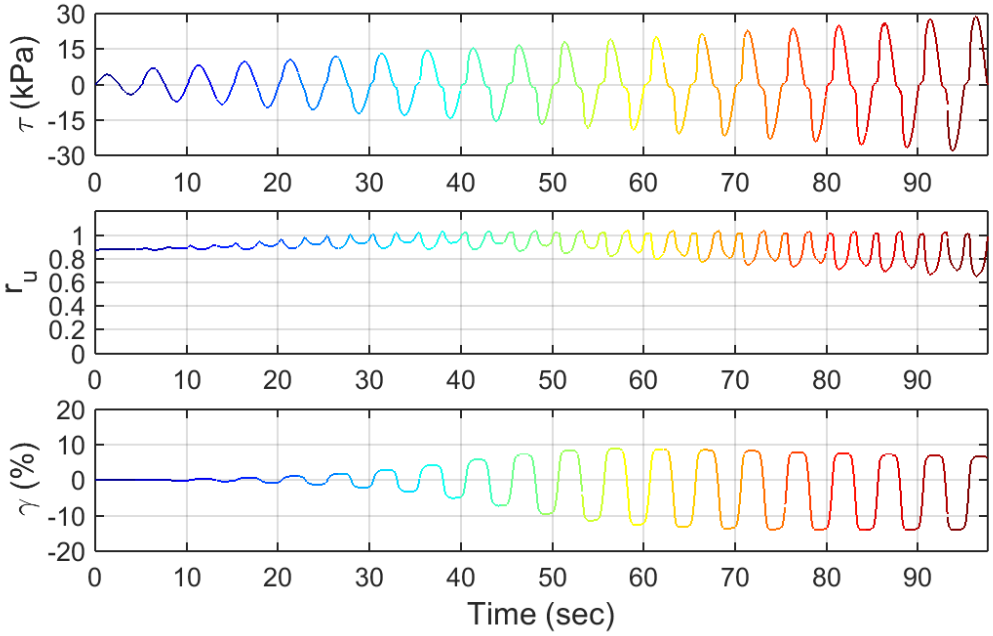

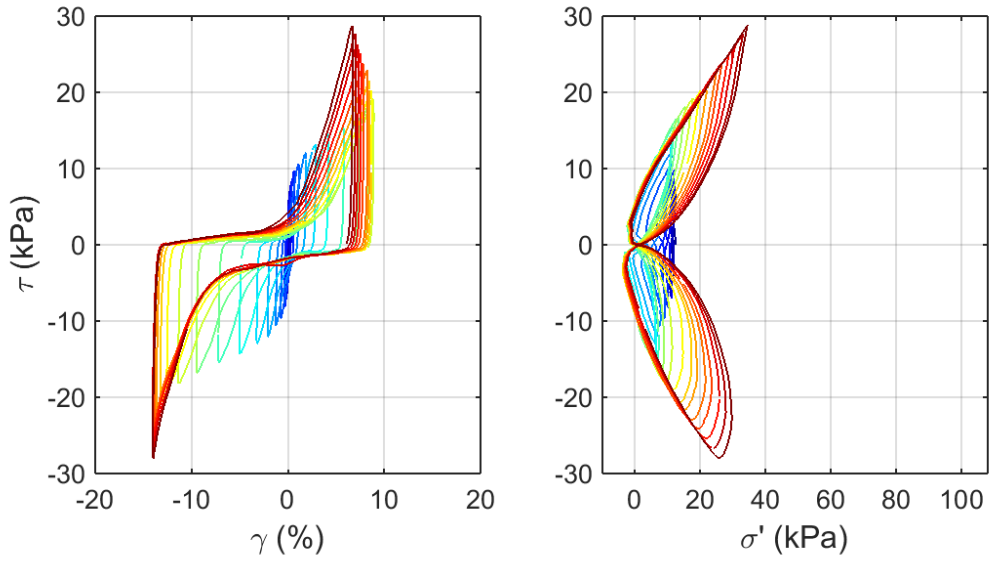

Test ID: 2013030702S2
Nevada Sand
D_r = 44 %
Motion: Taper-up

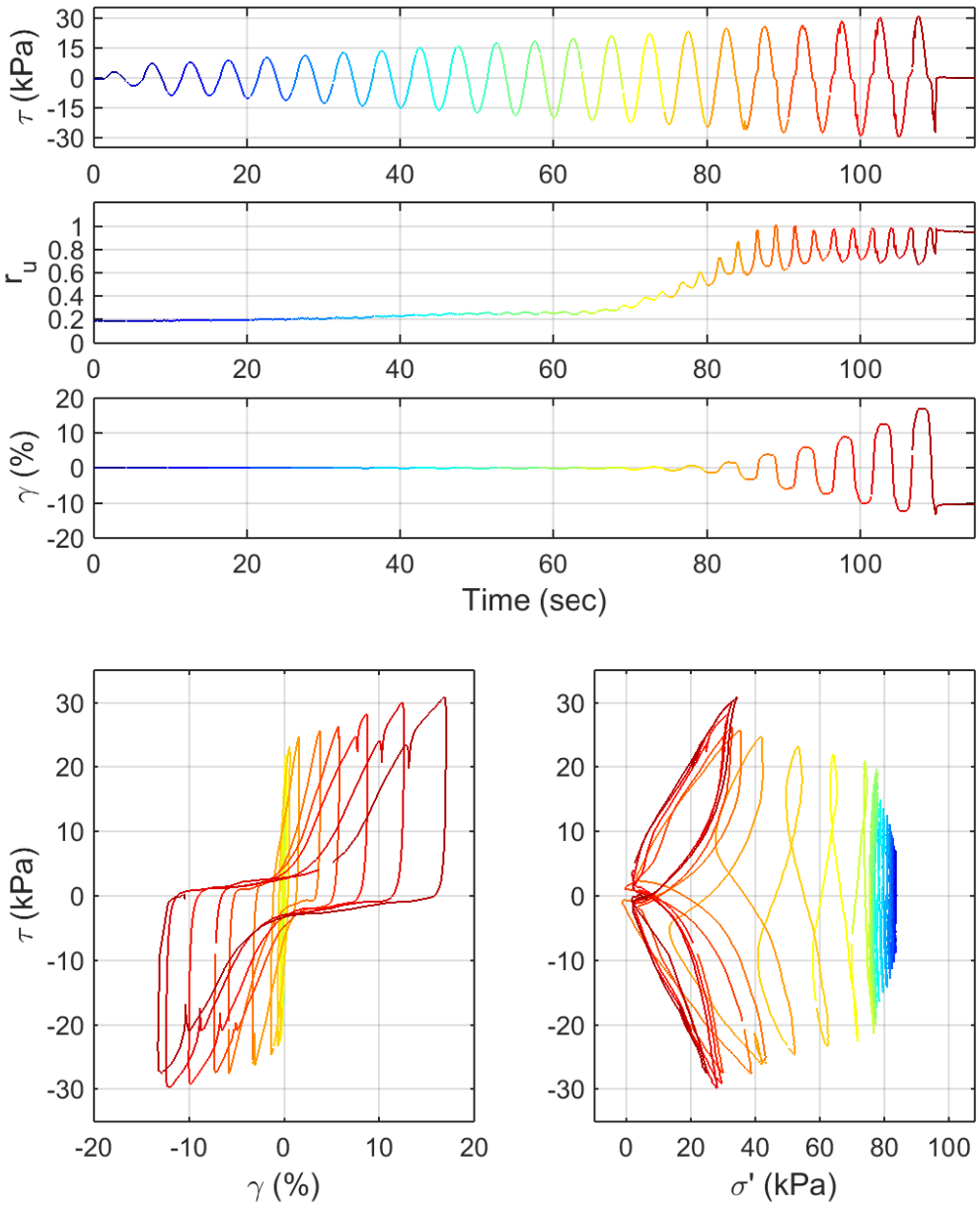

Test ID: 20130326S2
Nevada Sand
D_r = 43 %
Motion: Taper-up

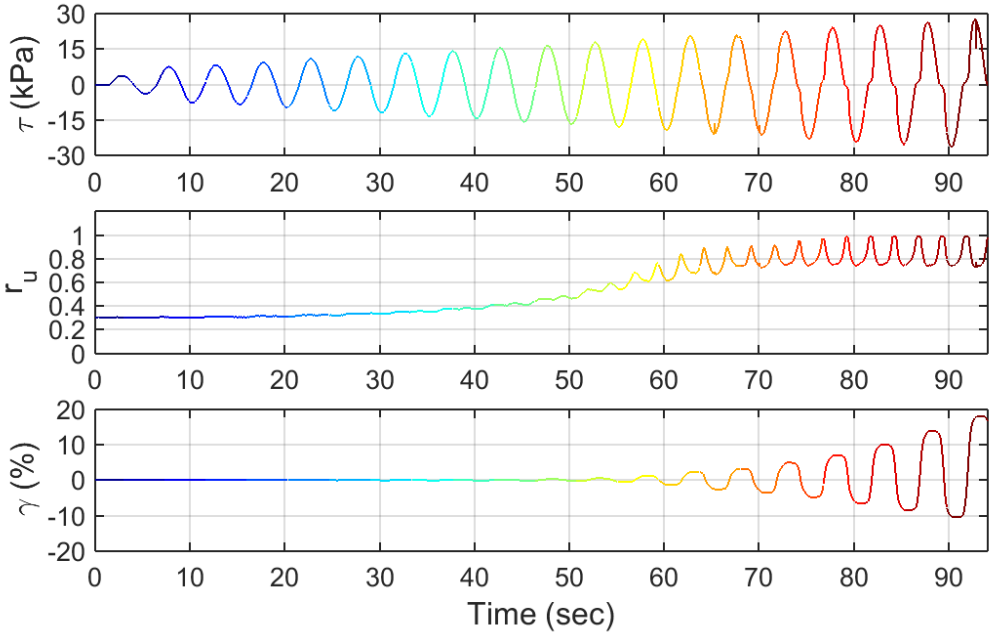

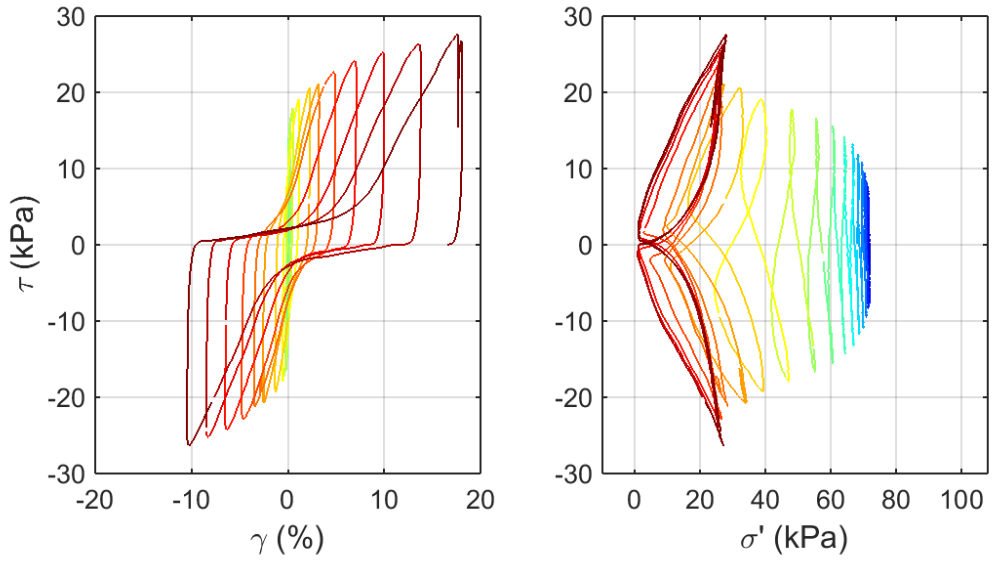

Test ID: 2013032602S2
Nevada Sand
$D_r = 41$ %
Motion: Taper-up

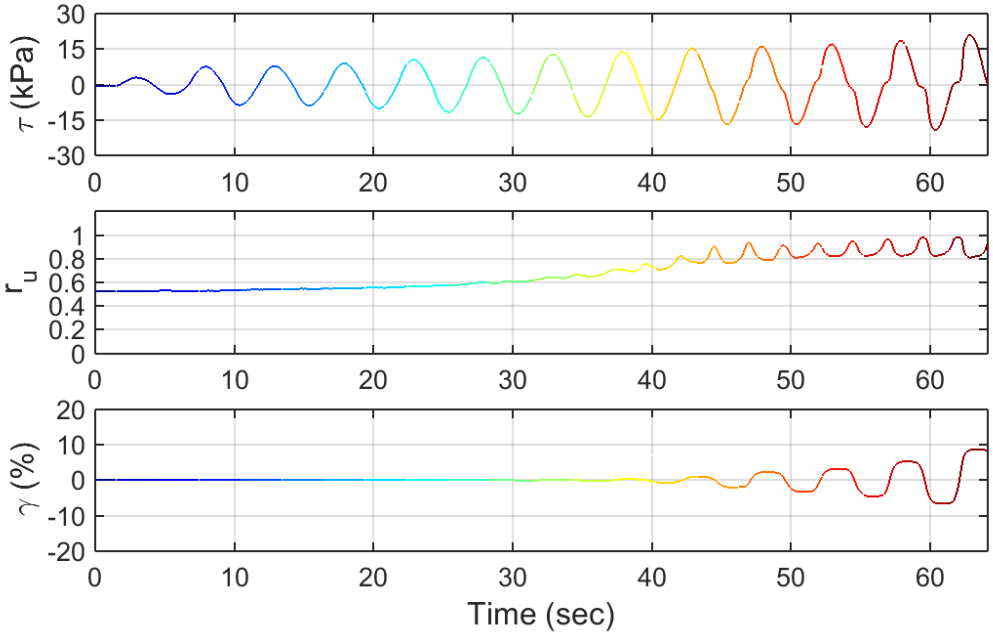

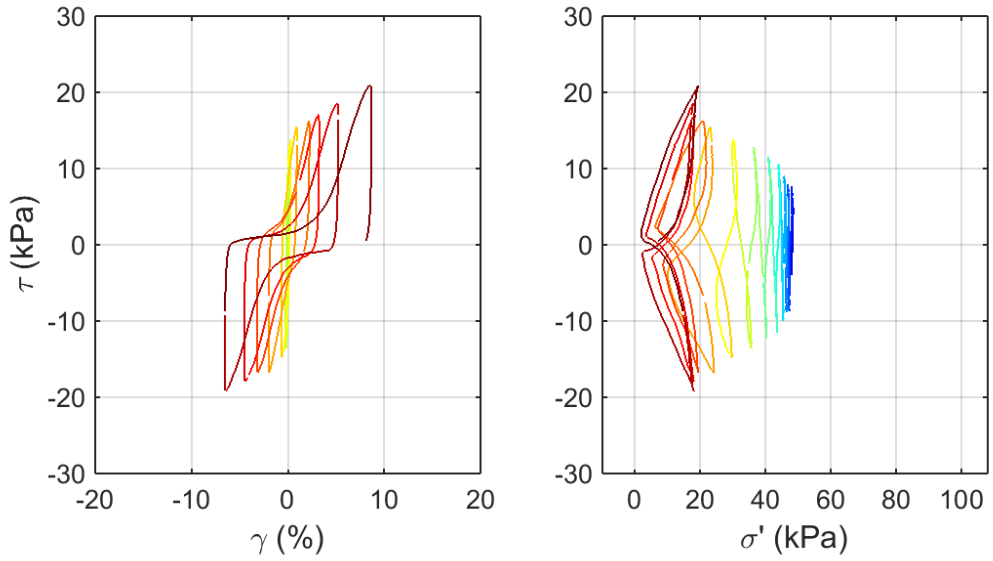

Test ID: 20130329S2
Nevada Sand
D_r = 43 %
Motion: Taper-up

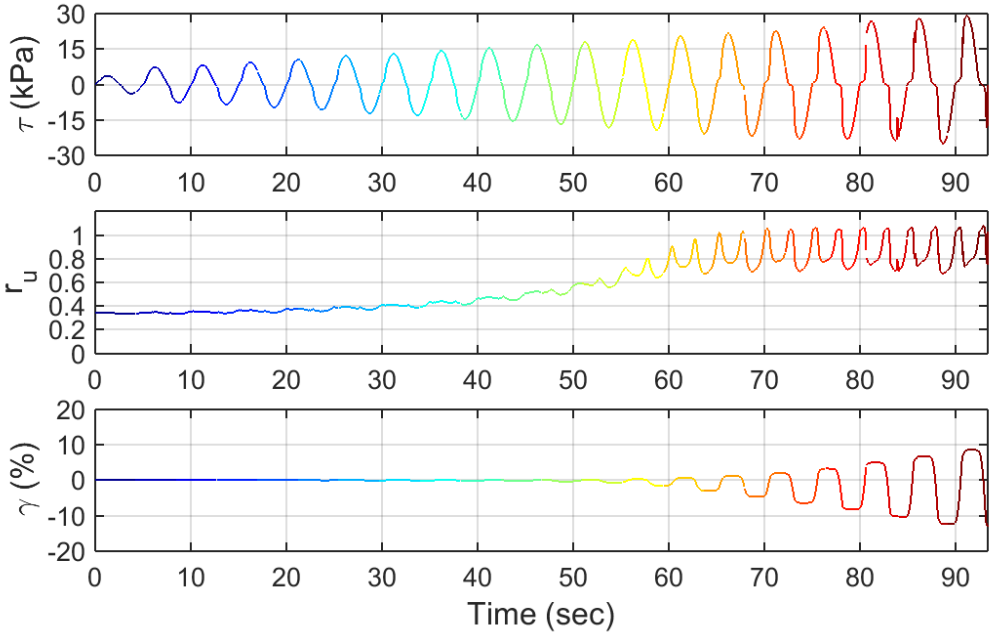

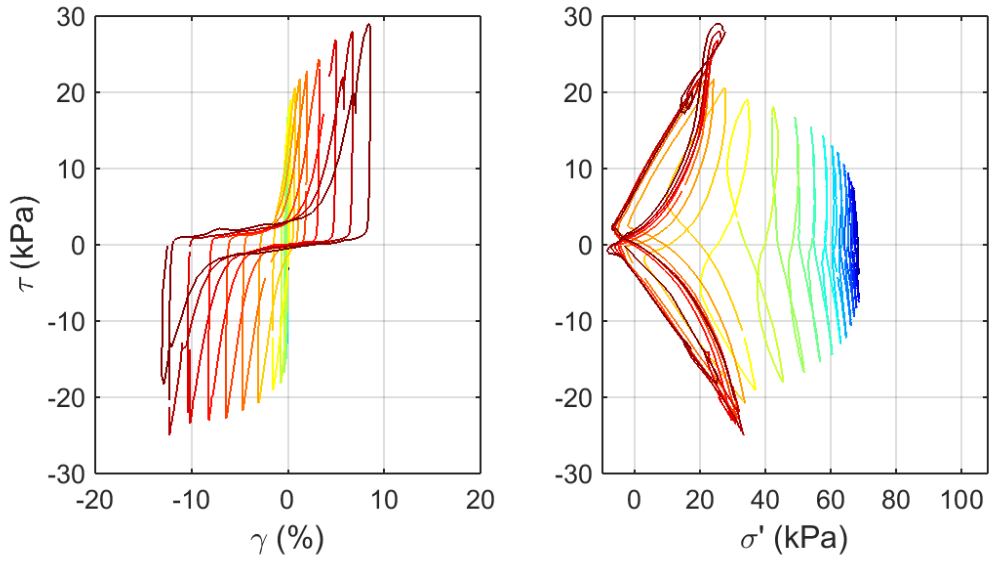

Test ID: 20130521S2
Nevada Sand
D_r = 42 %
Motion: Taper-up

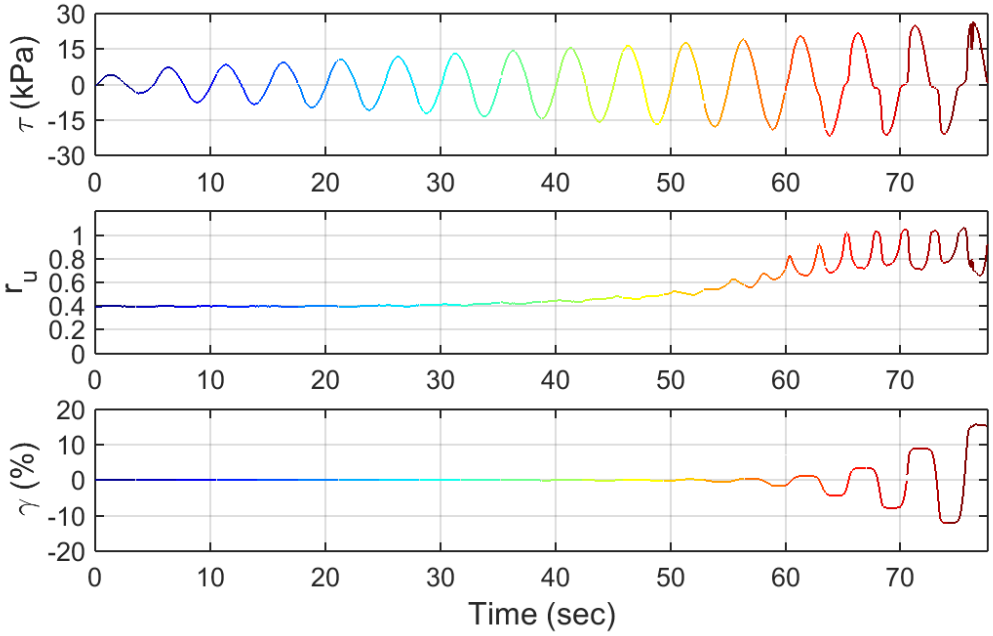

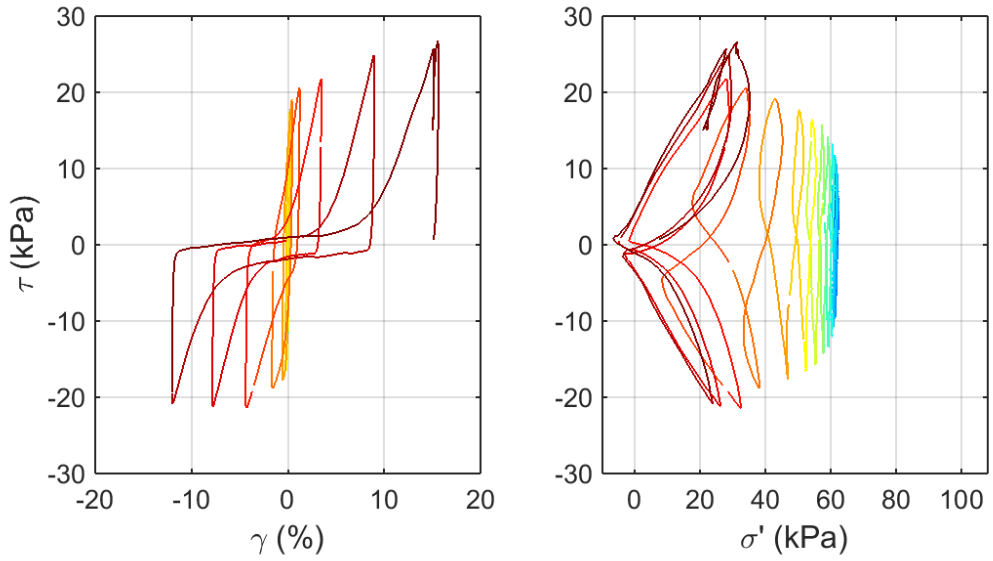

Test ID: 20130528S2
Nevada Sand
D_r = 47 %
Motion: Taper-up

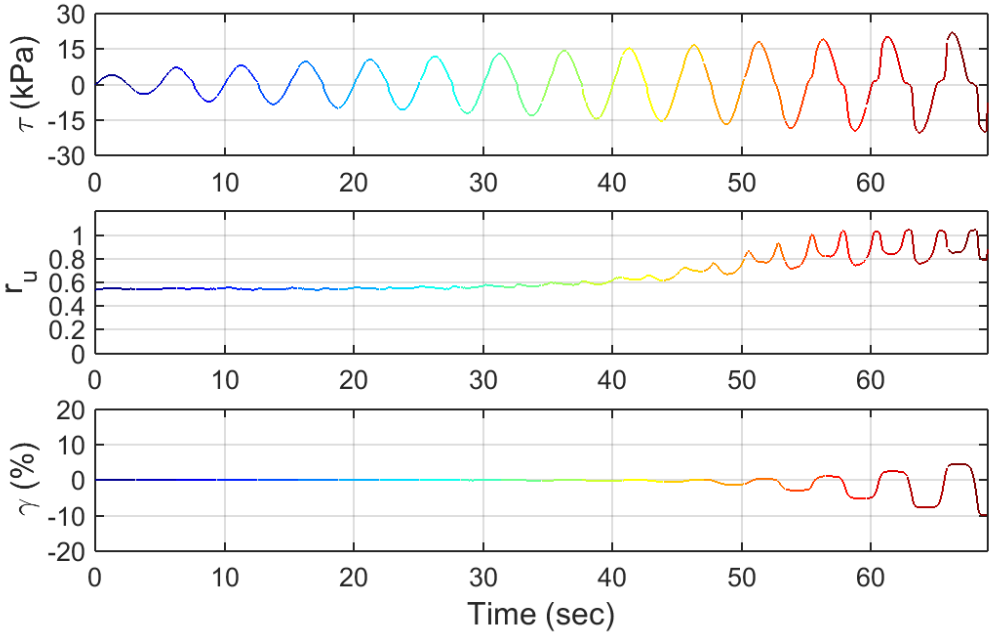

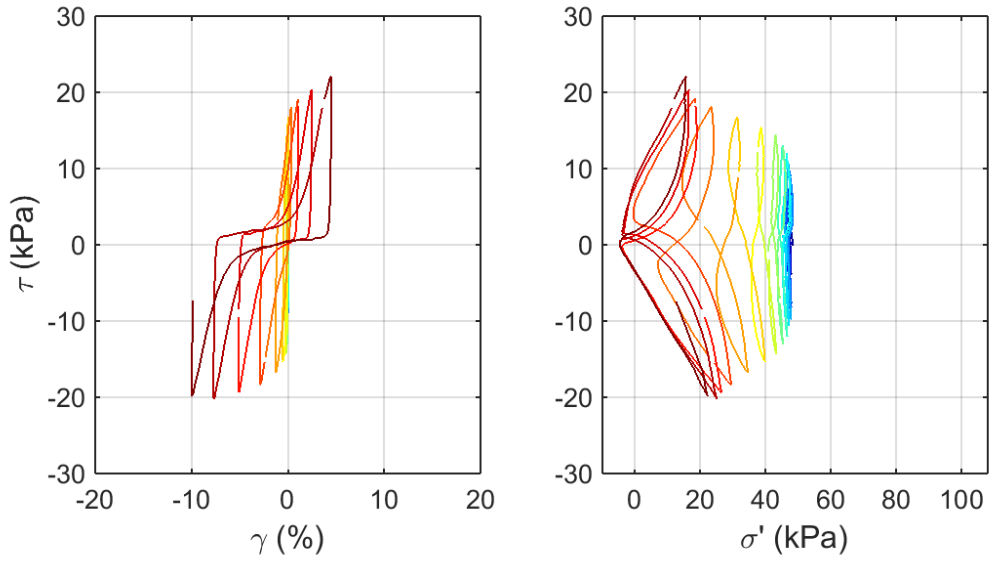

Test ID: 20130531S2
Nevada Sand
D_r = 56 %
Motion: Taper-up

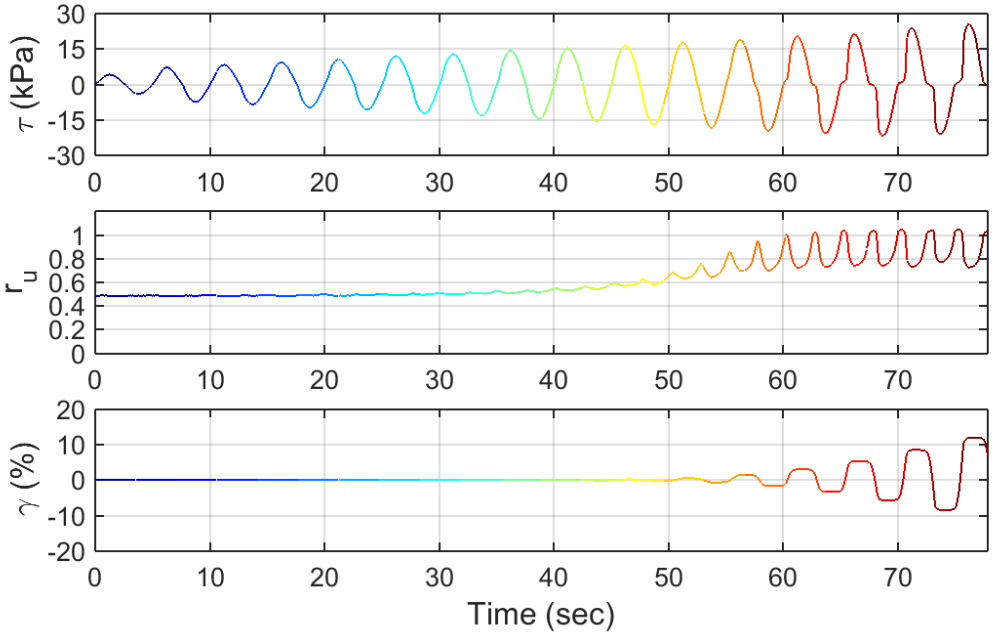

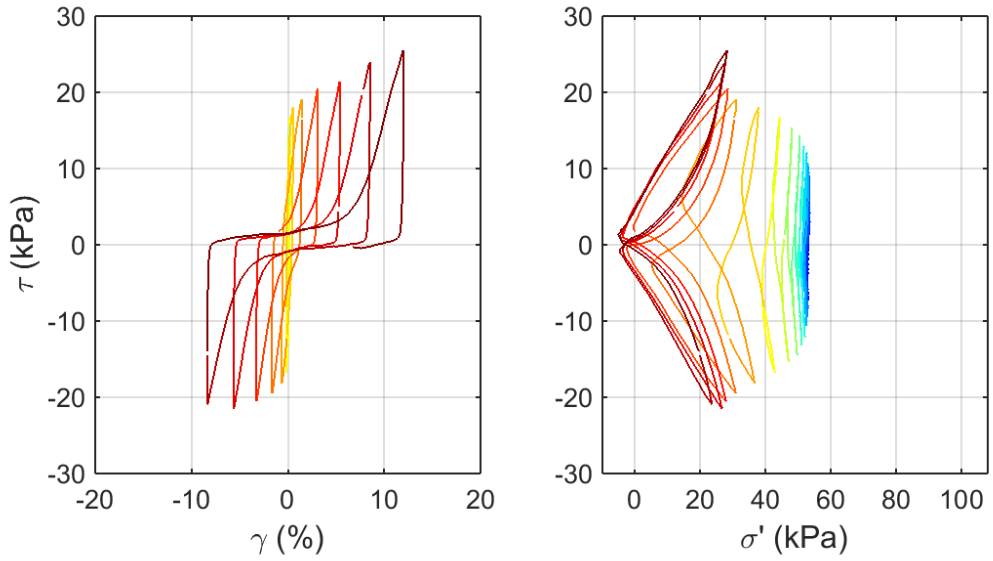

Test ID: 20130603S2
Nevada Sand
D_r = 52%
Motion: Taper-up

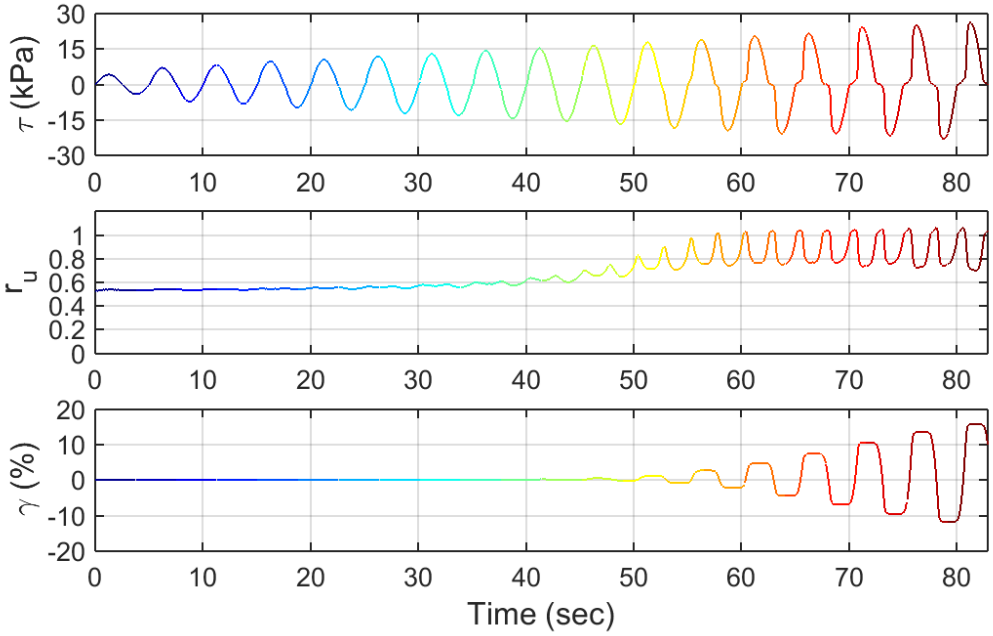

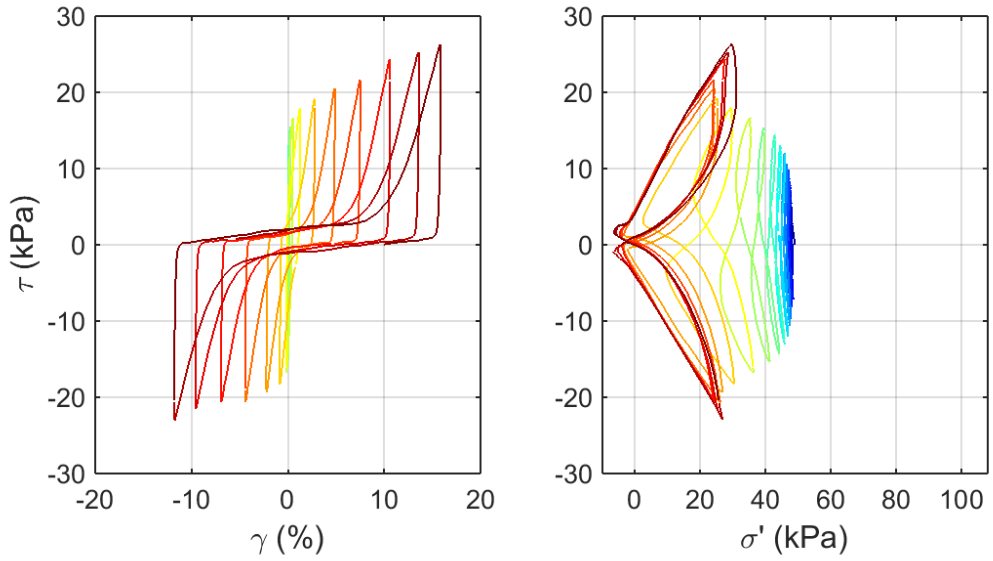

Test ID: 20130618S2
Nevada Sand
D_r = 52 %
Motion: Taper-up

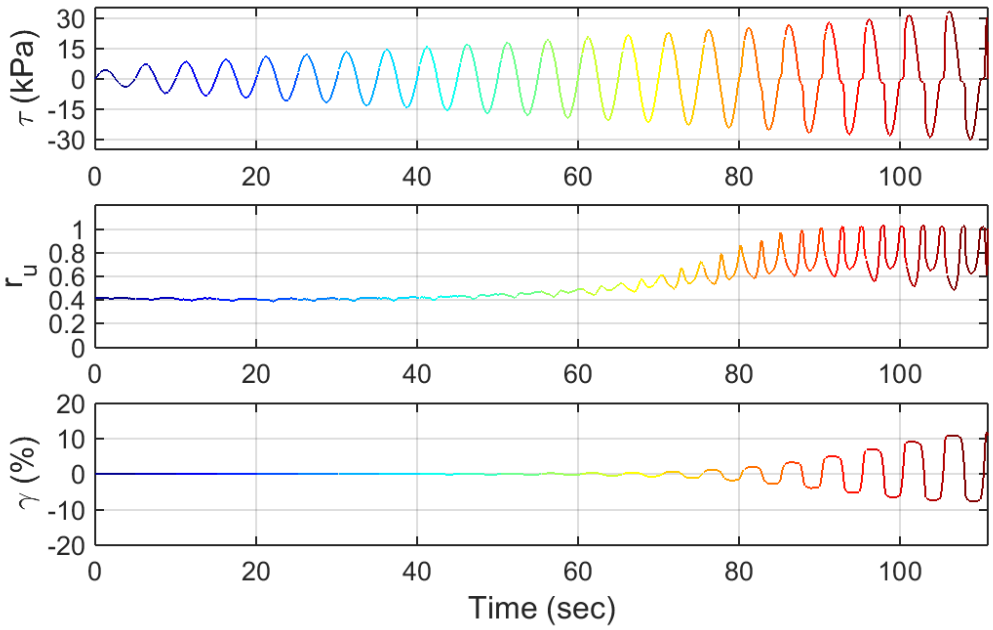

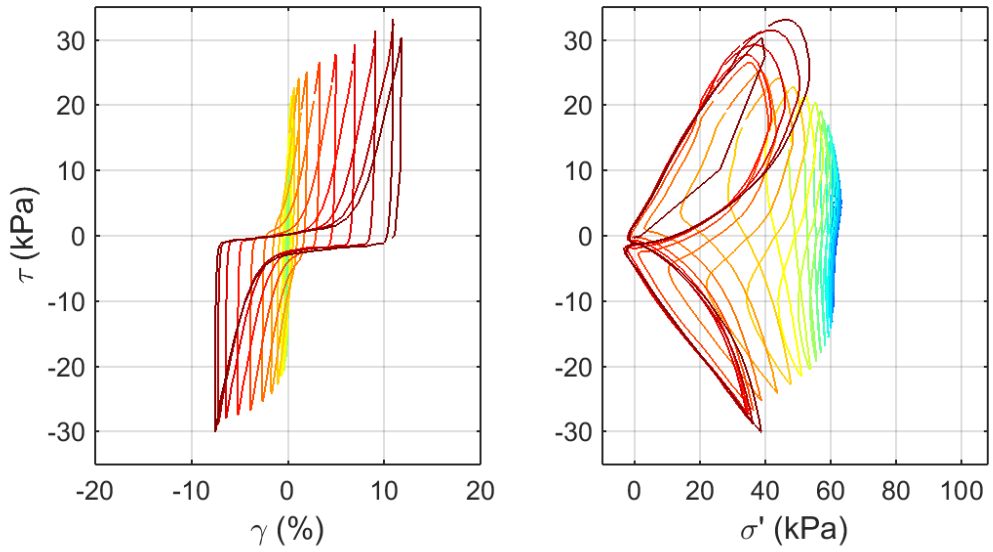

Test ID: 2013061902S2
Nevada Sand
D_r = 52 %
Motion: Taper-up

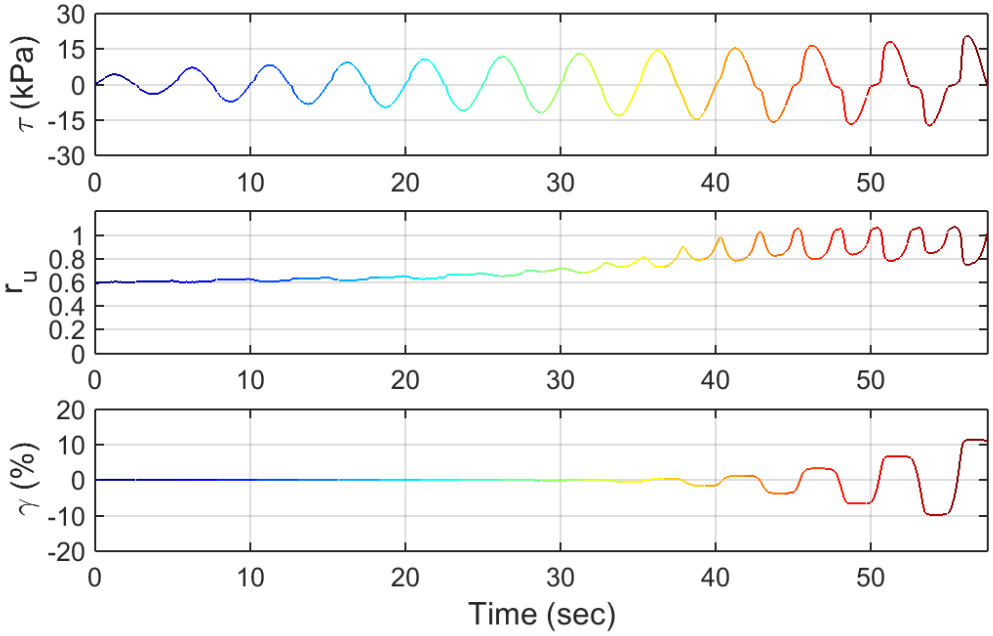

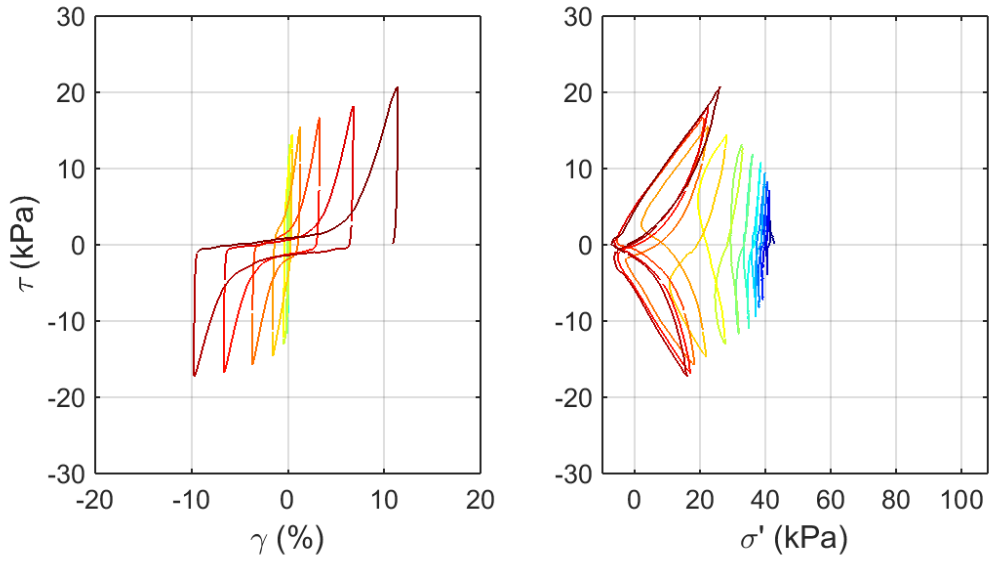

Test ID: 20130621S2
Nevada Sand
D_r = 43 %
Motion: Taper-up

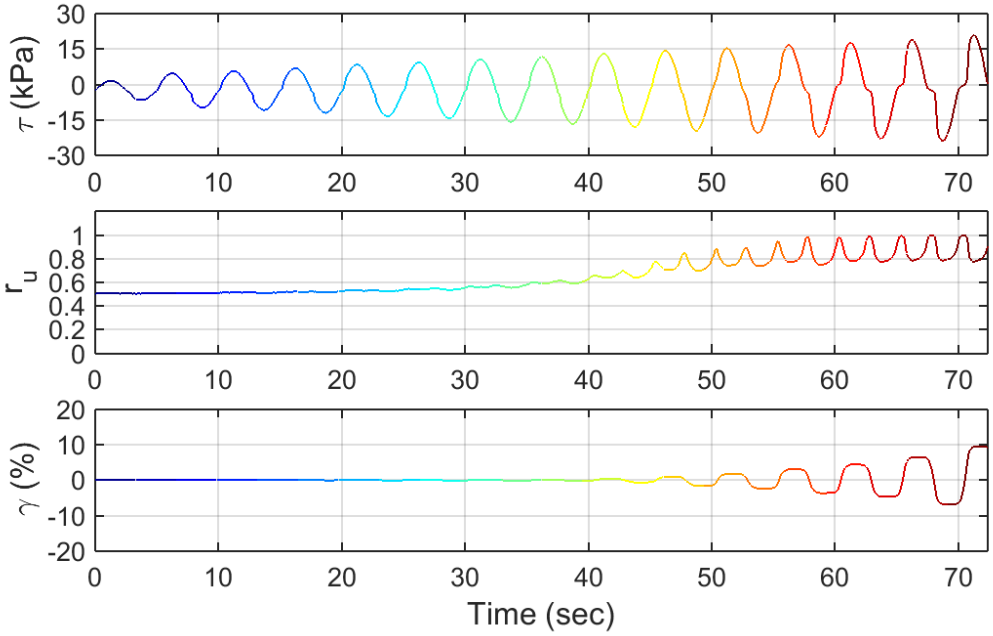

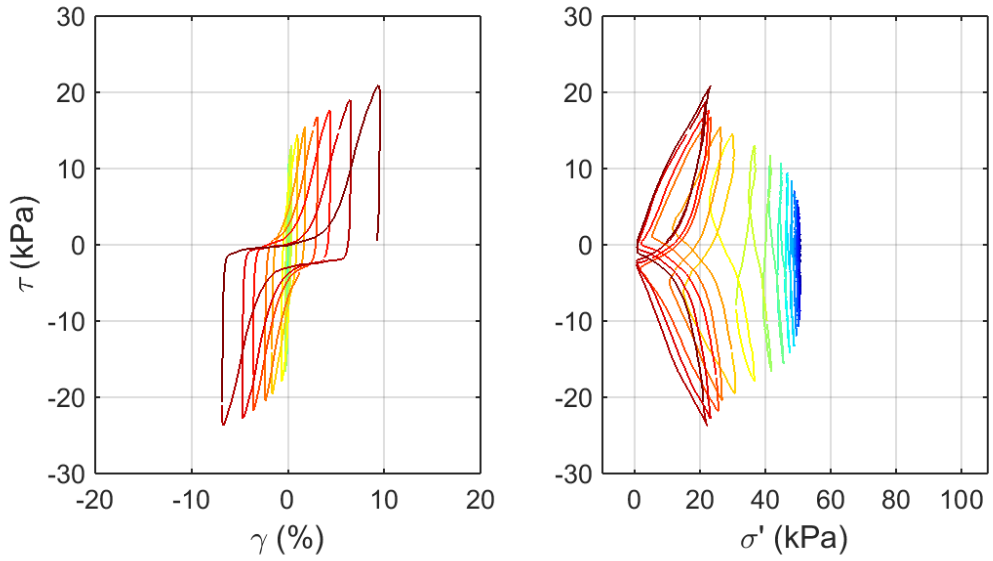

Test ID: 20130701S2
Nevada Sand
D_r = 36 %
Motion: Taper-up

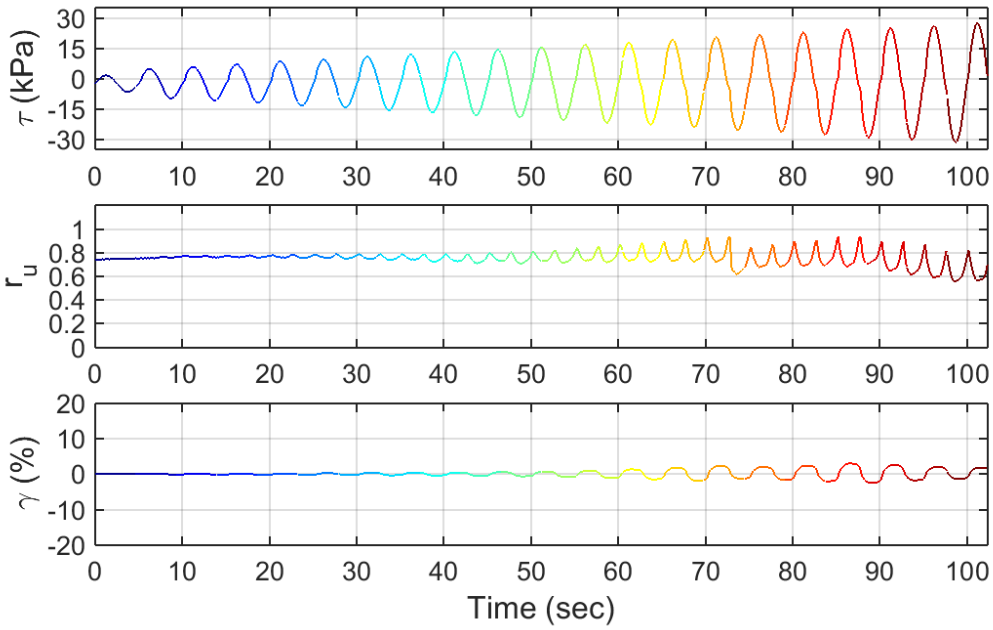

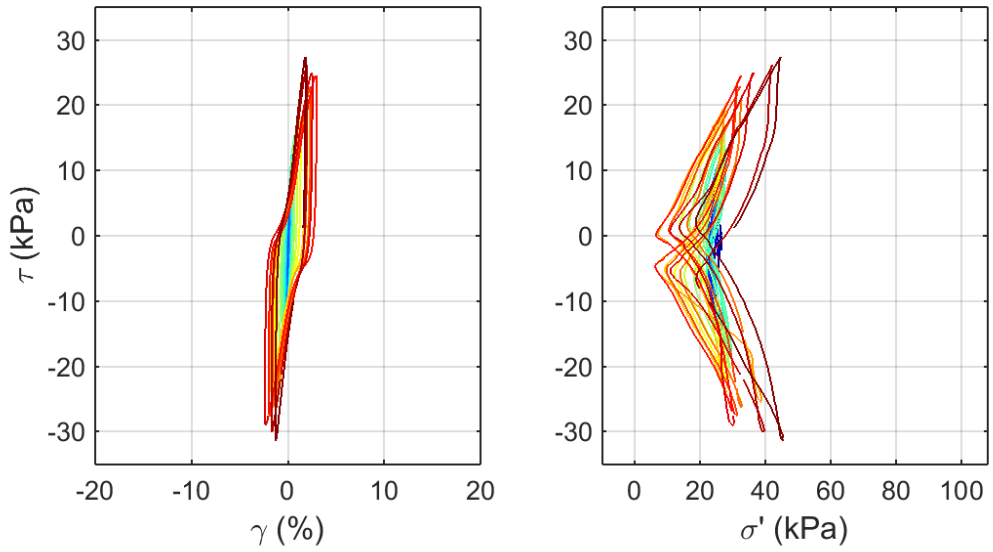

Test ID: 20130702S2
Nevada Sand
D_r = 50 %
Motion: Taper-up

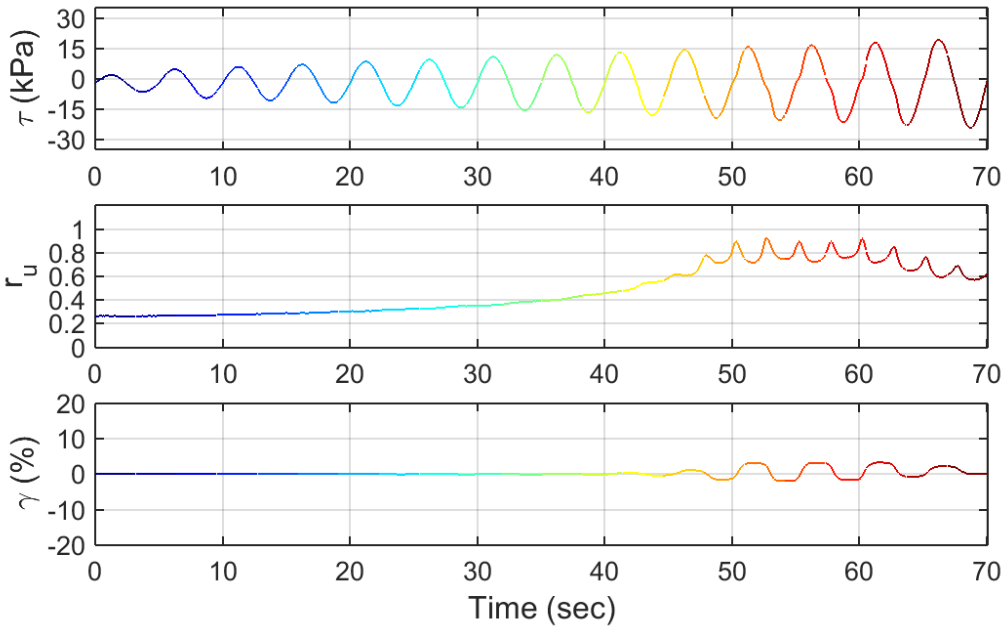

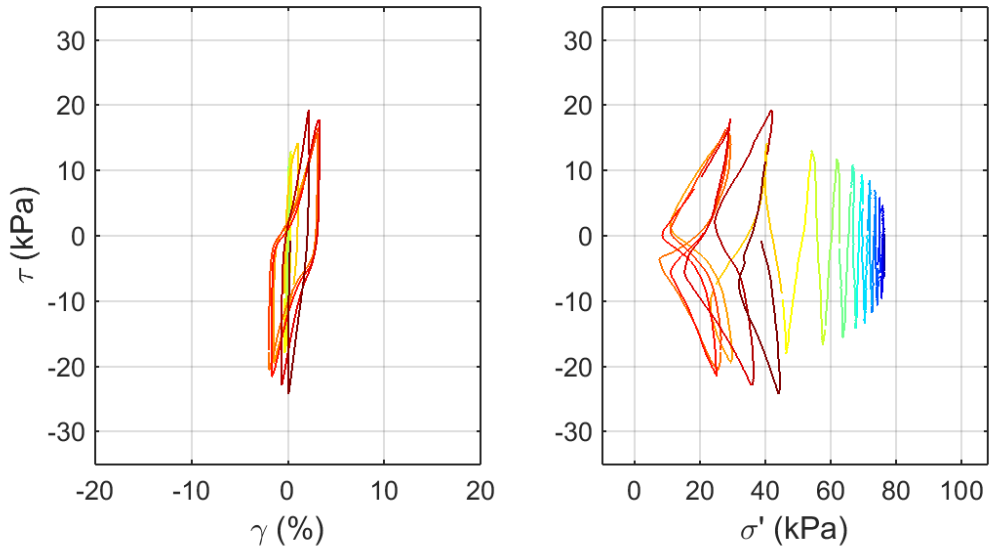

Test ID: 20130704S2
Nevada Sand
D_r = 42 %
Motion: Taper-up

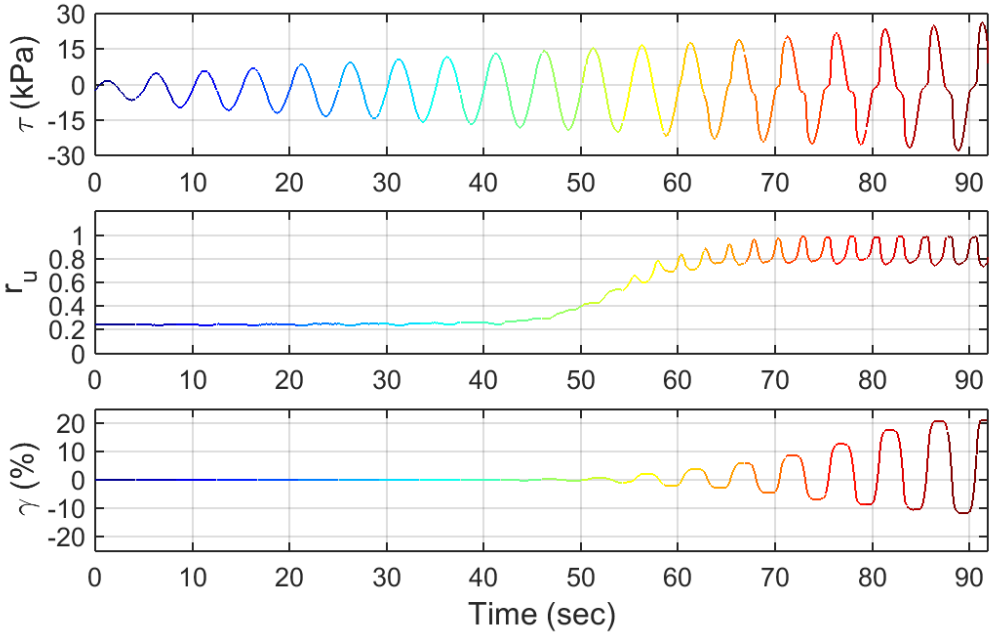

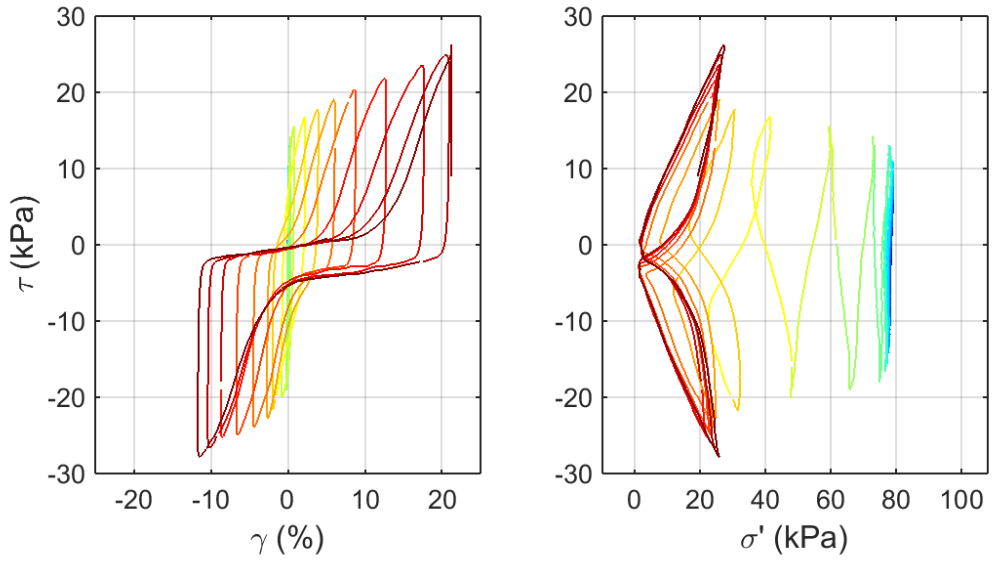

Test ID: 20130705S2
Nevada Sand
D_r = 45 %
Motion: Taper-up

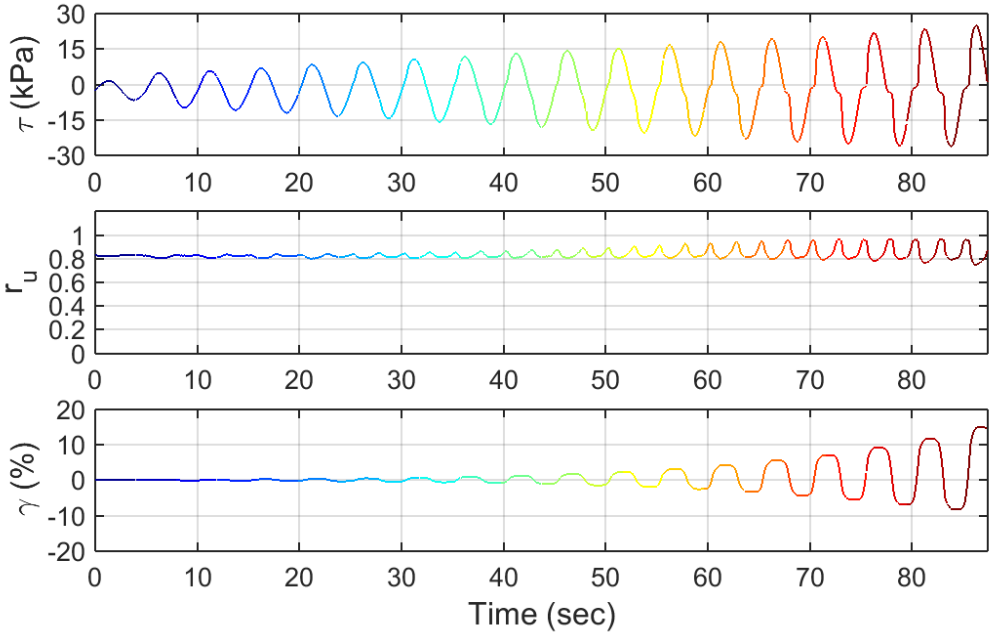

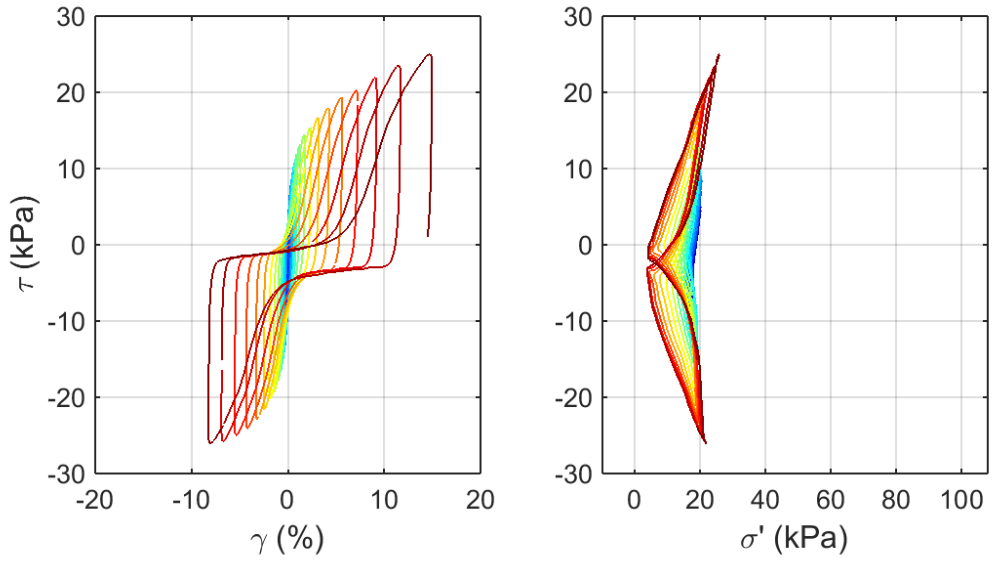

Test ID: 20130706S2
Nevada Sand
D_r = 49 %
Motion: Taper-up

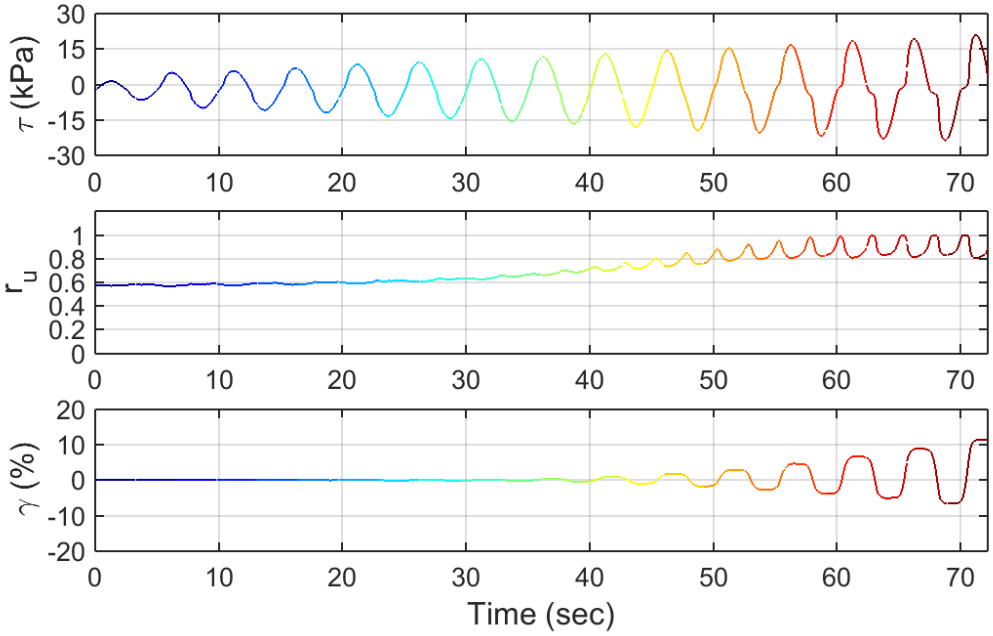

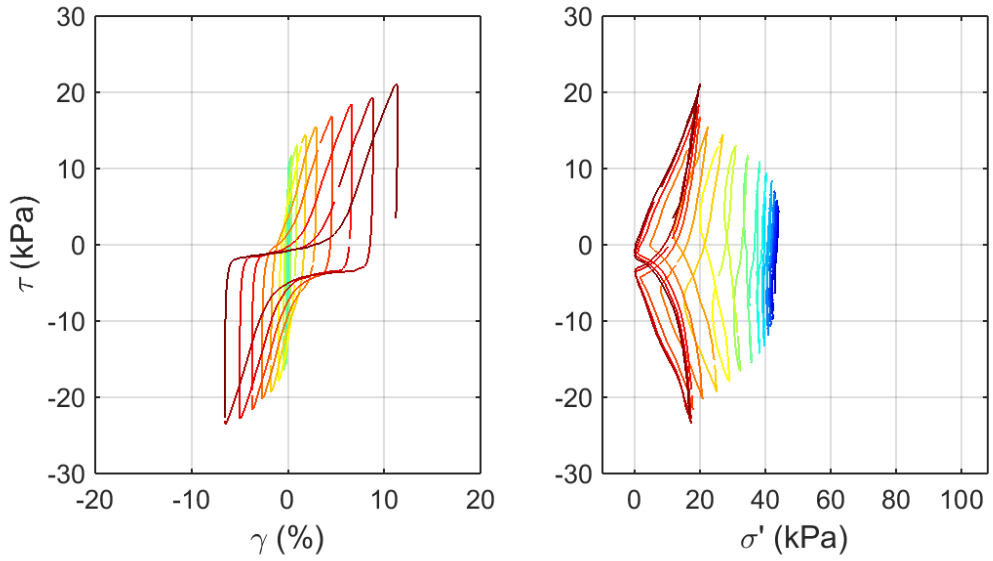

Test ID: 20130708S2
Nevada Sand
D_r = 43 %
Motion: Taper-up

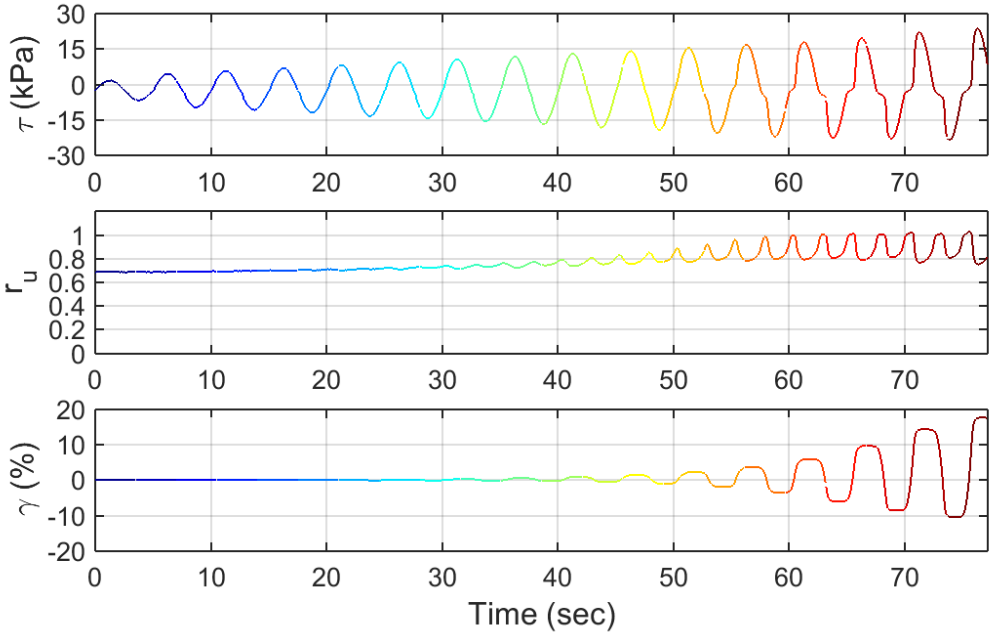

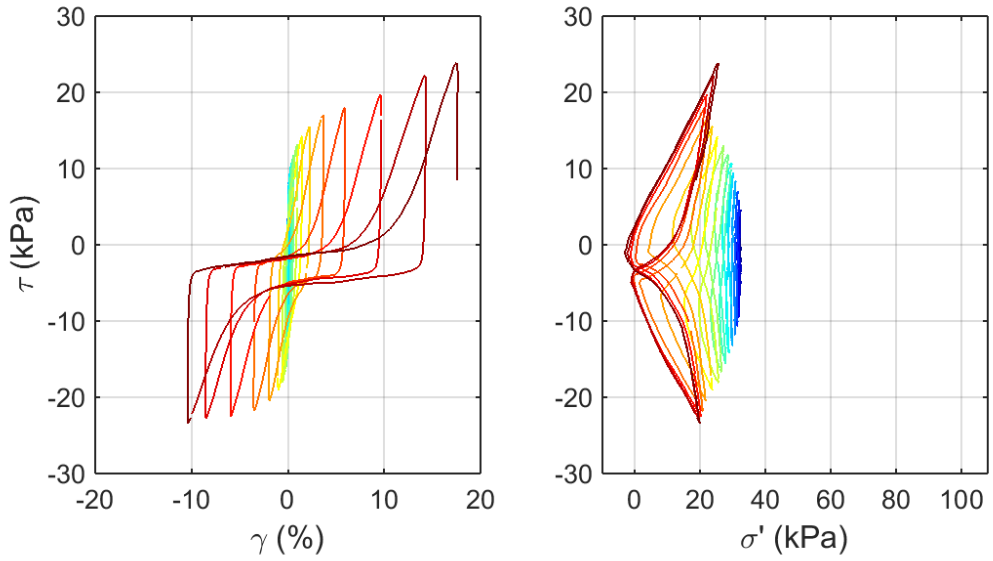

Test ID: 20130709S2
Nevada Sand
D_r = 39 %
Motion: Taper-up

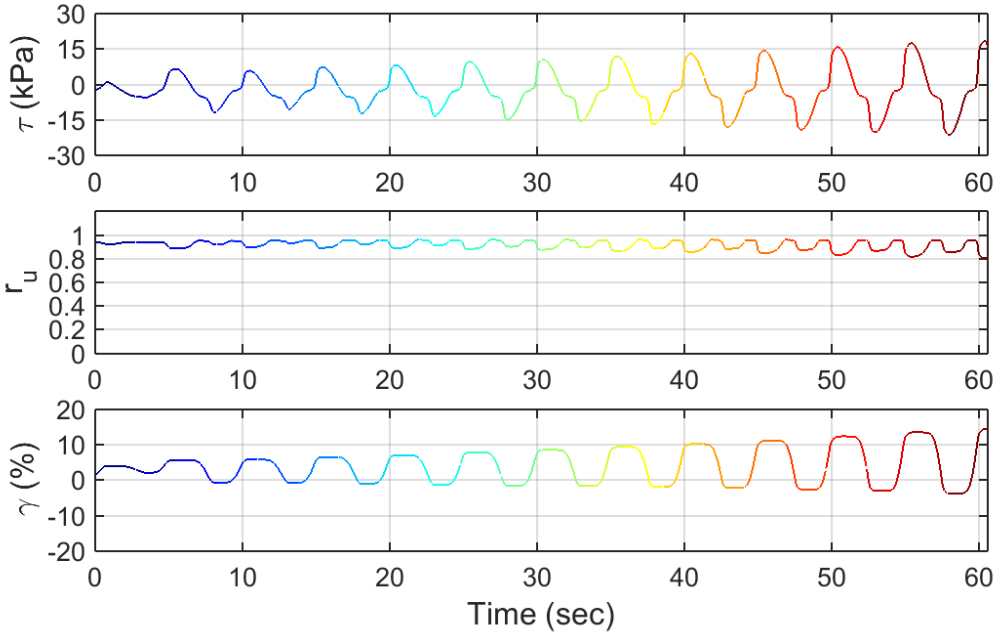

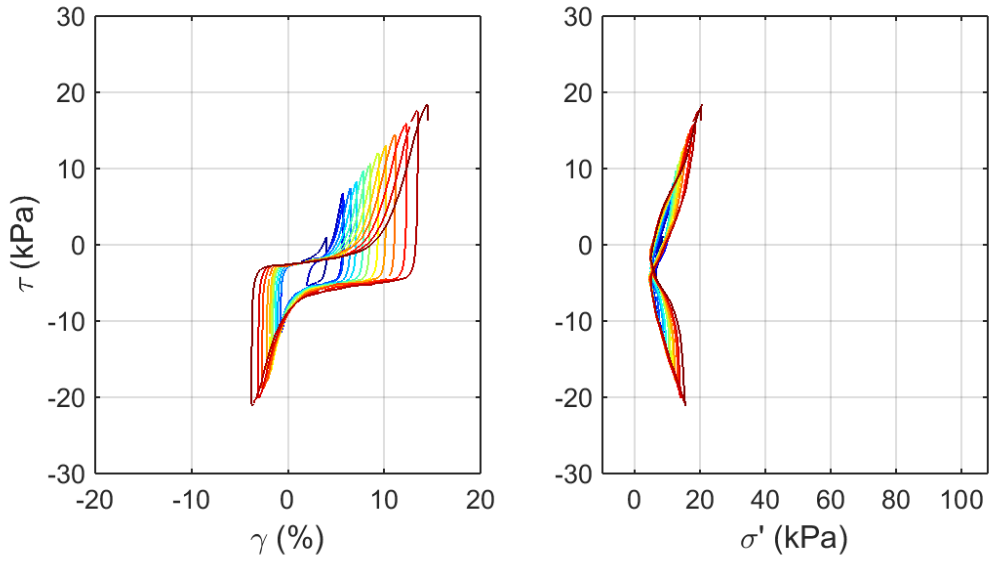

Test ID: 20130715S2
Nevada Sand
D_r = 39 %
Motion: Taper-up

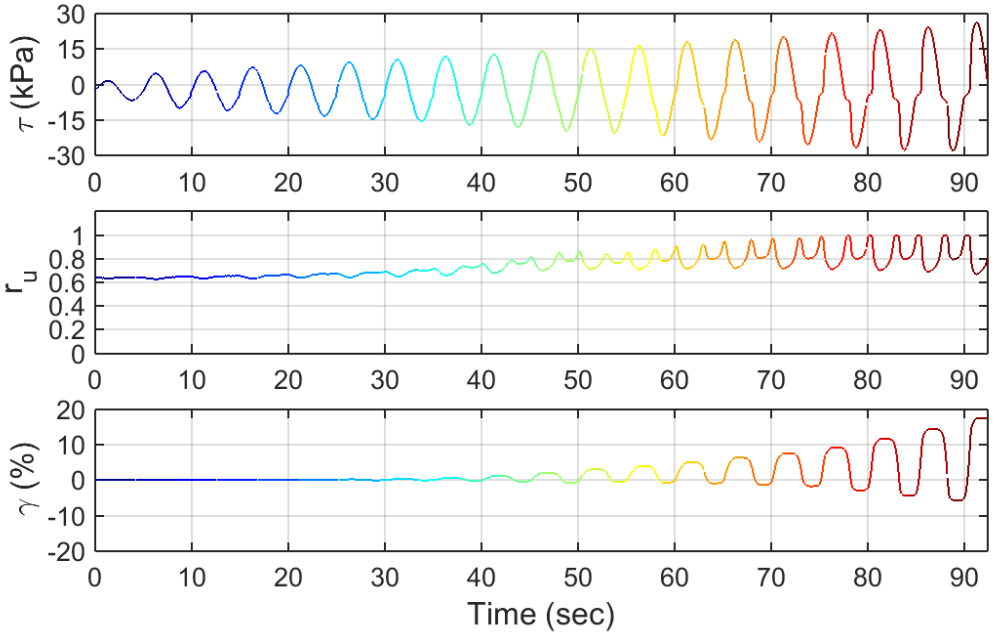

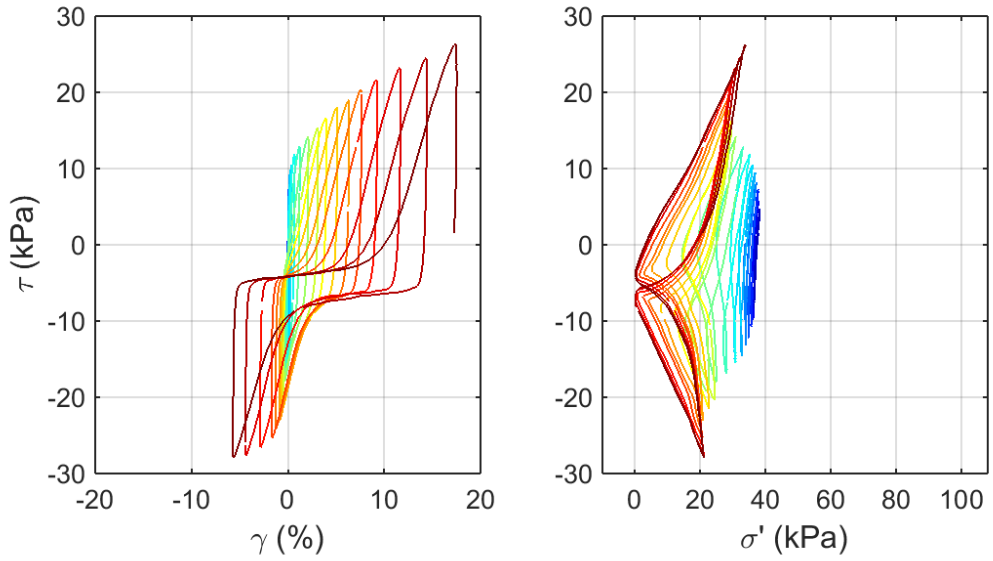

Test ID: 2013071802S2
Nevada Sand
$D_r = 41$ %
Motion: Taper-up

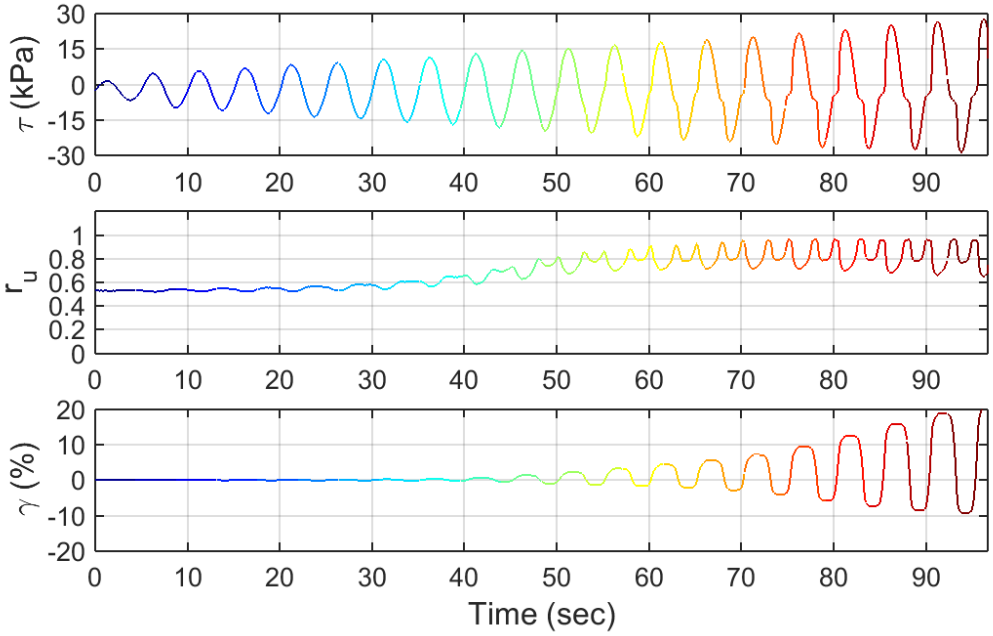

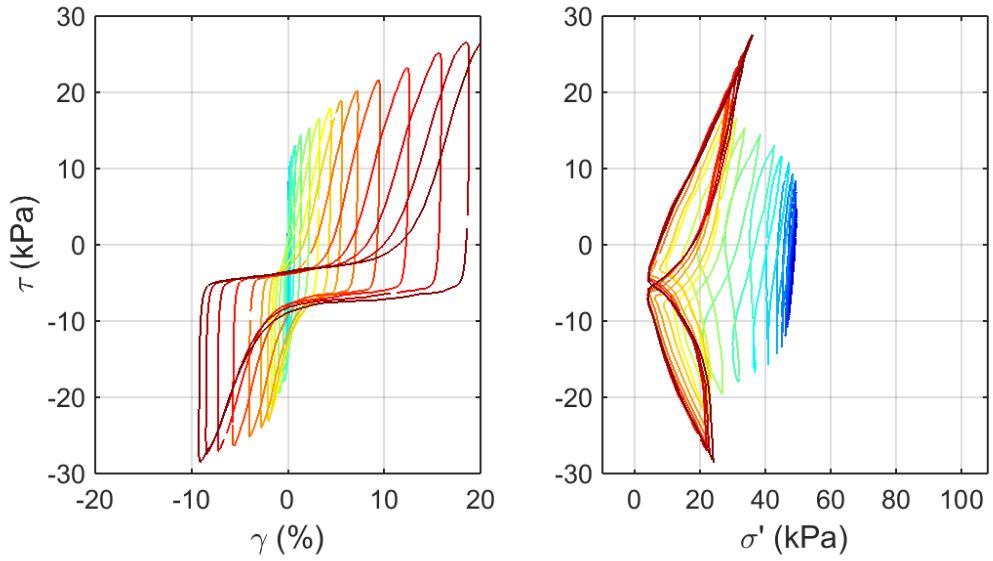

Test ID: 20130719S2
Nevada Sand
D_r = 44 %
Motion: Taper-up

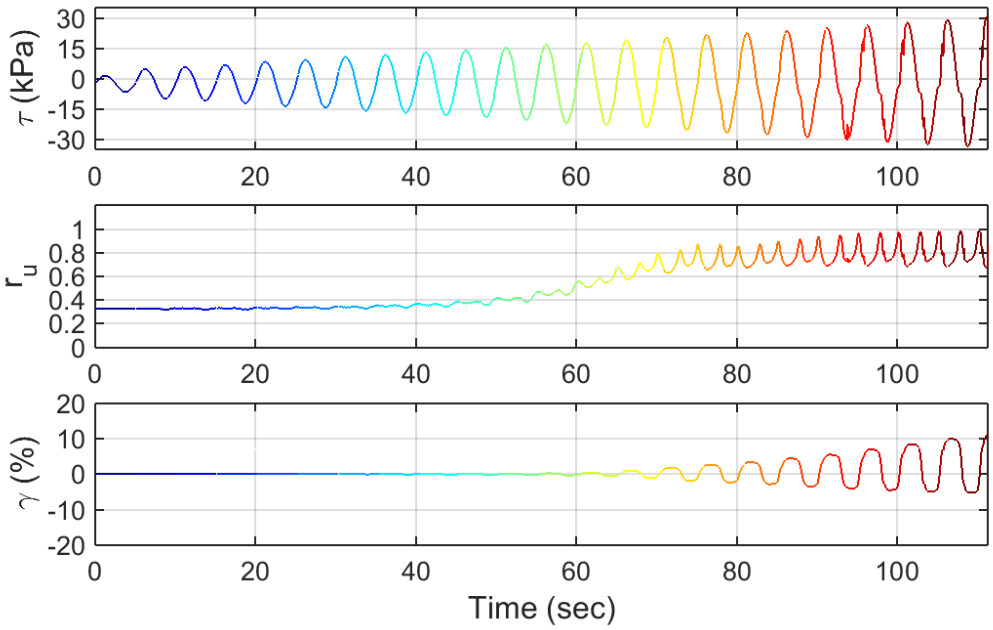

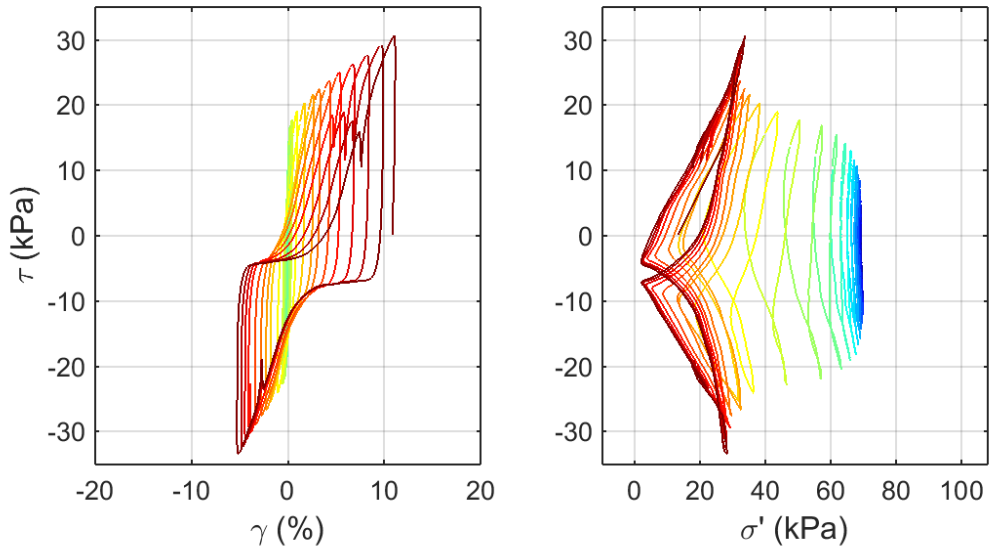

Test ID: 20130724S2
Nevada Sand
D_r = 53 %
Motion: Taper-up

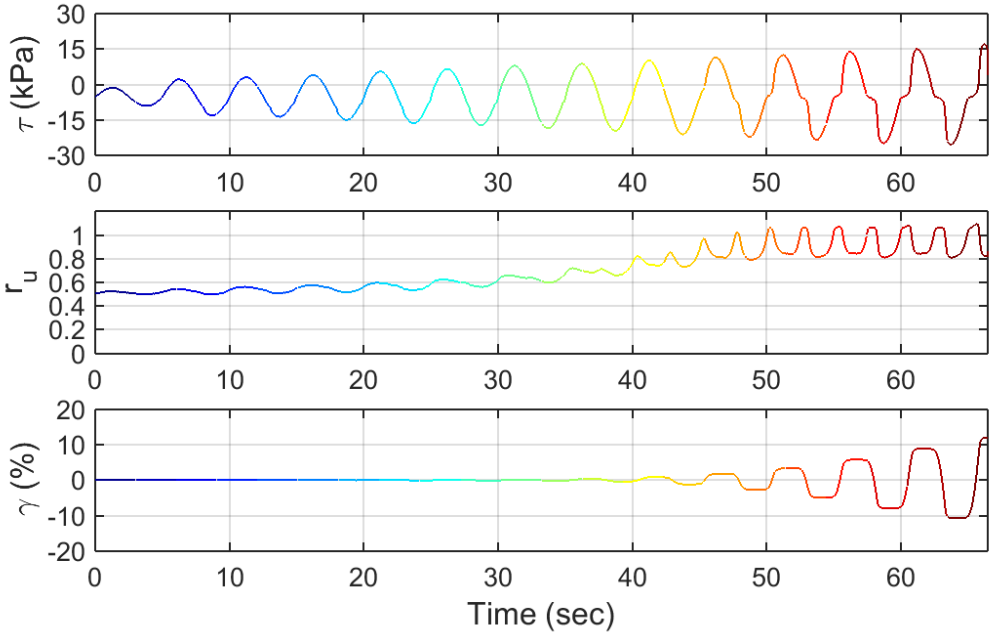

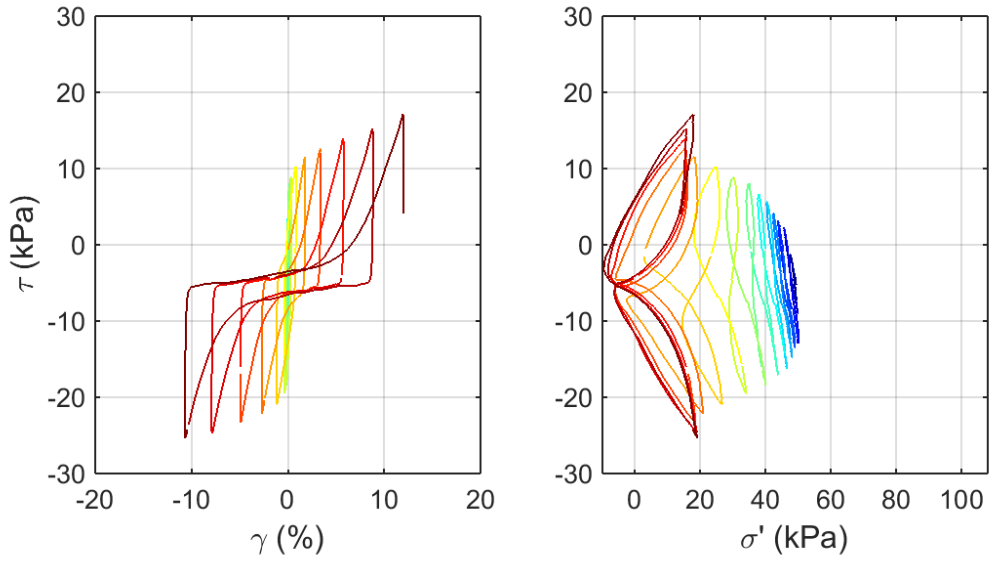

Test ID: 20130919S2
Nevada Sand
D_r = 55 %
Motion: Taper-up

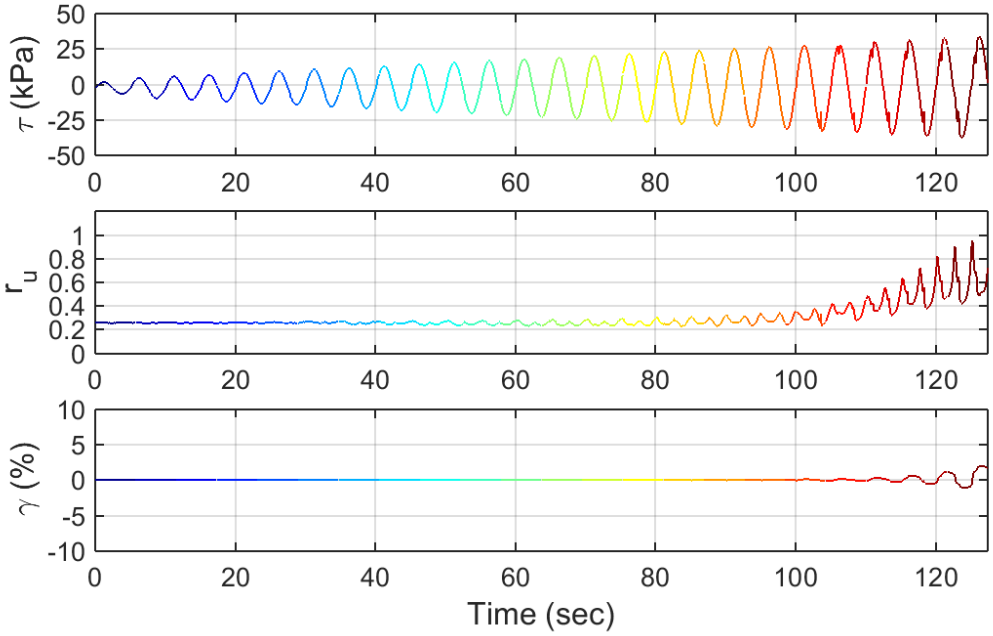

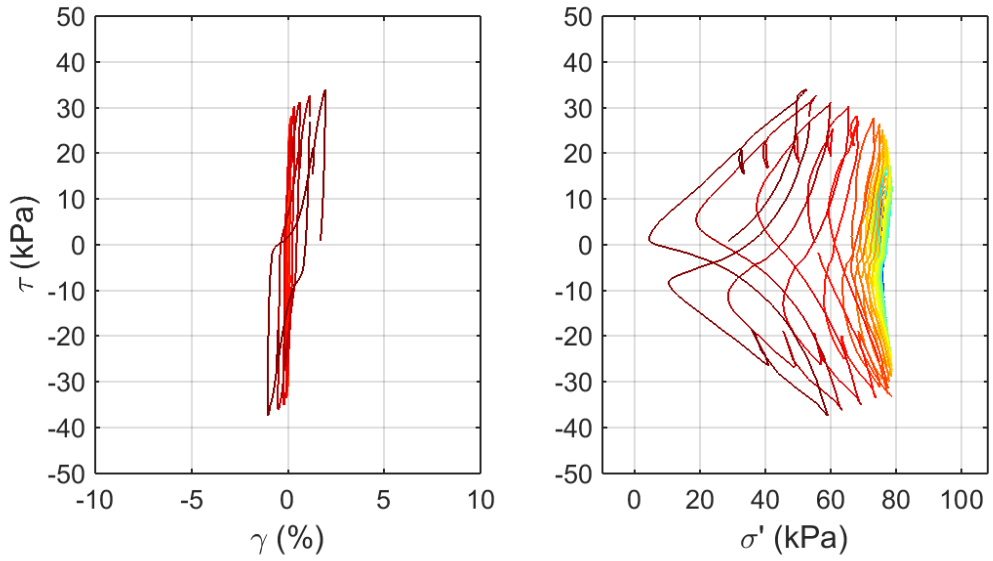

Test ID: 20130710S2
Nevada Sand
D_r = 80 %
Motion: Taper-up

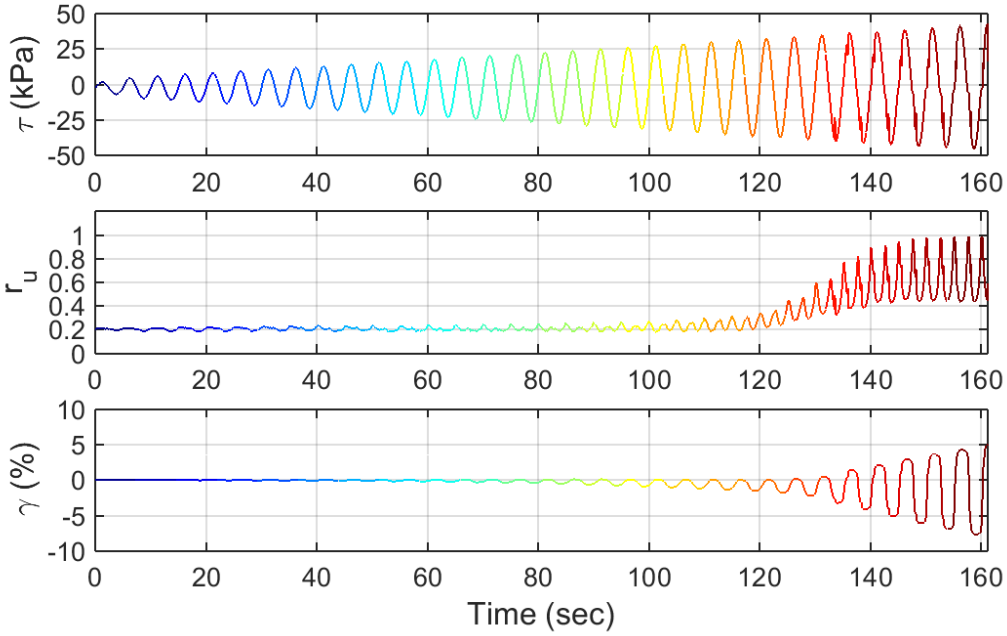

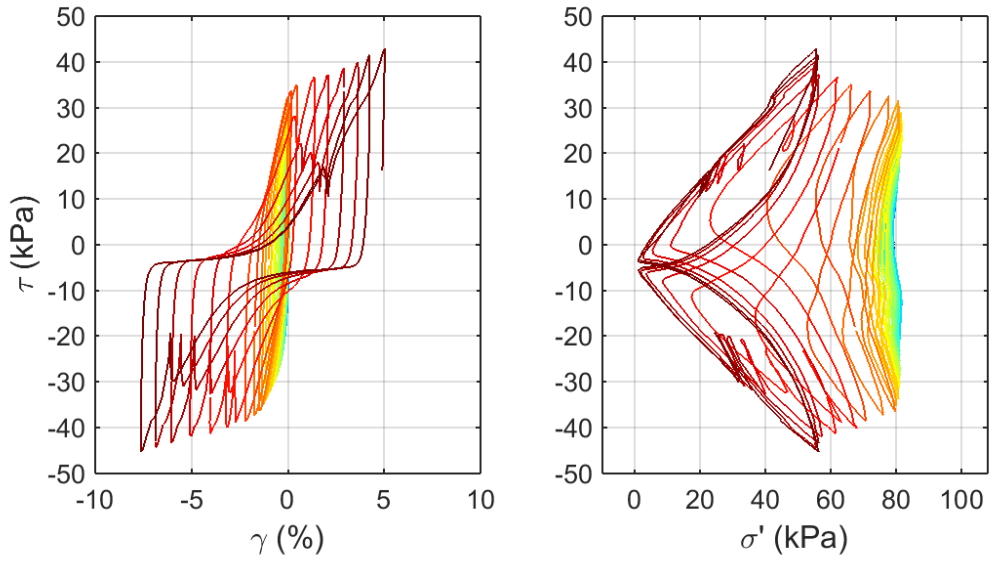

Test ID: 20130712S2
Nevada Sand
D_r = 77 %
Motion: Taper-up

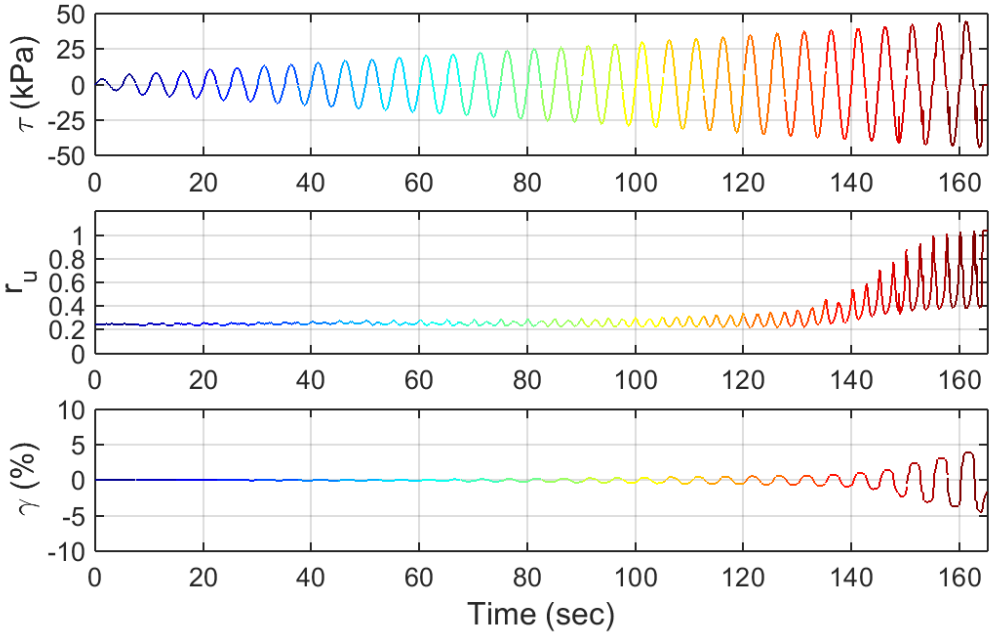

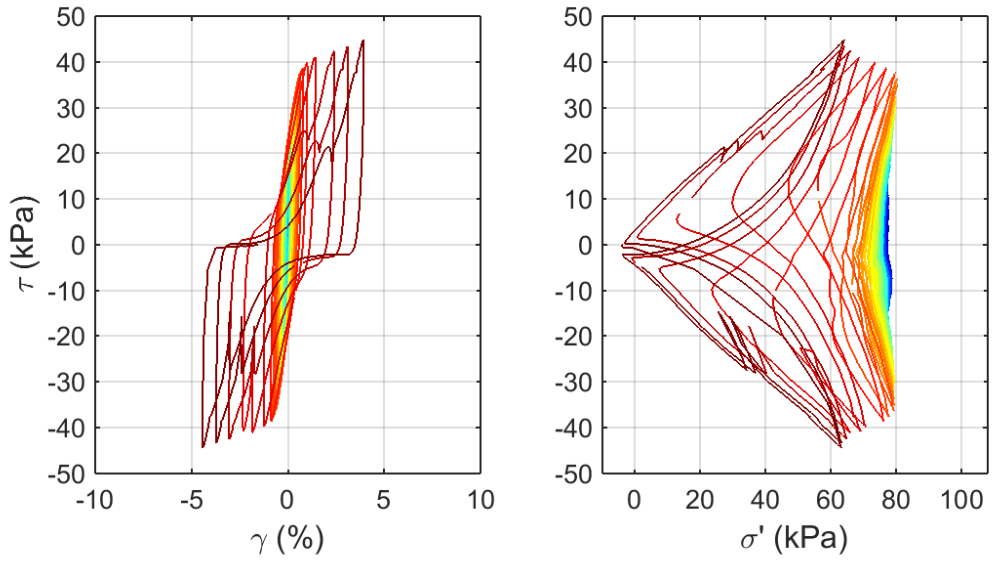

Test ID: 20130726S2
Nevada Sand
D_r = 74 %
Motion: Taper-up

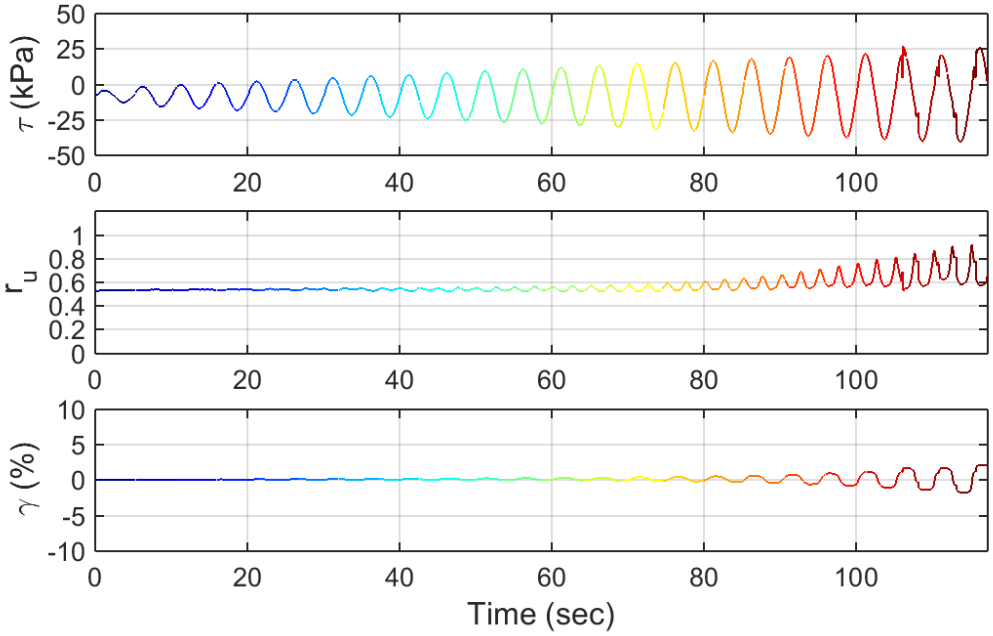

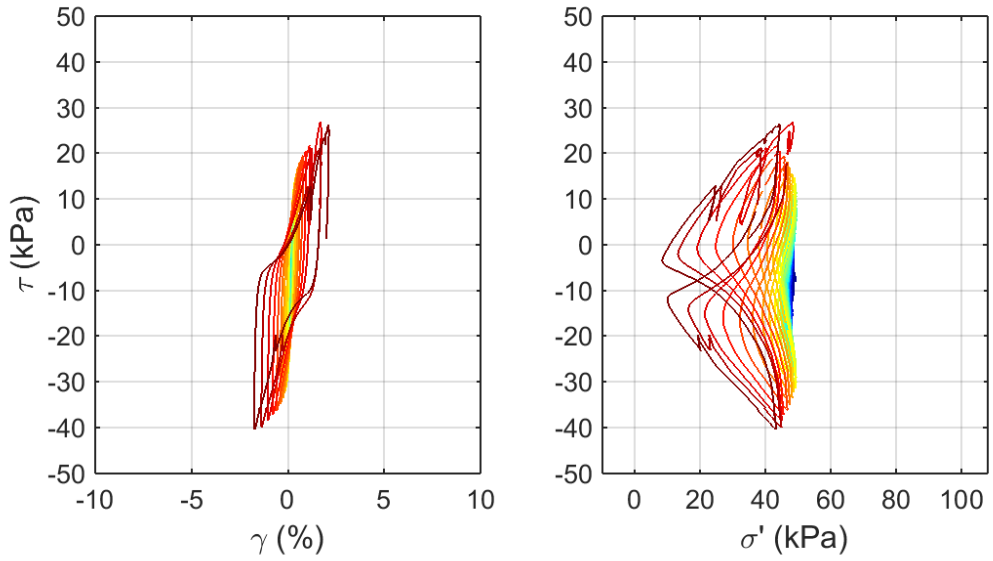

Test ID: 20130802S2
Nevada Sand
D_r = 94 %
Motion: Taper-up

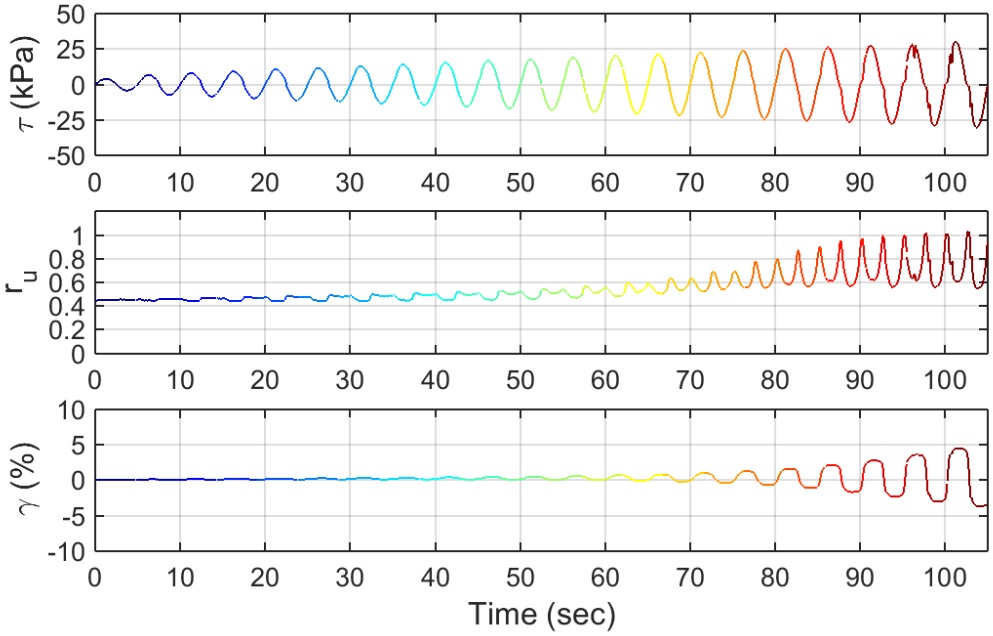

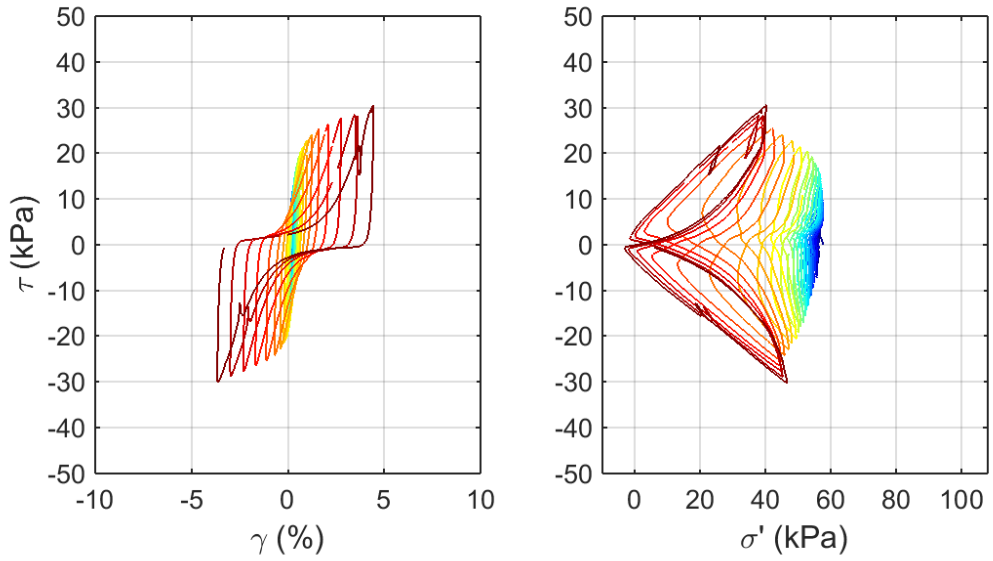

Test ID: 20130805S2
Nevada Sand
D_r = 77 %
Motion: Taper-up

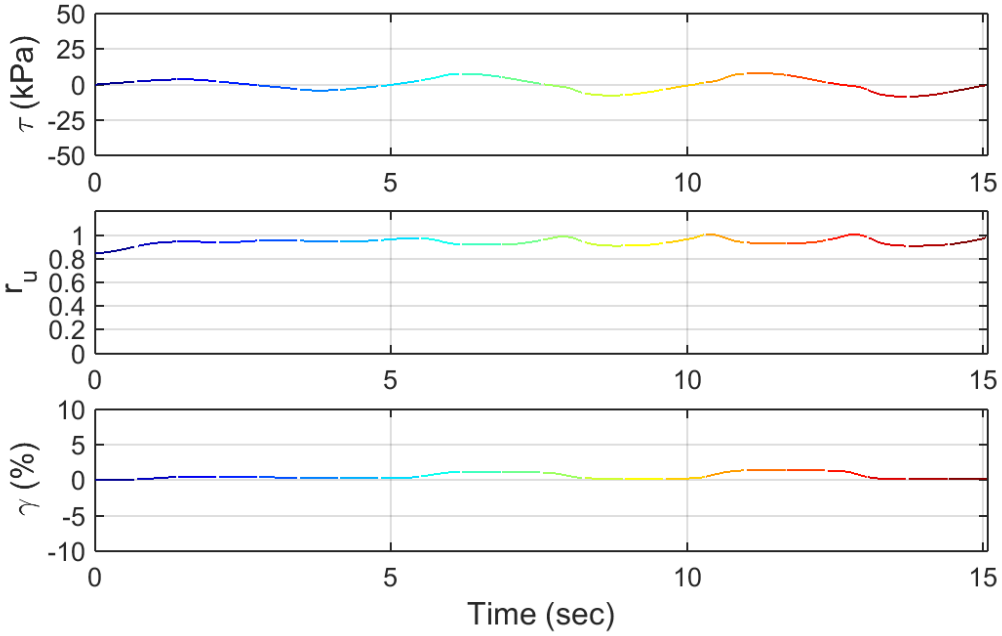

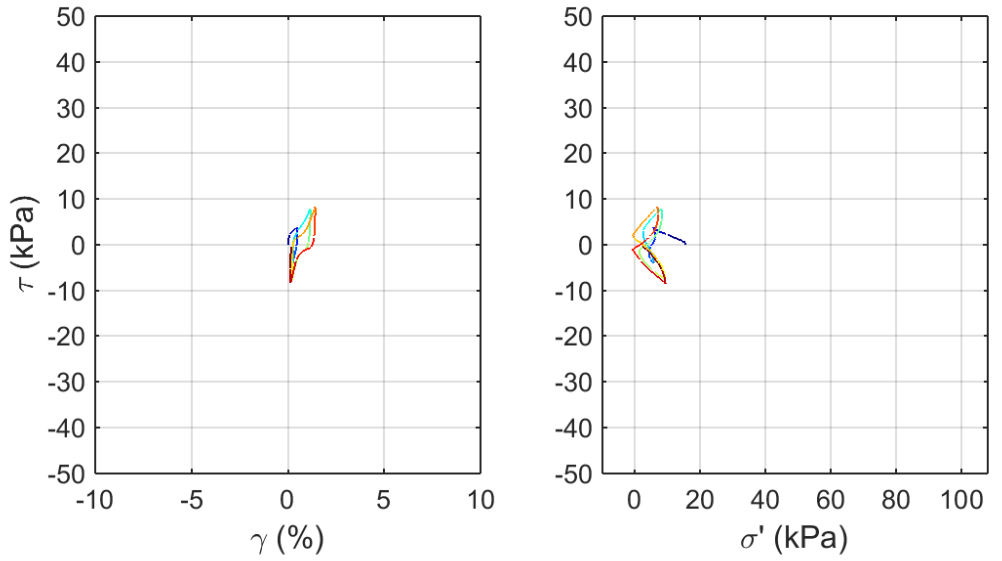

Test ID: 2013080702S2
Nevada Sand
D_r = 88 %
Motion: Taper-up

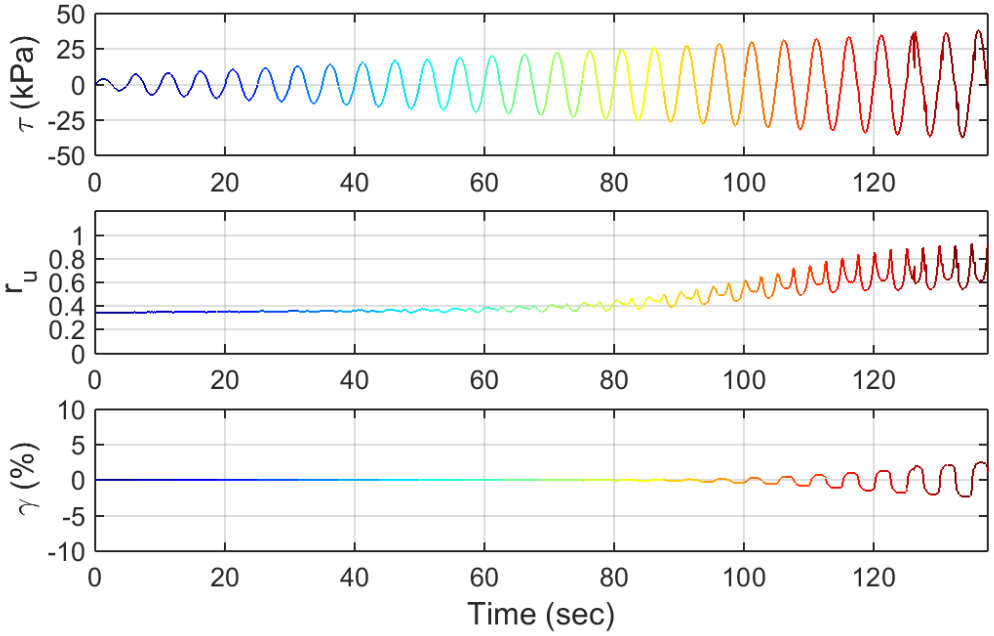

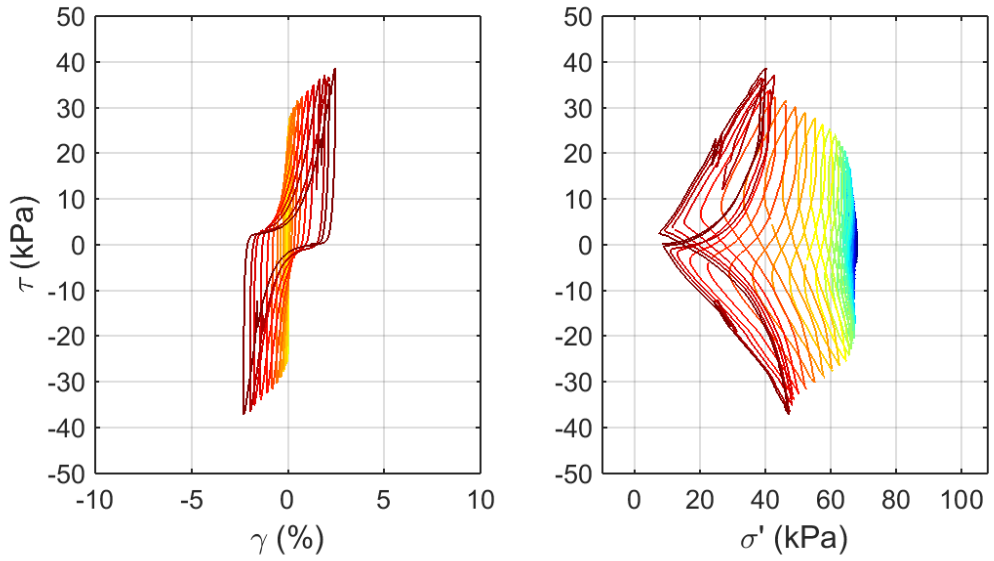

Test ID: 20130809S2
Nevada Sand
D_r = 90 %
Motion: Taper-up

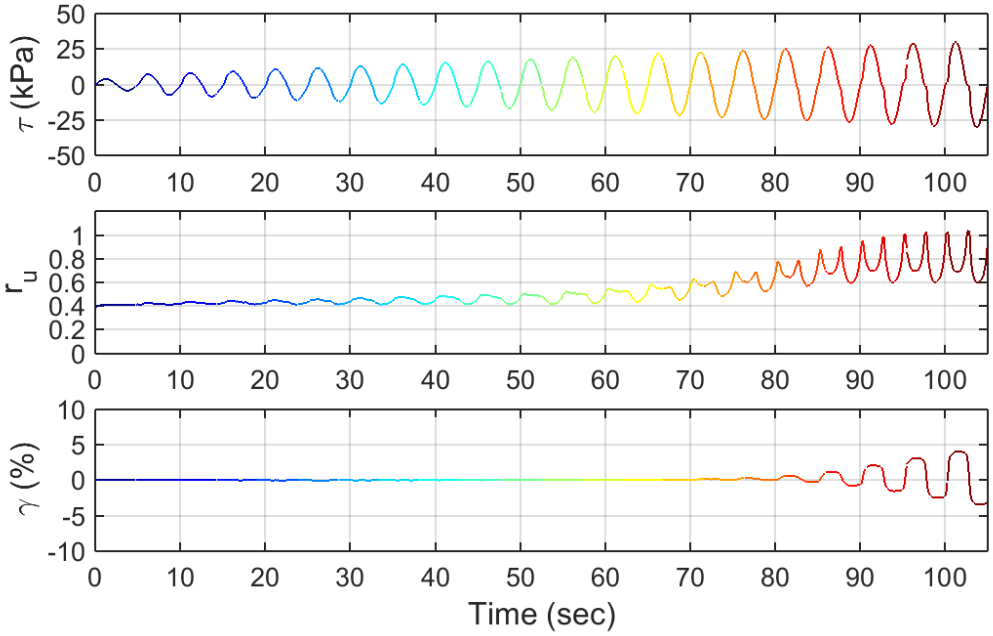

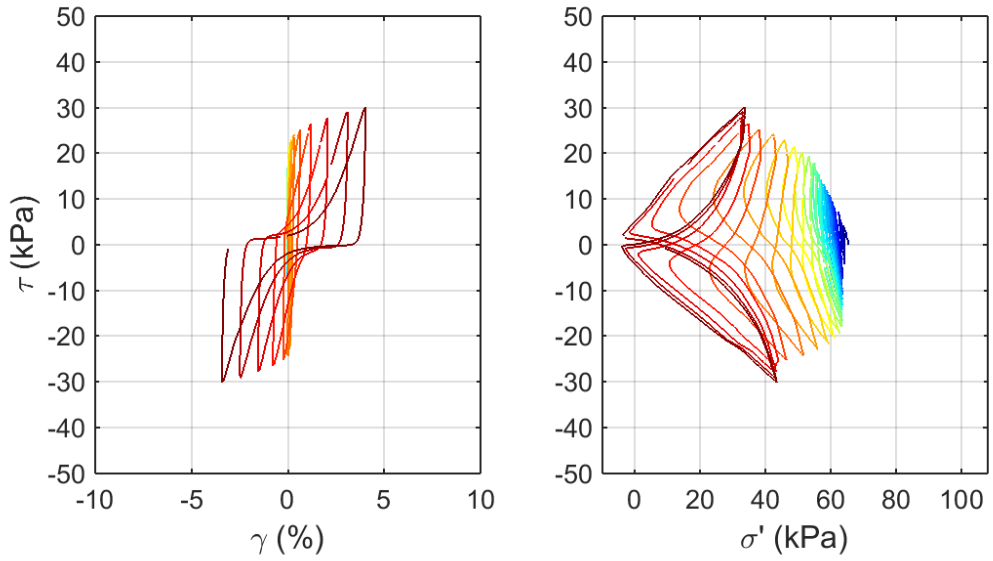

Test ID: 20130819S2
Nevada Sand
D_r = 70 %
Motion: Taper-up

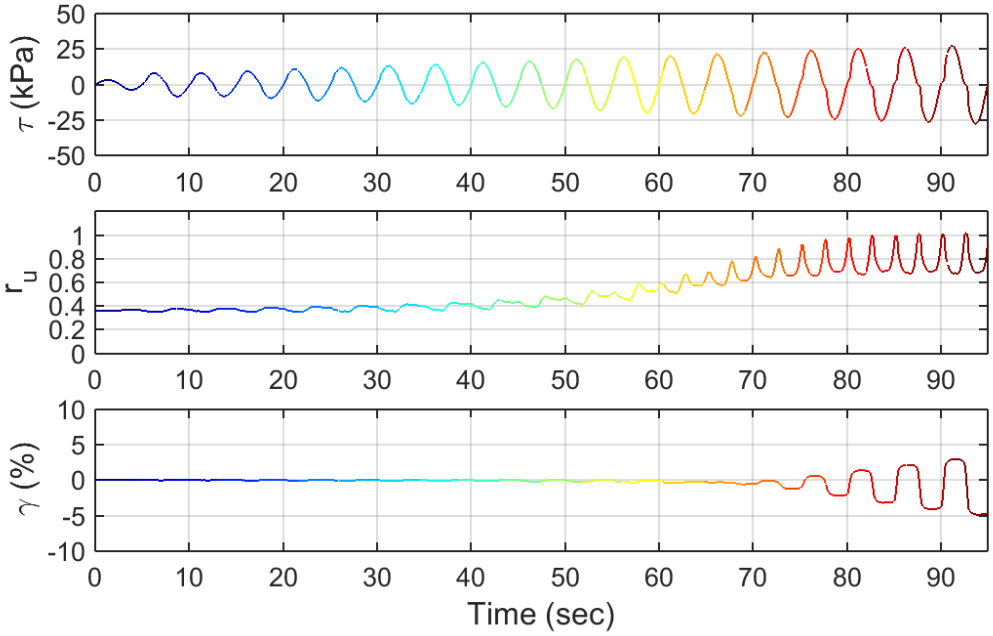

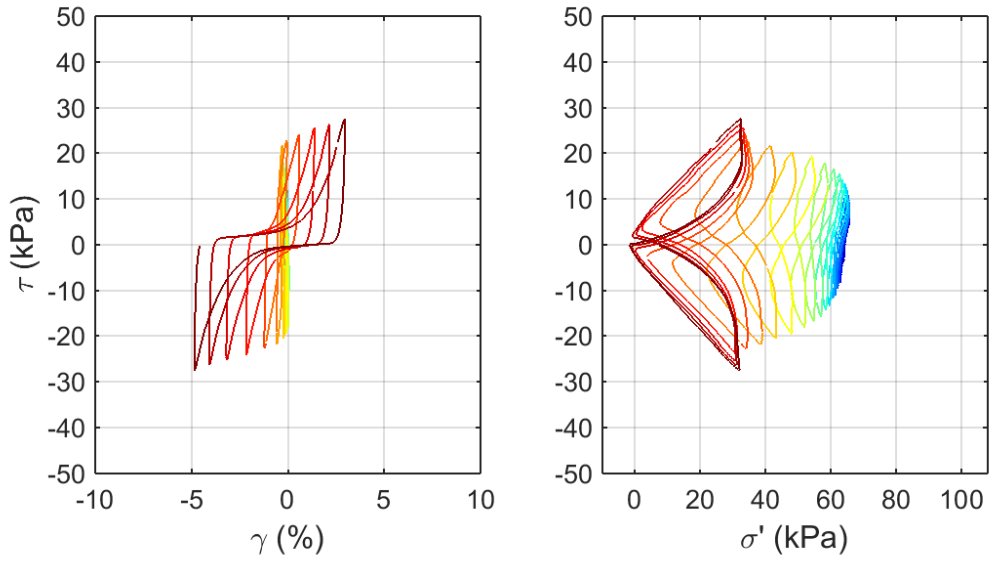

Test ID: 20130822S2
Nevada Sand
D_r = 78 %
Motion: Taper-up

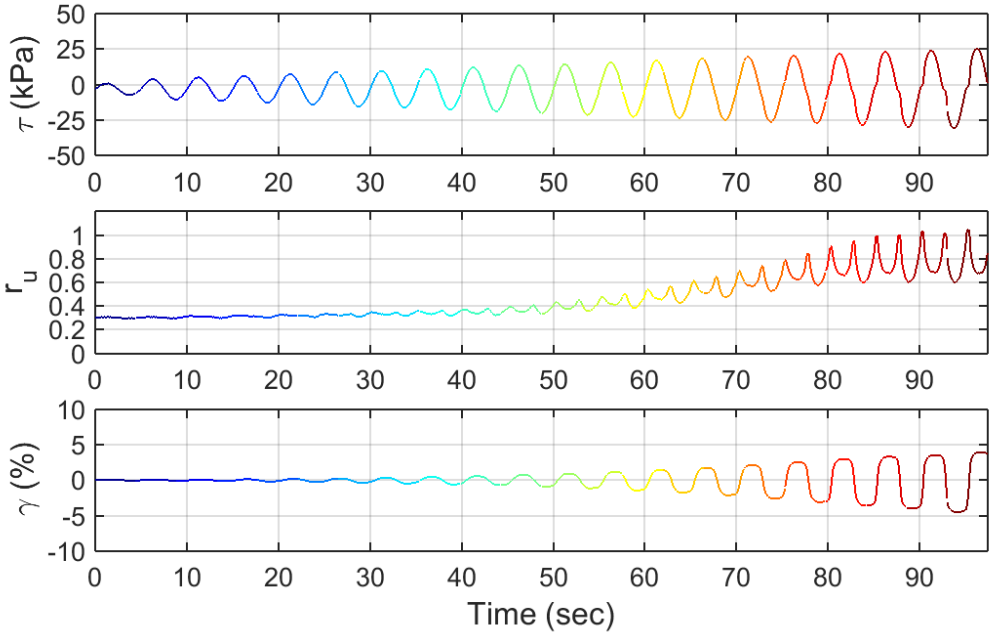

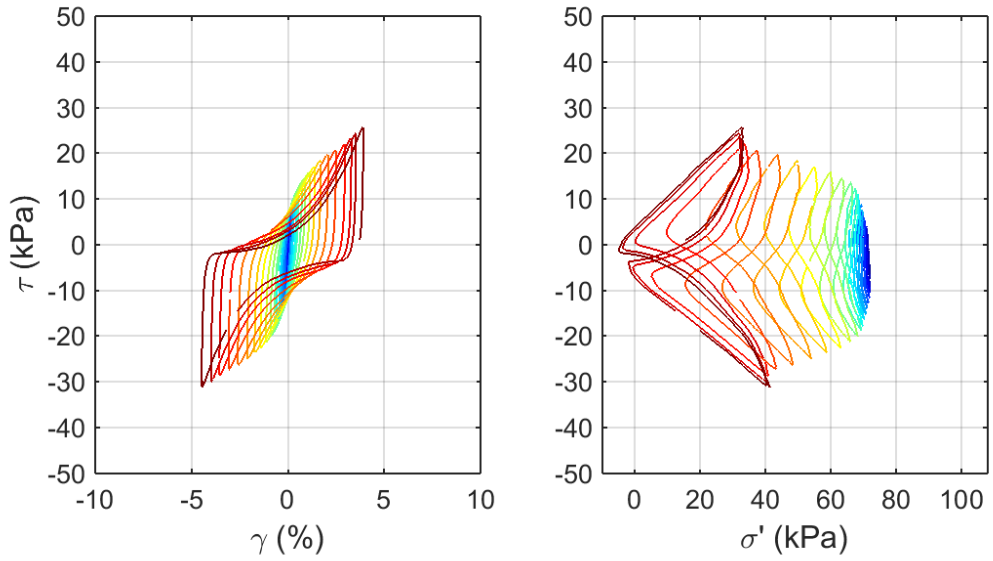

Test ID: 20130904S2
Nevada Sand
D_r = 83 %
Motion: Taper-up

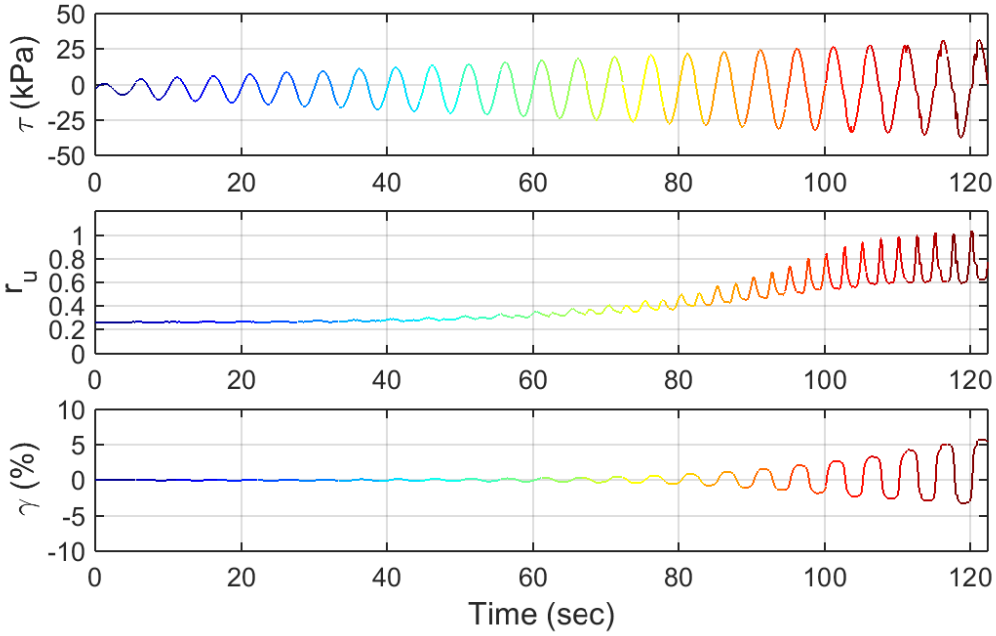

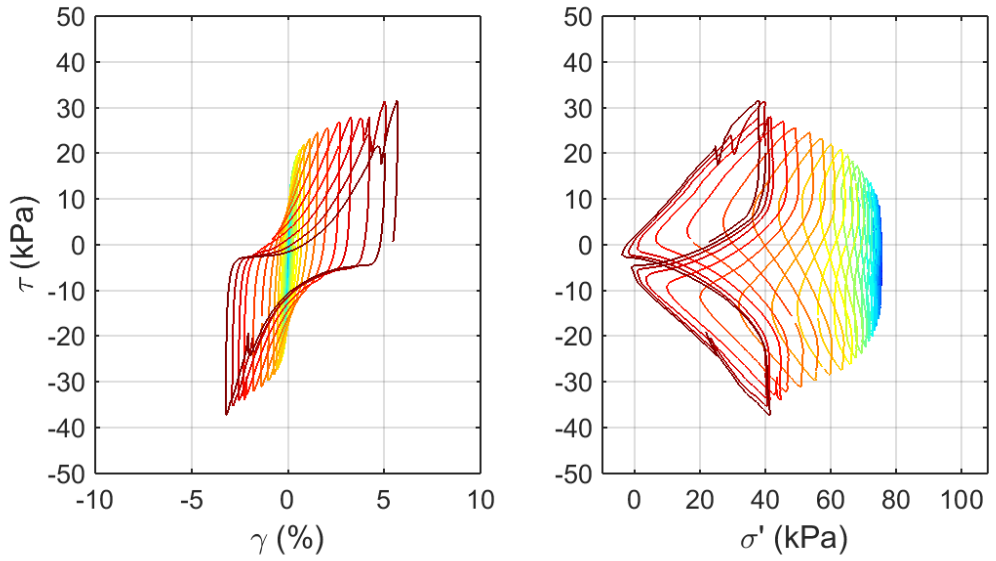

Test ID: 20130905S2
Nevada Sand
D_r = 91 %
Motion: Taper-up

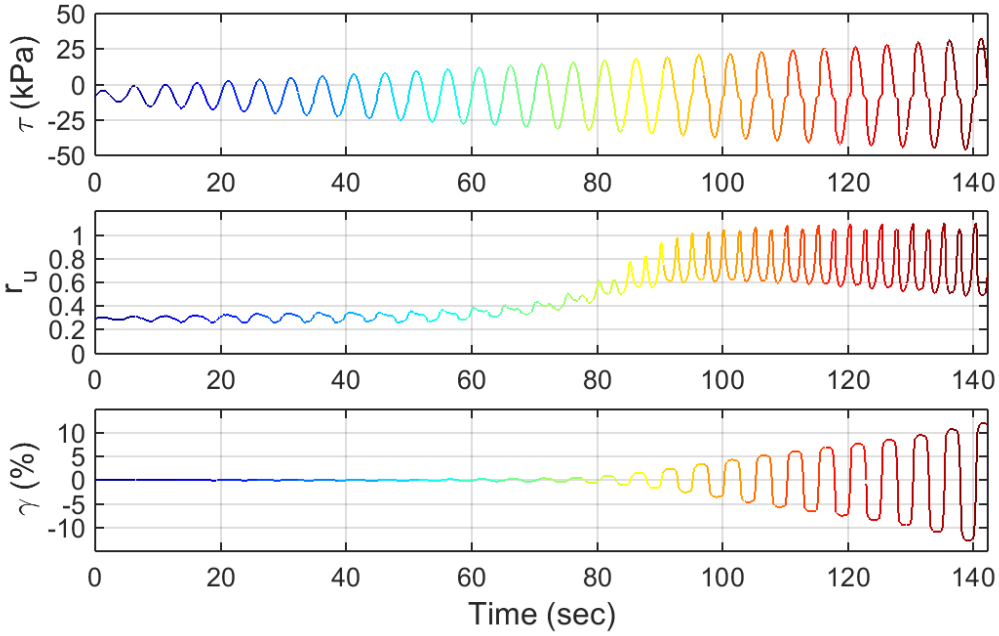

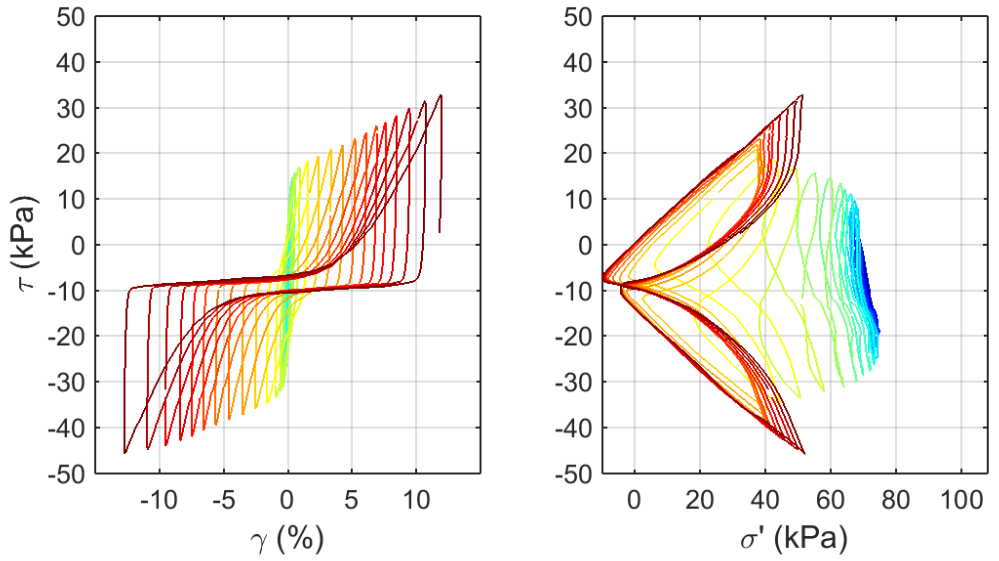

Test ID: 20131024S2
Nevada Sand
D_r = 76 %
Motion: Taper-up

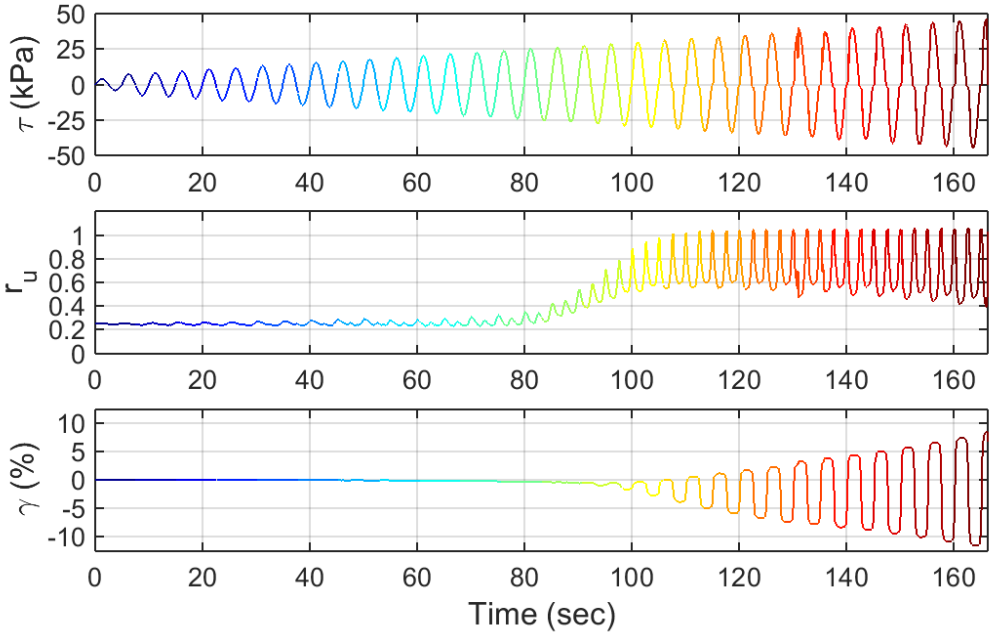

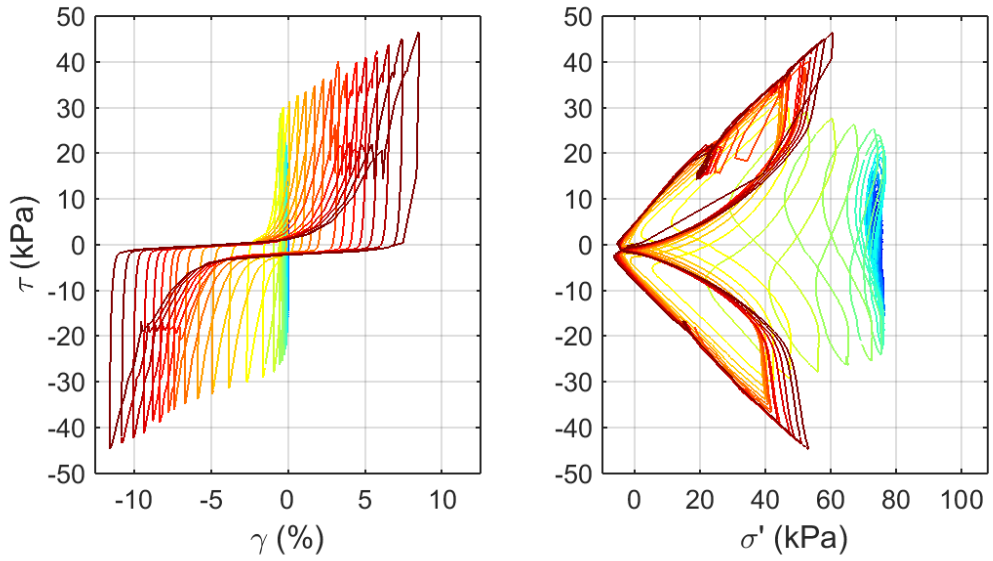

Test ID: 20131104S2
Nevada Sand
D_r = 80 %
Motion: Taper-up

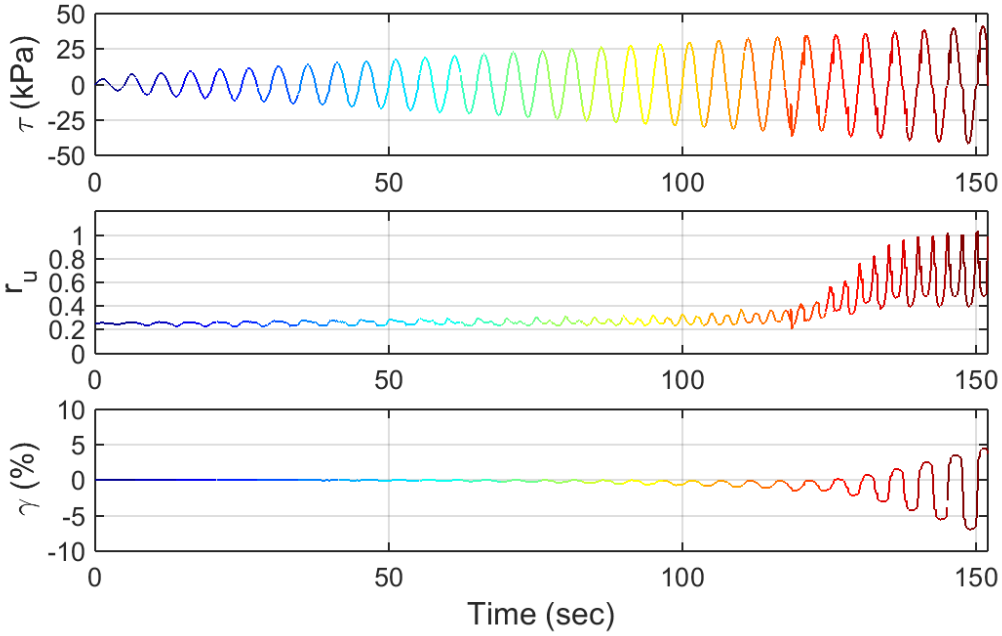

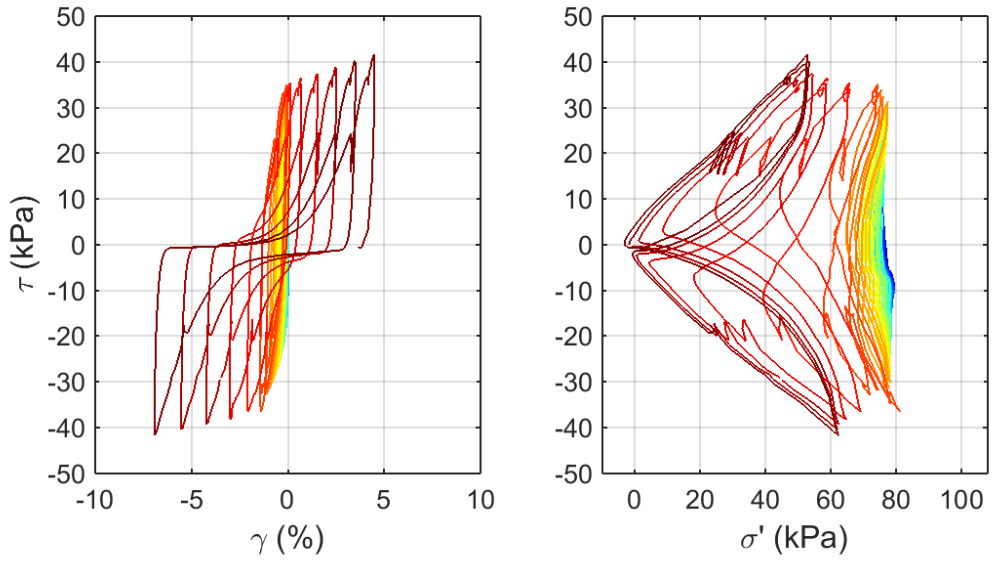

Test ID: 20131105S2
Nevada Sand
D_r = 73 %
Motion: Taper-up

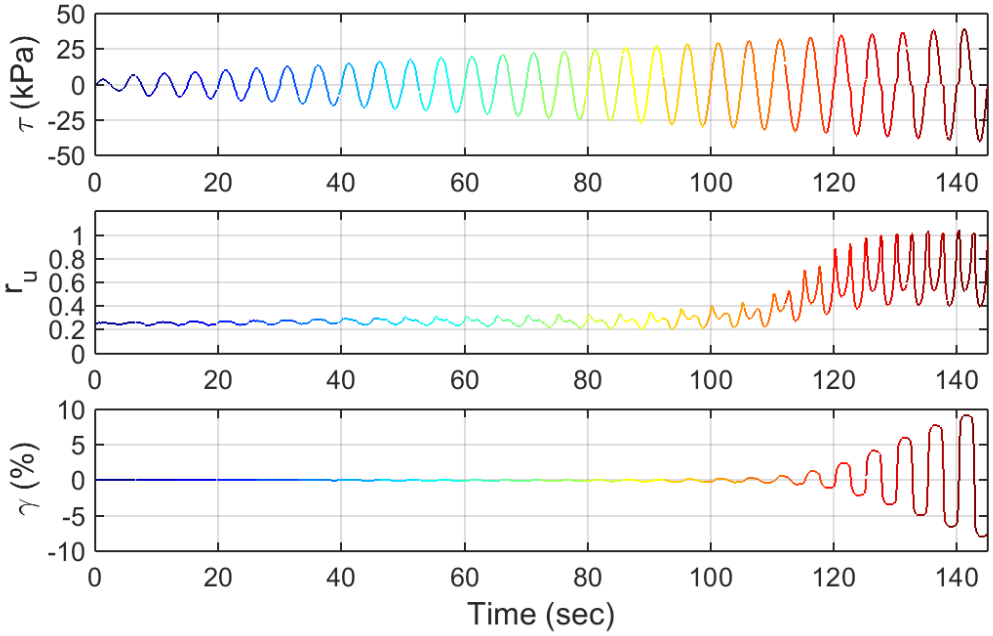

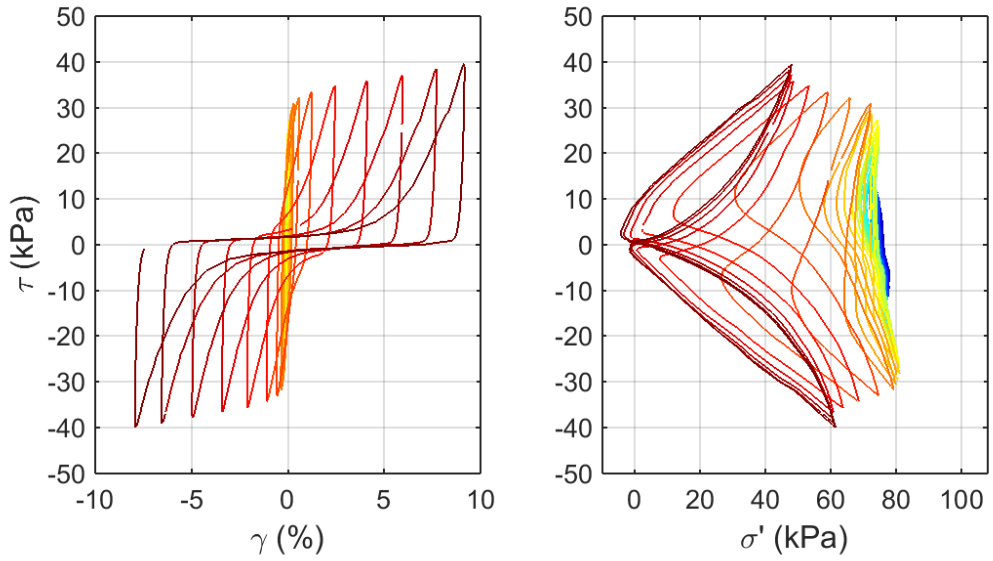

Test ID: 2013110603S2
Nevada Sand
D_r = 73 %
Motion: Taper-up

APPENDIX A.7. PRELIMINARY CSS DATA: POST-LIQUEFACTION MONOTONIC LOADING

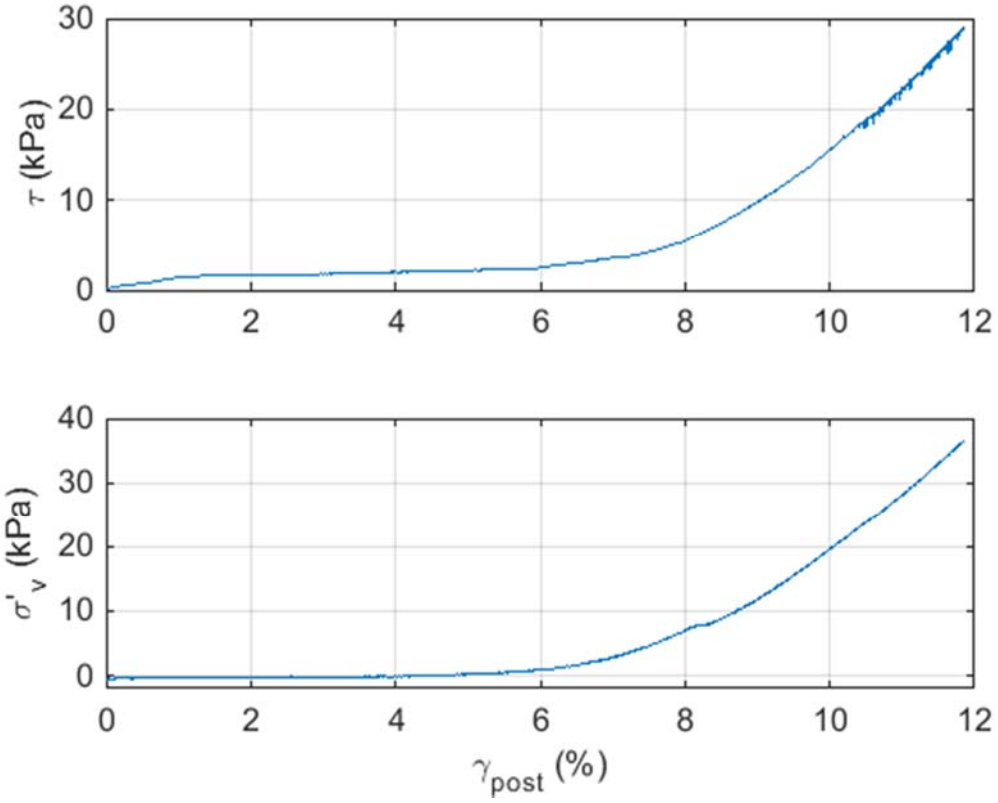

Test ID: 20130813P
Nevada Sand
D_r = 86 %
σ'_{vo} = 100kPa
Loading: Post-liquefaction Monotonic
Pre-liquefaction Loading: Modulated Taper Down (ID: 20130813)

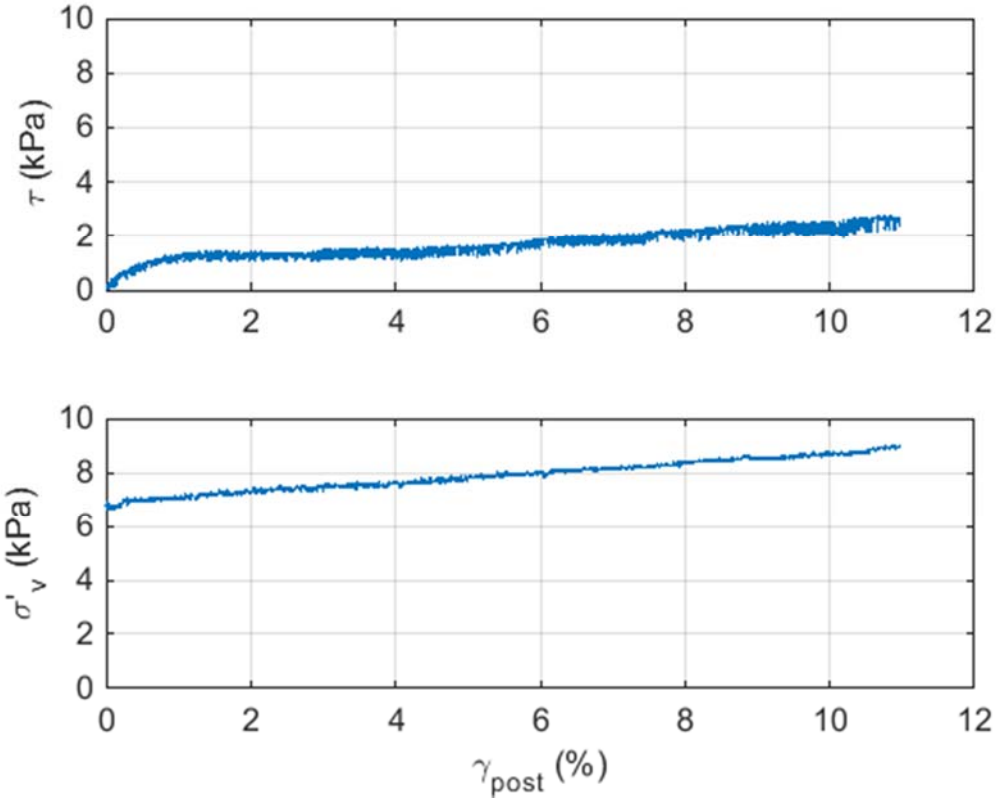

Test ID: 20130815P
Nevada Sand
D_r = 49 %
σ'_{vo} = 50kPa
Loading: Post-liquefaction Monotonic
Pre-liquefaction Loading: Harmonic Loading, CSR = 0.145

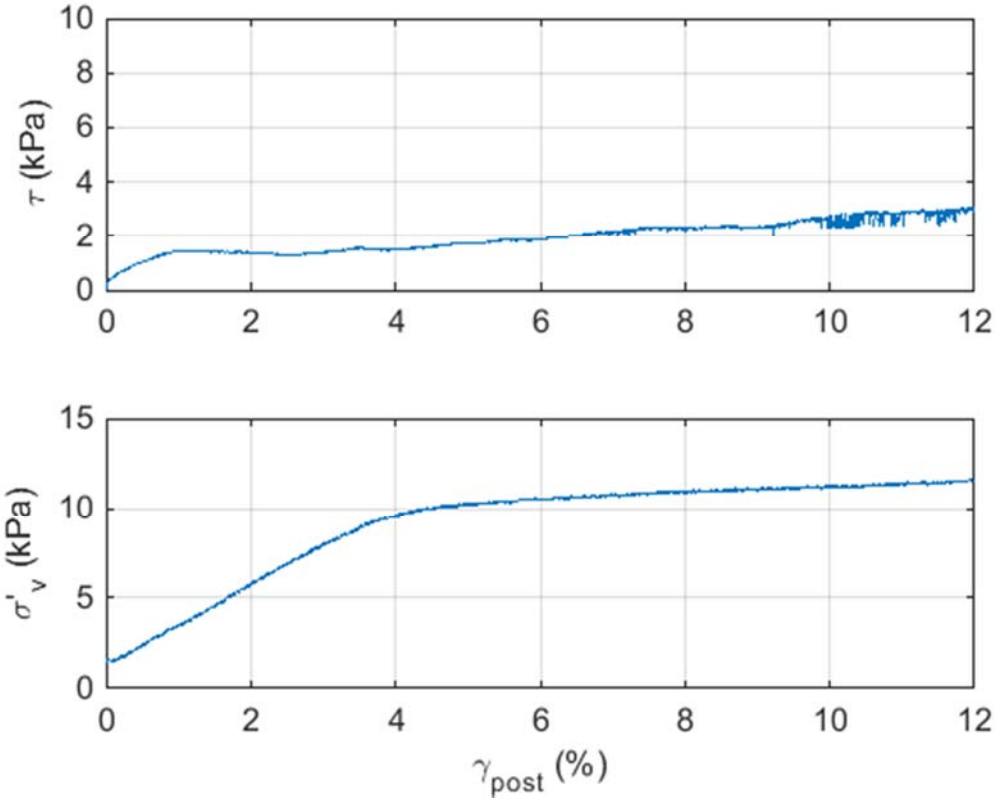

Test ID: 20130816P
Nevada Sand
D_r = 43 %
σ'_{vo} = 50kPa
Loading: Post-liquefaction Monotonic
Pre-liquefaction Loading: Harmonic Loading, CSR = 0.101

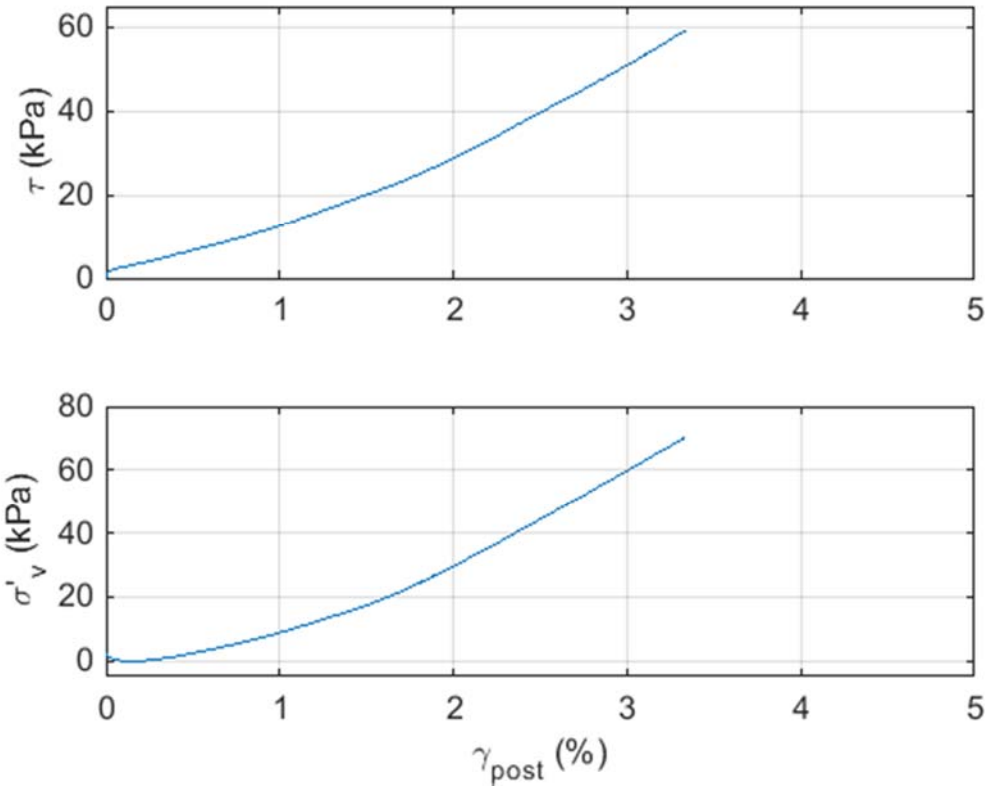

Test ID: 20130821P
Nevada Sand
D_r = 89 %
σ'_{vo} = 100kPa
Loading: Post-liquefaction Monotonic
Pre-liquefaction Loading: Transient (ID: 20130821)

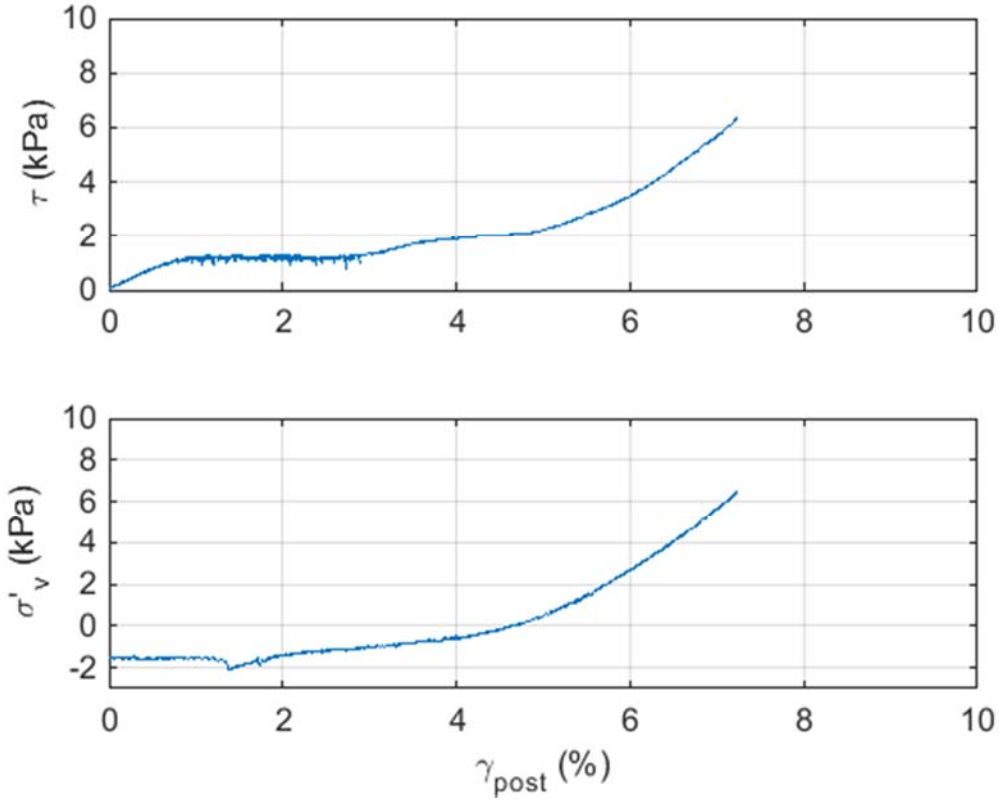

Test ID: 2013082702P
Nevada Sand
D_r = 97 %
σ'_{vo} = 100kPa
Loading: Post-liquefaction Monotonic
Pre-liquefaction Loading: Transient (ID: 20130827)

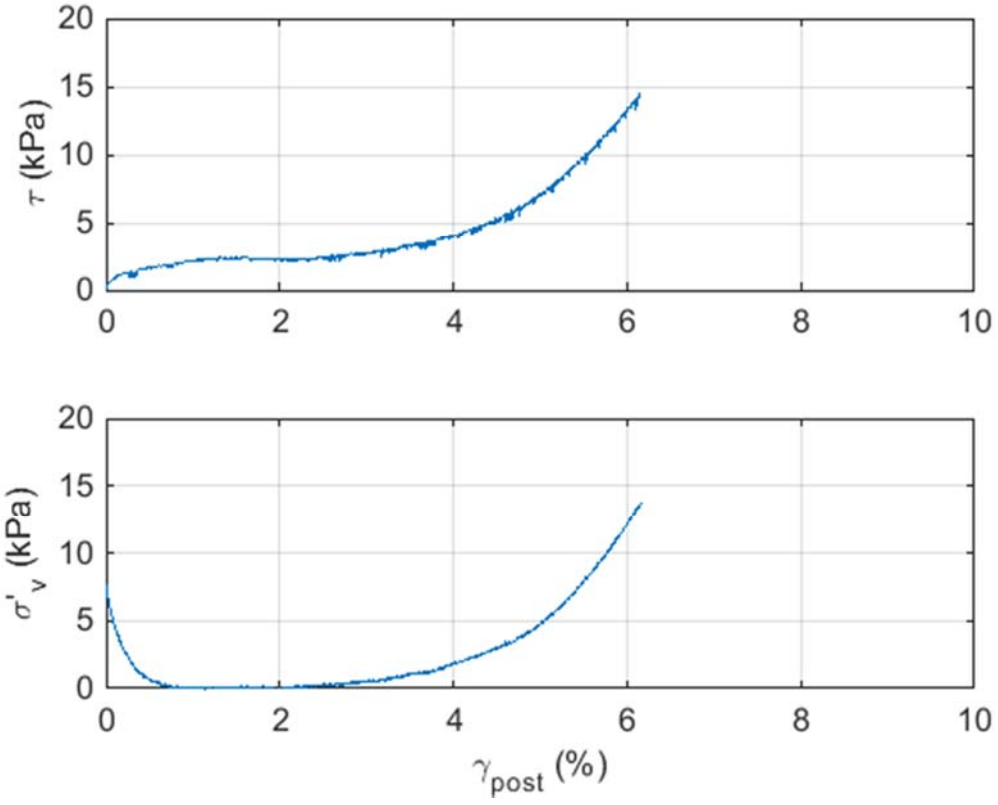

Test ID: 20130904P
Nevada Sand
D_r = 94 %
σ'_{vo} = 100kPa
Loading: Post-liquefaction Monotonic
Pre-liquefaction Loading: Transient (ID: 20130904) + Stage 2 Taper Up (ID:20130904S2)

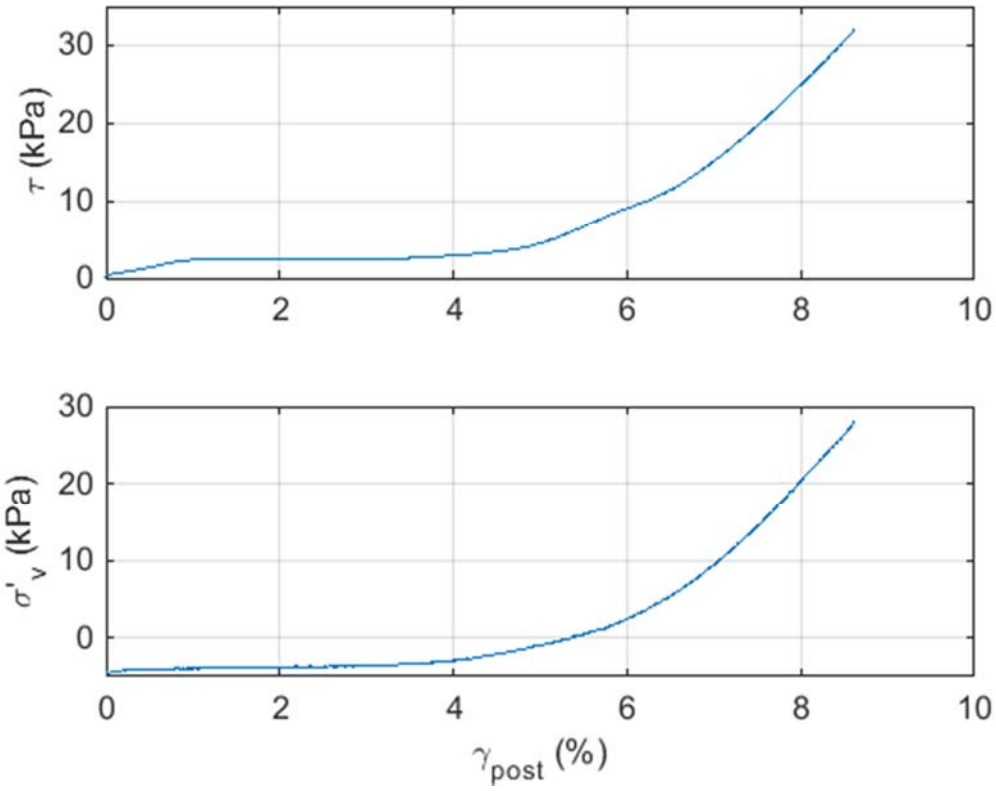

Test ID: 20130919P
Nevada Sand
D_r = 62 %
σ'_{vo} = 100kPa
Loading: Post-liquefaction Monotonic
Pre-liquefaction Loading: Transient (ID: 20130919) + Stage 2 Taper Up (ID:20130919S2)

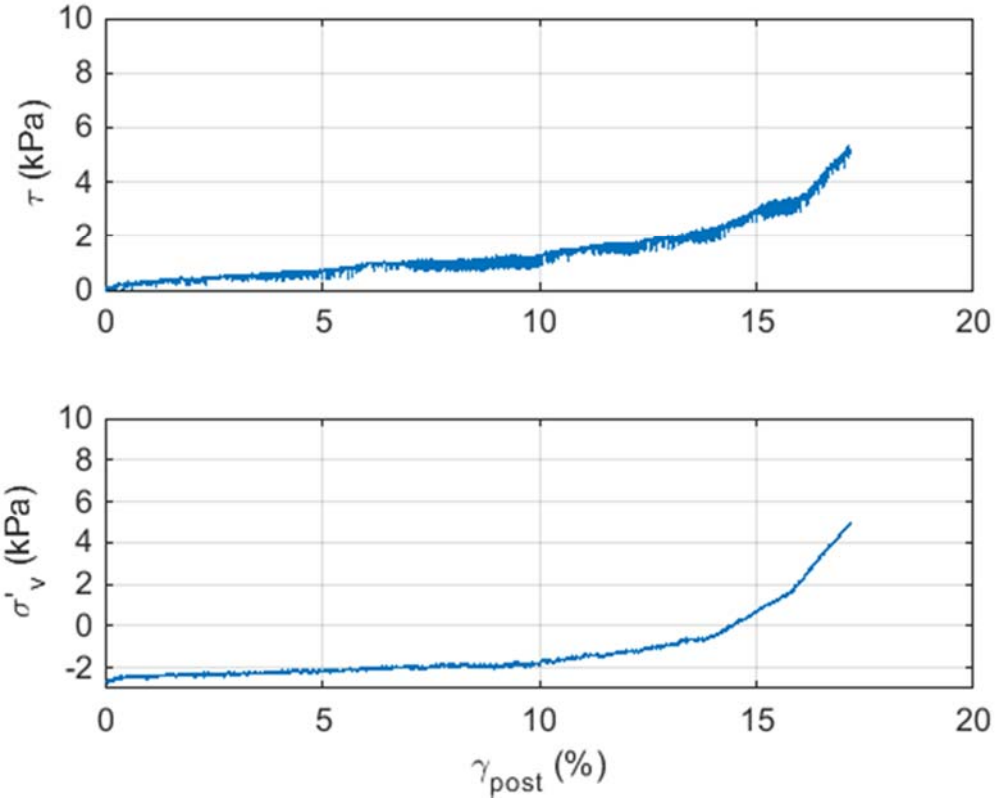

Test ID: 20131001P
Nevada Sand
D_r = 65 %
σ'_{vo} = 100kPa
Loading: Post-liquefaction Monotonic
Pre-liquefaction Loading: Transient (ID: 20131001)

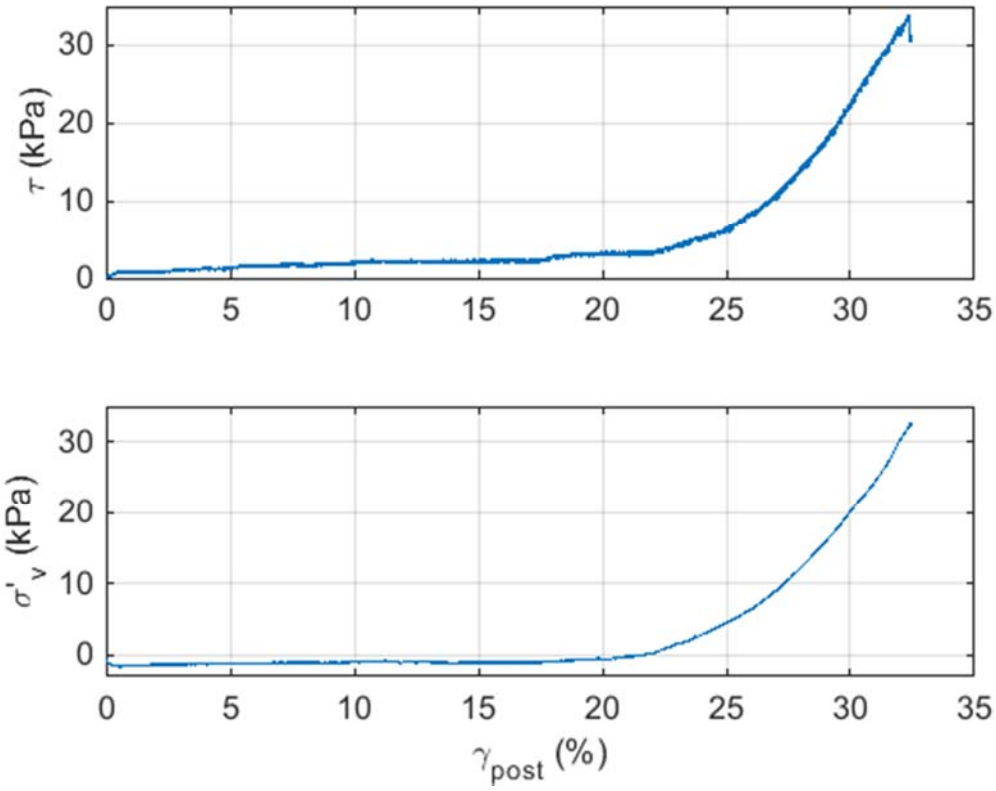

Test ID: 20131007P
Nevada Sand
D_r = 91 %
σ'_{vo} = 100kPa
Loading: Post-liquefaction Monotonic
Pre-liquefaction Loading: Transient (ID: 20131007)

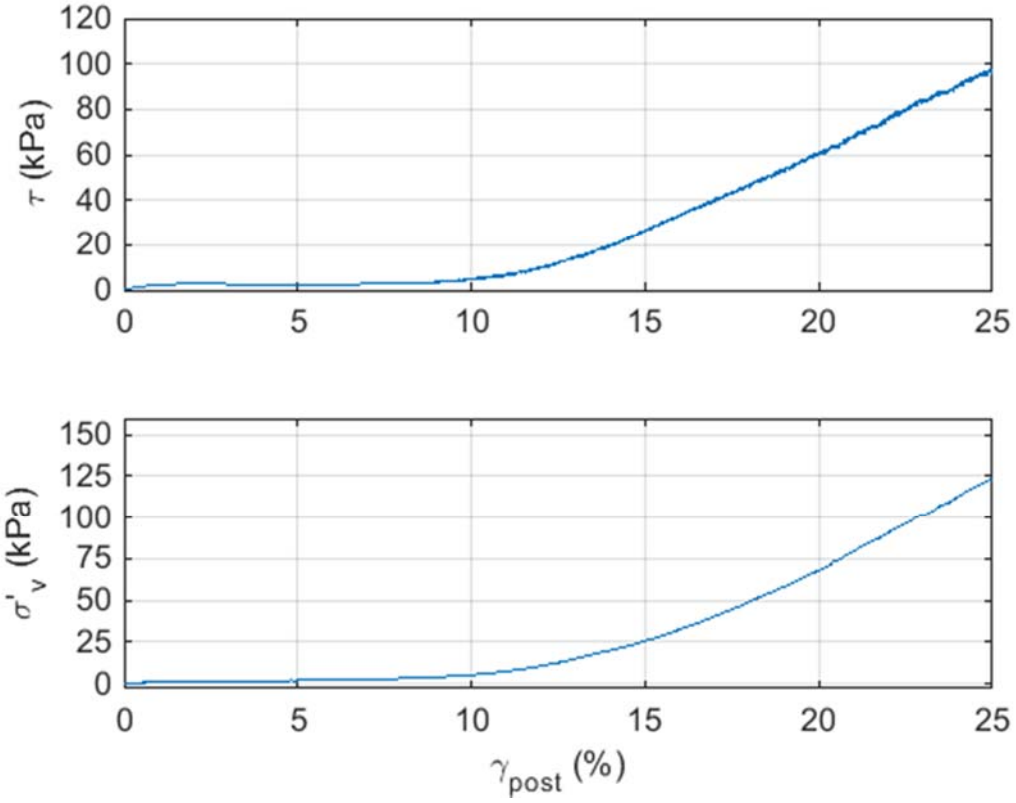

Test ID: 20131008P
Nevada Sand
D_r = 83 %
σ'_{vo} = 100kPa
Loading: Post-liquefaction Monotonic
Pre-liquefaction Loading: Transient (ID: 20131008)

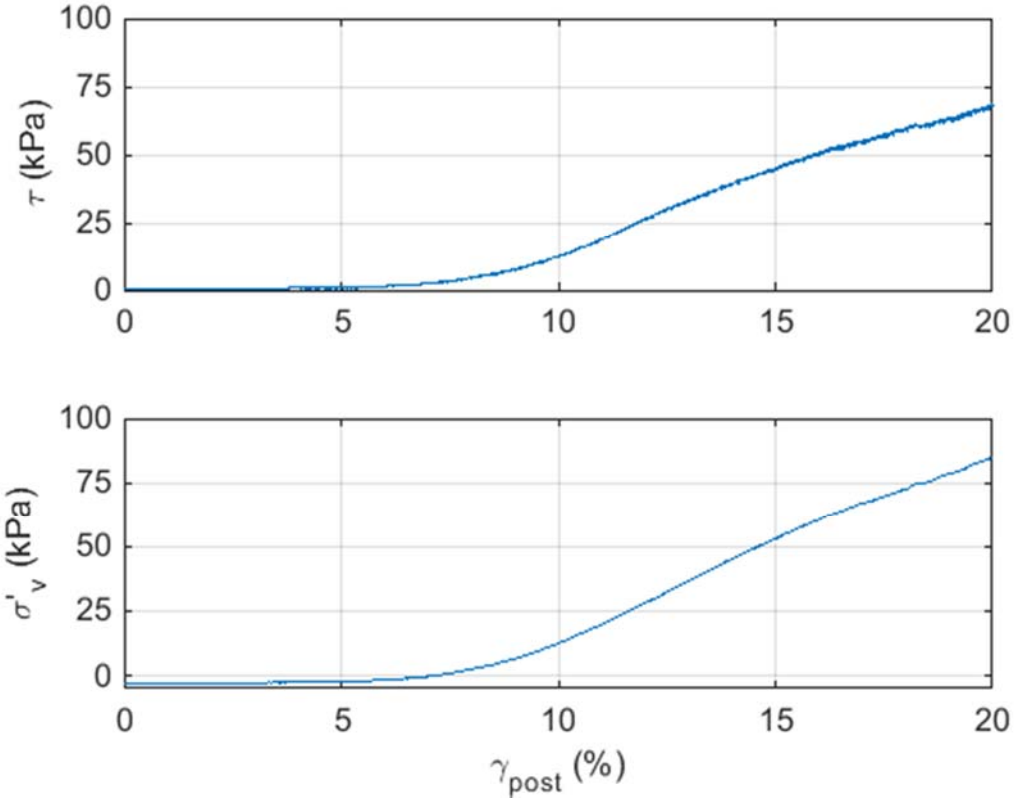

Test ID: 20131024P
Nevada Sand
D_r = 90 %
σ'_{vo} = 100kPa
Loading: Post-liquefaction Monotonic
Pre-liquefaction Loading: Transient (ID: 20131024) + Stage 2 Taper Up (ID:20131024S2)

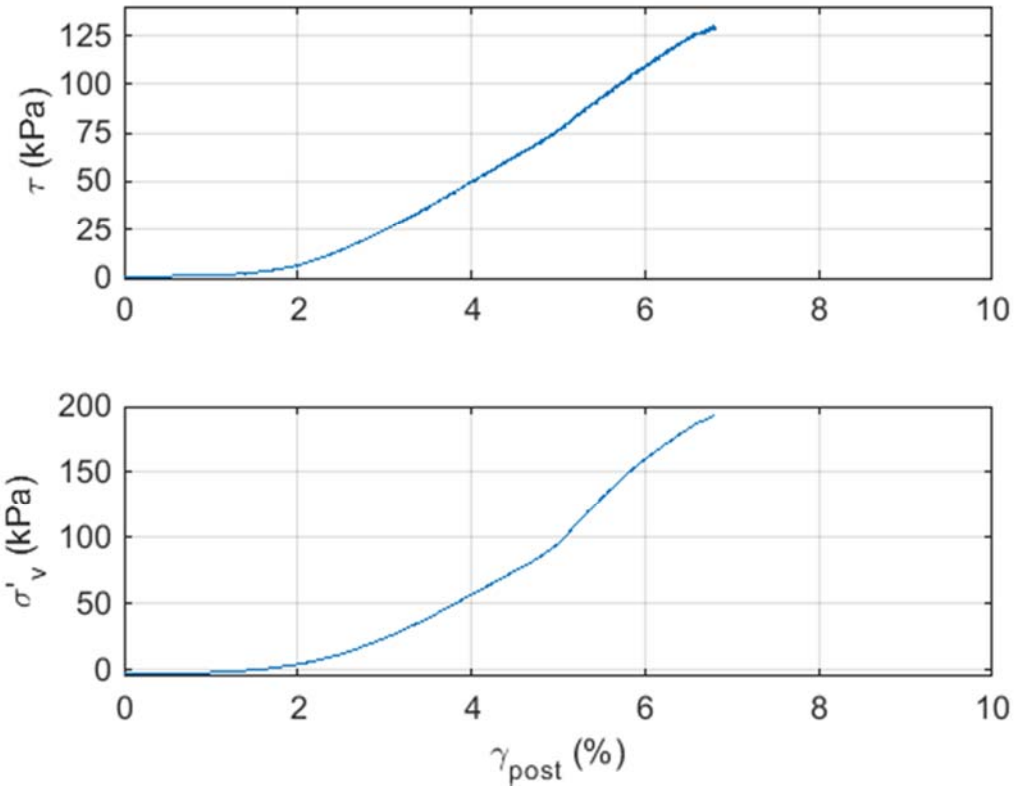

Test ID: 20131104P
Nevada Sand
D_r = 97 %
σ'_{vo} = 100kPa
Loading: Post-liquefaction Monotonic
Pre-liquefaction Loading: Transient (ID: 20131104) + Stage 2 Taper Up (ID:20131104S2)

Appendix B

UTCSS Soil Specimen Preparation Procedures

Wet Pluviation Procedure for UTCSS (both loose and dense specimens)

1. Boil the top and bottom platens for 45 minutes
2. Measure the desired amount of soil for the testing and put it in the flask. For preparing a loose specimen, place all the designated soil in one flask. For preparing a dense specimen, place the designated amount of soil into two flask (half and half).
3. Boil the soil for at least ½ hour
4. Fill the bottom of the cell with paper towels to try and absorb water that is spilled out of the specimen during preparations. Also put rags on top of the paper towels and rails to keep them dry
5. Keep the platens submerged in water and get the 2 bottom small drain lines and saturate them with water from the water panel.
6. Let some water flow out of the drain lines and connect the drain lines to the bottom platen under water
7. Secure the bottom platen on the shaking table using four screws.
8. Remove water from the sides of the bottom platen and apply vacuum grease to the sides of the platen, smoothing it around the surface
9. Fasten the membranes on the bottom platen with a large O-ring
10. Use an O-ring stretcher to secure the large O-ring to the grove of the bottom platen so as not to move the membrane
11. Connect the water line to the water panel to fill up the water panel, making sure the water line is saturated
12. Open the water line, and allow water to saturate membrane and fill up to about ½ inch height.
13. Remove any air bubbles between the membrane and the bottom platen using a small wrench or thin metal rod
14. Place O-rings at the base of the stacked ring base on the top edge (which is the edge with the groove)
15. Put the stacked rings on top of the bottom platen
16. Put hydraulic oil between the stacked rings to reduce shearing friction, making sure to apply with a clean finger.

17. Make sure the stacked rings are clean and free of sand particle, minimizing the effects of friction
18. Put oil on the inside of the rings and outside of the membranes to minimize friction during consolidation
19. Place the split mold (Figures 3.15 and 3.16) on top of the stacked rings, so that all rings are covered
20. Connect the vacuum line to the split mold
21. Wrap the membrane around the top edge of the split mold making sure the vacuum causes the membrane to stay touching the rings, creating a seal between the membranes and rings
22. Mark on the membrane one inch height from the bottom of the platen. This should be approximately the height of the stacked rings. This line represents the future height of the specimen
23. (For loose specimen construction only) Submerge the pluviation screen (Figure 3.23); place it on the top of the base platen, and try to remove air bubbles while submerged (vibration may help)
24. Fill up the inside of the membrane with water through the drainage from the bottom platen, bringing up the water to the edge of the split mold
25. Turn on the hydraulic pump using the GCTS software. Make sure the Shear LVDT reading is zero
26. When the water is at the rim of the split mold, make sure to fill up the water panel fully.
27. Disconnect the top drain water line that was connected the deaerator to the water panel
28. Connect the top drain line of the water panel to the CSS apparatus making sure the water line is saturated
29. Fill the saturated soil flask(s) with de-aired water to the rim (after being cool down)
30. Place a rubber stopper (a strip of membrane) on top of the flask to assure there is no air in the flask

The following steps are for creating loose specimens:

31. Invert the flask and insert into the saturated split mold making sure no air gets in the specimen
32. Remove the rubber stopper
33. Siphon the soil under water with a zero drop height to ensure a low density. Do this until all the soil has left the flask

34. Place the rubber stopper on the rim of the flask under the water. Remove the flask from the split mold making sure no air enters the sample
35. Lift up the screen very slowly to let the soil particles rain through the screen
36. Weigh the remaining soil on the screen to correct density readings

The following steps are for creating dense specimens:

31. Invert the first flask and insert into the saturated split mold making sure no air gets in the specimen
32. Remove the rubber stopper
33. Siphon the soil under water. Do this until all the soil has left the first flask
34. Place the custom made plastic plate (Figure 3.25) on the sand surface. Invert a small vibratory table and attached it to the tip of the metal thread of the plate. Apply the vibration until on further sand and water to come out from the predrilled holes.
35. Remove the plastic plate and weight the drained sand (after oven dry) to correct density readings
36. Repeat steps 31 to 35 for constructing second lift of dense specimen
37. Put the split rag around the split mold
38. Cover the specimen with a metal plate
39. Put on the X-bar
40. Put on the top cap of the CSS apparatus
41. Secure the top cap with 4 screws/nuts
42. Tighten the nuts loosely and make sure that the shear load is about zero. By tightening different nuts the shear load becomes more positive or negative
43. Place the rod through the x-bar
44. Secure the x-bar (tighten the screw) at the top position
45. Add on aluminum block to the bottom of the rod
46. Secure the rod by fastening the key screw on the top cap
47. Put 1 thick o-ring and 5 small o-rings on top of the submerged top platen
48. Connect a saturated water line from the apparatus to the top platen, making sure the connection is made under water
49. Place the top platen on the metal plate that is posited on the spilt mold
50. Lower the rod and connect the top platen with the rod and assemble
51. Apply vacuum grease to the outside of the top platen
52. Open the top drain such that water to move through the top platen and dripping out from the porous stone. Let the water drip until the porous stone is shiny on its surface, or water can be seen dripping a little bit

53. Remove the metal plate, making sure no water from the top platen splashes into the sample
54. Lower the top platen very slowly until there is a slight feeling of touching the sand surface, allowing water to spill out over the split mold
55. Remove the split rags.
56. Take measurements if the height of the specimen and platens to determine the density
57. Turn the top platen to the proper location for installation of the x-bar
58. Install the vertical load cell. The weight of the loading cell will help for better soil contact with the top platen
59. Wrap the membranes up and seal them with 2 small o-rings on the top of the split mold
60. Apply a small (10 kPa) vacuum to the top of the specimens. The pore pressure should be about -10kPa.
61. Remove the vacuum from the split mold and disassemble the split mold and remove it
62. Use the o-ring stretcher to install 1 large o-ring to the top platen. Move 5 small o-rings over the membrane making sure not to fold the membrane.
63. Bend the membrane back over the o-rings seal.
64. Remove all rags and paper towels
65. Install the L bar to the top platen by screwing in 2 bolts
66. Install the hose clamp the thin o-rings on the top platen and tighten it
67. Take the final height measurements at the 4 corners of the specimen
68. Lower the aluminum block and x-bar so they are sitting on top of the top platen
69. Align the aluminum block so it is in line with the shear motion
70. Tighten the x-bar so it cannot move up and down (keep an eye on the shear load, which should be maintain around zero reading).
71. Install the internal vertical LVDT and tighten
72. Install the internal horizontal LVDT and tighten
73. Adjust those internal LVDTs to be at zero positions
74. Lock the nuts at the top platen and remove the vertical load cell
75. Put the outer shell for the apparatus on
76. Put the top cap on the apparatus and secure the screws while watching the shear load to make sure it is balanced
77. Tighten the bar some if needed
78. Place the axial load cell back on the rod
79. Tighten the top cap again as needed
80. Connect the internal vertical LVDT cable and the axial load cable

81. Lower the loading frame until there is at least 3 mm between the vertical air piston and the axial load cell
82. Open the pressure valve
83. Increase the cell pressure to 15 kPa and corresponding axial load while also disconnecting the vacuum
84. Start back pressuring

Reference

Abegg, S. (2010). "Identification of Optimal Evolutionary Intensity Measures for Evaluation of Liquefaction Hazard." Master Thesis, University of Washington.

Ambraseys, N. N. (1988). "Engineering seismology." *Earthquake Eng. Struct. Dyn.*, 17(1), 1-105.

Amer, M. I., Kovacs, W. D., and Aggour, M. S. (1987). "Cyclic Simple Shear Size Effects." Journal of Geotechnical Engineering, 113(7), 693-707.

Andrus, R. D., and Stokoe II, K. H. (1997). "Liquefaction resistance based on shear wave velocity,." *Proceedings, NCEER Workshop on Evaluation of Liquefaction Resistance of Soils*, National Center for Earthquake Engineering Research, State University of New York at Buffalo, pp. 89–128.

Andrus, R. D., and Stokoe II, K. H. (2000). "Liquefaction resistance of soils from shear-wave velocity." *J. Geotech. Geoenviron. Eng.*, 126(11), 1015-1025.

Andrus, R. D., Hayati, H., and Mohanan, N. P. (2009). "Correcting Liquefaction Resistance for Aged Sands Using Measured to Estimated Velocity Ratio." *J. Geotech. Geoenviron. Eng.*, 135(6), 735-744.

Arango, I. (1996). "Magnitude scaling factors for soil liquefaction evaluations." *J. Geotech. Eng.*, 122(11), 929-936.

Arulmoli, K., Muraleetharan, K. K., Hossain, M. M., and Fruth, L. S. (1992). "VELACS: verification of liquefaction analyses by centrifuge studies, laboratory testing program, soil data report." Project no. 90-0562 Earth Technology Corp, Irvine, CA, USA.

ASTM D4253-00 (2006). “Standard test methods for maximum index density and unit weight of soils using a vibratory table,” American society for testing and materials, Philadelphia, PA.

ASTM D4254-00 (2006). “Standard test methods minimum index density and unit weight of soils and calculation of relative density,” American society for testing and materials, Philadelphia, PA.

Bartlett, S. F., and Youd, T. L. (1995). "Empirical Prediction of Liquefaction-Induced Lateral Spread." *Journal of Geotechnical Engineering*, 121(4), 316-329.

Baxter, B., Ochoa-Lavergne, and Hankour, R. (2010). "DSS Test Results Using Wire-Reinforced Membranes and Stacked Rings." *GeoFlorida 2010: Advances in Analysis, Modeling & DesignFlorida*, 600-607.

Beaty, M., and Byrne, P. (2011). "UBCSAND constitutive model: Version 904aR." *Documentation Report: UBCSAND Constitutive Model on Itasca* UDM Web Site.

Bjerrum, L., and Landva, A. (1966). "Direct simple-shear tests on a Norwegian quick clay." *Géotechnique*, 16(1), 1-20.

Byrne, P. M. (1991). "A cyclic Shear-Volume Coupling and Pore Pressure Model for Sand Proceeding." *Second International Conference on Recent Advances in Geotechnical Earthquake Engineering and Soil Dynamics,* St. Louis, Missouri, 47-55.

Boulanger, R. W., Seed, R. B., Chan, C. K., Seed, H. B., and Sousa, J. B. (1991). "Liquefaction Behavior of Saturated Sands under Uni-directional and Bi-directional Monotonic and Cyclic Simple Shear Loading."

Boulanger, R. W., Chan, C. K., Seed, H. B., Seed, R. B., and Sousa, J. B. (1993). "A Low-Compliance Bi-Directional Cyclic Simple Shear Apparatus." *Geotechnical Testing Journal*, 16(1), 36-45.

Boulanger, R. W., and Idriss, I. M. (2004). "Evaluating the Potential for Liquefaction or Cyclic Failure of Silts and Clays." *Report No. UCD/CGM-04/01*, Center for Geotechnical Modeling, Department of Civil and Environmental Engineering, University of California, Davis., 131 pp.

Boulanger, R. W., and Idriss, I. M. (2014). "CPT and SPT based liquefaction triggering procedures." *Report No. UCD/CGM-14/01* Center for Geotechnical Modeling, Department of Civil and Environmental Engineering, University of California, Davis, CA, 138 pp.

Boulanger, R. W., and Ziotopoulou, K. (2015). "PM4Sand (Version 3): A Sand Plasticity Model for Earthquake Engineering Applications." *Report No. UCD/CGM-15/01*, Center for Geotechnical Modeling, Department of Civil and Environmental Engineering, University of California, Davis, CA, 113 pp.

Casagrande, A. (1936). "Characteristics of cohesionless soils affecting the stability of slopes and earth fills." *Journal of the Boston Society of Civil Engineers*, 13-32.

Castro, G. (1969). "Liquefaction of Sands." PhD. Thesis, Harvard University, Cambridge Mass.

Cetin, K. O., and Seed, R. B. (2004). "Nonlinear shear mass participation factor (r_d) for cyclic shear stress ratio evaluation." *Soil Dynamics and Earthquake Engineering*, 24(2), 103-113.

Chern, J.-C. (1985). "Undrained response of saturated sands with emphasis on liquefaction and cyclic mobility." Ph.D. Dissertation, The University of British Columbia.

Cubrinovski, M., Bray, J. D., Taylor, M., Giorgini, S., Bradley, B., Wotherspoon, L., and Zupan, J. (2011). *Seismological Research Letters*, 82(6), 893-904.

Dafalias, Y. F., and Manzari, M. T. (2004). "Simple Plasticity Sand Model Accounting for Fabric Change Effects." *J. Eng. Mech*, 130(6), 622-634.

Dahl, K. R., DeJong, J. T., Boulanger, R. W., Pyke, R., and Wahl, D. (2014). "Characterization of an alluvial silt and clay deposit for monotonic, cyclic, and post-cyclic behavior." *Can. Geotech. J.*, 51(4), 432-440.

De Alba, P., Chan, C. K., and Seed, H. B. (1975). "Determination of Soil Liquefaction Characteristics by Large-Scale Laboratory Tests." *Report No. EERC 75-14*, Earthquake Engineering Research Center, Calif.

De Alba, P., Seed, H. B., and Chan, C. K. (1976). "Sand Liquefaction in Large-Scale Simple Shear Tests." *Journal of the Geotechnical Engineering Division* (GT9), 909-927.

Dobry, R., and Ladd, C. C. (1980). "Discuss to "Soil Liquefaction and cyclic mobility evaluation for level ground during earthquake" by H B Seed." *J. Geotech. Eng. Div. ASCE*, 106(6), 720-724.

Dobry, R., Ladd, R. S., Yokel, F. Y., Chung, R. M., and Powell, D. (1982). "Prediction of pore water pressure buildup and liquefaction of sands during earthquakes by the cyclic strain method." NBS Building Science Series 138, National Bureau of Standards, 150 pp.

Drnevich, V. P., and Richart, F. E. (1970). "Dynamic Prestraining of Dry Sand." *Journal of the Soil Mechanics and Foundations Division*, 96(SM2), 453-469.

Dyvik, R., Berre, T., and Lacasse, S. R., B. (1987). "Comparison of truly undrained and constant volume direct simple shear tests." *Géotechnique*, 37(1), 3-10.

Finn, W. D. L., and Byrne, P. M. (1976). "Seismic Response and Liquefaction of Sands." *J. geotech. Eng. div.*, 102(8), 841-856.

Finn, W. D. L. (1977). "An effective stress model for liquefaction." *Journal of Geotechnical Engineering Division, ASCE*, 103(6), 517-533.

Finn, W. D. L. (1982). "Dynamic Response Analyses of Saturated Sands." *Soil Mechanics - Transient and Cyclic Loads*, Pande, and Zienkiewicz, eds., Wiley, 105 -131.

Franke, E., Kiekbusch, M., and Schuppener, B. (1979). "A New Direct Simple Shear Device." Geotechnical Testing Journal, 2(4), 190-199.

Green, R. A. (2001). "Energy-based evaluation and remediation of liquefiable soils."PhD dissertation, Virginia Polytechnic Institute and State Univ., Blacksburg, Va.

Green, R. A., and Terri, G. A. (2005). "Number of Equivalent Cycles Concept for Liquefaction Evaluations—Revisited." *J. Geotech. Geoenviron. Eng.*, 131(4), 477-488.

Hazirbaba, K. (2005). "Pore Pressure Generation Characteristics of Sands and Silty Sands: A Strain Approach." PhD Dissertation, The University of Texas at Austin.

Hazen, A. (1920). "Hydraulic fill dams." *Transactions of the American Society of Civil Engineers* 83, 1713-1745.

Itasca (2011). FLAC – Fast Lagrangian Analysis of Continua, Version 7.0, Itasca Consulting Group, Inc., Minneapolis, Minnesota.

Ishihara, K. (1993). "Liquefaction and flow failure during earthquakes." *Géotechnique*, 43(3), 351-415.

Idriss, I. M. (1999). "An update to the Seed-Idriss simplified procedure for evaluating liquefaction potential." *TRB Workshop on New Approaches to Liquefaction*, Federal Highway Administration.

Idriss, I. M., and Boulanger, R. W. (2008). *Soil liquefaction during earthquakes*, Monograph MNO-12, Earthquake Engineering Research Institute, Oakland, CA, 261 pp.

Ishihara, K., and Yamazaki, F. (1980). "Cyclic Simple Shear Tests on Saturated Sand in Multi-Directional Loading." *Soils and Foundations*, 20(1), 45-59.

Jang, D.-J., and Frost, J. D. (1998) "Sand structure differences resulting from specimen preparation procedures." Proc., Proceedings of the Specialty Conference on Geotechnical Earthquake Engineering and Soil Dynamics, ASCE, 234-245.

Juang, C. H., J., C., Ku, C.-S., and Hsieh, Y.-H. (2012). "Unified CPTu-based probabilistic model for assessing probability of liquefaction of sand and clay." *Géotechnique*, 62(10), 877-892.

Kammerer, A. M., Wu, J., Pestana, J. M., Riemer, M., and Seed, R. B. (2000). "Cyclic Simple Shear Testing of Nevada Sand for Peer Center Project 2051999." Geotechnical Engineering Report No UCB/GT/00-01University of California, Berkeley, Jan 2000.

Kammerer, A.M, Pestana, J.M. and Seed, R.B. (2002) "Undrained Response of Monterey 0/30 Sand Under Multidirectional Cyclic Simple Shear Loading Conditions", Geotechnical Engineering Research Report No. UCB/GT/02-01, University of California, Berkeley, July 2002.

Kano, S., Kidera, H., Sasaki, Y., Ikeoka, T., and Ichii, K. (2008). "The Rigidity Recovery of Post Liquefied Soils." *Geotechnical Earthquake Engineering and Soil Dynamics IV*, 1-10.

Kayen, R. E., and Mitchell, J. K. (1997). "Assessment of Liquefaction Potential during Earthquakes by Arias Intensity." *J. Geotech. Geoenviron. Eng.*, 123(12), 1162-1174

Kayen, R., Moss, R. E. S., Thompson, E. M., Seed, R. B., Cetin, K. O., Kiureghian, A. D., Tanaka, Y., and Tokimatsu, K. (2013). "Shear-Wave Velocity–Based Probabilistic and Deterministic Assessment of Seismic Soil Liquefaction Potential." *J. Geotech. Geoenviron. Eng.*, 139(3), 407-419.

Kiku, H., and Tsujino, S. "Post Liquefaction Characteristic of Sand." *Proc., Eleventh World Conference on Earthquake Engineering*.

Kiyota, T., Sato, T., Koseki, J., and Abadimarand, M. (2008). "Behavior of liquefied sands under extremely large strain levels in cyclic torsional shear tests." *Soils and Foundations*, 48(5), 727-739.

Kokusho, T., Tadashi, H., and Hiraoka, R. (2004). "Undrained Shear Strength of Granular Soils with Different Particle Gradations." *J. Geotech. Geoenviron. Eng.*, 130(6), 621-629.

Kramer, S. L. (1996). *Geotechnical Earthquake Engineering*, Prentice Hall, Inc., Upper Saddle River, New Jersey.

Kramer, S. L., and Mitchell, R. A. (2006). "Ground Motion Intensity Measures for Liquefaction Hazard Evaluation." *Earthquake Spectra*, 22(2), 413-438.

Kwan, W. S., and El Mohtar, C. (2014). "Comparison between Shear Strength of Dry Sand Measured in CSS Device using Wire-reinforced Membranes and Stacked Rings." Geocongress 2014: Geo-Characterization and Modeling for Sustainability, Georgia, 1111-1119.

Kwan, W.S., Sideras, S., El Mohtar, C., and Kramer, S. L. (2014a). "Pore Pressure Generation under Different Transient Loading Histories." *Proceedings of the 10th National Conference in Earthquake Engineering*, Earthquake Engineering Research Institute, Anchorage, AK.

Wing Shun Kwan, Sam Sideras, Chadi El Mohtar, Steve Kramer (2014b). 33 to 56% Relative Density Cyclic Simple Shear Tests under Modulated Sine Loadings. Network for Earthquake Engineering Simulation (NEES) (distributor). Dataset. DOI: 10.4231/D3W66991S

Wing Shun Kwan, Sam Sideras, Chadi El Mohtar, Steve Kramer (2014c). 72 to 94% Relative Density Cyclic Simple Shear Tests under Modulated Sine Loadings. Network for Earthquake Engineering Simulation (NEES) (distributor). Dataset. DOI: 10.4231/D30Z70X6F

Wing Shun Kwan, Sam Sideras, Chadi El Mohtar, Steve Kramer (2014d). 36 to 55% Relative Density Cyclic Simple Shear Tests under Transient Loadings. Network for Earthquake Engineering Simulation (NEES) (distributor). Dataset. DOI: 10.4231/D34Q7QR0T

Wing Shun Kwan, Sam Sideras, Chadi El Mohtar, Steve Kramer (2014e). 70 to 91% Relative Density Cyclic Simple Shear Tests under Transient Loadings. Network for Earthquake Engineering Simulation (NEES) (distributor). Dataset. DOI: 10.4231/D3RJ48W0Z

Kwan, W. S., Nichols, A., and El Mohtar, C. (2015). "The Effect of Irregular Preliquefaction Loading and Particle Angularity on Postliquefaction Response." *Proceedings of the Tenth Pacific Conference on Earthquake Engineering,* Sydney, Australia.

Ladd, R. S., Dobry, R., Dutko, F. Y., Yokel, F. Y., and Chung, R. M. (1989). "Pore-Water Pressure Buildup in Clean Sands Because of Cyclic Straining." *Geotechnical Testing Journal*, 12(1), 77-86.

Lee, K. L., and Albeisa, A. (1974). "Earthquake Induced Settlements in Saturated Sand." *Journal of the Soil Mechanics and Foundations Division*, 100, 387-406.

Lee, K. L., and Seed, H. B. (1967). "Cyclic Stress Conditions Causing Liquefaction of Sand." *Journal of the Soil Mechanics and Foundations Division*, 93(SM1), 47-70.

Liu, A. H., Stewart, J. P., Abrahamson, N. A., and Moriwaki, Y. (2001). "Equivalent Number of Uniform Stress Cycles for Soil Liquefaction Analysis." *J. Geotech. Geoenviron. Eng.*, 127(12), 1017-1026.

Manzari, M. T., and Dafalias, Y. F. (1997). "A critical state two-surface plasticity model for sands." *Géotechnique*, 47(2), 255-272.

Marcuson, W. F., Ill (1978). "Definition of terms related to liquefaction." *J. Geotech. Engrg. Div., ASCE*, 104(9), 1197-1200.

Martin, G. R., Finn, W. D. L., and Seed, H. B. (1975). "Fundamentals of liquefaction under cyclic loading." *J. Geotech. Eng. Div. ASCE*, 101(GT5), 423-438.

Mayfield, R. T., Kramer, S. L., and Huang, Y.-M. (2010). "Simplified Approximation Procedure for Performance-Based Evaluation of Liquefaction Potential." *J. Geotech. Geoenviron. Eng.*, 136(1), 140-150.

Mitra, D. (2011). "Applicability of Equivalent Linear and Nonlinear Site Response Analyses." Master thesis, University of Washington.

Mogami, T., and Kubu, K. (1953). "The behavior of soil during vibration." *Proceeding, 3rd International Conference on Soil Mechanics and Foundation Engineering*, 152-155.

Moss, R. E. S., Seed, R. B., Kayen, R. E., Stewart, J. P., Der Kiureghian, A., and Cetin, K. O. (2006). "CPT-based probabilistic and deterministic assessment of in situ seismic soil liquefaction potential." *J. Geotech. Geoenviron. Eng., ASCE*, 132(8), 1032-1051.

Mulilis, J. P., Seed, H. B., Chan, C. K., Mitchell, J. K., and Arulanandan, K. (1977). "Effects of Sample Preparation on Sand Liquefaction." *Journal of geotechnical engineering Division*, GT2, 91-108.

Poulos, S. J. (1981). "The steady state of deformation." *Journal of the Geotechnical Engineering Division, ASCE*, 107(5), 553-562.

Pradhan, T. B. S., Tatsuoka, F., and Sato, Y. (1988). "Undrained stress strain behavior of sand subjected to earthquake wave loading." *Proc., Proc. of the 9th World Conference on Earthquake Engineering*, 267-272.

Riemer, M., Gookin, W. B., Bray, J. D., and Arango, I. (1994). "Effects of loading frequency and control of the liquefaction behavior of clean sands." Geotechncial Engineering Report No. UCB/GT/94-07, UC Berkeley, Dec 1994.

Robertson, P. K., and Wride, C. E. (1998). "Evaluating cyclic liquefaction potential using the cone penetration test." *Can. Geotech. J.*, 35, 442–459.

Roscoe, K. H. (1953) "An Apparatus for the Application of Simple Shear to Soil Samples." *Proc., 3rd International Conference on Soil Mechanics and Foundation Engineering*, 186-191.

Roscoe, K. H., Schofield, A. N., and Wroth, C. P. (1983). "On the yielding of soils." *Géotechnique*, 8(1), 22-53.

Rutherford, C. J. (2012). "Development of a Multi-Directional Direct Simple Shear Testing Device for Characterization of the Cycle Shear Response of Marine Clays." Ph.D. Dissertation, Texas A&M University.

Saada, A. S., Fries, G., and Ker, C. C. (1983). "An Evaluation of Laboratory Testing Techniques in Soil Mechanics." *Soils and Foundations*, 23(2), 98-112.

Seed, H. B., and Lee, K. L. (1966). "Liquefaction of Saturated Sands during Cyclic Loading." *Journal of the Soil Mechanics and Foundations Division*, 92(SM6), 105-134.

Seed, H. B., and Idriss, I. M. (1971). "Simplified Procedure for Evaluating Soil Liquefaction Potential." *Journal of the Soil Mechanics and Foundations Division*, 97(SM9), 1249-1273.

Seed, H. B., Idriss, I. M., Makdisi, F., and Banerjee, N. (1975). "Representation of irregular stress time histories by equivalent uniform stress series in liquefaction analyses." *Rep. No. UCB/EERC 75-29, Earthquake Engrg. Res. Ctr.* University of California, Berkeley, California.

Seed, H. B., Mori, K., and Chan, C. K. (1975). "Influence of seismic history on the liquefaction characteristics of sands." *Rep. No. UCB/EERC 75-25, Earthquake Engrg. Res. Ctr*, Berkeley, California.

Seed, H. B., and Idriss, I. M. (1982). "Ground motions and soil liquefaction during earthquakes." *Earthquake Engineering Research Institute, Monograph,* Oakland, Calif.

Seed, H. B. (1987). "Design Problem in Soil Liquefaction." *Journal of Geotechnical Engineering*, 113(8), 827-845.

Seed, R., Lee, S., and Jong, H. (1988). "Penetration and Liquefaction Resistances: Prior Seismic History Effects." *J. Geotech. Engrg*., 114(6), 691-697.

Seed, R. B., and Harder, L. F. J. (1990). "SPT-Based Analysis of Cyclic Pore Pressure Generation and Undrained Residual Strength." *Proceedings of Memorial Symposium for H. Bolton Seed*, J. M. D. ed., BiTech Publishers, Vancouver, B. C., Canada, 351-376.

Shamoto, Y., Zhang, J.-M., and Goto, S. (1997). "Mechanism of Large Post-liquefaction deformation in saturated sand." *Soils and Foundations*, 37(2), 71-80.

Shaw, P., and S.F., B. (1986). "Cyclic Simple Shear Testing of Granular Materials." *Geotechnical Testing Journal*, 9(4), 213-220.

Sideras, S. (2015). "Evolutionary Intensity Measures for More Accurate and Informative Liquefaction Hazard Evaluation." PhD Dissertation in progress, University of Washington.

Sitharam, T. G., Vinod, J. S., and Ravishankar, B. V. (2009). "Post-liquefaction undrained monotonic behaviour of sands: experiments and DEM simulations." *Géotechnique*, 59(9), 739-749.

Sivathayalan, S. (1994). "Static, Cyclic and Post Liquefaction Simple Shear Response of Sands." M.S. Thesis, The University of British Columbia.

Sivathayalan, S., and Yazdi, A. M. (2013). "Influence of Strain History on Postliquefaction Deformation Characteristics of Sands." *J. Geotech. Geoenviron. Eng.*, 140(3), 04013019.

Tatsuoka, F., and Silver, M. L. (1981). "Undrained stress-strain behavior of sand under irregular loading." *Soils and Foundations*, 21(1), 51-66.

Tatsuoka, F., Fujii, S., Yamada, S., and Maeda, S. (1982a). "Prediction of shear strain time history in dense sand subjected to undrained random loading." *Proc., Proc. the 5th Japanese Symposium Earthquake Engineering*, 537-544.

Tatsuoka, F., Fujii, S., and Yamada, S. (1982 b). "Undrained stress-strain behavior of sand under cyclic uniform and random loading." Proc., *Proc. Int. Sym. on Numerical Models in Geomechanics*, 419-426.

Tatsuoka, F., Maeda, S., Ochi, K., and Fujii, S. (1986). "Prediction of cyclic undrained strength of sand subjected to irregular loadings." *Soils and Foundations*, 26(2), 73-90.

Tatsuoka, F., Pradhan, T. B. S., and Yoshi-ie, H. (1989). "A Cyclic Undrained Simple Shear Testing Method for Soils." *Geotechnical Testing Journal*, 12(4), 269-280.

Terzaghi, K. (1947). "Shear Characteristics of Quicksand and Soft Clay." *Proc. of 7th Texas Conference on Soil Mechanics and Foundation Engineering*.

USCS (1971). “San Fernando, California, Earthquake February 1971”. < https://www.sciencebase.gov/catalog/item/51dc2817e4b0f81004b793c4> (July. 17, 2013)

Vaid, Y. P., and Thomas, J. (1995). "Liquefaction and Postliquefaction Behavior of Sand." *Journal of Geotechnical Engineering*, 121(2), 163-173.

Vaid, Y. P., Sivathayalan, S., and Stedman, D. (1999). "Influence of Specimen-Reconstituting Method on the Undrained Response of Sand." *Geotechnical Testing Journal*, 22(3), pp. 187-195.

Vucetic, M., and Lacasse, S. (1982). "Specimen size effect in simple shear test." *J. Geotech. Engrg. Div., ASCE*, 108(12), 1567-1585.

Wang, Z., Dafalias, Y. F., and Shen, C. (1990). "Bounding surface hypoplasticity model for sand." *Journal of Engineering Mechanics*, 116(5), 983-1001.

Wijewickreme, D. (2010). "Cyclic Shear Response of Low Plastic Fraser River Silt." *Proceedings of the 9th U.S. National and 10th Canadian Conference on Earthquake Engineering.* Toronto, Ontario, Canada.

Wood, F. M., and Yamamuro, J. A. "The effect of depositional method on the liquefaction behavior of silty sand." *Proc., 13th ASCE Engineering Mechanics Conference*, The Johns Hopkins University, Baltimore, MD.

Wu, J. (2002). "Liquefaction triggering and post-liquefaction deformation of Monterey 0/30 sand under uni-directional cyclic simple shear loading."Ph.D. Dissertation, University of California, Berkeley.

Wu, J., Kammerer, A. M., Riemer, M. F., Seed, R. B., and Pestana, J. M. (2004). "Laboratory Study of Liquefaction Triggering Criteria." *13th World Conference on Earthquake Engineering.* Vancouver, B.C., Canada.

Yang, Z., Elgamal, A., and Parra, E. (2003). "Computational model for cyclic mobility and associated shear deformation." *J. Geotech. Geoenviron. Eng.*, 129(12), 1119-1127.

Yoshida, N., Tsujino, S., Nakajima, T., and Yano, Y. (1993). "A Simplified Practical Model for the Use of Multi-Dimensional Analysis, Part 2, Consideration of Dilatancy." *Proc., 48th Annual Con f. of the Japan Society of Civil Engineering*, 1218-1219.

Yoshimi, Y., Tokhnatsu, K., and Ohara, J. (1994). "In situ liquefaction resistance of clean sands over a wide density range." *Géotechnique*, 44(3), 479-494.

Youd, T. L. (1972). "Compaction of Sands by repeated sand straining." *Journal of Soil Mechanics and Foundation Division*, ASCE, 99(SM7), 709-725.

Youd, T. L. (1977). "Packing changes and liquefaction susceptibility." *J. Geotech. Eng. Div. ASCE*, 103(GT8), 918-923.

Youd, T. L., and Noble, S. K. (1997). "Magnitude scaling factors." *Proceedings, NCEERWorkshop on Evaluation of Liquefaction Resistance of Soils*, National Center for Earthquake Engineering Research, State University of New York at Buffalo, 149-165.

Youd, T. L., Idriss, I. M., Andrus, R. D., Arango, I., Castro, G., Christian, J. T., Dobry, R., Finn, W. D. L., Harder, L. F., Hynes, M. E., Ishihara, K., Koester, J. P., Liao, S. C., Marcuson, W. F., Martin, G. R., Mitchell, J. K., Moriwaki, Y., Power, M. S., Robertson, P. K., Seed, R. B., and Stokoe II, K. H. (2001). "Liquefaction resistance of soils: Summary report from the 1996 NCEER and 1998 NCEER/NSF workshops on evaluation of liquefaction resistance of soils." *J. Geotech. Geoenviron. Eng.*, 127(10), 817-833.

Zalachoris, G. and Rathje, E. (2015). "Evaluation of One-Dimensional Site Response Techniques Using Borehole Arrays." *J. Geotech. Geoenviron. Eng.* ,

Ziotopoulou, K., Maharjan, M., Boulanger, R. W., Beaty, M., Armstrong, R., and Takahashi, A. (2014). "Constitutive Modeling of Liquefaction Effects in Sloping Ground." *10th National Conference in Earthquake Engineering*, Earthquake Engineering Research Institute, Anchorage, AK.